



UNIVERSITÀ DEGLI STUDI DI TRIESTE

XXX CICLO DEL DOTTORATO DI RICERCA IN  
FISICA

**STUDY OF ASTROPHYSICAL  
TRANSIENTS WITH THE MAGIC  
TELESCOPES**

Settore scientifico-disciplinare: FIS/01

DOTTORANDO  
ALESSIO BERTI

*Berti Alessio*

COORDINATORE  
PROF. LIVIO LANCERI

*Livio Lanceri*

SUPERVISORE DI TESI  
PROF. FRANCESCO LONGO

*Francesco Longo*

CO-SUPERVISORE DI TESI  
DOTT. VALTER BONVICINI

*Valter Bonvicini*

ANNO ACCADEMICO 2016/2017

## Declaration of Autorship

I, Alessio Berti, declare that this thesis titled "Study of astrophysical transients with the MAGIC telescopes" and the work presented in it are my own. I confirm that:

- This work was done wholly or mainly while in candidature for a research degree at this University.
- Where any part of this thesis has previously been submitted for a degree or any other qualification at this University or any other institution, this has been clearly stated.
- Where I have consulted the published work of others, this is always clearly attributed.
- Where I have quoted from the work of others, the source is always given. With the exception of such quotations, this thesis is entirely my own work.
- I have acknowledged all main sources of help.
- Where the thesis is based on work done by myself jointly with others, I have made clear exactly what was done by others and what I have contributed myself.

Signed: Berti Alessio

Date: 28/12/2017

*“Costanza: non chi comincia, ma quel che persevera.”*

Leonardo da Vinci



## Abstract

Questa tesi di Dottorato si concentra sullo studio dei transienti, eventi astrofisici che presentano una variabilità su brevi scale temporali. In particolare, sono stati studiati i Gamma-Ray Bursts (GRBs) e le eventuali controparti di onde gravitazionali usando i dati dell'esperimento MAGIC, due telescopi Cherenkov che rivelano raggi gamma nell'intervallo di energia 50 GeV-10 TeV (altissime energie) grazie alla cosiddetta *Imaging Atmospheric Cherenkov Technique*. I GRBs sono le sorgenti più violente nell'Universo che rilasciano una notevole quantità di energia in pochi secondi. Essi sono caratterizzati da una fase prompt, in cui viene emessa la maggior parte dei fotoni X e gamma, e una fase di afterglow, che è caratterizzata da una lunga durata ma più debole ed osservabile nelle altre bande (infrarossa, ottica, ultravioletto, radio, X,  $\gamma$ ). Una delle attuali domande sui GRBs riguarda la loro possibile emissione alle alte ( $E < 100$  GeV) ed altissime energie. Rivelare un GRB con MAGIC potrebbe aiutare a chiarire i processi di emissione in gioco, permettendo di distinguere fra i diversi modelli teorici proposti nel corso degli anni per spiegare l'emissione alle altissime energie. A tale scopo, è stato analizzato un insieme di GRBs osservati da MAGIC alla ricerca di un possibile segnale di raggi gamma. Per nessuno dei GRBs è stato evidenziato alcun segnale, quindi è stato possibile determinare solo i limiti superiori (integrali e differenziali) sul flusso di raggi gamma. Questi limiti superiori possono essere utilizzati per testare possibili modelli di emissione alle altissime energie.

La seconda parte di questo lavoro è stata dedicata alla ricerca di una possibile controparte elettromagnetica per gli eventi di onde gravitazionali rivelati dagli interferometri LIGO e Virgo. MAGIC ha eseguito il follow-up di GW151226, la seconda rivelazione di onde gravitazionali da un sistema binario di buchi neri. Poiché l'incertezza nella posizione dell'evento data da LIGO è più grande rispetto al campo di vista di MAGIC ( $3.5^\circ$ ), è stato necessario implementare un nuovo metodo di analisi per calcolare i flussi e i limiti superiori in un'ampia regione del campo di vista. Il metodo è stato utilizzato per produrre "upper limits skymaps" delle quattro posizioni osservate dopo il trigger GW151226. Anche in questo caso nessun segnale di raggi gamma è stato rivelato.

L'ultima parte della tesi si è concentrata su un lavoro tecnico sul sistema automatico di MAGIC che riceve ed elabora le allerta di eventi transienti provenienti dal Gamma-ray Coordinates Network (GCN), chiamato GSPOT (*Gamma Sources POinting Trigger*). Come estensione ad altri transienti astrofisici, è stata implementata la risposta automatica alle allerta di neutrini provenienti da IceCube, in modo simile a quanto viene fatto attualmente con le allerta di GRBs. I test preliminari eseguiti in remoto su GSPOT sono risultati in una corretta elaborazione delle allerta di neutrini, con un corretto calcolo dell'osservabilità secondo i criteri predefiniti.



## Abstract

This PhD work is focused on the study of transient sources, astrophysical events exhibiting short-time scale variability. In particular, Gamma-Ray Bursts (GRBs) and Gravitational Waves (GWs) counterparts were searched using the data of the MAGIC telescopes, two Cherenkov telescopes detecting gamma-rays in the energy range 50 GeV-10 TeV (very high energies, VHE) thanks to the Imaging Atmospheric Cherenkov Technique.

GRBs are the most violent sources in the Universe, releasing a huge amount of energy in few seconds. They are characterized by a prompt emission, where the bulk of photons in the hard-X and gamma energy range are emitted, and an afterglow phase, which is a long-lasting but dimmer emission observable in some of other bands (optical, infrared, ultraviolet, radio, X,  $\gamma$ ). One of the current questions about GRBs regards their possible High Energy (HE,  $E < 100$  GeV) and VHE emissions. Several models were proposed but no clear signature of any of them was found yet. Detecting a GRB in the MAGIC energy range would help in clarifying the emission processes at play. For this purpose, a set of several GRBs observed by the MAGIC telescopes was analyzed searching for a possible gamma-ray signal. None of the GRBs showed any signal, so only upper limits (integral and differential) on the gamma-ray flux could be determined. Nonetheless, these upper limits can be used to test possible emission models in the VHE range.

The second part of this work was dedicated to find a possible gamma-ray counterpart to GW candidate events detected by the LIGO/Virgo interferometers. MAGIC performed the follow-up of GW151226, the second detection of a GW signal from a binary black hole system. Since the uncertainty in the position of the event given by LIGO was too large compared to the MAGIC field of view (3.5 degrees), a new analysis method had to be implemented. Usually fluxes and spectra are computed at the nominal position of the source, but in the case of large error boxes the emission could be coming from any point of the field of view. For this reason a new tool built upon the existing MAGIC analysis software was developed in order to compute fluxes and upper limits in a wide region of the observed field of view. The method was used to produce “upper limits skymaps” of the four positions observed after the GW151226 trigger. No gamma-ray signal was found.

The last part of the thesis was focused on a technical work on the MAGIC automatic system which receives and processes the transient alerts coming from the Gamma-ray Coordinates Network (GCN), called GSPOT (*Gamma Sources POinting Trigger*). As an extension to other astrophysical transients, the automatic response to neutrino alerts coming from IceCube was implemented in a similar way to what is currently done with GRB alerts. Preliminary tests performed remotely on GSPOT resulted in a correct processing of the neutrino alerts, with a correct calculation of the observability according to predefined criteria.



# Contents

|  |           |
|--|-----------|
| <b>Introduction</b>  | <b>1</b>  |
| <b>1 HIGH-ENERGY GAMMA-RAY ASTRONOMY</b>   | <b>3</b>  |
| 1.1 Cosmic rays . . . . .  | 3         |
| 1.1.1 Cosmic rays spectrum and composition . . . . .                             | 5         |
| 1.1.2 Cosmic rays acceleration . . . . .   | 9         |
| 1.2 Gamma rays . . . . .   | 12        |
| 1.2.1 Mechanisms for the production of gamma rays . . . . .                      | 13        |
| 1.2.2 Propagation of gamma rays . . . . .  | 16        |
| 1.2.3 Detection techniques for gamma rays . . . . .                              | 19        |
| 1.2.4 Sources of gamma rays . . . . .  | 20        |
| 1.2.5 Supernova remnants and pulsar wind nebulae . . . . .                       | 22        |
| 1.3 Status and prospects of VHE astronomy . . . . .                              | 27        |
| <b>2 EXTENSIVE AIR SHOWERS</b>   | <b>31</b> |
| 2.1 Electromagnetic showers . . . . .  | 31        |
| 2.1.1 Introduction . . . . .   | 31        |
| 2.1.2 Bremsstrahlung . . . . .   | 32        |
| 2.1.3 Pair Production . . . . .  | 34        |
| 2.1.4 Heitler model for electromagnetic shower development . . . . .             | 35        |
| 2.1.5 Cascade equations for electromagnetic showers . . . . .                    | 35        |
| 2.1.6 Longitudinal development . . . . .   | 39        |
| 2.1.7 Lateral distribution function . . . . .                                    | 39        |
| 2.1.8 Other processes and effects involved in electromagnetic cascades . . . . . | 41        |
| 2.2 Hadronic showers . . . . .   | 42        |
| 2.2.1 Introduction . . . . .   | 42        |
| 2.2.2 Heitler model for hadronic showers . . . . .                               | 42        |
| 2.2.3 Superposition model for hadronic showers . . . . .                         | 45        |
| 2.2.4 Cascade equations for hadronic showers . . . . .                           | 45        |
| 2.3 Cherenkov Emission in EAS and IACT Technique . . . . .                       | 47        |
| 2.3.1 Historical excursus . . . . .  | 47        |
| 2.3.2 Cherenkov Radiation . . . . .  | 51        |
| 2.4 Monte Carlo simulation of Extensive Air Showers . . . . .                    | 59        |
| 2.5 The Imaging Atmospheric Cherenkov Technique . . . . .                        | 62        |
| 2.6 Other detection techniques for air showers . . . . .                         | 64        |
| 2.6.1 Examples of cosmic rays EAS detectors . . . . .                            | 66        |
| 2.6.2 Examples of $\gamma$ -rays EAS detectors . . . . .                         | 67        |

|          |   |           |
|----------|---|-----------|
| <b>3</b> | <b>THE MAGIC TELESCOPES SYSTEM</b>                        | <b>71</b> |
| 3.1      | Structure and drive system . . . . .                      | 71        |
| 3.2      | Optical system . . . . .                                  | 72        |
| 3.2.1    | Mirrors . . . . .   | 72        |
| 3.2.2    | Active Mirror Control (AMC) . . . . .                     | 74        |
| 3.2.3    | SBIG camera . . . . .                                     | 75        |
| 3.3      | Camera . . . . .  | 75        |
| 3.4      | Readout system . . . . .                                  | 76        |
| 3.4.1    | Brief description of the MAGIC signal chain . . . . .     | 76        |
| 3.4.2    | Readout system . . . . .                                  | 77        |
| 3.4.3    | Trigger system . . . . .                                  | 80        |
| 3.4.4    | Data Acquisition system . . . . .                         | 82        |
| 3.5      | Auxiliary systems . . . . .                               | 83        |
| 3.5.1    | Central Control . . . . .                                 | 83        |
| 3.5.2    | Calibration system . . . . .                              | 84        |
| 3.5.3    | LIDAR . . . . .   | 84        |
| 3.5.4    | Weather Monitoring System . . . . .                       | 85        |
| 3.5.5    | Cooling system . . . . .                                  | 86        |
| 3.5.6    | Starguider camera . . . . .                               | 86        |
| 3.5.7    | Pyrometer . . . . .                                       | 86        |
| 3.5.8    | AllSky Camera . . . . .                                   | 87        |
| 3.5.9    | Timing system . . . . .                                   | 87        |
| 3.5.10   | Central Pixel . . . . .                                   | 87        |
| 3.5.11   | GRB monitor: GSPOT . . . . .                              | 87        |
| 3.5.12   | OSA . . . . .   | 88        |
| 3.5.13   | MOLA . . . . .  | 89        |
| 3.6      | Telescope operation . . . . .                             | 89        |
| 3.6.1    | Pointing modes . . . . .                                  | 90        |
| 3.6.2    | Typical rates and Individual Pixel Rate Control . . . . . | 92        |
| <b>4</b> | <b>MAGIC DATA ANALYSIS</b>                                | <b>95</b> |
| 4.1      | Monte Carlo data . . . . .                                | 95        |
| 4.2      | MARS Data Formats . . . . .                               | 96        |
| 4.3      | Calibration . . . . .                                     | 98        |
| 4.4      | Image cleaning and parametrization . . . . .              | 100       |
| 4.4.1    | Other image cleanings . . . . .                           | 103       |
| 4.5      | Stereo parameter reconstruction . . . . .                 | 104       |
| 4.6      | Data selection . . . . .                                  | 105       |
| 4.7      | Event characterization . . . . .                          | 106       |
| 4.7.1    | Gamma/hadron separation . . . . .                         | 106       |
| 4.7.2    | Energy estimation . . . . .                               | 108       |
| 4.7.3    | Arrival direction estimation . . . . .                    | 108       |
| 4.8      | Application of RF, DISP RF and LUTs methods . . . . .     | 110       |
| 4.9      | Signal significance . . . . .                             | 110       |
| 4.10     | Sensitivity . . . . .                                     | 111       |
| 4.11     | Instrument Response Function . . . . .                    | 113       |
| 4.11.1   | Effective collection area . . . . .                       | 113       |
| 4.11.2   | Angular resolution . . . . .                              | 115       |
| 4.11.3   | Energy resolution . . . . .                               | 116       |
| 4.11.4   | Energy threshold . . . . .                                | 116       |
| 4.12     | High-level analysis . . . . .                             | 117       |
| 4.12.1   | Skymaps . . . . .   | 117       |

|          |   |            |
|----------|---|------------|
| 4.12.2   | Spectrum and light curve . . . . .  | 118        |
| 4.12.3   | Spectral unfolding . . . . .  | 119        |
| 4.12.4   | Upper limits . . . . .  | 120        |
| 4.13     | Systematics in MAGIC data analysis . . . . .  | 123        |
| 4.14     | Non-standard analyses . . . . .   | 124        |
| 4.14.1   | Observations under moonlight . . . . .  | 124        |
| 4.14.2   | Bad atmospheric conditions . . . . .  | 127        |
| 4.14.3   | GRB analysis . . . . .  | 127        |
| <b>5</b> | <b>ASTROPHYSICAL TRANSIENTS</b>   | <b>129</b> |
| 5.1      | Gamma-Ray Bursts . . . . .  | 129        |
| 5.1.1    | Introduction . . . . .  | 129        |
| 5.1.2    | History of GRBs . . . . .   | 130        |
| 5.1.3    | Fireball model for Gamma-Ray Bursts . . . . .                                       | 138        |
| 5.1.4    | Progenitors of Gamma-Ray Bursts . . . . .   | 143        |
| 5.1.5    | High Energy emission from GRBs . . . . .  | 146        |
| 5.1.6    | High and very high energy emission models for GRBs . . . . .                        | 153        |
| 5.1.7    | Other emission from GRBs . . . . .  | 156        |
| 5.1.8    | Observation of GRBs with MAGIC . . . . .  | 158        |
| 5.1.9    | Analysis of MAGIC GRBs . . . . .  | 161        |
| 5.1.10   | Summary of the observation of MAGIC GRBs . . . . .                                  | 170        |
| 5.1.11   | Summary of the analysis on MAGIC GRBs . . . . .                                     | 171        |
| 5.1.12   | Discussion and prospects for GRBs with MAGIC . . . . .                              | 172        |
| 5.2      | Gravitational Waves . . . . .   | 174        |
| 5.2.1    | Introduction . . . . .  | 174        |
| 5.2.2    | Sources of gravitational waves . . . . .  | 175        |
| 5.2.3    | The interferometric technique for GW detection and localization . . . . .           | 177        |
| 5.2.4    | MAGIC follow-up of GW candidate events from LVC: motivations and strategy . . . . . | 183        |
| 5.2.5    | Flux Upper Limits skymaps for Gravitational Waves candidate events . . . . .        | 186        |
| 5.2.6    | MAGIC follow-up of GW151226 . . . . .   | 193        |
| 5.2.7    | Discussion and prospects for GW follow-up with MAGIC . . . . .                      | 196        |
| 5.3      | Conclusions and prospects for transient science with MAGIC . . . . .                | 199        |
| <b>6</b> | <b>AUTOMATIC REPOINTING SYSTEM FOR MAGIC</b>  | <b>201</b> |
| 6.1      | The GCN system . . . . .  | 201        |
| 6.1.1    | Binary packets from the GCN . . . . .   | 202        |
| 6.2      | GSPOT . . . . .   | 203        |
| 6.2.1    | Threads in GSPOT . . . . .  | 203        |
| 6.2.2    | Observability computation and GRB observation strategy . . . . .                    | 205        |
| 6.3      | Automatic reaction implementation for HESE and EHE alerts . . . . .                 | 206        |
| 6.4      | Preliminary tests of the automatic reaction for neutrino alerts . . . . .           | 207        |
| 6.5      | Burst Advocate activity . . . . .   | 214        |
| 6.6      | Future updates and prospects . . . . .  | 215        |
| 6.7      | On-site tests of GSPOT . . . . .  | 219        |
| 6.7.1    | Test performed on 7th of December . . . . .   | 219        |
| 6.7.2    | Test performed on 22nd of December . . . . .  | 221        |
| <b>7</b> | <b>CONCLUSIONS AND FUTURE PROSPECTS</b>   | <b>225</b> |
| <b>A</b> | <b>CASCADE THEORY</b>   | <b>227</b> |

|   |            |
|---|------------|
| <b>B GRB LIGHTCURVES</b>                                | <b>229</b> |
| <b>C GRB ANALYSIS RESULTS</b>                           | <b>235</b> |
| <b>D GRB ENERGY THRESHOLD</b>                           | <b>249</b> |
| <b>E GRB DIFFERENTIAL UPPER LIMITS</b>                  | <b>257</b> |
| <b>F CRAB NEBULA CROSS CHECK FOR GW151226 FOLLOW-UP</b> | <b>263</b> |
| <b>Acknowledgments</b>                                  | <b>267</b> |
| <b>References</b>                                       | <b>290</b> |

# List of Figures

|      |  |    |
|------|--|----|
| 1.1  | <b>Left:</b> the electroscope used by Victor Hess for his measurements. From <a href="https://airandspace.si.edu/">https://airandspace.si.edu/</a> . <b>Right:</b> image of the trajectory followed by a positron in Anderson’s cloud chamber. From Anderson (1933). . . . .   | 4  |
| 1.2  | Energy spectrum of charged cosmic rays as determined by several experiment (in the legend). In the bottom the red and blue arrows indicate which are the current energies achievable at accelerators. From <a href="http://www.physics.utah.edu/~whanlon/spectrum.html">http://www.physics.utah.edu/~whanlon/spectrum.html</a> . . . . .   | 5  |
| 1.3  | Spectra of the nuclei in cosmic rays. From Olive (2014). . . . .   | 6  |
| 1.4  | Relative abundance of elements in galactic cosmic rays compared with the one found in the Solar System. From <a href="http://www.srl.caltech.edu/ACE">http://www.srl.caltech.edu/ACE</a> . . . . .   | 7  |
| 1.5  | Spectrum of the electrons in cosmic rays as measured by different experiments. The solid line is the prediction from GALPROP code. From Boezio and Mocchiutti 2012. . . . .  | 8  |
| 1.6  | Positron fraction as a function of the energy as measured by AMS-02, PAMELA and Fermi-LAT. From Aguilar et al. 2013. . . . .   | 8  |
| 1.7  | Antiproton to proton flux ratio as a function of the rigidity $\mathcal{R} = pc/ze$ from AMS-02 (red dots) and PAMELA (blue open circle). The inset shows a zoom on the 0.2-10 GeV kinetic energy range adding also the data from BESS-polar II. From Nozzoli (2017). . . . .  | 9  |
| 1.8  | Graphical depiction of the Fermi second order mechanism. From <a href="http://w3.iihe.ac.be/~aguilar/PHYS-467/PA3.html">http://w3.iihe.ac.be/~aguilar/PHYS-467/PA3.html</a> . . . . .  | 10 |
| 1.9  | Hillas plot: typical length scale versus magnetic field in sources potentially able to be cosmic-ray accelerators. From <a href="http://w3.iihe.ac.be/~aguilar/PHYS-467/PA3.html">http://w3.iihe.ac.be/~aguilar/PHYS-467/PA3.html</a> . . . . .  | 12 |
| 1.10 | Comparison of different EBL models (coloured lines), direct measurements (open symbols) and galaxy count lower limits (filled symbols). From Domínguez et al. (2011). . . . .  | 17 |
| 1.11 | Optical depth for pair production as a function of energy for different redshifts (see inset). The redshift increases from bottom to top. The solid thick black line corresponds to $z = 1$ . From Franceschini and Rodighiero (2017). . . . .   | 18 |
| 1.12 | Plot of the highest energy photons from blazars and GRBs used in the EBL analysis in Abdo et al. (2010b). The plot shows also the predictions of $\tau_{\gamma\gamma} = 1$ for different EBL models (see legend). From Abdo et al. (2010b). . . . .  | 18 |
| 1.13 | <b>Left:</b> principle of the gamma ray detection technique via pair production. From <a href="https://heasarc.gsfc.nasa.gov/docs/cgro/images/epo/gallery/glast/">https://heasarc.gsfc.nasa.gov/docs/cgro/images/epo/gallery/glast/</a> . <b>Right:</b> detection of gamma rays with the Compton mechanism. From <a href="https://heasarc.gsfc.nasa.gov/docs/cgro/comptel/">https://heasarc.gsfc.nasa.gov/docs/cgro/comptel/</a> . . . . . | 20 |
| 1.14 | Sketch of the magnetosphere of a pulsar. From Aliu et al. (2008a). . . . .   | 21 |
| 1.15 | Proton and gamma-ray spectra determined for IC443 and W44. From Hewitt and Lemoine-Goumard (2015). . . . .   | 23 |

|      |   |    |
|------|---|----|
| 1.16 | The for classes of binaries. (a) A high mass gamma-ray binary with a pulsar. (b) A microquasar. (c) A nova. (d) A colliding wind binary. From Dubus (2015). . . . .   | 24 |
| 1.17 | Wide-field image of the Galactic Centre performed in the radio band by the Very Large Array. The direction of the the Galactic Plane is from bottom-right to top-left. Several sources (SNRs and PWNe) are indicated by arrows with their names. The Galactic nucleus is the brightest spot in the image. The CMZ region extends from Sgr E (bottom right) to Sgr D (top left). From Su and van Eldik (2015). . . . . | 26 |
| 1.18 | AGN classification scheme. The following abbreviations are used: QSO (Quasistellar objects); Sy1 and Sy2 (Seyfert 1 and 2); FR1 and FR2 (Fanaroff-Riley 1 and 2). From Dermer and Giebels (2016). . . . .   | 28 |
| 1.19 | AGN unified scheme: AGN classes correspond to different accretion rates, black holes spin parameter and different orientation with respect to the observer. From Dermer and Giebels (2016). . . . .   | 28 |
| 1.20 | Skymap of the VHE sources detected up to date with the Fermi-LAT HE skymap on the background. Different colors correspond to different types of sources, see the legend on the right. From <a href="http://tevcat.uchicago.edu/">http://tevcat.uchicago.edu/</a> . . . . .  | 30 |
| 1.21 | Kifune plot showing the temporal evolution of the number of detected sources in different energy bands. Also an extrapolation to the expected number of sources detectable by the current Cherenkov array experiment CTA is shown. From Naurois and Mazin (2015). . . . .   | 30 |
| 2.1  | Definitions of the critical energy $E_c$ . Adapted from Olive (2014). . . . .   | 32 |
| 2.2  | Normalized cross section for Bremsstrahlung in lead versus the fractional photon energy $y = k/E$ . Adapted from Olive (2014). . . . .  | 33 |
| 2.3  | Normalized cross section for pair production versus the fractional electron energy $x = k/E$ . Adapted from Olive (2014). . . . .   | 34 |
| 2.4  | Heitler toy model for the development of electromagnetic showers. . . . .   | 36 |
| 2.5  | Electron size as function of the atmospheric depth $X$ in Approximation B for different initial $\gamma$ -ray energies. Shower age values and MAGIC altitude are also shown. Adapted from Naurois and Mazin (2015). . . . .   | 39 |
| 2.6  | Plot of the NKG formula as a function of the distance from the shower axis. . . . .   | 40 |
| 2.7  | Development of a hadronic shower initiated by a cosmic ray. From the production of different mesons (pions and kaons in particular), leptons (muons) and gamma-rays can be produced. The latter originate from the decay of neutral pions and initiate electromagnetic sub-showers. . . . .   | 43 |
| 2.8  | The experimental apparatus used by Gailbraith and Jelley to detect pulses from extensive air showers. From Mirzoyan (2012) . . . . .  | 47 |
| 2.9  | The Whipple telescope in Arizona. From <a href="http://www.astro.wisc.edu/~larson/Webpage/Gamma.html">http://www.astro.wisc.edu/~larson/Webpage/Gamma.html</a> . . . . .  | 48 |
| 2.10 | One of the telescopes of the HEGRA array in La Palma. From Mirzoyan (2012). . . . .   | 49 |
| 2.11 | <b>Left:</b> polarization of atoms when a charged particle passes through a medium with velocities lower or greater than the speed of light. <b>Right:</b> formation of the Cherenkov wave-front. Both figures adapted from Naurois and Mazin (2015). . . . .   | 52 |
| 2.12 | Photon density as a function of the distance from the shower axis for the simplified model of vertically moving charged particles emitting Cherenkov photons. Reproduced from Hillas (1982). . . . .  | 54 |
| 2.13 | Photon density as a function of the distance from the shower axis (solid curve). The dashed and dotted curves show the photon density for low and high developing showers respectively. In the former case the effect vanishes. Reproduced from Hillas (1982). . . . .  | 55 |

|      |   |    |
|------|---|----|
| 2.14 | Formation of the Cherenkov ring on the ground for a vertical shower. Adapted from Naurois and Mazin (2015). . . . .   | 55 |
| 2.15 | Lateral profile of showers at sea level for different energies of the primary particle. Adapted from Naurois and Mazin (2015). . . . .  | 56 |
| 2.16 | Time delay (in nanoseconds) of Cherenkov photons as a function of the distance from the shower axis and for different altitudes of emission. Adapted from Naurois and Mazin (2015). . . . .   | 56 |
| 2.17 | Magnitude of the geomagnetic field component perpendicular to the observation direction for the MAGIC site. From Commichau et al. (2008). . . . .   | 57 |
| 2.18 | Cherenkov light density as a function of the distance from shower axis for vertical 100 GeV showers simulated with CORSIKA. <b>Left:</b> different atmospheric profiles used in the simulations. <b>Right:</b> seasonal effects on the amount of Cherenkov light emitted in showers. Adapted from Bernlohr (2000). . . . .  | 58 |
| 2.19 | Transmission of light from 100 km to 2.2 km calculated with the MODTRAN program for different absorbers and scatterers. Adapted from Bernlohr (2000). . . . .   | 58 |
| 2.20 | Transmission of light from different altitudes to 2.2 km calculated with the MODTRAN program. The atmospheric profile used is written in the legend. Adapted from Bernlohr (2000). . . . .  | 59 |
| 2.21 | Lateral density of direct, aerosol and Rayleigh scattered light for vertical proton showers of 100 TeV with a tropical atmospheric profile. Different line dashes mean different integration times of the instrument. Adapted from Bernlohr (2000). . . . .   | 60 |
| 2.22 | Shower images produced with the CORSIKA Monte Carlo software. Red lines are photons, electrons or positrons. Green lines are muons, blue lines are hadrons. <b>Left:</b> longitudinal (top) and lateral (bottom) development of an electromagnetic shower initiated by a 100 GeV photon. <b>Right:</b> longitudinal (top) and lateral (bottom) development of a hadronic shower initiated by a 100 GeV proton. From <a href="https://www.ikp.kit.edu/corsika/">https://www.ikp.kit.edu/corsika/</a> . . . . . | 61 |
| 2.23 | The principle of the Imaging Atmospheric Cherenkov Technique (here a primary gamma ray is considered). From <a href="https://www.cta-observatory.org/about/how-cta-works/">https://www.cta-observatory.org/about/how-cta-works/</a> . . . . .   | 62 |
| 2.24 | Principle of the detection technique of EAS arrays. From Bauleo and Rodríguez Martino (2009). . . . .   | 65 |
| 2.25 | Scheme of the Pierre Auger Observatory array. Grey dots are the water Cherenkov surface detectors, while the blue dots are the 24 fluorescence telescopes with their field of view (blue lines). From Conceição (2013). . . . .   | 67 |
| 2.26 | One of the water Cherenkov surface detectors (left) and fluorescence telescopes (right) used in the Pierre Auger observatory. From Abraham et al. (2010). . . . .   | 68 |
| 2.27 | The HAWC observatory. From <a href="https://www.hawc-observatory.org/">https://www.hawc-observatory.org/</a> . . . . .  | 69 |
| 2.28 | Differential sensitivity of LHAASO for a point-like source compared to other experiments (see legend). The extrapolation up to 1 PeV of the Crab Nebula spectrum is reported, also scaled by a 0.1, 0.01 and 0.001 factor. From Di Sciacio (2016). . . . .  | 70 |
| 3.1  | Picture of MAGIC-I in parking position. The camera (on the left, leaning on its pillar) is kept at the right position from the reflector thanks to the arc and stiffness is maintained with steel wires. On the bottom right, one of the azimuth drive units (in yellow with the grey motor) with its carriage moving along the rail. The motor drives a double-toothed wheel gearing into the drive chain. . . . .   | 73 |

|      |   |     |
|------|---|-----|
| 3.2  | Picture of MAGIC-I reflector from the camera tower. Despite the reflection of the ground, the different measures of mirrors is visible (some mirrors are divided in four equal pieces, other are a unique piece). . . . .   | 74  |
| 3.3  | Rear view of the camera of MAGIC-II with the 169 PMTs clusters. From Borla Tridon et al. (2009). . . . .  | 75  |
| 3.4  | One of the 1039 PMTs of the cameras of the MAGIC telescopes. Each pixel, beside the photomultiplier tube, is completed by the HV generator, the preamplifier and the VCSEL. From Aleksić et al. (2016a). . . . .  | 76  |
| 3.5  | Scheme of the MAGIC electronic chain. Credits: Daniel Mazin, 3rd MAGIC Hardware School (May 2015) . . . . .   | 77  |
| 3.6  | <b>Left:</b> PULSAR board. From <a href="http://hep.uchicago.edu/~thliu/projects/Pulsar/">http://hep.uchicago.edu/~thliu/projects/Pulsar/</a> . <b>Right:</b> MONSTER board. . . . .  | 78  |
| 3.7  | The DRS4 mezzanine with the three DRS4 chips. On the left, the clock and trigger inputs and the analog connectors are visible. On the right of the chips, the FIFO memories, the connectors to the PULSAR board and the power connector complete the mezzanine. From Aleksić et al. (2016a). . . . .  | 79  |
| 3.8  | Scheme of the MAGIC camera. Cyan, green and red pixels belong to the trigger region, while the purple ones do not. The 19 L1 macrocell are denoted by the cyan pixels. Green and red pixels belong to two and three macrocells at the same time respectively. Moreover, thick black lines denote the 169 PMT clusters. From Aleksić et al. (2016a) . . . . .  | 81  |
| 3.9  | Scheme of the Sum-Trigger working principle. From García et al. (2014). . . . .   | 82  |
| 3.10 | Picture of the LIDAR used at the MAGIC site. From Fruck et al. (2014). . . . .  | 85  |
| 3.11 | The wobble pointing mode as seen in the camera plane for one wobble pointing. The blue circle has a radius of $0.4^\circ$ , equal to the wobble offset used during observations. The black pixel is at the center of the camera. The source is the red dot, while the other two semi-transparent red dots denote the path of the source in the camera plane during observations. The same holds for the green dots, which are the OFF regions used for background estimation. In this case, 3 OFF regions are used. . . . .   | 91  |
| 3.12 | <i>SuperArehucas</i> graphical user interface. Different panels are denoted with a different color. Brown: menu entries to give commands to different subsystems; black: MAGIC cameras with information about the PMTs (charge, DC current, pixel rates ecc. . . ); red: CC clock, GBM, pyrometer, GPS and LIDAR status; magenta: drive1 and drive2, with information about current source name and coordinates; violet: starguiders panel; blue: CaCo1 and Caco2 display info about HV settings, cameras and pixel temperature, internal humidity and lids status; cyan: calibration boxes panel; light green: trigger section, showing trigger tables, rates and prescaler bits; dark green: receivers and cooling status; yellow: IPRC settings and SumTrigger status; ocher: DAQs info (run number, acquisition rate, event number, disk space); orange: AMCs status. . . . . | 93  |
| 4.1  | <b>Left:</b> images of three events before the cleaning. From top to bottom, a gamma-like, a hadron-like and a muon-like event. <b>Right:</b> the corresponding cleaned images. . . . .   | 101 |
| 4.2  | Some of the Hillas parameters of a cleaned image. The central black dot is the center of the camera. The other black dot is the reconstructed position of the source, while the red dot is the true position of the source. . . . .   | 103 |
| 4.3  | Example of the reconstruction of some stereo parameters. . . . .  | 105 |

|      |   |     |
|------|---|-----|
| 4.4  | Graphical representation of the DISP method for the reconstruction of the arrival direction of the events. Given two images for the same event, there will be four reconstructed source positions, denoted by empty circles. The angular distances between them are shown by dotted lines: the closest pair is chosen (in this example 1B-2B) and their weighted average is taken as the final reconstructed position for the source (black dot). The solid line is $\theta$ , the angular distance between the true (empty diamond) and reconstructed position of the source. From Aleksić et al. (2016b). . . . .   | 109 |
| 4.5  | Example of a $\theta^2$ plot obtained with Crab Nebula data. The red points belong to the ON histogram, the black one to the OFF histogram. The dashed line correspond to $\theta_{\text{cut}}^2$ . This plot was produced using LE cuts. . . . .   | 111 |
| 4.6  | <b>Left:</b> integral sensitivity of the MAGIC telescopes as a function of the energy and for different periods. <i>Grey and dark grey dots:</i> mono era with Siegen and MUX readouts. <i>Black triangles:</i> stereo era with old MAGIC-I camera. <i>Red filled and blue empty squares:</i> stereo era after 2012-2013 upgrade at zenith lower than $30^\circ$ and between $30^\circ$ and $45^\circ$ respectively. <b>Right:</b> differential sensitivity of the MAGIC telescopes as a function of energy and for different periods. The same colors and symbols are used as in the left figure with the same meaning. From Aleksić et al. (2016b). . . . . | 112 |
| 4.7  | Effective collection area of MAGIC telescopes in two different zenith ranges (red lines $0 - 30^\circ$ , green lines $30^\circ - 45^\circ$ ) after the upgrade of MAGIC-I camera and use of DRS4 chips in both telescopes. Blue lines refer to the pre-upgrade period. Both trigger (dashed lines) and after-cuts (solid lines) effective areas are shown. Adapted from Aleksić et al. (2016b). . . . .   | 114 |
| 4.8  | <b>Left:</b> angular resolution of the MAGIC telescopes as a 2D Gaussian fit, obtained for a Crab Nebula data sample (filled dots) and from MC simulations (solid lines). <i>Red, blue, grey points:</i> low zenith ( $<30^\circ$ ), medium zenith ( $30^\circ - 45^\circ$ ) and low zenith angle before 2012-2013 upgrade. <b>Right:</b> energy bias (dashed lines) and resolution (solid lines) after reconstruction, obtained from MC simulations. The same colors and symbols are used as in the left figure with the same meaning. From Aleksić et al. (2016b). . . . .  | 116 |
| 4.9  | Energy threshold at different analysis stages: trigger level (blue dotted line), reconstruction level (after image cleaning and with $size > 50$ phe, black solid line) and signal extraction level (hadronness $< 0.5$ and $\theta^2 < 0.03^{\circ 2}$ (red dashed line). From Aleksić et al. (2016b). . . . .   | 117 |
| 4.10 | Example of a skymap created with <code>caspar</code> from Crab Nebula data. . . . .   | 118 |
| 4.11 | <b>Left:</b> energy threshold as a function of the sky brightness at the reconstruction level. <i>Filled dots:</i> low zenith ( $< 30^\circ$ ). <i>Empty squares:</i> medium zenith ( $30^\circ - 45^\circ$ ). <i>Blue, green, red:</i> hardware settings (nominal HV, reduced HV, UV filters respectively). <b>Right:</b> sensitivity of the MAGIC telescopes under moonlight with nominal HV as a ratio with the sensitivity for dark observations. From Ahnen et al. (2017). . . . .   | 127 |
| 5.1  | Spatial distribution of the GRBs observed by BATSE in the nine years of the mission. The number of GRBs recorded is 2704. Adapted from <a href="https://gammaray.nsstc.nasa.gov/batse/grb/skymap/">https://gammaray.nsstc.nasa.gov/batse/grb/skymap/</a> . . . . .  | 131 |
| 5.2  | Histogram of the duration ( $T_{90}$ ) of BATSE GRBs from the 4B catalog presented in Paciesas et al. (1999). Adapted from <a href="https://gammaray.nsstc.nasa.gov/batse/grb/duration/">https://gammaray.nsstc.nasa.gov/batse/grb/duration/</a> . . . . .  | 132 |
| 5.3  | Example of the Band function for GRB 990123. From Briggs et al. (1999). . . . .   | 132 |
| 5.4  | X-ray afterglow of GR970228. From Vietri (1997). . . . .  | 133 |

|      |   |     |
|------|---|-----|
| 5.5  | <b>Left:</b> achromatic break observed in the afterglow optical light curves of GRB990510. From Harrison et al. (1999). <b>Right:</b> evolution of the spectrum of GRB030329 and SN2003dh. While the early spectrum (top) shows a power-law continuum ( $F_\nu \propto \nu^{-0.9}$ ), the late spectra show peaks which are characteristic of a supernova. From Stanek et al. (2003). . . . .   | 134 |
| 5.6  | Sketch of the “canonical” X-ray afterglow light curve. From Zhang et al. (2006).  | 137 |
| 5.7  | Graphical representation of the fireball model. At first the outflow is not transparent to radiation, but after expansion it will let radiation escape. The prompt phase originates from the internal shocks, while the afterglow is caused by external shocks where the shock waves interact with the external medium. Both a forward and a reverse shock can form in this process. In the left part, also the progenitors of GRBs are represented, see Section 5.1.4. From Gomboc (2012). . . . . | 139 |
| 5.8  | The spectrum resulting from synchrotron radiation in the slow and fast cooling cases (left and right respectively). From Kumar and Zhang (2015). . . . .  | 142 |
| 5.9  | <b>Top:</b> photon energies detected by EGRET from GRB940217. The horizontal line is the time when EGRET was occulted by the Earth. <b>Bottom:</b> count rates of Ulysses in the 25-150 keV. The inset shows the first 200 seconds of the BATSE light curve and the photons detected by EGRET in that time interval. From Hurley et al. (1994). . . . .   | 146 |
| 5.10 | Light curves of GRB080916C for GBM and LAT observations. The first two graphs show the GBM light curves from the NaI and BGO detectors. The third shows the LAT lightcurve without any selection. The last two graphs show the LAT lightcurves with energy selection above 100 MeV and 1 GeV respectively. The insets are zooms on the first 15 seconds for each lightcurve. From Abdo et al. (2009c). . . . .  | 148 |
| 5.11 | Fermi-GBM and Fermi-LAT light curves for GRB090510 (top four panels). The fourth panel shows only events with energy above 100 MeV. The last panel shows the energies of the photons detected by Fermi-LAT as a function of time from the trigger $T_0$ . The insets are zooms on the first 1 second of the light curves. From Ackermann et al. (2010). . . . .   | 150 |
| 5.12 | <b>(a):</b> Fermi time-integrated spectrum of GRB090510 in the 0.5 s-1.0 s time range. The best fit is the sum of two components (dotted lines), a Band function and a power-law. The resulting spectrum is shown as a solid line with $\pm 1\sigma$ contours. <b>(b):</b> GRB090510 spectra with $\pm 1\sigma$ contours for different time ranges, shown in the legend together with the function which best fits the data in a given time range. From Ackermann et al. (2010). . . . .            | 150 |
| 5.13 | Energy flux light curves as measured by Fermi (LAT and GBM) and Swift (BAT and XRT) for GRB130427A (top panel). The second panel shows the evolution in time of the spectral index for the power-law used for fitting Fermi-LAT data. The last panel shows individual photon energies in time recorded by the LAT. It is clear from the time axis extending up to over $10^5$ s that the LAT emission is clearly extended in time. From Ackermann et al. (2014). . .                                | 152 |
| 5.14 | Fluence measured by Fermi-GBM (10 keV-1 MeV) versus the fluence measured by Fermi-LAT (100 MeV-10 GeV) for GRBs detected by both instruments. Blue points are long GRBs, while red ones are short GRBs. The green dashed lines correspond to 100%, 10% and 1% fluence ratios. From Ackermann et al. (2013b). . . . .  | 153 |
| 5.15 | Expected high energy emission signatures from GRBs in different emission phases, from both the prompt and afterglow. From Fan and Piran (2008). . .   | 155 |

|      |  |     |
|------|--|-----|
| 5.16 | Skymap (Aitoff projection) in galactic coordinates of the GRBs observed by MAGIC between 2004 and August 2017 (only those with good data are shown). Crosses are GRBs without redshift, while circles are GRBs with redshift determination. . . . .  | 159 |
| 5.17 | Delay of MAGIC observed GRBs with respect to the onset versus the zenith angle of observation. Red circles are bursts with $z < 1.5$ , blue have $z > 1.5$ while green ones do not have redshift determination. GRBs observed in stereo mode are denoted by a yellow cross. . . . .  | 160 |
| 5.18 | Cumulative redshift distribution of GRBs observed by MAGIC. The percentage of GRBs with $z < 1.5$ is around 38%. . . . .   | 160 |
| 5.19 | Effect of a gravitational wave having only the “+” or “ $\times$ ” polarization propagating through a ring of free test masses. . . . .  | 175 |
| 5.20 | Scheme of the possible scenarios for the merging of a BNS (top) or NS-BH (bottom). From Bartos, Brady, and Márka (2013). . . . .   | 176 |
| 5.21 | Decay of the orbital period from 1975 to 2005 in the binary system PSR B1913+16. The points are measurements, while the solid line is the theoretical prediction from the emission of gravitational waves. From Weisberg and Taylor (2005). . . . .  | 178 |
| 5.22 | Working principle of a power and a signal recycling mirrors (left and right) respectively. From Pitkin et al. (2011) . . . . .   | 179 |
| 5.23 | Antenna patterns in a Michelson interferometer. The beam-splitter is at the center of each pattern and the thick solid black lines denote the two interferometer arms. From left to right: + polarization, $\times$ polarization and unpolarized waves. From Riles (2013). . . . .   | 180 |
| 5.24 | Prospects for the sensitivities achievable by aLIGO and Adv. From Abbott et al. (2016c). . . . .   | 181 |
| 5.25 | Example of a posterior probability density skymap of a simulated CBC event produced by the BAYESTAR pipeline. The star denotes the true location of the event, which is located at 266 Mpc. From Abbott et al. (2016c). . . . .  | 182 |
| 5.26 | Binary neutron star sky localization in O2 with a 2 or 3 detectors network and for different pipelines (BAYESTAR and LALINFERENCE). The cumulative fraction of events is shown as a function of $CR_{0.9}$ , the smallest area enclosing 90% of the total posterior probability. From Abbott et al. (2016c). . . . .   | 183 |
| 5.27 | Possible electromagnetic counterparts of CBC mergers depending on the viewing angle $\theta_{\text{obs}}$ . The possible GRB emission can be seen by observers with $\theta_{\text{obs}} < \theta_j$ because of relativistic beaming. Optical and radio afterglow emission can be seen at different timescales. Another possible counterpart is a kilonova, emitting in the optical/IR bands due to the radioactive decay of r-process elements generated in the ejecta. From Berger (2014). . . . . | 185 |
| 5.28 | Example of the graphical output of the Python script developed by me to calculate the sky region visible by MAGIC below a certain zenith ( $70^\circ$ in this case, in red) at a certain time to assess the overlap with the LIGO/Virgo skymap. In this case the GW event is GW151226. . . . .   | 185 |
| 5.29 | <b>Top:</b> distribution of the ratio of the number of MC events and the distance from the camera center $R$ as a function of $R$ . ST.03.06 MC data were used. <b>Bottom:</b> values of the ring thickness for densely sampled values of $R$ . Since the distribution of MC data is flat up to $0.6^\circ$ , the focus is on larger radii (see text). . . . .   | 188 |
| 5.30 | Crab Nebula spectrum at $0.4^\circ$ offset. The red line is fit with the spectrum given by (5.34), while the blue line is the spectrum from Aleksić et al. 2016b. . . . .  | 189 |
| 5.31 | Crab Nebula spectrum at $0.7^\circ$ offset. The red line is fit with the spectrum given by (5.34), while the blue line is the spectrum from Aleksić et al. 2016b. . . . .  | 190 |

|      |   |     |
|------|---|-----|
| 5.32 | Crab Nebula spectrum at $1.0^\circ$ offset. The red line is fit with the spectrum given by (5.34), while the blue line is the spectrum from Aleksić et al. 2016b.   | 190 |
| 5.33 | Graphical representation of the situation considered in the sensitivity loss test.  | 190 |
| 5.34 | Flux upper limits skymap (left) and TS skymap (right) for the Crab Nebula using fixed cuts in <code>flute</code> .  | 192 |
| 5.35 | Flux upper limits skymap for the Crab Nebula using variable cuts from efficiency in <code>flute</code> .  | 193 |
| 5.36 | Sky localization provided by LIGO using the BAYESTAR algorithm. From <a href="https://gracedb.ligo.org/events/view/G211117">https://gracedb.ligo.org/events/view/G211117</a> .  | 193 |
| 5.37 | $\theta^2$ plots (LE cuts) for the four targets observed by MAGIC in the follow-up of the gravitational event GW151226.   | 196 |
| 5.38 | TS skymaps (LE cuts) for the four targets observed by MAGIC in the follow-up of the gravitational event GW151226.   | 197 |
| 5.39 | Flux upper limit skymaps for the four targets observed by MAGIC in the follow-up of the gravitational wave event GW151226.  | 198 |
| 6.1  | Positions of the target, the Sun and the Moon in the local azimuth-zenith reference system at the MAGIC site at the beginning and ending times as calculated by GSPOT for the test performed during 2017-07-14. The red dashed line is the zenith limit for the Sun ( $103^\circ$ ) while the blue one is the observability zenith limit for neutrino targets ( $50^\circ$ )        | 210 |
| 6.2  | Positions of the target, the Sun and the Moon in the local azimuth-zenith reference system at the MAGIC site at the beginning and ending times as calculated by GSPOT for the first test performed during 2017-07-16. The red dashed line is the zenith limit for the Sun ( $103^\circ$ ) while the blue one is the observability zenith limit for neutrino targets ( $50^\circ$ )  | 211 |
| 6.3  | Positions of the target, the Sun and the Moon in the local azimuth-zenith reference system at the MAGIC site at the beginning and ending times as calculated by GSPOT for the second test performed during 2017-07-16. The red dashed line is the zenith limit for the Sun ( $103^\circ$ ) while the blue one is the observability zenith limit for neutrino targets ( $50^\circ$ ) | 213 |
| 6.4  | Schematic structure of a VOEvent alert. From <a href="http://www.ivoa.net/documents/VOEvent/index.html">http://www.ivoa.net/documents/VOEvent/index.html</a> .  | 218 |
| 6.5  | <b>Left:</b> extract of the table of contents of the GSPOT User Guide. <b>Right:</b> An example of the Doxygen online documentation for GSPOT.  | 218 |
| A.1  | Plot of the functions $\lambda_1(s)$ and $\lambda_2(s)$ defined in equation (A.1).  | 228 |
| A.2  | Plot of the functions $A(s)$ , $B(s)$ and $C(s)$ defined in equations (A.3), (A.4) and (A.5) respectively.  | 228 |
| B.1  | Swift (BAT+XRT or XRT only) light curves for GRB130504A, with MAGIC observation window.   | 229 |
| B.2  | Swift (BAT+XRT or XRT only) light curves for GRB130606A, with MAGIC observation window.   | 230 |
| B.3  | Swift (BAT+XRT or XRT only) light curves for GRB130701A, with MAGIC observation window.   | 230 |
| B.4  | Swift (BAT+XRT or XRT only) light curves for GRB130903A, with MAGIC observation window.   | 231 |
| B.5  | Swift (BAT+XRT or XRT only) light curves for GRB140430A, with MAGIC observation window.   | 231 |
| B.6  | Swift (BAT+XRT or XRT only) light curves for GRB140709A, with MAGIC observation window.   | 232 |

|      |  |     |
|------|--|-----|
| B.7  | Swift (BAT+XRT or XRT only) light curves for GRB141026A, with MAGIC observation window. . . . .  | 232 |
| B.8  | Swift (BAT+XRT or XRT only) light curves for GRB141220A, with MAGIC observation window. . . . .  | 233 |
| B.9  | Swift (BAT+XRT or XRT only) light curves for GRB150819A, with MAGIC observation window. . . . .  | 233 |
| B.10 | Swift (BAT+XRT or XRT only) light curves for GRB151118A, with MAGIC observation window. . . . .  | 234 |
| B.11 | Swift (BAT+XRT or XRT only) light curves for GRB151215A, with MAGIC observation window. . . . .  | 234 |
|      |  |     |
| C.1  | $\theta^2$ plot, TS skymap and distribution and significance evolution in time for GRB130504A. . . . .   | 236 |
| C.2  | $\theta^2$ plot, TS skymap and distribution and significance evolution in time for GRB130606A. . . . .   | 237 |
| C.3  | $\theta^2$ plot, TS skymap and distribution and significance evolution in time for GRB130701A. . . . .   | 238 |
| C.4  | $\theta^2$ plot, TS skymap and distribution and significance evolution in time for GRB130903A. . . . .   | 239 |
| C.5  | $\theta^2$ plot, TS skymap and distribution and significance evolution in time for GRB140430A. . . . .   | 240 |
| C.6  | $\theta^2$ plot, TS skymap and distribution and significance evolution in time for GRB140709A. . . . .   | 241 |
| C.7  | $\theta^2$ plot, TS skymap and distribution and significance evolution in time for GRB141026A. . . . .   | 242 |
| C.8  | $\theta^2$ plot, TS skymap and distribution and significance evolution in time for GRB141220A. . . . .   | 243 |
| C.9  | $\theta^2$ plot, TS skymap and distribution and significance evolution in time for GRB150213A. . . . .   | 244 |
| C.10 | $\theta^2$ plot, TS skymap and distribution and significance evolution in time for GRB150819A. . . . .   | 245 |
| C.11 | $\theta^2$ plot, TS skymap and distribution and significance evolution in time for GRB151118A. . . . .   | 246 |
| C.12 | $\theta^2$ plot, TS skymap and distribution and significance evolution in time for GRB151215A. . . . .   | 247 |
|      |  |     |
| D.1  | Plot showing the MC data distribution in energy used for the calculation of the analysis energy threshold for GRB130504A. . . . .  | 249 |
| D.2  | Plot showing the MC data distribution in energy used for the calculation of the analysis energy threshold for GRB130606A. . . . .  | 250 |
| D.3  | Plot showing the MC data distribution in energy used for the calculation of the analysis energy threshold for GRB130701A. A higher cut size (80) was used because of the higher background due to the presence of the Moon, according to the values reported in Table 4.3. . . . . | 250 |
| D.4  | Plot showing the MC data distribution in energy used for the calculation of the analysis energy threshold for GRB130903A. . . . .  | 251 |
| D.5  | Plot showing the MC data distribution in energy used for the calculation of the analysis energy threshold for GRB140430A. . . . .  | 251 |
| D.6  | Plot showing the MC data distribution in energy used for the calculation of the analysis energy threshold for GRB140709A. . . . .  | 252 |

|      |  |     |
|------|--|-----|
| D.7  | Plot showing the MC data distribution in energy used for the calculation of the analysis energy threshold for GRB141026A. The zenith range used for the calculation of $E_{\text{thr}}$ is not the same as shown in Table 5.1 ( $10^\circ$ - $50^\circ$ ), but it is different ( $29^\circ$ - $50^\circ$ ) to take into account the fact that most of the initial part of the data used were affected by low and unstable transmission (see Figure D.8). | 252 |
| D.8  | Evolution in time of the atmospheric transmission at 9 km and 12 km for GRB141026A. The red line is the time at which the transmission becomes stable. The zenith of the GRB at that moment ( $29^\circ$ ) is the one taken as lower limit for the energy threshold calculation (see Figure D.7).  | 253 |
| D.9  | Plot showing the MC data distribution in energy used for the calculation of the analysis energy threshold for GRB141220A.  | 253 |
| D.10 | Plot showing the MC data distribution in energy used for the calculation of the analysis energy threshold for GRB150213A.  | 254 |
| D.11 | Plot showing the MC data distribution in energy used for the calculation of the analysis energy threshold for GRB150819A.  | 254 |
| D.12 | Plot showing the MC data distribution in energy used for the calculation of the analysis energy threshold for GRB151118A.  | 255 |
| D.13 | Plot showing the MC data distribution in energy used for the calculation of the analysis energy threshold for GRB151215A.  | 255 |
| F.1  | $\theta^2$ plot (LE cuts), light curve and SED for the Crab Nebula sample considered for cross-checking the settings used for the analysis of the targets GW3 and GW4.   | 264 |

# List of Tables

|      |   |     |
|------|---|-----|
| 2.1  | Main parameters of current IACTs experiments. . . . .   | 51  |
| 4.1  | Tag, time period and description of the different MC data sets used in this thesis. . . . .   | 96  |
| 4.2  | The standard cuts in the different energy ranges. Each cut results in a slight different final sensitivity. . . . .   | 110 |
| 4.3  | Pedestal distribution mean and RMS values, cleaning levels and size cuts for different brightness levels and hardware settings. These values are the “standard” values to be used in a moon analysis and were optimized on Crab Nebula data samples with different NSB levels. From Ahnen et al. (2017). . . . .  | 126 |
| 5.1  | List of MAGIC observed GRBs considered in this thesis. The columns are respectively: name of the GRB, satellite which detected the GRB, $T_{90}$ , redshift, zenith range during the observation, background conditions and delay between the onset and the beginning of the observation. All the reported $T_{90}$ are computed in the energy range 15 – 350 keV, except for GRB130903A and GRB150213A for which the energy range is 50 – 300 keV. . . . . | 162 |
| 5.2  | Main parameters of MAGIC observed GRBs considered in this thesis. The columns are respectively: name of the GRB, right ascension, declination, uncertainty in the position in arcmin, fluence in BAT (15-150 keV energy range) and BAT photon index (PL and CPL stand for power-law and cutoff power-law respectively). . . . .   | 163 |
| 5.3  | Summary of the observations of the GRBs observed by MAGIC considered in this thesis. The explanation of the meaning of the columns is given in the text.  | 171 |
| 5.4  | Summary of the results of the analysis performed on the GRBs listed in Table 5.1. The significance reported in the second column is the one computed using LE cuts in <i>odie</i> . . . . .   | 172 |
| 5.5  | CBC rates for different systems. $R_{\text{low}}$ , $R_{\text{re}}$ and $R_{\text{high}}$ are defined as plausible pessimistic, realistic and optimistic estimates respectively. The rates were calculated assuming a mass of $1.4M_{\odot}$ and $10M_{\odot}$ for NS and BH respectively. From Abadie et al. (2010). . . . .   | 177 |
| 5.6  | Results of the test to determine the separation between grid points. The three columns are the chosen MC ring (with $0.2^{\circ}$ thickness), the PSF value and the PSF overlap respectively. . . . .   | 188 |
| 5.7  | Results from the test for the data set taken with $0.4^{\circ}$ wobble offset. . . . .  | 191 |
| 5.8  | Results from the test for the data set taken with $0.7^{\circ}$ wobble offset. . . . .  | 191 |
| 5.9  | Results from the test for the data set taken with $1.0^{\circ}$ wobble offset. . . . .  | 191 |
| 5.10 | Summary of the values of the main parameters for GW151226. The reported numbers are median values with 90% credible intervals (statistical plus systematic errors). From Abbott et al. (2016a). . . . .   | 194 |

|      |   |     |
|------|---|-----|
| 5.11 | Summary of the four positions observed by MAGIC as a follow-up of GW151226. The second column shows the targets observed by optical partners and chosen to be observed by MAGIC. (1) <a href="https://gcn.gsfc.nasa.gov/gcn3/18804.gcn3">https://gcn.gsfc.nasa.gov/gcn3/18804.gcn3</a> . (2) <a href="https://gcn.gsfc.nasa.gov/gcn3/18734.gcn3">https://gcn.gsfc.nasa.gov/gcn3/18734.gcn3</a> . . . . .  | 195 |
| 5.12 | Summary of the results of the analysis performed on the four positions observed for the follow-up of GW151226 as listed in Table 5.11. The significance reported in the second column is the one computed using LE cuts in <i>odie</i> . The energy threshold for GW3 and GW4 is higher because of the higher NSB level due to the presence of the Moon during observations. Flux upper limits are calculated at the position of the targets. . . . . | 195 |
| 6.1  | List of the items always contained in a binary packet, with the positions (indexes) in the packets (always the same for different types of packets). . . . .  | 203 |
| 6.2  | Summary of the parameters used for the first test performed on 2017-07-16 . . . . .   | 209 |
| 6.3  | Summary of the parameters used for the second test performed on 2017-07-16 . . . . .  | 211 |
| 6.4  | Summary of the parameters used for the test performed on 2017-07-17 . . . . .   | 213 |
| 6.5  | Summary of the parameters used for the test performed on 2017-12-07. . . . .  | 219 |
| 6.6  | Summary of the parameters used for the test performed on 2017-12-22. . . . .  | 222 |
| E.1  | Differential flux upper limits in energy ranges $[E_1; E_2]$ for GRB130504A. Only upper limits above the energy threshold are reported. . . . .   | 257 |
| E.2  | Differential flux upper limits in energy ranges $[E_1; E_2]$ for GRB130606A. Only upper limits above the energy threshold are reported. . . . .   | 258 |
| E.3  | Differential flux upper limits in energy ranges $[E_1; E_2]$ for GRB130701A. Only upper limits above the energy threshold are reported. . . . .   | 258 |
| E.4  | Differential flux upper limits in energy ranges $[E_1; E_2]$ for GRB130903A. Only upper limits above the energy threshold are reported. . . . .   | 258 |
| E.5  | Differential flux upper limits in energy ranges $[E_1; E_2]$ for GRB140430A. Only upper limits above the energy threshold are reported. . . . .   | 259 |
| E.6  | Differential flux upper limits in energy ranges $[E_1; E_2]$ for GRB140709A. Only upper limits above the energy threshold are reported. . . . .   | 259 |
| E.7  | Differential flux upper limits in energy ranges $[E_1; E_2]$ for GRB141026A. Only upper limits above the energy threshold are reported. . . . .   | 259 |
| E.8  | Differential flux upper limits in energy ranges $[E_1; E_2]$ for GRB141220A. Only upper limits above the energy threshold are reported. . . . .   | 260 |
| E.9  | Differential flux upper limits in energy ranges $[E_1; E_2]$ for GRB150213A. Only upper limits above the energy threshold are reported. . . . .   | 260 |
| E.10 | Differential flux upper limits in energy ranges $[E_1; E_2]$ for GRB150819A. Only upper limits above the energy threshold are reported. . . . .   | 261 |
| E.11 | Differential flux upper limits in energy ranges $[E_1; E_2]$ for GRB151118A. Only upper limits above the energy threshold are reported. . . . .   | 261 |
| E.12 | Differential flux upper limits in energy ranges $[E_1; E_2]$ for GRB151215A. Only upper limits above the energy threshold are reported. . . . .   | 262 |
| F.1  | Pedestal distribution mean and RMS and cleaning levels adopted for GW3 and GW4. The same settings were applied since the NSB level was similar for both targets. . . . .  | 263 |

# Introduction

The field of very high-energy gamma-ray astronomy made a huge leap forward thanks to the current generation of ground-based telescopes. One of these instruments is MAGIC (*Major Atmospheric Gamma-ray Imaging Cherenkov*), a system of two Imaging Atmospheric Cherenkov Telescopes (IACTs) located in La Palma (Canary Islands). Among the several science cases, the search for Gamma-Ray Bursts (GRBs) is definitely one of the most interesting and intriguing. After the discovery of these explosive transient events, even before the operation of current generation Cherenkov telescopes, several theoretical models predicted that GRBs could have been detected by IACTs. MAGIC in particular was designed to have a low energy threshold, a fast repositioning and a good sensitivity at the lowest energies in order to be the key instrument in GRB science at very high energies. The first part of the work, presented in Chapter 5 of this thesis, is thus focused on GRBs observed with MAGIC and on the search of the possible VHE emission. The sample considered comprised 12 GRBs observed by MAGIC in the two year period 2013-2015, after the introduction of a new automatic repointing procedure which allowed to reduce drastically the hardware failures and related issues. My contribution in this regard was in the data analysis of these GRBs, whose results will be part of a dedicated paper comprising all the GRBs observed in the 2013-2015 period (19 in total). Unfortunately, no VHE signal was found in any of the GRBs considered. The second topic of this thesis is the follow-up of gravitational waves candidate events, which is intimately linked with GRBs. Indeed, a sub-class of GRBs with duration lower than 2 s (they are called *short GRBs*) is thought to originate from the merger of a binary system of two compact objects, namely two neutron stars or a neutron star and a black hole. The difficulty in the follow-up of such events is their localization: in the first run only the LIGO interferometer was taking data resulting in quite large localizations of the order of thousands of square degrees. The small field of view of MAGIC in this sense is a disadvantage but the presence of a whole electromagnetic community performing follow-up searches provides many possible counterparts to be observed by MAGIC. A similar strategy was adopted for the follow-up of the gravitational wave event GW151226 considered in this thesis. Despite being a merger of a black hole-black hole system, the hint of detection of electromagnetic emission by GBM for GW150914 (the very first detection of a gravitational from a binary black hole merger) triggered a huge theoretical activity trying to explain its origin in such kind of systems where EM counterparts are not expected. For this reason, MAGIC performed the follow-up of this event observing four sky positions according to the observations of other instruments. The second difficulty in this kind of observations is that localizations, in absence of a clear electromagnetic counterpart, are typically larger than the MAGIC field of view. The MAGIC software at the time did not have any self-consistent tool to compute quantities (e.g. flux, effective area) in a large portion of the field of view. My contribution was to develop, together with other two collaboration members, a tool to cope with this problem. The tool was tested and then applied to the four targets observed for the follow-up of GW151226. As the standard analysis suggested, the results are compatible with a background-only hypothesis.

The third and final topic of this thesis was a technical work performed on the automatic alert system of the MAGIC telescopes, GSPOT (*Gamma Sources POinting Trigger*): it receives

and processes the alerts coming from the *Gamma-ray Coordinates Network* (GCN). These alerts contain information about transient sources, in particular GRBs. In the last years, gravitational wave and neutrino alerts coming from LIGO/Virgo and IceCube respectively were added to the GCN stream and they are received by GSPOT. While for GRBs there is an automatic response to alerts i.e. if the target is observable the telescopes will reposition automatically without any human intervention, the same does not hold for neutrino alerts. As new responsible of GSPOT, I implemented the automatic response to neutrino alerts and tested it offline. The preliminary tests showed that the implementation works and that GSPOT processes correctly the neutrino alerts according to specific observational criteria. To have the final confirmation, tests performed at the MAGIC site are needed and they will be scheduled before the end of 2017.

The outline of this thesis is the following: Chapter 1 is an introduction to gamma-ray astronomy, describing cosmic rays and their acceleration, production of gamma-rays and the main sources of gamma-rays. Chapter 2 describes in detail the extensive air shower phenomenon and how gamma-rays can be detected with the Imaging Atmospheric Cherenkov Technique. Chapter 3 presents MAGIC with a description of its main mechanical, hardware and detector components. Chapter 4 focuses on the techniques used to analyze MAGIC data, which will be used in the following chapters. Chapter 5 introduces GRBs and presents the data analysis performed on the GRB sample. In the second part, the follow-up of gravitational wave events by MAGIC is described and the new tool for the analysis of these data is presented. Chapter 6 describes the MAGIC alert system GSPOT and the implementation of the automatic procedure for neutrino alerts. Finally, the conclusions and prospects for the future are presented.

# Chapter 1

## HIGH-ENERGY GAMMA-RAY ASTRONOMY

Throughout history, the first tools to study the Universe were the human eyes and the optical telescope used by Galileo. While the first observations were limited to collecting visible light, new discoveries and technological development led to the birth of new branches of astronomy: few examples are cosmic ray, radio, X-ray,  $\gamma$ -ray and neutrino astronomy and the most recent gravitational wave astronomy. This means that nowadays all the electromagnetic spectrum from radio waves to gamma rays is covered by astronomy, allowing to study sources at different wavelengths (the so-called *multi-wavelength* approach). Nonetheless, astrophysical sources do not emit only photons but we can get information on the sources by studying other messengers like neutrinos, cosmic rays and gravitational waves. This is the so-called *multi-messenger* approach, which allows to have a complete picture of a source, its environment and the occurring physical processes.

In this thesis I will deal with  $\gamma$ -ray astronomy and very high-energy astrophysics, with links to gravitational wave and neutrino astronomy. Since gamma rays are quite powerful photons, at least one million times more energetic than visible light ( $E \sim \mathcal{O}(1 \text{ eV})$ ), the first question that arises is how gamma rays are produced. The answer is quite simple: several astrophysical sources can accelerate cosmic rays in strong magnetic fields up to very high energies and these particles radiate gamma-rays through few basic emission mechanisms. So the study of gamma rays is at first order intimately linked with the origin of cosmic rays.

For this reason, this Chapter is organized as follows: first I will give a short overview of Cosmic Rays and how they are accelerated to the observed energies; then I will describe the physical processes through which gamma rays are produced and the different techniques used to detect them; finally I will briefly describe which are the classes of astrophysical sources of gamma rays and state the current status of very high energy (VHE,  $E \gtrsim 100 \text{ GeV}$ ) astronomy.

### 1.1 Cosmic rays

The discovery of *cosmic rays* goes back to 1912-1913. It was already known before that particles could be emitted by some materials which showed *spontaneous radioactivity* behavior, as discovered by Becquerel in 1896. Marie and Pierre Curie then started their studies on Polonium and Radium, using the electroscope to measure the level of radioactive emission. The electroscope was then improved with a closed vessel insulation and spontaneous discharge was observed, due to some radiation of unknown origin. There were three hypothesis on the source of this radiation: extraterrestrial (the Sun), the Earth crust or the atmosphere. To prove which was the correct explanation, several experiments were conducted measuring the ionization rate at different heights: a first attempt was made by Theodor Wulf who brought his electroscope up to the top of the Eiffel Tower ( $\sim 300 \text{ m}$ ). A second experiment was per-

formed by the Italian physicist Domenico Pacini: he measured the ionization rate at three meters underwater and he found a 20% decrease with respect to the one at sea level. This was the first proof that probably the radiation was not coming from the Earth crust. The issue was cleared thanks to balloon flights and especially to the one performed by Victor Hess: from his results, the ionization rate showed a minimum and then a clear increase with height (the maximum height that he reached was 5200 m). Since there was no clear difference between measurements performed during the day and the night, the Sun was not considered the source of the radiation. The radiation was coming from outside the Earth and given its high penetrating power it was considered to be comprised of  $\gamma$  rays. Following studies showed that the radiation was coming isotropically from all directions and that it was not composed of  $\gamma$  rays but of charged particles. The reason for that was found to be the ionization, which was increasing with latitude because of the interaction of the radiation with the geomagnetic field. In 1926 Millikan proposed the name *cosmic rays* for this penetrating radiation. With the introduction of the Geiger-Müller counter in 1928, the final confirmation that cosmic rays were charged particles was reached. Moreover, with experiments performed in 1933 by Alvarez and Compton, Johnson and Rossi it was found that most of the cosmic rays were positively charged particles because near the equator there were more particles coming from the West. So they concluded that cosmic rays are mainly composed by protons.



Figure 1.1.1

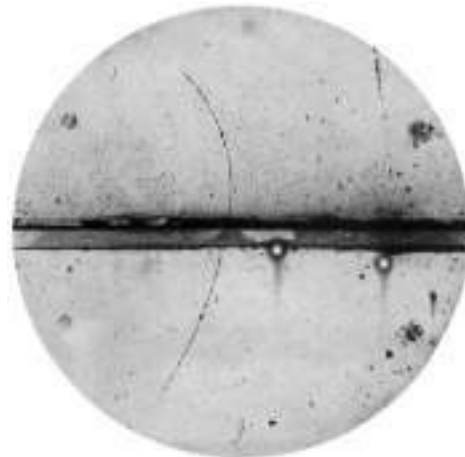


Figure 1.1.2

Figure 1.1: **Left:** the electroscopes used by Victor Hess for his measurements. From <https://airandspace.si.edu/>. **Right:** image of the trajectory followed by a positron in Anderson's cloud chamber. From Anderson (1933).

This is how particle physics started: cosmic rays, beside protons, contained other different kind of particles unknown at the time and they were used to study the interaction of charged particles with matter since no accelerator was available at the time. Soon many new particles (often predicted by the theory) were discovered: positrons (predicted by Dirac in 1928 and discovered by Anderson in 1933 with the cloud chamber, see Figure 1.1.2), pions, muons and strange particles.

An important step for ground-based astronomy, described in detail in Chapter 2, was the discovery with the coincidence technique first by Bruno Rossi in 1934 and then by Pierre Auger in 1937 of the development of extensive air shower (EAS) in the atmosphere due to the interaction of high energy cosmic rays with nuclei.

In the 1950s accelerator technology started to grow and the study of high energy particles moved to laboratories, where particles were produced instead of being hunted down in the atmosphere.

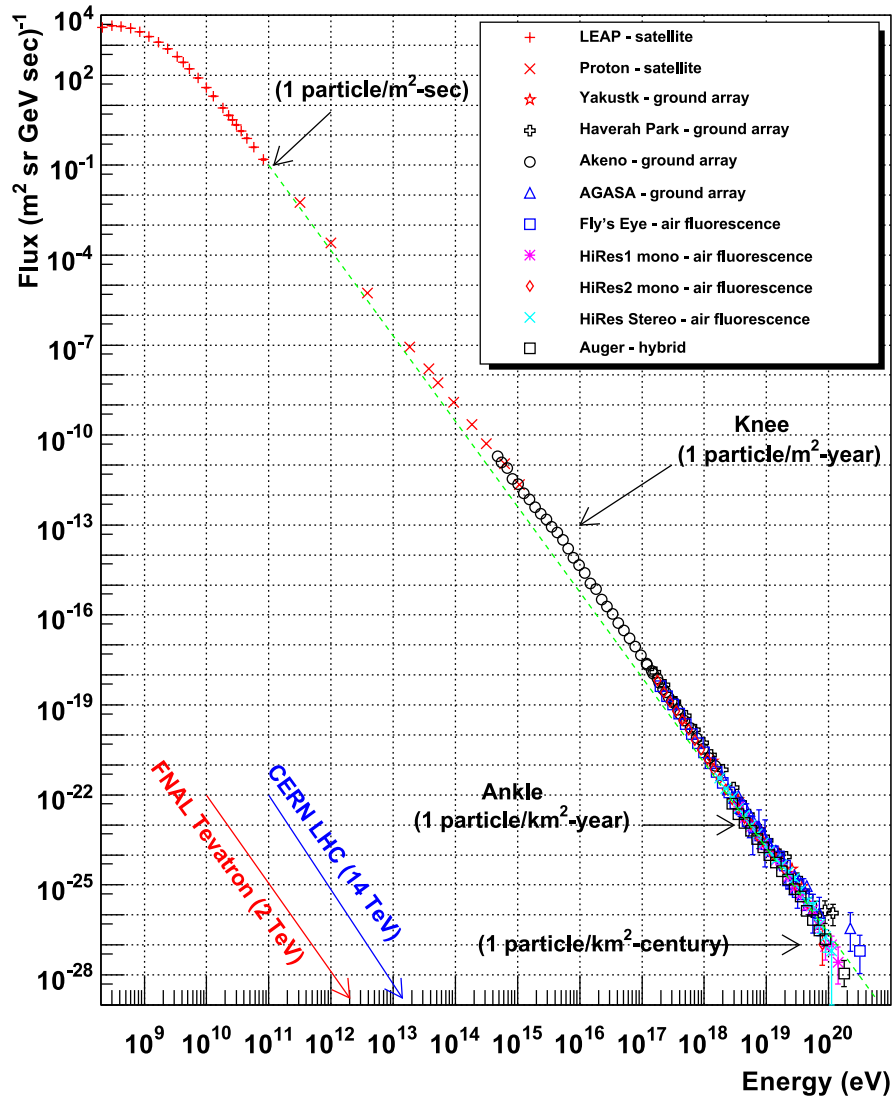


Figure 1.2: Energy spectrum of charged cosmic rays as determined by several experiment (in the legend). In the bottom the red and blue arrows indicate which are the current energies achievable at accelerators. From <http://www.physics.utah.edu/~whanlon/spectrum.html>.

### 1.1.1 Cosmic rays spectrum and composition

Through many years of measurements with balloons, satellites and extensive air shower arrays, it is currently known that cosmic rays have very different energies. The spectrum of cosmic rays, shown in Figure 1.2, extends from about  $10^9$  eV to  $\sim 10^{21}$  eV (well above current accelerators capabilities) and spans 24 orders of magnitude in flux: less energetic particles ( $E \sim$  GeV) have fluxes of the order of thousands of particles per square meter per second, while at the highest energies ( $E \sim 10^{20}$  eV) the number of particles reduces drastically to one per square kilometer per century. For this reason, different techniques are usually employed to detect cosmic rays: at low energies balloon or satellite based experiments are used while at high energies, given the low fluxes, detector arrays covering large areas are needed.

At energies below 10 GeV the cosmic ray spectrum is dominated by solar modulation and earth magnetic field effects. Above about 10 GeV it can be fitted by a power law:

$$\frac{dN}{dE} \propto E^{-\alpha} \quad (1.1)$$

with the spectral index  $\alpha$  changing at some specific energies. The first break, usually called *knee*, is at  $E \sim 5 \cdot 10^{15}$  eV and it is interpreted as the transition from galactic to extra-galactic cosmic rays. The spectral index changes from 2.7 to 3.1 after the knee. Moreover the composition of cosmic rays changes after the knee with more and more heavier nuclei dominating the spectrum. Above the second break (the *ankle*) at  $E \sim 5 \cdot 10^{18}$  eV, the spectrum hardens to a  $\alpha \sim 2.6$  spectral index. Finally, at  $E \sim 5 \cdot 10^{19}$  PeV the Greisen-Zatsepin-Kuz'min (GZK) cutoff makes the spectrum very soft. This cutoff was theoretically predicted by Greisen (1966) and Zatsepin and Kuz'min (1966) as a consequence of the interaction of the highest energy cosmic rays with the photons of the Cosmic Microwave Background (CMB). Other possible explanations are the change in composition, from protons to heavier nuclei which undergo photodisintegration, or exhaustion of sources.

As far as the composition is concerned, cosmic rays are mostly protons (90%), followed by helium nuclei ( $< 10\%$ ), ionized heavier elements, electrons/positrons and antiprotons. A small component of photons with energy greater than 100 MeV is also present. The spectra of the different hadronic components are shown in Figure 1.3 and have a very similar power-law shape.

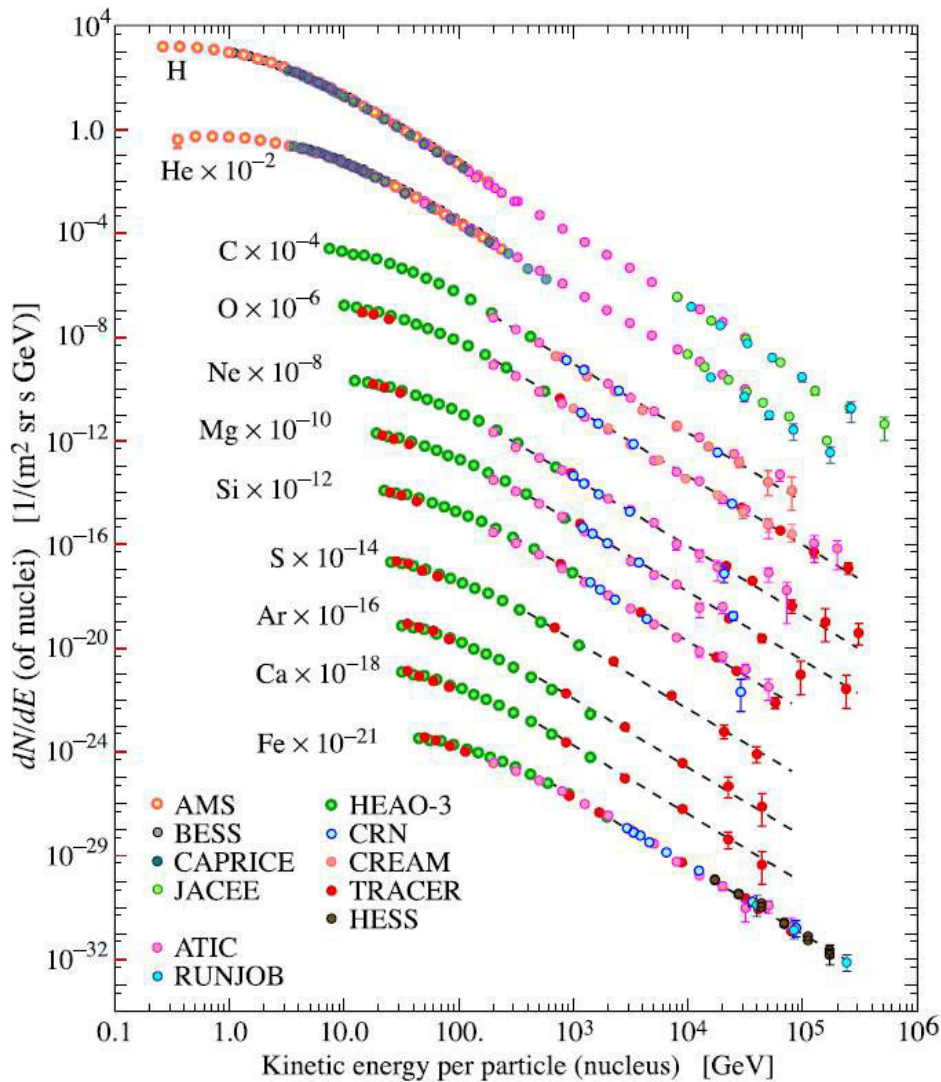


Figure 1.3: Spectra of the nuclei in cosmic rays. From Olive (2014).

An interesting comparison between the relative abundances of elements in cosmic rays compared to the ones in the Solar System is shown in Figure 1.4: most of the nuclei show a

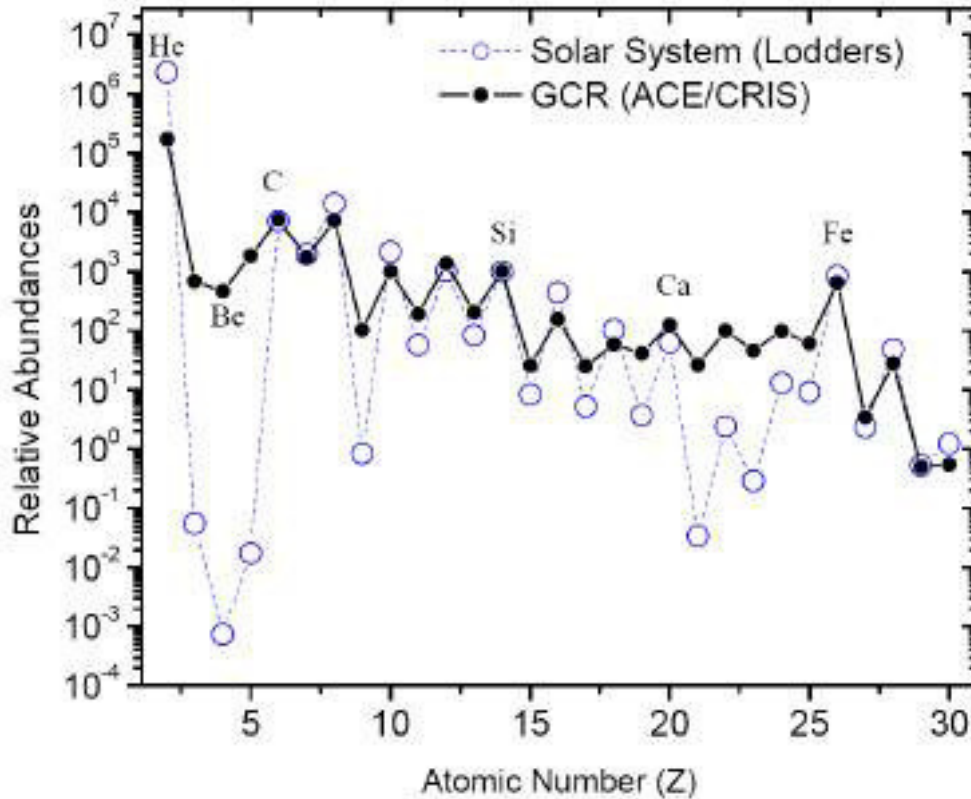


Figure 1.4: Relative abundance of elements in galactic cosmic rays compared with the one found in the Solar System. From <http://www.srl.caltech.edu/ACE>.

similar abundance but there are few exceptions. Light elements like lithium, beryllium and boron are more abundant in cosmic rays than in the Solar System and the same happens for the elements before iron. This difference can be explained by the spallation process: primary cosmic rays are heavy nuclei and are fragmented in the interstellar medium to produce lighter nuclei. This means that these abundant nuclei (Li, Be, B) are secondary products and are not produced directly at the sources of cosmic rays.

Electrons, due to their low mass, undergo severe energy losses during their propagation, so they are good probes about the propagation of cosmic rays in the Galaxy. Most of the electrons are primary, but they can be produced also as a secondary decay product of short-lived particles like pions. The electron spectrum is shown in Figure 1.5: all data are in agreement with the simulation (solid line) up to few tens of GeV, where a discrepancy is clear. Possible explanations are a harder injection spectra of the electrons at the source or the production of secondary electrons from hadronic interactions of accelerated protons. Also, additional sources of cosmic rays could explain the hardening above 70 GeV.

Positrons as well are produced as secondary products of primary cosmic rays interactions with the interstellar medium. Naively one would expect that the number of positrons would decrease with energy, but the positron fraction i.e. the ratio of the positron flux and the total flux of positrons plus electrons starts to rise at  $\sim 10$  GeV, as shown in Figure 1.6. Two possible explanations are the presence of nearby sources, Pulsars mainly, or decay of heavier particles into positrons (e.g. Dark Matter).

A similar behavior is seen in the antiproton to proton flux ratio: while it is expected that it should decrease with energy, measurements by AMS-02 show that it follows a flat behavior above 20 GeV (Nozzoli 2017, see Figure 1.7). This trend is more difficult to explain as a secondary production from primary cosmic rays or as originated from nearby sources and new measurements are needed to find a suitable theoretical explanation.

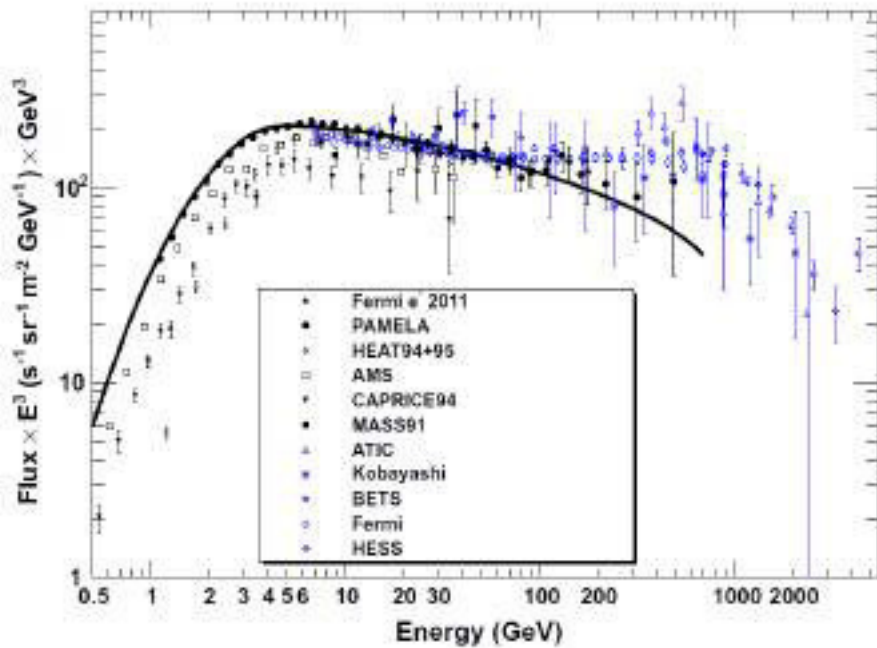


Figure 1.5: Spectrum of the electrons in cosmic rays as measured by different experiments. The solid line is the prediction from GALPROP (<https://galprop.stanford.edu/>) code. From Boezio and Mocchiutti 2012.

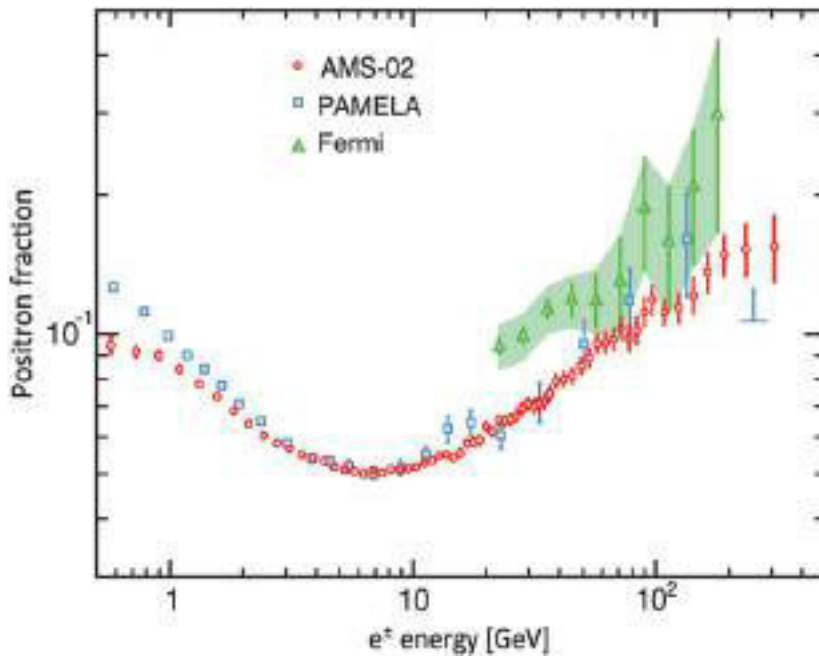


Figure 1.6: Positron fraction as a function of the energy as measured by AMS-02, PAMELA and Fermi-LAT. From Aguilar et al. 2013.

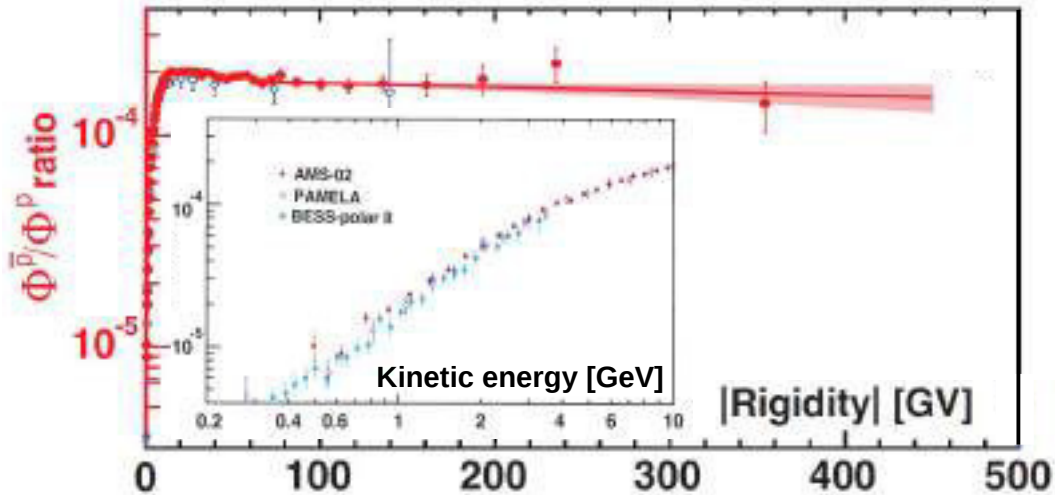


Figure 1.7: Antiproton to proton flux ratio as a function of the rigidity  $\mathcal{R} = pc/ze$  from AMS-02 (red dots) and PAMELA (blue open circle). The inset shows a zoom on the 0.2-10 GeV kinetic energy range adding also the data from BESS-polar II. From Nozzoli (2017).

### 1.1.2 Cosmic rays acceleration

The spectrum of cosmic rays shown in Figure 1.2 can be quite puzzling at first glance. The extension in energy is very broad and tells us that in some way astrophysical sources are able to accelerate particles up to  $10^{20}$  eV and that the resulting spectrum is a power law with index  $-2.7$ . For this reason, when trying to explain how cosmic rays are accelerated, one must try to reproduce the observational result i.e. the cosmic ray spectrum. Here I will give an overview of the acceleration processes, based mainly on Longair (2011) and Lemoine and Pelletier (2015).

#### Basic principles

Given the presence of an electric and magnetic fields in a region of space, a charged particle of mass  $m$ , Lorentz factor  $\gamma$ , velocity  $\mathbf{v}$  and charge  $q$  will be accelerated following the Lorentz force equation:

$$\frac{d\mathbf{p}}{dt} = \frac{d}{dt}(\gamma m \mathbf{v}) = q(\mathbf{E} + \mathbf{v} \times \mathbf{B}) \quad (1.2)$$

In most astrophysical sources, the environment is usually filled by ionized plasma which is highly conductive and so charges can move freely causing the short-circuiting of any electric field. This means that stationary electric fields are very difficult to maintain and that acceleration is associated with non-stationary magnetic fields or with magnetic fields varying in time. Usually this kind of situation is found within the ionized plasmas moving with a bulk velocity  $\mathbf{v}_p$ , which induces an electric field  $\mathbf{E}_p = -\mathbf{v}_p \times \mathbf{B}$  ( $\mathbf{B}$  here is in the laboratory frame and not in the rest frame). In the case of ideal magneto-hydrodynamics (MHD) conditions, as in general astrophysical settings, the acceleration time is bounded from above by Lemoine and Pelletier (2015):

$$t_{\text{acc}} \lesssim \left| \frac{1}{p} \frac{d\mathbf{p}}{dt} \right|^{-1} \sim \frac{t_g}{\beta_p} \quad (1.3)$$

where  $t_g = p/(eB)$  is the gyration time of the particle in the magnetic field and  $\beta_p = v_p/c$ . Since  $\mathbf{E}_p$  is transverse to  $\mathbf{B}$ , there should be also some force or scattering event pushing the particle across the magnetic field.

Finally, (1.2) can be also applied to rotating magnetic fields as happens in pulsars, where

$\mathbf{E} = -(\boldsymbol{\Omega} \times \mathbf{r}) \times \mathbf{B}$ , with  $\boldsymbol{\Omega}$  being the angular rotation of the pulsar and  $\mathbf{r}$  the position of the particle.

### Fermi acceleration mechanism

The first model to explain the acceleration of cosmic rays was proposed by Fermi. His original acceleration mechanism considered “magnetic mirrors” i.e. magnetic irregularities, having mass  $M \gg m$  moving randomly with velocity  $V$  (see Figure 1.8). Considering a charged particle of initial energy  $E$  and velocity  $\beta = v/c$  scattering with a magnetic cloud with an angle  $\theta$ , with a relativistic calculation, the energy of the particle after the scattering  $E'$  reads:

$$E' = \gamma_M^2 (1 - \beta\beta_m \cos \theta)(1 + \beta\beta_m \cos \theta') E \quad (1.4)$$

where  $\beta_M = V/c$ ,  $\gamma_M = (1 - \beta_M^2)^{-1/2}$  ( $\sim 1$  in the sub-relativistic limit) and  $\theta'$  is the scattering angle in the cloud rest frame. Averaging over  $\theta$  and  $\theta'$ , considered to be random, and weighting the energy gain by the frequency of the collision (proportional to  $|\beta - \beta_M|$ ) the energy gain reads:

$$\left\langle \frac{\Delta E}{E} \right\rangle \simeq \frac{4}{3} \beta_M^2 + \mathcal{O}(\beta_M^4) \quad (1.5)$$

(1.5) shows that the energy gain is proportional to  $\beta_m^2$  and it results in a very inefficient way to accelerate particles, since typical velocities of interstellar clouds are  $\beta_m \sim 10^{-4}$ . Moreover, ionization losses are dominant at low energies and particles should have enough energy when injected to be accelerated efficiently. Finally, the spectrum resulting by the Fermi second order mechanism is a power law with index  $x = 1 + (\alpha\tau_{\text{esc}})^{-1}$ , where  $\alpha = 4/3(V^2/cL)$  ( $L$  is the mean free path between clouds) and  $\tau_{\text{esc}}$  is the amount of time when the particle remains within the accelerating region. Unfortunately, it is very difficult that values of  $\alpha$  and  $\tau_{\text{esc}}$  for different sources could give the same value for the spectral index.

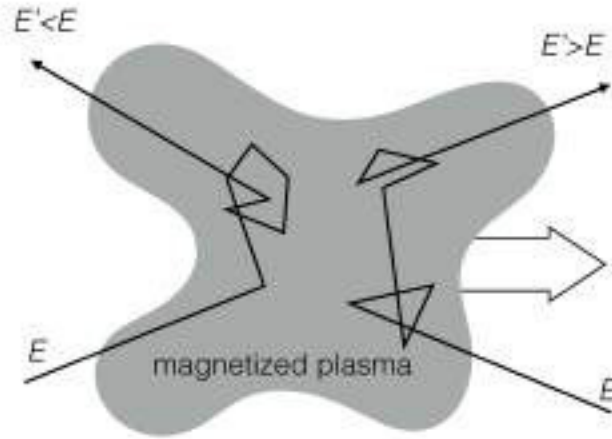


Figure 1.8: Graphical depiction of the Fermi second order mechanism. From <http://w3.iihe.ac.be/~aguilar/PHYS-467/PA3.html>.

A solution to these problems is given by considering the first order Fermi mechanism, also called *diffusive shock acceleration*. Instead of magnetic mirrors, this model considers shock waves propagating in the interstellar medium. In the reference system where the shock is at rest, two regions can be defined: the one with the unshocked plasma flowing into the shock (*upstream*) and the one behind the shock with shocked plasma flowing away at subsonic velocity (*downstream*). The advantage in this model is that particles moving from the downstream to the upstream region (or vice versa) will experience a head-on collision if they return downstream after the scattering.

To compute the average energy gain in this case, (1.4) can still be used replacing  $\beta_M$  by  $\beta_{\text{rel}}$ , that is the relative velocity between the downstream and upstream regions. Averaging on angles  $\theta$  and  $\theta'$ , the mean energy gain written in function of the Lorentz factor  $\gamma$  of the particle is:

$$\left\langle \frac{\Delta\gamma}{\gamma} \right\rangle \simeq \frac{4}{3}\beta_{\text{rel}} \quad (1.6)$$

Thus the energy gain depends linearly on  $\beta_{\text{rel}}$  and so the acceleration efficiency is higher than in the second-order Fermi mechanism. Moreover it can be shown that the resulting energy distribution of the particles due to the diffusive shock acceleration is a power law  $N(>\gamma) \propto \gamma^{1-p}$  with the spectral index  $p$  given by:

$$p \simeq 1 - \frac{\ln(1 - p_{\text{esc}})}{\ln(1 + \langle \Delta\gamma/\gamma \rangle)} \quad (1.7)$$

where  $p_{\text{esc}}$  is the escape probability from the acceleration region. Within the diffusive shock model, the escape probability is  $p_{\text{esc}} = 4\beta_{\text{sh}}/r$ , where  $\beta_{\text{sh}}$  is the velocity of the shock relative to the upstream and  $r = \beta_{\text{sh}}/(\beta_{\text{sh}} - \beta_{\text{rel}})$  is the compression ratio of the shock. The spectral index  $p$  from (1.7) now reads:

$$p \simeq 1 + \frac{3}{r-1} \quad (1.8)$$

For a strong non-relativistic shock the compression ratio is  $r = 4$  (from MHD simulations) and thus  $p \simeq 2$ . The simplicity of this model resides on the few assumptions required, namely the presence of strong shocks (like in supernovae remnants or active galactic nuclei) and of high-energy particles with random velocity vectors in the upstream and downstream regions. Despite the simplicity, the original diffusive shock model is limited in the maximum energy to which particles can be accelerated. An argument due to Syrovatskii (1971), a particle of charge  $Z$  accelerated in a magnetic field  $B$  with scale  $L$  and a shock moving with speed  $U$  attain the maximum energy:

$$E_{\text{max}} = ZeBUL \quad (1.9)$$

For typical parameters found in young SNR ( $B = 10^{10}$  T,  $U = 10^4$  km s $^{-1}$ ), the maximum energy is roughly  $E_{\text{max}} = 10^{14}$  eV. So diffusive shock acceleration can account for cosmic rays up to the knee, but cannot explain the highest energy cosmic rays with energies around  $10^{20}$  eV.

### Nonlinear diffusive shock acceleration

To overcome the maximum energy problem, some modifications are needed to the diffusive shock model. In particular, from observations of young SNRs (Cassiopeia A and Tycho in particular) values of magnetic fields of the order  $(3-10) \cdot 10^{-8}$  T were inferred and simulations show that the magnetic flux density can be enhanced behind shocks due to instabilities. This means that strong magnetic fields exist in shocks and that the maximum energy attainable by cosmic rays in (1.9) can reach values of  $10^{18}$  eV, thus around the ankle of the spectrum. Adding instabilities and magnetic field information into the diffusive shock acceleration model results again in a spectrum of the form  $N(E) \propto E^{-2}$ , independent of the particle type (see for example Figure 1.3), but the cutoff expected at the energy given by (1.9) is different depending on the cosmic ray charge. This means that heavier nuclei have the cutoff in their spectra at higher energies and this explains the origin of the knee: it is due to different maximum energies achievable by nuclei with different charge  $Z$ .

To explain cosmic rays with the highest energies ( $\sim 10^{20}$  eV), (1.9) can be used again in a slightly different form considering that we want to obtain energies as high as  $10^{20}$  eV and writing  $\beta = U/c$ :

$$\frac{3 \cdot 10^{11}}{Z\beta} = BL \quad (1.10)$$

This relation can be plotted and it is the famous *Hillas plot*, introduced by Hillas in 1984.

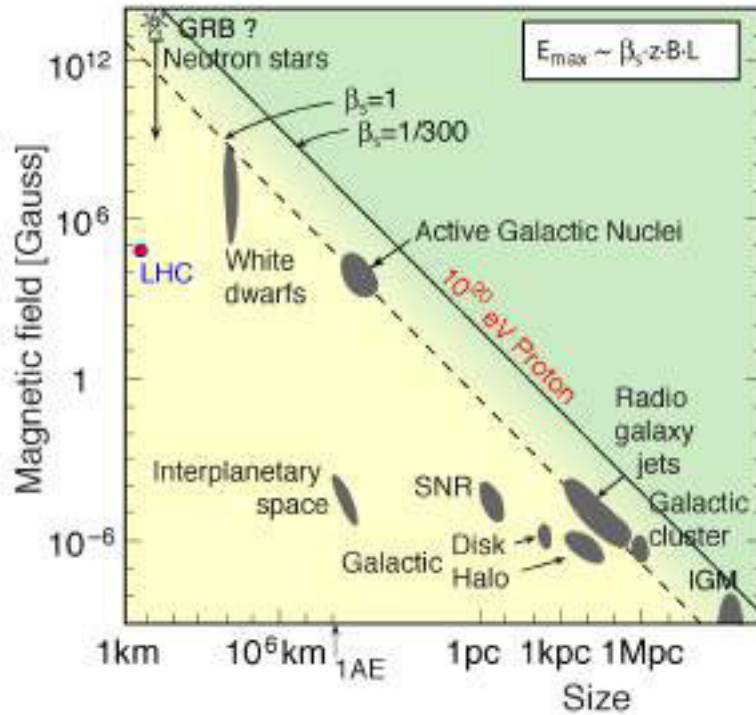


Figure 1.9: Hillas plot: typical length scale versus magnetic field in sources potentially able to be cosmic-ray accelerators. From <http://w3.iihe.ac.be/~aguilar/PHYS-467/PA3.html>.

The Hillas plot shows that there are many potential sites for cosmic ray acceleration up to the highest energies with shock velocities  $\beta \sim 1$  and with different sizes and magnetic field strength. The sources of the highest energy cosmic rays depend of course on their mass and charge: if they are protons, active galactic nuclei are preferred, but if they are iron nuclei lower shock velocities are needed to reach the same energy as shown by (1.10).

## 1.2 Gamma rays

Gamma rays are produced in extreme astrophysical environments. Since they are not charged particles like cosmic rays, they are not deflected by intergalactic magnetic fields and thus they point back directly to their sources. This allows to study their production sites through the spectra we measure with our instruments. The spectra are the results of the emission processes occurring at the source: a deep knowledge of the possible mechanisms responsible for the origin of gamma rays is needed to understand how such energetic particles could be produced. In this regard, gamma rays can give us information about the acceleration of cosmic rays.

Gamma rays can be used also as probes for fundamental physics problems: Lorentz Invariance Violation, Dark Matter and physics beyond the standard model (axion-like particles, supersymmetry).

Photons are usually defined as gamma rays in function of the  $e^+ - e^-$  annihilation process. So gamma rays have energies above  $\sim 0.5$  MeV. Since the energetic range of gamma-rays is very wide, the following classification scheme is used:

- High Energy (HE):  $0.5 \text{ MeV} \lesssim E \lesssim 100 \text{ GeV}$

- Very High Energy (VHE):  $100 \text{ GeV} \lesssim E \lesssim 100 \text{ TeV}$
- Ultra High Energy (UHE):  $100 \text{ TeV} \lesssim E \lesssim 100 \text{ PeV}$
- Extreme High Energy (EHE):  $E \gtrsim 100 \text{ PeV}$

This classification also reflects different techniques for the detection of gamma rays at different energies, see Section 1.2.3. In this thesis, the VHE range will be considered, with some references to the HE range.

In this Section I will describe how gamma rays are produced (Section 1.2.1), their detection techniques (Section 1.2.3), their sources (Section 1.2.4) and finally the processes affecting their propagation (Section 1.2.2).

### 1.2.1 Mechanisms for the production of gamma rays

Gamma rays can be produced in several ways, either from the interactions of charged particles with nuclear targets, magnetic fields and photon fields or by the decay of unstable particles. Usually the emission mechanism can be divided in leptonic and hadronic production models. They are described here below.

#### Synchrotron radiation

In the presence of a magnetic fields, charged particles will spiral around the magnetic field lines and will emit radiation. The total power emitted by a relativistic particle of charge  $q$  in a magnetic field  $B$  with acceleration perpendicular to its velocity is:

$$P = \frac{1}{6\pi\epsilon_0 c} \frac{q^4}{m^2} \gamma^2 \beta^2 B^2 \sin^2 \alpha \quad (1.11)$$

where  $\alpha$  is the angle between the particle velocity and the magnetic field. The  $P \propto 1/m^2$  dependence shows that the synchrotron radiation is more efficient for electrons than for protons.

In the specific case of synchrotron by electrons, the total energy loss rate is:

$$\frac{dE}{dt} = -\frac{4}{3} \sigma_T U_B \gamma_e^2 \beta_e^2 c \quad (1.12)$$

where  $\sigma_T$  is the Thomson cross section and  $U_B = B^2/2\mu_0$ . An exact treatment of the synchrotron process with Lienard-Weichert potentials leads to the power spectrum for a single particle:

$$P(\omega) = \frac{\sqrt{3}e^3 B \sin \alpha}{8\pi^2 \epsilon_0 m_e c} F(x) \quad (1.13)$$

where  $F(x)$  is given by:

$$F(x) = x \int_x^\infty K_{5/3}(\zeta) d\zeta \quad (1.14)$$

$x$  is defined as the ratio  $\omega/\omega_c$ , where the *critical frequency*  $\omega_c$  is defined as:

$$\omega_c = \frac{3}{2} \frac{eB}{m_e} \gamma^2 \sin \alpha \quad (1.15)$$

$\omega_c$  is the frequency above which the synchrotron spectrum exhibits a cutoff. For frequency well above or well below the critical frequency,  $F(x)$  has the following behavior:

$$F(x) \sim x^{1/2} e^{-x} \quad x \gg 1 \quad F(x) \sim x^{1/3} \quad x \ll 1 \quad (1.16)$$

To obtain the spectral shape due to a distribution of electrons, for example with a power law  $N(\gamma)d\gamma \propto \gamma^{-p}d\gamma$ , we have to convolve the power spectrum for a single particle with the distribution function:

$$P_{\text{tot}}(\omega) = \int P(\omega)N(\gamma)d\gamma \propto \omega^{-(p-1)/2} \int_{x_1}^{x_2} F(x)x^{(p-3)/2}dx \quad (1.17)$$

If we take a wide energy interval,  $x_1 \sim 0$  and  $x_2 \sim \infty$ , so that the integral is roughly constant and thus:

$$P_{\text{tot}}(\omega) \propto \omega^{-(p-1)/2} \quad (1.18)$$

This result can be obtained also in an exact way starting from (1.13).

### Inverse Compton

The Inverse Compton (IC) mechanism produces gamma rays through the upscattering of low energy photons with ultra-relativistic electrons, which cool down in the process. Usually two regimes can be defined:

- the Thomson regime, where the energy of the photon in the electron rest frame is lower than the electron rest mass energy:  $\gamma_e \epsilon_\gamma (1 - \beta_e \cos \theta) < m_e c^2$ , where  $\gamma_e$  is the Lorentz factor of the electron and  $\epsilon_\gamma$  is the energy of the photon before the scattering process
- the Klein-Nishina (KN) regime, where the energy of the photon exceed the rest mass energy of the electron in the electron rest frame:  $\gamma_e \epsilon_\gamma > m_e c^2$ .

In the two regimes, the total cross section of the process is given by:

$$\sigma_{\text{T}} = \frac{8}{3}\pi r_0^2 = \frac{e^4}{6\pi\epsilon_0 m_e^2 c^4} \quad (1.19)$$

$$\sigma_{\text{KN}} = \frac{3}{4}\sigma_{\text{T}} \left\{ \frac{1+x}{x^3} \left[ \frac{2x(1+x)}{1+2x} - \log(1+2x) \right] + \frac{1}{2x} \log(1+2x) - \frac{1+3x}{(1+2x)^3} \right\} \quad (1.20)$$

where  $x = h\nu/m_e c^2$ . The asymptotic behavior of the Klein-Nishina cross section is:

$$\sigma_{\text{KN}} \sim \frac{3}{8}\sigma_{\text{T}} x^{-1} \left( \log(2x) + \frac{1}{2} \right) \quad x \gg 1$$

It can be seen that for high photon energies the cross section decreases and the energy gain is limited to the energy of the electron. In the Thomson limit instead, the photon energy after scattering  $\epsilon'_\gamma$  is roughly  $\epsilon'_\gamma \simeq 2\gamma_e^2 \epsilon_\gamma$ . The rate at which an electron loses energy by Inverse Compton is given by:

$$\frac{dE}{dt} = -\frac{4}{3}\sigma_{\text{T}} c \gamma_e^2 \beta_e^2 U_\gamma$$

where  $U_\gamma$  is the radiation energy density. So the expression is very similar to the one obtained for synchrotron radiation.

The Inverse Compton spectrum from two distributions of electrons and photons is obtained by folding them with the differential cross section of the process. The resulting spectrum is, for a power law distribution for electrons with spectral index  $p$  and an isotropic distribution for photons peaked at  $\epsilon_\gamma$ , a power law with index  $-(p-1)/2$ , as in the synchrotron case, with a peak at  $2\gamma_{e,\text{min}}^2 \epsilon_\gamma$  ( $\gamma_{e,\text{min}}^2$  is the minimum Lorentz factor of the electrons). With different distributions of electrons and photons, other spectral dependencies are expected but all of them will exhibit a cutoff after the Klein-Nishina regime is reached.

### Synchrotron self-Compton

A particular situation arises when the photons emitted by synchrotron radiation are upscattered by the same electrons which produced them. This process is referred as *Synchrotron Self-Compton* (SSC). In the Thomson and Klein-Nishina regimes, the photon energy distribution is given by  $dN_\gamma/dE_\gamma \propto E_\gamma^{-(p+1)/2}$  and  $dN_\gamma/dE_\gamma \propto E_\gamma^{-(p+1)} \ln(E_\gamma)$  respectively, where  $p$  is the spectral index of the electron distribution and photons initial distribution is a blackbody with temperature  $T$ , as shown in De Angelis, Mansutti, and Persic (2008).

The two peaks, one due to synchrotron and the other to Compton, can be seen from the spectrum. The Compton peak in particular can be at GeV-TeV energies ( $\nu_{IC,peak} \simeq \langle \gamma_e^2 \rangle \nu_{syn,peak}$ ) and it is important for AGN emission and possibly for GRBs.

An interesting feature of SSC emission is that the yields of synchrotron and IC radiation are correlated during flares. Moreover, the ratio of the cooling rates through IC and synchrotron is:

$$\frac{P_{IC}}{P_{syn}} \simeq \frac{U_\gamma}{U_B}$$

and roughly corresponds to the Compton parameter  $Y \simeq \sigma_T n_e r \langle \gamma_e^2 \rangle$  ( $n_e$  is the electron density,  $r$  is the size of the emitting region).

### Hadronic processes

While previous processes were of leptonic origin, photons can be produced also by hadronic processes like  $pp$  collisions or  $p\gamma$  interactions. In both of these processes, pions are produced and photons can be the product of the decay of neutral pions. Charged pions instead will produce neutrino. In this regard, hadronic processes can link cosmic ray, gamma ray and neutrino astronomy.

$pp$  interaction is the possible responsible of the emission of gamma rays from the Milky Way disk, where cosmic ray protons interact with the interstellar gas. The same argument can be used to explain the gamma ray emission from SNRs: cosmic rays accelerated by shocks interact with molecular clouds producing gamma rays.

$p\gamma$  interactions produce pions via the reaction  $p + \gamma \rightarrow p + \pi^0$  and is kinematically allowed for:

$$\epsilon_\gamma E_p \geq \frac{m_\pi(m_\pi + 2m_p)c^4}{2(1 - \cos \theta)}$$

This interaction is the one thought to be responsible for the GZK cutoff in cosmic ray spectrum, where high-energy protons interact with CMB background photons. Gamma rays in this case are produced by the decay of neutral pions produced in the  $p\gamma$  interaction.

Given the high threshold and low cross section for the process, it is expected to be important in very compact sources with intense radiation fields, like GRBs and AGN.

### Other mechanisms

Beside the more “classical” mechanisms, gamma rays, especially those at the highest energies, can be produced as the decay products of remnant particles or topological structure that were created in the early universe. In these models, particles beyond the standard model (e.g. Grand Unified Theories) can decay into particles of the Standard Model, photons in particular. Thus, the highest energy cosmic rays in these models are photons.

In the VHE range, an appealing production mechanism is the decay or annihilation of Dark Matter particles. In this way, gamma rays could be used to probe physics beyond the Standard Model.

### 1.2.2 Propagation of gamma rays

After they are produced, gamma rays travel without being deflected by any magnetic field. Nevertheless, they can interact with background photons e.g. CMB photons. The relevant process is therefore pair production, where a high energy gamma-ray  $\gamma_{\text{VHE}}$  produces an electron-positron pair by the interaction with a low energy photon  $\gamma_{\text{BKG}}$ :

$$\gamma_{\text{BKG}} + \gamma_{\text{VHE}} \rightarrow e^+ + e^- \quad (1.21)$$

The cross section for this process is given by the Bethe-Heitler formula, as shown in Breit and Wheeler (1934):

$$\sigma_{\gamma\gamma}(\epsilon, E, \varphi) = \frac{1}{2}\pi r_0^2 \left[ 2\beta(\beta^2 - 2) + (3 - \beta^4) \ln \left( \frac{1 + \beta}{1 - \beta} \right) \right] \quad (1.22)$$

where

$$\beta(\epsilon, E, \varphi) = \left[ 1 - \frac{2m_e^2 c^4}{E\epsilon(1 - \cos \varphi)} \right]^{1/2} \quad (1.23)$$

$\epsilon$ ,  $E$  and  $\varphi$  are the cosmic background photon energy, source photon energy and the scattering angle respectively.

The pair production process is kinematically allowed for  $\beta^2 > 0$ , that is:

$$\epsilon > \epsilon_{\text{thr}}(E, \varphi) = \frac{2m_e^2 c^4}{E(1 - \cos \varphi)} \quad (1.24)$$

The cross section, in the case of an isotropic background of photons, is maximized for:

$$\epsilon(E) \simeq \left( \frac{900 \text{ GeV}}{E} \right) \text{ eV} \quad (1.25)$$

(1.25) tells us that higher the energy of the gamma rays, the lower is the energy of the background photon with which it will interact (most probably). This fact has consequences on the propagation of VHE and UHE gamma rays. In particular, VHE gamma rays, whose energy is between 100 GeV and 100 TeV, the pair production is relevant with photons in the UV/optical/infrared bands, while the dominant background absorbing UHE gamma rays is the CMB. At even higher energies, the radio background dominates.

For VHE gamma rays, the background of photons in the UV, optical and infrared bands is called *Extragalactic Background Light* (EBL). The EBL comprises the light (integrated over the whole cosmic evolution period) from all the resolved and unresolved extragalactic sources. Therefore it contains all the energy released through nuclear and gravitational processes from the recombination epoch. A fraction of this radiation is redshifted in the infrared (IR) by the cosmic expansion, absorption processes and reradiation by the dust. So the EBL intensity and spectrum can be used to set limits and study the galaxies formation process, their evolution and their stellar and interstellar contents throughout their cosmic story. Generally speaking, the density of EBL can be calculated numerically using different approaches, see Dwek and Krennrich (2013) and Figure 1.10. Another way to indirectly constrain the EBL density is through observations of HE and VHE sources. If one considers a source with a given intrinsic spectrum  $(dN/dE)_{\text{int}}$ , the observed spectrum  $(dN/dE)_{\text{obs}}$  will be given by:

$$\left( \frac{dN}{dE} \right)_{\text{obs}} = \left( \frac{dN}{dE} \right)_{\text{int}} e^{-\tau_{\gamma\gamma}(E_\gamma, z)} \quad (1.26)$$

Here  $e^{-\tau_{\gamma\gamma}(E_\gamma, z)}$  is the probability that a photon of energy  $E_\gamma$  survives from absorption while it travels from the source at redshift  $z$ . The coefficient  $\tau_{\gamma\gamma}(E_\gamma, z)$  is the *optical depth* and it depends on the pair production cross section  $\sigma_{\gamma\gamma}$ , the EBL density  $n_\gamma(\epsilon(z), z)$  and the

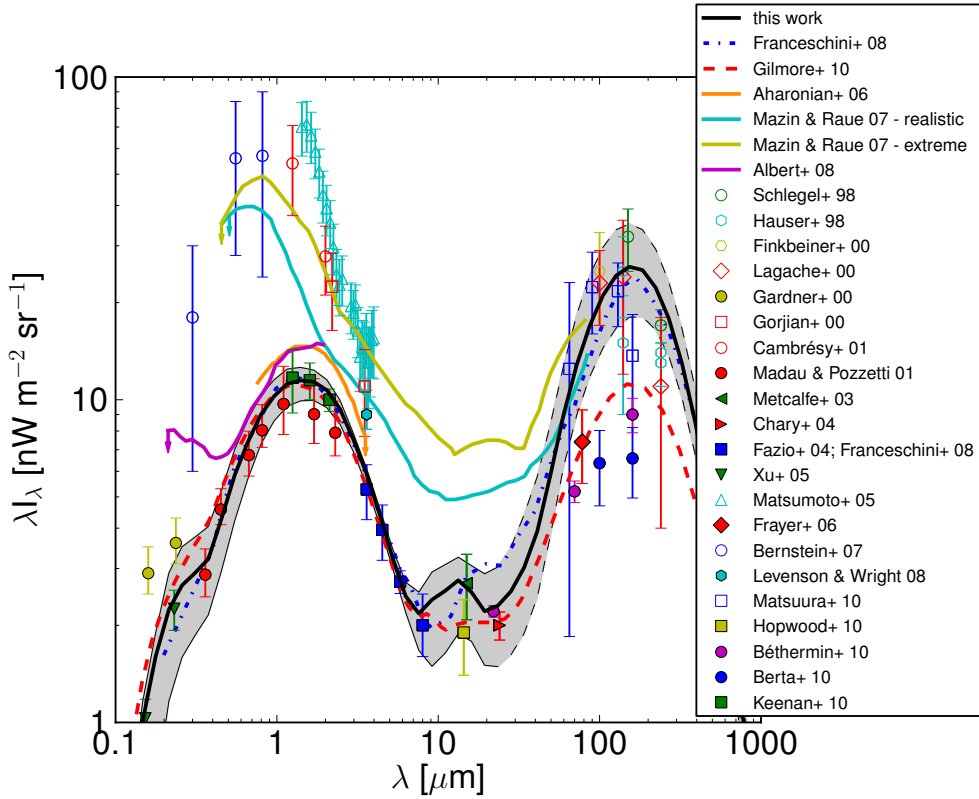


Figure 1.10: Comparison of different EBL models (coloured lines), direct measurements (open symbols) and galaxy count lower limits (filled symbols). From Domínguez et al. (2011).

distance as a function of redshift  $dl/dz$ . Given these elements, in De Angelis, Mansutti, and Persic (2008) the definition of the optical depth for a source at redshift  $z_s$  is given by:

$$\tau_{\gamma\gamma}(E_0, z_s) = \int_0^{z_s} dz \frac{dl(z)}{dz} \int_{-1}^1 d(\cos \varphi) \frac{1 - \cos \varphi}{2} \int_{\epsilon_{\text{thr}}(E(z), \varphi)}^{\infty} d\epsilon(z) n_{\gamma}(\epsilon(z), z) \sigma_{\gamma\gamma}(\epsilon(z), E(z), \varphi) \quad (1.27)$$

The distance travelled by a photon per unit redshift at redshift  $z$  in the standard  $\Lambda$ CDM cosmological model is given by:

$$\frac{dl(z)}{dz} = \frac{c}{H_0} \frac{1}{(1+z)\sqrt{\Omega_{\Lambda} + \Omega_M(1+z)^3}} \quad (1.28)$$

with Hubble parameter  $H_0 \simeq 70 \text{ km s}^{-1} \text{ Mpc}^{-1}$ ,  $\Omega_{\Lambda} \simeq 0.7$  and  $\Omega_M \simeq 0.3$  (average dark energy and matter density in units of the critical density  $\rho_{\text{cr}} \simeq 0.97 \cdot 10^{-29} \text{ g cm}^{-3}$ ).

The optical depth depends both on the energy and on the redshift. Since for more distant sources the probability of absorption is higher (the path is longer), the optical depth increases with redshift. The energy dependence is similar, that is an increasing trend with energy, see Figure 1.11. The end result, given (1.26), is that in the observed spectra of distant sources an exponential cutoff will be seen at an energy depending on the redshift of the source. Of course one must be careful that intrinsic cutoffs are not present at the source when constraining the EBL from observed spectra.

With the definition of optical depth, one can define the so-called *gamma-ray horizon*, that is the energies and redshift satisfying  $\tau_{\gamma\gamma}(E, z) = 1$ . Given a certain redshift, the gamma-ray horizon can be used to infer the energy above which the EBL attenuation starts to be non negligible: this is particularly important for distant sources like AGN and even more for GRBs (see Chapter 5).

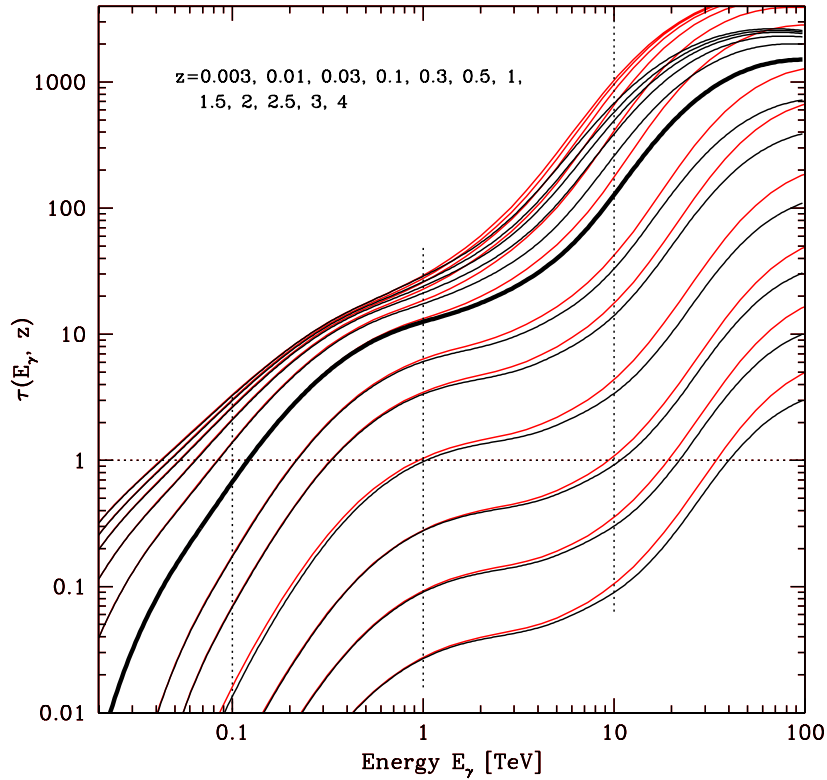


Figure 1.11: Optical depth for pair production as a function of energy for different redshifts (see inset). The redshift increases from bottom to top. The solid thick black line corresponds to  $z = 1$ . From Franceschini and Rodighiero (2017).

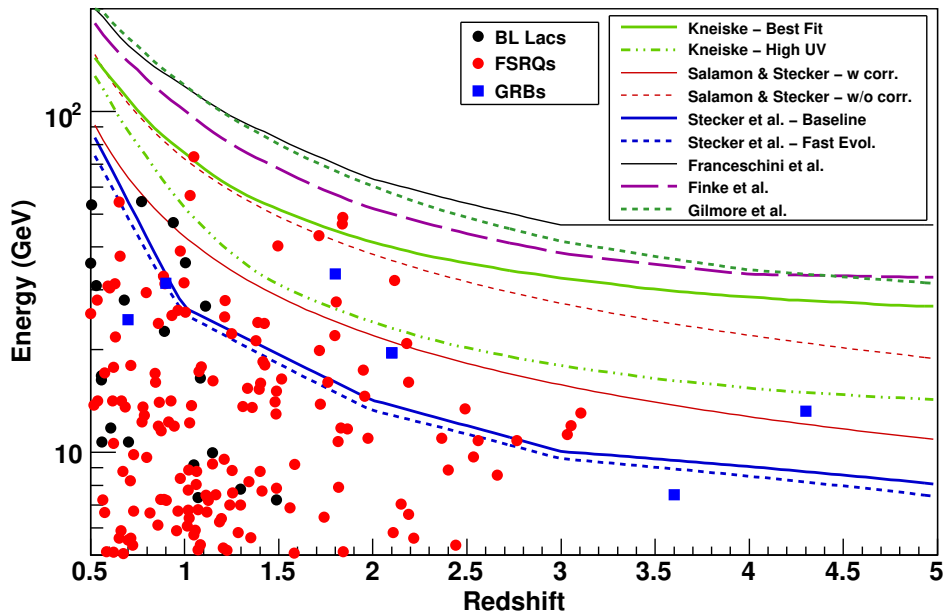


Figure 1.12: Plot of the highest energy photons from blazars and GRBs used in the EBL analysis in Abdo et al. (2010b). The plot shows also the predictions of  $\tau_{\gamma\gamma} = 1$  for different EBL models (see legend). From Abdo et al. (2010b).

Beside the pair production process, other mechanisms can affect the propagation of  $\gamma$ -rays. In particular, the presence of intergalactic magnetic fields (IGMF) could lead to the conversion of the gamma rays into axion-like particles (ALPs), see for example De Angelis, Galanti, and Roncadelli (2011). ALPs do not suffer of absorption due to the EBL, so they travel undisturbed. If reconversion of an ALP to a gamma ray occurs, the end result is that the photon traveled a shorter distance and so its probability to be absorbed is reduced. More conversions ALP-photon can occur, leading to an expansion of the gamma-ray horizon. Moreover, the flux of a source will be enhanced with respect to the case in which only EBL is taken into account.

A second possible non-standard effect could be attributed to the Lorentz Invariance Violation (LIV), see Kifune (1999). The change in the energy-momentum relation of the photon modifies the kinematical relations between the background photon and the gamma ray as well, leading in some cases to a larger mean free path for  $\gamma$ -rays.

### 1.2.3 Detection techniques for gamma rays

The detection of gamma rays is performed with different techniques depending on the energy. At low energies, the flux of gamma rays is high enough to detect them directly with satellite-based instruments.

Below 10 MeV, Compton scattering is the dominant process. This interaction was used to detect gamma rays by COMPTEL (*COMPTON TELescope*), one of the instruments on-board the CGRO (*Compton Gamma Ray Observatory*). It consisted of two detectors, one with low Z liquid scintillators and the other with high Z inorganic scintillators. Each detector is combined with photomultiplier tubes (PMTs) for light detection and surrounded by an anticoincidence system for background rejection. The photon interacts with the first detector through Compton scattering and its initial direction is changed. It then moves towards the second detector where it is completely absorbed. Given the energies released in the first and in the second detector,  $E_1$  and  $E_2$  respectively, the angle of the so called *Compton cone* is given by:

$$\cos \varphi = 1 - m_e c^2 \left( \frac{1}{E_2} - \frac{1}{E_1 + E_2} \right) \quad (1.29)$$

$\varphi$  is the half aperture angle of a cone whose circular base identifies a ring of possible direction for the initial photon, see Figure 1.13. So a degeneracy on the initial direction remains, but it can be removed if multiple photons are detected by the same source intersecting the several Compton cones obtained from the measurements. Recently, a new Compton satellite called *e-Astrogam* (De Angelis et al. 2017) has been proposed and, if selected for launch, it could become the most sensitive Compton telescope after COMPTEL.

Above 10 MeV the dominant process for gamma rays is pair production due to the interaction of the Coulomb field of a nucleus. For this reason, gamma ray satellites usually are composed by a converter-tracker to track the electron and positron created by the primary photon and a calorimeter for energy reconstruction, as shown in Figure 1.13. From the electron and positron tracks, the incident direction of the gamma ray can be inferred. An anticoincidence system is usually employed to reject the cosmic ray background. The limitation of gamma ray satellites is their small effective area ( $\sim 1 \text{ m}^2$ ), a limited sensitivity and a high cost (depending also on the weight). Nonetheless, they have a good angular and energy resolutions, quite large field of view and high duty cycles. The limitation on the angular resolution is given by the opening angle of the electron-positron pair and, especially at low energies, by multiple scattering. The energy resolution instead is limited by the size of the calorimeter: due to weight limitations, the calorimeter could be too small to contain the whole particle shower created by the initial electron and positron, degrading the energy measurement. So a gamma ray satellite should be designed accurately to achieve the best conversion efficiency and a good sampling of the electron/positron pairs.

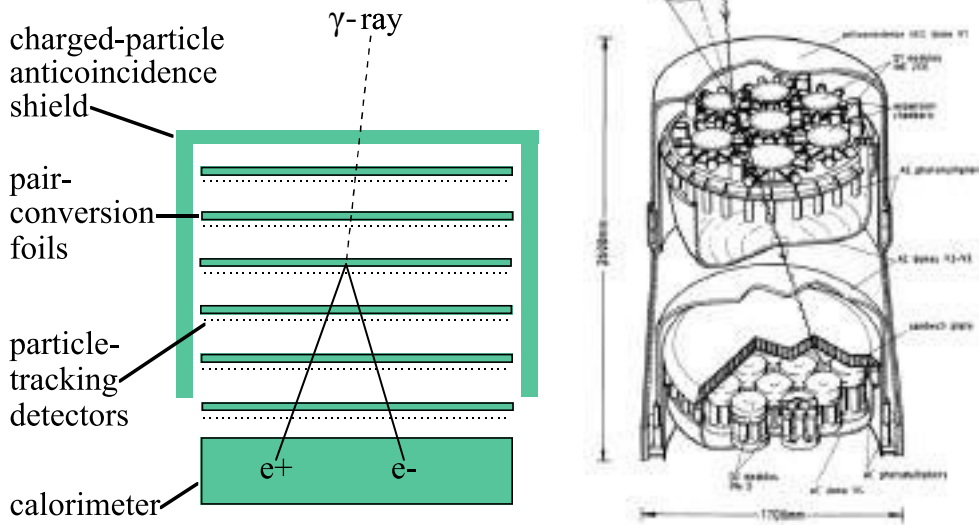


Figure 1.13: **Left:** principle of the gamma ray detection technique via pair production. From <https://heasarc.gsfc.nasa.gov/docs/cgro/images/epo/gallery/glast/>. **Right:** detection of gamma rays with the Compton mechanism. From <https://heasarc.gsfc.nasa.gov/docs/cgro/comptel/>.

An example of gamma ray telescope using the pair production technique is EGRET (*Energetic Gamma Ray Experiment Telescope*), one of the instruments on-board the CGRO. The gamma rays were converting in a spark chamber and the energy was measured in a calorimeter. This technology was well surpassed by the current generation of gamma ray telescopes, AGILE and Fermi. They both use silicon planes for tracking the electron/positron pairs, few of them preceded by a high Z material foil (usually tungsten) to increase the conversion probability. A calorimeter, usually made up of CsI(Tl) crystals, is used for energy measurement. Finally, the anticoincidence system covers the whole instrument and acts as a veto for charged particles background.

Finally, at energies higher than  $\sim 100$  GeV, satellites cannot be used due to their limited effective area and to the intrinsically low fluxes of photons. In this case, ground detectors must be used and the detection of gamma rays is performed indirectly. The reason is that the Earth atmosphere is opaque to gamma rays and, very much like cosmic rays, they produce extensive air showers in the atmosphere. The detection of gamma rays is then performed sampling either the Cherenkov light produced by secondary particles in the shower or sampling directly the secondary particles. In the first case they are called *Imaging Atmospheric Cherenkov Telescopes* (IACTs), in the second instead EAS arrays. The energy detectable by the two types of ground detectors is different: IACT can detect gamma rays from just below 100 GeV to few tens of TeV (or up to 100 TeV), while EAS arrays cover the UHE range. One of these ground facilities is the *Major Atmospheric Gamma-ray Imaging Cherenkov* (MAGIC) telescopes, which is the instrument from which I obtained the data used in my thesis. Since it is a basic piece of information for all the discussions in the following Chapters, the detection technique of gamma rays from the ground is described in detail in Chapter 2.

#### 1.2.4 Sources of gamma rays

There are several class of sources producing gamma rays through non-thermal processes: they are usually associated with compact objects, relativistic jets, violent stellar explosions and shocks. In this Section I will briefly describe the several sources from which we detect gamma

rays. They can be divided in two groups:

- galactic sources: pulsars, pulsar wind nebulae (PWN), supernova remnants, binary systems and the Galactic Centre
- extragalactic sources: starburst galaxies, active galactic nuclei and Gamma-Ray Bursts.

### Pulsars

*Pulsars* are neutron stars, very compact objects spinning rapidly with high magnetic fields from  $10^8$  to  $10^{11}$  T (see Grenier and Harding 2015 for a review). Neutron stars are formed in the collapse of the core of massive stars, while the outer layer is ejected in the interstellar medium in an explosive way i.e. a supernova. The high spin rate (as high as hundreds of revolutions per second in pulsars with periods of milliseconds) is due to the conservation of angular momentum: the object left after the collapse has a mass between one and two solar masses and a radius of about ten kilometers.

In this way the matter inside neutron stars obeys equations of state which are topic of investigation. Neutron stars were found to emit radiation in the radio band in periodic pulses in 1967 and then in optical, X-rays and finally  $\gamma$ -rays. For this reason they were called *pulsars* (*pulsating stars*). Since the strong magnetic field rotates together with the pulsar, strong electric fields are generated and the region around the neutron star is filled with dense plasma forming the so-called *magnetosphere* (see Figure 1.14). Moreover, the strength of the electric fields can extract particles from the surface of the pulsar and fill the magnetosphere with charges. Interaction of the plasma with the magnetic field can generate electron-positron pairs so that the force-free condition is reached:  $\rho\mathbf{E} + \mathbf{j} \times \mathbf{B} = 0$ . The density for which this condition is satisfied is the Goldreich-Julian charge density  $\rho_{GJ}$ . In this way the magnetosphere can rotate together with the neutron star. Moreover, particles can be accelerated along the magnetic field lines where the charge density value differs from the local value of  $\rho_{GJ}$ , so that an electric field parallel to the field lines is generated.

When accelerated, particles emit most of their radiation as gamma rays, which can produce electron-positron pairs in the outer part of the magnetosphere interacting with low energy photons or near the surface interacting with the strong magnetic fields.

The gamma radiation can be produced in different regions: the magnetosphere, the relativistic wind or the surrounding nebula. In each, different mechanisms can account for gamma ray emission. In magnetospheric models, different models put the acceleration region in different location. The most relevant are polar cap and outer gap models. In the former, the emission region is located near the polar caps of the neutron star and gamma rays are emitted mainly via curvature radiation and synchrotron from electron-positron pair cascades, while in the

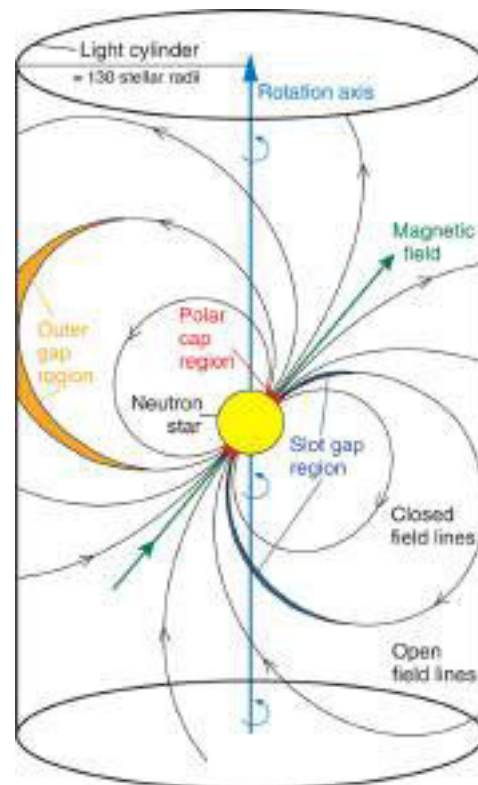


Figure 1.14: Sketch of the magnetosphere of a pulsar. From Aliu et al. (2008a).

latter acceleration happens near the last open field lines. With current observation and simulations, outer gap models seems favored but there is no clear proof yet. A particular type of pulsars are *millisecond pulsars*, which exhibit periods of the order of millisecond and “low” magnetic fields  $10^4$ - $10^6$  T. They are explained as old age pulsars which are recycled through the accretion of matter from a companion star. So the angular momentum is transferred from the accretion disk to the neutron star.

Many studies focus on pulsar variability, like pulsar “nulling” (sudden disappearance and reappearance of the pulses) or pulsars showing different pulse profiles in few minutes, as shown by Lyne et al. (2010). A particular case is the Crab Nebula<sup>1</sup>: it is the first source detected at VHE and it is used as a standard candle for the calibration of HE and VHE instruments due to its steady emission. It came as a complete surprise the observation of flares from the Crab Nebula by AGILE and Fermi-LAT (Wilson-Hodge et al. 2011; Tavani et al. 2011; Abdo et al. 2011), found to be coming from the nebula surrounding the pulsar since the flux of the latter was constant during the flare. To date, Crab Nebula flares are challenging all current models of emission.

In the high-energy range, Abdo et al. (2013) presents a catalog of 117 gamma-ray pulsars detected by Fermi-LAT, among which millisecond pulsars, young radio-loud pulsars, and young radio-quiet pulsars can be found. In the VHE range instead, the only detected pulsars are the Crab pulsar (see for example Aliu et al. 2008b) and the Vela pulsar (Djannati-Ataï et al. 2017).

### 1.2.5 Supernova remnants and pulsar wind nebulae

After the explosion of a supernova, the material ejected moves at speeds of the order of  $0.01c$  and it decelerates as it encounters the ambient medium in a timescale of the order of tens of thousands years. The resulting structure is called *supernova remnant* (SNR). These sources are usually classified as shell-type, *pulsar wind nebulae* and composite (a combination of shell-type and PWN). SNRs are thought to be the sources of galactic cosmic rays because of the presence of strong shocks in which diffusive shock acceleration can take place. Usually, three phases can describe the evolution of a SNR: i) ejecta-dominated phase (swept-up mass less than the ejecta mass), ii) Sedov-Taylor phase where the swept-up mass is larger than the ejecta mass and the SNR undergoes adiabatic expansion, iii) a radiative phase with gas recombination and cooling of the swept-up gas, ending with the SNR becoming indistinguishable from the interstellar medium.

The study of young SNRs like SN1987A (H.E.S.S. Collaboration et al. 2015), Cassiopeia A (Aharonian et al. 2001) and Tycho (Acciari et al. 2011a) can give information about diffusive shock acceleration in the earlier periods of the SNR life and proton acceleration. In particular SN1987A can be used to test when the transition from SN to SNR occurs and when diffusive shock acceleration becomes efficient.

Also shell-type SNRs can be used to probe the radiation mechanisms producing gamma rays. Here the study focuses on the five young shell-type SNRs detected by H.E.S.S. (*High Energy Stereoscopic System*) in the VHE range: RXJ1713.7-3946 (Muraishi et al. 2000), RXJ0852.0-4622 (Katagiri 2005), RCW86 (Aharonian et al. 2009a), SN1006 (Acero et al. 2010) and HESSJ1731-347 (H.E.S.S. Collaboration et al. 2011). In these cases, the detected VHE emission could be explained either as  $\pi^0$  decay emission or IC from leptons. Quite hard spectra observed at HE suggest that probably the hadronic scenario should be discarded. Regardless of the origin of VHE radiation, SNRs are for sure able to accelerate particles up to at least 100 TeV.

Hadronic processes were clearly detected in two middle-aged SNRs, IC443 and W44 (Ackermann et al. 2013a; Giuliani et al. 2011), as shown in Figure 1.15. In this case the SNR

---

<sup>1</sup>To be exact, the Crab is classified as a pulsar wind nebula.

interacts with dense molecular clouds and the  $\pi^0$  bump is clearly evident in the observed spectrum.

Pulsar Wind Nebulae (PWNe) are young and energetic pulsars powering a highly magnetized nebulae and constitute the most abundant class of TeV emitters. They can probably account also for most of the current unidentified sources (e.g. old PWNe offset from the pulsar powering it). PWNe emission is likely to be of leptonic origin as in the case of HESSJ1825-137 (Aharonian et al. 2005a): the X-ray and gamma-ray morphologies are very similar and low magnetic fields imply that the X-ray emission is due to synchrotron by electrons with energies higher than the observed one for gamma-rays, which are then produced via IC scattering.

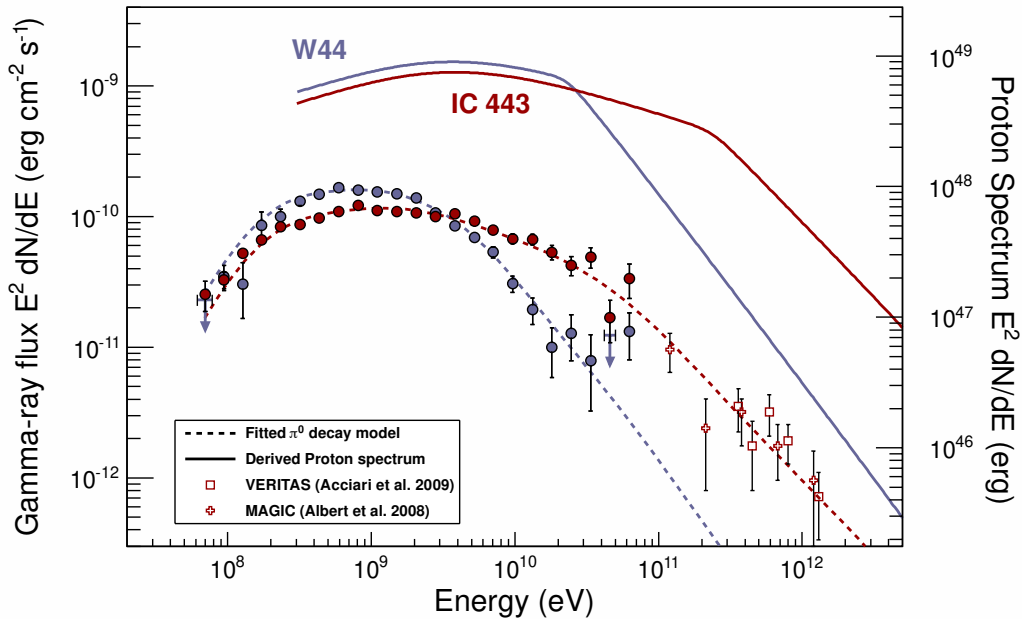


Figure 1.15: Proton and gamma-ray spectra determined for IC443 and W44. From Hewitt and Lemoine-Goumard (2015).

### Binary systems

VHE and HE emission can be produced by binary systems, which can be classified in four classes: *gamma-ray binaries*, *microquasars*, *novae* and *colliding wind binaries*. A sketch is shown in Figure 1.16. See Dubus (2015) for a review.

Gamma-ray binaries (high- and low-mass) are powered usually by pulsars, like in the case of PSRB1259-63 (Aharonian et al. 2005b), a binary system with a 48 ms pulsar and a star of  $\sim 30M_{\odot}$ . In this case VHE emission is seen in the pre- and post-periastron passage, when the pulsar wind interacts with the dense stellar wind of the companion.

Microquasars are powered by the accretion onto a black hole or neutron star of material coming from the companion, consequent release of gravitational energy and possible formation of a relativistic jet. Cyg X-3 and Cyg X-1 (Bodaghee et al. 2013; Malyshev, Zdziarski, and Chernyakova 2013) are detected clearly at HE and this emission is related to radio emission and thus it is associated with the relativistic jet. Cyg X-1 has an evidence of VHE emission by MAGIC when it was observed during a flare (Albert et al. 2007), but it was not confirmed after observations of other flares. As of today, no other X-ray binary was detected at HE or VHE.

Novae are due to the deposition of material on the surface of a white dwarf from a companion star, usually a red dwarf. When a critical pressure is reached, thermonuclear burning is triggered and gamma rays are produced, probably when the material is ejected. The rate

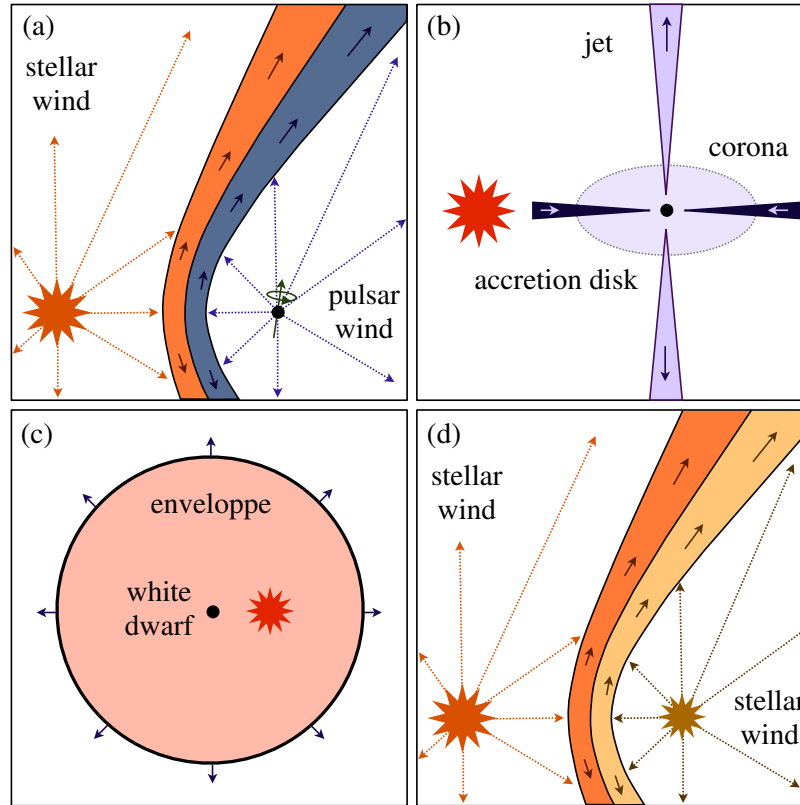


Figure 1.16: The for classes of binaries. (a) A high mass gamma-ray binary with a pulsar. (b) A microquasar. (c) A nova. (d) A colliding wind binary. From Dubus (2015).

of deposition changes strongly the time needed to reach the critical pressure, from tens to thousands of years. Usually most of the energy radiated is released in the optical band. Currently five novae have been detected by Fermi-LAT (Dubus 2015).

Finally, colliding wind binaries (CWB) consists of massive O or Wolf-Rayet stars. Strong winds are produced due to radiation pressure and their interaction forms a (non-relativistic) shock where particles can be accelerated and produce gamma rays. Most of the emission is in the X-ray band from the heating of the gas during the winds collision. Given the high photon and matter densities, gamma ray emission is expected in many cases, but currently only in one CWB, Eta Car (Tavani et al. 2009a; Abdo et al. 2010c), high energy emission was detected. Search for HE emission from similar CWBs resulted in non-detections, signaling that probably diffusive shock acceleration is not as efficient as in SNRs.

### The Galactic Centre

The Galactic Centre hosts a black hole with mass of million times the one of the Sun, associated with the radio source Sgr A\*. Beside the central black hole, many other sources can be observed e.g. star forming regions, SNRs, PWNe and X-ray binaries, as shown in Figure 1.17. The average density of the ISM is one order of magnitude higher than in other regions of the Galactic disk, while magnetic fields are expected to be strong at the level of 5 nT. Many sources were discovered by IACT instruments in the GC region, mainly by the H.E.S.S. experiment which is favored by its location in the Southern hemisphere. The H.E.S.S. measurements of the GC (HESSJ1745-290, Aharonian et al. 2009d) provided a spectrum with relatively hard index  $\Gamma = 2.10 \pm 0.04$  and an exponential cutoff at  $\sim 14$  TeV (Aharonian et al. 2009d). The spectrum suggests that particles could undergo Fermi-type acceleration. The cutoff instead could be explained as absorption of gamma rays by IR background near the

source. With more recent data, the cutoff moved to  $\sim 7$  TeV when considering the effect of diffuse  $\gamma$ -ray emission.

Beside the Galactic Centre, observations were made also in the Central Molecular Zone (CMZ), which extends for  $\sim 300$  pc in galactic longitude. Many sources of different type were discovered, like G0.9+0.1, a composite SNR where protons likely interact with the molecular material (Aharonian et al. 2006).

An interesting structure arising from the GC are the so-called *Fermi bubbles*: they are two symmetric structures with lobe shape and they extend for about 50 degrees from the GC. The interpretation of the nature of the Fermi bubbles is still unclear, but they are probably associated with the IC scattering of high energy electrons accelerated by a large injection in the GC region in the past, likely accretion on the central black hole or a nuclear starburst (Su and van Eldik 2015).

Finally, despite the goodness of current diffuse  $\gamma$ -ray emission models, there is an underestimation of the flux measured by Fermi above few GeV in the GC region. The excess could be explained as decay of dark matter particles (Daylan et al. 2016), but the uncertainties on the modeling of diffuse emission, CR propagation, strength of the magnetic could lead to different explanations.

### Starburst galaxies

*Starburst galaxies* are regions with high star formation rate (SFR) compared to our Galaxy or to other galaxies, see Ohm (2016) for a review. In these systems the gas reservoir is consumed on a timescale of about 1 Gyr (or less) and the starburst event can last up to few 100 Myr. Starburst galaxies can be used to study indirectly CR feedback mainly through  $\gamma$ -ray and X-ray emission. Indeed, cosmic rays have an important role in the star formation since they can trigger complex chemical reactions in the ISM. Since most of Galactic sources are usually associated with the end products of stellar evolution (SNR, PWN, binary systems), starburst galaxies give the chance to study how cosmic rays affect the ISM given their high SFR and supernova explosion rate.

Up to now,  $\gamma$ -ray emission at TeV energies was detected both from nearby starburst galaxies like M82 (Acciari et al. 2009) and NGC253 (Acero et al. 2009) and from other star-forming galaxies like the Large Magellanic Cloud (LMC) (Abramowski et al. 2015). Several models can explain the gamma ray emission, among which the most relevant are hadronic interactions producing charged and neutral pions decaying into gamma rays, synchrotron, IC and bremsstrahlung from electrons or protons or advection of CR in the starburst wind after diffusive escape. The starburst conditions must be taken properly into account in the modeling, in particular the different properties of the ISM, which is much denser. The increased SFR leads to a higher number of stars and thus UV photons which are absorbed by dust and re-emitted in the IR band. Magnetic fields as well are stronger than those present in the Milky Way, resulting in a faster cooling of non-thermal particles. Moreover, the relative importance of the previous processes depends strongly on the electron-to-proton ratio.

### Active Galactic Nuclei

*Active Galactic Nuclei* (AGN) are sources powered by the accretion and infalling of matter onto a central supermassive ( $10^6 - 10^{10} M_{\odot}$ ) black hole and the conversion of the gravitational potential energy of the infalling matter can power a relativistic jet. They are characterized by high luminosities ( $L_{\text{bol}} \sim 10^{48}$  erg/s), small emitting regions ( $\mathcal{O}(\text{mpc})$ ), rapid variability and emission covering the whole electromagnetic spectrum. For a review of AGN, see for example Dermer and Giebels (2016) or Padovani et al. (2017).

The classification of AGN comprises several sub-classes but the basic dichotomy is between *radio-quiet* and *radio-loud* AGN. Most of the AGN, roughly 90%, are radio-quiet. A sketch

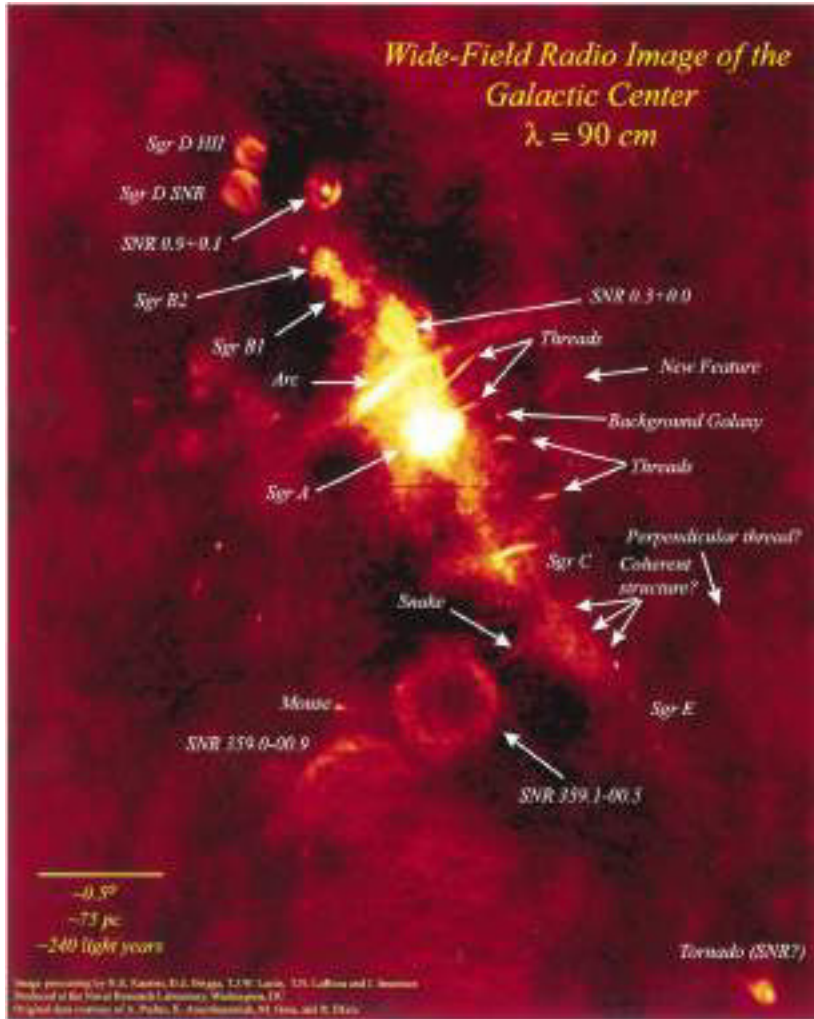


Figure 1.17: Wide-field image of the Galactic Centre performed in the radio band by the Very Large Array. The direction of the the Galactic Plane is from bottom-right to top-left. Several sources (SNRs and PWNe) are indicated by arrows with their names. The Galactic nucleus is the brightest spot in the image. The CMZ region extends from Sgr E (bottom right) to Sgr D (top left). From Su and van Eldik (2015).

of the main classes of AGN is shown in Figure 1.18. The classification is made based on observational properties, like the presence of optical lines or their radio loudness, but following the so-called *unification scheme* (Urry and Padovani 1995; Netzer 2015), the several classes are associated to the change of few basic parameters, namely the orientation between the jet and the line of sight, accretion rate and black hole spin parameter, as shown in Figure 1.19. At VHE, most of the detected AGN are *blazars*, that is AGN with the jet aligned with the line of sight. Blazars are further classified in *BL Lac* objects and *Flat Spectrum Radio Quasars* (FSRQs), characterized by a low and high luminosity respectively (see Figure 1.19) and by the presence or absence of broad optical emission lines. Moreover FSRQs get their name from the quite flat spectrum (spectral index  $\sim 0$ ) at few GHz. Beside blazars, also few radio galaxies were detected in the VHE range.

The spectral energy distribution (SED) of blazars has a double-humped shape and covers the whole electromagnetic spectrum from radio to gamma ray energies. The first hump is generally attributed to synchrotron radiation from relativistic electrons and is located between the IR and X-ray bands. Based on the location of the synchrotron peak, blazars are called *low synchrotron peak* (LSP) if  $\nu_{\text{syn,peak}} < 10^{14}$  Hz or *high synchrotron peak* (HSP) if

$\nu_{\text{syn,peak}} > 10^{15}$  Hz. Blazars with the synchrotron peak at intermediate frequencies are called *intermediate synchrotron peak* (ISP). The explanation for the second peak in the SED of AGN is more challenging to explain. Leptonic models propose the SSC mechanism (electrons up-scatter the photons they produced by synchrotron) or the external inverse Compton process (electrons up-scatter photon in an external field) as the origin of the second hump. Hadronic models instead consider gamma rays to be produced via synchrotron radiation by protons or photo-meson interactions. In the latter case, neutrinos are also expected to be produced. Another interesting topic in AGN studies is their variability, which occurs at different timescales ranging from minutes to months. The origin of this variability is still matter of debate. Nevertheless, multiwavelength observations of AGN during variable states can provide information on the size of the emitting region and on its location with respect to the central black hole. Finally, distant AGN can be used to constrain the EBL. Two examples are PKS 1441+25 and QSO B0218+357. The first one is a FSRQ at redshift  $z = 0.939$  detected by MAGIC during a flare (Mirzoyan 2015; Ahnen et al. 2015) and confirmed by VERITAS (*Very Energetic Radiation Imaging Telescope Array System*, Abeysekara et al. 2015a). The second one is a gravitationally lensed blazar, probably a FSRQ, at  $z = 0.944$  which showed a flare in HE in July 2014 (Buson and Cheung 2014). Due to the gravitational lensing, the emission is split in two components delayed by about 11 days. MAGIC observed the source at the time when the second component was expected after the HE flare and detected it at a significance of  $5.7\sigma$  (Mirzoyan 2014; Ahnen et al. 2016). The inferred spectra of such distant sources are very useful to put constraints on the scaling parameters of the optical depth predicted by different models and put upper limits on the density of the EBL for a particular distance and wavelength range, see for example Ahnen et al. (2015).

### Gamma-Ray Bursts

Gamma-Ray Bursts (GRBs) are the most luminous and violent explosions occurring in the Universe, because they release a huge amount of energy as high as  $10^{51}$  erg on a timescales of seconds and even less. GRBs link together many branches of physics: special and general relativity, astroparticle physics, theoretical physics, cosmology and many others. They are the perfect target for both multi-wavelength and multi-messenger astrophysics thanks to their emission in several bands of the electromagnetic spectrum and to the very recent observation of a GRB (GRB170817A) associated with a gravitational wave signal detected by LIGO and Virgo, GW170817.

Since it is one of the main topics of my thesis, GRBs are described in detail in Chapter 5.

## 1.3 Status and prospects of VHE astronomy

As described in the previous Section, the VHE sky is populated by a wealth of sources, see Figure 1.20. Currently, more than 200 sources are detected in this band (see <http://tevcat.uchicago.edu/>). The reason behind this success is to be attributed to the better sensitivity of current ground-based facilities and to the more sophisticated analysis techniques with respect to the previous generations of ground-based telescopes. Also multiwavelength campaigns are one of the main drivers of current VHE astronomy. Before the operation of current IACTs, only a handful of sources (14) were discovered at VHE but with the new generation the number of sources exponentially increased during the years. This trend is shown by the so called *Kifune plot* (Figure 1.21): it displays the evolution in time of the number of sources in different energy bands (X,  $\gamma$ -rays and VHE  $\gamma$ -rays). The conclusion that can be drawn from the Kifune plot is that currently (and the same was in the past) the sensitivity of the instruments limits the number of detectable sources. Since the brightest have probably been already detected, only a boost in sensitivity or very deep exposures are needed to discover new sources. In this sense, the future of ground gamma-ray astronomy

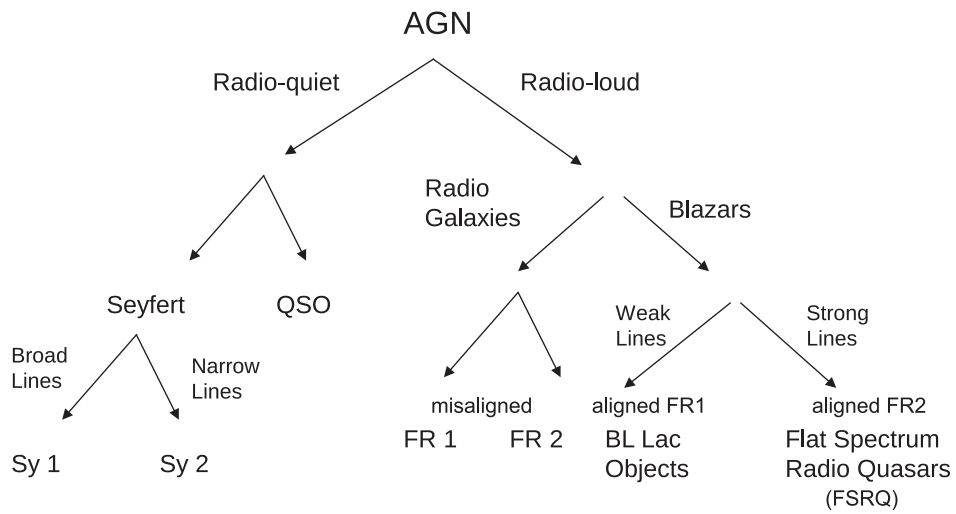


Figure 1.18: AGN classification scheme. The following abbreviations are used: QSO (Quasistellar objects); Sy1 and Sy2 (Seyfert 1 and 2); FR1 and FR2 (Fanaroff-Riley 1 and 2). From Dermer and Giebels (2016).

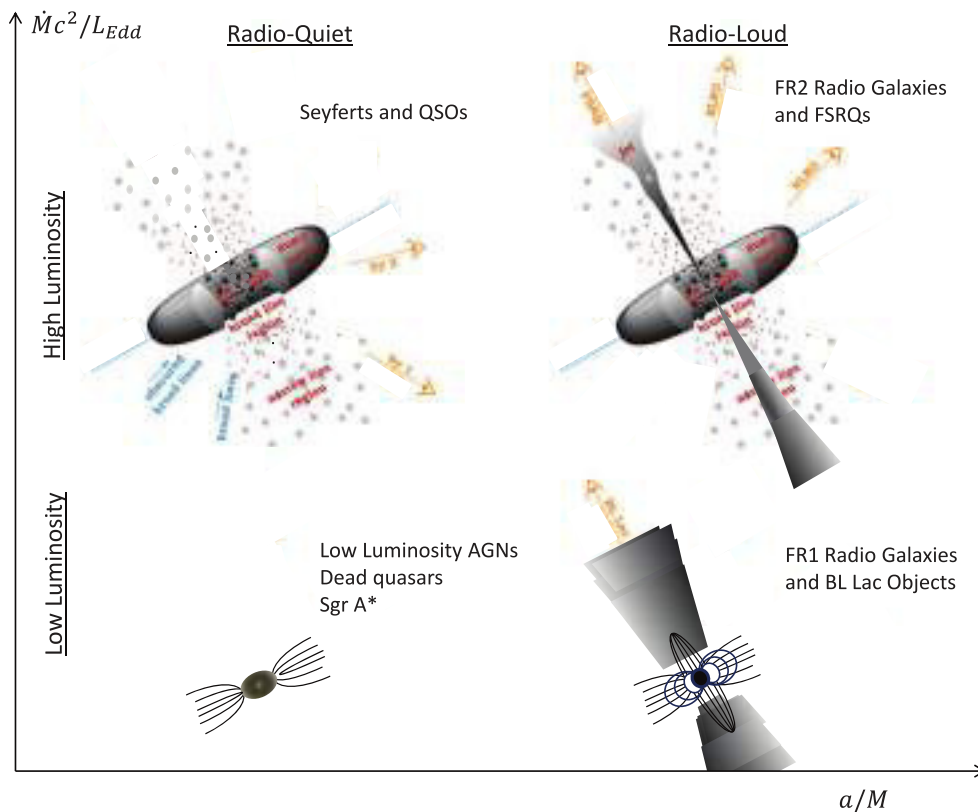


Figure 1.19: AGN unified scheme: AGN classes correspond to different accretion rates, black holes spin parameter and different orientation with respect to the observer. From Dermer and Giebels (2016).

seems to be bright thanks to the new experiment *Cherenkov Telescope Array* (CTA, Acharya et al. 2013), that will cover the energy range from  $\sim 20$  GeV to few hundreds of TeV with unprecedented sensitivity (a factor about three better at low energies and up to one order of magnitude better around few TeV) thanks to a large number of telescopes of different sizes to cover different energy ranges. The Large Area Telescopes (LSTs, Cortina and Teshima 2015) will be 23 m diameter Cherenkov telescopes mostly sensitive in the low energy regime below 200 GeV. Moreover it will have fast slewing capabilities allowing to reposition the telescopes in less than 20 s, which is ideal for transient searches. The Medium Size Telescopes (MSTs, Garczarczyk et al. 2015) will cover the core energy range from around 100 GeV to about 10 TeV and they will increase the effective area at those energies.

Finally, the Small Size Telescopes (SSTs, Montaruli et al. 2015) will try to catch the gamma-rays at the highest energies, around few hundreds of TeV.

In order to have a better sky coverage and perform different kind of studies, CTA will be split in two sites, one in the Northern and one in the Southern hemisphere. In their final configurations, CTA North will host 4 LSTs and 15 MSTs in the La Palma site (the same as MAGIC) while CTA South will have 4 LST, 25 MSTs and 70 SSTs covering a huge area in Paranal, Chile. The northern site will focus on the Extragalactic sky and on transient phenomena. The southern site instead, given its position, will focus on Galactic science.

Thanks to the improvements envisioned for CTA in angular and energy resolutions, energy coverage, sensitivity and field of view, hopefully some of the questions of current VHE astronomy will find an answer, namely (see also Cherenkov Telescope Array Consortium et al. 2017):

- the origin of Dark Matter, both studying dwarf galaxies or the Galactic Halo;
- the existence of VHE emission from GRBs;
- nature of the sources of astrophysical neutrinos;
- sources of UHECRs (the so called *PeVatrons*);
- identification of sources detected in the VHE range but with no X-ray or radio counterpart, so that they are not classified; because some acceleration mechanism is expected to produce the VHE emission, they are called *dark accelerators*

Currently the first LST is being built in La Palma and the first prototypes of both MSTs and SSTs were already built and tested. Few years of waiting are between us and a new era of many discoveries and new challenges.

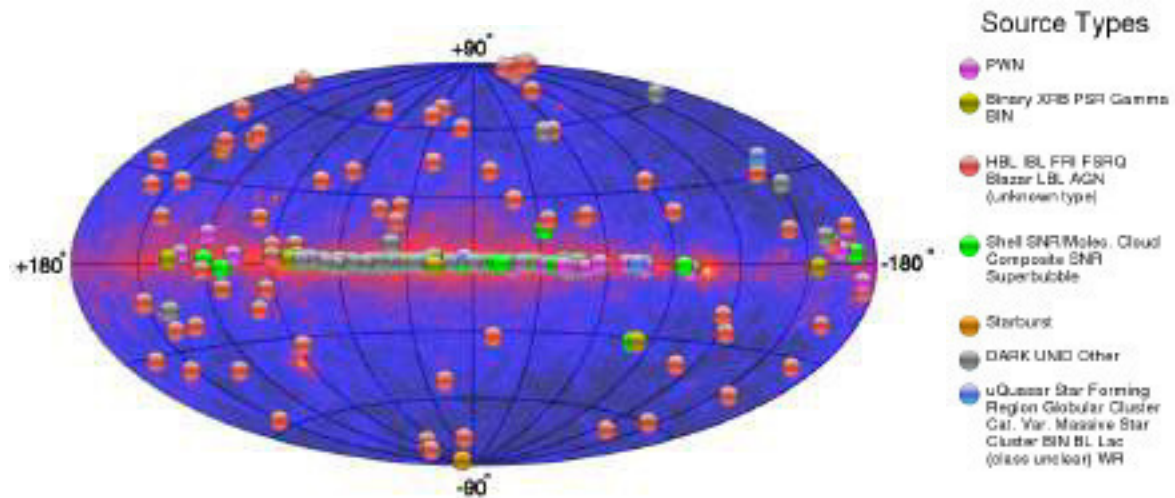


Figure 1.20: Skymap of the VHE sources detected up to date with the Fermi-LAT HE skymap on the background. Different colors correspond to different types of sources, see the legend on the right. From <http://tevcat.uchicago.edu/>.

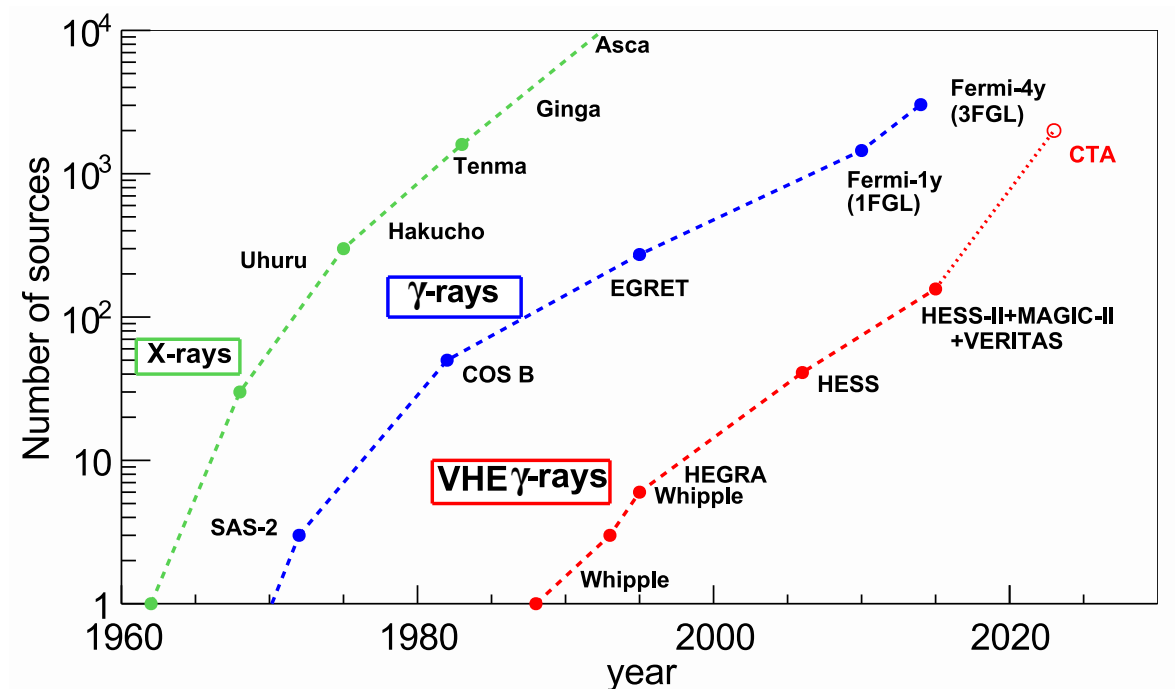


Figure 1.21: Kifune plot showing the temporal evolution of the number of detected sources in different energy bands. Also an extrapolation to the expected number of sources detectable by the current Cherenkov array experiment CTA is shown. From Naurois and Mazin (2015).

## Chapter 2

# EXTENSIVE AIR SHOWERS

The detection technique used by MAGIC and by the other Cherenkov telescopes is based on the development of *extensive air showers* (EAS), discovered at the end of the thirties in the twentieth century (for an historical review see (Kampert and Watson 2012)). A primary particle, being a cosmic ray or a gamma ray, interacting with the atmosphere produces many secondary particles which can decay (e.g. pions, kaons) or interact with the atmospheric medium. Many of these secondary particles are energetic electrons, positrons and muons which produce flashes of Cherenkov light. This effect is exploited by Cherenkov telescopes like MAGIC to obtain information on the primary particle producing the air shower. In particular, MAGIC is interested in air showers initiated by  $\gamma$ -rays, called *electromagnetic showers* (the same term is used for electron initiated showers). Cherenkov telescopes do not record only electromagnetic showers, but most of the showers recorded have a cosmic ray as parent (mostly protons): they are called *hadronic showers*. These events constitute an unwanted background to the events of interest (gamma rays), but can be removed almost completely thanks to the analysis techniques developed during the years, described in Chapter 4.

This Chapter is devoted to the description of the main properties of electromagnetic and hadronic showers (Sections 2.1 and 2.2). Then in Section 2.3 I will focus on the Cherenkov emission in EAS, underlining the features which make possible the Imaging Atmospheric Cherenkov Technique. I will also introduce the simulation of extensive air showers with CORSIKA (Section 2.4). Finally, other detection technique for EAS will be described in Section 2.6.

## 2.1 Electromagnetic showers

### 2.1.1 Introduction

Electromagnetic showers are initiated by high-energy electrons or  $\gamma$ -rays interacting with the atmosphere.

In the following I will focus on  $\gamma$ -ray-initiated showers, but all the considerations hold true for electron-initiated showers. From the interactions point of view, the processes in a shower produced by a primary electron or a gamma ray are the same. Going more in detail, the main physical processes involved in electromagnetic showers are the following:

- *pair production*, when a gamma ray, interacting with the Coulomb field of the nuclei in the atmosphere, produces an electron-positron pair;
- *bremstrahlung*, when an electron or positron emits a photon interacting with the Coulomb field of the nuclei.

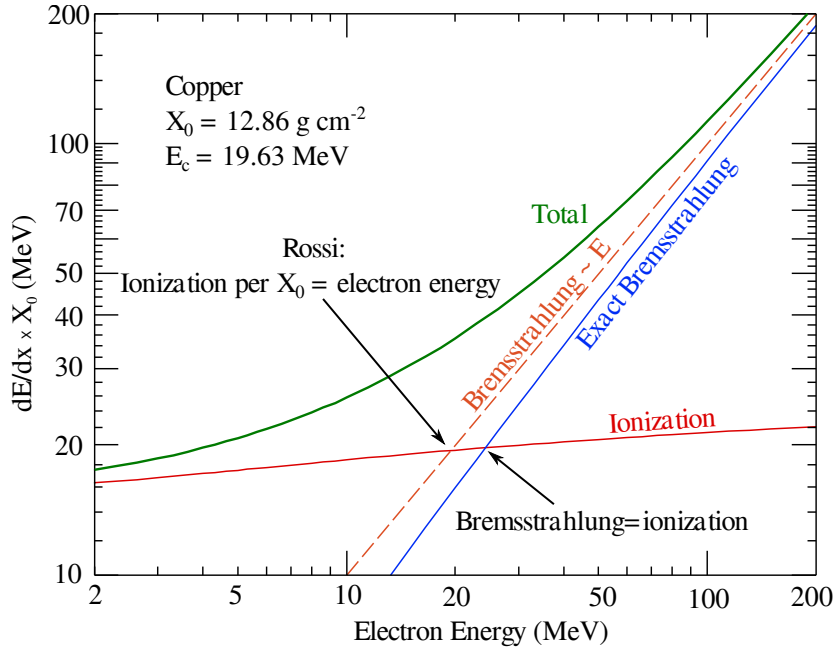


Figure 2.1: Definitions of the critical energy  $E_c$ . Adapted from Olive (2014).

Before going in detail for these two processes, it is useful to introduce two quantities. The first one is the so-called *critical energy*,  $E_c$ , and can be defined as follows: it is the energy at which a particle loses equal amounts of energy per unit radiation length,  $X_0$  (defined later), by ionization and bremsstrahlung. Another definition, given by Rossi and Greisen, is that  $E_c$  is the energy at which ionization loss per unit radiation length is equal to the electron energy. See Figure 2.1 for a graphical representation of the two definitions, which are equal if in the first case the approximation  $|dE/dx|_{\text{br}} \approx E/X_0$  is valid. An important factor in these processes is the *screening* of the nucleus (and consequently the screening of the nuclear field) by the outer electrons. If the distance at which the radiation process occurs is larger than the nuclear radius but smaller than the atomic radius, the nuclear field can be thought as the one produced by a point-like particle of charge  $Z$ . If the distance is comparable with the atomic radius or larger, the nucleus will be partially or completely screened by the outer electrons. Finally, if the distance is of the order of the nuclear radius, then the point-like field approximation no longer holds. For most applications, it is enough to determine an energy scale, called the *screening energy*  $E_{\text{scr}}$ , to distinguish between screening or no screening situation. The screening energy is defined as (Grieder 2010):

$$E_{\text{scr}} = \frac{m_e c^2}{\alpha Z^{1/3}} \quad (2.1)$$

where  $Z$  is the atomic number of the medium. If energies are well above the screening energy, we have complete screening.

I will now describe in more detail the bremsstrahlung and pair production processes.

### 2.1.2 Bremsstrahlung

Bremsstrahlung is the main process through which electrons and positrons lose energy at high and very high energies in extensive air showers. At low energies energy losses by ionization (described by the famous Bethe-Block formula) are dominant, but are not relevant in the development of electromagnetic showers. In air we have  $E_c > E_{\text{scr}}$  (84 MeV and 36.5 MeV respectively) and since we want to consider energies above the critical energy, we are in the complete screening case. In this limit and for very high energies, the bremsstrahlung cross

section as a function of the radiated photon energy  $k$  is (Olive 2014):

$$\frac{d\sigma_{\text{br}}}{dk} = \frac{4\alpha r_e^2}{k} \left\{ \left( \frac{4}{3} - \frac{4}{3}y + y^2 \right) [Z^2(L_{\text{rad}} - f(Z)) + ZL'_{\text{rad}}] + \frac{1}{9}(1-y)(Z^2 + Z) \right\} \quad (2.2)$$

where  $y = k/E$ , with  $E$  the electron energy, and  $r_e$  is the classical radius of the electron. In this expression,  $L_{\text{rad}} = \ln(184.15 Z^{-1/3})$ ,  $L'_{\text{rad}} = \ln(1194 Z^{-2/3})$  and  $f(Z)$  is called *Coulomb correction*, see Tsai (1974). In the infrared limit (small  $y$ ), the second term in the curly braces can be neglected. The first term can be simplified if we calculate the average energy loss of an electron by bremsstrahlung:

$$-\left\langle \frac{dE}{dx} \right\rangle_{\text{br}} = 4\alpha r_e^2 \frac{N_A}{A} [Z^2(L_{\text{rad}} - f(Z)) + ZL'_{\text{rad}}] E = \frac{E}{X_0} \quad (2.3)$$

where  $N_A$  is the Avogadro's number and  $A$  the mass number of the medium. Here we have introduced the aforementioned *radiation length*  $X_0$ , which for bremsstrahlung corresponds to the mean distance traveled by an electron to lose all but a factor  $1/e$  of its energy. So the cross section now reads:

$$\frac{d\sigma_{\text{br}}}{dk} = \frac{A}{X_0 N_A k} \left( \frac{4}{3} - \frac{4}{3}y + y^2 \right) \quad (2.4)$$

For  $y = 1$  this expression is no longer valid because the screening may not be complete anymore, while for  $y \approx 0$  some suppression effects arises which reduce the radiation emitted.

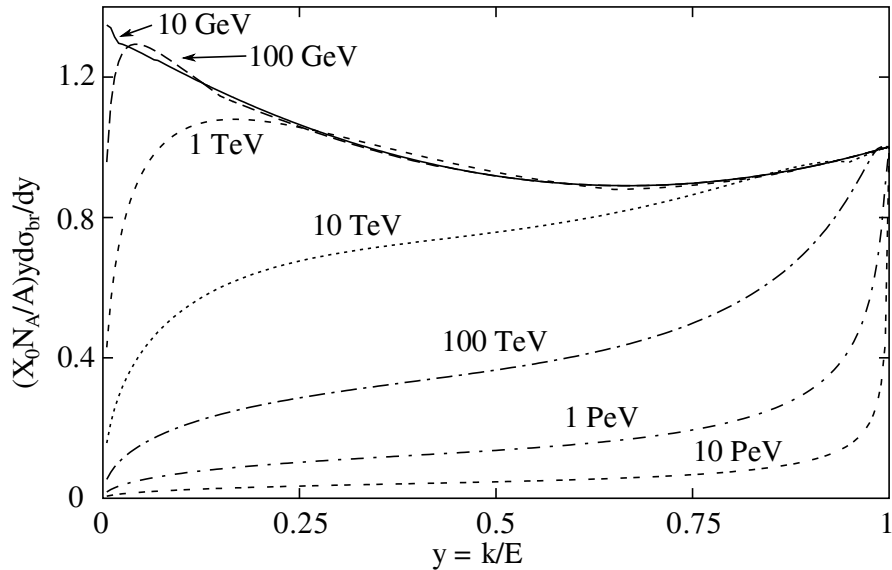


Figure 2.2: Normalized cross section for Bremsstrahlung in lead versus the fractional photon energy  $y = k/E$ . Adapted from Olive (2014).

Remaining in the complete screening approximation, the number of photons emitted between energies  $k_{\text{min}}$  and  $k_{\text{max}}$  by an electron of energy  $E$  traveling a distance  $d$  much smaller than the radiation length of the medium is given by (Olive 2014):

$$N_\gamma = \frac{d}{X_0} \left[ \frac{4}{3} \log \left( \frac{k_{\text{max}}}{k_{\text{min}}} \right) - \frac{4}{3} \frac{(k_{\text{max}} - k_{\text{min}})}{E} + \frac{k_{\text{max}}^2 - k_{\text{min}}^2}{2E^2} \right] \quad (2.5)$$

For the following discussion it is useful to introduce also the *reduced depth*  $t = x/X_0$ , that is simply a thickness measured in radiation lengths. The average energy loss per radiation

length is linked with the differential radiation probability per radiation length which, in the case of high energies with complete screening, is given by (Grieder 2010):

$$\varphi_0(y)dy = \left[ 1 + (1-y)^2 - (1-y) \left( \frac{2}{3} - 2b \right) \right] \frac{dy}{y} \quad (2.6)$$

with  $b = 1/[18 \log(184.15Z^{-1/3})]$ . So we have:

$$-\frac{1}{E} \left\langle \frac{dE}{dt} \right\rangle_{\text{br}} = -X_0 \frac{1}{E} \left\langle \frac{dE}{dx} \right\rangle_{\text{br}} \approx \int_0^1 y \varphi_0(y) dy = 1 + b \quad (2.7)$$

The parameter  $b$  gives a contribution to the average energy loss, but for different values of the atomic number it ranges from 0.012 to 0.015 if we consider the case of air ( $Z = 7.3$ ) and lead ( $Z = 82$ ), so it can be neglected without harm.

### 2.1.3 Pair Production

At high energies (tens of MeV), photons lose energy through pair production. At low energies process like the photoelectric effect, the Rayleigh scattering and the Compton scattering are dominant.

In the case of high energies and complete screening, the differential cross section for pair production as a function of the fractional energy transfer  $x = E/k$  to the produced electron (or positron), with  $k$  the photon energy and  $E$  the electron (positron) energy, is given by (Olive 2014):

$$\frac{d\sigma_{\text{pair}}}{dx} = \frac{A}{X_0 N_A} \left[ 1 - \frac{4}{3}x(1-x) \right] \quad (2.8)$$

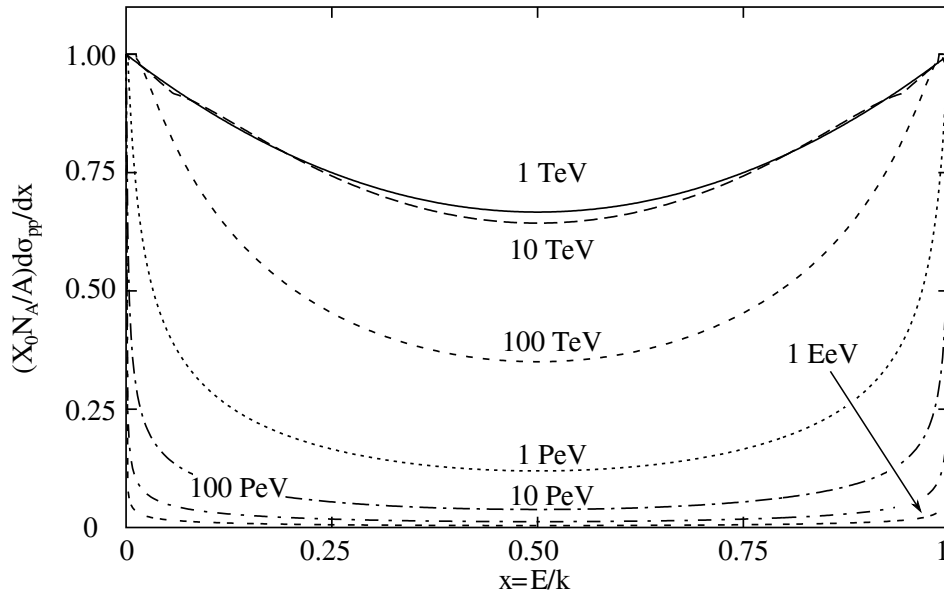


Figure 2.3: Normalized cross section for pair production versus the fractional electron energy  $x = k/E$ . Adapted from Olive (2014).

In the case of pair production, the radiation length is defined as the average track after which the photon will convert into a pair and is strictly linked with the radiation length for bremsstrahlung:

$$X_{0,\text{pair}} = \frac{9}{7} X_{0,\text{br}} \quad (2.9)$$

Finally I give the differential probability per unit radiation length  $X_{0,\text{pair}}$  for a photon to produce an electron-positron pair, see Lipari (2009):

$$\psi_0(x)dx = \left[ x^2 + (1-x)^2 + \left( \frac{2}{3} + 2b \right) x(1-x) \right] dx \quad (2.10)$$

From this one can obtain the total pair production probability per radiation length:

$$\sigma_0 = \int_0^1 dx \psi_0(x) = \frac{7}{9} - \frac{b}{3} \quad (2.11)$$

#### 2.1.4 Heitler model for electromagnetic shower development

The development of an electromagnetic shower, from the point view of the number of particles (electrons, positrons and photons) and energy partition, can be quantitatively and qualitatively understood in an approximate way using the so-called *Heitler model* (Heitler 1954). In this one dimensional model, the primary particle is considered to be a photon of energy  $E_0$  interacting in the atmosphere. After an average thickness  $X_0$  of air, the photon will undergo pair production and produce an electron and positron, which in turn will radiate photons by bremsstrahlung after an average path of  $X_0$ , then the process repeats for the newly created photons and electrons/positrons. At each step the energy is split among the new particles involved, until the energy goes below the critical energy  $E_c$ . At this point ionization losses for electrons/positrons and low energy processes for photons reduce the number of particles in the shower until they are completely absorbed.

If  $n$  is the number of steps considered for the toy model, then after  $n$  steps the number of particles will be  $2^n$ . Assuming that the energy is split equally between the parent particle and the particles produced by bremsstrahlung or pair production, then at the  $n$ -th step the energy of each particle is  $E_n = E_0/2^n$ . A more realistic model should consider also the energy distribution of bremsstrahlung photons, see for example Gaisser (1990).

From this toy model the depth of the shower maximum can be inferred, that is the depth, calculated in units of radiation lengths, at which the maximum number of particles is reached. Of course this occurs when the particles have an energy equal to the critical energy, because after that the number of particles will be certainly reduced. Since the Heitler model assumes as natural scale the radiation length, the reduced radiation length  $t$  can be used to characterize the longitudinal development of the shower instead of the number of steps  $n$ . After  $t$  radiation lengths the shower will have  $N = 2^t$  particles, but the maximum number will be reached at a reduced depth  $t_{\text{max}}$  such that:

$$\int_0^{t_{\text{max}}} 2^t dt = \frac{E_0}{E_c} \quad (2.12)$$

So  $t_{\text{max}}$  reads:

$$t_{\text{max}} \simeq \frac{\log(E_0/E_c)}{\log(2)} \quad (2.13)$$

Since the maximum number of particles is linked with  $2^{t_{\text{max}}}$ ,  $N$  is proportional to the energy of the primary particle  $E_0$ .

Despite being so simple, the Heitler model gives qualitatively the same trends which can be derived in a more difficult way using the whole analytic treatment.

#### 2.1.5 Cascade equations for electromagnetic showers

The development of an electromagnetic shower was studied in detail by Rossi and Greisen (1941), giving analytic expressions for the differential energy spectra of electrons and photons at a depth  $t$ , called  $n_e(E, t)$  and  $n_\gamma(E, t)$  respectively. These solutions were given in two approximations:

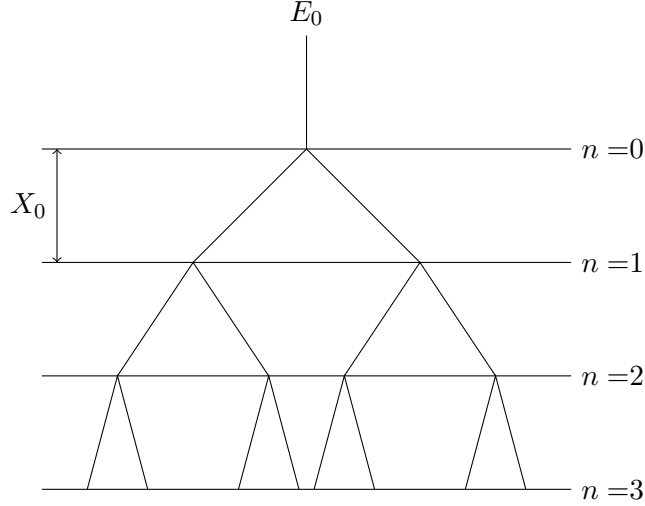


Figure 2.4: Heitler toy model for the development of electromagnetic showers.

- *Approximation A*: the energies involved in the shower development are higher than the critical energy and so only bremsstrahlung for electrons and pair production for photons are considered;
- *Approximation B*: near the critical energy, energy losses of electrons by collisions are taken into account as an energy independent loss  $\varepsilon$  per radiation length.

The differential spectra for electrons and photons follow the so-called *cascade equations*, which can be found easily with the following considerations:

- the number of electrons in a layer  $dt$  with energy between  $dE$  and  $E + dE$  can change if photons with  $E_\gamma > E$  pair produce electrons/positrons in the range  $(E, dE)$ , if electrons with  $E' > E$  radiate and losing energy they end up with an energy between  $E$  and  $dE$  or if electrons leave this energy interval after radiating;
- the number of photons in a layer  $dt$  with energy between  $dE$  and  $E + dE$  changes if electrons radiate photons in that energy interval or if photons in the same interval are absorbed by pair production.

With these considerations, the cascade equations in Approximation A can be written as (Rossi and Greisen 1941; Lipari 2009):

$$\left. \frac{\partial n_e(E, t)}{\partial t} \right|_{\text{ApproxA}} = - \int_0^1 dy \varphi_0(y) \left[ n_e(E, t) - \frac{1}{1-y} n_e\left(\frac{E}{1-y}, t\right) \right] + 2 \int_0^1 \frac{dx}{x} \psi(x) n_\gamma\left(\frac{E}{x}, t\right) \quad (2.14)$$

$$\left. \frac{\partial n_\gamma(E, t)}{\partial t} \right|_{\text{ApproxA}} = \int_0^1 \frac{dy}{y} \varphi_0(y) n_e\left(\frac{E}{y}, t\right) - \sigma_0 n_\gamma(E, t) \quad (2.15)$$

The cascade equations have some trivial solutions of the form:

$$n_e(E, t) = E^{-(s+1)} \left[ a_1 e^{\lambda_1(s)t} + a_2 e^{\lambda_2(s)t} \right] \quad (2.16)$$

$$n_\gamma(E, t) = E^{-(s+1)} \left[ b_1 e^{\lambda_1(s)t} + b_2 e^{\lambda_2(s)t} \right] \quad (2.17)$$

where the coefficients  $a_{1,2}$  and  $b_{1,2}$  and the functions  $\lambda_{1,2}(s)$  are given in Appendix A. The cases with an initial photon or electron as boundary conditions make the calculation more difficult, but with the use of the Mellin and Laplace transforms and the saddle point method, an analytic, well approximated solution can be found:

$$n_\alpha(E_0, E, t) \simeq \frac{1}{E_0} \frac{1}{\sqrt{2\pi}} \left[ \frac{G_\alpha(s)}{\sqrt{\lambda_1''(s)t}} \left( \frac{E}{E_0} \right)^{-(s+1)} e^{\lambda_1(s)t} \right]_{s=\bar{s}(E/E_0, t)} \quad (2.18)$$

with:

$$\bar{s}(E/E_0, t) \simeq \frac{3t}{t - 2 \log(E/E_0)} \simeq \frac{3t}{t - 2t_{\max}} \quad (2.19)$$

and  $\alpha$  indicates whether we are considering an initial electron or photon and the electron or photon spectrum (so four cases in total). See Appendix A for the definition of the functions  $G_\alpha(s)$ .

From the differential spectra we can obtain the integral one:

$$N_\alpha(E_0, E, t) \simeq \frac{1}{\sqrt{2\pi}} \left[ \frac{1}{s} \frac{G_\alpha(s)}{\sqrt{\lambda_1''(s)t}} \left( \frac{E_{\min}}{E_0} \right)^{-s} e^{\lambda_1(s)t} \right]_{s=\bar{s}(E/E_0, t)} \quad (2.20)$$

The parameter  $\bar{s}$ , or simply  $s$ , is called *shower age*. Its name comes from the fact that the energy dependent part of the spectrum is approximately a power law with spectral index  $-(s+1)$ : for  $s < 1$  the spectrum describes the growing phase of the shower development, while for  $s > 1$  the declining phase.  $s = 1$ , as the following will prove, corresponds to the shower maximum. So the parameter  $s$  can be effectively used to describe the longitudinal development of an electromagnetic shower.

Rossi's and Greisen's Approximation A is a good starting point to understand general properties of electromagnetic showers, but it does not take into account the ionization losses of electrons. As anticipated, Approximation B deals with this problem. The cascade equation (2.14) is modified by adding the ionization loss term in the right hand side, while (2.15) remains unchanged. The cascade equations in Approximation B reads (Rossi and Greisen 1941; Lipari 2009):

$$\begin{aligned} \left. \frac{\partial n_e(E, t)}{\partial t} \right|_{\text{ApproxB}} &= - \int_0^1 dy \varphi_0(y) \left[ n_e(E, t) - \frac{1}{1-y} n_e \left( \frac{E}{1-y}, t \right) \right] + \\ &+ 2 \int_0^1 \frac{dx}{x} \psi(x) n_\gamma \left( \frac{E}{x}, t \right) + \epsilon \frac{\partial n_e(E, t)}{\partial t} \end{aligned} \quad (2.21)$$

$$\left. \frac{\partial n_\gamma(E, t)}{\partial t} \right|_{\text{ApproxB}} = \int_0^1 \frac{dy}{y} \varphi_0(y) n_e \left( \frac{E}{y}, t \right) - \sigma_0 n_\gamma(E, t) \quad (2.22)$$

The ionization energy loss per unit radiation length  $\epsilon$  is considered to be constant and equal to the critical energy in the medium, which in air is  $\simeq 84$  MeV. In this case it is not possible to find an exact close form for the electron and photon spectra for an initial photon or electron, but the solutions for the cascade equations in Approximation A can be used to write down an approximation of the solutions in Approximation B:

$$n_{e(\gamma) \rightarrow e}(E_0, E, t) \simeq [n_{e(\gamma) \rightarrow e}(E_0, E, t)]_{\text{ApproxA}} \times p_1 \left[ \bar{s} \left( \frac{\epsilon}{E_0}, t \right), \frac{E}{\epsilon} \right] \quad (2.23)$$

$$n_{e(\gamma) \rightarrow \gamma}(E_0, E, t) \simeq [n_{e(\gamma) \rightarrow \gamma}(E_0, E, t)]_{\text{ApproxA}} \times g_1 \left[ \bar{s} \left( \frac{\epsilon}{E_0}, t \right), \frac{E}{\epsilon} \right] \quad (2.24)$$

The effect of ionization losses are taken into account by  $p_1$  and  $g_1$  functions, which have the asymptotic behaviors:

$$\lim_{x \rightarrow \infty} p_1(s, x) = 1 \quad \lim_{x \rightarrow \infty} g_1(s, x) = 1 \quad (2.25)$$

$$p_1(s, x) \propto_{x \rightarrow 0} x^{s+1} \quad g_1(s, x) \propto_{x \rightarrow 0} x^s \quad (2.26)$$

with  $x = E/\varepsilon$ . Equations (2.25) follow from the fact that at high energies with respect to the critical energies, ionization losses can be safely neglected and so the solutions obtained in Approximation A are expected. Equation (2.26) instead reflects the behavior near and below the critical energy. For the electron spectrum one expects a cutoff due to the ionization losses, while for the photon spectrum below the critical energy we expect a  $E^{-1}$  dependence from the bremsstrahlung cross section.

In the case of Approximation B, analogously to Approximation A, the natural definition of the age parameter is given by (Lipari 2009):

$$\bar{s}(E/E_0, t) \simeq \frac{3t}{t - 2 \log(E/\varepsilon)} \quad (2.27)$$

Using again the saddle point method, one can obtain the integral spectra for electrons, or *total electron size*:

$$N_{\gamma(e) \rightarrow e}(E_0, t) \simeq \frac{1}{\sqrt{2\pi}} \left[ \left( \frac{E_0}{\varepsilon} \right)^s \frac{K_1(s, -s)}{s} \frac{G_{\gamma(e) \rightarrow e}(s)}{\sqrt{\lambda_1''(s)t}} e^{\lambda_1(s)t} \right]_{s=\bar{s}(E/E_0, t)} \quad (2.28)$$

where

$$K_1(s, -s) = s \int_0^\infty dx x^{-(s+1)} p_1(s, x) \quad (2.29)$$

The shower maximum correspond to the depth where the electron size is maximum as well, and this corresponds to the condition  $\lambda_1(s) = 0$ . The functional form of  $\lambda_1$  depends on the momenta of the two functions  $\varphi_0$  and  $\psi_0$ , but a very good approximation, deviating less than 2% from the exact expression, was given by Greisen (1960):

$$\lambda_1(s) = \frac{1}{2}(s - 1 - 3 \log s) \quad (2.30)$$

So the condition  $\lambda_1(s) = 0$  requires that  $s = 1$  and from (2.27) it follows that:

$$t_{\max} \simeq \log \left( \frac{E_0}{\varepsilon} \right) \quad (2.31)$$

So (2.19) still holds in Approximation B, of course with the different definition of the maximum depth of the shower of (2.31). A more general way to define the shower age is to consider that the longitudinal development as a function of the depth is governed by the exponential term through the function  $\lambda_1(s)$ , which can be always written as:

$$\lambda_1(s) = \frac{1}{N(t)} \frac{dN(t)}{dt} \quad (2.32)$$

From this expression the shower age can be defined as (Lipari 2009):

$$s = \lambda_1^{-1}(\lambda) = \lambda_1^{-1} \left( \frac{1}{N(t)} \frac{dN(t)}{dt} \right) \quad (2.33)$$

In any case, equation (2.30) can be used without problems to represent the mapping between  $\lambda$  and  $s$ .

### 2.1.6 Longitudinal development

For practical applications, the expression which describes the longitudinal development of an electron/photon initiated cascade, given by (2.20), is of difficult usage. An accurate approximation was given again by Greisen (1960). It combines (2.30) and (2.32), with shower age given by (2.19). The differential equation has the boundary condition  $N(t_{\max}) = N_{\max}$ , which can be found recalling that at the shower maximum  $s = 1$  and from (2.28) we have:

$$N_{\max} = \frac{1}{\sqrt{2\pi}} \frac{G_{\gamma \rightarrow e}(1)}{\sqrt{\lambda_1''(1)}} K_1(1, -1) \frac{1}{\sqrt{\log(E_0/\varepsilon)}} \frac{E_0}{\varepsilon} \simeq \frac{0.31}{\sqrt{\log(E_0/\varepsilon)}} \frac{E_0}{\varepsilon} \quad (2.34)$$

So the longitudinal development of the shower in Greisen's approximation is given by:

$$N_{e, \text{Greisen}}(E_0, t) = \frac{0.31}{\sqrt{\log(E/\varepsilon)}} \exp \left[ t \left( 1 - \frac{3}{2} \log s \right) \right] \quad (2.35)$$

and is the formula usually used to do practical calculations in Approximation B.

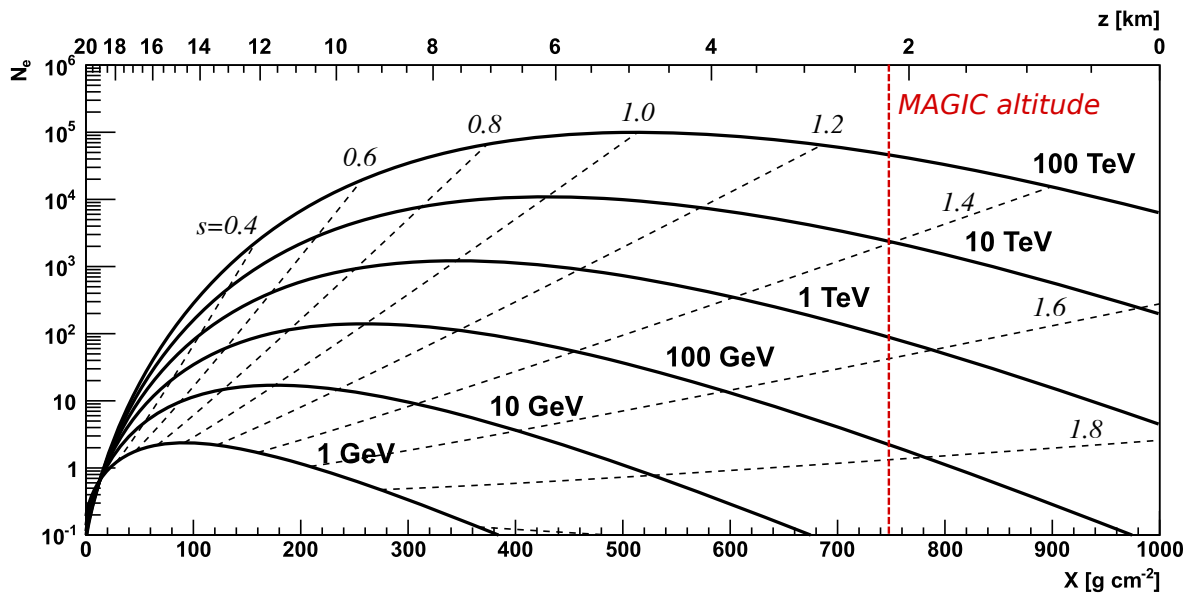


Figure 2.5: Electron size as function of the atmospheric depth  $X$  in Approximation B for different initial  $\gamma$ -ray energies. Shower age values and MAGIC altitude are also shown. Adapted from Naurois and Mazin (2015).

Figure 2.5 shows the longitudinal development of showers for different initial energies of the primary  $\gamma$ -ray. It can be seen that the value  $s = 1$  effectively corresponds to the shower maximum and that at MAGIC altitudes, that is about 2200 m a.s.l., the number of electrons coming from low energy primary photons ( $E < 100$  GeV) is very low, so that it is not possible to use the particle sampler technique to detect the showers.

### 2.1.7 Lateral distribution function

The longitudinal development of a shower comes from solving the cascade equations in one dimension, in this case the reduced depth  $t$ . This is not correct anymore when the lateral distribution of the particles in a shower is considered. The cascade equations (2.21)-(2.22) must be modified once more and there are two main approaches to this problem (Kamata and Nishimura 1958; Grieder 2010):

- the *Landau approximation*, which makes use of the Focker-Planck equation:

$$\left( \frac{\partial}{\partial t} + \boldsymbol{\theta} \frac{\partial}{\partial \mathbf{r}} \right) n_e = -A'n_e + B'n_\gamma + \varepsilon \frac{\partial n_e}{\partial E} + \frac{E_s^2}{4E^2} \left( \frac{\partial^2}{\partial \theta_1^2} + \frac{\partial^2}{\partial \theta_2^2} \right) n_e \quad (2.36)$$

$$\left(\frac{\partial}{\partial t} + \boldsymbol{\theta} \frac{\partial}{\partial \mathbf{r}}\right) n_\gamma = -\sigma_0 n_\gamma + C' n_e \quad (2.37)$$

- *Moliere scattering theory* without Landau approximation:

$$\left(\frac{\partial}{\partial t} + \boldsymbol{\theta} \frac{\partial}{\partial \mathbf{r}}\right) n_e = -A' n_e + B' n_\gamma + \varepsilon \frac{\partial n_e}{\partial E} + \int (n_e(\boldsymbol{\theta} - \boldsymbol{\theta}') - n_e(\boldsymbol{\theta}') \sigma(\boldsymbol{\theta}')) d\boldsymbol{\theta}' \quad (2.38)$$

$$\left(\frac{\partial}{\partial t} + \boldsymbol{\theta} \frac{\partial}{\partial \mathbf{r}}\right) n_\gamma = -\sigma_0 n_\gamma + C' n_e \quad (2.39)$$

where  $\boldsymbol{\theta}$ ,  $\boldsymbol{\theta}'$  and  $\mathbf{r}$  are the angles and the radial distance in the  $x-y$  plane and  $\sigma(\boldsymbol{\theta}') d\boldsymbol{\theta}'$  is the probability of deflection of the particle by an angle between  $\boldsymbol{\theta}'$  and  $\boldsymbol{\theta}' + d\boldsymbol{\theta}'$  in an infinitesimal layer of thickness  $dx$ .

In the previous equations,  $\mathbf{r}$  is the position vector while  $\boldsymbol{\theta} = (\theta_1, \theta_2)$ , where  $\theta_1$  and  $\theta_2$  are the angles in two perpendicular planes intersecting in a line parallel to the  $z$ -axis of the propagation of the shower. The term  $A' n_e$  corresponds to the loss of electrons due to bremsstrahlung,  $B' n_\gamma$  is the gain of  $e^+/e^-$  from pair production and  $C' n_e$  is the gain of photons from bremsstrahlung.

In any case, the lateral distribution of the particles in three dimensions is originated mainly by the multiple Coulomb scattering: the opening angles of electron-positron pairs in the pair production process and the emission angle of photons in bremsstrahlung give a negligible contribution with respect to the angles involved in multiple scattering. From this theory we have a mean square scattering angle in infinitesimal thickness layer given by:

$$\langle \theta_{\text{scatt}}^2 \rangle dx = 16\pi N_A \left(\frac{Z^2}{A}\right) r_e^2 \left(\frac{m_e^2 c^4}{p^2 \beta^2 c^2}\right) \log(b) dx \quad (2.40)$$

Including the multiple scattering contribution finally leads to the *lateral distribution function* of particles in the showers:

$$\rho(r) = \frac{N_e}{2\pi r_M^2} \left(\frac{r}{r_M}\right)^{s-2} \left(1 + \frac{r}{r_M}\right)^{s-4.5} \left(\frac{\Gamma(4.5-s)}{\Gamma(s)\Gamma(4.5-2s)}\right) \quad (2.41)$$

This expression is often called *NKG formula* (Nishimura-Kamata-Greisen) (Kamata and Nishimura 1958; Greisen 1960) and is shown in Figure 2.6.

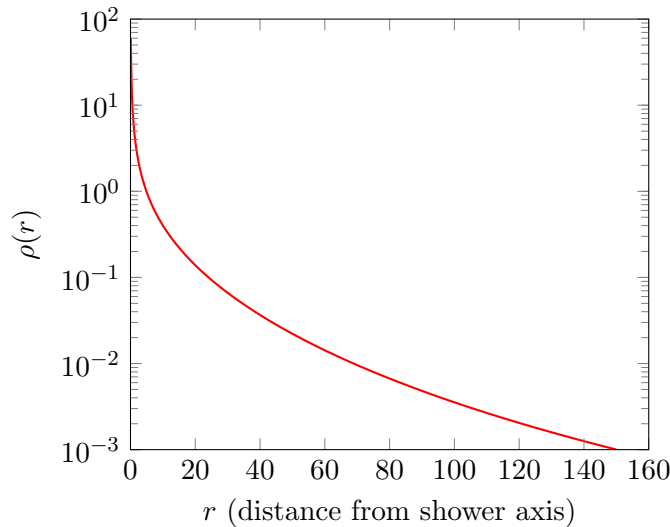


Figure 2.6: Plot of the NKG formula as a function of the distance from the shower axis.

The relevant scale for the lateral distribution is the *Moliere radius* defined as (in  $\text{g cm}^{-2}$ ):

$$r_M = X_0 \frac{E_{\text{scatt}}}{E_c} \quad E_{\text{scatt}} = m_e c^2 \sqrt{\frac{4\pi}{\alpha}} \simeq 21.1 \text{ MeV} \quad (2.42)$$

At sea level, the Moliere radius is  $\sim 79 \text{ m}$ . To some extent, the NKG function could be used to describe the lateral distribution of hadronic showers as well, but there are (of course) discrepancies between the theoretical curve and the experimental one due for example to the fact that in the hadronic case there is a superposition of several electromagnetic sub-showers. For more details, refer to Grieder (2010).

### 2.1.8 Other processes and effects involved in electromagnetic cascades

The processes described until now for the development of an electromagnetic shower are the main ones. Less relevant processes which are involved in electromagnetic cascades are (Grieder 2010):

- Photonuclear interactions, like  $\gamma p \rightarrow p\pi$ , through which pions can be created, which then decay into muons. However the number of muons is very low since:

$$\frac{\sigma(\gamma p \rightarrow p\pi)}{\sigma(\gamma p \rightarrow p e^+ e^-)} \sim 3 \cdot 10^{-3} \quad (2.43)$$

This ratio explains why electromagnetic showers should be muon-poor.

- Fluorescence emission, due to the excitation and successive de-excitation of nitrogen molecules in the air due to the energy deposit by the air showers. It is emitted isotropically and is used in EAS experiment for the reconstruction of events.
- The Landau-Pomeranchuk-Migdal (LPM) effect, which suppresses the bremsstrahlung cross section and makes the showers initiated by a ultra high-energy photon or cosmic ray to penetrate deeper in the atmosphere, stretching it in the initial development phase. The LPM effect is due to the non point-like nature of bremsstrahlung and is enhanced in dense media. In the atmosphere it can be safely neglected.
- Magnetic bremsstrahlung and pair production, which are the analogous of standard bremsstrahlung and pair production in the electric field of the nuclei but in a strong magnetic field. The energy above which these effects are relevant is proportional to the primary particle mass and a critical field strength  $B_{\text{crit}} \sim 4 \cdot 10^{13} \text{ G}$  and inversely proportional to the magnetic field strength of the component perpendicular to the direction of the particle motion. In atmospheric showers the effect is negligible, but is very important in the so called *pre-showering* phenomenon. It occurs in the geomagnetic field outside Earth's atmosphere, where a ultra high-energy photon can interact and produce some secondary electrons and positrons, which in turn can produce other photons if their energy is high enough. The net effect is a packet of photons, electrons and positrons entering the atmosphere, each of them initiating its own shower, mimicking a shower from a hadron if not taken into consideration.
- Radio emission from few to hundreds of MHz, probably caused by an excess of negative charge due to Compton scattering, delta rays production and positron annihilation in flight.

## 2.2 Hadronic showers

### 2.2.1 Introduction

The cosmic rays arriving at the Earth atmosphere are mostly protons, while heavier nuclei constitute a less populated component. Of course electrons are there as well: they produce an electromagnetic shower, as described in Section 2.1. Protons and nuclei instead produce hadronic showers. The phenomenology of this kind of showers is different from the electromagnetic ones, starting from the particle content (see Figure 2.7). Since hadronic processes are involved between the primary particle and the nuclei in the atmosphere, a plethora of different particles are produced, depending on the initial energy: pions, kaons, nucleon and antinucleon pairs, hyperons, antihyperons, charmed particles and so on. These secondary particles can interact or decay if they are unstable, depending on their interaction length, mean lifetime at rest and Lorentz factor: for example charged pions can decay in muons and muonic neutrinos, so that hadronic showers are muon rich. Muons have a “long” lifetime and low energy losses in a medium, so almost all of them reach the ground level. An important contribution comes from neutral pions, which have a very short lifetime ( $\tau_0 = 8.4 \cdot 10^{-17}$  s). They decay into a pair of gamma rays, which in turn initiate electromagnetic sub-showers. This means that hadronic showers have an electromagnetic component, which in average takes one third of the total energy available from the primary particle. The electromagnetic sub-showers can be initiated also by electrons and positrons produced by the decay of muons or other unstable particles. The longitudinal and lateral development of hadronic showers is different from the one in electromagnetic showers. In particular secondaries have large transverse momenta, which makes the shower asymmetric if seen from the plane perpendicular to the shower axis. Low energy muons can be scattered far away from the axis due to Coulomb scattering. Another effect at play in hadronic showers is the *leading particle effect*, that is the primary particle, or its fragments if it undergoes fragmentation, keep a large fraction of the initial kinetic energy when interacting with a nucleon or a nucleus. With other words, there is a high *elasticity* in the process.

The difficulty in the study of hadronic shower is the knowledge of the cross sections of the processes involved, especially at the highest energies, which is not a problem in electromagnetic showers. However, the energies that can be reached in modern accelerators are several orders of magnitude below the energies that primary particles can have when reaching the atmosphere. So EAS measurements of hadronic showers can give hints on the behavior of cross sections at energies higher than those achievable with current technology. The most important cross sections to be considered are the ones between pions, nucleons, kaons and the air nuclei, namely nitrogen and oxygen. Also fragmentation must be taken properly into account. All these processes must be considered when simulating the development of hadronic showers.

Despite the intrinsic complexity of hadronic EAS, simplified models like the Heitler model for electromagnetic showers can be found, as discussed in the following section.

### 2.2.2 Heitler model for hadronic showers

As for electromagnetic showers, a Heitler model can be constructed also for hadronic showers in order to understand qualitatively their development (see Matthews 2001; Matthews 2005). In the first interaction between the initial hadron, in this case a proton, and the nuclei in the atmosphere, two components are produced: one containing charged pions  $\pi^\pm$  and one containing neutral pions  $\pi^0$ . The former component interacts producing more pions (charged and neutral) until the pion critical energy  $E_c^\pi$  is reached, after which the charged pions decay into muons reaching the ground.  $E_c^\pi$  is defined as the energy at which the decay length of a charged pion becomes less than the next interaction point. In the latter component, the neutral pions decay into  $\gamma$ -ray pairs, which initiate electromagnetic sub-cascades.

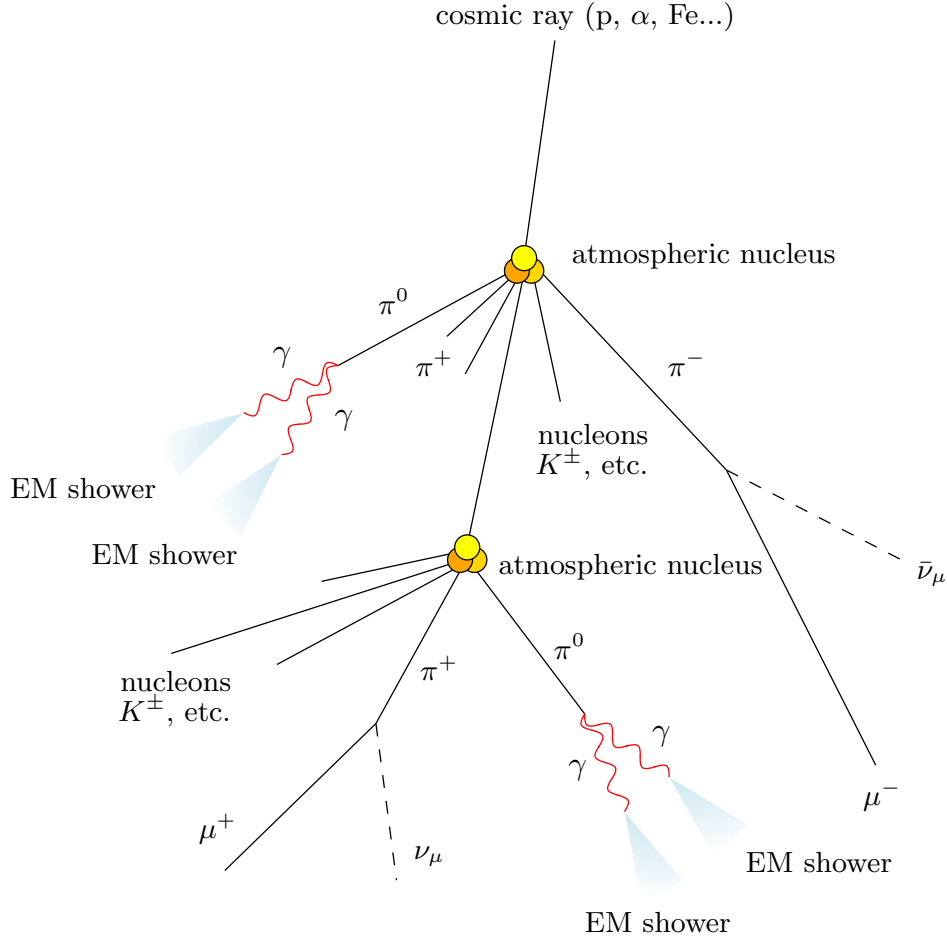


Figure 2.7: Development of a hadronic shower initiated by a cosmic ray. From the production of different mesons (pions and kaons in particular), leptons (muons) and gamma-rays can be produced. The latter originate from the decay of neutral pions and initiate electromagnetic sub-showers.

In the model of Matthews (2005) the atmosphere is divided in layers of thickness  $\lambda_I \ln 2$ , where  $\lambda_I$  is the interaction length of hadrons (for pions  $\sim 120 \text{ g cm}^{-2}$ ). In each layer,  $N_{\text{ch}}$  and  $1/2 N_{\text{ch}}$  charged and neutral pions respectively are produced. So, after  $n$  layers, there will be  $N_\pi = (N_{\text{ch}})^n$  charged pions, carrying a total energy of  $(2/3)^n E_0$  assuming equipartition of the energy between the particles. The rest of the energy goes into the neutral pions and therefore in the electromagnetic part of the shower. The energy per charged pion after the  $n$ -th interaction can be written as:

$$E_\pi = \frac{E_0}{\left(\frac{3}{2} N_{\text{ch}}\right)^n} \quad (2.44)$$

If  $E_\pi < E_c^\pi$ , the charged pions will die out as muons. If  $E_\pi$  is put equal to  $E_c^\pi$  in (2.44), the number of generations  $n_c$  needed to reach the critical energy is found:

$$n_c = \frac{\ln(E_0/E_c^\pi)}{\ln(\frac{3}{2} N_{\text{ch}})} \quad (2.45)$$

To have a numerical estimate, the model proposed in Matthews (2005) uses as reference values  $N_{\text{ch}} = 10$  and  $E_c^\pi = 20 \text{ GeV}$ . It can be shown that different values do not change the

final estimates. With these values it can be seen that:

$$n_c = 0.85 \log_{10} \left( \frac{E_0}{E_c^\pi} \right) \quad (2.46)$$

At this point, the initial energy must be linked with observable quantities. In this hadronic Heitler model, all the primary energy will be divided between  $N_\pi$  pions and  $N_{\max}$  particles from the electromagnetic subshowers. Since instead of pions we observe muons at ground, which are the results of charged pion decay,  $N_\mu (= N_\pi)$  can be used. It follows that:

$$E_0 = E_c N_{\max} + E_c^\pi N_\mu \quad (2.47)$$

$N_{\max}$  can be rescaled to give the total electron size of the hadronic showers, namely  $N_e = N_{\max}/g$ , and (2.47) becomes (Spurio 2015):

$$E_0 = g E_c \left( N_e + \frac{E_c^\pi}{g E_c} N_\mu \right) \sim 0.85 \text{ GeV} (N_e + 24 N_\mu) \quad (2.48)$$

where  $g = 10$  was used, as suggested by simulations. (2.48) can be used as long as the numbers  $N_e$  and  $N_\mu$  are known. This can be not straightforward since most of the measurements are done after the shower maximum and different experiments are sensitive to photons and electrons in a different way, leading to a uncertainty in the value of  $N_e$ . Nevertheless, (2.48) is insensitive to primary particle type and fluctuations, and accounts for the different energy splitting between the hadronic and electromagnetic components.

From (2.45) the number of muons  $N_\mu$  as a function of the primary energy can be derived:

$$N_\mu = \left( \frac{E_0}{E_c^\pi} \right)^\beta \quad \beta = \frac{\ln(N_{\text{ch}})}{\ln\left(\frac{3}{2}N_{\text{ch}}\right)} = 0.85 \quad (2.49)$$

Given the number of muons, it is easy to obtain the fraction of the primary energy going into the electromagnetic component of the shower:

$$\frac{E_{\text{em}}}{E_0} = \frac{E_0 - E_c^\pi N_\mu}{E_0} = 1 - \left( \frac{E_0}{E_c^\pi} \right)^{\beta-1} \quad (2.50)$$

For the maximum number of electrons in hadronic showers, we can think that we have  $N_0$  neutral pions in the shower and each one carries an energy  $E_0/N_{\text{ch}}$ ,  $N_0/N_{\text{ch}} = 1/3$ . Then from equation (2.34):

$$N_{e,\text{max}} = N_0 \frac{1}{g} \left( \frac{E_0/N_{\text{ch}}}{\varepsilon} \right) = \left( \frac{E_0}{3g\varepsilon} \right) = 4 \cdot 10^5 \left( \frac{E_0}{\text{PeV}} \right) \quad (2.51)$$

Equation (2.51) underestimates the real electron number since they are not produced only from neutral pions. A better estimation is given by the following equation, showing that the electron size grows not exactly linearly with energy (Spurio 2015):

$$N_{e,\text{max}} = 6 \cdot 10^5 \left( \frac{E_0}{\text{PeV}} \right)^{1.046} \quad (2.52)$$

The other important quantity is the depth of shower maximum  $X_{\max}$ : it can be calculated as the sum of the depth at which the first interaction occurs and the maximum depth of an electromagnetic shower of initial energy  $E_0/(3N_{\text{ch}})$ . This approximation uses only the first generation of photons, so the resulting maximum depth will be underestimated (Spurio 2015):

$$X_{\max}^p = \lambda_I \ln 2 + X_0 \ln \left( \frac{E_0}{3N_{\text{ch}} E_c} \right) = X_{\max}^\gamma + \lambda_I \ln 2 - X_0 \ln(3N_{\text{ch}}) \quad (2.53)$$

where  $X_{\max}^\gamma$  is the maximum depth for an electromagnetic shower of initial energy  $E_0$ .

### 2.2.3 Superposition model for hadronic showers

The Heitler model presented in the previous section started with the hypothesis of a hadronic shower initiated by a high-energy proton. If the primary particle is a nucleus, the argument can be extended with the *superposition model*: a nucleus with mass number  $A$  and energy  $E_0$  is equivalent to  $A$  nucleons, each with energy  $E_0/A$ . So the shower will be just the sum of  $A$  proton initiated showers starting in the same interaction point. This model makes easy to derive the equations for the quantities we considered before, because we only need to replace  $E_0$  with  $E_0/A$  and summing over  $A$  showers.

That said, starting from (2.51) the number of electrons reads:

$$N_{e,max}^A = A \left( \frac{E_0/A}{3g\varepsilon} \right) = \left( \frac{E_0}{3g\varepsilon} \right) = N_{e,max} \quad (2.54)$$

So electrons cannot be used to distinguish a primary proton from a primary nucleus, since their number should be the same.

The number of muons can be generalized from (2.49):

$$N_{\mu}^A = A \left( \frac{E_0/A}{E_c^{\pi}} \right)^{\beta} = A^{1-\beta} N_{\mu} \quad (2.55)$$

The number of muons increases slightly with the mass number  $A$  with an index  $1 - \beta \sim 0.15$ . For example, if we take a primary iron nucleus ( $A = 56$ ), the number of muons will be a factor two more than the one found for a proton shower.

Finally, for the shower maximum depth (2.53) is used replacing  $\lambda_I$  with  $\lambda_I^A$ :

$$X_{\max}^A = \lambda_I^A \ln 2 + X_0 \ln \left( \frac{E_0/A}{3N_{\text{ch}} E_c} \right) = X_{\max}^p - X_0 \ln A \quad (2.56)$$

### 2.2.4 Cascade equations for hadronic showers

Similarly to what was showed in Section 2.1.5, the cascade equations for a hadronic shower can be written. The difficulty, as already explained, is the huge variety of particles involved, so that the equations will be heavily coupled one with another. Despite this, the transport equation for protons is the starting point (Gaisser 1990):

$$\frac{d\Phi_p(E, X)}{dX} = -\frac{\Phi_p(E, X)}{\lambda_{I,p}(E)} + \int_E^{\infty} \frac{\Phi_p(E', X)}{\lambda_{\text{int},p}(E)} \frac{dn_{p \rightarrow p}(E')}{dE'} dE' \quad (2.57)$$

Here  $\lambda_{I,p}$  is the interaction length of protons in air and  $dn_{p \rightarrow p}$  is the number of protons produced in the energy bin  $dE'$ . Assuming a solution of the kind:

$$\Phi_p(E, X) = A(X)E^{-\gamma} \quad (2.58)$$

equation (2.57) becomes:

$$\frac{d\Phi_p(E, X)}{dX} = -\frac{\Phi_p(E, X)}{\lambda_{I,p}(E)} + Z_{pp} \frac{\Phi_p(E, X)}{\lambda_{I,p}(E)} = -\frac{\Phi_p(E, X)}{\lambda_{I,p}(E)} + S(p \rightarrow p, E) \quad (2.59)$$

where  $Z_{pp}$  is linked with the differential number of protons by:

$$Z_{pp} = \int_0^1 x^{\gamma-1} \frac{dn_{p \rightarrow p}(x, E)}{dx} dx \quad x = \frac{E}{E'} \quad (2.60)$$

The solution for  $\Phi_p$  now reads:

$$\Phi_p(E, X) = A(0)e^{-X/\Lambda} E^{-\gamma} \quad \frac{1}{\Lambda} = \frac{1}{\lambda_{I,p}} [1 - Z_{pp}] \quad (2.61)$$

Here we made an assumption, similar to Approximation A for electromagnetic showers, that the interaction length and  $dn_{p \rightarrow p}$  do not depend on the energy  $E$ , which is not true if a wide energy range is considered.

From equation (2.59) the last equality has two terms: the former is the sink term (depletion of protons), the latter instead is the source term (enrichment of the cascade with protons). A similar equation for pions holds:

$$\frac{d\Phi_\pi(E, X)}{dX} = -\frac{\Phi_\pi(E, X)}{\lambda_{I,\pi}} - \frac{\Phi_\pi(E, X)}{d_\pi} + \sum_h S(h \rightarrow \pi, E) \quad (2.62)$$

Since pions decay, the sink term will have also the contributions due to the decays. Moreover, the source term now comes from all hadrons which can produce pions. To simplify the model, only the pions coming from the interaction with other pions, protons and neutron can be considered. Similarly to equation (2.59), dropping the dependencies on  $E$  and  $X$  since they are implicit, the equation for pions reads (Gaisser 1990):

$$\frac{d\Phi_\pi}{dX} = -\frac{\Phi_\pi}{\lambda_{I,\pi}} - \frac{\Phi_\pi}{d_\pi} + Z_{\pi\pi} \frac{\Phi_\pi}{\lambda_{I,\pi}} + Z_{p\pi} \frac{\Phi_p}{\lambda_{I,p}} + Z_{n\pi} \frac{\Phi_n}{\lambda_{I,n}} \quad (2.63)$$

The last two terms couple the pions with nucleons. Now, assuming that muons are produced only by charged pions decay:

$$\frac{d\Phi_\mu}{dX} = -\frac{\Phi_\mu}{\lambda_{I,\mu}} + Z_{\pi \rightarrow \mu}^D \frac{\Phi_\pi}{d_\pi} \quad (2.64)$$

where  $Z_{\pi \rightarrow \mu}^D$  accounts for the decay of pions and is equal to:

$$Z_{\pi \rightarrow \mu}^D = \text{BR}(\pi \rightarrow \mu) \int_0^1 x^{\gamma-1} \frac{dn_{\pi \rightarrow \mu}}{dx} dx \quad (2.65)$$

$\text{BR}(\pi \rightarrow \mu)$  is the branching ratio of the pion decay into muons.

After writing the equations for protons, pions and muons, the generic form of the transport equation for a generic particle  $h$  with energy  $E$  at depth  $X$  can be written as:

$$\frac{d\Phi_h(E, X)}{dX} = -\frac{\Phi_h(E, X)}{\lambda_{I,h}(E)} - \frac{\Phi_h(E, X)}{d_h(E)} + \frac{\partial}{\partial E}(b(E)\Phi_h(E, X)) + \quad (2.66)$$

$$+ \sum_l S(l \rightarrow h, E) + \sum_l S^D(l \rightarrow h, E) \quad (2.67)$$

The first two terms are the depletion of particles of type  $h$  due to interactions and decays, the third is the continuous energy loss, while the last two terms are the source terms, by interaction or by decay of particles of type  $l$ . The interaction and decay depletion terms are in competition: the interaction length depends weakly on the energy through the inelastic cross section of the particle  $h$  with air, while the decay length increase linearly with energy. Usually a critical energy is defined as the energy at which the decay and interaction rates are equal. For example, muons have a critical energy of 1 GeV, while it is about 115 GeV for pions.

Solving analytically or even numerically the cascade equations, even in the simplified case of nucleons, pions and muons system, is heavily demanding. Beside the pion channel, other meson channels have to be taken into account, especially for muons and electrons production. The most important ones are the kaon and D channels, producing pions, muons and electrons. Taking into account many particle types makes the use of the cascade equations even more difficult. For this reason, both hadronic and electromagnetic showers are simulated using Monte Carlo codes, tackled in Section 2.4. This approach allows to obtain not only average values of several shower parameters, but fluctuations and correlations can be inferred as well. With the cascade equation approach, this is not possible.

## 2.3 Cherenkov Emission in EAS and the Imaging Atmospheric Cherenkov Technique

### 2.3.1 Historical excursus

Commonly it is said that the Cherenkov effect was discovered in 1934 by Pavel Cherenkov, but the truth is that the Cherenkov light was expected theoretically and observed many years before Cherenkov did. Oliver Heaviside, in a series of publication in 1888-1889, predicted that a charged particle should emit radiation when moving faster than light in a transparent medium. In 1912 he also computed the geometry of this emission. The blue light typical of the Cherenkov radiation was observed by Marie Curie in 1910, but it was thought that it was some kind of luminescence, so she did not go in depth of the phenomenon. Only in 1934 Cherenkov, at that time PhD student of Sergej Vavilov, understood that the radiation was peculiar and different from other kinds of radiation (for example bremsstrahlung). The experimental discovery was followed later by the theoretical explanation of Ilya Frank and Igor Tamm. Cherenkov, Tamm and Frank received the Nobel Prize in Physics in 1958 for this discovery. Vavilov, regardless of the fact that he had an important role in it, unfortunately died before the assignation of the prize.

After that, many experiments confirmed the emission of Cherenkov light in liquids and solids, but nothing was made to prove the emission in gases as well. In 1948 Blackett (Blackett 1948) pointed out that the Cherenkov effect should have existed also in gases and took as an example the Cherenkov light produced by cosmic-rays particles in the atmosphere, which would give a contribution to the night sky background (NSB). Some experiments on the Cherenkov effect in gases were carried on by two Italian scientists who used an experimental apparatus with a mixture of air and chloroform, a photomultiplier and a group of counters for coincidence measurement (Balzanelli and Ascoli 1953; Ascoli Balzanelli and Ascoli 1954). From the results, they concluded that the excess events detected were originated by the Cherenkov light produced by the particles in atmospheric showers.

From these results, in 1953 Gailbraith and Jelley supposed that they could detect the Cherenkov light from high energy cosmic-ray particles as short pulses of Cherenkov light (Galbraith and Jelley 1953).

In their first attempts, there was no direct evidence that the observed pulses were caused by Cherenkov radiation (they were using as a detector a garbage can with a mirror in the bottom and a photomultiplier in the focus, see Figure 2.8), but later they changed the experimental apparatus to investigate the properties of the observed radiation (polarization, directional properties and color). Eventually they proved that the pulses were associated with Cherenkov light produced in air showers (Galbraith and Jelley 1955; Jelley and Galbraith 1955). A similar experiment was performed by N. M. Nesterova and A. E. Chudakov (Nesterova and Chudakov 1955), where they confirmed the possibility of observing Cherenkov radiation from air showers with energy of  $10^{14}$  eV. These discoveries led to the idea of using gamma rays to do astronomy like it was done with optical light, X-rays and in the radio band. The



Figure 2.8: The experimental apparatus used by Gailbraith and Jelley to detect pulses from extensive air showers. From Mirzoyan (2012)

Italian physicist Cocconi proposed to use EAS to detect gamma-rays at VHE, giving also an estimation of the Crab Nebula flux. His conclusion was that the Crab Nebula could be detectable since the expected signal was  $10^3$  times larger than the background (Cocconi 1960). No signal was detected because of the high energy threshold of the instruments of the time. The first Atmospheric Cherenkov Telescope (ACT) for gamma ray astronomy was built by a team led by Chudakov. The experiment was designed as an array of 12 mirrors of 1.5 m diameter and it was operative from 1960 to 1964 in Crimea. During its operation, the observed sources were mainly radio galaxies, SNRs and the Crab Nebula, on which it was possible to set an upper limit on the flux expected from neutral pions decay. Beside these results, there was no significant discovery because of the strong cosmic rays background. At the same time, D. A. Hill and N. A. Porter developed an image intensifier system with which they recorded the first Cherenkov image from air showers (Hill and Porter 1961). J.V. Jelley and Porter added some observable sources (quasars and variable stars) to the list by Chudakov and used two 90 cm mirrors on a Bofors gun mounting from the Second World War in Glencullen, Ireland. Also in this case, there was no significant result (Jelley and Porter 1963). Nevertheless, it was clear that using the images from Cherenkov light produced by showers could be used for retrieving information about the energy and direction of the primary particles.



Figure 2.9: The Whipple telescope in Arizona. From <http://www.astro.wisc.edu/~larson/Webpage/Gamma.html>.

All these experiments belong to the so called first generation ACTs and were not able to discriminate between the Cherenkov images from gamma rays and those from cosmic rays. A step further was done with the construction of the Whipple telescope in Mount Hopkins in Arizona (see Figure 2.9, from a proposal of Fazio, Helmken, Rieke and Weekes (Fazio et al. 1968). The telescope was finished in 1968 and its design was a reflector of almost 10 m of diameter with 252 hexagonal mirrors and a single phototube. In 1971, Grindlay proposed the so called “double-beam technique” (Grindlay 1971): a two-telescope system, each with two pixels, one to detect the shower maximum (and so the arrival direction) and one to select events probably initiated by gamma rays. This research led the Whipple team to add a second phototube in 1972 and a third one with a guard ring of seven tubes in 1976. From 1978 to 1982 Whipple was inoperative because of the lack of fundings. Despite of this, Weekes proposed to use electronic cameras with multiple phototubes in the focal plane to record the images of the Cherenkov light in a workshop in Frascati, Italy, in 1977. In 1981 he then

proposed to equip the Whipple telescope with a camera with 37 pixel, which was finished and mounted in 1983 (Weekes 1996).

The next step was to understand how to discriminate between images from gamma rays and cosmic rays. A first attempt was to use the image parameter  $Frac2$ , defined as the ratio between the signal in the two brightest pixels and the total signal in the image. This led to a first indication of a significant signal from the Crab and from other sources, but the credibility of these detection was not so high. But in 1985, A. M. Hillas proposed to use the second moments ( $Width$ ,  $Length$ ) and other parameters of the images ( $Dist$ ,  $Azwidth$ ,  $Alpha$ ,  $Asymmetry$ , see Section 4.4 for their definition) to distinguish between hadronic and electromagnetic showers (Hillas 1985; Plyasheshnikov and Bignami 1985). This was motivated by the different physical processes involved in the showers, which lead to different shapes of the images. Moreover the images coming from primary gamma rays should have their major axis intersecting the center of the field of view and this guarantees a good angular resolution. These developments marked the beginning of the second generation of Cherenkov instruments. Using the parameters of the images for the discrimination finally led to the detection of the Crab Nebula in 1989 at a level of  $9\sigma$  after an observation time of 60 h, presented in Weekes et al. (1989).

The following step was to take advantage of the stereoscopic technique: a first stereoscopic instrument was built by Arnold Stepanian in Crimea. In 1984 (so before the detection of the Crab Nebula) Weekes made a proposal for an array of seven telescopes with 15 m reflectors (Weekes 1985). This configuration is the one used by VERITAS, although the number of telescopes was reduced from seven to four. But the stereoscopic technique was fully adopted with the construction of the HEGRA (*High Energy Gamma Ray Astronomy*) experiment in La Palma (Canary Islands, see Figure 2.10): the proposal was made in 1991 and in summer 1992 the first telescope started data taking. In the following years, till 1996, other five telescopes were added and allowed a better background rejection, angular resolution and sensitivity. After HEGRA stopped operations, in 2011 a camera with Geiger-mode avalanche photodiodes (G-APDs) was mounted in the focus of one of the former HEGRA telescopes and became the FACT (First APGDs Cherenkov Telescope) telescope. Nowadays, the MAGIC telescopes are operative at the HEGRA site.



Figure 2.10: One of the telescopes of the HEGRA array in La Palma. From Mirzoyan (2012).

Other examples of stereoscopic system are 1) the one built by a Japanese collaboration in Utah in 1997 (Utah Seven Telescope Array), which consisted of seven telescopes (there was also a very risky moment when an american test missile hit two trailers used to support telescope operations) and 2) the one in Narrabri, Australia, which consisted of three 7 m mir-

rors, operational between 1986 and 2000. After Whipple many Cherenkov telescopes were built around the world: the Cherenkov Array at Themis in the Pyrenees (CAT, led by a French collaboration, started in 1996), CANGAROO (*Collaboration of Australia and Nippon for a Gamma Ray Observatory in the Outback*) in Woomera, Australia (led by a Japanese-Australian collaboration; the first telescope was operative since 1992), SHALON in Russia and TACTIC in India (both started operation in 2001). Nowadays all these experiment are no longer running.

From all these experiments, it became clear that the only way to improve the imaging technique was to adopt the following measures:

- Using a fine pixelized camera to improve the granularity of the images;
- Using of very fast electronics and thus taking advantage of the time properties of the Cherenkov light produced by electromagnetic showers;
- Building stereoscopic arrays with two or more telescopes to improve background rejection, reconstruction of arrival directions and sensitivity.

As an example the use of more pixelized cameras led, in 1992, the Whipple collaboration to detect Markarian 421, the first extragalactic source seen in the VHE range, after upgrading the camera from the initial 37 to 109 pixels (Punch et al. 1992).

In April 1997 there was the first multi-detection of the Mrk 501 flare by CAT, HEGRA and Whipple, presented at the 5th workshop on TeV Gamma Ray Astrophysics in Kruger, South Africa. From that moment on, the atmospheric imaging technique was fully accepted by the whole community and an effort was made by some groups towards the third generation instruments. The goal was to lower the energy threshold down to energies less than 100 GeV by developing larger dishes, to have better image resolution (and so better image analysis) with more fine grained cameras and to have more than one telescope, as demonstrated by HEGRA, in order to improve the angular resolution and sensitivity.

The first step was made by the CANGAROO collaboration, which added three telescopes to the original one (CANGAROO-II and CANGAROO-III) in 1999 and in the period 2002-2004, but they did not have a competing sensitivity with the other third generation instruments which started to take data while CANGAROO was operative: H.E.S.S., MAGIC and VERITAS (in chronological order of the “first light”).

H.E.S.S. is a system of five Cherenkov telescopes, four 12 m hexagonal telescopes operational from 2003 (H.E.S.S.-I) with a FoV of  $5^\circ$  and a fifth 28 m telescope operational from 2012 (H.E.S.S.-II), having a smaller FoV ( $3.5^\circ$ ). It is located in Namibia, near the Gamsberg mountain. The initial four telescopes are arranged to form a square of 120 m side length and then the fifth telescope was added at the center increasing the energy coverage, sensitivity and angular resolution. The sensitivity reached by H.E.S.S. I+II is better compared to the MAGIC one above  $\sim 150$  GeV; the energy and angular resolution are  $\simeq 15\%$  and  $0.06^\circ$  ( $0.1^\circ$  with a single telescope) respectively. Thanks to the fifth telescope, the energy threshold of H.E.S.S. was decreased down to  $\sim 30$  GeV, competing with MAGIC and giving the opportunity to study sources emitting in that energy range (e.g. pulsars or GRB).

VERITAS is an array of four 12 m optical reflectors for gamma-ray astronomy located in Tucson, Arizona, at the Fred Lawrence Whipple Observatory with a peak effective area of  $\sim 100\,000$  m<sup>2</sup>. Its energy coverage is from  $\sim 100$  GeV (but spectral reconstruction starts at 150 GeV) to  $> 30$  TeV, with an energy resolution of 15% at 1 TeV. The telescopes have an angular resolution of  $0.1^\circ$  at 1 TeV,  $0.14^\circ$  at 200 GeV and can locate sources with an accuracy of 50 arcoseconds. The array was reconfigured in 2009, increasing the point source sensitivity to 1% of the Crab flux in less than 30 h of observations and 10% of the Crab flux in 30 min. Each telescope has 350 hexagonal spherical mirrors with a total area of 110 m<sup>2</sup> and at the focal plane of the telescopes is placed the 1.8 m  $\times$  1.8 m camera, having a total FoV of  $3.5^\circ$ .

---

|                               | H.E.S.S.-I                | H.E.S.S.-II | VERITAS      | MAGIC         |
|-------------------------------|---------------------------|-------------|--------------|---------------|
| Telescopes                    | 4                         | 1           | 4            | 2             |
| Site                          | Khomas Highland (Namibia) |             | Arizona (US) | La Palma (ES) |
| Latitude (°)                  | -23.27                    |             | 31.68        | 28.76         |
| Longitude (°)                 | 16.50                     |             | -110.95      | -17.89        |
| Altitude (m a.s.l.)           | 1800                      |             | 1268         | 2231          |
| Dish diameter (m)             | 12                        | 28          | 12           | 17            |
| Mirror area (m <sup>2</sup> ) | 107                       | 614         | 110          | 236           |
| Pixels per camera             | 960                       | 2048        | 499          | 1039          |
| FoV (°)                       | 5                         | 3.5         | 3.5          | 3.5           |
| Threshold (TeV)               | 0.1                       | < 0.05      | 0.08         | 0.05          |
| Sensitivity (% Crab)          | 0.7                       | tbd         | 0.7          | 0.7           |
| > 1 TeV                       |                           |             |              |               |

Table 2.1: Main parameters of current IACTs experiments.

Since MAGIC is the instrument whose data are used in this thesis, it is described in detail in Chapter 3.

The main parameters characterizing current IACT facilities are summarized in Table 2.1.

### 2.3.2 Cherenkov Radiation

I will now briefly describe the phenomenon of Cherenkov radiation by charged particles, in particular connected to extensive air showers and with the Imaging Atmospheric Cherenkov technique.

Cherenkov radiation is a so-called threshold effect, that is a phenomenon occurring when particular conditions are satisfied. In this case there's only one condition: the particle (charged) must travel faster than the phase velocity of the light in the medium. Of course it means that a neutral particle cannot emit Cherenkov radiation and the same applies if the charged particle travels in the vacuum. The previous condition have a simple physical explanation: when a particle travels through a medium, it polarizes the atoms/molecules of the medium in a symmetrical way in the azimuthal plane but not along the axis of motion (see Figure 2.11). This polarization causes the formation of dipoles, which in turn emit radiation while relaxing. The radiation can interfere destructively or constructively if the particle moves slower or faster than the light in the medium respectively. The threshold condition mathematically translates to:

$$\beta_{\text{thr}} = \frac{1}{n} \quad (2.68)$$

where  $n$  is the refraction index of the medium. An important feature of the Cherenkov radiation is that it is emitted along the mantle of a cone with semi-opening angle  $\theta_{\text{ch}}$  and apex lying on the particle track (Figure 2.11). The angle  $\theta$  is connected to the particle velocity and to the refraction index of the medium by the so-called *Cherenkov relation*<sup>1</sup>:

$$\cos \theta_{\text{ch}} = \frac{1}{\beta n} \quad (2.70)$$

<sup>1</sup>If one takes into account the recoil of the particle caused by the emitted photon, the Cherenkov relation is modified as

$$\cos \theta_{\text{ch}} = \frac{1}{\beta n} + \frac{\hbar k}{2p} \left( 1 - \frac{1}{n^2} \right) \quad (2.69)$$

where  $\hbar k$  and  $p$  are the photon and particle momentum respectively. This modification has very little effect and can be neglected for all practical applications.

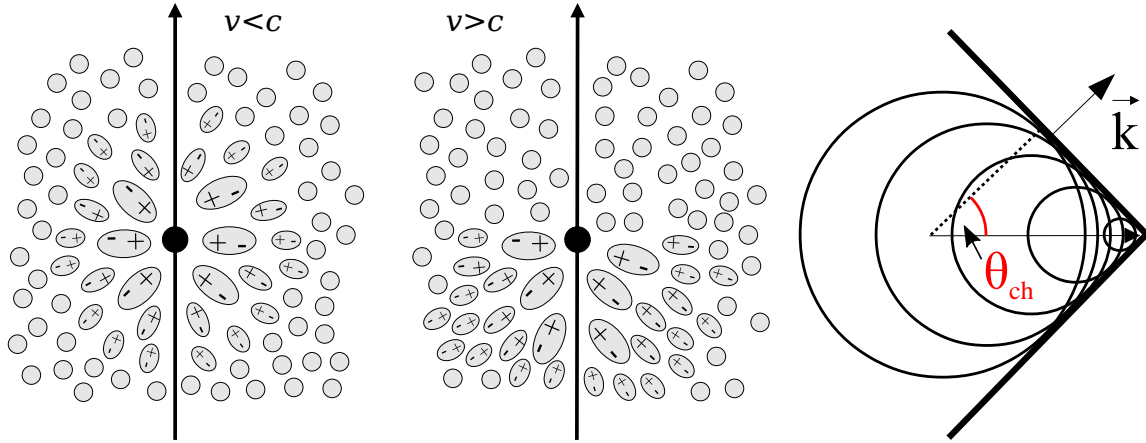


Figure 2.11: **Left:** polarization of atoms when a charged particle passes through a medium with velocities lower or greater than the speed of light. **Right:** formation of the Cherenkov wave-front. Both figures adapted from Naurois and Mazin (2015).

$\theta_{ch}$  can range from 0 (that is, the radiation is emitted in the same direction of the particle track and this happens at threshold) to a maximum value  $\theta_{max}$ , sometimes called *Cherenkov angle*, when  $\beta = 1$  (ultrarelativistic case):

$$\theta_{max} = \arccos\left(\frac{1}{n}\right) \quad (2.71)$$

Since the cosine of an angle must not be greater than one (in absolute value), it follows that  $n > 1/\beta$  and it holds true for  $\beta = 1$  as well. Then it means that Cherenkov radiation is produced in media with  $n(\omega) > 1$ . Another feature is that Cherenkov radiation is highly polarized: the vector of the electric field is perpendicular to the mantle of the cone, while the vector of the magnetic field is tangential to it.

### Energy loss and spectral distribution

The energy loss due to Cherenkov radiation was computed both classically and quantum mechanically essentially with the same result. The classical formula reads:

$$\left.\frac{dE}{dx}\right|_{ch} = 4\pi \left(\frac{Ze}{c}\right)^2 \int_{\beta n > 1} \left(1 - \frac{1}{\beta^2 n^2}\right) \omega d\omega \quad (2.72)$$

where  $\omega$  is the angular frequency of the emitted radiation and  $Ze$  is the charge of the particle. Typically the energy loss is of the order of few keV/cm and is about 0.1% of the energy loss by ionization. So it means that in an atmospheric shower the energy lost from Cherenkov radiation gives a negligible contribute to the total energy loss: pair production and bremsstrahlung are the main processes through which the energy of the initial photon/electron is dissipated and cause the dying of the shower.

The spectral distribution of the Cherenkov radiation, that is the number of photon per unit path length and unit wavelength interval, is given by:

$$\frac{d^2 N}{dx d\lambda} = \frac{2\pi\alpha Z}{\lambda^2} \left(1 - \frac{1}{\beta^2 n^2(\lambda)}\right) = \frac{2\pi\alpha Z}{\lambda^2} \sin^2 \theta \quad (2.73)$$

The scaling as  $\lambda^{-2}$  is the one responsible to give the Cherenkov light the bluish hue in typical media like water and air. It is now straightforward to obtain the total number of photons

emitted along a path of length  $\ell$  between the wavelengths  $\lambda_1$  and  $\lambda_2$ , assuming a constant index of refraction:

$$N = 2\pi Z^2 \alpha \ell \left( \frac{1}{\lambda_1^2} - \frac{1}{\lambda_2^2} \right) \sin^2 \theta \quad (2.74)$$

For Cherenkov radiation in air, we have  $n = 1.00029$ , giving for an electron an threshold energy of 21 MeV, a Cherenkov angle of  $1.3^\circ$  and 0.3 photons/cm in the wavelength interval between 400 and 500 nm.

The number of Cherenkov photons per unit wavelength in an atmospheric shower of course depends on the distribution of electrons and positrons in the shower as a function of the reduced depth  $t = X/X_0$ . Moreover the atmosphere is not homogeneous, but its density changes with the altitude and so the refraction index changes as well. Its dependence on the pressure (or density) is given by the relation (Naurois and Mazin 2015):

$$(n - 1) = 2.92 \cdot 10^{-4} \cdot \frac{P}{P_0} \cdot \frac{288.15 \text{ K}}{T} \quad (2.75)$$

Assuming the atmosphere as hydrostatic and isothermal, the density will have an exponential dependence on the altitude:

$$\rho(z) = \rho_0 e^{-z/z_0} \quad \rho_0 = 1.2 \text{ kg/m}^3 \quad z_0 = \frac{RT}{gM} = 8.4 \text{ km} \quad (2.76)$$

Using the thickness instead of the altitude and applying the approximation  $\sin^2 \theta \approx 2(n - 1)$  valid for small angles (as for Cherenkov radiation in air following the previous numerical example), we obtain:

$$\frac{d^2 N}{dX d\lambda} \approx 2.92 \cdot 10^{-4} \cdot \frac{4\pi\alpha Z^2}{\rho_0 \lambda} \cdot \frac{288.15 \text{ K}}{T} \quad (2.77)$$

Finally the number of Cherenkov photons per unit wavelength produced in an electromagnetic shower can be computed (Naurois and Mazin 2015):

$$\begin{aligned} \frac{dN}{d\lambda} &= \int dX N_e(t) \cdot \frac{d^2 N}{dX d\lambda} = \\ &= 1.86 \sqrt{y} X_0 \cdot \frac{E_0}{E_c} \cdot \frac{d^2 N}{dX d\lambda} \int \frac{ds}{(3-s)^2} \exp\left(\frac{2s}{3-s} \left(1 - \frac{3}{2} \log s\right)\right) \end{aligned} \quad (2.78)$$

with  $y = \log(E_0/E_c)$ . The correction factor  $\sqrt{y}$  ranges between 2.2 and 3.4 for energies between 10 GeV and 10 TeV, meaning that in an electromagnetic shower the total amount of Cherenkov light is proportional to the energy of the primary particle  $E_0$ , allowing a calorimetric measurement.

### Angular and temporal structure

An important effect on ground is the *Cherenkov ring*. In a simplified model presented in Hillas (1982) where charged particles move vertically and emit Cherenkov radiation, the resulting density of photons at ground is shown in Figure 2.12: the density rises and there is a sharp cusp around 150 m and then the density drops to zero.

The behavior shown in Figure 2.12 is very different from the one observed in real showers. One must include scattering effects of the photons to obtain a more realistic picture. This is shown in Figure 2.13: around the same distance from shower axis as before the ring where the photon density is higher is clear (in this lateral profile, the ‘‘peak’’ in light density is called also *hump*, whereas the area in the ground with almost constant light density before the hump is called ‘‘light pool’’).

The reason of the creation of this ring is very simple and is shown in Figure 2.14 for a vertical

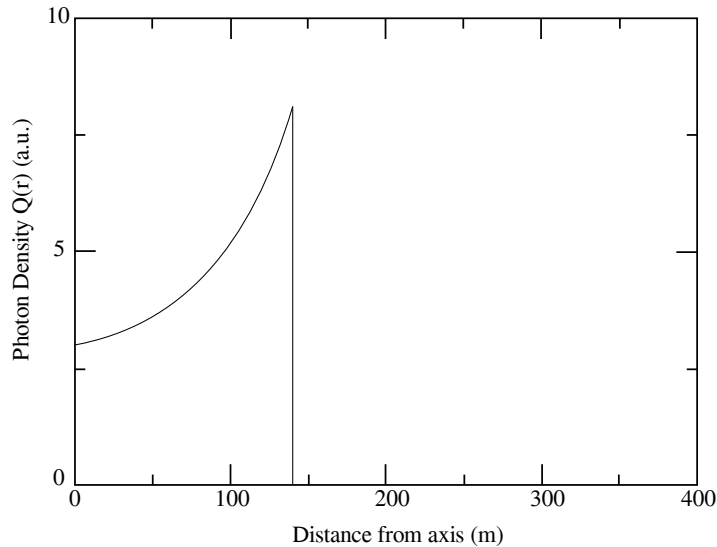


Figure 2.12: Photon density as a function of the distance from the shower axis for the simplified model of vertically moving charged particles emitting Cherenkov photons. Reproduced from Hillas (1982).

shower: charged particles near the first interaction emit Cherenkov radiation with a small angle ( $\sim 0.2^\circ$ ). As the shower develops deeper in the atmosphere, the air density and the index of refraction change, causing the Cherenkov angle to increase up to  $\sim 1.5^\circ$  at sea level. So there is a constructive contribution of light from different heights, causing the formation of the Cherenkov ring at a distance of about 150 m from the shower axis.

The presence of the Cherenkov ring is proved by Monte Carlo simulations as well, as shown in Figure 2.15. In this case different energies result in a less or more prominent ring. Moreover the geomagnetic field introduces an azimuthal asymmetry, making the ring elliptical.

It must be noted that the hump is present only if the electron-positron shower dies before reaching the ground, otherwise the density profile shows a higher photon density at the shower core with a fast drop as the distance from the axis increases.

The Cherenkov light front has a very peculiar shape, shown in Figure 2.16. The effect is caused by the fact that electrons and positrons in the shower move faster than the Cherenkov light that they emitted. Close to the shower core the light from the shower tail arrives before the light emitted from the top of the shower. Far from the shower core instead the trend is inverted and the light from the top arrives first, because the photons from the shower tail have a longer geometrical path, which is the sum of the track of the electron/positron to the point where it emits the Cherenkov light and the track of the Cherenkov photon itself. As Figure 2.16 shows, at  $\sim 120$  m from the shower core the two effects compensate and it results in a short pulse of  $\sim 2$  ns duration, while at the core the pulse can last  $\sim 5$  ns.

### Geomagnetic field effect on EAS and IACT technique

EAS are also affected by the geomagnetic field. Of course the effect depends on the IACT site, since direction and magnitude of the geomagnetic field are different. The geomagnetic field deviates electrons and positrons in opposite directions and the deflection of particles is proportional to the component of the geomagnetic field perpendicular to the observation direction,  $B_\perp$  (Szanecki et al. 2013):

$$B_\perp = [H^2 (\cos^2 \theta + \sin^2 \theta \sin^2 \phi) - HZ \sin(2\theta) \cos \phi + Z^2 \sin^2 \theta]^{1/2} \quad (2.79)$$

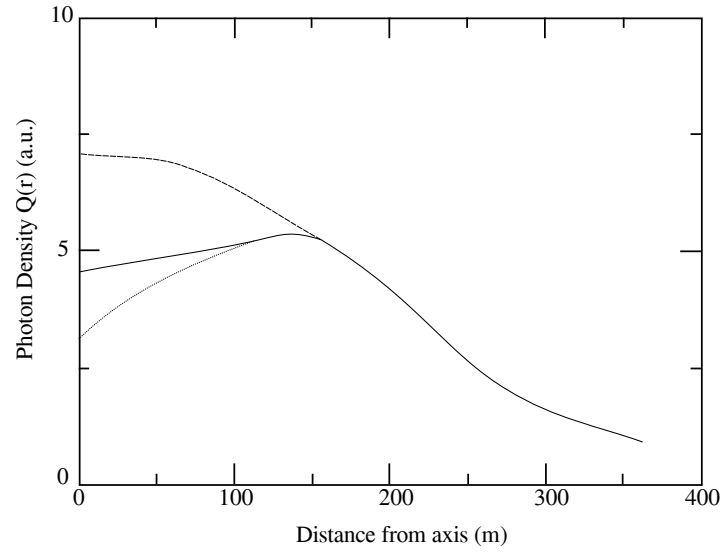


Figure 2.13: Photon density as a function of the distance from the shower axis (solid curve). The dashed and dotted curves show the photon density for low and high developing showers respectively. In the former case the effect vanishes. Reproduced from Hillas (1982).

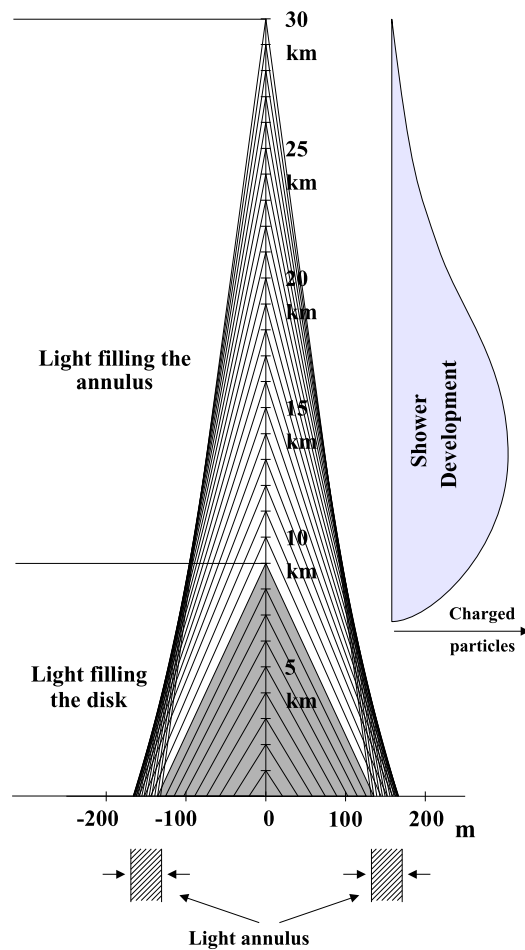


Figure 2.14: Formation of the Cherenkov ring on the ground for a vertical shower. Adapted from Naurois and Mazin (2015).

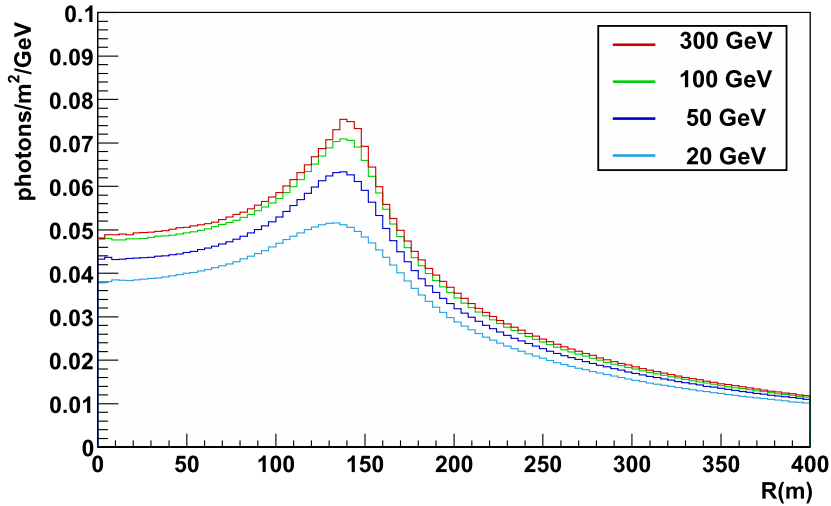


Figure 2.15: Lateral profile of showers at sea level for different energies of the primary particle. Adapted from Naurois and Mazin (2015).

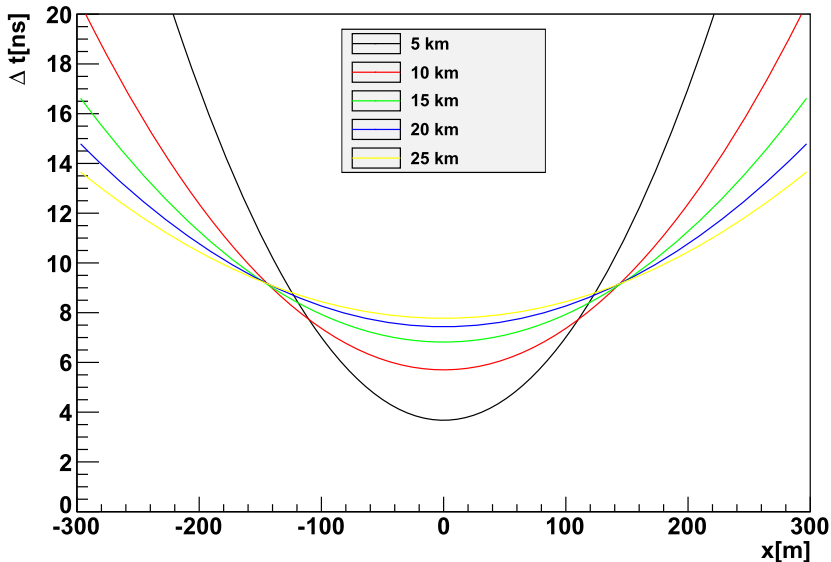


Figure 2.16: Time delay (in nanoseconds) of Cherenkov photons as a function of the distance from the shower axis and for different altitudes of emission. Adapted from Naurois and Mazin (2015).

where  $\theta$  and  $\phi$  are the zenith and azimuth angle respectively, while  $H$  and  $Z$  are the  $x$  and  $z$  component of the geomagnetic field<sup>2</sup>. Figure 2.17 for example shows the magnitude of  $B_{\perp}$  at the MAGIC site.

This deviation influences the distribution of Cherenkov light on the ground. In particular, the light pool is stretched decreasing the Cherenkov photon density and the shower images are distorted (both the shape and the orientation are modified) leading to a worse gamma/hadron separation and a worse sensitivity. The effect of the geomagnetic field is stronger on gamma-initiated showers and for low energy showers. If the energy of the primary particle is sufficiently high, the photon density in the light pool is high enough to trigger the IACT (see Commichau et al. 2008 for a detailed study of the effect of the geomagnetic field for the MAGIC site or Szanecki et al. 2013 for CTA, included the effects of the altitude

<sup>2</sup>The reference system used with the geomagnetic field is such that  $\mathbf{B} = (H, 0, Z)$ , with the  $x$  axis pointing to the local magnetic north, the  $y$  axis pointing to east and the  $z$  axis pointing downwards.

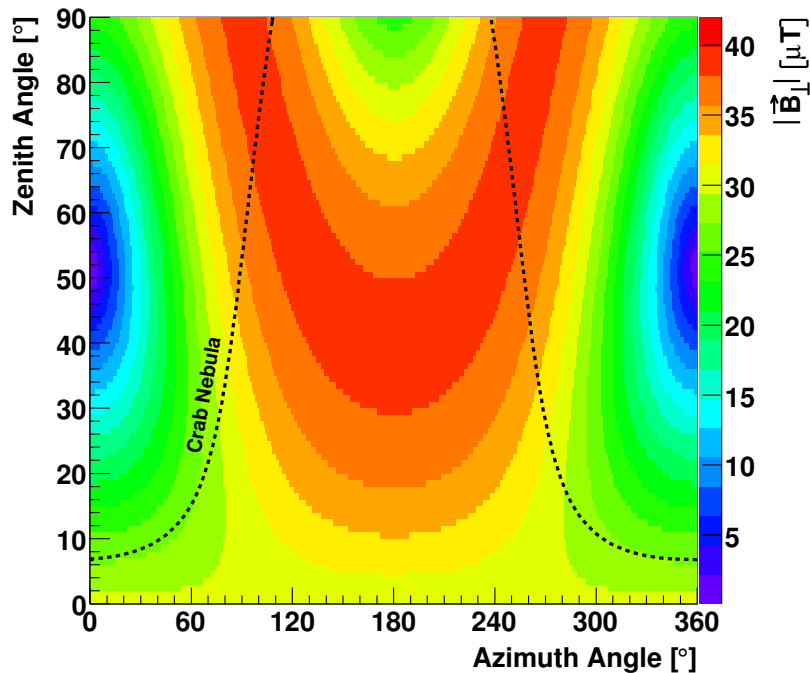


Figure 2.17: Magnitude of the geomagnetic field component perpendicular to the observation direction for the MAGIC site. From Commichau et al. (2008).

on the site choice).

### Absorption and scattering of Cherenkov light in the atmosphere

While the atmosphere is an essential element of the IACT technique since it allows a calorimetric measurement of the showers, it affects the Cherenkov light produced in EAS with absorption and scattering processes, degrading the performance of the telescopes, as shown in detail in Bernlohr (2000).

The amount of Cherenkov light produced in an EAS depends on the density profile chosen for the atmosphere, since the light is sampled from all altitudes and the index of refraction changes as the shower develops through the atmosphere. What is particularly affected by the change in refraction index is the light density in the light pool: this comes mostly from a cylindrical region centered on the shower maximum and different density profiles changes the amount of light produced in this region. Figure 2.18 shows on the left the Cherenkov photon density in the wavelength range 300 – 600 nm for different atmospheric profiles for an experiment at 2200 m above sea level. Between the tropical and the antarctic winter profile there is a 60% difference in light density, showing the high impact of the atmospheric profile choice in the simulation of the response of a IACT. On the right instead, Figure 2.18 shows the impact of seasonal effects on the amount of Cherenkov density. In this case the difference is of the order of 15 – 20%.

Another effect on Cherenkov light due to the atmosphere is its extinction due to absorption and scattering by molecules and aerosols. The presence of different kinds of absorbers and scatterers modifies the transmission of Cherenkov light to the detection site. In Figure 2.19 the transmission of light from 100 km to 2.2 km along a vertical path is shown for different absorbers and scatterers. In the range most important for the IACT technique, 300 – 600 nm, absorption by ozone ( $O_3$ ) and scattering by molecules/aerosols are the principal processes affecting Cherenkov light transmission. While the contribution of molecular scattering is

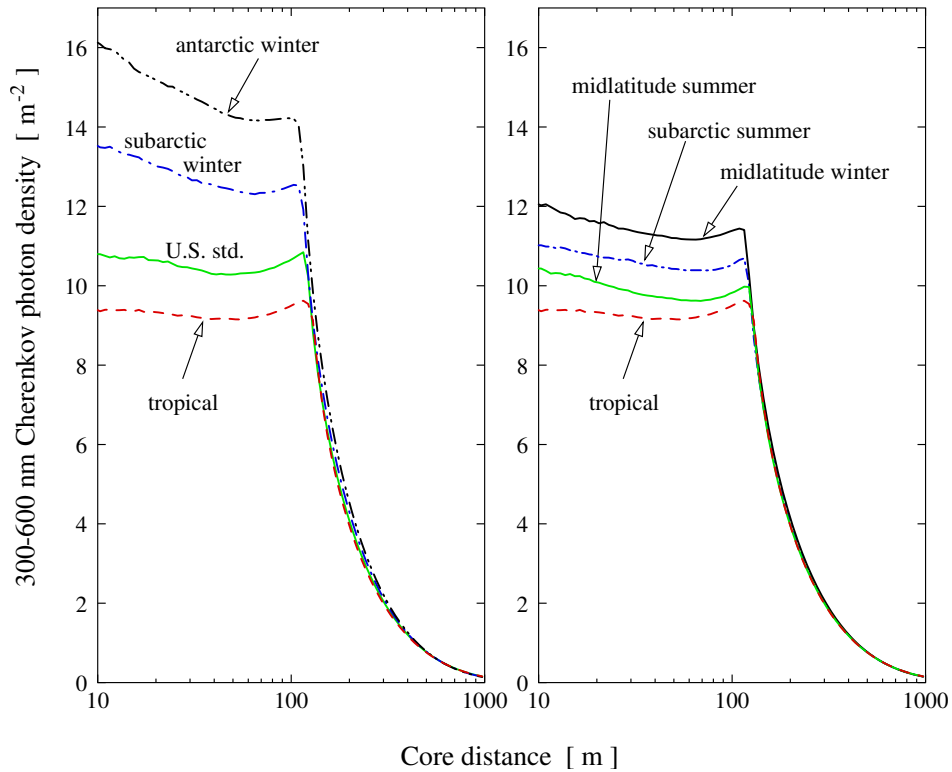


Figure 2.18: Cherenkov light density as a function of the distance from shower axis for vertical 100 GeV showers simulated with CORSIKA. **Left:** different atmospheric profiles used in the simulations. **Right:** seasonal effects on the amount of Cherenkov light emitted in showers. Adapted from Bernlohr (2000).

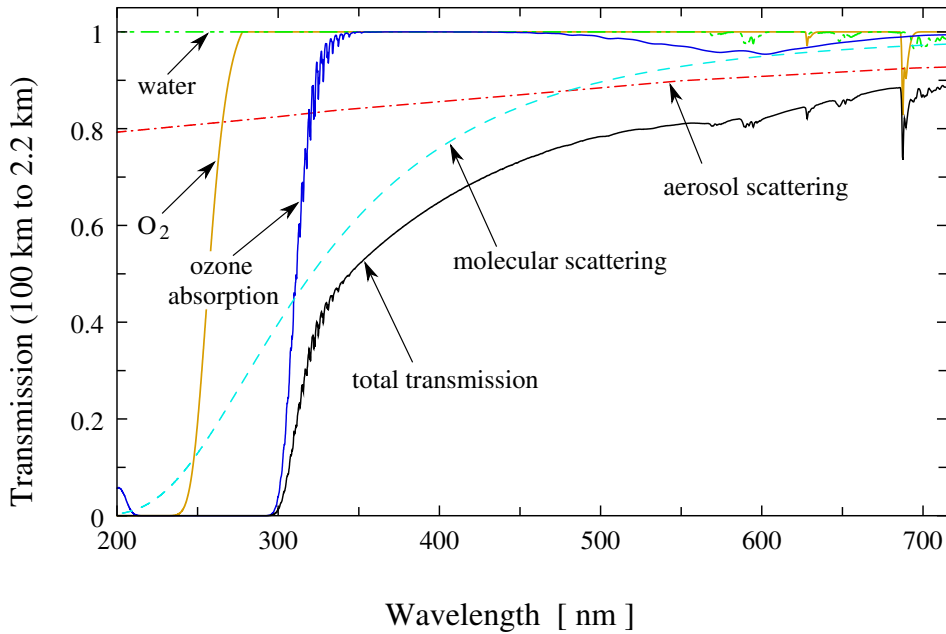


Figure 2.19: Transmission of light from 100 km to 2.2 km calculated with the MODTRAN program for different absorbers and scatterers. Adapted from Bernlohr (2000).

almost constant at each site, the one from aerosols and ozone depends on the site location. For MAGIC in particular, one major component of aerosols is the so-called *calima*, a wind from Sahara which brings desert dust to the MAGIC site, especially in summer. For aerosols

the contribution can vary in the boundary layer of 1 – 2.5 km thickness above ground, where the ground heating by solar radiation leads to turbulences and consequent exchange of air and dust. The density of aerosols cannot be taken to be proportional to the air density because it would lead to an overestimate of Cherenkov light intensity at the site location. Figure 2.20 shows the atmospheric transmission from different altitudes to 2.2 km with a suitable model of aerosols.

Till now both molecular and aerosol scattering were treated as an absorption process, but an estimate of scattered light in showers can be given using the theory of Rayleigh and Mie scattering for molecules and aerosols respectively. This is shown in Figure 2.21. In the case of scattered light the integration time of the instrument must be taken into account and for IACTs, where it is of the order of  $\sim 20$  ns, small-angle scattering is predominant but it accounts for only  $10^{-3}$  of the total light emitted even for small integration times and field of view.

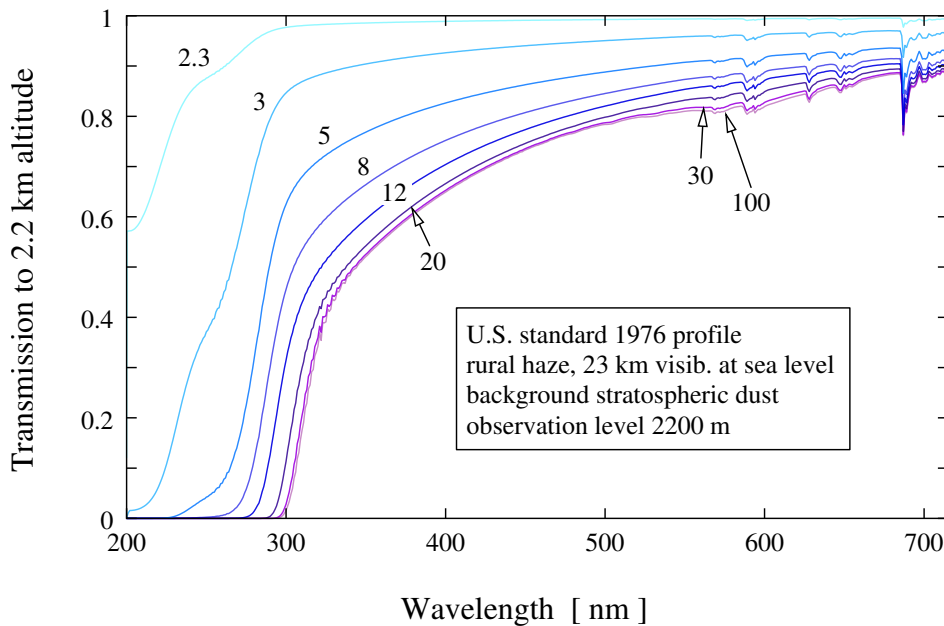


Figure 2.20: Transmission of light from different altitudes to 2.2 km calculated with the MODTRAN program. The atmospheric profile used is written in the legend. Adapted from Bernlohr (2000).

## 2.4 Monte Carlo simulation of Extensive Air Showers

As anticipated in Section 2.2, the simulation of electromagnetic or hadronic showers is performed via Monte Carlo methods. For Cherenkov telescopes like MAGIC having simulated data is of utter importance, since there is no beam of gamma rays through which the instrument can be calibrated. For this reason  $\gamma$ -ray initiated showers are simulated and are used in the analysis to estimate the energy and arrival direction of real showers. Showers with primary protons or nuclei can be used for the background estimation but they require more time for the simulation to complete, so usually a real sample of hadronic events are used for this purpose. Moreover, hadronic models can have many uncertainties, especially at the highest energies. Electromagnetic processes are known much better so that simulation results are highly reliable: in this case the problem is the high number of particles produced in the shower, which increases the computation time.

The main difficulty in a Monte Carlo simulation is the number of particles, processes and observables to be taken into account. Each particle must be propagated and tracked until it

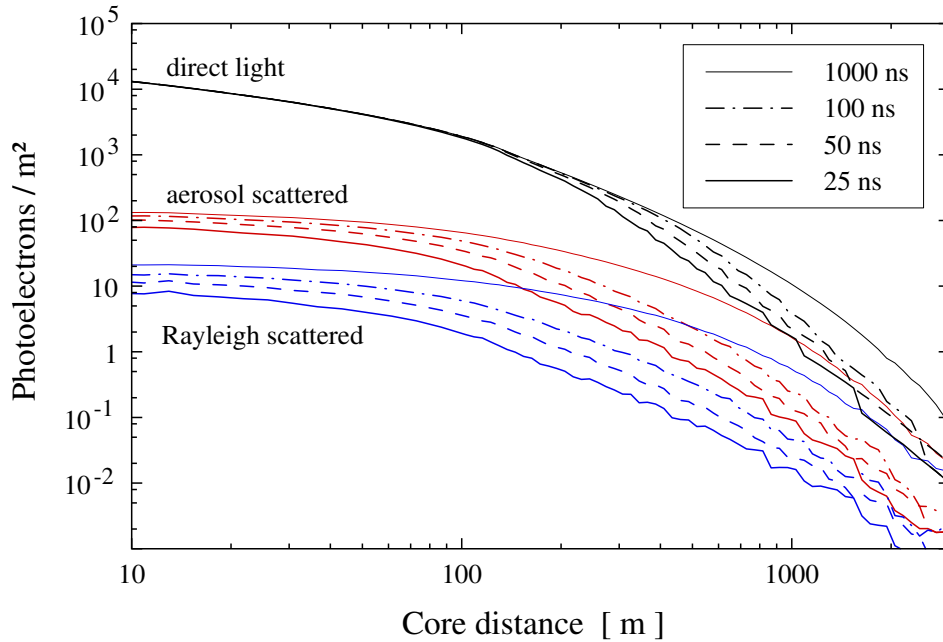


Figure 2.21: Lateral density of direct, aerosol and Rayleigh scattered light for vertical proton showers of 100 TeV with a tropical atmospheric profile. Different line dashes mean different integration times of the instrument. Adapted from Bernlohr (2000).

interacts or decays (if unstable): the interaction is selected from the set of possible processes for the selected particle. At this point the particle properties (momentum, energy, position, time, angular orientation ecc.) are saved in a temporary stack memory. The particle parameters are saved only if the particle crosses one of the *observation levels*: they are imaginary layers at different heights and their purpose is to have information about the longitudinal and lateral development of the showers. Usually the last observation level is located at the same height of the experimental site in consideration (e.g. for MAGIC it would be at 2200 m). When a particle crosses the last observation level, it is not tracked anymore. This is done for all the particles generated in the shower. The previous is, very roughly, the workflow of a Monte Carlo code.

The software usually used for the simulation of the development of extensive air showers is CORSIKA (COsmic Ray SIMulations for KASCADE, Heck et al. 1998), a code originally developed by the members of the KASCADE collaboration. In the years it became the standard software used by all the experiments studying air showers. The primary particle can be chosen to be a gamma-ray, a proton or a nucleus up to iron in a wide energy range. The secondary particles can be elementary particles (50 types: leptons, mesons, baryons, anti-baryons, resonances, neutrinos) or nuclei and can interact, decay or annihilate. The particles propagate through the atmosphere: in CORSIKA it is made up of nitrogen, oxygen and argon in a 78.1 : 21.0 : 0.9 ratio, with five layers to take into account the density variation with height. Different models for the atmosphere density profile can be adopted depending on the experimental site location. The processes taken into account are particle dependent and different routines take care of different interactions. For electrons and photons, the EGS4 routine is used. For hadronic processes, since there are many uncertainties in the high energy range, there are five models available: VENUS (Werner 1993), QGSJET (Kalmykov, Ostapchenko, and Pavlov 1997), DPMJET (Ranft 1995), SIBYLL (Fletcher et al. 1994) and HDPM (Heck et al. 1998). At low energies, below 12 GeV in the center of mass frame, GHEISHA (Fesefeldt, H. 1985) or UrQMD (Bleicher et al. 1999) can be selected. Regarding decays, only channels with branching ratio greater than 1% are considered.

CORSIKA was initially thought to simulate only the production of particles (see Figure 2.22),

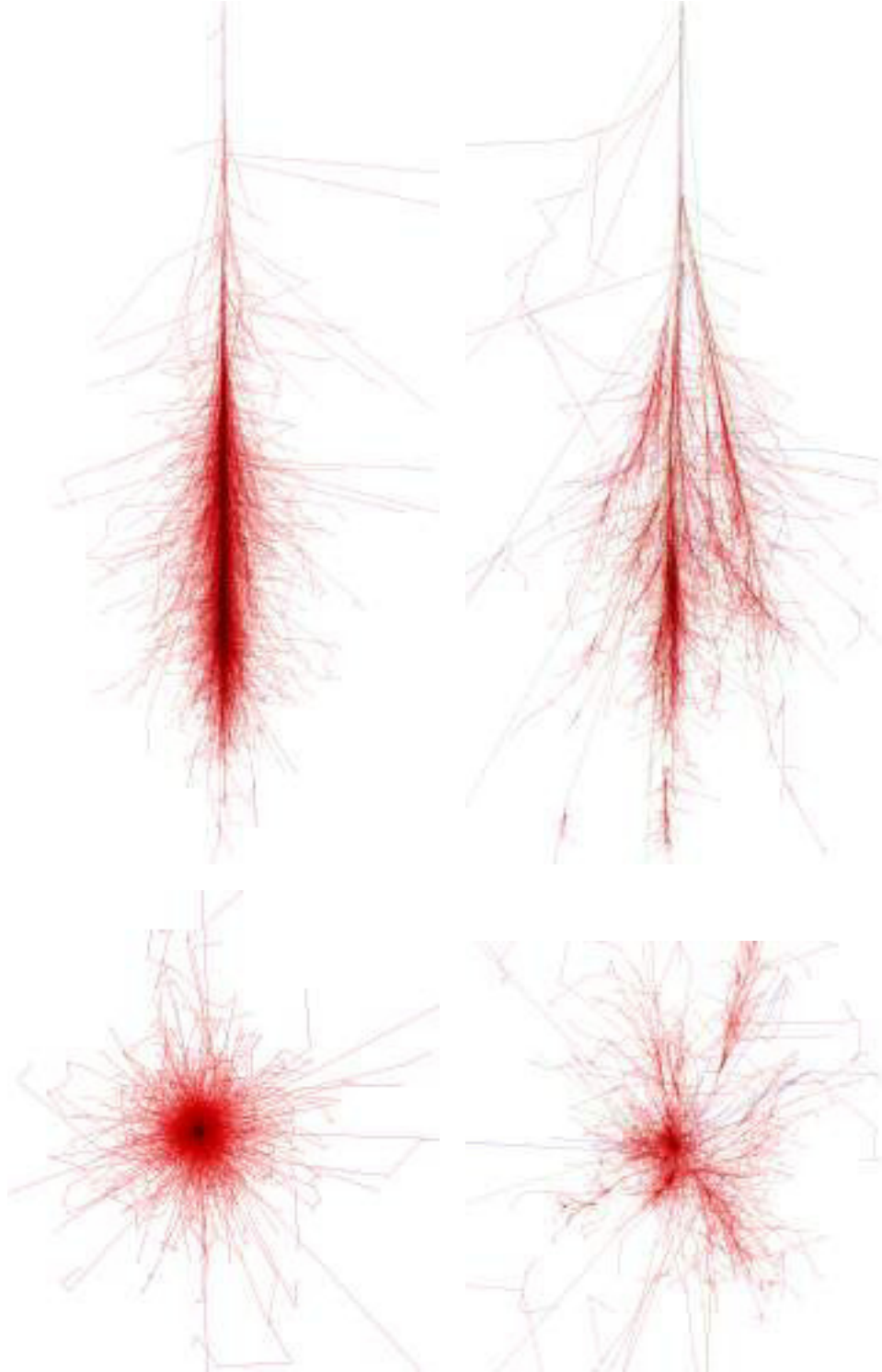


Figure 2.22: Shower images produced with the CORSIKA Monte Carlo software. Red lines are photons, electrons or positrons. Green lines are muons, blue lines are hadrons. **Left:** longitudinal (top) and lateral (bottom) development of an electromagnetic shower initiated by a 100 GeV photon. **Right:** longitudinal (top) and lateral (bottom) development of a hadronic shower initiated by a 100 GeV proton. From <https://www.ikp.kit.edu/corsika/>.

but with the development of the ACT technique, the simulation of the emission of Cherenkov light from the secondary particles of the shower was implemented. Other additional effects

---

can be simulated, like fluorescence or radio emission. Of course, taking Cherenkov emission as an example, the number of photons produced can be quite large, so the computation time will be affected accordingly. The simulation of Cherenkov light takes into account all the processes described in Section 2.3.2 and in order to have an efficient simulation, Cherenkov photons are grouped in bunches of adjustable size. Moreover, in the case of IACT experiments, the telescopes are represented by spheres enclosing them completely. Only the bunches crossing this sphere will be saved, because they will be actually reflected by the mirrors into the camera. For more details on the Monte Carlo chain used in MAGIC, see Section 4.1.

## 2.5 The Imaging Atmospheric Cherenkov Technique

In the previous sections I described in detail the development of hadronic and electromagnetic showers, focusing on the emission of Cherenkov light by secondary particles. In this section I will describe how all the previous pieces fit together into the Imaging Atmospheric Cherenkov Technique (IACT).

The basic principle of this technique can be inferred by the name itself (see Figure 2.23): the atmosphere is used as a calorimeter where primary particles ( $\gamma$  or cosmic rays) produce air showers. Secondary charged particles (mostly electrons and positrons) emit Cherenkov light, which is collected by large mirrors and focused on a camera comprised of PMTs. The light recorded forms an image in the camera and the properties of the primary particle (energy, direction, type) are inferred from it.

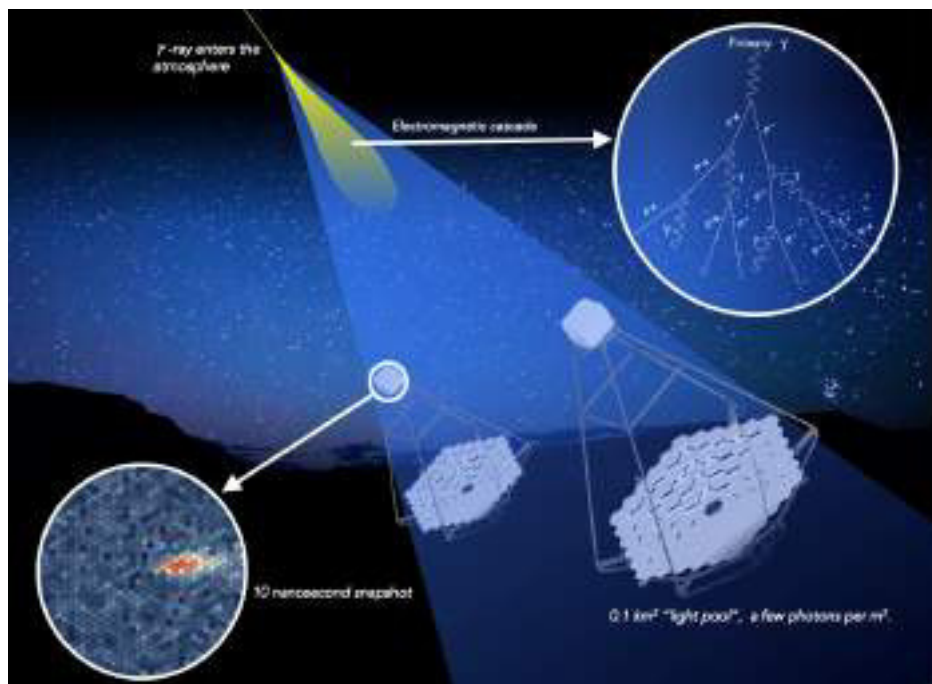


Figure 2.23: The principle of the Imaging Atmospheric Cherenkov Technique (here a primary gamma ray is considered). From <https://www.cta-observatory.org/about/how-cta-works/>.

The reflectors required are large (several meters of diameter) in order to collect as many Cherenkov photons as possible. The angular size of the image is  $0.5\text{-}1.0^\circ$  so the requirements for the optical system of a Cherenkov telescope are not as high as the ones for optical astronomy. To reach large areas, the reflector is composed by many mirrors of the same focal length. The shape of the reflector can be spherical or parabolic (as in MAGIC): in the latter case the arrival times of Cherenkov photons are preserved but the construction cost of the

single mirrors is higher. The telescope structure supporting the reflector is altazimuthal and allows to point the targets moving in the azimuth and zenith directions. The structure must be rigid enough in order to avoid huge deformations due to the weight of the structure itself and of the other components of the telescopes (reflector and camera in particular). The camera is composed by a large number of photon detectors, namely PMTs. They should be most sensitive in the same wavelength range where Cherenkov light is mostly produced. Because of the time duration of Cherenkov pulses (few nanoseconds for gamma-ray showers, around 20 nanoseconds for hadronic ones), their timing response should be fast. The large number of PMTs ensures to generate a shower image with high precision, which is fundamental for the following reconstruction of the events. Finally, fast electronics should be used to record the events.

The most challenging difficulty for IACTs is background rejection (also called gamma-hadron separation): most of the recorded events are of hadronic origin, about three order of magnitude more than gamma-ray events. The discrimination between the two types of events is done analyzing the recorded images: gamma-ray initiated showers form elliptical and narrow images, while hadronic ones, due to their different development in the atmosphere, create more broader and scattered images (see for example Section 4.4, Figure 4.1). Each image can be fit by an ellipse characterized by the so called *Hillas parameters* (see Figure 4.2), introduced in Section 2.3.1: the distribution of these parameters is different if they belong to a  $\gamma$  or a hadronic shower and this fact is used to reject most part of the hadronic events using classification methods (see Section 4.7.1). Moreover, the orientation of major axis of the ellipse, which gives ultimately the arrival direction of the events, will be different for gamma-ray showers, since they come from a discrete source. Hadronic events are instead and isotropic distribution for their arrival direction.

The reconstruction of the events and consequently the gamma-hadron separation are improved by the stereoscopic technique, as pioneered by HEGRA: more Cherenkov telescope view the same events from a different point of view, allowing a better geometrical reconstruction of the shower properties. In particular, the stereoscopic technique allows to reject other sources of background: for example muons produced near the reflectors can trigger a single telescope forming a ring-like image in the camera. With a stereoscopic system, where an event is recorded only if it triggers all the telescopes (or a minimum number), the muon event will be discarded since only one telescope will trigger. Beside muons, the most relevant source of background is the *Night Sky Background* (NSB): this will produce a continuous signal in the PMTs, while Cherenkov photons will produce a much higher signal. To discriminate between pixels activated by the NSB and those belonging to the shower, a cleaning technique is used (see Section 4.4). After removing these pixels, the image can be characterized by its Hillas parameters. Finally, cosmic  $e^+/e^-$  with isotropic arrival direction and diffuse  $\gamma$ -rays are irreducible sources of background, since they produce electromagnetic showers with the same development as those initiated by VHE gamma rays.

As far as the angular resolution is concerned, the stereoscopic technique allows to better reconstruct the arrival direction of the events from the geometrical reconstruction of the shower parameters: in this way a IACT can reach an angular resolution as good as  $0.05^\circ$ . The angular resolution is energy dependent, because high-energy showers will be better reconstructed than low energy ones (see Section 4.11.2).

Other figures of merit of the Imaging Atmospheric Cherenkov technique are the collection area, the energy threshold and their sensitivity. The collection area of a Cherenkov telescope can be estimated recalling that the Cherenkov light from an air shower creates on the ground a light pool with circular shape of about 120 m radius: if a Cherenkov telescope is located inside the light pool, it will be triggered. From this simple argument, the collection area of a IACT is of the order of  $10^4 \text{ m}^2$ . As it will be shown in Section 4.11.1, the collection area depends on the energy and on the zenith of the observations. The energy threshold of a Cherenkov telescope depends mainly on the surface of the reflector and on the efficiency

of the PMTs. The former is needed to collect more Cherenkov photons from low energy showers, where their number is small, while the second ensures that all Cherenkov photons are effectively collected. In general, a larger reflector means a lower energy threshold. In the case of MAGIC, the reflectors have a diameter of 17 m and the resulting energy threshold is  $\sim 70$  GeV (after analysis cuts). This is important because it allows to have an overlap with satellite-based instruments like Fermi. The energy threshold, like the collection area, depends on the zenith angle of the observation: a shower coming from a high zenith will create a larger light pool on the ground, resulting in a lower Cherenkov photon density. Moreover, since the path traveled by photons is longer, they are more attenuated in the atmosphere. These two factors have the result that only higher energy showers will trigger at higher zenith and so the energy threshold increases. Despite this, this effect is compensated by the increase of the collection area because of the larger light pool. This allow IACT to detect gamma rays up to few tens of TeV. At higher energies, the images will leak outside the camera and so no proper reconstruction is possible. The large collection area of IACT is also responsible of their high sensitivity, especially above few hundreds of GeV (see Section 4.10).

The Imaging Atmospheric Cherenkov technique has also few drawbacks: the most relevant is the duty cycle, because IACT can operate only during the night and when the background due to the Moon is not too high (it would damage the PMTs). Moreover, also weather conditions can affect the measurement, sometimes making it impossible to take data. Another limitation of IACTs is their small field of view: for MAGIC it is  $3.5^\circ$ , but it can be as high as  $9^\circ$  (e.g. the SSTs of CTA). For this reason IACTs must point directly the sources to be observed.

## 2.6 Other detection techniques for air showers

The IACT technique is not the only one able to detect very high energy  $\gamma$ -rays, or cosmic rays in general. Cherenkov telescopes operates in the energy range from some tens of GeV to some tens of TeV with high sensitivity, with the main limitations of a small FoV and low duty cycle. We know that the CR spectrum goes up to energies of  $10^{20}$  eV with a power law spectrum approximately of  $E^{-2.7}$ . Here the flux of particles is about 1 particle/km<sup>2</sup>/yr: this means that detectors covering large areas and with a duty cycle as high as possible are needed.

This is the principle behind the so called EAS detectors, which exploit the “particle sampling” technique: the charged particles of the shower are detected by an array (sparse or covering the entire area) of detectors spread over a large area, see Figure 2.24. The energy threshold is rather high, of the order of TeV energies, but there is a gain in effective area ( $\sim 10^4$  m<sup>2</sup>), in duty cycle ( $\sim 100\%$ ) and FoV ( $\sim \pi$  sr). Several types of detectors were and are used in EAS experiments such as scintillators, resistive-plate chambers, water Cherenkov tanks, muon detectors and fluorescence telescopes. Since the bulk of the particles is around the shower axis (200 m to 300 m), usually the central region of the array is more detector-dense, while in the outer region the detectors can be placed farther away one from each other.

The arrival direction estimation is divided in two parts: first the impact point on ground is found using a fit with the NKG formula of the lateral distribution of the particle density from the detectors signals. Then the arrival direction is reconstructed from the arrival times of the signals in the detectors and assuming the shower front as a plane perpendicular to the arrival direction. If fluorescence telescopes are used in the experimental setup, a signal in those detectors constrain even better the geometrical reconstruction. The advantage of fluorescence light is that it is isotropic, but with low intensity, so that detectors can be used only during moonless nights (duty cycle about 10%). The achievable angular resolution depends on the electron size ( $N_e$ ), being of the order of  $0.1^\circ$  for showers with  $N_e \sim 10^6$ .

The energy of the events is proportional to  $N_e$ , so first the shower size must be computed.

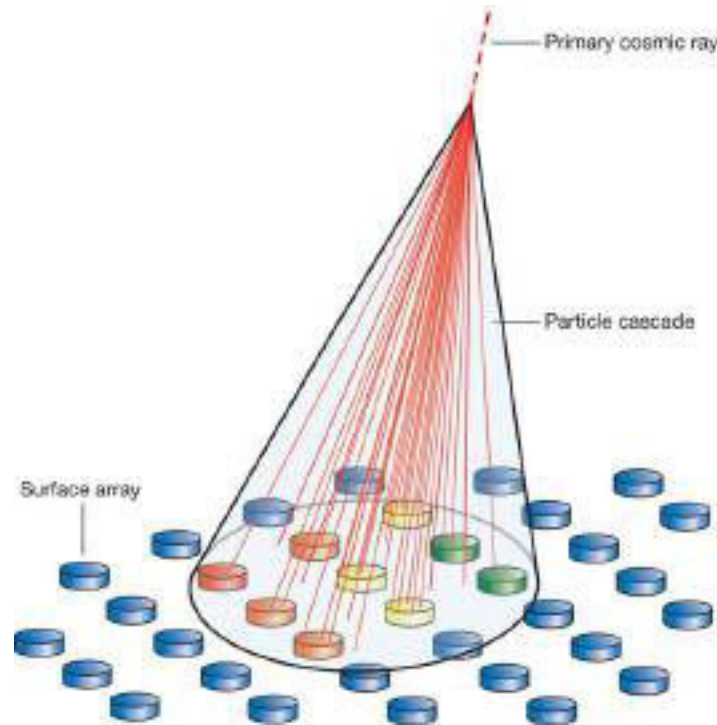


Figure 2.24: Principle of the detection technique of EAS arrays. From Bauleo and Rodríguez Martino (2009).

The NKG is used again, with the age  $s$  not a priori known. A solution is to use the value of  $s$  for the height of the experimental site from MC or the data itself, otherwise a global fit can be performed where axis impact point, direction and shower age are left as free parameters. When the fitting function is found, the total size  $N_e$  can be computed starting from equation (2.41). Results from EAS-TOP show that the agreement with the NKG formula with an average value for the shower age is at most 10%. KASCADE could achieve an accuracy of about 1% with the global fitting technique. For the primary particle energy, equation (2.52) can be inverted to obtain  $E_0$ .

Finally, cosmic rays are composed of different nuclei, from hydrogen up to iron. EAS experiments are able to discriminate between different primary nuclei and producing in this way an all-particle spectrum. There are two methods to infer the mass number of the primary particle. The first uses  $N_e$  to derive the initial energy and  $N_\mu$  to find the primary mass through equation (2.55). The second method exploits the dependence of the shower maximum  $X_{\max}$  on the mass number (equation 2.56).  $X_{\max}$  can be measured with fluorescence detectors or with integrating Cherenkov telescopes, arrays of PMTs over a large area looking in the upward direction. The latter can measure both the lateral and longitudinal distribution of Cherenkov light, giving an estimate for  $X_{\max}$ .

As far as  $\gamma$ -rays are concerned, the EAS technique can be used in the same way as described above. The energy threshold achievable is of the order of hundreds of GeV but with a sensitivity much lower than IACTs. EAS gamma detectors are most sensible in the region from some tens of TeV up to hundreds of TeV. Of course the same detector will be triggered by hadronic events as well, so a discrimination technique is needed. This is usually done by muon detectors, since gamma-ray induced showers should be muon poor, or by MC data in a IACT-like manner (see Section 4.7.1).

### 2.6.1 Examples of cosmic rays EAS detectors

The history of EAS detectors for cosmic rays is rather long, starting in the sixties of the twentieth century with the first large arrays Volcano Ranch (New Mexico, 1770 m), Haverah Park (UK, 25 km away from the University of Leeds) and Yakutsk Array (Siberia, 105 m). Here I will focus on more recent experiments, but for an historical review see Kampert and Watson (2012).

The largest array before the current operative ones was AGASA (Akeno Giant Air Shower Array, Chiba et al. 1992) in Akeno, Japan, at 900 m of altitude. Operative from 1990 to 2004, it comprised 111 unshielded scintillator detectors ( $2.2 \text{ m}^2$ ) spaced of 1 km one from each other. 27 of the 111 detectors mounted muon detectors of different areas. With AGASA some research and develop was performed, especially on the use of water Cherenkov tanks and on the different components of showers (electrons, photons and muons). AGASA reported a CR spectrum extending up and beyond  $10^{20} \text{ eV}$  without any cut-off with 11 events in Takeda et al. (1998), but this was disproved by current experiments.

Regarding the detection of fluorescence light, the milestone was the Fly's Eye detector (Bird et al. 1995). The first phase, Fly's Eye I, had 67 camera units: each one consisted of a 1.5 m diameter spherical section mirror, PMTs with Winston cones and the electronics. Each station could observe a  $5^\circ \times 5^\circ$  region of the sky, resulting in a complete coverage of the sky. A first test with 3 units taken to the Volcano Ranch site allowed the detection of 44 showers in 12 consecutive nights with energies up to  $10^{18} \text{ eV}$ . The second phase, Fly's Eye II, added 36 units. With Fly's Eye, the fluorescence detection technique found its way up to current detectors.

More recent experiments comprise the italian EAS-TOP (Extensive Air Shower on Top, Campo Imperatore, Italy, 2005 m), the german KASCADE (KARlsruhe Shower Core and Array Detector, Karlsruhe, Germany, 110 m) and KASCADE-Grande and the successor of Fly's Eye, HiRes (High Resolution Fly's Eye, Dugway, Utah, USA).

EAS-TOP, operative from 1989 to 2000, consisted of 35 scintillator detectors of  $10 \text{ m}^2$  each, separated by 20 m near the center of the array and by 80 m at the edge, for a total area covered of  $0.1 \text{ m}^2$  (Aglietta et al. 1989). At the core of the array there was a  $140 \text{ m}^2$  iron-lead calorimeter for hadron and muon detection above 30 GeV and 1 GeV respectively. Since it was on top of Gran Sasso, there was the possibility of performing correlated measurements of muons with the underground experiment MACRO.

KASCADE (Antoni et al. 2003) was operative from 1996 to 2013: it consisted of 252 stations with shielded and unshielded detectors for electrons and muons detection spread over a  $200 - 200 \text{ m}^2$  area and spaced of 13 m one from each other. Muon-tracking detectors were distributed across the 192 outer stations with lead-iron shielding (to stop the EM component) and plastic scintillators with coupled PMTs. After EAS-TOP stopped operation, 37 of its electromagnetic stations were recycled by KASCADE, renamed KASCADE-Grande after the extension (Apel et al. 2010). The KASCADE experiments achieved quite important results in the testing of the several hadronic models and in the CR composition in the knee region, showing that different mass groups had a knee in their spectrum shifted towards higher energies for higher masses.

HiRes was an upgrade of Fly's Eye, with two sites, HiRes I and HiRes II, 12.6 km apart. Basically the fluorescence telescopes were the same as in Fly's Eye with smaller PMTs, reducing to  $1^\circ \times 1^\circ$  the region covered in the sky by each unit. The most important result was the proof of a cutoff in the energy spectrum around the region where the GZK cutoff was expected (Sokolosky and HiRes Collaboration 2011). HiRes is not operational anymore since 2006.

The most recent EAS detectors for CR detection are the Pierre Auger Observatory (PAO, Argentina) and the Telescope Array (TA, Utah, USA). PAO (Abraham et al. 2004) is the largest EAS detector of all time: an area of around  $3000 \text{ km}^2$  is covered by 1600 water Cherenkov

tanks on a 1.5 km side triangular grid and 24 fluorescence detectors on four stations for an hybrid detection of the showers (see Figure 2.25). The water tanks (see Figure 2.26) are cylinders of 1.5 m height and  $10\text{ m}^2$  base filled with 12 t of pure water, in which charged particles emit Cherenkov light collected by three PMTs on the top of the tank. Each of them has a GPS time unit and power unit with solar panels. The signals are transmitted to the elaboration system with radio waves. The fluorescence detectors are Schmidt telescopes with 3.5 m spherical section mirrors and a camera composed of 440 PMTs (see Figure 2.26). Auger clearly detected a flux suppression above  $4 \cdot 10^{19}$  eV, observed the anisotropy in the arrival direction above  $5.7 \cdot 10^{19}$  eV and measured the mass composition above  $10^{19}$  eV. Moreover it put upper limits on EeV photon and neutrino fluxes, ruling out (almost) the model where highest energy CRs are produced in exotic physics interactions.

The Telescope Array (Tameda 2009) is very similar to PAO: it covers about  $800\text{ km}^2$  with an hybrid approach of 506 surface scintillator detectors on a 1.2 km square grid and 38 fluorescence telescopes distributed in 3 stations.

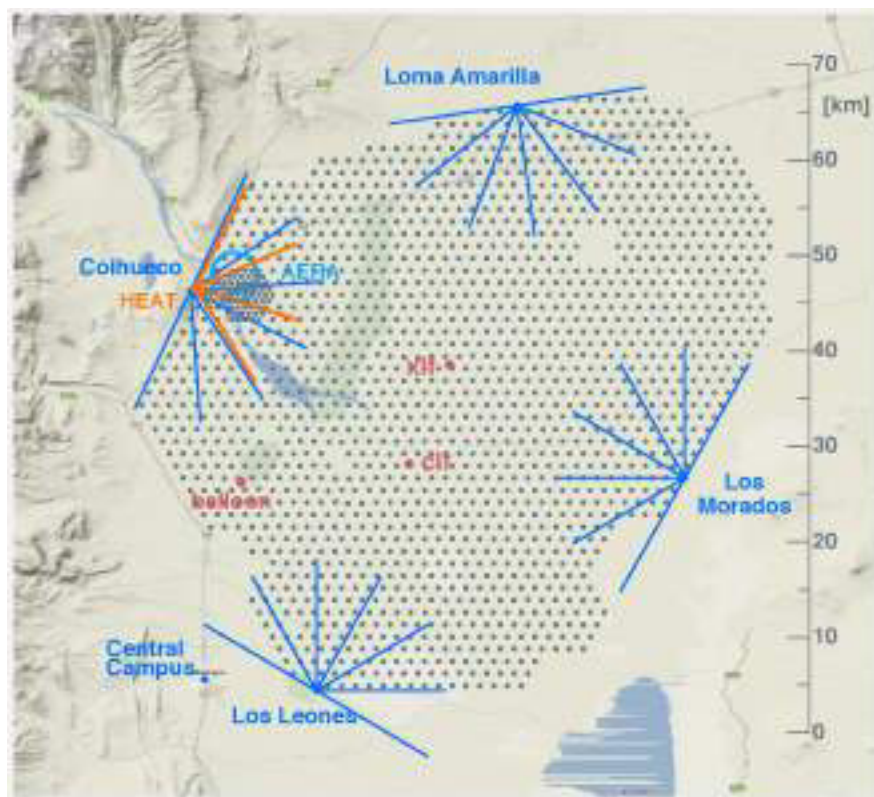


Figure 2.25: Scheme of the Pierre Auger Observatory array. Grey dots are the water Cherenkov surface detectors, while the blue dots are the 24 fluorescence telescopes with their field of view (blue lines). From Conceição (2013).

### 2.6.2 Examples of $\gamma$ -rays EAS detectors

As already mentioned, EAS detectors for  $\gamma$ -rays exploit the same technique as the ones for CRs, adding the hadron/gamma discrimination to retain only gamma ray initiated showers. The most notable  $\gamma$ -ray EAS detectors are ARGO-YBJ, MILAGRO and HAWC (see Bacci et al. 2002; Atkins et al. 2003; Abeysekara et al. 2013). For the future, LHAASO will probably be deployed in China (Di Sciascio 2016).

ARGO-YBJ (Astrophysical Radiation with Ground-based Observatory at YangBaJing, operative up to 2013) is located in Tibet at 4300 m and is a full coverage  $78 \times 74\text{ m}^2$  detector with a single layer of Resistive Plate Chambers (RPCs). A guard ring surrounds the core of

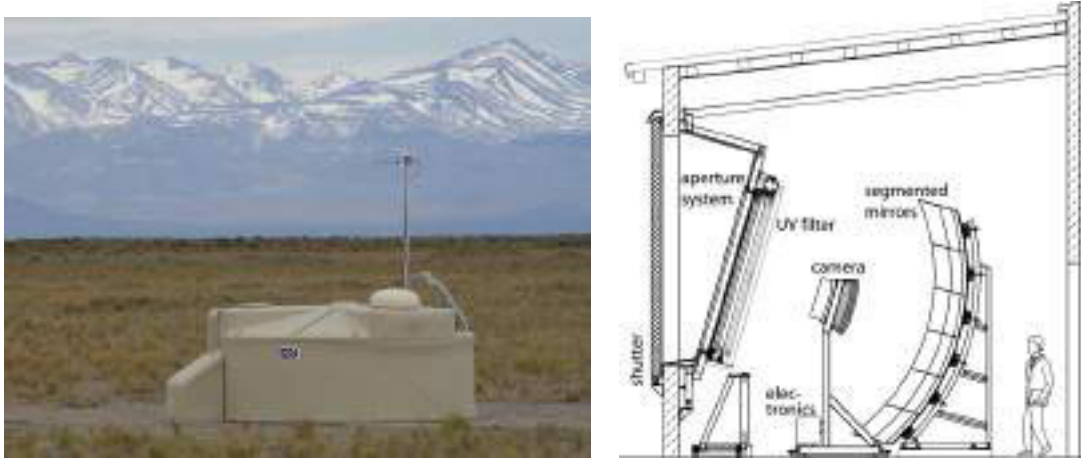


Figure 2.26: One of the water Cherenkov surface detectors (left) and fluorescence telescopes (right) used in the Pierre Auger observatory. From Abraham et al. (2010).

the instruments with other RPCs. There are 18480 pads of  $56 \times 60 \text{ cm}^2$ , each with a RPC, constituting the pixels of the array. ARGO-YBJ could detect the emission from the Crab at  $5\sigma$  in 50 days (Bartoli et al. 2015) and the flare from Mrk421 in 2008, monitoring the source for the whole year and detecting a variable flux (Aielli et al. 2010).

MILAGRO was located in New Mexico at 2630 m and it was equipped with a  $80 \text{ m} \times 60 \text{ m} \times 8 \text{ m}$  central pond detector of  $5000 \text{ m}^2$  filled with  $6 \cdot 10^6$  gallons of water and 175 outer water Cherenkov tanks on a total area of  $40\,000 \text{ m}^2$ . The central pond had two layer of PMTs on a  $2.8 \text{ m} \times 2.8 \text{ m}$  grid: the first layer has 450 PMTs at 1.5 m depth, the second layer has 273 PMTs at 6 m depth, ensuring that all the charged particles could be detected if entering the pond. Moreover, also the secondary gamma rays of the showers could be detected. The outer water tanks were used mostly to determine the correct core position of the shower if it falls outside the central pond. MILAGRO detected for the first time TeV gamma rays from the Galactic plane, from the Cygnus region and detected the Crab Nebula at  $5\sigma$  in 100 days (see Atkins et al. 2005; Abdo et al. 2007; Atkins et al. 2003).

The HAWC (High Altitude Water Cherenkov, Abeysekara et al. 2017) experiment is located in Mexico at 4100 m: 300 water Cherenkov tanks, each with 3 PMTS, cover an area of about  $20\,000 \text{ m}^2$  (see Figure 2.27). HAWC sensitivity is 15 times better than MILAGRO thanks to the improvements in gamma/hadron separation from the signal pattern in the detectors, angular resolution ( $0.1^\circ$  for energies above 10 TeV, five times better than MILAGRO) and energy resolution (below 50% above 10 TeV). The 1-year sensitivity is about 5-10% of the Crab Nebula flux, the instantaneous FoV is  $1.5 \text{ sr}$  and the duty cycle greater than 90%. HAWC pursues many science cases (GRBs, Dark Matter, Pulsars, Galactic plane emission, Transients) and recently published the first catalog with 39 TeV gamma ray sources, comprising the observations made from its completion in 2015 (Abeysekara et al. 2017).

The new generation EAS experiment is the Large High Altitude Air Shower Observatory (LHAASO), which is supposed to be built in Sichuan, China, at 4410 m (Di Sciascio 2016). It will be both a CR and gamma ray detector comprised of:

- a  $1 \text{ km}^2$  array with a central part of 4931 scintillators ( $1 \text{ m}^2$ , spaced by 15 m) and a guard ring with electromagnetic particle detectors
- an underground  $1 \text{ km}^2$  array overlapping with the previous one made of water Cherenkov tanks for muons detection
- a surface water Cherenkov detector covering about  $78\,000 \text{ m}^2$



Figure 2.27: The HAWC observatory. From <https://www.hawc-observatory.org/>.

- 12 air Cherenkov telescopes

LHAASO is expected to be completed in 2021, while one fourth of the total site should be finished by 2018. At energies above few TeV, LHAASO 1-year sensitivity is better than the 50h sensitivity of current IACT telescopes, due to the low duty cycle of the latter (see Figure 2.28). It will search for  $\gamma$ -ray emission in the 100 GeV-PeV energy range, possibly discovering new classes of sources, checking for transient sources, mapping the diffuse gamma emission. Regarding CRs, LHAASO will improve the statistics in the  $10^{12}$  eV to  $10^{17}$  eV range, discriminating different mass groups and searching for anisotropy in the region around the knee. Detecting different components of the showers (electronic, muonic and Cherenkov) will test thoroughly the hadronic models, giving hints for possible correction of current MC simulation for hadronic showers. Finally, DM searches are expected, looking for a possible WIMP signature. Together with CTA, LHAASO will be the most sensitive instrument to gamma-rays in the UHE range in the northern hemisphere.

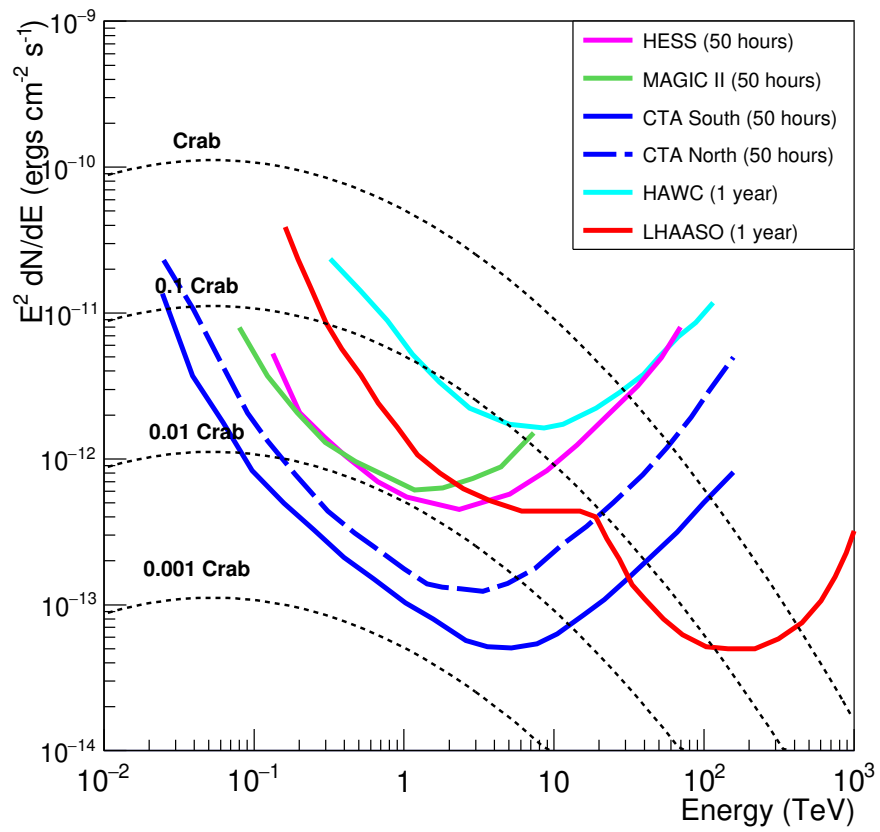


Figure 2.28: Differential sensitivity of LHAASO for a point-like source compared to other experiments (see legend). The extrapolation up to 1 PeV of the Crab Nebula spectrum is reported, also scaled by a 0.1, 0.01 and 0.001 factor. From Di Sciascio (2016).

## Chapter 3

# THE MAGIC TELESCOPES SYSTEM

MAGIC is a system of two Cherenkov telescopes located in La Palma, one of the Canary Islands, Spain ( $28^{\circ} 45' \text{ N}$ ,  $17^{\circ} 53' \text{ W}$ ). The site is at 2200 m above sea level, almost on top of the Roque de Los Muchachos mountain, in the so called ORM (Observatorio del Roque de Los Muchachos). MAGIC was designed to exploit the Imaging Atmospheric Cherenkov Technique for the indirect detection of VHE gamma-rays, with the particular goal of achieving a lower energy threshold with respect to previous generations IACTs.

The Imaging Atmospheric Cherenkov technique needs a specific hardware to work. Building a IACT requires taking into account several aspects to take full advantage from the detection technique described in Chapter 2. In particular, some design and structural choices were driven by the scientific goals pursued by MAGIC, like Gamma-Ray Bursts. Since MAGIC detects Cherenkov light from extensive air showers, basically it is an optical telescope. The Cherenkov light is detected as rapid flashes of few nanoseconds duration, so that the both the light detectors and the electronics must be very fast. Having two telescopes can help drastically in rejecting events belonging to background fluctuations and this is accomplished by having a stereoscopic trigger. Once an event triggers, it can be saved to disk through the Data Acquisition System and finally it can be brought to the analyzers.

In this section I will describe the main structural and hardware components of MAGIC: the structure, the drive system, the cameras, the readout system and the several auxiliary subsystem. The last part describes how telescopes are operated and how the observation of sources are performed. This will be fundamental in order to understand some analysis approaches as described in Chapter 4.

### 3.1 Structure and drive system

The MAGIC telescopes were designed to be light in order to be fast when repositioning, for example after a GRB alert. The total weight of each telescope is  $\sim 70 \text{ t}$  distributed between the camera ( $\sim 0.89 \text{ t}$ ), the camera bow and counterweights ( $\sim 3.4 \text{ t}$ ), the carbon fiber dish ( $\sim 8 \text{ t}$ ), the mirrors and Active Mirror Control ( $\sim 9 \text{ t}$ ), the towers to access some parts of the telescopes ( $\sim 20.2 \text{ t}$ ) and the six carriages ( $\sim 25 \text{ t}$ ). Despite the reduced weight, enough stiffness is required to avoid deformations and sustain the weight of the telescope. This is accomplished using a carbon fiber structure which is at the same time robust and light.

To point, track sources and repoint, MAGIC has a drive system which allows the movement in both the azimuthal and zenith axis, described in Bretz et al. (2009).

For the azimuthal movement, there are 6 digitally controlled industrial drive units with servo motors. Two of them are equipped with a 11 kW motor (Bosch Rexroth MHD112C-058) and are coupled by torque control in a master-slave setup. The motors exert their power on a

drive chain, which guarantees the minimum slip while rotating.

On the elevation axis there is only one digitally controlled drive unit equipped with a 1 kW motor. Also in this case there is a drive chain on which the motor exerts its power. To prevent the backlash, the elevation axis must be properly balanced. The movement of the telescopes during repositioning is performed at the angular speed of  $4^\circ/\text{s}$ , but in the so called *fast movement mode* (or GRB mode), the speed is increased to  $7^\circ/\text{s}$ . This allows to reposition the telescopes in less than 30 s.

The drive system allows a movement of more than  $400^\circ$  in the azimuthal axis and in the range  $-73^\circ - 100^\circ$  in the elevation axis. Both of the axis are also equipped with end-switches to know in which direction the telescope is moving. This is important in the case the telescopes have to be moved manually.

The telescope movements are controlled by two 13 bit shaft encoders (one in the west tower and the second at the top of the central axis), which read the motor positions at 1 kHz frequency.

When the telescopes are not taking data (daytime) or the weather conditions are bad (e.g. strong wind), the telescopes are secured with bolts, which are manually removed by the shifters before switching on the motor power and taking data.

Even with its robust structure, there can be imperfections and deformations of the mechanical structure. This requires a pointing model which parametrizes the deviations from an “ideal” telescope. The pointing model is created thanks to the TPoint package: the Starguider camera (see Section 3.2.3), located in the center of the dish, looks for the stars spread in the sky (the so called TPoints) and record on each occasion the telescope readout, which is then fed to TPoint. The software then identifies and measures misalignments and flexures in the telescope structure, which are included in the drive and starguider bending models (multi-parameter calibration functions). The former is applied directly in the software controlling the drive system, called *Cosy*, while the latter is applied during data analysis (usually at star level, see Section 4.4).

## 3.2 Optical system

### 3.2.1 Mirrors

The mirrors of a Cherenkov telescope have peculiar features. Since the IACTs detection technique is based on the collection of the Cherenkov light produced by the atmospheric showers, the mirrors must be designed to have optimal performance for this task. There are intrinsic limits: for example the showers starts developing at an average height of 10 km; for this reason the source is somewhat extended from the telescope point of view and this puts a limit on the achievable precision. Moreover the Cherenkov light can be scattered and absorbed in the atmosphere, so that the spectrum at ground is different from the original one when the light was produced. Because of that, the wavelength range of most of the light is between 300-350 nm and mirrors reflectivity must be maximum in this range. MAGIC optics, as any other, is not perfect and suffers from aberrations, in particular coma aberrations because of its parabolic shape. The parabolic shape allows to preserve the temporal features (coaxial photons travel the same path) of Cherenkov flashes but at the cost of a more difficult production. It is not possible to produce a parabolic mirror from the start, so each mirrors has two different radii. At each point of the mirror the average of these radii is the radius at that point of the paraboloid. The mirrors surface can be characterized by the following parameters:

- The P-V valley, the difference between the perfect geometrical shape and the real one. This determines the goodness of the PSF;
- The RMS roughness, which determines the reflection of the mirrors.



Figure 3.1: Picture of MAGIC-I in parking position. The camera (on the left, leaning on its pillar) is kept at the right position from the reflector thanks to the arc and stiffness is maintained with steel wires. On the bottom right, one of the azimuth drive units (in yellow with the grey motor) with its carriage moving along the rail. The motor drives a double-toothed wheel gearing into the drive chain.

PSF is a key parameter for MAGIC, because it affects the sensitivity and the reconstruction of extended sources. Its value is made up by the contribution of all the mirrors, but the contribution is different considering the direction of light. For on-axis light, edge and central dishes contribute equally to the resulting PSF, while for tilted light the most of the contribution comes from edge mirrors. There's also a worsening of the PSF by going off-axis. The MAGIC PSF is measured every night before the observations with the SBIG camera, see Section 3.2.3.

Unfortunately, sometimes mirrors take external damage and it is needed to replace them. The most common problems are:

- inelastic modification of the mirrors structure due to temperature cycles;
- humidity absorbed in the mirrors and turned into water and eventually ice modifying the mirrors surface;
- bad micro roughness of the surface due to the diamond-milling technique causing high scattered light.

The two MAGIC telescopes mount different kinds of mirrors, see Doro et al. (2008). MAGIC-I has most INFN-PD aluminum-honeycomb sandwich  $50 \times 50$  cm mirrors, some MPI aluminum-honeycomb sandwich  $50 \times 50$  cm mirrors and from 2011 some INAF aluminum-honeycomb sandwich and cold-slumped  $1 \times 1$  m mirrors. In addition the disposition of MAGIC-I panels (on which mirrors are mounted) is chess-board-like, since the mirrors were touching during AMC adjustment because of a wrong consideration of mirror thickness and backpanels.

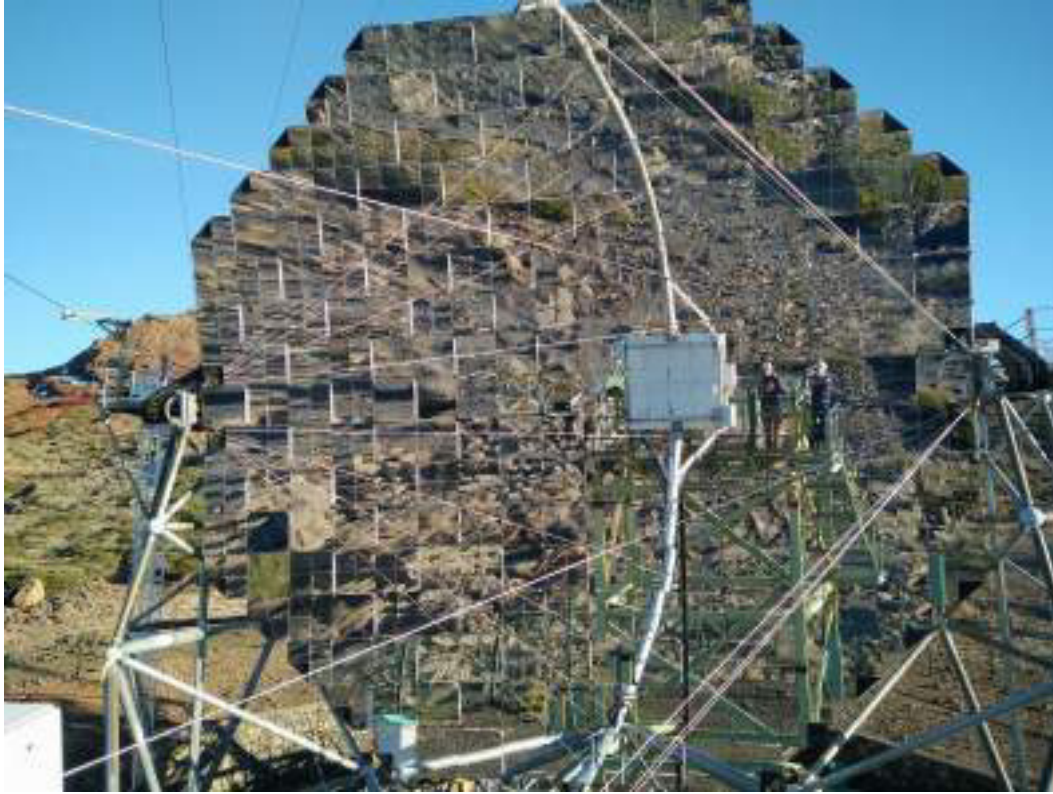


Figure 3.2: Picture of MAGIC-I reflector from the camera tower. Despite the reflection of the ground, the different measures of mirrors is visible (some mirrors are divided in four equal pieces, other are a unique piece).

This problem was solved by lowering or raising the panels accordingly to allow the correct adjustment without the contact between mirrors. MAGIC-II instead has 143 INFN-PD aluminum-honeycomb sandwich  $1 \times 1$  m mirrors and 104 INAF cold-slumped  $1 \times 1$  m mirrors. Overall, the MAGIC telescopes reflectors have a diameter and focal length of 17 m and a total reflective surface of about  $236 \text{ m}^2$ .

### 3.2.2 Active Mirror Control (AMC)

As discussed in the mirror section, a good alignment is mandatory to achieve a good PSF: such alignment is guaranteed by using the Active Mirror Control (AMC, Biland et al. 2008). It is a system with actuators in cardan and axial joints which can move the panels on which the mirrors are mounted and align them so that they are correctly focused. In the past the alignment was done with the help of laser modules which shot a laser beam from the center of the mirrors towards the camera. The problem with this method was the long focusing time ( $\sim 3$  min, too much for GRB observations; also there is a loss in duty cycle), the fact that the focus operation was possible only when the pointing position was reached and the not so good pointing accuracy.

The layout of the AMC system is a little different between MAGIC-I and MAGIC-II:

- MAGIC-I has eight independent chains with eight AMC electronics boxes each. These chains are horizontally aligned for better maintenance. The chains structure guarantees that only a small part of panels cannot be moved in case of failure (max 36). The computer with the interface to its AMC is placed in the Counting House.
- MAGIC-II has seven independent chains with eight or nine boxes each and they are

organized in sectors to minimize the cable length from the central box. The box containing the computer with the interface to its AMC is close to the telescope structure.

Each mirror has three fixing points: one is fixed, while the other two are connected to the actuators and allow the mirror to be moved and focused. The actuator positions are saved in so called Look Up Tables (LUTs), which are binned in zenith and azimuth angle. At the beginning of the night the AMC is used to center and adjust the mirrors in order to assess the quality of the optical PSF with the SBIG camera (see Section 3.2.3). For each source, during the repositioning of the telescopes (so also when changing wobble position, see Section 3.6.1 for details), the proper values of the actuator positions are read from the LUTs according to the zenith and azimuth of the observation, so that the mirrors are always focused. The same happens when a GRB alert comes and the telescopes repoint in fast mode.

### 3.2.3 SBIG camera

The SBIG camera is a CCD camera designed for measuring the (optical) PSF for individual mirrors or for the complete reflector and it is part of the AMC system. Three filters are available for different purposes: for the PSF measurement, performed at the beginning of each night of observation, the blue filter is used. In this case the SBIG camera looks at the reflection of a star on a spectralon plate in the camera (see next Section) and it is used to assess the optical PSF of the telescopes.

## 3.3 Camera

Once the photons are reflected by the mirrors, they reach the camera, made up of close photomultipliers (PMTs) to form a circular shape. Photons are then converted in photoelectrons by the PMTs and create an electrical signal which is processed by the readout and trigger systems (see Sections 3.4.2 and 3.4.3).

Each camera has 1039 PMTs (see Figure 3.3), R10408 Hamamatsu photosensors modules, hemispherical window, low profile, wide angle of acceptance, bialkali photocathode, 6-stage, head-on type (see for example Aleksić et al. 2016a; Borla Tridon et al. 2009). Each PMT (see Figure 3.4) has a diameter of one inch and a field of view of  $0.1^\circ$ , for a total of  $3.5^\circ$  of the whole camera. The peak quantum efficiency is 34% for light with 350 nm of wavelength. On top a hexagonal Winston cone focuses the light on the PMT window and prevent NSB light coming from large angles to enter the PMTs. The power unit for the bias voltages is a Cockroft-Walton DC-DC converter with a peak voltage of 1250 V. Since the operational gain is of the order of  $3 \cdot 10^4$ , the signal is amplified by an AC coupled pre-amplifier. The PMTs are grouped in clusters of 7 pixels (169 total, those at the camera edge are not fully populated) which allows a simple installation and maintenance. The photomultipliers are responsible of generating an



Figure 3.3: Rear view of the camera of MAGIC-II with the 169 PMTs clusters. From Borla Tridon et al. (2009).

electrical signal from the photons interacting

with the photocathode. This electrical signal is then converted into an analog optical signal: the benefits from this choice are that over long distances the dispersion of the signal is very low over a large bandwidth and crosstalk effects are not present. The conversion is performed by Vertical Cavity Surface Emitting Lasers (VCSELs): the light produced has a wavelength of 850 nm (near infrared) and a pulse width (FWHM) of 2.5 ns. The resulting signal of each pixel is transmitted from the camera to the electronics room in the counting house with  $\sim 160$  m long fiber cables, grouped in 19 bundles of 72 fibers each. In order to test the PMTs during daytime as well, at their base an electrical signal can be injected with a FWHM of 2.6 ns and a configurable amplitude to simulate the flash of a Cherenkov shower.

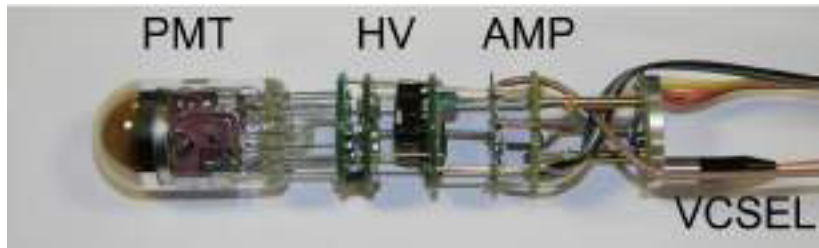


Figure 3.4: One of the 1039 PMTs of the cameras of the MAGIC telescopes. Each pixel, beside the photomultiplier tube, is completed by the HV generator, the preamplifier and the VCSEL. From Aleksić et al. (2016a).

Each camera is completed by other several components:

- two cooling aluminum plates to keep stable the pixel temperature; the cooling units are placed on the telescope undercarriage
- 8 temperature and 4 humidity sensors to monitor the two parameters
- two low voltage power supplies, one for each half of the camera
- a drying unit to lower, when possible, the humidity level
- the camera lids, controlled by the lid drive box on the camera side. They are used to protect PMTs during day and during bad weather conditions (high wind or humidity, rain)
- a spectralon plate, commonly called target, used to focus star images when assessing the telescope PSF
- starguider LEDs, used by the starguider camera (see Section 3.5.6) to find the camera center

All these elements make up the cameras of the MAGIC telescopes, each reaching a weight of almost 1 t.

The operators can check the status of the two cameras and control them through the LabView based programs CaCo1 and CaCo2 (CaCo stands for Camera Control), which interact with the Central Control program of the MAGIC telescope, see Section 3.5.1.

## 3.4 Readout system

### 3.4.1 Brief description of the MAGIC signal chain

Before going into the details of the readout system, it is worth to have an overview of the signal chain in the MAGIC telescopes.

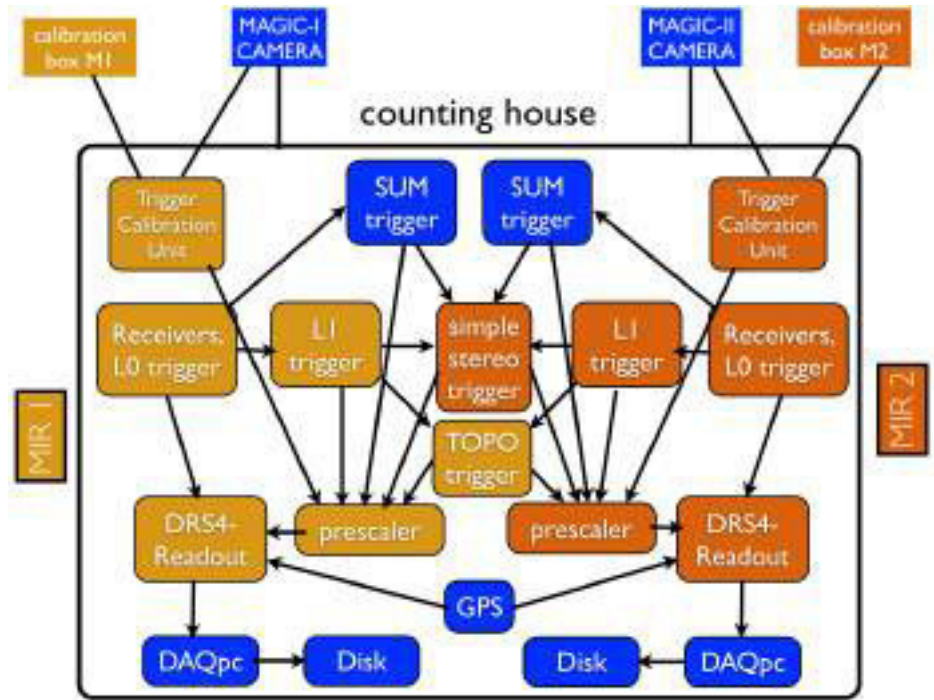


Figure 3.5: Scheme of the MAGIC electronic chain. Credits: Daniel Mazin, 3rd MAGIC Hardware School (May 2015)

As already mentioned in Section 3.3, the signal generated by the PMTs is electrical and it is converted into an analog optical signal by the VCSELs. Thanks to optical fibers going from the PMTs base to the counting house, the signal is transmitted to the so called *receiver boards*, or just *receivers*. Here the signal is converted back to an electric analog signal and split into two branches:

- a digitization branch, where the Domino Ring Sampler version 4 (DRS4) based readout stores the signal waiting for the trigger decision (see Sections 3.4.2)
- a trigger branch, with two sub-branches: a digital one (L0 trigger) which is sent to the L1 trigger (see Section 3.4.3) and a copy of the starting analog signal, which is sent to the Sum-Trigger (SUMT), if used (see Section 3.4.3)

After the first trigger decision (L1 or SUMT, one per telescope), the signal is digital and is sent through the L3 trigger (stereoscopic). If the L3 trigger is positive, the signals stored in the DRS4 buffers (one per telescope) are sent to the *Data Acquisition System* (DAQ) after being digitized by a standard Analog-to-Digital Converter (ADC). Eventually the events are stored on disk.

A scheme of the electronic chain is given in Figure 3.5.

### 3.4.2 Readout system

All the readout system is hosted in VME crates, six per telescope, plus one crate for the trigger system. Each crate has a 6U VME bridge plugged to the backplane, so that a daisy chain using optical fibers can be used to connect the seven crates with the computer which controls the readout and trigger through the MIR (MAGIC Integrated Readout) software. To do so, the computer needs a VME PCI card.

The optical fibers connect to the back side of the MONSTER (MAGIC Optical NanoSecond Trigger and Readout, Figure 3.6.2) boards, otherwise called receiver boards: each board can host 24 channels i.e. 24 optical fibers. The purposes of a receiver board are the following:

- conversion of the optical signals transmitted by the fibers into an electrical analog signal
- bringing the analog signal to the DRS4 digitization chips, hosted by the PULSAR boards (see below)
- generation of the L0 and L1 triggers
- feeding of a copy of the analog signals to the Sum-Trigger

The L0 trigger is produced for each individual pixel using adjustable discriminators thresholds (DTs): the output pulse can be programmed to have a specific width and delay for each channel independently. Moreover, the receiver boards host the Individual Pixel Rate Control (IPRC), which monitors the L0 rate of each pixel.

Each receiver board has four outputs: three trigger outputs (8 channels each) to be sent to the L1 trigger and one analog output to be sent to the Sum-Trigger.

As will be shown in Section 3.4.3, only the inner pixels of the camera participate to the L1 trigger: this is called the trigger region and is almost the same for the Sum-Trigger. There are two flavors of the receiver boards, version 2.1 and version 4.3, which basically differ for the low gain and high noise of the Sum-Trigger output of the former. For this reason, version 2.1 receiver boards are used for the outer pixels while version 4.3 is used for the pixels in the trigger region.



Figure 3.6.1



Figure 3.6.2

Figure 3.6: **Left:** PULSAR board. From <http://hep.uchicago.edu/~thliu/projects/Pulsar/>. **Right:** MONSTER board.

For the digitization (sampling) of the signals, a motherboard-mezzanine logic is used: the former is the PULSAR (PULSer And Recorder, Figure 3.6.1) board, the latter is the Domino mezzanine (four per PULSAR board), hosting the DRS4 chips (see Section 3.4.2). There are 12 PULSAR boards per telescope, located in a total of four VME crates, each one able to digitize 96 channels. Beside the standard PULSAR boards, there are two additional boards: the BUSY PULSAR and the DIGI PULSAR. The former gives the busy signal, which stops the triggers when the readout system is processing an event and the latter propagates the trigger arrival information to the other PULSAR boards.

Each PULSAR board has three main FPGAs: two DATAIO FPGAs (DATAIO1 and DATAIO2) to control the DRS4 and store the data in the SRAM and one CONTROL FPGA to check for data and preparing data packets to be sent to the DAQ. Four Domino mezzanines can be hosted in one PULSAR board in its bottom side: the first two are controlled by the DATAIO1 FPGA, the other two by DATAIO2.

The PULSAR boards have two front panel connectors, the L1 INPUTS, each one carrying 32 bits for a total of 64 bits. Using a VME P3 connector, the PULSAR board is connected to the HOLA (High-speed Optical Link for Atlas) board, hosting the BUSY circuit and an optical transmitter. An optical fiber (SLink protocol) transmits the data from the HOLA board to the FILAR (Four Input Links for Atlas Readout) board, which is connected to the PCI bus of the DAQ computers. Each FILAR board has 4 SLink channels and for each DAQ pc, 4 FILARS are connected, leaving room for some spare channels.

#### Domino Mezzanine and DRS4 chips

The Domino mezzanines host the DRS4 chips (Sitarek et al. 2013; Bitossi, Paoletti, and Tescaro 2016), three per mezzanine, as shown in Figure 3.7. Each chip can sample 8 channels, for a total of 24 channels per mezzanine. On the side of the mezzanine, three inputs can be connected:

- the reference clock and trigger synchronization signals
- the analog connector which brings in the signal

The 40 MHz clock and the trigger signals are distributed to the mezzanines thanks to the Trigger and Clock Fanout board, which produces 80 copies of the signals.

Each DRS4 chip has 1024 capacitors forming a ring buffer, whose time length depends on the sampling frequency of the chip, set to 1.64 Gsamples/s. This is particularly important for some telescope orientations, because the buffer time length could not be enough to produce a stereoscopic trigger if the sampling speed is too high. The DRS4 chip has a Region of Interest (RoI), that is only a part of the buffer which is read out, reducing the dead time of the electronics. Currently, the dead time is 27  $\mu$ s, actually negligible in standard data taking operation. If a trigger occurs, the DRS4 sampling memory is read out by a 14-bit nominal resolution ADC (one for each chip), clocked at 32 MHz. Despite their versatility, the DRS4 chips need a proper and accurate calibration of their response, described in Section 3.4.4.

Finally, the mezzanine is completed by three built-in FIFO memories, the connectors to the PULSAR board and the power connector, distributing  $\pm 5$  V.

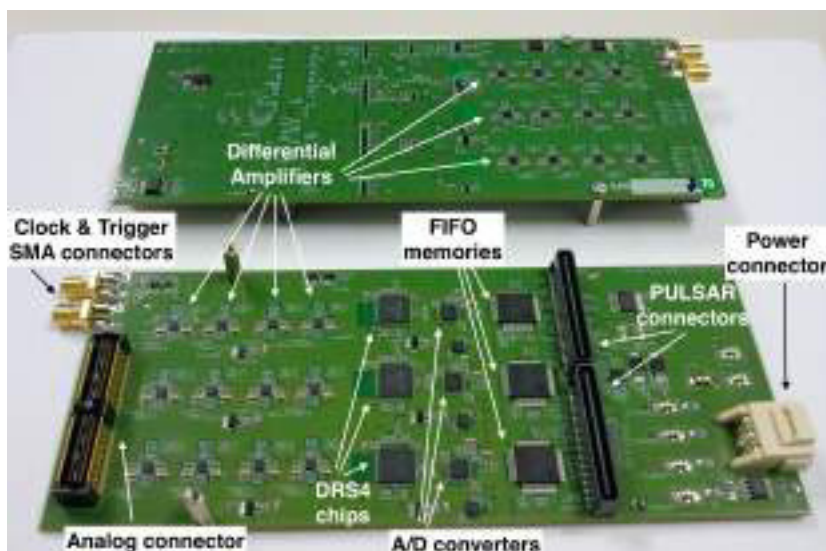


Figure 3.7: The DRS4 mezzanine with the three DRS4 chips. On the left, the clock and trigger inputs and the analog connectors are visible. On the right of the chips, the FIFO memories, the connectors to the PULSAR board and the power connector complete the mezzanine. From Aleksić et al. (2016a).

### 3.4.3 Trigger system

The standard trigger used by MAGIC has three levels: L0, L1 and L3. The first level, L0, digitizes the signals from the 547 inner pixels of the cameras (trigger region) thanks to a discriminator threshold. The width and delay of the digitized signal can and must be adjusted to have a compromise between the L1 trigger rate, dependent from the L0 signals width, and a good spread of the arrival times at the L1 board. The times spread has mostly electronic nature: there are intrinsic differences between the PMTs e.g. the High Voltage applied, which modifies the transit time of the electrons, the optical fibers transmitting the signal to the receivers and the components of the electronics which cause a time spread in the arrival times of the signal. For high-energy showers with large impact distance, there is also an intrinsic spread up to 2 ns which cannot be minimized in any way since it is a physical effect and not hardware related. The widths and delays adjustment is performed thanks to the program called HYDRA (HYperfast Delay and Rate Adjustment), developed by MAGIC collaboration members: this results in a reasonable gate for the L1 trigger reducing the rate of accidental triggers. The DTs should be calibrated as well: different FOVs have different NSB, so that for extragalactic sources the DTs are set to 4.25 phe, while for the galactic sky the DTs are 15% higher. If the observation is performed with the Moon, higher DTs are used and, if needed, reduced High Voltage is set for the PMTs.

As already mentioned, the L0 trigger is implemented directly in the receiver boards, see Section 3.4.2. After that, the signals are handled by the actual trigger system of the MAGIC telescope, comprised of:

- L1 trigger
- L3 trigger
- Sum-Trigger
- Time Calibration Unit (TCU) and Prescaler
- Topological trigger

After the L0 trigger, the digitized signals is transmitted with MDR cables to the LT1 back-plane, which distributes them to the right LT1 boards. There is a total of 19 LT1 boards per telescope: the trigger region pixels of the MAGIC cameras are arranged in 19 regions of 36 pixels each, called *macrocells*, with some pixels belonging to two or three macrocells at the same time as shown in Figure 3.8. In each macrocell, the L1 trigger searches for any combination of compact active pixels in a next-neighbor logic (only one at a time, set before observations): 2NN, 3NN, 4NN, 5NN.

The signals of the 19 macrocells are sent to the Trigger Processing Unit (TPU), which creates the final trigger performing a global logical OR of the signals. In the case of a trigger, the L1 trigger signals (one per telescope) are sent to the L3 board and prescaler board, after being stretched to 100 ns and delayed according to the telescopes orientation, which causes the light paths at the focal planes to be different. The L3 or stereoscopic trigger is hosted in a specific PULSAR board (L3T) with two mezzanines, one for the standard trigger (L1) and the other for the Sum-Trigger signals. The L3 trigger executes a logical OR between the two L1 trigger signals: if a trigger is generated, the L3 trigger signal is sent to the readout of the two telescopes. A L3 trigger number is generated as well by the mezzanines and is used later in the offline analysis.

The readout loop now closes: the sampled signals in the DRS4 chips can be read out and sent to the DAQ system, which performs some calibration and correction of the readout data and transmits it to the storage computers, see Section 3.4.4.

The trigger system is completed by the prescaler and the TCU boards. The former accepts

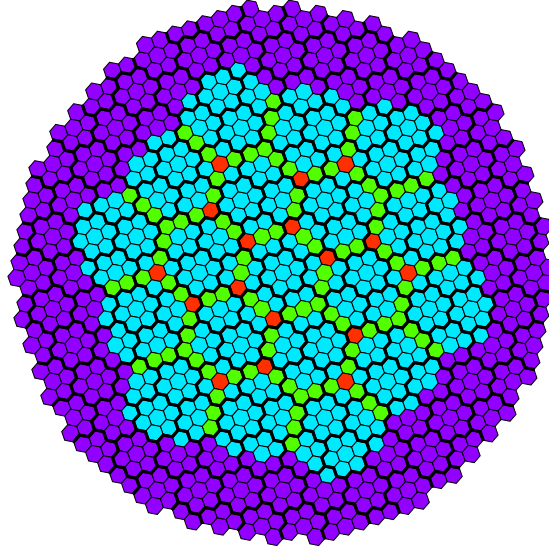


Figure 3.8: Scheme of the MAGIC camera. Cyan, green and red pixels belong to the trigger region, while the purple ones do not. The 19 L1 macrocell are denoted by the cyan pixels. Green and red pixels belong to two and three macrocells at the same time respectively. Moreover, thick black lines denote the 169 PMT clusters. From Aleksić et al. (2016a)

as input different triggers (L1, L3, LIDAR, PEDESTAL, CALIBRATION, SUMTRIGGER, TOPOTRIGGER, PULSEINJECTION) and allows to select a subset with a prescaler factor (bit). In this way, the total trigger rate can be reduced. Moreover, the trigger pattern provided by the prescaler is written into the data stream.

The TCU board is responsible of controlling and monitoring the calibration box, issuing the pedestal, calibration and pulse injection triggers. The calibration pattern, which contains the filter wheel positions, is written in the data stream for each event. For more details on the calibration system of the MAGIC telescopes, see Section 3.5.2.

### Sum and Topological Trigger

Beside the standard trigger described in Section 3.4.3, other two trigger systems can be selected: the Sum-Trigger and the Topological Trigger.

The Sum-Trigger (García et al. 2014) is an analog trigger without any topological logic. The electronics of the Sum-Trigger, one per telescope, is hosted in two separate racks in the electronics room of the MAGIC counting house. Each rack comprises 18 Clip-boards with their power unit, 19 Sum-boards, 1 Astro-board, 1 SPI-backplane, 1 Sum-backplane and a power unit. The signals for the Sum-Trigger come from the receiver boards, where a dedicated mezzanine transmits the copy of the analog signals to the Clip Boards. Here the signals are adjusted in time, equalized and clipped to 7-8 phe so that afterpulses in the PMTs do not produce fake triggers. As in the case of the standard L1 trigger, the inner pixels are grouped in 55 overlapping macrocells of 19 pixels each. Each signal from the Clip-board is assigned the right macrocell thanks to the Sum-backplane. For each macrocell, the analog sum of the 19 pixels is performed: a settable discriminator threshold is used at this point to issue a trigger for each macrocell and is sent to the Astro-board, which executes a global logical OR (see Figure 3.9). The individual Sum-Trigger signals of the two telescopes are then used to perform the L3 trigger as described in Section 3.4.3.

The advantages of the Sum-Trigger is the lack of a strong topological constraint and putting the discriminator threshold after the pulse sum, which allows to get more showers. Because of this, the single telescope rate produced by the Sum trigger is higher than the corresponding

L1 of the standard trigger. Summing the analog signals of the pixels in each macrocell is a way to lower the energy threshold, because even if the single pixel signal is low, the sum of more pixels will pass the discriminator threshold level. In this way the energy threshold at the trigger level can be lowered down to about 30 GeV. The Sum-Trigger (stereo version) is currently under testing, but it is used to perform the observation of sources like Pulsars, namely the Crab and Geminga, with the goal to catch the low energy pulsed emission. The mono version of the Sum Trigger instead was used to detect successfully the pulsed emission from the Crab Nebula down to 25 GeV, see Aleksić et al. (2011a). As far as GRBs are concerned, many tests were performed to check the stability of the Sum-Trigger just after the fast repositioning of the telescopes. Up to now, GRB observations are performed using the standard trigger but in the future the plan is to use the Sum-Trigger in order to lower as much as possible the energy threshold at the trigger level and consequently at the analysis level.

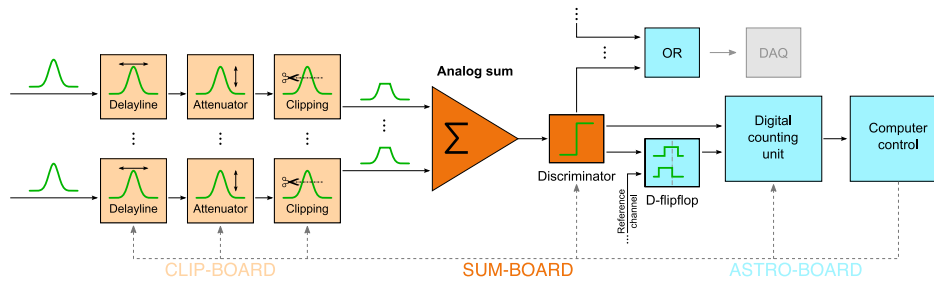


Figure 3.9: Scheme of the Sum-Trigger working principle. From García et al. (2014).

The Topological Trigger (Topo-Trigger) uses the spatial information at the trigger level. In particular it uses the information about the 19 L1 macrocells. The basic idea is that gamma-ray initiated showers will trigger the same macrocells in the two cameras or, if one fixes a macrocell in the first telescope, the surrounding ones will be triggered in the second telescope. Adding the azimuth information of the source, one can even predict which of the macrocells in the second telescope will be triggered. This leads to a rejection of accidentals of about 85% and 2.4% for gamma rays. Since the stereo accidental trigger is lowered, the discriminator thresholds can be set at a lower value, improving the energy threshold by 8% at the analysis level. Also the collection area at the energy threshold improves between 10% and 20%. Special MC simulations were made to check that the topological constraints on the macrocells with the standard DT values do not change the performance of the system. From the hardware point of view, the Topo-Trigger receives a copy of the L1 macrocells information from the TPU in a dedicated board, the Test Evaluation and Debug (TED) board. A mezzanine sends the macrocell trigger information to the readout system after stretching the signal when a L3 trigger is issued, so that the macrocell information is recorded for stereo events. For more details, see López Coto (2017).

Unfortunately, the output events of only one trigger type can be sent to the DAQ, so the triggers are mutually exclusives in this sense.

### 3.4.4 Data Acquisition system

If a trigger is issued, the data stored in the DRS4 chips are sent from the HOLA cards to the FILAR cards through the SLink connection. Each event is made up of 24 data packets: they are built by the PULSAR firmware and one packet is created by two Domino mezzanines. Additional information is needed when sending the data packets to the DAQ, like the time stamp, the trigger and calibration pattern and L3 trigger number, which are always available thanks to some cables connected to some of the PULSAR boards. In the case of a trigger, this info is copied in the data packets.

The DAQ computers run a program called *Domino4Readout* which performs the following operations, as described in Tescaro et al. (2013):

1. reading the data packets from the FILAR boards and building the complete event, checking the integrity of the data
2. correction and calibration of the DRS4 chips response
3. storing the data on disk
4. send charge and arrival time information for each event to the MOLA program, see Section 3.5.13.

The second point in the list is crucial. The DRS4 chips exhibit some features in noise and time resolution which must be corrected to obtain a good response. The first correction is the calibration of the mean cell offset of the chips, defined as the raw mean ADC count value for a certain capacitor during a pedestal run i.e. random triggers. Without calibration, differences up to 15% can be seen in the baseline, higher than the single RMS, which is unacceptable. To correct this behavior, a pedestal run taken once at the beginning of the night is used to obtain a flat baseline of the DRS4 chips. During data taking, interleaved pedestal runs at fixed frequency of 25 Hz are taken to monitor and possibly correct changes in the baseline. The second correction takes into account the elapsed time between two consecutive readings of a capacitor: the dependence of the baseline on the time lapse is a simple power law which can be used to regain a flat baseline. For more details, see Sitarek et al. (2013). An additional calibration is needed for the signal arrival time, but it is applied in the offline analysis, see Section 4.3.

After the corrections of the DRS4 chips response, the events are grouped in bunches of 100 to optimize the writing into disks. As described in Section 4.2, the events are saved in the so called raw files (binary), each containing about 14000 events and about 2GB in size. The DAQ system can write events up to a rate of about 800 Hz, more than double of the sum of the L3 trigger rate in normal conditions (about 270 Hz) and of the interleaved calibration and pedestal rates (25 Hz each). Finally, each second a random event is taken from the DAQ and displayed in the GUI of the Central Control program of MAGIC (see Section 3.5.1), so that operators can monitor and spot possible problems in the data taking.

## 3.5 Auxiliary systems

### 3.5.1 Central Control

Taken as a whole, the MAGIC telescopes are a complex system. To ensure the correct and safe operation of all the subsystems involved, it is important to be able to monitor their status at any time (when they are working). For this purpose, the so called Central Control (CC) of the MAGIC telescopes, named *SuperArehucas* (SA), was designed. It is a complex program written with the LabView software which is used to monitor the status of all the subsystems of the MAGIC telescopes. Each subsystem has its own monitoring software (e.g. CaCo1 and CaCo2 for the two cameras, MIR1 and MIR2 for the readout and so on) which can run independently, but usually do not provide an easy and graphical interface to understand if there is a problem or to send a specific command. SA provides this functionality: each subsystem communicates via TCP/IP socket connections with SA alone, sending reports with their status every one second. SA sends to the subsystems a CC report every ten seconds and in this case the subsystems are in CC mode, so that they can receive commands from SA. Only two subsystems communicate with both the Weather Station and SA: the first are CaCo1 and CaCo2 and the second is the LIDAR. The reason is to have automatic reactions e.g. close the camera lids if the wind is too strong, if the operational safety limits are not

---

fulfilled during observation.

Given the modular organization of the MAGIC hardware, SA provides a graphical interface with different panels, each referring to a specific subsystem: the circular LEDs tell if the communication between SA and the subsystem is established while the clocks show the time when the last report was sent by the subsystems to SA (see Figure 3.12). Some subsystems may have additional LEDs to specify the status of one of its subpart or to display additional information. Finally, several menus and buttons are there to issue commands from SA to specific subsystems.

### 3.5.2 Calibration system

As any other experimental apparatus, the MAGIC telescopes need a calibration system to ensure the good response of the instrument. This is accomplished by using the so called *calibration boxes*, hosted at the center of the telescopes mirrors. A calibration box has the following main components:

- a passively Q-switched Nd:YAG laser of 355 nm wavelength, whose pulses have FWHM of 0.4 ns to be as close as possible to a Cherenkov flash
- two filter wheels, each with six filters for a total of 36 combinations, to change the light intensity (up to 80 kphe)
- an Ulbricht sphere in spectralon to make the output light uniform by multiple scattering reflections
- temperature and humidity sensors and a heating system

The main purpose of the calibration box is to get the conversion factor between the FADC counts and the number of photoelectrons by illuminating uniformly the camera. This is achieved by means of a dedicated run before the observation of any source, called *calibration run*, where 2000 calibration events are collected at fixed light intensity. Moreover, during data taking the so called *interleaved calibration events*, that is calibration pulses fired at a frequency of 25 Hz, are used to check the gain evolution in each pixel during the observation. The calibration box can be used also to test the linearity of the readout chain from the PMTs and to perform when needed the flat-fielding of the PMT gains. This last procedure sets the High Voltage of the PMTs so that the signal from a calibration signal is the same in readout counts in all the pixels.

### 3.5.3 LIDAR

Since the Cherenkov light produced in air showers propagates in the atmosphere, it undergoes scattering and absorption processes as described in Section 2.3.2. This will affect the reconstruction of the main parameters of a shower, in particular the estimation of the energy of the primary particle: this will lead to a wrong computation of quantities like the effective area and the flux. So it is important to have a way to estimate the effect of clouds and aerosols on the transmission of the atmosphere and have an algorithm to correct the data taken in non optimal weather conditions.

The purpose of the MAGIC single-wavelength elastic Rayleigh LIDAR, shortly LIDAR, is to monitor the same sky region observed by the MAGIC telescopes. It is located on a tower on the side of the MAGIC Counting House and when inoperative it is protected by a dome (see Figure 3.10). It is described in details in Fruck et al. (2014) and its main components are:

- a Nd:YAG laser operating at 532 nm, with pulse energy and width of 5  $\mu$ J and 0.5 ns
- a 60 cm diameter milled aluminum mirror with a focal length of 1.5 cm



Figure 3.10: Picture of the LIDAR used at the MAGIC site. From Fruck et al. (2014).

- the detector module with a 6 mm diameter diaphragm, a pair of lenses with interference filter and a Hybrid Photo Detector (HPD, Hamamatsu R9792U-40) with 55% peak quantum efficiency
- an equatorial telescope mount which is controlled by computer.

In order not to interfere with MAGIC and other telescopes operations, the LIDAR is a low power instrument, with as low as 5 mW for the laser. Moreover, when tracking the MAGIC telescopes, the LIDAR points a sky position few degrees away from the pointed source to reduce the possibility of effects on the trigger rates. In any case, even if the laser shots increase the rates, they are properly tagged in the data stream so that they can be easily removed in the offline analysis.

The signal obtained by the LIDAR, which fires its laser every few minutes, is processed by two different algorithms to calculate the integral aerosol transmission profile  $T_a(h)$  as a function of the altitude above the MAGIC site  $h$ . The corrected estimated energy of the primary particle can be calculated as:

$$E_{\text{est,corr}} = \frac{E_{\text{est}}}{\bar{\tau}} \quad (3.1)$$

$\bar{\tau}$  is the weighted aerosol transmission of the atmosphere:

$$\bar{\tau} = \int_0^{\infty} \varepsilon(h) \cdot T_a(h) dh \quad (3.2)$$

where  $\varepsilon(h)$  is the normalized estimated light emission profile of the photons of the air shower contained in the camera image.

For spectrum and flux calculations, the corrected effective area must be known. In this case, the basic assumption is that events affected by atmospheric extinction look like events of lower energy. Applying the correction to the events will make them migrate to a different energy bin, so that a migration matrix can be constructed. This migration matrix is finally used to compute the corrected effective area and its related quantities, see Section 4.11.

### 3.5.4 Weather Monitoring System

Monitoring the weather at the MAGIC site is crucial to ensure a safe operation of the telescopes and protect from damages the subsystems which operate in open air e.g. the camera

(PMTs in particular) and the mirrors.

For this purpose, a weather station (model Reinhardt MWS 5MW) is installed on the roof of the MAGIC Counting House. It provides measurements of several quantities:

- temperature (in °C)
- relative humidity (in %)
- wind speed (current, average and peaks) in  $\text{km h}^{-1}$  and direction
- pressure in hPa.

The data collected by the weather station is sent every 2 seconds to the Central Control program of the MAGIC telescopes and to CaCo1 and CaCo2, so that if the safety limits for operation are exceeded, automatic reactions are performed to ensure the safety of the the telescopes.

### 3.5.5 Cooling system

The electronics of the MAGIC telescopes needs to be cooled because of the heat produced when it is on and working, consuming about 8.4 kW. This task is performed by the cooling system which consists of:

- three chillers: they cool down the hot water received from the heat exchangers and pump the cold water again in the circuit
- eight heat exchangers: six are placed above the six racks containing the readout electronics and two are placed on the side of the racks structure
- other two heat exchangers placed above the two racks of the Sum-Trigger electronics
- circuits for the distribution of water to and from the heat exchangers and of cool air inside the racks.

The temperature of the air inside the racks can be monitored from the LED screens of the heat exchangers: they will start working at the temperature of 22 °C (25 °C for Sum-Trigger) and will give a warning if the temperature value reaches 36 °C (35 °C for Sum-Trigger).

### 3.5.6 Starguider camera

Despite the good pointing accuracy of the drive system, there can be a possible mispointing which can be corrected offline at the analysis level (see Section 4.4) with the help of starguider cameras. They are two CCD cameras at the center of each reflector, aligned with the optical axis of the telescopes. The cameras observe both part of the MAGIC Cameras and part of the sky behind them i.e. the sky region observed by MAGIC. Six LEDs at the edge of the Cameras are used to find their center. The starguider then looks at the bright stars in the sky, comparing the measured position with the one from a catalog. This information is then used to estimate the mispointing.

### 3.5.7 Pyrometer

A radiation pyrometer (model Heitronics KT 19.82), mounted close to the west tower of MAGIC-I, is used to assess the presence of clouds in the sky region observed by the telescopes. The working principle of the pyrometer is that the clouds, reflecting the thermal radiation from the earth, have a greater sky temperature  $T_{\text{sky}}$  with respect to a clear sky. Once  $T_{\text{sky}}$  is measured, an empirical function is used to compute the so called *cloudiness*, whose value runs

---

from 0 to 100 i.e. no clouds or completely covered sky respectively. For the computation, the zenith of the observation, the air temperature  $T_{\text{air}}$  and the humidity must be known as well. In any case, for a more precise assessment of the presence of clouds, the LIDAR is used.

### 3.5.8 AllSky Camera

An AllSky Camera (model KAI 340 CCD,  $640 \times 480$  pixels) takes images of the sky above the MAGIC site every two minutes with exposure time automatically adjusted. The camera is located on the roof of the counting house together with the other weather systems. The images are then used to inspect visually the sky condition e.g. to see if the sky is cloudy.

### 3.5.9 Timing system

The timing system of the MAGIC telescopes consists of two modules:

- A GPS module (Symmetricom XLi) with a Rubidium clock with stability of  $3 \cdot 10^{-11}$  s over 1 s. This stability holds only for short timescales, so the clock is synchronized with the signal received by the GPS with a frequency of 1 Hz, achieving an accuracy of better than 30 ns RMS.
- A Timing Rack module, which exports the time information in LVDS format and sends it to MAGIC-I and MAGIC-II PULSAR boards.

Once the time information is converted in the right format by the Timing Rack module, each recorded event will be assigned with a timestamp.

### 3.5.10 Central Pixel

The central pixel of MAGIC-II is a modified PMT able to perform optical observations. The purpose of the Central Pixel is to study slow variations of the flux of optical sources like pulsars (e.g. Crab). The signal received is sent through the standard MAGIC readout chain and a dedicated readout, so that  $\gamma$  and optical observations can be performed at the same time.

Since the central pixel needs to receive the light from the source, the data taking must be performed in ON mode (see Section 3.6.1).

### 3.5.11 GRB monitor: GSPOT

As will be described in detail in Section 5.1, GRBs are transient sources occurring unpredictably in any position of the sky. The detection of VHE emission from GRBs is one of the Key Observational Program (KOP) of the MAGIC experiment. However the observation of GRBs by IACTs is intrinsically difficult due to several reasons:

1. the FoV of an IACT is small (e.g.  $3.5^\circ$  for MAGIC) compared to satellite-based instruments, which can cover almost all sky in any moment. This intrinsic limit points to the need of an external trigger from satellite instruments to know the location of potentially observable GRBs;
2. GRBs occur regardless of the day/night and regardless the atmospheric conditions. This of course limits the chance to observe an interesting GRB;
3. GRBs are cosmological sources, with median redshift of  $z \sim 2$ . This means that the absorption of gamma rays by the Extragalactic Background Light (EBL) is considerable and so the possibility of catching the VHE emission is reduced.

Regarding the first point, the Gamma-ray Coordinates Network (GCN) disseminates the coordinates of GRBs detected by space-based instruments (e.g. Swift, Fermi, INTEGRAL, CALET ecc.) through the so called *Notices*, which are packets containing the GRB info sent through socket to the sites subscribed to the GCN.

MAGIC receives the GCN notices but not all the targets contained in the alert packets will be observable by MAGIC. Moreover, one can apply other observational criteria i.e. zenith of observation, time of observation, constraints on the physical properties of the GRB ecc. to determine if the follow-up of the target is possible or not. This task is performed by the software called *GSPOT* (*Gamma Sources POinting Trigger*, Galante 2006): it reads from the socket the GCN notices and it checks if the coordinates contained are observable from the MAGIC site according to some predefined observational criteria (following the so called GRB strategy). If the criteria are met, *GSPOT* will tell the Central Control to repoint automatically the telescopes to the GRB position and start the follow-up. A more detailed description of *GSPOT* and the GRB strategy can be found in Chapter 6.

A web page (<http://www.magic.iac.es/site/grbm/index.html>), usually called the Burst Monitor, is available for the MAGIC operators to check the connection status to the GCN and the CC and the info about the last GCN packet received.

### 3.5.12 OSA

When raw data are saved to disk, their size is considerable, about 2 GB or 1 GB when compressed. The permanent data storage is not in La Palma, but at the Port d'Informació Científica (PIC) in Barcelona. Even if a high-speed connection connects La Palma and the continent, moving the raw data files would take too much time.

For this reason, in several machines installed in La Palma, called *ana*, the so called On-Site Analysis (OSA) software is running, which reduces the data size by performing the standard MAGIC analysis. As soon as raw data and metadata from the DAQ or reports from SuperArehucas are available, they are copied in a shared storage (GFS2) and inserted in a MySQL database. Basically the OSA software runs the standard MAGIC analysis tool, MARS, on the event files created during observation. The difference is that the analysis is managed through several jobs that are executed in parallel with a proper distribution of CPU resources thanks to some scripts developed for this purpose.

Currently, OSA reduces the data up to the **superstar** level (see Section 4.5), since for the energy and direction estimation proper Random Forest is needed. When the reduced data are available, they are ready to be transferred to the PIC. Generally **star** data are available at around 12:00 UTC the morning after the observation; all the others (calibrated and superstar), are available soon after. Beside the transfer problem, the reduction performed by OSA is useful because makes available the data for the analyzers few hours after they were taken. This is important specially if a flare or a transient was observed during the night: the real time analysis performed by MOLA (see Section 3.5.13) is indeed very preliminary, mostly if the observation was not performed in dark conditions, so in order to obtain more robust results the data need to be analyzed properly by the analyzers. Thank to OSA, the first steps of the analysis are already done so that producing high-level results i.e.  $\theta^2$  plots, skymaps, light curves and spectra will be faster for the analyzers. Of course this is valid only if the data are taken under dark conditions: in this case the analyzers can start directly from **superstar** data. However, for example if the data is affected by moonlight, the analysis will start from calibrated files. In this eventuality as well OSA helps greatly, since the conversion and calibration of the raw files is done on site and the analyzers do not have to download several gigabytes of data.

---

### 3.5.13 MOLA

In order to get a feeling of the behavior of a source during the observation, for example to check for a possible variability of the flux, a preliminary real time analysis is mandatory. The preliminary results can then be used to issue alerts to other observatories which can perform follow-ups of the source.

In MAGIC, the real time analysis is performed by MOLA (MAGIC OnLine Analysis, Tescaro et al. 2013), a multithreaded C++ program which takes the charge and time arrival information for each pixel from the two DAQ systems independently and performs the first steps of the standard MAGIC analysis, the calibration and the image parameters calculation. A separate thread, called *analysis thread*, performs the stereo analysis and the gamma/hadron separation, finally producing high level products like the  $\theta^2$  plots, skymaps and light curves. The analysis is performed in two energy ranges, Low Energy (LE) and High Energy (HE), defined by the conditions image size greater than 40 phe and 125 phe respectively. These values correspond roughly to 110 GeV and 350 GeV during Crab Nebula observations at low zenith. For a detailed description of the analysis, see Chapter 4. MOLA can achieve a sensitivity of 1% of the Crab Nebula flux in 50 h or, equivalently, 10% in 30 min, which is fundamental in the case a transient source is observed.

MOLA works without significant data loss up to 600 Hz, so well within the rates usually recorded at the DAQ level, while for higher rates the performance will be lower due to the loss of events when reading them from the DAQ.

## 3.6 Telescope operation

MAGIC telescopes has been operating during all nights since 2004, except for the days of full moon and the ones right before and after them. No observation was done, of course, during all the hardware updates. The observation is divided in yearly cycles, made up of 13 periods with the same duration of the lunar cycle (28 days). In each period, a different shift crew of 4 people (5 in some days) belonging to the MAGIC collaboration operates the telescopes during the nights, following the source schedule prepared in advance by the MAGIC scheduling group. The shifters have to perform the required observations and to be able to solve problems if they occur during data taking. There are three roles among shifters: Operators (two per shift), usually they are at the site for the first time and they have to learn all the basics in data taking and telescope operation; a Deputy Shift Leader (DSL), who has to transfer the knowledge to the operators and shares the responsibilities with the Shift Leader (SL), the more experienced among the shifters, who has done at least two data taking shifts and has the responsibility on everything (safety, decision taking, teaching to the other shifters). The roles are progressive and usually after one shift everyone is upgraded to the next role. Beside shifters, in La Palma there are two postdocs who are on call during the nights if some particular problems occur. Usually they can be on site during the day to perform the maintenance of the telescopes together with other two technicians. They can join the shifters during the night to perform technical tests e.g. tests of the automatic GRB procedure. Both the postdocs and the technicians have a very good knowledge of all the subsystems of the MAGIC telescopes and perform almost all the maintenance works at the MAGIC site, allowing the shifters to participate in order to teach them more about the subsystems, always following the safety rules.

During a year, the so called dark time (with no Moon) is about 1600 hours in total, resulting in a duty cycle of 18%. Taking into account the time lost due to bad weather, technical problems and repointing times, the duty cycle decreases. The efficiency, that is the fraction of dark time actually observed, is usually around 60%. The duty cycle, as long as MAGIC is concerned, is increased up to 40% thanks to the observation during moonlight and twilight time, even if with a higher energy threshold due to the increased NSB but extremely important

---

for the follow-up of transient or flaring sources.

### 3.6.1 Pointing modes

MAGIC was born as a single telescope system, so until MAGIC-II was added, it was operating in the so called *mono mode*. When the second telescopes began operation, the default mode of operation was the *stereoscopic mode*. The stereo mode produces an effect called *stereo blob*: more showers are recorded if they are produced between the telescopes and this affects the acceptance of the system, which depends on the relative pointing of the telescopes. It can be seen that if the acceptance is binned in azimuth for a given zenith range, the stereo blob rotates according to the pointing of the telescopes. Another effect caused by the stereoscopic mode is the so called *L3 deadzone*: as already mentioned, the Cherenkov photons arrive at the camera focus with a delay in the two telescopes depending on their relative position and this affects the time when the L3 trigger signal is issued to read the events from the DRS4 analog buffer. Since the DRS4 buffer is 512 ns and the digitization and storing of the signal is of the order of 300 ns, the maximum delay that can be applied to take the L3 trigger decision is around 220 ns. For high zenith observations and for some azimuth orientations, the L3 delay is more than 220 ns and so this means that the events, even if seen by both telescopes, cannot be recorded because after being delayed they fall outside the buffer time duration. This causes a drastic decrease of the L3 stereo rate. For this reason, in November 2014 the DRS4 chips sampling speed was decreased from 2 Gsamples/s to 1.64 Gsamples/s, increasing the buffer length by 210 ns and removing the L3 deadzone. This is particularly important for transient sources, since they occur in any sky position and in some cases they should be followed up even at high zenith angles.

Regarding the pointing mode, two different techniques are used:

- *ON mode*,
- *wobble mode* (or false source tracking mode).

In the ON mode, the position of the source is pointed directly and tracked during all the observation, so that the source lies always in the center of the camera. This is called the ON observation. To have an estimation of the background, a second observation must be performed, called OFF observation: a patch of the sky without gamma ray sources with the same zenith and azimuth distribution (or as close as possible) is observed for the same time as the ON observation. The underlying hypothesis is that the background in the ON observation is the same as calculated from the OFF observation, which is not completely true since even for OFF data taken during the same night there can be different data taking conditions and because different portions of the skies have different backgrounds (like extragalactic and galactic fields). The clear drawback of this method is that for each source the double of the time must be allocated to take into account the OFF observation, reducing the already low duty cycle.

The aforementioned problem can be solved by using the false source tracking method, usually known as wobble mode, introduced in Fomin et al. (1994). In this pointing mode the source is not directly pointed, but rather a position with a certain offset from the source. This offset has to be optimized using MC simulations: for point-like sources, MAGIC uses an offset of  $0.4^\circ$ , while it can be increased if an extended source is observed. Since the camera response is not homogeneous, to have an unbiased estimation of the background, at least another pointing, symmetric to the first one with respect to the source, is needed. These two pointing are commonly called *wobble positions* and are denoted as W1 and W2: the former is  $0.4^\circ$  degrees from the source along the positive direction of the RA axis, while the latter is along the negative direction of the same axis. In almost all cases, other two wobble pairs are used, denoted as W3 and W4, which lies on the axis perpendicular to the line connecting

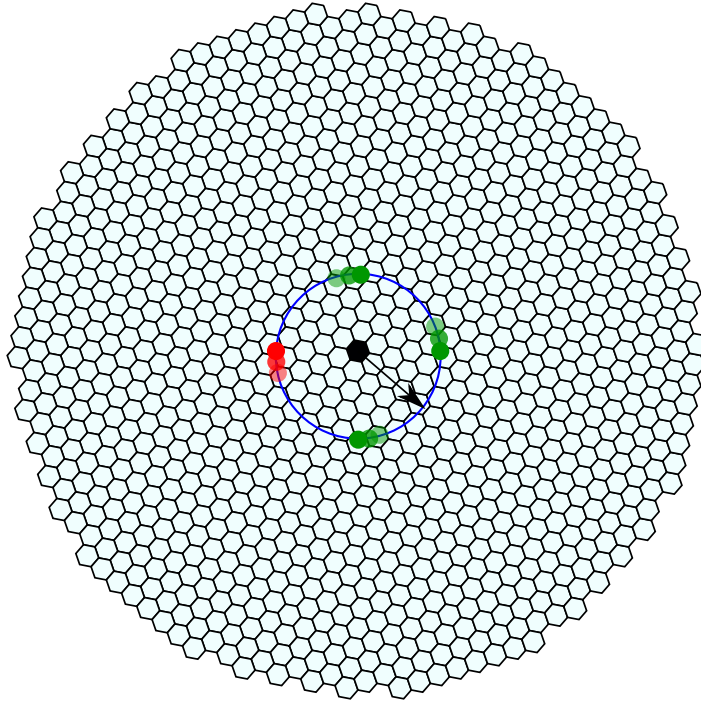


Figure 3.11: The wobble pointing mode as seen in the camera plane for one wobble pointing. The blue circle has a radius of  $0.4^\circ$ , equal to the wobble offset used during observations. The black pixel is at the center of the camera. The source is the red dot, while the other two semi-transparent red dots denote the path of the source in the camera plane during observations. The same holds for the green dots, which are the OFF regions used for background estimation. In this case, 3 OFF regions are used.

W1 and W2. So the observation of a source usually starts with W1, then switches to W2, W3 and W4. The cycle then repeats. The duration of the wobble pointings depend on how much time is allocated for each source, but it is important that the time is the same and that a complete wobble pair is taken. The wobble mode is versatile: in the case of sky fields with a lot of stars, the wobble pointing can be organized such that the contribution from stars are minimized, leaving them at the edge of the trigger region. The same can be done if another gamma ray source is in the field of view.

The clear advantage of the wobble mode is that the signal from the source and the background are collected at the same time and with the same conditions despite losing in gamma ray efficiency because the source is not in the camera center anymore. The wobble method requires the MC events to be simulated on a ring with radius equal to the wobble offset: during the observation, a tracked source will follow in the camera an arc of circle of radius  $0.4^\circ$  because of the alt-azimuthal structure of the telescope. Usually we refer to this MC data as *ring wobble*.

Regarding the background, usually its estimation is done with the simultaneous method using OFF regions: in the case of only 1 OFF region, the background is taken from the region opposite to the one where the source lies in the camera. If more than one OFF region is used, they will lie equidistant one from each other and from the source on the circle centered on the camera center with  $0.4^\circ$  radius, as shown in Figure 3.11.

The wobble method with  $0.4^\circ$  in stereoscopic mode is the default pointing mode used by MAGIC. Only in few situations the ON mode is used, like for fake sources called DarkPatch, used to collect OFF data for the Random Forest training (see Section 4.7.1), or for observations with the Central Pixel (see Section 3.5.10). Up to 2013, GRB observations were made in ON mode as well, but with the new automatic procedure the wobble method was adopted.

### 3.6.2 Typical rates and Individual Pixel Rate Control

The event rates (L0, L1 or L3) of a system like MAGIC depend very much on the observation conditions, for example if stars, the moon or clouds are in the field of view. For a clear night in dark conditions i.e no Moon, the typical L0 rate is around 800 kHz. The average DT applied at the L0 level is 4.25 phe, which was optimized in order to get the highest L3 rate triggering the lowest number of accidentals and cosmic rays initiated showers. The DT of each single pixel can be changed by the Individual Pixel Rate Control (IPRC): if the L0 rate of a pixel is above 1.2 MHz, the IPRC will increase the DT of that pixel in order to have a not too high L1 rate and to re-establish the L0 rate in the range 200 kHz-1.2 MHz. If the L0 rate instead falls below 100 kHz, the IPRC will lower the DT to the standard value. This usually happens when stars are in the FoV of the source observed: sometimes even the DC in the PMTs goes above the limit and for that reason the High Voltage of the affected pixels is lowered to prevent problems for the PMTs. Thanks to the IPRC, the L1 typical rates are between 10 kHz and 20 kHz while for L3 it is around 250-350 Hz. Using Sum-Trigger, the L3 rate increases to 500-600 Hz. The accidental L3 rate, that is the rate of accidental triggers due to background only, assuming a typical L1 rate of 15 kHz and a time coincidence window of 180 ns between the telescopes and the DRS4 chips, is about 40 Hz, so that the majority of recorded events are from Cherenkov showers.

The final DAQ rate is the sum of the L3 rate and the triggering rate of interleaved calibration and pedestal events, which is 25 Hz for both: this results in a DAQ rate of 300-400 Hz for a typical dark night.

The DT set for the L0 trigger depends on the FoV as well, so that a galactic field will have higher DT ( $\sim 15\%$ ) with respect to an extragalactic sky region. When the Moon is present, DT are increased, so that the rates are lower. If the moonlight is too strong, the HV of the PMTs is reduced in order to avoid their fast aging.

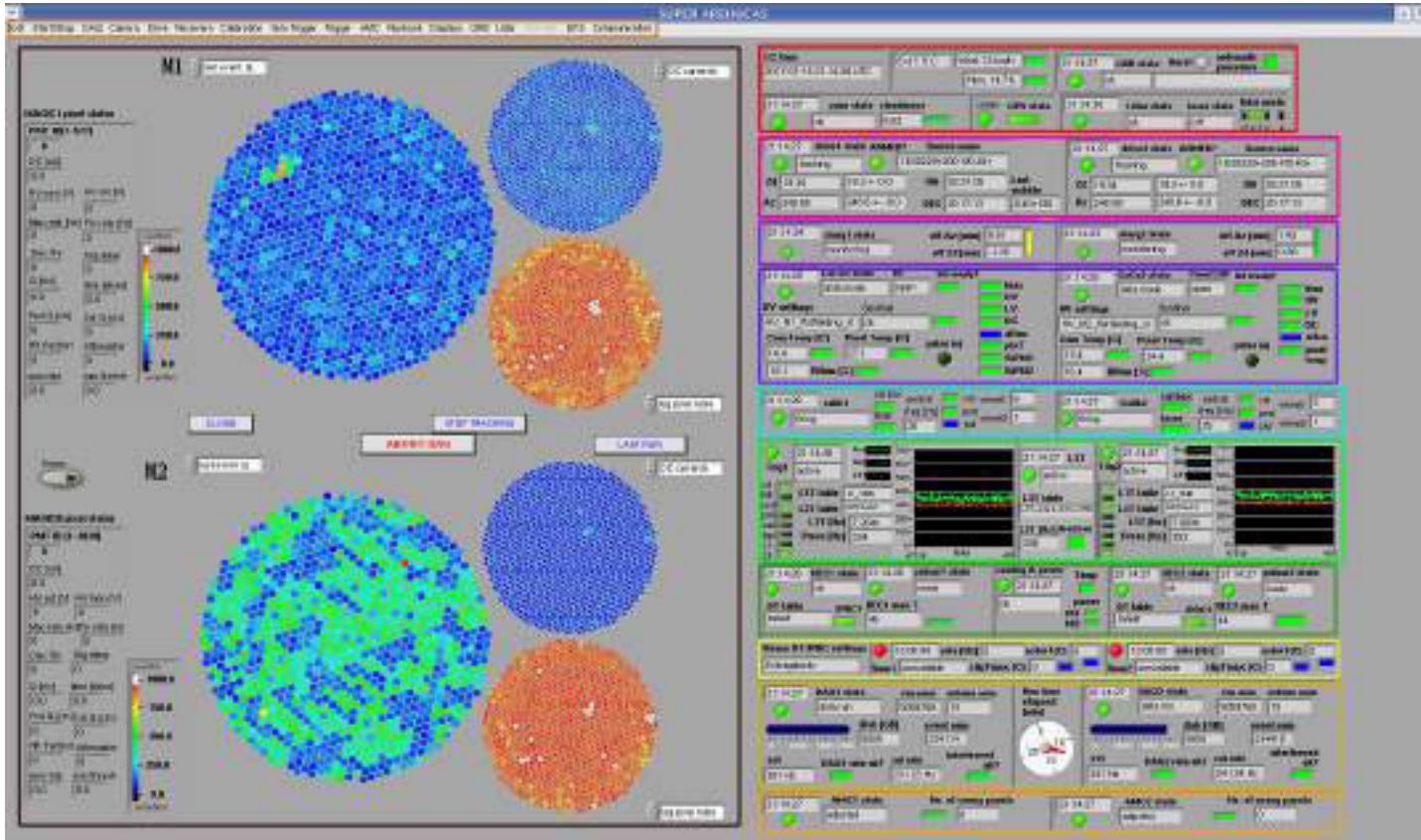


Figure 3.12: *SuperArehucas* graphical user interface. Different panels are denoted with a different color. Brown: menu entries to give commands to different subsystems; black: MAGIC cameras with information about the PMTs (charge, DC current, pixel rates ecc. . . ); red: CC clock, GBM, pyrometer, GPS and LIDAR status; magenta: drive1 and drive2, with information about current source name and coordinates; violet: starguiders panel; blue: CaCo1 and Caco2 display info about HV settings, cameras and pixel temperature, internal humidity and lids status; cyan: calibration boxes panel; light green: trigger section, showing trigger tables, rates and prescaler bits; dark green: receivers and cooling status; yellow: IPRC settings and SumTrigger status; ocher: DAQs info (run number, acquisition rate, event number, disk space); orange: AMCs status.



## Chapter 4

# MAGIC DATA ANALYSIS

Since the designing and commissioning of the first MAGIC telescope, an object-oriented software based on the ROOT framework was developed to be able to analyze the collected data and give scientific results. The name of this software is **MARS**, the **MAGIC Analysis Reconstruction Software**, see Zanin (2013). It has  $\sim 36$  executables (even if not all of them are used with the current version of the data) and some macros which perform common tasks. The executables use  $\sim 900$  classes, for a total of  $\sim 700000$  lines of code. One note about MARS is that even if its development goes on since 2000, it is backward compatible so that newer versions of MARS can still be used to analyze old data (for example taken in mono mode).

Usually the reconstruction of the events has three levels:

- low level, from raw data to image cleaning and calculation of Hillas parameters;
- intermediate level, from stereo reconstruction to estimation of the energy and arrival direction of the events;
- high level, that is the production of skymaps, spectrum, flux and light curve calculation, signal search and more.

Analyzers usually deal with the intermediate and high stages of the analysis, while the low-level reconstruction is done automatically by the On-Site Analysis (OSA) chain. Only in the case of non-standard analysis e.g. analysis of data taken in moon conditions or the analysis of GRB data, analyzers need to start from the low reconstruction level.

In this chapter I will describe the processing of the data taken by the MAGIC telescopes in stereoscopic mode, from raw to high level science products. The software tool developed by me and other two MAGIC members to produce what we call *upper limits skymaps* will be described in Section 5.2.5.

### 4.1 Monte Carlo data

The analysis of real data relies on the availability of enough Monte Carlo data, already anticipated in Section 2.4. MAGIC relies on a modified version of CORSIKA, Mmcs, to obtain the Cherenkov photons produced in a electromagnetic shower, as described in Majumdar et al. (2005). The initial spectrum of the  $\gamma$ -rays is a power law with spectral index  $-1.6$ . Since MAGIC pointing mode is wobble with  $0.4^\circ$  offset, the arrival directions of the gammas are on a circle of radius equal to the wobble offset. These MC are used for the analysis of point like sources and are called ring wobble MC. For extended sources or sources observed with a different wobble offset, diffuse MC data must be used, which are produced on a circle of radius  $1.5^\circ$  (or  $2.5^\circ$ ). After the Cherenkov photons are stored from the CORSIKA simulation, their propagation and absorption in the atmosphere is computed with the `reflector`

program. It takes into account the reflectivity of mirrors and records the position and time of photons when arriving at the camera. After that the `camera` program simulates the response of the PMTs and of the whole electronic chain. At this stage also noise, both from NSB and electronics, is added. At the end of the whole simulation chain, the events are saved in ROOT files and can be analyzed like real data with MARS.

MC data used in the MAGIC data analysis are produced directly by the MAGIC collaboration in dedicated clusters. The MC productions are divided in wide energy ranges:  $5^\circ$ - $35^\circ$ ,  $35^\circ$ - $50^\circ$ ,  $50^\circ$ - $62^\circ$  and  $62^\circ$ - $70^\circ$ , with a flat distribution in  $\cos(zd)$ . Since MC data should reproduce as closely as possible real data, hardware changes correspond usually to a change in the production of MC. MAGIC has different MC productions depending on the telescope and hardware status. The data used in the thesis are all taken after the major upgrade of the MAGIC telescopes in 2012.

The MAGIC collaboration provide another tool, still in testing phase, to simulate the telescopes response called `matelsim` (MAGic TELEscope SIMulation, Lopez 2013): it replaces `camera` and `reflector` and has a structure more suitable to be used with MARS.

During the analysis, only gamma MC data are used for the training of the Random Forest (i.e. teach to the Random Forest how gamma showers look like) and for the calculation of the effective area of the instrument. Proton MC data can be used in the Random Forest to recognize hadronic showers in the real data, but since the simulation of proton showers is CPU and time demanding, real data with no gamma rays, called OFF data, are used for this purpose. One could use proton or heavier nuclei MC data to try to distinguish between different species in the cosmic rays detected by MAGIC: hadrons are not the background in this case, but the signal. So MAGIC could be effectively used as a cosmic ray detector.

Since MAGIC underwent several hardware changes during the years e.g. change of MAGIC-I camera, change of readout from DRS2 to DRS4, downsampling and so on (see Aleksić et al. 2016a for the most recent upgrades in 2012-2013), in order to keep the match between MC data and real data, the parameters used in all the simulation chain (`Mmcs`, `reflector` and `camera`) must be updated and MC data must be produced again. This means that for data taken in different time periods, a different MC data set should be used. In MAGIC MC data for different analysis periods are tagged as `ST.XX.YY`, where `ST` means “stereo” (no mono data were used in this thesis), `XX` defines major hardware changes (it is equal to 03 for data after the 2012-2013 upgrade) and `YY` is the analysis period corresponding to minor changes in the hardware which nonetheless require a new MC production. The MC data used in this thesis with their tag and time period validity are summarized in Table 4.1.

| Tag                   | Time Period  | Description                |
|-----------------------|--|----------------------------|
| <code>ST.03.06</code> | 2014.11.24 - 2016.04.28                            | Data after downsampling    |
| <code>ST.03.05</code> | 2014.08.31 - 2014.11.22                            | Data after mirror exchange |
| <code>ST.03.03</code> | 2013.07.27 - 2014.06.18<br>2014.07.05 - 2014.08.05 | New AMC LUTs in MAGIC-I    |
| <code>ST.03.02</code> | 2013.01.18 - 2013.07.26                            | New AMC LUTs in MAGIC-I    |

Table 4.1: Tag, time period and description of the different MC data sets used in this thesis.

## 4.2 MARS Data Formats

Before going into the details of the MAGIC analysis chain, it is useful to have an overview of the data format used in MARS.

The most basic information (date, data type, telescope, source name ecc...) regarding a data file used in MARS can be retrieved from the filename itself. Usually the data files are in ROOT format, except for raw (binary format with `.raw.gz` or `.raw` extension, depending if

they are compressed or not) and report files (ASCII files with `.rep` extension). An example of a data filename is:

$$\underbrace{20170211}_1 \underbrace{M1}_2 \underbrace{05432109.001}_3 \underbrace{I}_4 \underbrace{GRB170211}_5 \underbrace{-W0.40+090}_6 \underbrace{.root}_7$$

where the different pieces have the following meanings:

1. date when the data was taken in the format `YYYYMMDD`. The convention in MAGIC is to put the date of the day after the night in which the data was taken;
2. telescope to which the file belongs. Possible values are `M1` and `M2`. This part of the filename is removed when the file contains stereo information i.e. if it is from `superstar` or `melibe` output;
3. data run and subrun in the format `RRRRRRRR.SSS`. The data run is the basic unit used in MAGIC data taking and corresponds to one wobble position, usually lasting 20 or 15 minutes. To have smaller files, each run is divided into multiple subruns. The subrun part of the filename is removed when the file contains stereo information. If the run number starts with `05`, then the data was taken with both telescopes, otherwise it will start with `01` or `02` if it was taken only with MAGIC-I or MAGIC-II respectively (i.e. mono observation);
4. data file tag specifying the data type;
5. name of the source;
6. wobble information (see Section 3.6.1) in the format `WY.YY+XXX`, where `Y.YY` denotes the wobble offset in degrees (e.g `0.40` or `1.00`) and `+XXX` is the angle between the right ascension axis and the offset direction as measured in the direction of the declination axis. For example, `W1` is denoted usually as `W0.40+000`, while `W2` as `W0.40+180`.
7. extension of the file: `.raw` and `raw.gz` for non-compressed/compressed files, `.rep` for report files and `.root` for the other data types.

A list of the possible data types is given here below:

`*_D_*.raw`: raw files in binary format, containing information about the subrun (date, time, software version used, source information ecc.) and the events (waveforms of the signals for each pixel, timestamps, event number ecc.).

`*_D_*.rep`: ASCII files containing the reports sent from the several subsystems (drive, camera, trigger, DAQ, receivers, starguider, LIDAR and so on) to the central control program, `SuperArehucas`. They are crucial for data analysis and they are later merged with the raw files.

`*_P_*.raw`: pedestal run, taken with constant frequency triggers.

`*_C_*.raw`: calibration run, where the camera is uniformly illuminated by the light produced by the calibration box.

`*_B_*.raw`: baseline subtraction run.

`*_Y_*.root`: calibrated files containing for each pixel the charge and time information.

`*_I_*.root`: star files containing the Hillas parameters for each event.

`*_S_*.root`: superstar files containing the stereo parameters combining the star files for both telescopes.

`*_Q_*.root`: melibea files containing for each event the direction and energy reconstruction and the hadronness calculation.

MARS ROOT files have a common structure: they contain several ROOT trees, with data containers as branches and data values as leafs. Some of these trees are:

- **RunHeaders** tree with only one entry per file, containing information about the (sub)run e.g. the software version used for the processing, the command line arguments used with the executables used before in the analysis chain ecc.
- **Events** tree containing information for each event. It is updated adding branches to it as more information is found through the analysis chain.
- **subsystems** trees containing the information from the report files. They are usually copied from file to file as the analysis chain goes from the low to the high level.
- **RunTails** tree, similar to the RunHeaders one. It is created and filled after the file is processed with informations regarding the execution of a specific program.

Note that for MonteCarlo data additional trees are present, containing information about how the MC events were produced, like the true energy of the events.

The raw files can be converted into ROOT format with the proper MARS containers using the `merpp` (**M**erging and **P**reprocessing **P**rogram) executable. The same program is used to merge the report files with the ROOT files, creating a tree for each subsystem. The merging of the subsystem reports can be done on ROOT converted raw files or directly on calibrated files (they are not needed at the calibration level), like it is done by the Online Site Analysis (OSA).

### 4.3 Calibration

Raw files contain the waveforms of the signal for each event and for each pixel. The next step in the analysis is the *signal extraction*, that is the calculation of the charge in photoelectrons and the arrival time of the signals.

The waveform is just the signal binned in several time slices, in MAGIC case 50 slices of 0.5 ns each. Before the signal extraction, the baseline of the waveform must be evaluated. The baseline will then be subtracted from the waveform to get a precise value of the signal charge. The current method for the baseline estimation uses the so called *pedestal events*, taken at the beginning of each source observation and during data taking as interleaved pedestal events. The pedestal events are events with random triggers and so without any pulse. To estimate the baseline, the signal from each time slice is binned into a single histogram and fitted with a gaussian, whose mean is taken as the baseline.

When the baseline is known, the signal can be extracted. In Albert et al. (2008a) several signal extraction methods are presented:

- **fixed time window extractor**: the signal is integrated over several consecutive slices in an a priori know position;
- **sliding window extractor**: similar to the fixed window algorithm, but the integration window can be moved and the signal charge (in readout counts) is taken as the largest sum of several consecutive slices;
- **digital filter extractor**: the signal waveform is fitted by a pulse shape;
- **spline extractor**: similar to the sliding window with integration performed by a polynomial function.

The current signal extractor used in MAGIC data analysis is the sliding window over five consecutive slices. It is not sensitive to afterpulses because they give a lower integral value with respect to the main pulse. On the other hand, this method will always find a signal even from background fluctuations (bias).

After signals have been extracted, they have to be calibrated: the signals are given in integrated readout counts, while their value in photoelectrons is needed. The *calibration* process computes the conversion factors from readout counts to photoelectrons for all the pixels. The computation is done with the *F-factor method* (Mirzoyan and Lorenz 1997), where the basic assumption is that the number of photoelectrons follows a Poisson distribution. One can derive the relation between the number of photoelectrons  $N_{\text{phe}}$  and readout counts  $\mu$  (in average) :

$$N_{\text{phe}} = \frac{\mu}{\sigma_{\text{signal}}^2 - \sigma_{\text{noise}}^2} \cdot F^2 \quad (4.1)$$

where  $F^2$  is the *excess noise factor* of the photomultiplier,  $\sigma_{\text{signal}}$  is the standard deviation of the signal and  $\sigma_{\text{noise}}$  is the standard deviation of the noise.  $\mu$  and  $\sigma_{\text{signal}}$  are computed from the *calibration runs* (see calibration box section): one calibration run is taken before each source observation (2000 events at 300 Hz) and many of them are taken with a 25 Hz frequency during data taking as interleaved calibration runs to monitor the behavior of the PMTs during time.  $\sigma_{\text{noise}}$  instead is calculated from the aforementioned pedestal runs.

Given (4.1), the conversion factor  $C$  will be:

$$C = \frac{N_{\text{phe}}}{\mu} = \frac{\mu}{\sigma_{\text{signal}}^2 - \sigma_{\text{noise}}^2} \cdot F^2 \quad (4.2)$$

Another important point to take into account in the F-factor method is the different response (different gain at fixed HV) of each photomultiplier to the same signal, e.g. the one during a calibration run. The *flatfielding procedure* allows to adjust the HVs of the photomultipliers so that the signal, in readout counts, from the calibration events is the same for all the pixels. This means that the calibration is done not to real photoelectrons but to *equivalent photoelectrons*:

$$C = \frac{N_{\text{phe,average}}}{\mu} \quad (4.3)$$

where  $N_{\text{phe,average}}$  is averaged over all the camera pixels.

After the charge extraction, the arrival time  $t_{\text{arrival}}$  of the signal is estimated as the average time slice of the integrated window weighted with the signal in the same slices:

$$t_{\text{arrival}} = \frac{\sum_i i \cdot s_i}{\sum_i s_i} \quad (4.4)$$

where  $i$  is the time slice number and  $s_i$  is the signal in the  $i$ -th slice. The index  $i$  runs over the slice numbers belonging to the final integration window.

There are some pixel to pixel differences due to the different length of the optical fibers and the transit times of the electrons in the photomultipliers (due to the different HVs set after flatfielding), so that even with a synchronous light pulse in the whole camera, it will not be recorded at the same DRS sample in the readout channels. To calibrate these time differences, the mean arrival time from a calibration pulse is computed and then subtracted from the arrival times in each pixel to get an estimate of the difference.

The MARS executable taking care of the whole calibration process is **sorcerer** (*Simple, Out-right Raw Calibration; Easy, Reliable Extraction Routines*): there are two running modes, usually called *C-mode* and *Y-mode*. In the former, \*\_P\_\* and \*\_C\_\* files are processed to get the baseline, the pedestal bias and RMS, mean arrival times and conversion factors. The latter runs over \*\_Y\_\* files (in raw or ROOT format after running **merpp**) and uses the output files of the C-mode: the events are calibrated in this step and the pedestal/calibrated

interleaved events are used to update the values calculated previously in the C-mode. The output is again a \*\_Y\_\*.root file and two other ROOT files, usually called *scalib* and *ssignal* files, containing information about the calibration.

## 4.4 Image cleaning and parametrization

After the calibration, the *image cleaning* and *image parametrization* are performed by the MARS executable *star* (*STandard Analysis and image Reconstruction*), which takes as input calibrated files (\*\_Y\_\*.root) and creates the so called star files (\*\_I\_\*.root).

The image cleaning is essential to remove from the image those pixel whose signal does not come from a Cherenkov shower but from the NSB or electronic noise. Several cleaning algorithms were developed across the years, which were efficient with some specific hardware configurations (MAGIC as a mono system, MAGIC as a stereo system before and after the upgrade). For stereo data taken after the major MAGIC upgrade, the default cleaning method is divided in two steps, see Aleksić et al. (2011b) for details:

- **sum image cleaning:** after the clipping of the pixels signal to remove accidental signal<sup>1</sup> (e.g afterpulses or strong NSB fluctuations), compact groups of 2, 3 or 4 neighboring pixels (usually referred as 2NN, 3NN and 4NN respectively) are considered in every possible combination. The pixels of each combination are not discarded if the sum of their charge is above a certain threshold and the difference between the time of arrival of the pixels is within a predefined time window. Given the number of neighboring pixels, the values for the charge threshold and the time difference change, becoming more relaxed for larger groups. See Aleksić et al. (2016b) for the values used in the sum image cleaning.
- **time-constrained absolute image cleaning**<sup>2</sup>: after the application of the sum cleaning, the survived pixels are tagged as *core* or *boundary* pixels. First, all pixels with charge greater than a reference value  $Q_{\text{core}}$  are selected. A pixel will be tagged as core if at least one neighbor pixels survived the previous step. Moreover, the mean time of arrival for the core pixels forming the main island of the image will be computed. If the time of arrival of a core pixel is not within a time window of 4.5 ns, it is rejected. After that, all the pixels with a core pixel as a neighbor, charge above a second reference level  $Q_{\text{boundary}}$  and time difference with respect to the core pixels within 1.5 ns will be added to the image and tagged as boundary pixels.

Moreover, it can happen that during the observation one or more stars are present in the field of view. If they are bright enough they can provide a signal in one or more pixels. *star* is capable of removing these "hot" pixels looking at the mean and rms of the pixels pedestal rms distribution and comparing it with two reference values.

The use of this two-steps cleaning ensures robustness, efficiency and a lower energy threshold compared to old cleaning methods where the time information was not exploited. In particular the sum cleaning allows to choose lower values for the reference values  $Q_{\text{core}}$  and  $Q_{\text{boundary}}$ , which are set to 6 phes and 3.5 phes respectively for the current MAGIC configuration, and to have a probability less than 6% to have an image with NSB or electronic noise only. An example of events before and after image cleaning is shown in Figure 4.1.

The cleaned images at this point undergo the parametrization process, which is just the computation of the so called *image parameters*. Some of them are still the ones that Hillas used for the first time to discriminate between hadron and gamma initiated showers, as he presented in Hillas (1985).

<sup>1</sup>the clipping level is set to 750 phe

<sup>2</sup>Cleaning method used also with MAGIC-I 2 GSamples/s MUX FADC system.

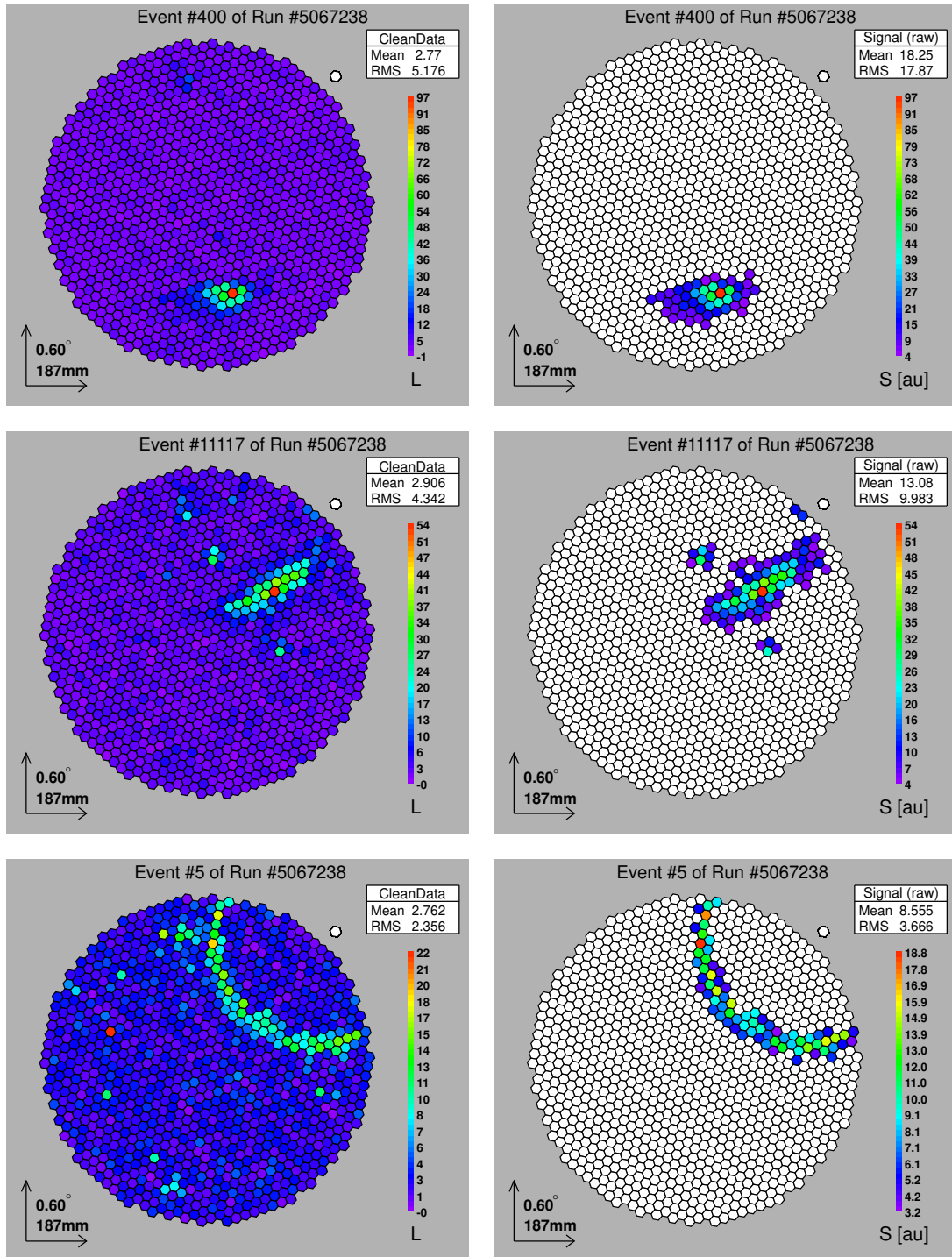


Figure 4.1: **Left:** images of three events before the cleaning. From top to bottom, a gamma-like, a hadron-like and a muon-like event. **Right:** the corresponding cleaned images.

We can divide the image parameters in three categories:

- parameters independent on a reference direction or point on the camera plane, describing the general shape of the image (ND);
- parameters depending on a reference direction (RD);
- parameters depending on a reference point (RP, for example the camera center or the source position in the camera plane).

Here I give a list of the main image parameters considered in the image parametrization. To visualize some of them refer to Figure 4.2.

- **size**: total number of photoelectrons in the image. In first approximation, it is proportional to the energy of the primary particle
- **length**: half length of the major axis of the ellipse
- **width**: half of the minor axis of the ellipse
- **center of gravity**: pair of values (X and Y in the camera reference frame) representing the center of gravity of the shower image
- **conc-n**: given the  $n$  brightest pixel, it represents the fraction of photoelectrons contained in those pixels
- **leakage1/2**: given the last or the last two camera pixel rings, it is the fraction of signal distributed in them with respect to the image *size*
- **M3long**: third momentum of the image along the major axis of the ellipse
- **asym**: difference between the peak of the charge distribution in the image and the center of gravity
- **number of islands**: number of different islands of the image (an island is a group of isolated pixels survived after the cleaning)
- **alpha**: angle between the major axis of the ellipse and the line connecting the reference point and the center of gravity
- **dist**: distance of the center of gravity from the reference point
- **time-gradient**: angular coefficient of the linear function used to fit the arrival time distribution of each pixel after their coordinates have been projected on the major axis of the ellipse
- **time-rms**: spread of the arrival time distribution of the pixels belonging to the image.

In addition to the image cleaning and parametrization, **star** can artificially add noise in the data before the cleaning. A new mean and RMS for the pedestal must be specified (the two values can be extracted directly from the interleaved pedestal events taken during every observation) and **star** will degrade the signal both in charge and time. A second possibility is to specify a file containing the distributions in charge and time of the pedestal. This feature is useful in the case of observation under moon conditions, in which the NSB is higher than in dark conditions: standard MC data produced for MAGIC analysis are produced with a NSB level compatible with the one found in dark observations, so if moonlight is present there is a mismatch between MC and real data. This leads to a wrong estimation of the energy of the events, of the effective area and related quantities (e.g. flux, LC and SED). A good tuning

---

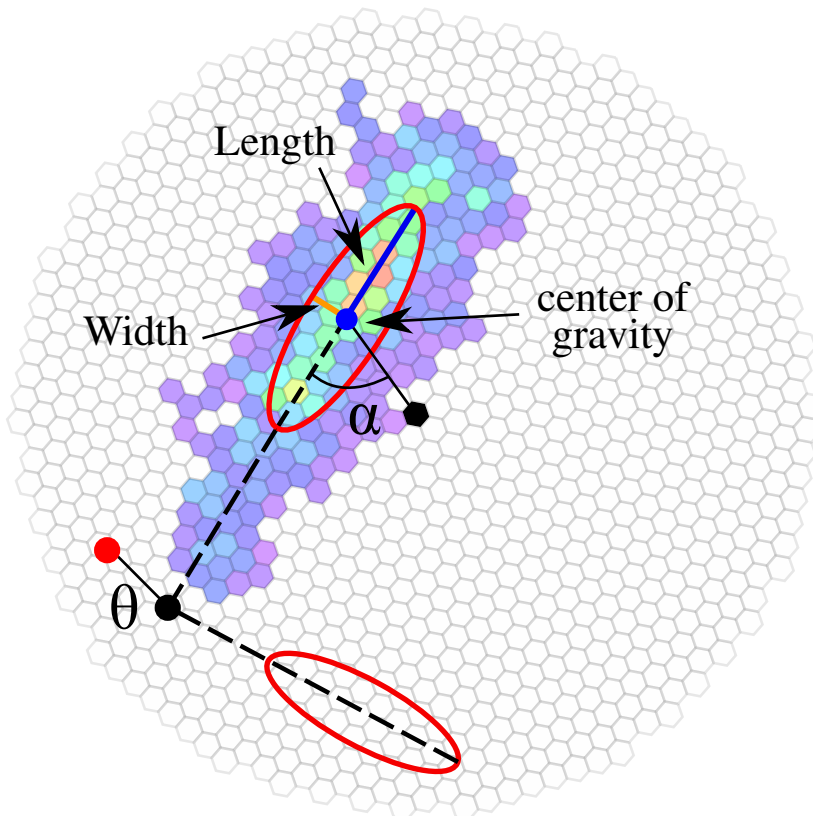


Figure 4.2: Some of the Hillas parameters of a cleaned image. The central black dot is the center of the camera. The other black dot is the reconstructed position of the source, while the red dot is the true position of the source.

of MC data with a proper choice of the cleaning levels and other cuts (size and hadronness in particular) allows to obtain correct results for fluxes, LCs and SEDs, although there will be a degradation of the sensitivity, especially for strong NSB, and additional systematics to be taken into account.

Another task performed during `star` execution is the *pointing correction*. The mispointing is caused by the gravitational load, so that the dishes bend and the cameras sag. In order to correct for this effect, a drive bending model, which is created from a special observation procedure called *TPoints* and takes into account the dependence of the bending on the orientation of the telescopes, is applied to the data. Moreover, during observations, the starguider camera monitors the camera and the stars in the field of view behind it at the same time. Comparing the position of the stars from catalogs with the one obtained from the starguider, a correction to the pointing position of the telescopes can be applied for each event. Since also the starguider camera behavior can change depending on the telescopes position, it needs to be calibrated as well using a starguider bending model. With this method the pointing position can be calibrated down to less than  $0.025^\circ$ .

#### 4.4.1 Other image cleanings

Other image cleaning methods available in `star` are reported here for completeness.

- **Absolute image cleaning:** used with MAGIC-I 300 MSamples/s FADC system. It relies on the distinction between core and boundary pixels, as defined within the time-constrained absolute image cleaning but without the constrain on the time information, which is not taken into account and so increases the achievable energy threshold. The

two reference levels are higher,  $Q_{\text{core}} = 10$  phes and  $Q_{\text{boundary}} = 5$  phes, so this cleaning method is not much affected by different levels of NSB.

- **Dynamical Image Cleaning:** alternative cleaning method, where the two reference values are calculated for each event starting from the default values, which are scaled by a factor dependent on the event size estimated with the default reference values (6 and 3.5 phes). If the scaling factor is less than unity, then no scaling is applied i.e. the standard cleaning is applied to the event.

## 4.5 Stereo parameter reconstruction

Up to this point, the analysis is performed individually for MAGIC-I and MAGIC-II data. Given the stereoscopic nature of MAGIC, the information about the same event recorded by individual telescopes is combined to get a three dimensional shower reconstruction. This is performed by the MARS executable `superstar`, which calculates the so called *stereo parameters* starting from `*_I_*.root` files (one per telescope and subrun). The most relevant are:

- **shower axis:** a shower axis is characterized by a direction and an impact point on the ground. The direction is defined as the intersection of the major axes of the two images, once superimposed on a camera plane (crossing method). The impact point on the ground is determined by the intersection of the major axes of the two elliptical images starting from the telescope positions (taking into account the distance between the two telescopes). The accuracy of shower axis determination depends on the relative positions of the telescopes and the shower: the more parallel the two images on camera planes are, the larger the uncertainty in the reconstructed parameters. The shower axis is used to calculate  $\theta$ , the angular distance between the estimated shower direction and the true source position. Since we are only interested in the modulus of this distance,  $\theta^2$  is used.
- **impact parameter:** the perpendicular distance between the shower axis and the telescope pointing axis.
- **shower maximum height:** the height of the shower maximum is obtained by using the angle at which the image CoG is viewed from each telescope. So it will be the intersection point between the shower axis and the lines going from each telescope to the centroid direction in the sky. Being a three dimensional problem, it is difficult to have a perfect intersection of three lines, so the maximum height is computed as the altitude which minimizes the distance of the lines or better, the altitude which minimizes the perimeter of the triangle formed by the three lines. The height of the shower maximum depends on the primary energy: higher energy showers penetrate deeper into the atmosphere, hence their maxima are closer to the ground (smaller values). This parameter has a high discriminating power mainly at low energies. In fact, while the shower maximum height distribution has a single Gaussian shape for  $\gamma$ -ray events, it shows a second peak at the height of 2 – 3 km for low energy (size < 300 ph.e.) background events (for high energy background events the distribution has a single peak, but broader than the one for  $\gamma$ -ray events). This second peak is produced by single muon events.
- **Cherenkov radius and density:** radius and density of the Cherenkov light pool on the ground. They are calculated assuming Cherenkov emission from a single electron at the shower maximum height and with energy equal to the critical energy in air (86 MeV). The light density is calculated from the annulus generated by the electron after it traveled a one-meter track.

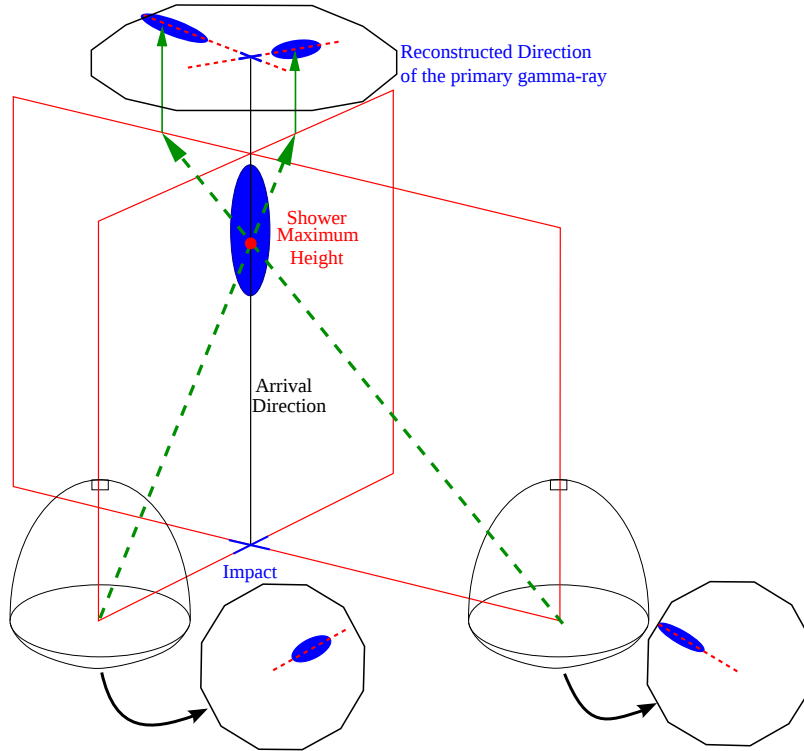


Figure 4.3: Example of the reconstruction of some stereo parameters.

From now on, files are not divided by subrun or telescope anymore. The results are stored in \*\_S\_\*.root files, one for each data run, in a ROOT tree called **MStereoPar**.

## 4.6 Data selection

MAGIC and Cherenkov telescopes operate without any protection (e.g. a dome) against bad weather conditions. This means that in some situations data cannot be collected if some parameters are outside the so called *safety limits*: some examples are the average wind speed which must not exceed  $40 \text{ km h}^{-1}$  and the humidity which must be below 90% in order not to damage the PMTs (HV's are turned off in any case). Even if these safety limits are respected, the quality of the data can be affected by hardware failures, cars passing at the MAGIC site (the so called car flashes, increasing the trigger rate for few seconds) and especially by atmospheric conditions. The quantity of aerosols and water vapors depends on the presence of clouds or calima and affects the Cherenkov yield through photon scattering, absorption and the change of the refractive index of the atmosphere. Thanks to simulations with different atmospheric profiles, it was found that the critical parameter is the total transmission of the atmosphere, introduced in Section 3.5.3 when the LIDAR was described. The LIDAR software is able to calculate the atmosphere transmission, but the correction of energy estimation and spectrum is not always possible, depending on the value of the transmission. For this reason, usually data are divided in different quality classes according to their transmission calculated at 9 km  $T_{9\text{km}}$  (this is because 10 km is the average height where the showers develop; the LIDAR computes the transmission at 3 km, 6 km, 9 km and 12 km):

- $0.85 < T_{9\text{km}} < 1.00$ : transmission is very good, there is no need to correct the data
- $0.70 < T_{9\text{km}} < 0.85$ : transmission is good but data need to be corrected
- $0.55 < T_{9\text{km}} < 0.70$ : poor transmission, correction is mandatory

- $T_{9\text{km}} < 0.55$ : the transmission is too low and data cannot be corrected, so they cannot be analyzed.

To keep systematic uncertainties under control, bad quality data must be removed from the dataset. Usually the selection is performed according to the value of  $T_{9\text{km}}$ , removing all the data below 0.55 transmission and dividing the data in two subsets, one which will need corrections and the other which is good as it is. The executable used for this purpose is called `quate`. Beside the selection based on the transmission value, the user can perform selections according to several other parameters like zenith and azimuth angles, rates and cloudiness. If the LIDAR information is not available (e.g. the LIDAR was not working), the cloudiness or rate information can be used, even if less reliable. In this case, no correction can be applied to the data.

The selection can be performed at `star` or `superstar` level. If performed at `star` level, `quate` can divide the data in three subsets *good*, *bad* and *out-of-range* with the subruns respecting or not the cuts selected by the user. If `quate` is run at `superstar` level, the data are divided in time slices of predefined duration and only those where the selection parameters have good values are selected. The time slices found at this step can then be used in `melibea` to remove bad quality data.

## 4.7 Event characterization

After the image and stereo parameters have been calculated, the nature and properties of the events need to be determined. Regarding the nature, the events triggering the telescopes are mostly hadrons constituting the background in MAGIC observations. Gamma events need to be recognized from this dominant background. The other two properties needed for the high-level analysis are the energy and arrival direction of the events.

The discrimination between gammas and hadrons (*gamma/hadron separation*) is performed using a classification method called *Random Forest* (RF), the energy estimation with *Look Up Tables* (LUTs) and the arrival direction uses the so called *DISP* parameter. These methods are described in Sections 4.7.1, 4.7.2 and 4.7.3 respectively and they are implemented in the MARS executable called `coach`. The actual estimation of the nature of the particle, its energy and arrival direction is performed by the executable `melibea` after `coach` creates the files needed for the computation.

### 4.7.1 Gamma/hadron separation

As every particle experiment, MAGIC needs to draw out the signal ( $\gamma$ -rays) from a dominant background (hadron originated showers): even in a strong source like the Crab Nebula the number of hadrons is three orders of magnitude greater than the gammas. This points out to the need of a powerful method to reject almost all hadrons while retaining most of the gamma events. This is accomplished by using the classification method called Random Forest, described in Albert et al. (2008b), from now RF for short: image and stereo parameters and timing information are combined at the same time to reach the highest degree of separation between the hadronic and gamma samples.

The ultimate goal of the RF method is to assign to each event a value for the *hadronness*. This classification parameter is limited between 0 and 1: events with hadronness close to zero are most likely gamma events. To compute the hadronness, the RF builds a decision tree. The inputs needed are a MC dataset of simulated gamma-ray events and a set of “OFF” data with only hadronic events. Since simulating hadronic showers is computationally costly and subject to uncertainties, real data with no gamma events are used. As far as the MC gamma sample is concerned, it is divided in two subset: one, called the *training sample*, is used in the RF method while the second, the *test sample* is used for the computation of the

---

instrument response function. The two samples must be independent one from each other in order not to obtain biased results. Both the gamma MC and OFF samples must be chosen in the same zenith range of the ON data (the data to be analyzed). Specifically for OFF data, they should be chosen with the same data taking conditions as the ON data (dark or moon, galactic or extragalactic). Before the decision tree is built, a *rezenithing* is applied to the OFF sample in order to have the same size and zenith/azimuth angle distributions of the MC sample. This procedure ensures that no artifacts are present when the RF method is used in the event characterization.

The idea behind the classification tree is that each event can be represented by a multidimensional array with the values of the parameters describing the event found in the previous analysis steps (**star** and **superstar**). If  $N$  parameters are used, a  $N$ -dimensional hypercube will contain all the events. Starting from this hypercube, a first parameter is randomly selected and a cut on this parameter is computed. The choice of the parameter cut is optimized in the sense that the cut will separate in the best possible way the hadronic and gamma samples according to that parameter. The initial hypercube is divided in two nodes. Each node is taken and the previous operation is repeated: a parameter is chosen (different for the two nodes) and the optimized cut is found, creating more nodes. The procedure is stopped when a node contains only gammas or hadrons or if the number of events in a node is below a predefined value. The final nodes will be tagged with a different value for the hadronness: 0 (1) if the node is comprised of only gamma (hadron) events or a value between 0 and 1 if the node contains both event types. In this case the hadronness value is computed according to the fraction of gamma and hadron events in the node. When the final nodes are reached, the decisional tree is built.

Regarding the choice of the parameter and the optimized cuts in each node splitting, the method uses the so called *Gini index*  $Q_{\text{Gini}}$ , used to assess the inequality of two statistical populations (gammas and hadrons in this specific case). In the RF method it is defined as:

$$Q_{\text{Gini}}(K) = 4 \cdot \frac{N_{\gamma}N_{\text{h}}}{(N_{\gamma} + N_{\text{h}})^2} \quad (4.5)$$

where  $K$  is the node where the index is being computed, while  $N_{\gamma}$  and  $N_{\text{h}}$  are the numbers of gamma and hadron events in the node.

The cut optimization is performed as follows:

- starting from a specific node (starting node), the remaining parameters are selected;
- for each parameter different cuts are tried and for each trial cut the Gini index decrease is computed as the difference between the Gini indexes in the node created applying the cut on the parameter and in the starting node;
- for each parameter, the selected cut is the one resulting in the maximal decrease of the Gini index (i.e. maximal distinction between gamma and hadrons according to that parameter);
- the parameter chosen to create the new nodes is the one with the maximal decrease in the Gini index between all the parameters involved.

The parameters used in the RF method can be simple image parameters (e.g. width, length of the images) or stereo parameters (MaxHeight). The distribution of these parameters for gamma and hadron events is very different and so their separation power is high. Other parameters, like the zenith angle, do not have a huge direct separation power but they can be combined with other parameters to increase it. Other combination of parameters can be found by MC simulations.

Now that the decision tree is created, each event will be assigned an hadronness value by

feeding it to the decision tree. If only a single decision tree would be used, the error on the hadronness would be rather large. Creating more trees ensures the convergence of the error. Usually 100 trees are created, but the number depends on how many parameters are used in the classification. Having  $k$  trees, an event will be fed to all the decisional trees, resulting in a value  $h_i$  for its hadronness ( $i$  represents the  $i$ -th tree). The final hadronness value for the event will be just the average of the hadronness values from each tree:

$$h = \frac{1}{k} \sum_{i=1}^k h_i \quad (4.6)$$

The RF method is quite efficient: it removes more than 90% of the hadronic events while keeping about 50% of the gamma events. The performance of the method depends on energy, being better at higher energies. At low energies the images are smaller and sloppier, causing the RF method to perform worse. Moreover, at the lowest energies hadronic and gamma showers are very similar.

### 4.7.2 Energy estimation

The standard method for the estimation of energy for stereo observations relies on Look Up Tables (LUTs, Aleksić et al. 2012). The gamma MC sample is binned according to some parameters chosen for the energy estimation. For each bin, the mean energy and RMS is computed. A real event will belong to one of these bins and its energy will be the energy value contained in that bin.

The basic assumption in this method is that the energy of the primary particle is proportional to the number of Cherenkov photons in the shower. This translates in a proportionality between the energy and the *size* of the images. This zero order approximation is used in a first step to fill the LUT with the value  $E_{\text{true}} \cdot (\rho_c / \text{size})$ , where  $\rho_c$  is the Cherenkov density (see Section 4.5). The ratio  $\text{size} / \rho_c$  is an estimation of the number of electrons at the shower maximum. In a second approximation, the LUT has two dimensions  $\text{sqrt}(\log_{10}(\text{size}))$  and  $\text{impact} / r_C$  ( $r_C$  is the Cherenkov radius defined in Section 4.5). They take into account the non perfectly linear dependence of the energy on *size* and the decrease of  $\rho_c$  with the impact parameter. At this point the LUTs bins contain the mean values of  $E_{\text{true}} \cdot (\rho_c / \text{size})$  and their RMS.

A second correction based on the zenith angle, leakage and geomagnetic field is applied assuming that they do not depend on other parameters. The zenith correction is particularly important at high zenith angles, where the Cherenkov light gets more absorbed. The leakage correction is applied only for the events having non-zero leakage parameter (those at the edge of the camera). The geomagnetic field decreases the Cherenkov density because it causes a spreading of the shower depending on the relative angle between the geomagnetic field and the shower axis. All these corrections are applied with some predefined empirical formulas. The LUTs method is applied for the events of each telescopes separately, resulting in two estimated energies  $E_{\text{est},1}$  and  $E_{\text{est},2}$ . The final energy estimation  $E_{\text{est}}$  is an average between  $E_{\text{est},1}$  and  $E_{\text{est},2}$  weighted with the inverse of their RMS.

### 4.7.3 Arrival direction estimation

The arrival direction of the primary gamma ray can be determined in a rather straight-forward way in case of arrays of IACTs, but requires a complex method based on MC simulations in case of stand-alone IACTs. It is the so-called *DISP RF* method (Aleksić et al. 2016b).

Since the major axis of the image ellipse is the projection of the shower incoming direction on the camera plane, the source position lies on this axis at a certain distance from the image CoG. This distance, *DISP*, can be estimated from the shower elongation (width/length) as

follows:

$$\text{DISP} = A(\text{size}) + B(\text{size}) \cdot \frac{\text{width}}{\text{length} + \eta(\text{size}) \cdot \text{leakage}^2} \quad (4.7)$$

The correction term added to length accounts for the truncation of large images at the edge of the camera (expressed in terms of the leakage parameter). Also a second order polynomial dependence of the parameters on the logarithm of the image size is included. The optimization of the coefficients  $A$ ,  $B$ , and  $\eta$  is performed with gamma MC with a regression method using a Random Forest on a continuous quantity. The parameter set is similar to the one used in the RF for the gamma/hadron separation. In this case, the DISP is computed for each event and for each telescope, resulting in two DISP values for each event.

Once the DISP is known, the reconstructed source position is not unequivocally determined: there are two possible solutions along the major axis of the ellipse. To solve this head-tail discrimination (or ghost busting) in the case of stereoscopic observations, the two images of the same event are taken on the same plane and the four reconstructed source positions (2 per image) are found. The four distances between these positions are computed and the pair with the smallest distance is taken. The final estimated source position is an average of these two positions weighted by the number of pixels in each image. The estimated arrival direction will be the line connecting the CoG to the reconstructed source position. The full method is shown in Figure 4.4.

When applied to hadronic events, sometimes the DISP method can give inconsistent results because the training was performed on gamma MC events. If the distances between the four points in the camera plane are not close enough ( $0.22^\circ$  is the limit), it means that no reconstructed source position was found for the event and so it is discarded. This way the gamma/hadron separation is further improved. Moreover, the DISP value can be used for a better estimation of other parameters like the impact. The DISP RF joined with the stereoscopic reconstruction leads to an almost perfect ghost busting, of the order of less than 1% at high energies and of 10% at low energies.

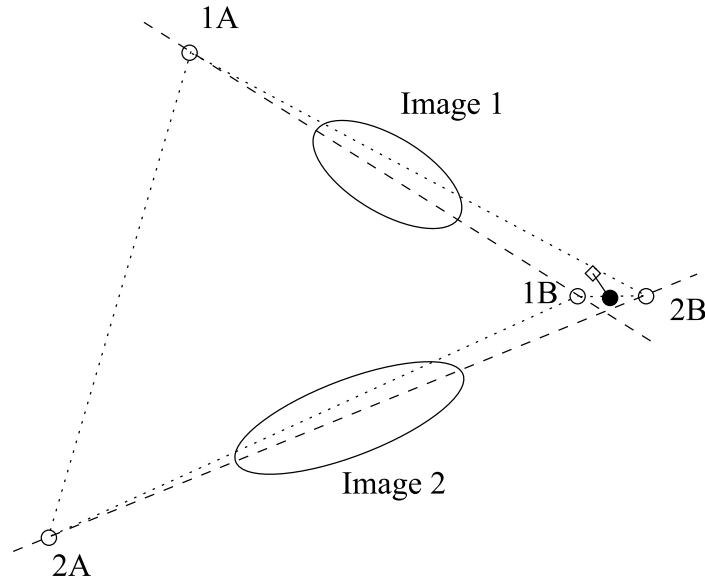


Figure 4.4: Graphical representation of the DISP method for the reconstruction of the arrival direction of the events. Given two images for the same event, there will be four reconstructed source positions, denoted by empty circles. The angular distances between them are shown by dotted lines: the closest pair is chosen (in this example 1B-2B) and their weighted average is taken as the final reconstructed position for the source (black dot). The solid line is  $\theta$ , the angular distance between the true (empty diamond) and reconstructed position of the source. From Aleksić et al. (2016b).

## 4.8 Application of RF, DISP RF and LUTs methods

Once `coach` is run, the RF, the energy LUTs and the DISP RF are created. The final hadronness calculation, energy and arrival direction estimation is done by applying those three outputs to the data respectively. This is performed by the MARS executable `melibea`. It takes as an input the `*_S_*.root` superstar files and the output files from `coach`: `RF.root` containing the RF for the gamma/hadron separation, two `DispRF.root` (one per telescope) for the DISP estimation and `EnergyTable.root` containing the energy LUTs. The output files from `melibea` are `*_Q_*.root` files (one for each superstar input file) with additional containers for the new computed quantities: `MImageParDisp_x`, `MEnergyEst_x` and `MHadronness` (`x` stands for 1 or 2 depending on the telescope). Moreover, the `MStereoParDisp` container is added, containing the stereo parameters recalculated with the DISP values. In particular  $\theta^2$  is computed again, obtaining a more robust estimation.

As anticipated, `melibea` can be fed with a file containing time slices: events with a time stamp in these slices will be retained and processed, while the others will be left untouched and not added to the output files.

In order to produce spectra, SEDs and light curves, `melibea` must be run on the test MC sample as well.

## 4.9 Signal significance

Once `melibea` processed the ON data, the next step is to assess the presence of a  $\gamma$ -ray signal. In MARS, the executable `odie` is responsible for this task.

The basic assumption is that the distribution of  $\theta^2$  peaks at small values for  $\gamma$ -ray events while is flat for hadronic events on the whole  $\theta^2$  range. Cutting on these parameters (one or the other) defines the so called *signal region*. The program which performs this task is called `odie`.

Starting from the ON data (`melibea *_Q_*.root` files), cuts on several parameters, especially size and hadronness, can be applied to the events and fill the so called *ON histogram*, a simple 1D histogram where the events are binned according to their  $\theta^2$  value. To maximize the chance of discovery, `odie` calculates the value of the cut on  $\theta^2$ ,  $\theta_{\text{cut}}^2$  which defines the range  $0 - \theta_{\text{cut}}^2$  in the  $\theta^2$  axis, called *signal region*. Currently there are three sets of standard cuts used for signal search in three energy ranges: Low Energy (LE), High Energy (HE) and Full Range (FR), see Table 4.2.

| Parameter        | LE                | FR                 | HE                      |
|------------------|-------------------|--------------------|-------------------------|
| $\theta^2$       | $\theta^2 < 0.02$ | $\theta^2 < 0.009$ | $\theta^2 < 0.007$      |
| hadronness       | hadronness < 0.28 | hadronness < 0.16  | hadronness < 0.1        |
| size             | size > 60         | size > 300         | size > 400              |
| $E_{\text{est}}$ | /                 | /                  | $E_{\text{est}} > 1000$ |

Table 4.2: The standard cuts in the different energy ranges. Each cut results in a slight different final sensitivity.

As the ON histogram is filled, the number of events in the signal region,  $N_{\text{on}}$  is found. These events are the  $\gamma$ -ray candidates coming from the source, but some of them are hadronic events ( $\gamma$ -like), diffuse gamma rays or events with primary electrons/positrons. In order to estimate the number of background events in the signal region  $N_{\text{off}}$ , a second histogram called *OFF histogram* is filled with the events coming from the OFF regions and binned according to  $\theta^2$ , now calculated as the angular distance between the event arrival direction and the OFF region position. As described in Section 3.6.1, the OFF region depends on the wobble pointing and it is taken as the region symmetrically opposite to the wobble position (*symmetrical region*

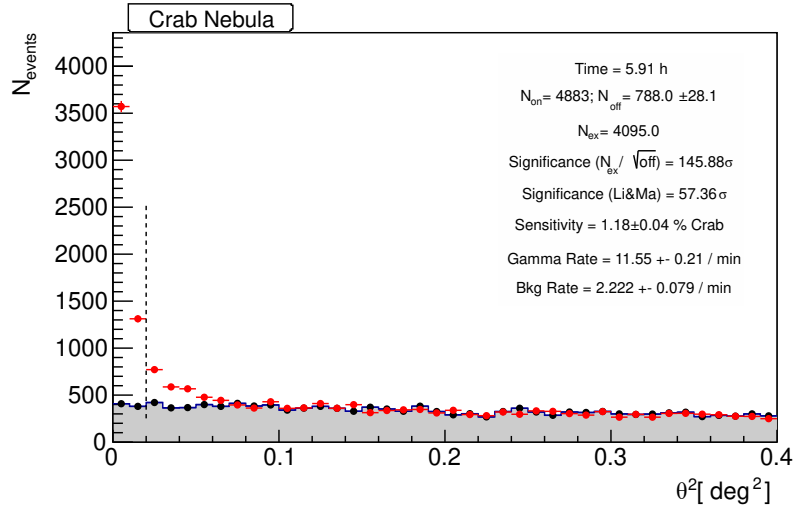


Figure 4.5: Example of a  $\theta^2$  plot obtained with Crab Nebula data. The red points belong to the ON histogram, the black one to the OFF histogram. The dashed line correspond to  $\theta_{\text{cut}}^2$ . This plot was produced using LE cuts.

background estimation). To improve the background estimation, more than one OFF regions are used (*multi-OFF* background estimation). Since each wobble pointing will have different OFF region, the ON and OFF histograms are created for each different wobble position and stacked. The ON and OFF histograms outside the signal region can have a mismatch, especially for quite strong sources. For this reason a *normalization region* is defined: if the integral in this region for anyone of the OFF histograms deviates more than one standard deviation from the one in the normalization region of the ON histogram, that OFF histogram will be renormalized. For very strong sources (e.g. Crab Nebula), the renormalization is skipped and one can see a contamination of events in the normalization region. After the total OFF histogram is created,  $N_{\text{off}}$  is determined as the sum of the events in the signal region in the OFF histogram. The resulting plot is usually called  $\theta^2$  plot and an example is shown in Figure 4.5.

The expected number of gamma-ray events, called “excess events”,  $N_{\text{ex}}$ , is calculated as:

$$N_{\text{ex}} = N_{\text{on}} - \tau \cdot N_{\text{off}} \quad (4.8)$$

where  $\tau$  is the ratio of OFF to ON exposure, that is the inverse of the number of OFF regions if the symmetrical region or multi-OFF background estimation methods are used.

The detection significance  $S$  can be finally computed with a statistical test, with a null hypothesis assuming that the expected signal is from background emission.  $S$  is given by the so called Li&Ma expression, from Li and Ma (1983):

$$S = \sqrt{2} \left\{ N_{\text{on}} \cdot \ln \left[ \left( \frac{1 + \tau}{\tau} \right) \left( \frac{N_{\text{on}}}{N_{\text{on}} + N_{\text{off}}} \right) \right] + \frac{N_{\text{off}}}{\tau} \cdot \ln \left[ (1 + \tau) \left( \frac{N_{\text{on}}}{\tau \cdot N_{\text{on}} + N_{\text{off}}} \right) \right] \right\}^{1/2} \quad (4.9)$$

As a convention, the detection of a source can be claimed if its significance level equal or surpasses  $S = 5\sigma$ .

## 4.10 Sensitivity

Besides signal significance, one can use the sensitivity, defined as the gamma-ray flux detected with a significance of  $5\sigma$  after 50 h of observation, to quantify the performance of an instrument. It can be used to make a fast comparison of the performance of different instruments.

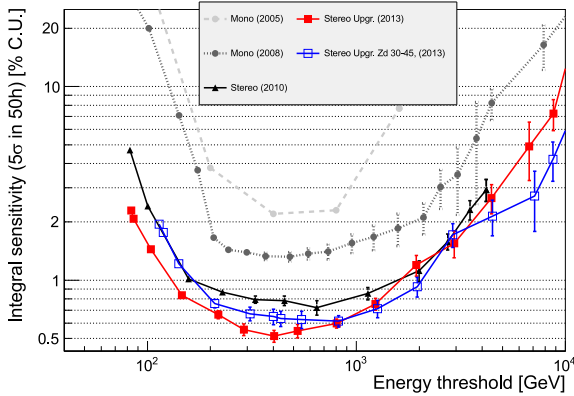


Figure 4.6.1

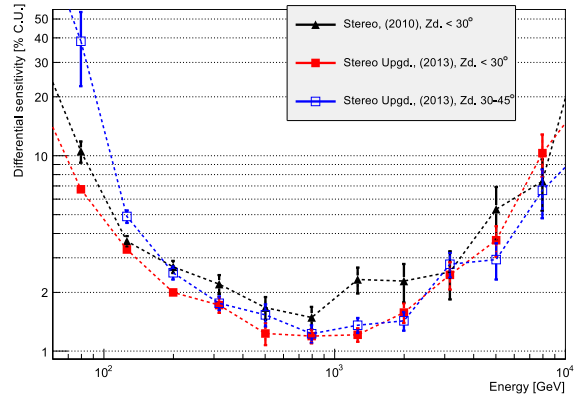


Figure 4.6.2

Figure 4.6: **Left**: integral sensitivity of the MAGIC telescopes as a function of the energy and for different periods. *Grey and dark grey dots*: mono era with Siegen and MUX readouts. *Black triangles*: stereo era with old MAGIC-I camera. *Red filled and blue empty squares*: stereo era after 2012-2013 upgrade at zenith lower than  $30^\circ$  and between  $30^\circ$  and  $45^\circ$  respectively. **Right**: differential sensitivity of the MAGIC telescopes as a function of energy and for different periods. The same colors and symbols are used as in the left figure with the same meaning. From Aleksić et al. (2016b).

Usually it is reported as a fraction of the Crab Nebula flux in a particular energy range, called Crab Unit (C.U.).

Under Gaussian approximation, the significance of an observation giving  $N_{\text{ex}}$  excess events and  $N_{\text{off}}$  background events can be calculated as  $N_{\text{ex}}/\sqrt{N_{\text{off}}}$ . The sensitivity will be the flux of a source giving a significance, computed with the previous formula, equal to 5 in 50 h of observation. According to (Aleksić et al. 2016b), the constraints  $N_{\text{ex}} > 10$  and  $N_{\text{ex}} > 0.05N_{\text{off}}$  make the sensitivity estimation more robust ensuring that the Gaussian approximation is valid and that no artifacts in the signal significance are created due to a large residual background.

Usually the sensitivity is calculated in two ways:

- *integral sensitivity*, global optimized cuts on hadronness and  $\theta^2$  above different energy thresholds are used for the sensitivity computation;
- *differential sensitivity*, cuts on hadronness and  $\theta^2$  are optimized in each energy bin, usually 5 bins per decade.

The optimization of the cuts is done on a Crab Nebula dataset. The integral sensitivity can be used only for sources with a Crab-like spectrum ( $-2.6$  spectral index), while the differential sensitivity is valid for sources with any spectral shape because the optimization is performed in narrow bins of energy so that the spectrum dependence can be neglected.

After the 2012 upgrade, the integral sensitivity is as low as 0.55% C.U. at few hundreds of GeV, while the pre-upgrade value was around 0.8% Crab Units (see Figure 4.6.1). For the differential sensitivity, in the lowest energy bin 60-100 GeV its value decreased from 10.5% to 6.7% C.U. and improved in all the energy range up to few TeV as shown in Figure 4.6.2 and Aleksić et al. (2016b). The good sensitivity at low energies is particularly important for transient sources, but of course the sensitivity is time-dependent. For short observation times the integral sensitivity follows a dependence  $\propto 1/t$  while saturates for long observation times at low energies.

## 4.11 Instrument Response Function

The response function of an IACT is governed by its hardware design, reconstruction algorithms, selection criteria for quality of the events and for discrimination between gamma-rays and hadrons. It is computed by means of full MC simulations and for each analysis separately, as it depends on the particular cuts applied to the data as well as on the overall technical settings and performance of the instrument at the time of the observations.

The three functions describing the IRF are the effective collection area, the angular resolution and the energy resolution. The former one is particularly important since it is used in the calculation of the spectrum and light curves.

### 4.11.1 Effective collection area

The effective area  $A_{\text{eff}}$  is the geometrical area around the telescope where a  $\gamma$ -ray shower produces a trigger,  $A_{\text{sim}}$ , folded with the gamma-ray efficiency  $\epsilon_\gamma$  of all the cuts applied in the analysis and the trigger. The efficiency  $\epsilon_\gamma$  depends on the spatial coordinates but also of gamma-ray energy, zenith angle and azimuth angle. In first approximation, an estimate of the effective area can be given recalling that in the light pool the Cherenkov light density is approximately constant, so that if the telescope is in the light pool then it is triggered by the event. Of course this is not true anymore if we have a low energy event with light density too low to trigger the telescope. Remembering that the light pool has a radius of  $\sim 120$  m, a rough estimate of the effective area is  $\sim 4 \cdot 10^4 \text{ m}^2$  at energies of hundreds of GeV.

As said before, the effective area depends on the gamma-ray energy and on the zenith angle. This can be intuitively understood looking at showers coming from different zenith angle. If the zenith angle is low, the light pool is smaller but the photon density is enough to get a trigger. This means that the energy threshold is lower but the effective area becomes smaller and smaller as energy decreases. If the zenith angle is high instead, the Cherenkov photons must travel a longer path in the atmosphere and absorption processes kill low energy events. In this case the light pool is larger but with a lower photon density compared to a shower with the same energy but a lower zenith angle. This results in an higher energy threshold and larger effective area at high energies (see Figure 4.7). Given the definition of the effective area, calculating it is pretty straightforward. Given  $N_{\gamma,\text{sim}}$  Monte Carlo simulated gamma-ray events on an area  $A_{\text{MC,total}}$  (defined as  $\pi r_{\text{max}}^2$ ,  $r_{\text{max}}$  being the maximum shower impact simulated) and the number  $N_{\gamma,\text{final}}$  of gamma-ray events surviving after the analysis cuts, the effective area is defined as:

$$A_{\text{eff}} = A_{\text{MC,total}} \cdot \frac{N_{\gamma,\text{final}}}{N_{\gamma,\text{total}}} \quad (4.10)$$

The area  $A_{\text{MC,total}}$  is chosen so that the probability that a gamma-ray beyond it could trigger the telescopes and remain after all analysis cuts is negligible: small simulation areas leads to an underestimation of  $A_{\text{eff}}$  while big areas can lead to waste of computing time with no visible effect on the final computation of the effective area.

Since the effective area depends on many parameters, it is calculated in bins of these parameters (energy, zenith and azimuth angle...). Regarding the dependence on the gamma-ray energy, the effective area is well defined in energy since in Monte Carlo simulation the initial energy of the events is known (and the energy spectrum as well). Unfortunately producing Monte Carlo events is very time consuming and so the number of simulated events is limited. This limited statistics forces to calculate the effective area in energy bins and get an average value in each bin. In this case the average effective area in the energy bin  $[E_1, E_2]$  can be calculated as:

$$\langle A_{\text{eff}} \rangle_{[E_1, E_2]} = A_{\text{MC,total}} \cdot \frac{N_{\gamma,\text{final}}(E_1, E_2)}{N_{\gamma,\text{total}}(E_1, E_2)} \quad (4.11)$$

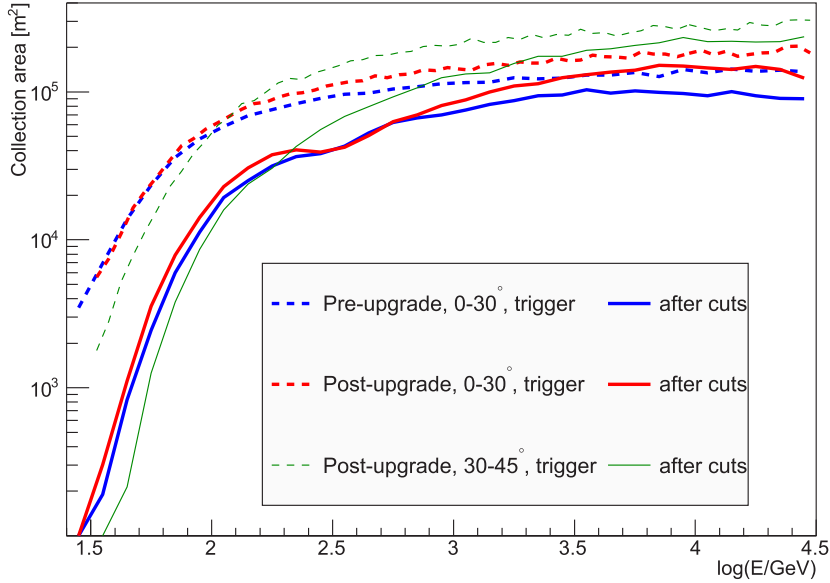


Figure 4.7: Effective collection area of MAGIC telescopes in two different zenith ranges (red lines  $0 - 30^\circ$ , green lines  $30^\circ - 45^\circ$ ) after the upgrade of MAGIC-I camera and use of DRS4 chips in both telescopes. Blue lines refer to the pre-upgrade period. Both trigger (dashed lines) and after-cuts (solid lines) effective areas are shown. Adapted from Aleksić et al. (2016b).

The value obtained from (4.11) depends on the spectrum with which the Monte Carlo events were produced and from the width of the bins. The best thing should be to produce the Monte Carlo events with the same spectrum of the observed source since this would guarantee to find the correct instrument response, but for time/computing reasons it can not be done. If one observed a source with spectrum  $d\Phi/dE$  and produced enough Monte Carlo data with the very same spectrum, (4.11) would become:

$$\langle A_{\text{eff}} \rangle_{[E_1, E_2]} = \frac{\int_{E_1}^{E_2} \frac{d\Phi}{dE} A_{\text{eff}}(E) dE}{\int_{E_1}^{E_2} \frac{d\Phi}{dE} dE} \quad (4.12)$$

It is clear that the spectrum of the source is not always known in advance (let us think for example about a source which has a rather stable flux and known spectrum in the gamma-ray band and suddenly has a flare), so for the effective area calculation a tentative spectrum is needed and the result will be more or less accurate depending on the difference between real and tentative spectrum. In reality this cannot be done, so the averaging of the effective area in a given energy bin is done with energy-dependent weights on  $A_{\text{eff}}(E)$  in narrow bins.

The same procedure must be applied when we want to average the effective area in zenith bins. In this case:

$$\langle A_{\text{eff}} \rangle_{[ZD_1, ZD_2]} = \int_{ZD_1}^{ZD_2} f(ZD) A_{\text{eff}}(ZD) d(ZD) \quad (4.13)$$

where  $f(ZD)$  is the observation time fraction the telescope pointed at zenith  $ZD$ .

Finally geomagnetic field effects and the change in the relative distance between the telescopes introduce a dependence of the effective area on the azimuthal angle, especially at medium and large zenith.

As explained in Section 2.3.2, the geomagnetic field causes the positrons and electrons to move in opposite directions, resulting in an elongation of the light pool in the E-W direction and lowering the peak density. This has a direct effect on the value of the effective area.

The relative telescope position introduces an azimuthal asymmetry as well. When MAGIC had only the MAGIC-I telescope, the azimuthal dependence of the effective area was caused only by the geomagnetic field. Adding a second telescope led to a different overlap of the two FoVs depending on their relative position and consequently to a different effective area. Moreover, most (if not all) MAGIC observations are done in the so called Wobble mode, where the source has an offset (usually  $0.4^\circ$ ) from the camera center and rotates around it during the tracking. So using standard MC in which the source is simulated to be in the camera center as in ON observations would lead to a wrong estimate of the effective area. The problem is solved by using *ring wobble MC*, that is gamma-rays are simulated with directions along a cone with semi-aperture angle equal to  $0.4^\circ$  (the normal offset used in Wobble observations) and axis along the telescopes' pointing direction. This kind of MC data works only for point sources, but for extended sources or sources observed with a different offset diffuse MC data, generated in a disk of radius  $1.5^\circ$  with constant density of events per square degree, are available and can be selected according to the data with `selectmc`, one of the programs included in the MARS package. In this way the analyzer can obtain a good estimate of the effective area and all the quantities depending on it, namely flux and spectrum.

Averaging of effective area also in bins of azimuthal angle is not done by default in MARS, but must be turned on by the analyzer case by case. The reason for that is the loss of MC data since only Monte Carlo data with the same azimuthal angle as the one of the observed source will be used in the computation. This can introduce greater statistical fluctuations in the final value of the effective area.

Another problem arises when we want to use the effective area in the calculation of fluxes and spectral points. As described in Section 4.12.2, the calculation of these quantities need the knowledge of the number of excess events in bins of estimated energy, because we do not know the true energy of our events. The effective area instead is known in bins of true energy of the Monte Carlo data. Using these two quantities, one binned in estimated energy and the other in true energy, causes the so-called *spillover* or *migration* of events: given an energy bin  $E_1 < E_{\text{true}} < E_2$  and events contained in such bin, not all of them will be contained in the bin  $E_1 < E_{\text{est}} < E_2$  but will fall outside. If this effect is not taken into account, it leads to a wrong estimation of the flux and consequently of the spectrum and light curve.

For this reason one needs an *unfolding* method to correct for the spillover of the events. The most simple method, called *poor's man unfolding*, use a modified definition of the collection area in which the number of events surviving the analysis cuts is given in bins of estimated energy instead of the true one:

$$\langle A'_{\text{eff}} \rangle_{E_1 < E < E_2} = A_{\text{MC, total}} \cdot \frac{N_{\gamma, \text{final}}(E_1 < E_{\text{est}} < E_2)}{N_{\gamma, \text{total}}(E_1 < E_{\text{true}} < E_2)} \quad (4.14)$$

This definition depend on the assumed spectral shape of the source and gives better results if it is close to the real one. In any case, an iterative procedure can be used to get the source spectrum and usually it converges quickly (one or two iterations). The assumed spectrum is needed to get an average value of the spillover in the energy bins and find correction factors used in the spectrum calculation.

#### 4.11.2 Angular resolution

The angular resolution describes the capability of the instrument to reconstruct the gamma-ray incident direction. Two definitions can be used:

1. standard deviation of the 2-dimensional Gaussian function fitting the distribution of the reconstructed arrival direction of the gamma-ray excesses, denoted as  $\Theta_{\text{gauss}}$ ;

2. angular distance from the source position enclosing 68% of the excess events, denoted as  $\Theta_{68}$ .

In general the values obtained by the two methods are different and usually  $\Theta_{\text{gauss}} < \Theta_{68}$ . The angular resolution is energy-dependent: showers corresponding to high-energy events are better reconstructed, so the angular resolution improves. Taking as a reference  $\Theta_{\text{gauss}}$ , at low energies ( $\sim 100$  GeV) the angular resolution is about  $0.1^\circ$ , while it improves down to  $0.04^\circ$  starting from TeV energies, as shown in Figure 4.8.1 and in Aleksić et al. (2016b).

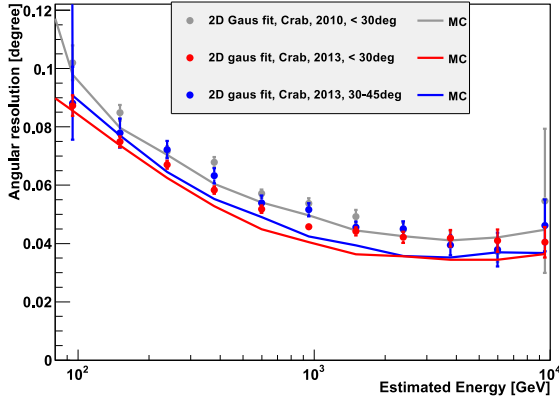


Figure 4.8.1

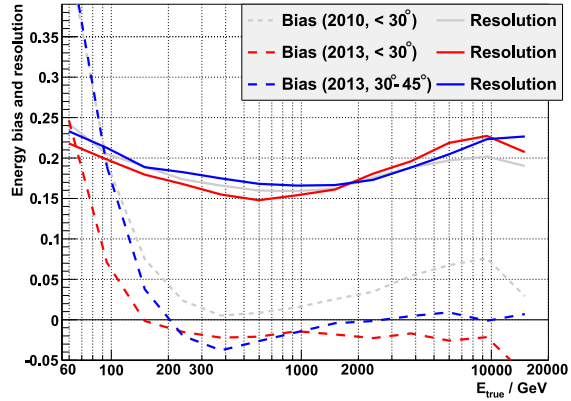


Figure 4.8.2

Figure 4.8: **Left:** angular resolution of the MAGIC telescopes as a 2D Gaussian fit, obtained for a Crab Nebula data sample (filled dots) and from MC simulations (solid lines). *Red, blue, grey points:* low zenith ( $<30^\circ$ ), medium zenith ( $30^\circ$ - $45^\circ$ ) and low zenith angle before 2012-2013 upgrade. **Right:** energy bias (dashed lines) and resolution (solid lines) after reconstruction, obtained from MC simulations. The same colors and symbols are used as in the left figure with the same meaning. From Aleksić et al. (2016b).

### 4.11.3 Energy resolution

The energy resolution is defined as the standard deviation of a Gaussian fit to the peak of the  $(E_{\text{est}} - E_{\text{true}})/E_{\text{true}}$  distribution. This value provides an estimation of the goodness of the energy reconstruction for the bulk of events excluding all the outliers. The difference from zero of the peak of the  $(E_{\text{est}} - E_{\text{true}})/E_{\text{true}}$  distribution gives the mean *energy bias*.

For stereo analysis, the energy resolution is as good as 15% for a low zenith sample between few hundreds of GeV and 1 TeV. At low and high energies it degrades at  $\sim 20\%$  due to the worse reconstruction of image parameters and truncated images respectively, see Aleksić et al. (2016b).

The energy bias is less than 5% for low zenith observations above few hundreds GeV while at low energies it increases up to 20% due to threshold effects.

Figure 4.8.2 shows both the energy bias and resolution as a function of the true energy.

### 4.11.4 Energy threshold

The energy threshold of an observation is defined as the peak energy of the distribution in energy of simulated MC data for a source with a power law spectrum with  $-2.6$  spectral index, see Aleksić et al. (2016b). Usually the peak is fitted with a Gaussian function. The energy threshold depends on the trigger used and its settings and on the zenith of the observation. It can be evaluated at different analysis stages:

- at trigger level no cuts are applied, all MC events triggering are used: the energy threshold is around 50 GeV

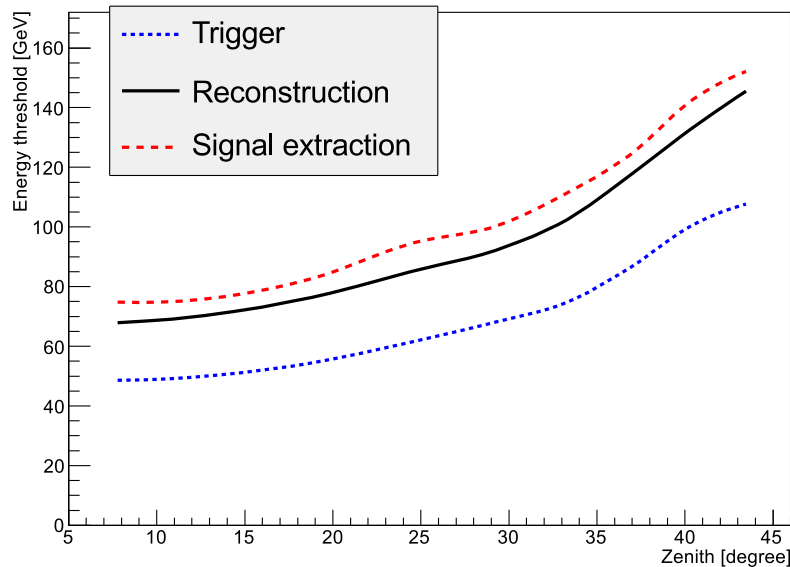


Figure 4.9: Energy threshold at different analysis stages: trigger level (blue dotted line), reconstruction level (after image cleaning and with  $size > 50$  phe, black solid line) and signal extraction level (hadronness  $< 0.5$  and  $\theta^2 < 0.03^{\circ 2}$  (red dashed line). From Aleksić et al. (2016b).

- after the reconstruction and applying a cut  $size > 50$  phe: the energy threshold rises to about 70 GeV (75 GeV if hadronness and  $\theta^2$  cuts are included)

In the zenith range  $0^\circ - 45^\circ$  the energy threshold can be described as a function of the zenith angle  $zd$  by the formula:

$$E_{\text{thr}}(zd) = 74 \times \cos(zd)^{-2.3} \text{GeV} \quad (4.15)$$

so that  $E_{\text{thr}}$  doubles at  $\sim 40^\circ$ , as shown in Figure 4.9. Having a low energy threshold is especially important for distant sources, for which a strong absorption by the EBL is expected. This is true for AGNs but mainly for GRBs, which are detected at high redshift, so a low energy threshold allows to operate in an energy range unaffected by absorption effects.

## 4.12 High-level analysis

After the data are selected with optimized cuts, one can generate higher level results: sky maps, light curves, integral and differential spectra (in case of signal detection) or upper limits (in case of no detection). These results depends widely on the *instrument response function* (IRF) of the MAGIC telescopes, see Section 4.11.

### 4.12.1 Skymaps

Sky map refers to a 2-dimensional histogram that contains arrival directions, in sky coordinates, of all gamma-ray events that remain after the analysis cuts and after the subtraction of the expected background. In MARS, the executable `caspar` is responsible of creating skymaps starting from `melibea` data.

The skymap creation is divided in two steps: estimation of the camera exposure model and sampling of the background event distribution from that model. The camera exposure model can be created in two ways: *blind map*, without assuming the position of the source, and *wobble map*, assuming the source to be where expected. In both ways the non homogeneity

of the camera acceptance is taken into account by dividing the data in hour angle bins. From the exposure model, the OFF background map is created, while the events in the data are used for the ON map.

Both the histograms are smoothed by the PSF ( $\sigma_{\text{PSF}}$ ) and by a Gaussian Kernel ( $\sigma_{\text{smear}}$ ) added in quadrature, whose value depends on the purpose of the skymap (e.g. discovering a source or studying the morphology). Usually the smearing Gaussian kernel has the same value as the PSF, so that the total smearing is  $\sqrt{2}\sigma_{\text{PSF}}$ .

`caspar` creates several skymaps: the ON, OFF and ON-minus-OFF map, the relative flux map and its fit. Probably the most important is the significance map, computed with the Test Statistics (TS) significance, defined as the Li&Ma significance applied on a smoothed and modeled background model. The null hypothesis generally has a Gaussian-like form but can have a different shape.

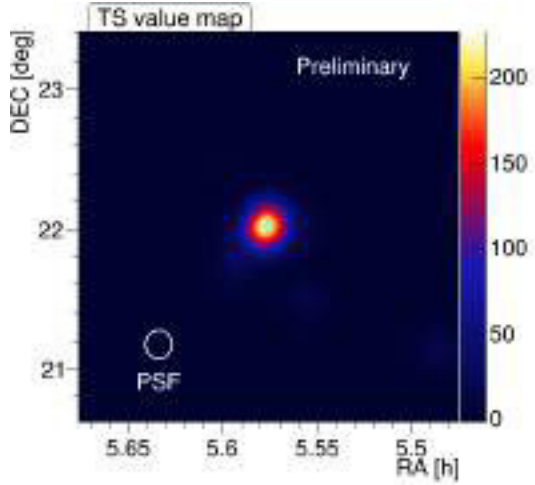


Figure 4.10: Example of a skymap created with `caspar` from Crab Nebula data.

#### 4.12.2 Spectrum and light curve

The differential gamma-ray spectrum is defined as the total number of photons coming from the source and reaching the observer, in unit of energy, area and time:

$$\frac{d\Phi}{dE} = \frac{dN_{\gamma}(E)}{dt_{\text{eff}}dA_{\text{eff}}(E)dE} \quad (4.16)$$

where  $N_{\gamma}$  is the total number of gamma-rays from the source at energy  $E$ ,  $t_{\text{eff}}$  is the effective observation time, and  $A_{\text{eff}}$  is the effective area of the instrument. The calculations of these quantities is performed by the executable `flute`, which takes as inputs the ON and MC data in `melibe` format. The former are used for the computation of  $N_{\gamma}$  and  $t_{\text{eff}}$ , while the latter is used for  $A_{\text{eff}}$  estimation.

The effective time is corrected for the dead time of the readout system electronics and for possible gaps between events or data runs, so that the effective observation time does not coincide with the real elapsed observation time. Assuming a Poissonian statistics for the arrival time of the events, it can be shown that the time difference between the arrival time of one event and the next is an exponential. The expression of the probability that the next event comes after a time  $t$  as a function of time is:

$$\frac{dP(t_{\text{next}} = t)}{dt} = \lambda e^{-\lambda t} \quad (4.17)$$

where  $\lambda$  is the true rate of events. The distribution of the time differences between triggered events as a function of time will simply be:

$$\frac{dN}{dt} = N_0 \lambda e^{-\lambda t} \quad (4.18)$$

with  $N_0$  the total number of triggered events. By fitting this distribution, obtained from the data itself, the value of  $\lambda$  can be found and finally the effective time is estimated as:

$$t_{\text{eff}} = t_{\text{elapsed}} / (1 + \lambda \cdot d) \quad (4.19)$$

where  $t_{\text{elapsed}}$  is the time elapsed during the observation and  $d$  is the dead time of the electronics (26  $\mu\text{s}$  with DRS4 digitization electronics). The effective time calculation is reliable if  $\lambda$  is constant, which is true only for relatively short periods of time. In `flute`, the calculation of  $\lambda$  is done every 2 min to ensure a robust estimation of the effective time.

The number of gamma rays in the energy range  $E$  is estimated as the number of excess events in that energy range. The calculation is quite similar to the one performed by `odie`. One difference is that the cuts on hadronness and  $\theta^2$  are optimized for each energy range according to a predefined efficiency: MC data are binned in energy and in hadronness. For each energy bin, the optimal cut is the one where the number of events is above the efficiency. The same is done for  $\theta^2$ . In general, the cuts found with this method are looser than the one found in `odie` since we are not searching for a signal. Another option is to have cuts fixed by the user in each energy range. Moreover, in `flute` another background method is available, called *off-from-wobble partner*. The idea is that for the wobble pointing W1, for example, the proper OFF region should be taken from the other pointings W2, W3, . . . , in which at least one of the OFF regions follows the same path as the source in W1. The same is applied to the other wobble pointings.

The effective collection area calculation was already described in detail in Section 4.11.1.

Once  $N_\gamma$ ,  $t_{\text{eff}}$  and  $A_{\text{eff}}$  are computed in each energy bin, the differential energy spectrum in the energy range  $[E_1, E_2]$  is:

$$\frac{d\Phi}{dE}(E_{\text{LW}}) = \frac{N_{\gamma, E_1 < E < E_2}}{(E_2 - E_1)t_{\text{eff}}\langle A_{\text{eff}} \rangle_{E_1 < E < E_2}} \quad (4.20)$$

where  $E_{\text{LW}}$  is the energy value where the spectral point will be put, according to Lafferty and Wyatt (1995).

Once the differential energy spectrum is computed, the creation of the lightcurve is trivial. Usually the light curve is defined as the integral flux above an energy  $E_0$  in a certain time bin, so that:

$$\Phi_{E > E_0} = \int_{E_0}^{\infty} \frac{d\Phi}{dE} dE = \frac{N_{\gamma, E > E_0}}{t_{\text{eff}}\langle A_{\text{eff}} \rangle_{E > E_0}} \quad (4.21)$$

### 4.12.3 Spectral unfolding

When computing the number of excesses in the energy bins, since these events are from the data and not MC data, we only know their estimated energy  $E_{\text{est}}$ . As discussed in Section 4.11.3, the energy estimation has a certain resolution around 15% in the few hundreds GeV energy range. The effective area instead is computed in bins of the true energy  $E_{\text{true}}$  of the events, which is known *a priori*. When computing the differential spectrum, the number of excesses in bins of estimated energy is divided by the effective area in bins of true energy. As already mentioned in Section 4.11.1, a spillover of events emerges. To correct for this effects and others deriving from the non-perfection of the detector (limited acceptance, limited energy resolution, detection efficiency and so on), from the statistical analysis (binning of the variables) or systematic distortion (threshold effects), an *unfolding* procedure is needed to obtain a spectrum as a function of the true energy.

The starting point of the unfolding is the *Fredholm equation*:

$$g(y) = \int M(x, y)f(x)dx + b(y) \quad (4.22)$$

$g(y)$  is the distribution of the measured observable ( $E_{\text{est}}$ ),  $M(x, y)$  is the migration matrix (or response function) calculated from MC data,  $f(x)$  is the distribution of the sought observable ( $E_{\text{true}}$ ) and  $b(y)$  is the distribution of the background.

Equation (4.22) can be written in discretized/matrix form:

$$g_i = \sum_j M_{ij}f_j + b_i \Rightarrow \mathbf{g} = \mathbf{M} \cdot \mathbf{f} + \mathbf{b} \quad (4.23)$$

$M_{ij}$  indicates the probability that an event with true energy in bin  $j$  is measured in bin  $i$  of estimated energy due to the response of the detector. Generally  $\mathbf{M}$  is not a squared matrix, because the binning in  $E_{\text{est}}$  might be different from the one in  $E_{\text{true}}$ .

The simplest approach to solve equation (4.23) is to invert the migration matrix. If one restricts to the case  $\mathbf{b} = \mathbf{0}$  (solutions for  $\mathbf{b} \neq \mathbf{0}$  are similar), the solution would read:

$$\mathbf{f} = \mathbf{M}^{-1} \cdot \mathbf{g} \quad (4.24)$$

This equation is equal to a system of equations which can have one, infinite or no solutions. For this reason, usually minimization techniques are used, as the least squares expression:

$$\chi_0^2 = (\mathbf{g} - \mathbf{M} \cdot \mathbf{f})^T \cdot V[\mathbf{g}] \cdot (\mathbf{g} - \mathbf{M} \cdot \mathbf{f}) \quad (4.25)$$

The limitation of the least square method is its validity for Gaussian distributions only, which is not the case for bins with few events. To account for the possible Poissonian distribution, a likelihood expression can be used. Both methods can give strong fluctuations in the found solution, where small contributions in the migration matrix gets amplified in the unfolding process and produce unwanted noise in the result. For this reason usually a *regularization* is performed, adding a regularization term to equation (4.25):

$$\chi^2 = \frac{\omega}{2} \chi_0^2 + \text{Reg}(\mathbf{f}) \quad (4.26)$$

$\omega$  is a weight applied to  $\chi_0^2$  while  $\text{Reg}(\mathbf{f})$  is the regularization term. A small value for  $\omega$  results in a strong regularization, so that fluctuations in the solution are kept as low as possible. Too small values should be avoided, because otherwise the resulting distribution would deviate too much from the data. In MAGIC analysis, different regularization choices can be applied to the data, called Tikhonov, Schmelling and Bertero methods (Tikhonov and Arsenin 1977; Schmelling 1994; Bertero 1989).

A simpler solution to the unfolding problem is the *forward unfolding*: the distribution  $\mathbf{f}$  is assumed to be a function  $f(x, \mathbf{a})$  with parameters  $\mathbf{a} = (a_1, \dots, a_n)$ . This makes the forward unfolding dependent from the assumed model. The solution is found by minimizing  $\chi_0^2$  without any regularization:  $f(x)$  will be a smooth function (it is defined as a continuous function).

Usually the forward unfolding can be used as a cross-check or to compare two different spectral models. In MAGIC, the spectral parameters are computed with the forward unfolding, while spectral points are obtained with one of the unfolding methods with regularization (they should give consistent results).

#### 4.12.4 Upper limits

In `flute`, if in any of the energy bins there are not enough excess events, an upper limit will be calculated. This happens when a spectral point has a relative error on the estimated flux greater than 0.5. The upper limits calculated by `flute` are both differential (one for energy bin) and integral (above a certain energy).

The starting point of the flux upper limit calculation is the upper limit on the number of excesses. It relies on the likelihood machinery and on the computation of confidence intervals. The complication in this particular case is the presence of nuisance parameters, so that the application of methods like the *likelihood ratio test* (LRT) is not straightforward. Despite this, one can construct the so called *profile likelihood*. Assuming a set of parameters to be measured  $\theta = (\theta_1, \dots, \theta_k)$ , a set of nuisance parameters  $\nu = (\nu_1, \dots, \nu_l)$  and a data set  $\mathbf{X} = (X_1, \dots, X_n)$ , the likelihood reads:

$$\mathcal{L}(\theta, \nu | \mathbf{X}) = \prod_{i=1}^n f(X_i | \theta, \nu) \quad (4.27)$$

where  $f(X_i|\theta, \nu)$  is the probability distribution function for the measurement  $X_i$ . The profile likelihood is defined starting from equation 4.27 as:

$$\mathcal{L}(\theta, \nu''(\theta)|\mathbf{X}) \quad (4.28)$$

$\nu''(\theta)$  maximizes  $\mathcal{L}$  for a given value of  $\theta$ . As before, we can use the *profile likelihood ratio test*:

$$\lambda_P(\theta; \mathbf{X}) = \frac{\mathcal{L}(\theta, \nu''(\theta)|\mathbf{X})}{\mathcal{L}(\theta', \nu'|\mathbf{X})} \quad (4.29)$$

where  $\theta'$  and  $\nu'$  maximize  $\mathcal{L}$ . The likelihood ratio test and Wilk's theorem tell us that  $-2 \ln \lambda_P(\theta; \mathbf{X})$  will behave as a Chi-square distribution with  $n$  degrees of freedom. The confidence interval at the  $100(1-\alpha)\%$  confidence level (CL) can then be found by computing the  $\alpha$  percentiles of the Chi-square distribution with  $n$  degrees of freedom.

In MAGIC, the likelihood used in upper limits calculation is the following:

$$\mathcal{L}(g, b, \varepsilon; N_{\text{on}}, N_{\text{off}}) = \frac{(\varepsilon g + b)^{N_{\text{on}}}}{N_{\text{on}}!} e^{-(\varepsilon g + b)} \cdot \frac{(\tau b)^{N_{\text{off}}}}{N_{\text{off}}!} e^{-(\tau b)} \cdot \frac{1}{\sqrt{2\pi}\sigma_\varepsilon} e^{-\frac{1}{2}\left(\frac{\varepsilon - \varepsilon_0}{\sigma_\varepsilon}\right)^2} \quad (4.30)$$

The parameters appearing in (4.30) are the following:

- $N_{\text{on}}$  and  $N_{\text{off}}$  are the measured number of events in the ON and OFF region respectively;
- $\tau$  is the ratio between OFF and ON exposure, which is assumed to be known exactly;
- $g$  is the estimated gamma-ray signal events in the ON region;
- $b$  is the estimated number of background events in the OFF region;
- $\varepsilon$  is the efficiency of the detector, whose distribution is assumed to be a Gaussian with mean  $\varepsilon_0 = 1$  and  $\sigma_\varepsilon = 0.3$ .

The first two factors of (4.30) are the same that would be found in the ideal case (dropping the  $\varepsilon$  factors) with a 100% efficient system. The last factor takes into account a 30% of global systematic uncertainty in the detection efficiency of gamma rays after applying the analysis cuts. It should be noted that the probability distribution functions for the background and for the efficiency can be different from a Poissonian or a Gaussian. In MARS, other PDF can be chosen, like the binomial and the Dirac-delta distributions. In general, for the background PDF, a Gaussian or a Poissonian distribution is chosen if  $N_{\text{OFF}}$  is greater or lower than 10 events respectively.

Given the likelihood function defined by (4.30), the profile likelihood ratio test can be applied considering  $b$  and  $\varepsilon$  as nuisance parameters, so that the only parameter to be estimated will be  $g$ . The resulting function is  $\lambda_P(g; N_{\text{on}}, N_{\text{off}})$ .

Starting from the value  $g'$  which minimizes  $-2 \ln \lambda_P$ , the confidence interval at the  $100(1-\alpha)\%$  CL is denoted  $[g_{\text{low}}, g_{\text{up}}]$ . At the edges of this confidence interval, the function  $-2 \ln \lambda_P$  increases of the  $\alpha$  percentile of a Chi-square distribution with one degree of freedom (only  $g$  is estimated). The default CL level in the computation of upper limits is 95%.

The problem that could arise in this kind of statistical computation is that  $g'$  could be negative or that part of confidence interval falls into the negative region of  $g$  values. While statistically this is totally acceptable, physically we expect that both  $g'$  and the confidence interval comprise non-negative values. This "regularization" can be performed in many ways: in MARS the Rolke method is used, described in Rolke, López, and Conrad (2005).

The Rolke method treats the cases where  $g'$  is small or negative in different ways:

- if  $g' > 0$  but small,  $-2 \ln \lambda_P$  probably cannot increase enough in the region  $g \geq 0$ , so that  $g_{\text{low}}$  could be negative. To avoid this,  $g_{\text{low}}$  is set to 0 and  $g_{\text{up}}$  is computed as usual

- if  $g' < 0$  and  $g_{\text{up}} < 0$  two methods are available:
  1. *unbounded likelihood method*:  $b$ ,  $\varepsilon$  and  $\tau$  are kept fixed and  $N_{\text{on}}$  is increased by one until  $g'$  is positive
  2. *bounded likelihood method*: the increase of  $-2 \ln \lambda_P$  is calculated starting from the point  $g = 0$ . It is the default one in MARS.
- if  $g < 0$  and  $g_{\text{up}} > 0$ ,  $g_{\text{low}}$  is set to 0 and  $g_{\text{up}}$  is computed as usual.

Special care should be taken in the cases  $N_{\text{on}} = 0$  and/or  $N_{\text{off}} = 0$ . Since the logarithm of the likelihood does not have any minimum in this situation, the solution is extrapolated from the cases  $N_{\text{on}} = 1, 2$  and/or  $N_{\text{off}} = 1, 2$ .

Despite the Rolke method is an ad-hoc solution to obtain physical confidence intervals, its use is justified by its good coverage: if the experiment is repeated many times, the resulting confidence interval would cover the true parameter value at least  $100(1 - \alpha)\%$  of the time. For more details, see Rolke, López, and Conrad (2005).

Once  $N_{\text{UL}}$  is computed with the Rolke method, an upper limit to the integral flux can be found. An assumption on the spectrum is needed:

$$\Phi(E) = K \cdot S(E) = K \cdot \left(\frac{E}{E_0}\right)^{-\Gamma} \quad (4.31)$$

The integral flux above the energy  $E_{\text{min}}$  can be determined as:

$$K \int_{E_{\text{min}}}^{\infty} \left(\frac{E}{E_0}\right)^{-\Gamma} = \frac{N_{\text{UL}}(E_{\text{est}} > E_{\text{min}})}{\int_{E_0}^{\infty} \int_0^{t_{\text{obs}}} A_{\text{eff}}(E, E_{\text{est}} > E_{\text{min}}) dE dt} \quad (4.32)$$

The upper limit on the normalization  $K^{\text{UL}}$  is ultimately given by:

$$K^{\text{UL}} = \frac{N_{\text{UL}}(E_{\text{est}} > E_{\text{min}})}{t_{\text{obs}} \cdot \int_{E_{\text{min}}}^{\infty} S(E) A_{\text{eff}}(E, E_{\text{est}} > E_{\text{min}}) dE} \quad (4.33)$$

For the integral flux upper limit above the energy  $E_{\text{min}}$ , we integrate equation (4.31):

$$\Phi(E > E_{\text{min}}) = K \int_{E_{\text{min}}}^{\infty} S(E) dE \quad (4.34)$$

We substitute the value of  $K^{\text{UL}}$  given by (4.33) into (4.34) to obtain the integral flux upper limit above energy  $E_{\text{min}}$ :

$$\Phi^{\text{UL}}(E > E_{\text{min}}) = \frac{N_{\text{UL}}(E_{\text{est}} > E_{\text{min}}) \int_{E_{\text{min}}}^{\infty} S(E) dE}{t_{\text{obs}} \cdot \int_{E_{\text{min}}}^{\infty} S(E) A_{\text{eff}}(E, E_{\text{est}} > E_{\text{min}}) dE} \quad (4.35)$$

For the differential upper limits, we know that at the energy  $E^*$  the differential flux is given by:

$$\frac{d\Phi(E^*)}{dE} = K \cdot S(E^*) \quad (4.36)$$

Using again (4.33) in the range  $E_{\text{min}} < E' < E_{\text{max}}$  we have:

$$\frac{d\Phi^{\text{UL}}(E^*)}{dE} = \frac{N_{\text{UL}}(E_{\text{min}} < E' < E_{\text{max}}) S(E^*)}{t_{\text{obs}} \cdot \int_{E_{\text{min}}}^{\infty} S(E) A_{\text{eff}}(E, E_{\text{min}} < E' < E_{\text{max}}) dE} \quad (4.37)$$

The energy bin  $[E_{\text{min}}, < E_{\text{max}}]$  should be narrow in order not to have effects from the assumed spectral shape (especially if a steep spectrum is used), but wide enough to have enough events. The energy  $E^*$  is chosen as done in `flute`, see Section 4.12.2 and Lafferty and Wyatt (1995).

### 4.13 Systematics in MAGIC data analysis

As every instrumental apparatus, MAGIC has systematic uncertainties stemming from the IACT technique. There are many factors which contribute to the total systematics, most of them not constant throughout a single night or with night-to-night variations. The sources of systematics are several: the atmosphere, the approximations used in the MC simulations, the PMT response and aging, PMT to PMT differences, mirrors reflectivity and inhomogeneities in the cameras are some of the causes of systematics in the IACT technique.

Here I summarize the systematic uncertainties for the MAGIC telescopes due to different factors, as shown in (Aleksić et al. 2016b; Aleksić et al. 2012).

**Background subtraction** The distribution of events in the camera is not homogeneous due to PMT to PMT differences, stars in the FoV and generic NSB variations. To estimate how much this affects the estimation of the background, the number of background events in two reflected regions in the sky without any gamma-ray signal was estimated. The difference between the number of estimated events is  $\lesssim 1\%$ , which is then the level of accuracy at which the background is known. The background uncertainty has a direct effect on the flux normalization and spectral index depending on the signal to the signal to noise ratio: for strong sources the systematic uncertainty is few percent and roughly 20% for a high and low signal to background ratio respectively for both the flux normalization and spectral index.

**Pointing position systematics** The pointing accuracy of MAGIC is modified by the fact that the structure of the telescopes is not fixed but can be deformed by the gravitational load e.g. when the camera sags due to its own weight. The AMC and the starguider camera correct for most of this effect, but some residual mispointing can be there spoiling the accuracy of the determination of the sources position. From Crab Nebula data taken during several nights, the mispointing between the nominal position of the source in the camera and the reconstructed position was evaluated, resulting in a systematic uncertainty  $\lesssim 0.02^\circ$ .

**Energy scale** A difficult parameter to be determined for IACTs is their light scale i.e. the amount of light generated by an event at a given energy. MAGIC-I and MAGIC-II have a slightly different light scale, with MAGIC-II having a response larger of about 11%. This difference is properly taken into account in the MC simulation in order to have a better agreement between real and simulated events. However this improves the relative size scale and not the light scale, which depends mostly on the atmospheric transmission, on the reflectivity of the mirrors and PMTs response. The miscalibration in the energy/light scale of the telescopes affects especially the spectrum reconstruction at low energies and near the threshold. They can lead to a lower collection area and so to a lower flux and to a migration of events to lower energies. A pile-up effect is expected below the energy threshold because of the fast decrease in the collection area.

To assess the effect of the energy scale, in Aleksić et al. (2016b) the energy threshold was changed in two ways, first by using data in different zenith ranges and then using a higher size cut. In both cases the light scale in MC simulations was shifted by -25%, -10%, -5%, +5%, +10%, +25% and the Crab Nebula spectrum was reconstructed to compare it with the historical Crab Nebula spectra. From this study the systematic uncertainty of the absolute energy scale is assessed to be below 15%.

**Flux normalization and slope** The previous effects affect the systematic uncertainty on the flux normalization and spectral index when reconstruction source spectra. To this the possible mismatch in cut efficiencies must be added, but for the flux normalization the

systematic uncertainty is kept below 12%. For the spectral index, as already mentioned, the systematic uncertainty is about 15% considering a source with at least 25% of signal to background ratio.

**Night to night variations** Due to night to night variations, the flux of a steady source measured in different nights will be slightly different. This depends mostly on the atmospheric conditions. Part of this systematic is kept under control using the LIDAR corrections, but a residual will still be there. Estimating the flux for different sub-samples from the same data set and trying to fit it with a constant, the relative systematic uncertainty is estimated to be around 11%.

## 4.14 Non-standard analyses

The imaging atmospheric technique is heavily affected by weather conditions, therefore the response of the instrument, its subsystems and the reconstruction of the events is modified. The MAGIC telescopes were designed and tuned to be at the top of their performance for observations during dark nights without Moon and good weather conditions, but such conditions are found in a relatively small amount of hours compared to the total number of hours available. The Moon of course will be present at different zenith and illumination phases increasing the background level and clouds, showing up at different altitudes above MAGIC, together with dust will change the atmospheric transmission. The resulting images and reconstruction of the events will be unavoidably affected. Despite this, ad-hoc analysis methods were developed inside the MAGIC collaboration to analyze data taken under specific observational conditions. This allows to increase the duty cycle of the telescopes and to obtain scientific results at the price of a slightly reduced performance and longer times for the analysis.

In this Section, three non-standard analyses will be briefly described:

- analysis of data taken under moonlight (Section 4.14.1), based on the results presented in Ahnen et al. (2017)
- analysis of data taken with low atmospheric transmission (Section 4.14.2), based on the work presented in Fruck (2015)
- analysis of data taken with the automatic repointing during GRB alerts (Section 4.14.3)

These three analysis methods were used in this thesis in the GRBs analysis, so a proper knowledge of the technicalities involved is fundamental.

### 4.14.1 Observations under moonlight

Being an IACT, MAGIC does not always observe sources in dark conditions, defined when a target is observed during astronomical night, with the Moon below the horizon and good weather without clouds and with low dust content. The night sky background level in these conditions can be referred as  $NSB_{\text{dark}}$ . Unfortunately, having the Moon in the sky is an unavoidable fact, leading to a different NSB level, of course higher than  $NSB_{\text{dark}}$ . In order to extend the duty cycle of the MAGIC telescopes, the hardware and the analysis techniques were adapted to cope with observations performed under moonlight.

The Moon affects both data taking and data analysis. Depending on the Moon zenith, phase, angular distance from the target, distance from the Earth and its position in the sky, the NSB level will be different. To assess its level, it is compared to  $NSB_{\text{dark}}$  and in particular to the DC in the two cameras pixels. A different level of background will change the DC, so that there is a direct correspondence between NSB and DC. Taking as a reference the median

DC in MAGIC-I and Crab Nebula observations performed in dark conditions, at low zenith and with nominal HV,  $\text{NSB}_{\text{dark}}$  corresponds to a median DC between 1.1 and 1.3  $\mu\text{A}$ . When the Moon is in the sky, the median DC value will be higher and from it the NSB level as a multiple of  $\text{NSB}_{\text{dark}}$  can be inferred.

In order not to damage PMTs and to have the best performance, the observations can be performed with nominal HV until the safety limits for the DC are reached (47  $\mu\text{A}$  for a single pixel and 15  $\mu\text{A}$  for the median), corresponding to a  $12 \times \text{NSB}_{\text{dark}}$ . MAGIC PMTs can be also operated at a lower voltage (about a factor 1.7) and consequently lower gain, so that the DC will be lower and  $20 \times \text{NSB}_{\text{dark}}$  levels can be reached. This operation mode is usually referred as *reduced HV* observation: targets cannot be observed if the Moon phase is above 90%. In order to increase the NSB level at which observations can be performed, UV-pass filters can be installed in the cameras and they allow observations up to  $50 \times \text{NSB}_{\text{dark}}$  ( $100 \times \text{NSB}_{\text{dark}}$ ) if nominal (reduced) HV are used.

The first effect of a higher NSB levels is higher accidental L0 rates, so that DTs are increased by the IPRC and consequently the energy threshold at trigger level will be higher. At the calibration level, the distribution of pedestal events is modified: the mean value shifts towards higher values (in phe) and the RMS increases with higher NSB level at fixed hardware conditions (nominal or reduced HV, UV filters). As far as real events are concerned, the NSB will affect especially weak signals, because the Cherenkov pulse can be lower than the noise fluctuations and so the reconstruction of the pulse time and amplitude will be not correct. For strong signals, the NSB will not induce a huge bias so that the time and amplitude estimation are almost left unmodified.

At the analysis level, the first difference with respect to the standard analysis described in the previous sections is at **star** level. The standard cleaning levels (6 phe and 3.5 phe) must be increased for moonlight analysis because noise fluctuations are higher. The new cleaning levels depend on the NSB and, according to Ahnen et al. (2017), are chosen so that less than 10% of the pedestal events survive the cleaning process.

The second major difference of moonlight analysis concerns Monte Carlo data: the standard MC produced have a NSB level for dark observations, so they are not suitable for data taken under moonlight, for which the background level is much higher than  $\text{NSB}_{\text{dark}}$ . All the data reconstruction in MAGIC analysis is based on the comparison with  $\gamma$  MC data, so the higher noise due to the NSB must be incorporated in MC data. As mentioned in Section 4.4, **star** can add noise to the data: once the mean and RMS of the pedestal distribution of real data taken under moonlight are known, they can be used in **star** to adapt the MC data to the noise level present during observations. Of course, the same cleaning values must be used for real and MC data. This process must be performed for both the test sample, used for RF, LUTs and DISP estimation, and for the test sample, used for the computation of the collection area. Also the OFF data sample used as input of **coach** should be chosen so that its NSB level is similar to the one of ON data.

Finally, after the reconstruction stage, a higher cut on the size parameter must be applied. The reason for this is that the simulations do not reproduce the trigger and IPRC behavior under moonlight, which are very difficult to take into account. The size cut depends on the NSB level and its value is chosen as the minimum one for match MC and ON data.

The values of pedestal distribution mean and RMS, cleaning levels and size cut according to the NSB level are reported in Table 2 of Ahnen et al. (2017), which I report here in Table 4.3 since one of the GRBs considered in my thesis was observed under moonlight and so a moon analysis was performed.

### Performance for moonlight observations

The analysis of data taken under moonlight has a different performance with respect to the standard analysis for dark night observations. This is due mainly to the higher background,

| Sky Brightness<br>( $\text{NSB}_{\text{dark}}$ ) | Hardware Settings | Pedestal Distr<br>mean/rms<br>[phe] | Cleaning Level factors<br>Lv11/Lv12<br>[phe] | Size Cut<br>[phe] |
|--|-------------------|-------------------------------------|--|-------------------|
| 1 (Dark)   | nominal HV        | 2.0 / 1.0                           | 6.0 / 3.5                                    | 50                |
| 1–2  | nominal HV        | 2.5 / 1.2                           | 6.0 / 3.5                                    | 60                |
| 2–3  | nominal HV        | 3.0 / 1.3                           | 7.0 / 4.5                                    | 80                |
| 3–5  | nominal HV        | 3.6 / 1.5                           | 8.0 / 5.0                                    | 110               |
| 5–8  | nominal HV        | 4.2 / 1.7                           | 9.0 / 5.5                                    | 150               |
| 5–8  | reduced HV        | 4.8 / 2.0                           | 11.0 / 7.0                                   | 135               |
| 8–12   | reduced HV        | 5.8 / 2.3                           | 13.0 / 8.0                                   | 170               |
| 12–18  | reduced HV        | 6.6 / 2.6                           | 14.0 / 9.0                                   | 220               |
| 8–15   | UV-pass filters   | 3.7 / 1.6                           | 8.0 / 5.0                                    | 100               |
| 15–30  | UV-pass filters   | 4.3 / 1.8                           | 9.0 / 5.5                                    | 135               |

Table 4.3: Pedestal distribution mean and RMS values, cleaning levels and size cuts for different brightness levels and hardware settings. These values are the “standard” values to be used in a moon analysis and were optimized on Crab Nebula data samples with different NSB levels. From Ahnen et al. (2017).

higher cleaning levels, higher size cuts, higher electronic noise (for reduced HV observations), possible mismatch between MC and data and different response of PMTs. All these variables will affect the performance parameters of the MAGIC telescopes and their effect was studied by Ahnen et al. (2017).

The first intuitive effect of the moon analysis is a higher energy threshold: higher cleaning levels and size cuts will remove the low energy events and will modify the distribution of the rates of  $\gamma$  MC events as a function of energy, whose peak shifts towards higher energies for higher background level. In the case of worst case scenario ( $15 - 30 \times \text{NSB}_{\text{dark}}$  with UV filters), the energy threshold for low (medium) zenith observation increases from  $\sim 70$  GeV ( $\sim 110$  GeV) to  $\sim 300$  GeV ( $\sim 500$  GeV), as shown in Figure 4.11.1.

Having higher cleanings and size cuts reduces also the collection area at low energies and the plateau is reached at higher energies for higher NSB levels. After 1 TeV, in all cases the collection area is flat and is reduced of a factor less than 10% for UV filters and background  $8 - 15 \times \text{NSB}_{\text{dark}}$ .

The tracking accuracy is unaffected by the moonlight and also the angular resolution is in agreement with the one measured in dark conditions for all the NSB and hardware settings shown in Table 4.3.

As far as the integral sensitivity is concerned, for nominal HV observations its degradation is constrained to be less than 10% up to 1 TeV, with a similar sensitivity up to 300 GeV and  $5 - 8 \times \text{NSB}_{\text{dark}}$ , as shown in Figure 4.11.2. For reduced HV and UV filters the degradation is higher, 15-30% and 60-80% respectively.

Finally, the different response of the subsystems can induce additional systematics to the measurement, in particular with reduced HV or UV filters. Comparing the daily light curves of the Crab Nebula with different NSB levels and hardware settings, the additional systematics on the flux is  $\sim 10\%$  and  $\sim 15\%$  for NSB lower than  $8 \times \text{NSB}_{\text{dark}}$  (nominal HV) and  $18 \times \text{NSB}_{\text{dark}}$  (reduced HV) respectively. This leads to a flux normalization uncertainty at hundreds of GeV of 15% and 19% respectively, and even higher (30%) for UV filters. The spectral index instead has a negligible additional systematic around 4%. Regarding the energy scale and pointing accuracy, the moonlight does not introduce additional systematics.

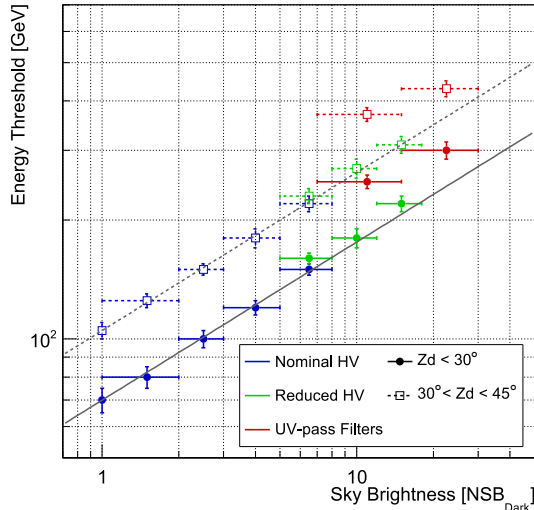


Figure 4.11.1

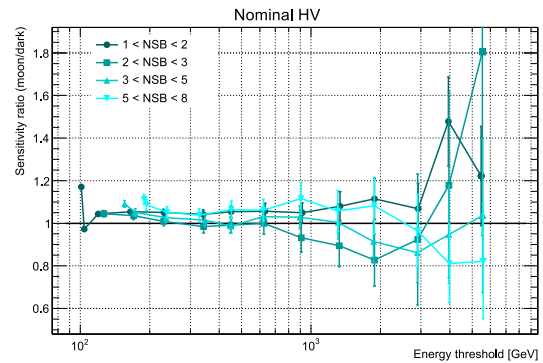


Figure 4.11.2

Figure 4.11: **Left:** energy threshold as a function of the sky brightness at the reconstruction level. *Filled dots:* low zenith ( $< 30^\circ$ ). *Empty squares:* medium zenith ( $30^\circ$ - $45^\circ$ ). *Blue, green, red:* hardware settings (nominal HV, reduced HV, UV filters respectively). **Right:** sensitivity of the MAGIC telescopes under moonlight with nominal HV as a ratio with the sensitivity for dark observations. From Ahnen et al. (2017).

#### 4.14.2 Bad atmospheric conditions

As mentioned in Section 3.5.3, the atmospheric transmission affects the event reconstruction, in particular the energy estimation, the effective area computation and its related quantities. Thanks to the LIDAR software, the atmospheric transmission is known during observation and its value can be used to correct data. Usually, the reference value used in the corrections is  $T_{9\text{km}}$ . A low atmospheric transmission will also degrade the shower parameters estimation, since the images will be modified. For this reason, using looser cuts on hadronness and  $\theta^2$  is necessary, as shown in Fruck (2015). The corrections to the events are applied at `flute` level, so the user should only provide a dataset with a high enough transmission using `quate` (usually  $T_{9\text{km}} > 0.6 - 0.65$ ) and data will be corrected.

#### 4.14.3 GRB analysis

Before 2013, the analysis of GRB data taken by MAGIC was quite non-standard. The main reason is that the observations were performed in ON mode instead of wobble mode, so a different analysis was required. After 2013, the GRB automatic procedure was modified so that GRB observations began to be carried out in wobble mode as any other source. This allows to use the standard MARS tools to perform the analysis. The particularity of the new automatic procedure is that the DAQ is not stopped while the telescopes are slewing from the position of the source that was observed to the GRB one. This means that events will trigger the telescope during the movement, but they will come from a direction different from the GRB one until the telescopes will reach the target sky position. For this reason, the data subrun taken during the slewing (I refer to it as *pre-GRB subrun*), still with the name of the source observed before the GRB, has to be treated in a different way with respect to the others subruns, which have the GRB name.

The pre-GRB subruns (one per telescope) must be downloaded as calibrated files and `star` must be run on them specifying the right ascension and declination of the GRB. In this way the position of the GRB in the camera is known. At `superstar` level, the two pre-GRB

subruns are processed to calculate the stereo parameters. As before, the sky position of the GRB must be specified so that the parameters,  $\theta^2$  in particular, are computed with respect to the correct source position in the camera. In some cases, the association of the images from the two telescopes to the same event is spoiled in the pre-GRB subruns. Usually the association is based on the L3 stereo number, but it can be reset during the slewing. In such a case, the temporal coincidence method, which compares the arrival times of the events in the two telescopes, can be used at a price of a reduced precision.

All the other subruns belonging to the GRB can be analyzed in the standard way. As the coordinates of the GRB can be refined by satellites after data have been analyzed, usually few hours after the trigger, and this position will be slightly different from the one pointed during MAGIC observation, the best coordinates can be specified in `odie`, `flute` and `caspar`. In this way  $\theta^2$  will be calculated with respect to the position specified and not to the one saved in the RunHeader of the data files. As soon as the two sky positions are not too different, no other steps are necessary. On the contrary, if they are not close, probably MC data with the right distance from the camera center should be used to compute correctly the effective area in `flute`.

---

## Chapter 5

# ASTROPHYSICAL TRANSIENTS

*Transients* are astrophysical events exhibiting short-time scale variability. Sources belonging to this class are Gamma-Ray Bursts, Active Galactic Nuclei, gamma-ray binaries, flaring sources, Gravitational Waves counterparts, very high energy neutrinos and many others. The challenge in the transient field is that most of the times it cannot be predicted when and where they will happen (e.g. GRBs). In the multi-wavelength and multi-messenger era of astrophysics it then becomes crucial to have a synergy between the observatories spread around the world and in space to detect these events and perform a follow-up as soon as possible. The scientific reward is guaranteed: one simple example is VHE neutrinos. A temporal and directional detection of a neutrino and an electromagnetic signal would reveal the sources emitting them. Moreover they trace back to the sites where hadronic interactions happens and so where Cosmic Rays are produced.

Among transient sources GRBs are probably the ones studied for the longest time and still many questions about their origin are without answer despite the huge collection of data at different wavelengths. Some mysteries about GRBs could be unveiled only thanks to the multi-messenger approach. In this regard, gravitational waves represent the most promising messenger in order to solve some GRB-related problems. Very recently the era of Gravitational Waves has begun thanks to the detection of four signals from black holes binary systems and the first one from a binary neutron star system. This new branch in astrophysics will give a better understanding of how general relativity works and of binary systems of compact objects.

This chapter is structured as follows: section 5.1 introduces and describes the GRB phenomenon, with special care to their high-energy emission. The analysis of several GRBs observed by MAGIC in the two years period 2013-2015 is then presented. Section 5.2 describes the development of an analysis tool to analyze the data collected from the follow-up of the gravitational wave event GW151226, with prospects for future follow-up campaigns.

## 5.1 Gamma-Ray Bursts

### 5.1.1 Introduction

Gamma-Ray Bursts (GRBs for short) are transient sources releasing a large amount of energy as high as  $10^{52}$  erg- $10^{53}$  erg in a very short time, from a fraction of a second to hundreds of seconds. This feature makes GRBs the most violent explosive events in the Universe. They happen suddenly and unpredictably with no repetition from random directions in the sky as flashes of hard-X and gamma-ray radiation. This first emission, called *prompt* phase, is non-thermal and usually ranges between 100 keV and 10 MeV. The prompt phase is then followed by the *afterglow*, a much fainter and fading emission observable in different bands of the electromagnetic spectrum, namely radio, optical, UV, infrared, X-rays and  $\gamma$ -rays. The fading timescale can be very different from burst to burst, ranging from hours to weeks or

even months. The observations of the afterglow emission can sometimes lead to the identification of their host galaxies and estimation of their distance through redshift measurement: this revealed the cosmological nature of GRBs. Regarding their origin, their variable light curves led to the conclusion that very compact objects like black holes and neutron stars are involved. Moreover, GRB outflows are highly relativistic.

GRBs are usually classified in two different classes according to their duration: those lasting less than 2s are called *short* GRBs, while those lasting more than 2s. It is thought that short GRBs originate from the mergers of compact objects, while some long GRBs were seen to be associated with supernovae collapses. The different nature of the progenitors reflects the observational features of the two classes.

Since their discovery, GRB properties were studied deeply to understand their emission mechanism. As more advanced instruments were developed in the years, few questions were cleared, but some are still without answer. Section 5.1.2 will briefly review the history of GRBs highlighting the observational properties and their interpretations. Section 5.1.3 will describe the so called *fireball model* to explain the prompt and the afterglow phases. Section 5.1.4 instead will focus on the progenitors of GRBs. Finally, Section 5.1.5 will describe the models to explain the high-energy emission from GRBs and their implications on the observations in the VHE range.

### 5.1.2 History of GRBs

The history of GRBs usually can be split in several eras, each determined by some milestones in the progress of our understanding of GRBs. These eras are the following:

- the *dark era*, when GRBs were discovered but almost nothing was known about them
- the *BATSE era*, where the spatial distribution of GRBs was measured
- the *BeppoSAX era* with the discovery of the afterglow and the identification of some host galaxies allowing to determine the distance of GRBs
- the *HETE-2 era*, when some long GRBs were associated to the explosions of supernovae
- the *Swift era*, where it began possible to study the early afterglow of long and short GRBs
- the *Fermi era*, partially overlapping with the previous one, is characterized by the detailed study of high-energy emission from GRBs.

The discovery of GRBs happened by chance: the USA had a constellation of satellites orbiting around the Earth called Vela satellites. They were equipped with X-ray and gamma-ray instruments to detect possible nuclear threats during the Cold War. In 1967 a very fast and strong gamma-ray signal was detected by the Vela satellites. Subsequent analyses revealed that the signal did not have origin from Earth or the Solar System, but it was made public only few years later in 1973 together with other fifteen events in Klebesadel, Strong, and Olson (1973). The origin of these flashes was unknown, but many theoretical models appeared after their discovery despite observations were just a few and with poor localization.

The dark era finished as soon as the BATSE (*Burst and Transient Source Experiment*) instrument started operation in 1991 (Fishman et al. 1985). BATSE was one the instruments onboard the *Compton Gamma-Ray Observatory* (CGRO) together with OSSE, COMPTEL and EGRET. BATSE comprised 8 NaI scintillators for the detection of X-rays and gamma-rays in the 20 keV-2 MeV. The orientation and position of the BATSE detectors in the CGRO was such that the field of view was the whole sky. This features made BATSE the perfect instrument to detect and characterize GRBs: in its entire lifetime BATSE detected 2704

GRBs. Moreover it could measure light curves and spectra, which was not possible before. The main findings of BATSE can be summarized as follows:

- the spatial distribution of GRBs is isotropic in the sky (see Figure 5.1), suggesting but not proving without doubt an extragalactic origin for GRBs (Meegan et al. 1996)

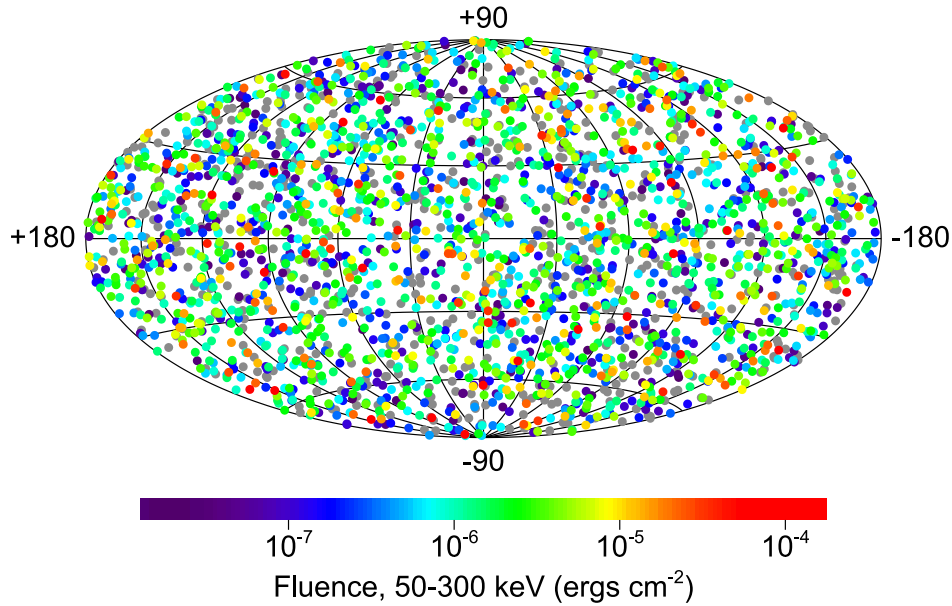


Figure 5.1: Spatial distribution of the GRBs observed by BATSE in the nine years of the mission. The number of GRBs recorded is 2704. Adapted from <https://gammaray.nsstc.nasa.gov/batse/grb/skymap/>.

- the temporal behavior from gamma-ray light curves is different from burst to burst. Some light curves were characterized by single peaks with a *Fast Rise Exponential Decay* (FRED) shape, other had double peaks or extended structures, as shown in Fishman et al. (1993). A standard classification of GRBs from their light curves is therefore not possible
- the durations of GRBs were different one from each other, from milliseconds to thousands of seconds. Despite this, two classes can be identified looking at the distribution of the parameter  $T_{90}$ , defined as the time interval where the counts goes from 5% to 95% of the total counts (Fishman et al. 1994). The distribution is bimodal with two peaks at 0.3 s and 3 s respectively and the separation is at 2 s, see Figure 5.2 and Meegan et al. (1996). So GRBs with  $T_{90} < 2$  s are called short while those with  $T_{90} > 2$  s are called long GRBs.
- the spectra are non thermal and are harder for short GRBs. They can be fit with a smooth broken power law with peak energy around 200-300 keV, see Figure 5.3. The functional form of this broken power law takes the name of *Band function* (Band et al. 1993) and is characterized by a low and a high energy spectral index,  $\alpha$  and  $\beta$  respectively:

$$N(E) = \begin{cases} A \left( \frac{E}{100 \text{ keV}} \right)^\alpha \exp\left(-\frac{E}{E_0}\right) & E < (\alpha - \beta)E_0 \\ A \left( \frac{(\alpha - \beta)E_0}{100 \text{ keV}} \right)^{\alpha - \beta} \exp(\beta - \alpha) \left( \frac{E}{100 \text{ keV}} \right)^\beta & E \geq (\alpha - \beta)E_0 \end{cases} \quad (5.1)$$

Here  $N(E)$  is the photon number spectrum and  $E_0$  is the break energy. The spectral energy distribution (SED)  $E^2 N(E)$  peaks at the energy  $E_p$  which is related to  $E_0$  by:

$$E_p = (2 + \alpha)E_0 \quad (5.2)$$

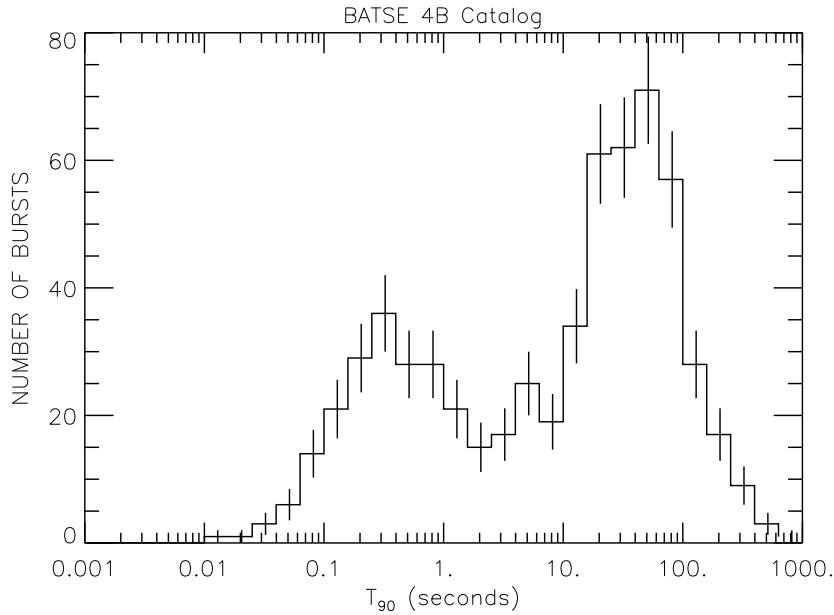


Figure 5.2: Histogram of the duration ( $T_{90}$ ) of BATSE GRBs from the 4B catalog presented in Paciesas et al. (1999). Adapted from <https://gammaray.nsstc.nasa.gov/batse/grb/duration/>.

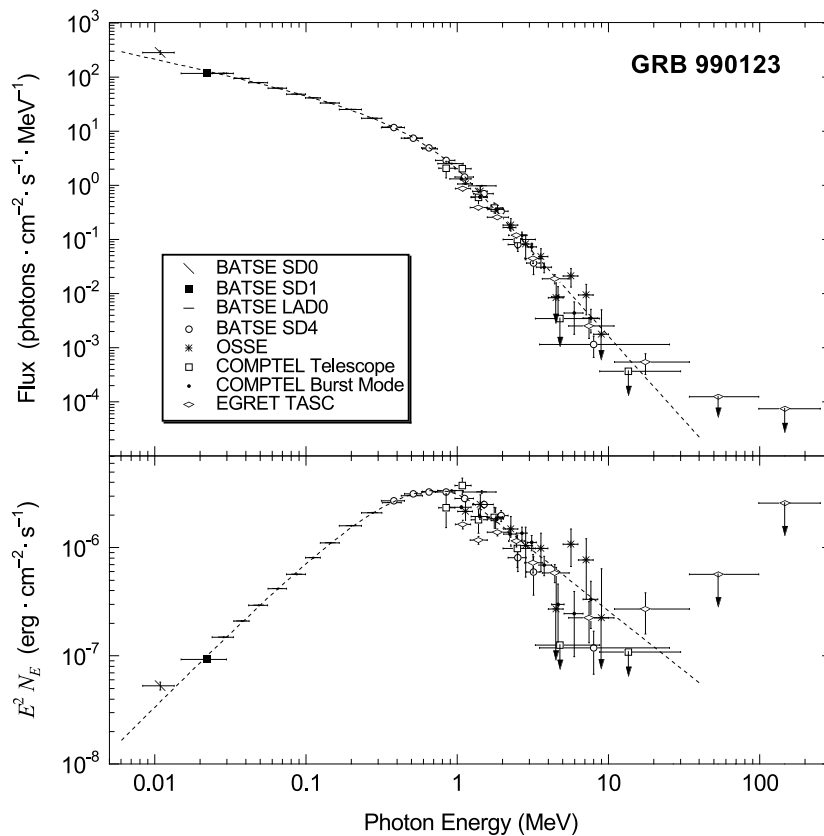


Figure 5.3: Example of the Band function for GRB 990123. From Briggs et al. (1999).

BATSE observations were affected by large error boxes, so the identification of a counterpart was not possible. So the debate between the galactic or extragalactic origin of GRBs was still on. The debate was closed with the observations performed by the Italian-Dutch satellite *BeppoSAX* (Boella et al. 1997). Three main instruments were onboard: the Narrow Field

Instruments (NFI), X-ray focusing telescopes sensitive between 0.1 and 200 keV; the Wide Field Cameras (WFC), two coded mask proportional counters with a  $20^\circ \times 20^\circ$  field of view in the range 2-30 keV; the GRB Monitor (GRBM), 4 CsI scintillators with large field of view and sensitive between 40 and 700 keV. The GRBM was used for GRB triggering and the WFC were aligned with it so that a monitoring of the GRB region could be performed with a resolution of  $5'$ . The first GRB to be detected simultaneously by the GRBM and the WFC was GRB960720<sup>1</sup>, presented in Piro et al. (1996). The milestone reached with BeppoSAX was the discovery of the afterglow, a fading X-ray emission, after the detection of GRB970228, see Figure 5.4 (Costa et al. 1997a; Costa et al. 1997b). Also an optical counterpart was detected for this GRB (Groot et al. 1997). For other GRBs counterparts were detected also at other wavelengths e.g. radio: the first radio afterglow was detected from GRB970508 (Frail and Kulkarni 1997). The presence of optical afterglows allowed to identify the host galaxies of the GRBs and to determine their distance through spectroscopic techniques. GRB970508 was the first GRB to have a measured redshift of  $z = 0.835$  (Metzger et al. 1997), while GRB970228 had  $z = 0.65$ : this was the proof without any doubt that GRBs had an extragalactic origin. It has to be noted that the redshift measurement is not possible for every GRB: sometimes the optical afterglow is not present and usually these bursts are called *dark GRBs*. The most accepted reason is dust intervening between the GRB and the observer causing extinction of the optical light passing through it (see for example Groot et al. 1998).

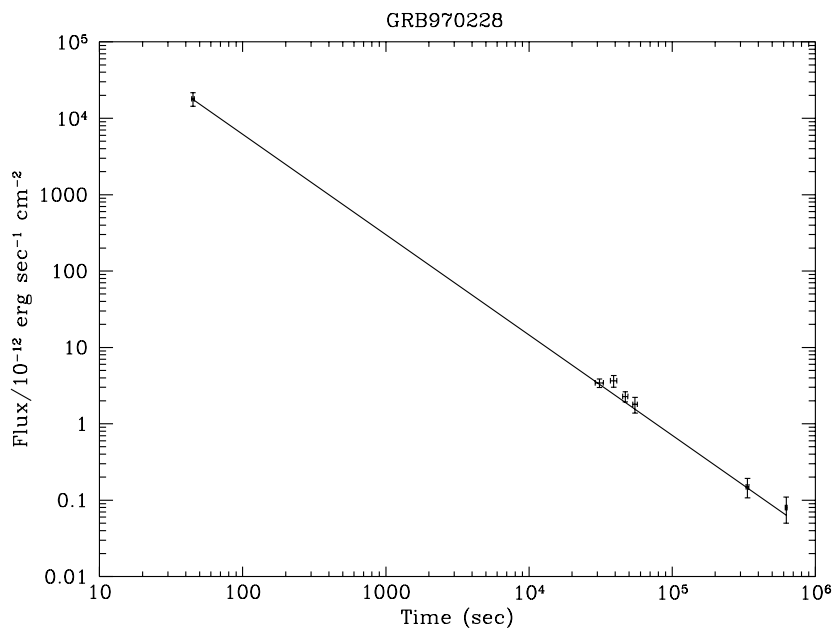


Figure 5.4: X-ray afterglow of GR970228. From Vietri (1997).

While GRB970228 and GRB970508 had moderately low redshift, BeppoSAX detected in 1997 another GRB, GRB971214, with an optical afterglow: the measured redshift was  $z = 3.42$ , corresponding to 2 billion years after the Big Bang (Kulkarni et al. 1998). Given the high luminosity observed at Earth and the cosmological distances, the energy output  $E_{\text{iso}}$  of GRBs, if assumed isotropic, is of the order of  $10^{52}$  erg- $10^{53}$  erg. This makes GRBs the most energetic and violent transient sources in the Universe.

Measurements of the GRB energetics posed a problem when the inferred  $E_{\text{iso}}$  was found to be more than the mass of the Sun converted into energy: it was the example of GRB990123 with

<sup>1</sup>GRB names nomenclature is GRBYMMDD followed by a letter (A,B,C,...) if more than one is detected on the same day. The current rule is to put the letter A even if only one GRB is detected on a day, but in the past it was omitted.

$E_{\text{iso}} \sim 4.5 \cdot 10^{54}$  erg. It was the first hint of the collimation of GRB emission. This means that the emission is collimated in two jets of opposite directions, each having an half opening angle  $\theta_j$ , so that the energy released in gamma rays was  $E_\gamma = (\theta_j^2/2)E_{\text{iso}}$ . The proof of the collimation of GRB emission was found studying the light curves of the optical afterglows: they presented an *achromatic break* (or *jet break*) independent from the filter used for the observation as shown in Figure 5.5. The break is caused by the relativistic motion of the outflow whose emission is then beamed within an angle  $\theta_b \sim 1/\Gamma$ , being  $\Gamma$  the Lorentz factor of the moving outflow. As long as  $\theta_b < \theta_j$ , the observer sees the emission from inside an angle  $\theta_b$ . But when the outflows slows down, at some point the condition  $\theta_b > \theta_j$  will be satisfied and so the observer will see less light with respect to the spherical outflow emission creating in the light curve a break after which the decay is faster. The jet opening angle  $\theta_j$  is related to the time of the break and so the correct energy value emitted in gamma-rays can be computed, as shown in Frail et al. (2001). Two consequences of the beaming of GRBs is that we observe only those whose jet is pointing towards the Earth (assuming isotropy in the direction of the jets) and that some GRBs could be seen as *orphan afterglows*, where the strongly beamed prompt emission is not seen while the afterglow, being mildly beamed, is detected.

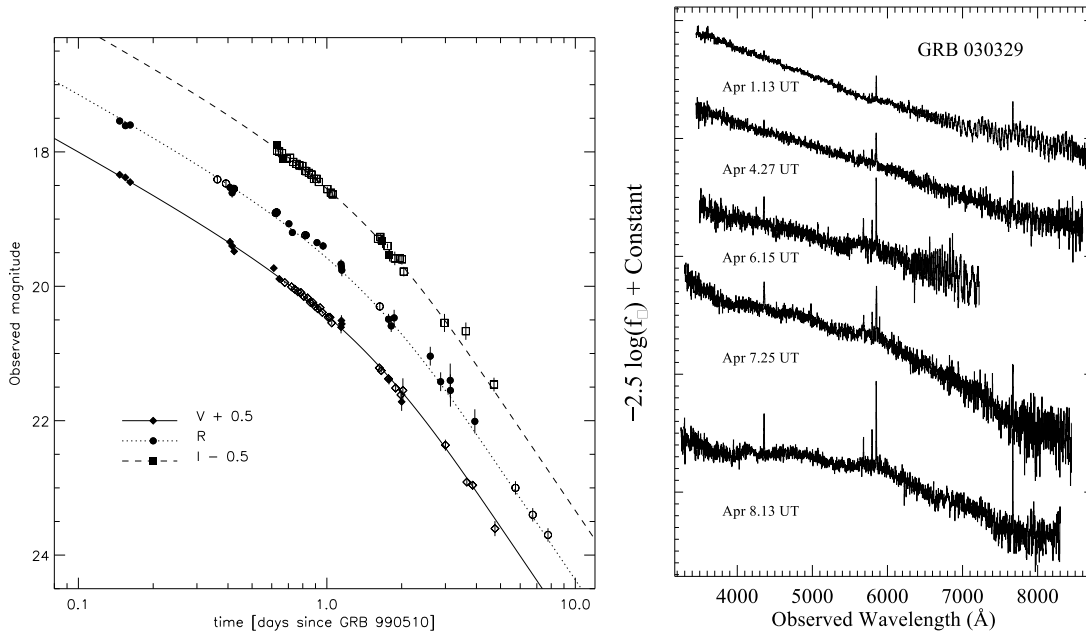


Figure 5.5: **Left:** achromatic break observed in the afterglow optical light curves of GRB990510. From Harrison et al. (1999). **Right:** evolution of the spectrum of GRB030329 and SN2003dh. While the early spectrum (top) shows a power-law continuum ( $F_\nu \propto \nu^{-0.9}$ ), the late spectra show peaks which are characteristic of a supernova. From Stanek et al. (2003).

Another important result of BeppoSAX was the association of some long GRBs to supernovae. As a matter of fact, the *progenitors* of GRBs, that is the objects which lead to the explosion of GRBs, were not identified until 1998. Several models predicted supernovae to be the progenitor of GRBs due to their similar energy output. The first indication of the association between supernovae and GRBs was found with GRB980425, detected and localized by the WFC of BeppoSAX. This GRB was found to be in temporal and spatial coincidence with SN1998bw, a Type Ic supernova (Pian et al. 1999). Both the GRB and the SN were unusual: the low redshift,  $z = 0.0085$  implied a “small” energy for the burst of the order of  $10^{48}$  erg, while the SN was brighter than in the typical case. Still one single event was not enough to

confirm this association. Before 2003, several afterglow optical light curves showed bumps after  $\sim 10$  days from the GRB onset. The final confirmation of the GRB-SN association was found with the coincident observation of GRB030329 and SN2003dh done by HETE-2: about 6 days after the burst, a bump was seen in the optical light curve (see Figure 5.5). The SN spectrum was isolated removing the afterglow spectrum and it was found to follow closely a SN1998bw-like spectrum. These discoveries led to the general thought that some long GRBs are associated with core collapse supernovae.

BeppoSAX, as discussed, gave major contributions<sup>2</sup> on the progress of our understanding of GRBs afterglow but had a limitation: its findings are connected to long GRBs only, since it was not able to localize short GRBs with the WFC. The first information about short GRBs came from the HETE-2 satellite, a mission entirely dedicated to GRBs (Ricker et al. 2003). It comprised three instruments: four wide-field gamma-ray detectors (6-400 keV), a wide-field coded-aperture X-ray imager (2-25 keV) and two CCD-based coded-aperture imagers called soft X-ray cameras (SXC). There were also additional optical CCD cameras to track stars. One of the novelty of HETE-2 with respect to BeppoSAX was the onboard processing of the data to quickly determine the position of the bursts. This feature allowed to send the position of the GRBs to the so called GRB Coordinates Network (GCN), which then disseminates the information to all the other observatories interested in performing follow-ups. HETE-2 was launched in October 2000, but the implementation of the fully automatic release of HETE localizations started in the 31st of May 2001 (see <https://gcn.gsfc.nasa.gov/gcn3/1064.gcn3>). The dissemination of GRBs positions was performed in matter of tens of seconds, allowing for fast reaction and follow-up of ground instruments of the afterglow, which could be characterized better than before. One remarkable result achieved by HETE-2 was the detection of GRB030329, then found to be associated with SN2003dh, as already anticipated (Stanek et al. 2003). Nevertheless, HETE-2 helped in obtaining other important results. One was the first detection of an optical afterglow from GRB050709, a short GRB with  $T_{90} = 0.07$  s at  $z = 0.16$  (Hjorth et al. 2005). This was the proof that both long and short GRBs were due to ultra-relativistic jets followed by an afterglow detectable in the optical, radio and X-ray band. Despite this similarity, also differences arose between the two classes: short GRBs are closer, so less energetic, than long GRBs and are associated with galaxies with low or no star formation. Moreover, they are not associated with supernovae and so their progenitors are different. From the study of the optical afterglow light curves, the best hypothesis was that short GRBs were the result of the merging of compact objects like black holes and neutron stars. A direct consequence of this theory is that this kind of binary systems with at least one neutron star are emitters of gravitational waves possibly detectable by current interferometers like LIGO and Virgo.

Another achievement of HETE-2 was the confirmation of the nature of X-Ray Flashes (XRF) as soft GRBs. XRF were discovered by BeppoSAX: some events seen in the WFC did not trigger the GRBM and their signal was GRB-like, as shown in Heise et al. (2001). Some of these events were detected also by BATSE in its low energy range (20-100 keV). To understand the nature of XRF, HETE-2 was the key instrument given its broad energy coverage. It observed many XRF determining their peak energies, concluding that they were lower than the ones of usual GRBs. Nevertheless, duration and spectra were quite similar (Barraud et al. 2003; Sakamoto et al. 2005). Being fainter than GRBs, XRF are detected at low redshift and can be used to look for supernovae association. Two predominant models explains the nature of XRF: they could be standard GRBs whose jet is seen at large angles or they could be GRBs which produce intrinsically softer radiation.

A huge contribution in the study of GRBs came (and comes nowadays) with the launch of the *Swift* satellite in 2004. It was designed with three instruments: the *Burst Alert Telescope*

---

<sup>2</sup>I would like to stress that many of the discoveries were not done by BeppoSAX itself, but by ground observatories performing follow-ups of BeppoSAX-detected GRBs. So the merit should be shared.

(BAT), the X-Ray Telescope (XRT) and the Ultra-Violet/Optical Telescope (UVOT) (Gehrels et al. 2004). BAT is detector with 32768 CdZnTe elements and a D-shaped coded mask with 54000 lead tiles 1 m above the detector, with a field of view is 1.4sr. BAT cover the energy range 15-150 keV. The second instrument, XRT, is a focusing X-ray telescope with a 2.5 m focal length. Its field of view is a square of 23.6' side and 18'' resolution. The precision of the determination of the GRB positions is 5-6'' if determined on-flight, otherwise 2-3''. Its energy range covers the 0.2-10 keV band. Finally, the UVOT, which is aligned with the XRT, is a Ritchie Chretien telescope detecting light in the wavelength range from 170 to 600 nm. It has a field of view of 17'  $\times$  17' with 0.3'' positional accuracy. The different energy ranges covered by the three detectors allows Swift to perform multi-wavelength observations. The Swift observing strategy is the following: GRBs usually trigger the BAT detector, which can calculate the position of the bursts with an accuracy better than 4'. The Swift spacecraft is able to slew automatically to the position provided by BAT and perform simultaneous XRT and UVOT observations. XRT is able to determine the position up to 5'', while UVOT produces images of the sky field searching for a possible optical counterpart. The burst position found by BAT or by XRT are immediately sent to the GCN for prompt follow-up of the ground instruments. The delay between the GRB onset and the beginning of XRT observations is well below 100s: this is a huge improvement compared to BeppoSAX, which was able to repoint only in hours after the initial trigger. This unique feature of Swift allowed to characterize in an unprecedented way the behavior of the first hours of the X-ray afterglow light curves and the transition between the prompt and afterglow emission. Thanks to the high number of GRBs detected by Swift, a "canonical" X-ray early afterglow light curve could be extracted, which is valid for most of the bursts, shown in Zhang et al. (2006). It can be described by a piecewise function with several power laws, see Figure 5.6. It is common to divide such light curves in different pieces:

- I: *steep decay phase*, described by a  $\propto t^{-3}$  power law; it is the tail of the prompt emission and lasts until about  $10^2$ - $10^3$  s
- II: *shallow decay phase*, decaying as  $t^{-0.5}$  (for this reason is also called *plateau*) until  $10^3$ - $10^4$  s
- III: *normal decay phase* ( $\propto t^{-1.2}$  up to  $10^4$ - $10^5$  s)
- IV: *late steepening phase* ( $\propto t^{-1.2}$ )
- V: during the shallow decay phase *X-ray flares* are sometimes observed.

Parts III and IV were already observed with BeppoSAX, while parts I, II and especially V were characterized for the first time thanks to Swift.

The high Swift sensitivity allowed also the detection of very distant GRBs. The most distant GRB up to date is GRB090423 with a redshift of  $z = 8.2$ , corresponding to a look-back time of 13.2 billion years (Fernandez-Soto et al. 2009). This high-redshift GRBs make possible to associate them with Population III stars as their progenitors. Additionally, distant GRBs could be used for cosmology purposes, shedding light on the star formation in the first phases of the Universe.

Finally Swift detected many short hard GRBs beside the ones observed by HETE-2 and characterized their afterglow light curves and their host galaxies. As suggested already from HETE-2 observations, short GRBs afterglows are fainter than long GRB ones and have different progenitors, supporting the idea that compact binary mergers are responsible of their origin.

Up to 2007, GRBs were studied especially in the X-band and in lower energy bands (optical, radio, UV). With the launch of AGILE (*Astro-rivelatore Gamma a Immagini LEggero*) in 2007 (Tavani et al. 2009b) and Fermi in 2008 (Atwood et al. 2009), it became possible to

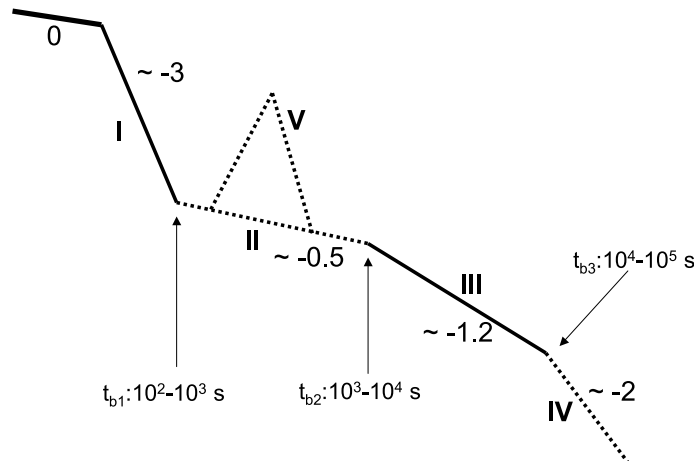


Figure 5.6: Sketch of the “canonical” X-ray afterglow light curve. From Zhang et al. (2006).

have an insight of the features of GRBs at High Energy. AGILE is a compact satellite for high-energy astrophysics, comprised of a hard X-ray imager (Super-AGILE, 18-60 keV), a Gamma Ray Imaging Detector (GRID, 30 MeV-30 GeV), a non-imaging Mini Calorimeter (MCAL, 250 keV-100 MeV) and anti-coincidence shield. Its good angular resolution in both X and gamma-ray band,  $1'-2'$  and  $0.1^\circ-0.2^\circ$  respectively, is a key factor in the study of GRBs. The Fermi satellite has two main instruments: the *Gamma-ray Burst Monitor* (GBM) and the *Large Area Telescope* (LAT). The GBM focuses on the low energy band, namely between 8 keV and 40 MeV, thanks to twelve sodium iodide (NaI) scintillators and two cylindrical bismuth germanate (BGO) scintillators. Given its energy coverage and huge field of view (all the unocculted sky), GBM triggers  $\sim 200$  GRBs per year but the uncertainty on their position is quite large (several degrees). The LAT is a pair production telescope sensitive in the high-energy band between 20 MeV and 300 GeV. Its field of view is small compared to GBM, about 20% of the sky at any instant, but has a good angular resolution improving at higher energies ( $0.15^\circ$  at 10 GeV).

AGILE and Fermi revealed some interesting and unexpected features of the high energy component of GRBs, which will be discussed in more detail in Section 5.1.5:

- not all GRBs have HE emission, but the rate is  $\sim 10$  GRBs per year
- GRBs detected in the GeV band are the brightest and their minimum Lorentz factors are high, between 600 and 100
- both long and short GRBs can emit in the HE band
- additional spectral components could be present at HE, together with a thermal component)
- the HE emission is seen to be extended in time (up to hours, with a  $t^{-1}$  decay) and delayed with respect to the low energy components

The origin of the high energy emission is still unknown and is not clear if it is produced during the prompt or afterglow phase. In any case, since most of the HE photons are seen close to the prompt emission, the current picture of the prompt phase is under heavy discussion. A huge contribute on this matter could be given by observing and possibly detecting GRBs

in the VHE band where MAGIC and the other Cherenkov telescopes operate. This will be discussed in Section 5.1.5.

### 5.1.3 Fireball model for Gamma-Ray Bursts

Given the extreme energies and short variability of GRBs, it is quite difficult to understand how the GRB explosion results in the radiation observed at Earth. Despite different progenitors give rise to short and long GRBs, the evolution of the initial explosion can be considered independent by the particular progenitor involved.

As already mentioned, the energies released by GRBs are of the order of  $10^{52}$ - $10^{53}$  erg and the temporal variability can happen on timescales of milliseconds. This implies that the dimension of the source is not bigger than few thousands kilometers and the huge amount of energy contained in that volume gives rise to a so called fireball of electrons, positrons and gamma-rays, plus possible barions. The presence of this fireball should result in a high opacity to gamma rays: most of them should not be able to escape but they should be lost due to the pair production process. This is in contrast with observations, since gamma radiation is clearly detected from GRBs and the spectrum is non-thermal. The opacity (or optical depth)  $\tau_{\gamma\gamma}$  for pair creation can be estimated easily given the GRB observed flux  $F$ , its distance  $d$ , its variability timescale  $\delta t$  and the mean gamma ray energy  $\bar{E}_\gamma$ :

$$\tau_{\gamma\gamma} \approx \frac{f_{e^\pm} \sigma_T 4\pi d^2 F}{\bar{E}_\gamma c^2 \delta t} = \frac{f_{e^\pm} \sigma_T E_{\text{iso}}}{\bar{E}_\gamma c^2 \delta t} \quad (5.3)$$

where  $f_{e^\pm}$  denotes the average probability for gamma rays to undergo pair production and  $\sigma_T$  is the Thomson cross section. Inserting in Equation (5.3) typical values from GRB observations,  $\tau_{\gamma\gamma}$  assumes values much larger than one so that the fireball should be heavily opaque to gamma rays. This is true as soon as the matter emitting the radiation is not moving relativistically towards the observer. If the outflows moves relativistically with a Lorentz factor  $\Gamma$  (much greater than 1), two effects result in an optically thin fireball. The first is the blueshifting of observed photon energies compared to the ones in the outflow frame while the second is the modification of the source size from  $c\delta t$  to  $c\delta t\Gamma^2$ . The complete calculation of the relativistic optical depth can be found in Lithwick and Sari (2001):

$$\tau_{\gamma\gamma} = \frac{11}{180} \frac{\sigma_T d^2 (m_e c^2)^{-\alpha+1} \mathcal{F}}{c^2 \delta t (\alpha - 1)} \times \left( \frac{E_{\text{max}}}{m_e c^2} \right)^{\alpha-1} \Gamma^{-(2\alpha+2)} (1+z)^{-(2\alpha+2)} \quad (5.4)$$

where  $\alpha$  is the spectral index of the gamma rays spectrum and  $E_{\text{max}}$  is the maximal photon energy. Equating (5.4) to unity gives a lower limit on the required Lorentz factor for an optically thin fireball. The basic requirement to observe non-thermal spectra of gamma-rays from GRBs is  $\Gamma \gtrsim 100$ .

Having solved the compactness problem assuming the relativistic motion of the outflow, the dynamics of the fireball can be studied, see for example Vedrenne and Atteia (2009). Denoting the baryon loading and the starting energy of the fireball as  $M_0$  and  $E_0$  respectively, it leads to an energy-to-mass ratio  $\eta = E_0/M_0 c^2 \gg 1$ . Assuming an initial radius for the fireball  $R_{\text{in}}$ , the particles inside will be almost at rest. As the fireball starts to expand, the internal energy will be converted totally in bulk kinetic energy. Assuming an adiabatic expansion, the temperature of the fireball in the rest frame  $T'$  will be proportional to  $R^{-1}$ , with  $R$  being the fireball radius. At this point the internal energy is dominant, so that  $E_0 \propto \Gamma T'$ . From this it follows that  $T' \propto \Gamma^{-1}$  and  $\Gamma \propto R$  because  $E_0$  is constant. This means that in the first acceleration phase the fireball Lorentz factor increases linearly with its radius.  $\Gamma$  will reach a saturation value at radius  $R_{\text{sat}} = \eta R_{\text{in}}$ . After the fireball reaches the saturation radius, it will move with constant Lorentz factor  $\Gamma_{\text{max}} \sim \eta$ . As soon as the fireball reaches the circumburst medium, it will decelerate, usually at radius  $R_d > R_{\text{sat}}$ .

In the fireball model, relativistic shocks are expected. In shocks the bulk kinetic energy of the flow is converted into internal energy of particles. In particular electrons can be accelerated and can radiate through synchrotron or Inverse Compton. There are two kinds of shocks in the fireball model (see Figure 5.7):

- *external shocks* (ES), where the fireball blastwave interacts with the circumburst medium, see Rees and Meszaros (1992). Usually the ES explains the afterglow emission of GRBs. The ES usually is a forward shock, but in the presence of magnetic fields a reverse shock propagating in the opposite direction of the blastwave can be created
- *internal shocks* (IS), where outflows with different Lorentz factors interact one with each other, giving rise to the fast time variability seen in observations. The internal shocks are used to explain the prompt emission, see Rees and Meszaros (1994).

The internal shocks should appear after the blastwave reached the photospheric radius  $R_{ph}$ , that is the radius at which the outflow becomes optically thin. This puts constraints on  $\eta$ , which ranges from few tens to few hundreds.

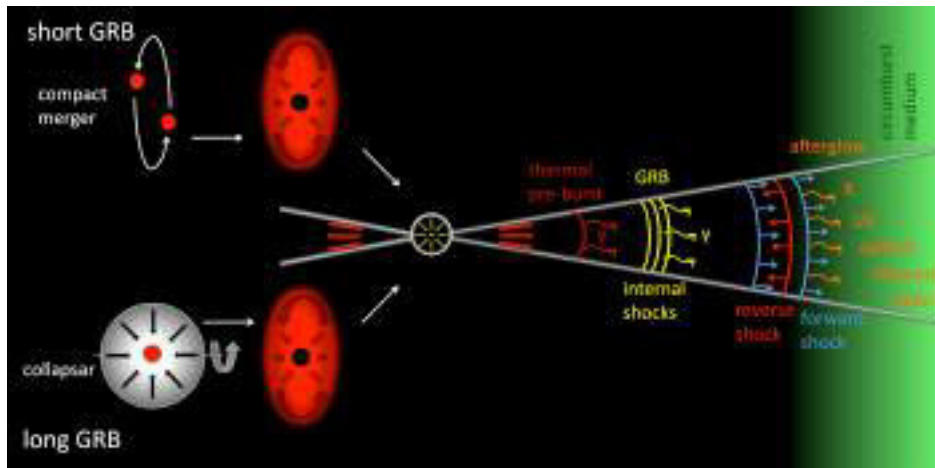


Figure 5.7: Graphical representation of the fireball model. At first the outflow is not transparent to radiation, but after expansion it will let radiation escape. The prompt phase originates from the internal shocks, while the afterglow is caused by external shocks where the shock waves interact with the external medium. Both a forward and a reverse shock can form in this process. In the left part, also the progenitors of GRBs are represented, see Section 5.1.4. From Gomboc (2012).

The presence of relativistic shocks leads to the acceleration of electrons. In shocks, a downstream and upstream region can be defined, where the physical properties have a jump in their values, described by the Hugoniot shock jump conditions, see Blandford and McKee (1976):

$$n_2 = 4\Gamma n_1 \quad (5.5)$$

$$e_2 = 4\Gamma n_1 m_p c^2 \quad (5.6)$$

$$\Gamma_{sh}^2 = 2\Gamma^2 \quad (5.7)$$

$n_{1,1}$  and  $e_{1,2}$  are the number and energy density respectively measured in the local rest frame. The subscript 1 denotes the upstream region, the subscript 2 denotes the downstream region.  $\Gamma_{sh}$  is the Lorentz factor of the shock, while  $\Gamma$  is the one for the fluid behind the shock. From equation (5.5) it can be seen that matter is compressed of a factor  $4\Gamma$  behind the shock. The pressure instead is given by  $4\Gamma n_1 m_p c^2$ . This conditions makes an ultrarelativistic shock to increase the velocities of the particles downstream to ultrarelativistic ones. The magnetic field

is changed as well: the component parallel to the front expansion direction is compressed and amplified by a factor  $\Gamma$ , while the perpendicular component is left unchanged. Since synchrotron radiation is expected, it implies a good knowledge of the energy distributions of the electrons and of the magnetic field in the downstream region. For the latter, usually two parameters are used to describe the microscopic details of the shock:  $\varepsilon_B$ , the ratio of the magnetic energy and the energy behind the shock, and  $\varepsilon_E$ , the ratio of the electron energy and the energy behind the shock. Despite the outflow evolution, these two parameters are considered to be constant throughout the burst.

Thanks to the presence of shocks, particles (electrons) can be accelerated to ultrarelativistic energies when crossing repeatedly the shock front (this process is called *diffusive shock acceleration*) in a similar way proposed by Fermi. This model works well in the non-relativistic case, but needs some modifications in the GRB case, where shocks move relativistically. In particular a magnetic field in the upstream region is needed to scatter the particles at large angles and in the downstream region large magnetic fluctuations should allow particles to cross again the shock. The resulting electron spectrum is a power law with a quite universal value for the spectral index  $p \sim 2.2 - 2.3$ .

Once electrons are accelerated, they can cool through synchrotron emission: this is true especially for the afterglow phase. Synchrotron radiation is characterized by three parameters: the Lorentz factor of electrons  $\gamma_e$ , the strength of the magnetic field  $B$  and the Lorentz factor of the moving outflow. In the observer frame, the characteristic photon energy is given by:

$$(h\nu_{syn})_{obs} = \frac{\hbar q_e B}{m_e c} \gamma_e^2 \Gamma \quad (5.8)$$

This leads to the emitted power by a single electron in the rest frame:

$$P_{syn} = \frac{4}{3} \sigma_T c U_B \gamma_e^2 \quad (5.9)$$

where  $U_B = B^2/8\pi = \varepsilon_B e$  is the magnetic energy density. If the power emitted is known, the time needed to cool the electron in the rest and observer frame can be computed, since they differ only by a  $\Gamma$  factor:

$$t_{syn}(\gamma_e)_{rest} = \frac{3m_e c}{4\sigma_T U_B \gamma_e} \quad t_{syn}(\gamma_e)_{obs} = \frac{3m_e c}{4\sigma_T U_B \gamma_e \Gamma} = \frac{3}{\sigma_T} \sqrt{\frac{2\pi c m_e q_e}{B^3 \Gamma}} \nu^{-1/2} \quad (5.10)$$

The last equality follows from the value of  $\gamma_e$  obtained from (5.8). It can be noted that the cooling time in the observer frame does not depend on  $\gamma_e$  and consequently on the energy distribution of the electrons. This relation holds as soon as electrons have  $\gamma_e$  high enough to produce photons with frequency  $\nu$ . It could be concluded that the observed variability in GRBs is due to the cooling time of electrons: the rising trail of the spikes could be attributed to the heating of electrons, while the decaying phase is a consequence of the cooling. This explanation however is too simplistic and not satisfactory, since the decay time of the spikes resulting from the cooling time is too short compared to the one observed if reasonable parameters are inserted in (5.10). If instead the cooling time is long, there could be adiabatic losses of the shocked region and the efficiency would be dramatically decreased. So synchrotron radiation, at least for the prompt radiation, is not fully responsible for the observed light curves of GRBs.

The previous relations were found for a single electron. In the fireball model, electrons have an energy spectrum  $N(\gamma_e) \propto \gamma_e^{-p}$  due to the diffusive shock acceleration. This spectrum is valid only for  $\gamma_e > \gamma_m$ , where  $\gamma_m$  is the minimum Lorentz factor of the electron distribution whose value is determined by the electron energy density  $e_e$  and the electron number density  $n_e$  (Piran 2004):

$$\gamma_m = \frac{p-2}{p-1} \frac{e_e}{n_e m_e c^2} = \frac{p-2}{p-1} \langle \gamma_e \rangle \quad \rightarrow \gamma_m \propto \langle \gamma_e \rangle \quad (5.11)$$

The last proportionality implies that  $\gamma_m$  represents the typical Lorentz factor of the electron population and consequently the typical frequency of the synchrotron emission, so that  $\nu_m = \nu_{syn}(\gamma_m)$ . To obtain the full synchrotron spectrum, it is simpler to treat different parts of the spectrum separately. In the lowest part, all electrons will contribute to the synchrotron spectrum, since the tails of the electrons emission will sum up. This is a typical behavior of synchrotron radiation and leads to a spectrum  $F_\nu \propto \nu^{-1/3}$ . The most energetic electrons cool rapidly, emitting almost all their energy into synchrotron radiation at the specific frequency determined by their Lorentz factor. Since the number of electrons with Lorentz factor  $\gamma$  is  $\propto \gamma^{1-p}$  and their energy is  $\propto \gamma^{2-p}$ , from (5.8) we obtain  $\nu \propto \gamma^2$  and therefore  $F_\nu \propto \gamma^{-p} \propto \nu^{-p/2}$ . This means that the high energy part of the synchrotron can be used to infer the spectral index  $p$  of the electron population.

The intermediate part of the spectrum has different behaviors depending on the cooling: there are two regimes called *fast cooling* and *slow cooling*. The former indicates that electrons cool on a hydrodynamic timescale (the time of interaction between the shocks and the surrounding medium in the afterglow, or between shocks in the prompt) while in the latter case they do not. The dominant regime can be found comparing  $\gamma_m$  with the critical value  $\gamma_c$  defined as:

$$\gamma_c = \frac{3m_e c}{4\sigma_T U_B \Gamma t_{hyd}} \quad (5.12)$$

where  $t_{hyd}$  is the hydrodynamic timescale in the observer frame. The slow cooling is defined by the condition  $\gamma_m < \gamma_c$ , while fast cooling by  $\gamma_m > \gamma_c$ . The minimum and critical Lorentz factor can be used to define the following synchrotron frequencies:

$$\nu_m = \nu_{syn}(\gamma_m) \quad \nu_c = \nu_{syn}(\gamma_c) \quad (5.13)$$

The spectrum in the intermediate region depends on the cooling regime, see Figure 5.8 and Piran (2004):

- in the fast cooling regime all electrons cool down to  $\gamma_c$ . The resulting spectrum is:

$$F_\nu = \begin{cases} F_{\nu,max} \left(\frac{\nu_a}{\nu_c}\right)^{1/3} \left(\frac{\nu}{\nu_a}\right)^2 & \nu < \nu_a \\ F_{\nu,max} \left(\frac{\nu}{\nu_c}\right)^{1/3} & \nu_a < \nu < \nu_c \\ F_{\nu,max} \left(\frac{\nu}{\nu_c}\right)^{-1/2} & \nu_c < \nu < \nu_m \\ F_{\nu,max} \left(\frac{\nu_m}{\nu_c}\right)^{-1/2} \left(\frac{\nu}{\nu_m}\right)^{-p/2} & \nu > \nu_m \end{cases} \quad (5.14)$$

$F_{\nu,max}$  is the observed maximum flux density, equal to  $F_\nu(\nu_c)$  for the fast cooling regime

- in the slow cooling regime only electrons with Lorentz factor greater than  $\gamma_c$  can cool efficiently, while the bulk of the electrons have Lorentz factor  $\sim \gamma_m$  but they are not able to cool down. The resulting spectrum is therefore:

$$F_\nu = \begin{cases} F_{\nu,max} \left(\frac{\nu_a}{\nu_m}\right)^{1/3} \left(\frac{\nu}{\nu_a}\right)^2 & \nu < \nu_a \\ F_{\nu,max} \left(\frac{\nu}{\nu_m}\right)^{1/3} & \nu_a < \nu < \nu_m \\ F_{\nu,max} \left(\frac{\nu}{\nu_c}\right)^{-(p-1)/2} & \nu_m < \nu < \nu_c \\ F_{\nu,max} \left(\frac{\nu_c}{\nu_m}\right)^{-(p-1)/2} \left(\frac{\nu}{\nu_c}\right)^{-p/2} & \nu > \nu_c \end{cases} \quad (5.15)$$

In this case,  $F_{\nu,max} = F_\nu(\nu_m)$

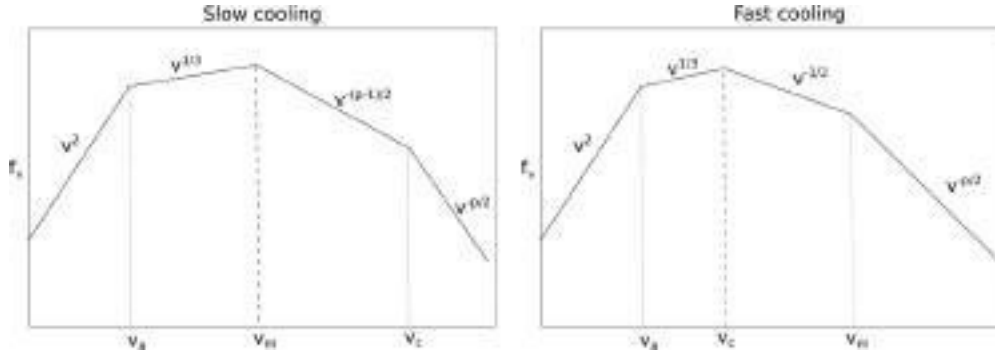


Figure 5.8: The spectrum resulting from synchrotron radiation in the slow and fast cooling cases (left and right respectively). From Kumar and Zhang (2015).

In the previous spectra another characteristic frequency was introduced, the *self-absorption frequency*  $\nu_a$ . At the lowest energies, synchrotron self-absorption is relevant and produces a steep cut-off of the spectrum. In this case photons are absorbed by the inverse-synchrotron process.

The two cooling regimes are both present in GRBs: fast cooling must take place otherwise the energy transfer from shocks to particles would be highly inefficient. A transition from fast to slow cooling could arise in external shocks, so in the afterglow phase.

The shocks in the fireball model will accelerate particle up to a maximum energy, which in turn will reflect on the maximum energy of photons produced via synchrotron radiation. It can be shown that synchrotron photons by electrons can reach energies up to  $50 \text{ MeV} \cdot \Gamma$  or more by a factor of a few if a highly inhomogeneous magnetic field is present in the downstream region.

An important role during the prompt phase could be played by the Inverse Compton (IC) process. Depending on the conditions within the fireball, the IC scattering can take place and increase the energy of the photons above the Klein-Nishina energy ( $m_e c^2 \sim 0.5 \text{ MeV}$ ). Above this energy the IC cross section decreases with photon energy as  $\nu^{-1}$  and so usually photons scatter only once. Below the Klein-Nishina regime, upscattered photons have an average frequency  $\nu_s \sim \nu \gamma_e^2$ . The total power of IC-scattered photons  $P_{IC}$  by electrons moving in a region with a photon density  $u_\gamma$  is given by:

$$P_{IC} \sim \sigma_T u_\gamma \gamma_e^2 c \quad (5.16)$$

The importance of the Inverse Compton with respect to the synchrotron radiation is estimated by the Comptonization parameter  $Y$ , which in the fast cooling regime can be written as:

$$Y = \begin{cases} \varepsilon_e / U_B & U_e \ll U_B \\ \sqrt{U_e / U_B} & U_e \gg U_B \end{cases} \quad (5.17)$$

If  $Y < 1$  the IC can be ignored. If  $Y > 1$  the low energy photons produced via synchrotron radiation will be upscattered via the IC scattering. This will affect the cooling time of electrons, since they will lose energy through two processes. Another consequence of the IC process is that high energy radiation in the GeV-TeV is expected, since the photons energy is boosted by a factor  $\gamma_e^2$ .

As introduced in Section 1.2.1, a particular case of IC process is when the seed photons are produced via the synchrotron process and the up-scattering of photons is on their parent electrons, the SSC process. The possible presence of the SSC process introduces an extra cooling to electrons and an additional spectral component at high energies. More details on SSC emission will be described in Section 5.1.5.

### 5.1.4 Progenitors of Gamma-Ray Bursts

In Section 5.1.3 the GRBs prompt and afterglow phases were explained as internal and external shocks, regardless of the progenitor and central engine giving birth to the burst. In this Section, the different models for GRB progenitors will be described.

As already mentioned, the observational features of GRBs give precious hints on the nature of the central engine. These features are the following:

1. huge amount of energy released, about  $10^{52}$  erg- $10^{53}$  erg
2. collimation of the outflow within a small angle
3. different durations for bursts (long versus short)
4. the GRB rate is one every  $3 \cdot 10^5$  yr per galaxy, which is a factor  $\sim 3000$  less than the one for supernovae
5. fast time variability, down to millisecond time scales.

The first two points require that the central engine should be able to generate an amount of energy comparable to the one observed and to accelerate the outflow to relativistic velocities with a collimation. The third point implies that the progenitors of short and long GRBs are different. The fourth point suggests that the central engine can exhibit a prolonged activity, ruling out explosive events where the energy is released at once in a single explosion. The last point more specifically implies that the progenitors are compact objects due to the fast variability seen in GRB light curves. To account for the bursts duration, matter accreting onto the compact object is needed. This suggest that GRB accompany the formation of black holes, in a similar but more extreme way to what happens for AGN.

Different models were developed to explain the different types of GRBs. They are briefly described in the following sections.

#### Collapsar model

Collapsars are rotating massive stars which can be isolated or in binary systems, see Woosley (1993). These objects will collapse forming a black hole onto which the remaining matter from the star core accretes forming the relativistic jet which is then observed if directed towards our line of sight. The star should have lost most of its hydrogen envelop so that the baryon loading is not significant. For this reason, Wolf-Rayet stars are the natural candidates for the GRB progenitors in the collapsar model and are closely linked with the progenitors of type Ib/Ic supernovae. Beside a massive core and lack of the hydrogen envelope, an additional condition in the collapsar model is an high angular momentum of the core which translates in a torus which accretes onto the black hole. This is needed to power the GRB.

According to MacFadyen and Woosley (1999), the collapsar model can be summarized as follows : the iron core of a rapidly rotating star with mass greater than  $30M_{\odot}$  collapses to a black hole and an accretion disk is created. The accretion happens in the equatorial plane perpendicular to the rotation axis so that in the polar region there is almost no accretion. In the disk neutrino annihilation ( $\nu + \bar{\nu} \rightarrow e^+ + e^-$ ) dissipates the energy and power polar outflows, where the rotational support is low (a funnel). Here radiation bubbles, pairs and baryons are compressed into jets which eventually break out from the star surface. Beside neutrino annihilation, the energy can be extracted from the disk to form a jet through the Blandford-Znajek mechanism, see Blandford and Znajek (1977), or with MHD processes (Blandford and Payne 1982; Koide, Shibata, and Kudoh 1999; Meier 1999).

In the former case, charges around the black hole will induce an electrical field which usually has a non-zero component along the magnetic field lines created by currents in the disk. Charged particles can therefore be accelerated and radiate photons, which in turn produce

electron-positron pairs. This free charge production makes the electromagnetic field in the horizon vicinity almost force-free and the magnetic field lines will corotate with the black hole. Induced current loops will be produced, which couple to the magnetic field of the accretion disk. The force exerted by this coupling brakes the black hole, effectively extracting angular momentum from it and energy from the disk itself. The energy extracted through the Blandford-Znajek mechanism can be huge, up to 9% of the rest mass energy of the black hole.

In the latter case, MHD processes which could form a jet are magneto-centrifugal forces, neutrino energy deposition or magnetic reconnection in the disk. In the first situation, cold jets are produced, with thermal energy not large compared to its rest mass or kinetic energy. The jet can be collimated in this case by magnetic fields.

The whole process (core collapse, accretion and jet propagation) in the collapsar model requires at least  $\sim 10$  s. This means that the collapsar model is expected to explain the origin of long GRBs. Another consequence of this model is that GRBs are connected to the death of massive stars, so that they should be found in galaxies with active star formation. Observations strongly support this idea, showing that GRBs are found in the active star-forming galaxies, namely blue dwarf ones.

Currently the collapsar model seems to be the preferred one, since many observations like the SN-GRB association and the presence of bumps in the optical afterglow light curve as signature of a SN support it.

### Supranova model

The supranova model considers a supermassive neutron star which in its initial phase loses angular momentum via magnetic dipole radiation and gravitational waves. When centrifugal forces are not supporting the neutron star anymore, it collapses into a black hole. The same could happen if the neutron star accretes material from a close accretion disk, see Vietri and Stella (1998). The situation is then similar to the one seen in the collapsar scenario, with the important difference that no baryons are present around the black hole. This is because the supranova model is a two-step process: first a supernova creates the neutron star, which after few weeks or months collapses into the black hole. In the first explosion all the baryons are swept away and so the contamination is low, as required by the fireball model to form an efficient relativistic jet. This same fact has the consequence that the jet propagates in an almost matter-free medium instead of breaking out from a stellar envelope.

### Pulsar model

Progenitor models involving pulsars are particularly interesting since in the context of the fireball model a low baryonic load is needed. In these kind of models the energy is transported through vacuum thanks to the Poynting flux, so it requires very strong magnetic fields of the order of  $10^{15}$  G. This situation can be found during the formation of rapidly rotating and highly magnetized neutron stars, so that the rotational energy is lost in a very short amount of time, of the order of few seconds, see Usov (1992). A strong electric field, created by the rotation of the magnetic field, will induce electron-positron pair production. The same happens with photons interacting with the strong magnetic field or with other photons. In this way a pair plasma is produced which moves away from the pulsar at relativistic speeds. The expanding plasma will become optically thin at a radius  $r_{rad} \sim 10^8 - 10^9$  cm, so that gamma radiation with energy of 0.1-1 MeV (with a tail extending to few hundreds MeV) can escape. This model was used to explain both long and short GRBs. The resulting spectrum has two components, one thermal with equivalent temperature of  $\sim 10^{10}$  K and one non-thermal resulting from the gamma-ray photosphere. When reaching  $r_{rad}$ , the magnetic field is not frozen anymore in the plasma and strong electromagnetic waves are emitted, allowing

particles to be accelerated to Lorentz factors as high as  $10^6$ .

Beside the standard pulsar model, a variant involving magnetars was proposed in Duncan and Thompson (1992). In this case, since magnetars are characterized by very strong magnetic fields, the GRB would be the result of the magnetic reconnection in the magnetosphere.

### Compact binary mergers

Previous models dealt with the progenitors of long GRBs, with an exception for the pulsar model. To explain the formation of short GRBs, the preferred model involves the merging of compact objects like neutron stars or black holes. As in collapsar models, this results in the formation of a black hole with matter from the original objects forming an accretion disk or torus. When matter falls onto the black hole, it will release part of its gravitational energy. The binary systems leading to these scenarios are neutron star-neutron star (NS-NS), neutron star-black hole (NS-BH), black hole-white dwarf (BH-WD) or black hole-helium star (BH-He).

In the case of NS-NS systems, after the black hole and accretion disk are created, the jet can be formed in ways similar to the ones described for the collapsar model in Section 5.1.4. The most simple way is neutrino-antineutrino annihilation, but the viscosity of the disk plays an important role. Depending on the value of the viscosity of the material of the torus, the energy released in neutrinos is larger if the viscosity is low. In this case the accretion timescale is of the order of 0.4 s to 1 s, giving enough time to radiate the internal energy through neutrino emission. If only this process is at play, the energy available to produce the relativistic fireball is around  $10^{50}$  erg, but to account for the apparent isotropic energy of  $10^{52}$  erg a very small collimation angle of  $10^{-2}$  sr would be needed. This strong beaming seems possible to achieve but to relax this condition other processes like the Blandford-Znajek mechanism can be invoked to extract enough additional energy. The simulations of these processes, including General Relativity (GR) hydrodynamics and realistic Equation Of State (EOS), show that the isotropic equivalent energy attainable spans a range from  $10^{49}$  to  $10^{51}$  erg and that the collimation angle is larger ( $5^\circ$ - $10^\circ$ ).

In BH-NS binary systems, the neutron star is tidally disrupted and the debris form a torus around the black hole. First simulations of BH-NS system showed that for different values of the ratio between the NS and BH masses the neutron star is totally disrupted and that the mass of the accretion disk is few tenths of a solar mass, as showed by Lee and Kluźniak (1999). The resulting accretion rate is high, between 2 and  $6M_\odot\text{s}^{-1}$ , so that the torus lifetime is short, of the order of 50 ms. The region corresponding to the rotational axis of the system is almost matter-free and the relativistic fireball can be formed. These results strongly depend from the EOS used: some of them require a high mass ratio for the torus to be created and to totally disrupt the NS. If the accretion disk is formed, the energy available in BH-NS systems is generally larger compared to NS-NS systems, even if it depends on the conversion efficiency. The formation of the torus is also affected by the mass of the black hole. Studies with explored masses from 14 to  $20M_\odot$  show that a) a torus is formed but it is thin and cold or b) the torus is not created at all. So in this kind of system, solar mass black holes accompanied by a neutron star are the possible progenitors of short GRBs, given the short timescales involved.

Other binary systems proposed to be responsible of the formation of GRBs are black hole-helium star and black hole (or neutron star)-white dwarf. In the former case, the time needed to gain enough energy to power a GRB is of the order of tens of seconds, so that it could be responsible of long GRBs, see Fryer and Woosley (1998). A similar situation holds for BH-WD or NS-WD systems, see Fryer et al. (1999): the accretion disk in some cases could be convection-dominated with matter escaping and not falling onto the black hole. This lowers the accretion rate: the energy available as neutrino-antineutrino pairs depends heavily on it and low accretion rates mean a low energy budget available. In any case, the timescale of

the disruption of the WD and the formation of the torus is 10-70 s, so BH-WD and NS-WD system would generate long GRBs.

Very recently it has been proven that binary neutron star systems are the progenitors of short GRBs (or at least of one class of short GRBs), thanks to the detection of GW170817 and GRB170817A, see for example Abbott et al. (2017e) and Goldstein et al. (2017). This topic will be addressed in more detail in Section 5.2.

### 5.1.5 High Energy emission from GRBs

The first detection of High Energy emission from GRBs was found by EGRET, one of the instruments on-board the CGRO (Hughes et al. 1980). It consisted of a spark chamber for the direction measurement of gamma-rays and a calorimeter, called *Total Absorption Shower Counter* (TASC), for energy measurement. EGRET was sensitive in the energy range 20 MeV-30 GeV and this made it the best instrument at the time to detect high energy emission from GRBs. EGRET detected five bursts (GRB910503, GRB910601, GRB930131, GRB940217, GRB940301; see for example Merck et al. (1995)) with its spark chamber and few others with the TASC, sensitive in the lower energy range 1-200 MeV. The common feature among EGRET-detected GRBs is the GeV delayed emission: the most striking case in this sense was GRB940217 (Hurley et al. 1994), which presented emission of gamma-rays (28 in total) up to 5400 s after the onset, with a 18 GeV detected at  $\sim T_0 + 4500$  s (see Figure 5.9). Ten of the eighteen photons detected by EGRET were detected while the low energy emission was still active, as seen by Ulysses and BATSE, but additional 18 photons were detected starting from  $T_0 + 4500$  s after EGRET occultation by the Earth for  $\sim 3700$  s, when low energy emission ceased. This was a hint to the long-lasting activity of GeV emission with respect to the low energy one and of the possible presence of additional spectral components to explain the HE emission.

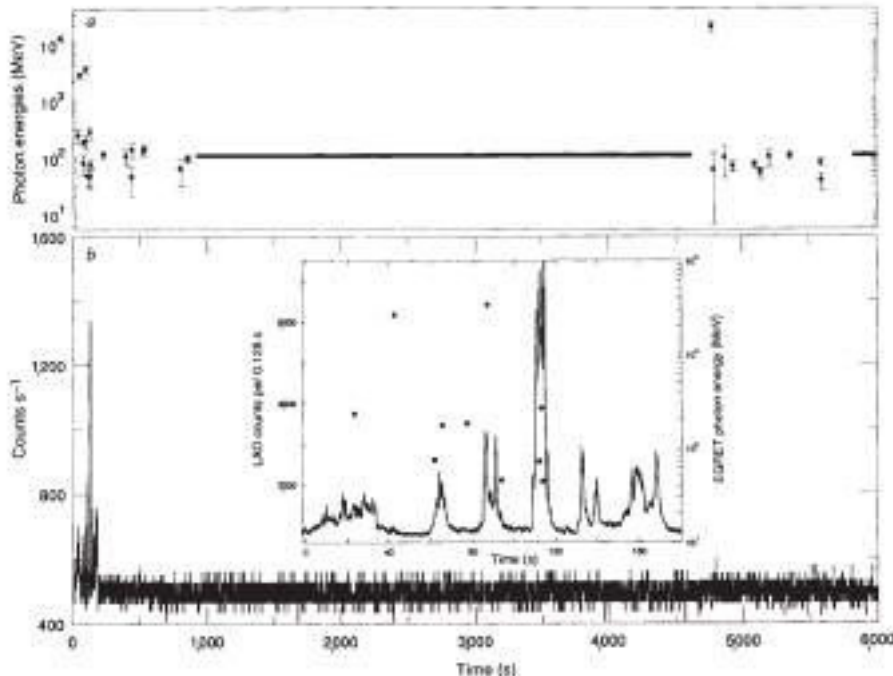


Figure 5.9: **Top:** photon energies detected by EGRET from GRB940217. The horizontal line is the time when EGRET was occulted by the Earth. **Bottom:** count rates of Ulysses in the 25-150 keV. The inset shows the first 200 seconds of the BATSE light curve and the photons detected by EGRET in that time interval. From Hurley et al. (1994).

This was the case for GRB941017 (González et al. 2003), detected by EGRET, BATSE and

COMPTEL: the high energy component detected by EGRET's calorimeter TASC is well fitted with a power-law with index  $\sim -1$  up to 200 MeV throughout all the burst duration, has a fluence above 30 keV three times larger than the one estimated in the BATSE energy range and lasted about 200 s. The low energy portion of the data was fitted instead with a Band function in different temporal bins. The data were inconsistent with the emission of  $\gamma$ -rays by synchrotron alone and prompted for other theoretical explanations. The most fitting ones were found in Granot and Guetta (2003a) to be synchrotron self-Compton from the reverse shock created when the GRB ejecta are decelerated by the ambient medium and Inverse Compton in the reverse shock by electrons in the forward shock with synchrotron self-absorption taken into account as shown in Pe'er and Waxman (2004). The first model seems to be disfavored because it requires very high Lorentz factors  $\gtrsim 10^4$  and a value of the magnetic field much lower from the ones implied by afterglow observations.

It was clear from these observations that the high-energy component of GRBs had different features with respect to the low-energy emission. The open questions after the EGRET era were mostly related to the jet physics and particle acceleration (collimation, value of the Lorentz factor) and to the nature of the high energy emission (a second emission component? is it present also during the prompt phase or only in the afterglow?).

A more in-depth study of high energy emission from GRBs came with the launch of AGILE in 2007 (Tavani et al. 2009b) and Fermi in 2008 (Atwood et al. 2009). The old generation of gamma-ray imagers like EGRET had the limitations of a small FoV and a large dead time. With the use of silicon trackers these difficulties are overcome and AGILE was the first satellite with this kind of technology, then followed by Fermi.

One of the most interesting GRBs observed by AGILE is GRB080514B (Giuliani et al. 2008), which was detected by all the instruments on-board AGILE (SuperAGILE, GRID and MCAL). In particular, the GRID detector allowed the detection of photons above 25 MeV, with the maximum energy photon of about 300 MeV. The light curve of the burst in SuperAGILE in hard X-rays (17-50 keV) shows a duration of 7 s and a multipeak structure, but the high energy photons do not coincide with these peaks. Only three photons with energy  $\sim 30$  MeV were detected within 2 s from  $T_0$  while the others arrived when the X-ray emission already faded to levels compatible with the background up to  $\sim 30$  s after the burst onset. Since the statistic was not limited by the instrumental dead time like in the EGRET case, these results are robust and confirm the delayed and relatively long-lasting of the high energy emission, whose evolution in time seems to be very different from the one in X-rays, suggesting a rapid variation in the  $\gamma$ -ray to X-ray flux ratio.

Another interesting GRB detected by AGILE-GRID is GRB100427B (Del Monte et al. 2011), which turned out to be the brightest GRB detected by AGILE in gamma rays with a total fluence between 22 MeV and 3.5 GeV of  $(0.25 \pm 0.05)$  ph/cm<sup>2</sup>. Both the MeV and GeV light curves show two bumps with the second peak broader than the first one and no significant delay with respect to the X-ray emission was observed. Spectral evolution between the bumps and the interbump region in MCAL data was detected at the level of  $4.0\sigma$ , with the second bump being harder than the first. The time integrated spectrum for both MCAL and GRID data has a spectral index of  $-2.13$ , compatible with the  $-2.04_{-0.14}^{+0.31}$  index measured for GRID data only, showing that a single power law is adequate to model the spectrum from 500 keV to 3.5 GeV. Finally, the highest energy photon detected during the burst, a 3.5 GeV photon arrived at  $T_0 + 65.9$  s allowed to put a constraint on the minimum Lorentz factor during the prompt emission between 50 and 900 depending on the redshift, which was not determined for this GRB.

For other GRBs observed by AGILE, not detected by GRID, upper limits were derived and found to be consistent with an extrapolation of the Band spectrum up to GeV energies, see Longo et al. (2012).

Regarding the study of the high energy emission, the Fermi satellite with its two instruments GBM and LAT (Atwood et al. 2009) for sure is the one giving us more detailed results and

the highest statistics. This is possible mainly because GBM is an all-sky monitor sending real-time repointing requests to the LAT instrument in case of interesting GRBs. Thus they are placed in the center of the LAT FoV in order to maximize sensitivity. In order to find common properties in the high energy emission of LAT-detected GRBs, it is useful to consider some of them one by one.

The first GRB detected by LAT was GRB080825C (Abdo et al. 2009b). It was a long GRB with  $T_{90} = 27$  s as calculated in the 50-300 keV energy range. The GBM lightcurve shows a multi-peak structure, with the emission almost fading at  $T_0 + 25$  s. The LAT lightcurve instead shows one first peak with three events in coincidence with the second GBM peak and then a quite emission with no events up to  $\sim T_0 + 16$  s. After that, more photons were detected by the LAT, both within and after  $T_{90}$ . In particular, the highest energy photon ( $(572 \pm 58)$  MeV) from this GRB was detected at  $\sim T_0 + 28$  s, so just after the NaI emission decreased almost at background level. As far as the time-resolved spectroscopy is concerned, the spectrum in time bins considered in Abdo et al. (2009b) is well fitted by a Band function with the typical hard-to-soft evolution for  $E_{\text{peak}}$ , except for the last one which is compatible with a power law with a harder index  $-1.95 \pm 0.05$ . This fact and the low flux between the first two peaks in the LAT lightcurve may suggest a different region for their emission (internal and external shock respectively).

The second LAT-detected burst, GRB080916C, is particularly interesting because it is one

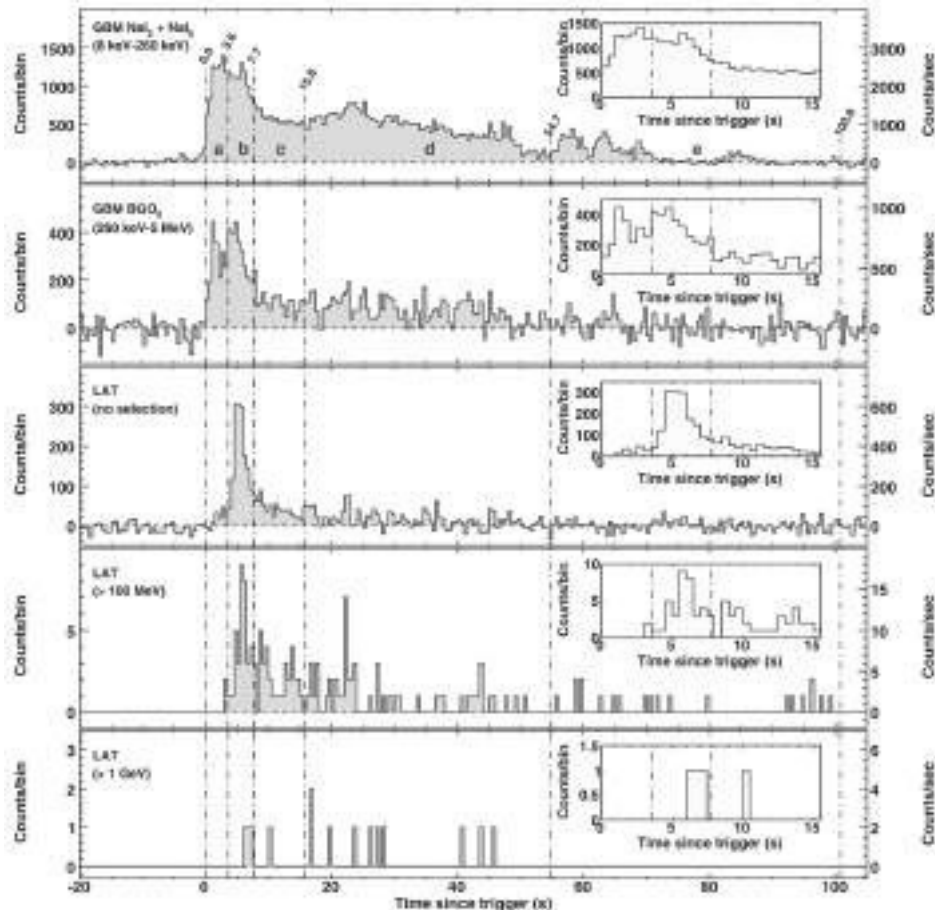


Figure 5.10: Light curves of GRB080916C for GBM and LAT observations. The first two graphs show the GBM light curves from the NaI and BGO detectors. The third shows the LAT lightcurve without any selection. The last two graphs show the LAT lightcurves with energy selection above 100 MeV and 1 GeV respectively. The insets are zooms on the first 15 seconds for each lightcurve. From Abdo et al. (2009c).

of the brightest ones and has a measured redshift of  $z = 4.35 \pm 0.15$  (Abdo et al. 2009c). GRB080916C exhibited two features then confirmed in other LAT detected GRBs: the delayed onset of the LAT pulse and the long-lived emission for  $E > 100$  MeV. The former is clear from the comparison of the GBM (BGO, 260 keV-5 MeV) and the LAT ( $> 100$  MeV) lightcurves shown in Figure 5.10: the first GBM peak, from  $T_0$  to  $T_0 + 3.6$  s, has no corresponding peak in the LAT lightcurve. Instead, the first LAT pulse is seen in coincidence with the second GBM peak, from  $T_0 + 3.6$  s to  $T_0 + 7.7$  s. This suggests a common origin for the two peaks but in a spatially different region, likely different pairs of colliding shells within the internal shock scenario. The long-lived emission was proved with a maximum likelihood analysis and was found to be significantly present up to  $T_0 + 1400$  s above 100 MeV, well after the fading of the GBM emission at background level. Including the other time intervals, the declining high energy flux is well fitted by a power law  $t^{-\alpha}$  with  $\alpha = -1.2 \pm 0.2$ . The GBM flux instead shows a quite different behavior: the flux decays as  $t^{-0.6}$  up to  $T_0 + 55$  s, then it decays faster as  $t^{-3.3}$ . This would be a hint to the different nature of the high energy emission, but no spectral hardening is seen in the LAT late spectrum, as in the case of GRB080825C. The observation of GRB080916C allowed to set a lower limit to the Lorentz factor of the relativistic jet equal to  $\Gamma_{\min} = 887 \pm 21$ , taking into account that the highest energy photon detected had  $E = 13.2$  GeV. Finally, GRB080916C holds the record as the GRB with the highest source frame energy release of  $E_{\text{iso}} = 8.8 \cdot 10^{54}$  erg, calculated in a standard cold matter cosmology. Such high value, which is 4.9 times the rest mass of the Sun, suggests an highly collimated jet.

Beside long GRBs, LAT detected also some short GRBs: some interesting cases are GRB081024B (Abdo et al. 2010a) and GRB090510 (Giuliani et al. 2010; Ackermann et al. 2010).

The former is the first short GRB detected by LAT, with a duration of 0.8 s below 5 MeV. The emission above 100 MeV is seen to be delayed (the first photon detected by LAT comes 0.229 s after the trigger) and long lasting ( $T_{90} = 2.6$  s above 100 MeV) up to  $T_0 + 3$  s.

GRB090510 is a short GRB detected by both AGILE and Fermi. Both instruments data show a delayed high energy emission at  $\sim 0.1$  s after the onset, as shown in Figure 5.11 (interval *a*). During the prompt phase, LAT detected a photon with energy 30.5 GeV, implying a lower limit for the Lorentz factor  $\Gamma_{\min} \gtrsim 1200$  assuming the estimated redshift  $z = 0.903$ . The most striking feature of GRB090510 is its time integrated spectrum for the prompt emission: the usual Band is not enough to fit the GBM+LAT data, but an additional power law with index  $-1.62 \pm 0.03$ , dominant below 20 keV and above 100 MeV, is necessary (see Figure 5.12). Moreover, the afterglow emission has been detected by LAT to extend up to  $\sim T_0 + 150$  s. This prompted several theoretical interpretation for both the prompt and afterglow phase of this particular burst, like synchrotron for the Band function and SSC for the hard component. However difficulties arise in explaining the delayed onset of the high energy emission, since the SSC model predicts a too short delay in the assumptions of weak magnetic field. Also hadronic scenarios were proposed but as shown in Asano, Guiriec, and Mészáros (2009) the proton injection isotropic-equivalent energy required is more than two orders higher than the one actually measured for the burst ( $E_{\text{iso}} = (1.80 \pm 0.06) \cdot 10^{53}$  erg). These observations of short GRBs, in particular of GRB090510, show that SGRBs are as relativistic as long GRBs and that they seem to have a better efficiency in emitting gamma-rays since the energy emitted at high energy (100 MeV-10 GeV) is greater than the one at low energy (20 keV-2 MeV), but the statistic is still limited to few bursts to draw a definitive conclusion.

Other GRBs showing a delayed emission with an additional component are GRB090902B and GRB090926A, presented in Abdo et al. (2009a) and Ackermann et al. (2011) respectively.

For the former, a long GRB with  $T_{90} = 21.9$  s the delayed  $> 100$  MeV emission started at  $\sim T_0 + 9$  s and was detected in LAT data up to  $T_0 + 1000$  s, with the lightcurve showing a temporal behavior as a power law  $t^{-1.5 \pm 0.1}$ . The upper limits obtained for times after  $T_0 + 3600$  s when the Earth's limb exited the FoV are compatible with the extrapolation of

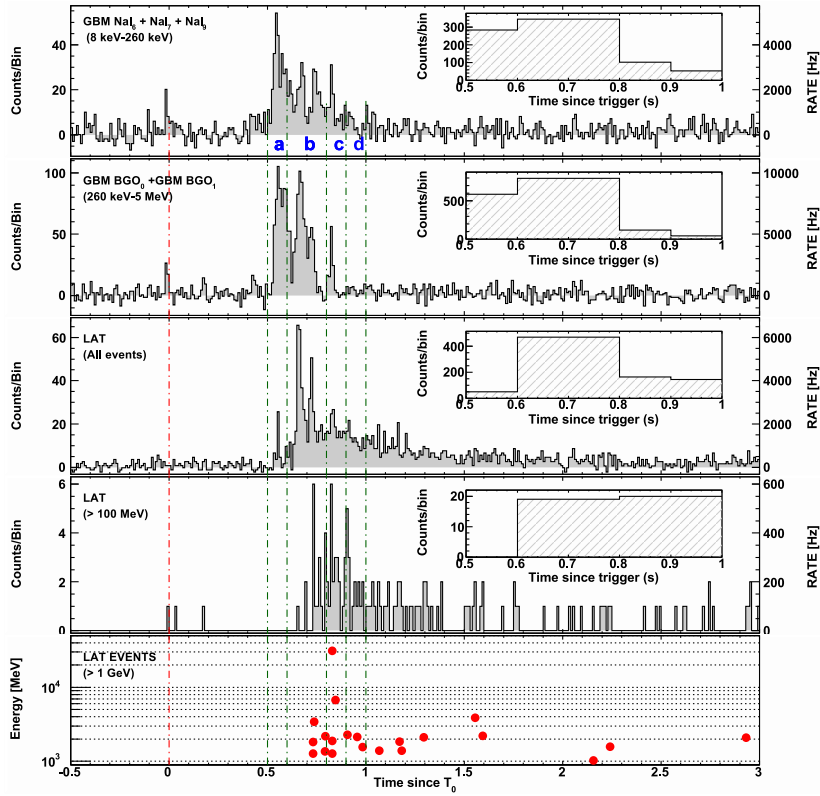


Figure 5.11: Fermi-GBM and Fermi-LAT light curves for GRB090510 (top four panels). The fourth panel shows only events with energy above 100 MeV. The last panel shows the energies of the photons detected by Fermi-LAT as a function of time from the trigger  $T_0$ . The insets are zooms on the first 1 second of the light curves. From Ackermann et al. (2010).

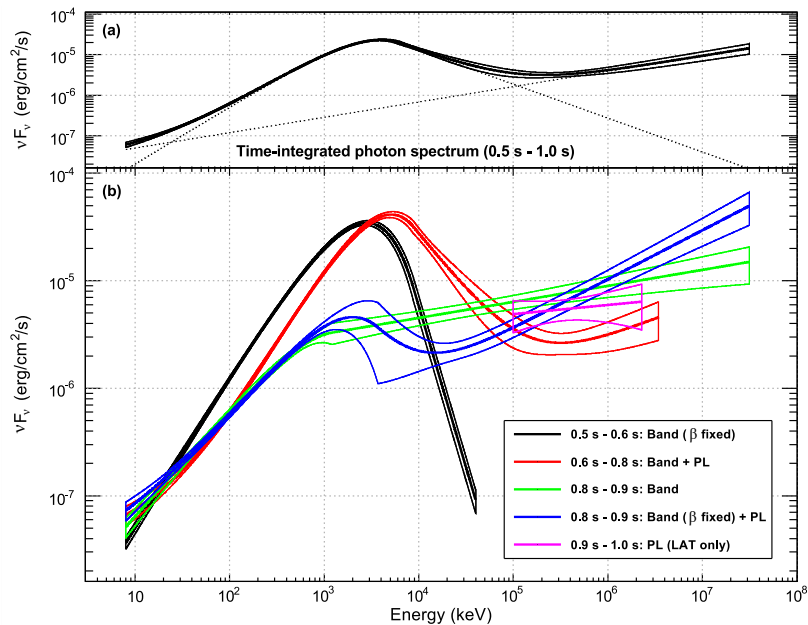


Figure 5.12: **(a)**: Fermi time-integrated spectrum of GRB090510 in the 0.5 s-1.0 s time range. The best fit is the sum of two components (dotted lines), a Band function and a power-law. The resulting spectrum is shown as a solid line with  $\pm 1\sigma$  contours. **(b)**: GRB090510 spectra with  $\pm 1\sigma$  contours for different time ranges, shown in the legend together with the function which best fits the data in a given time range. From Ackermann et al. (2010).

that power law. Moreover the time integrated spectrum of the prompt phase shows a clear additional power law component to the Band function with a spectral index  $\sim -1.9$  during all the prompt emission. The most energetic photon had  $E = 33.4$  GeV and was detected after 82 s from the trigger, so already in the early afterglow phase. To constrain the bulk Lorentz factor, the 11.16 GeV photon detected during the prompt phase was used to derive a minimum value  $\Gamma_{min} \approx 1000$ , taking into account of the variability timescale of 53 ms seen in BGO data.

GRB090926A is another long GRB with  $T_{90} = (13.1 \pm 0.2)$  s. It shows a delayed LAT emission by 3.3 s with respect to the GBM emission which lasts up to  $\sim T_0 + 4800$  s. The time decay is well fitted with a power law  $t^{-1.66 \pm 0.03}$ . The most interesting feature of this GRB is the additional high energy component to the Band function: the time integrated GBM+LAT joint spectrum shows a spectral break at 1.4 GeV. This result is important since it allows to calculate a value for the bulk Lorentz factor and not just an upper limit, considering a simple assumption of a uniform, isotropic and time independent in the comoving frame photon field. The result of this analysis yielded  $\Gamma \simeq 720 \pm 76$  while taking into account a full-time dependent model, as tried by Granot, Cohen-Tanugi, and Silva (2008), this value reduces to  $\Gamma \simeq 220$ .

Even if in most of the GRBs the additional component to the Band function needed to describe the joint LAT/GBM data is a power law, in other cases a thermal spectral component is observed, like in GRB100724B, detected by GBM (Guiriec et al. 2011) and AGILE (Del Monte et al. 2011). In the first work (Guiriec et al. 2011), the GBM prompt spectrum integrated in time ( $T_0 - 1.024$  s to  $T_0 + 83.969$  s) is best fitted by a Band function plus a thermal blackbody spectrum with  $kT = (38.14 \pm 0.87)$  keV. This additional component is seen to not vary during time, while the Band component evolves showing a decreasing value for  $E_{peak}$ , so it seems to be a different spectral emission. From the theoretical point of view, the blackbody spectrum points to the presence of a photospheric emission in the context of the standard fireball scenario. A more recent analysis, see Vianello et al. (2017) but also Ackermann et al. (2013b), shows that the GBM and LAT Low Energy (LLE) data can be fitted by a Band function with an high-energy cutoff at  $E_c = (48 \pm 6)$  MeV, to be interpreted in the most natural way as due to the intrinsic opacity to pair production in the source. The optional explanation as an intrinsic cutoff in the emission process e.g. synchrotron was ruled out in Vianello et al. (2017).

As a final example of Fermi detected bursts, GRB130427A is the brightest one observed, see Ackermann et al. (2014). It is, to date, the record holder as far as fluence ( $4.2 \cdot 10^{-3}$  erg/cm<sup>2</sup> from 10 keV to 20 MeV), highest energy photon (95 GeV at  $T_0 + 244$  s) and high-energy emission duration (up to 100 ks after the trigger, see Figure 5.13) are concerned. The total apparent isotropic gamma-ray energy,  $E_{\gamma,iso} = 1.4 \cdot 10^{54}$  erg given the redshift estimate  $z = 0.34$ , is second only to other LAT GRBs like GRB080916C, GRB090902B and GRB090926A. As other LAT detected GRBs, GRB130427A shows a delayed emission starting about 10 s after the trigger when GBM brightest emission already ended. The main difference in this case is that the LAT emission appears to be temporally and spatially uncorrelated to the GBM one, pointing to a different region or mechanism for the two emissions. GRB130427A challenges also theoretical models: having a 95 GeV photon in the early afterglow and a 32 GeV at  $T_0 + 34.4$  ks does not find any explanation in the standard synchrotron emission from electrons accelerated in the external shock or in the SSC scenario, at least according to Ackermann et al. (2014). The combined Fermi, Swift, NuSTAR and ground-based optical data were used in Kouveliotou et al. (2013) to fit the spectrum from optical to GeV energies with a single synchrotron component. In Liu, Wang, and Wu (2013) an afterglow SSC emission is proposed to explain the long-lasting emission. This shows that high energy emission from GRBs still lacks a clear physical explanation, both in the prompt and in the afterglow.

After all these examples, it is advisable to briefly summarize the features of high energy emission from GRBs, as shown by the examples by AGILE and Fermi:

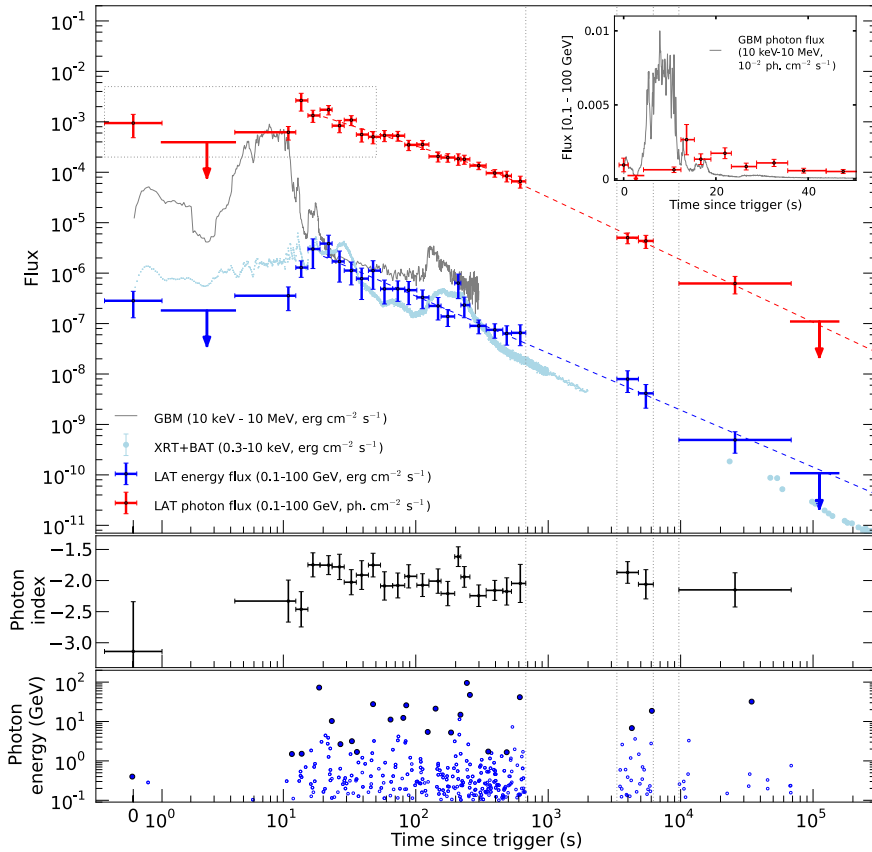


Figure 5.13: Energy flux light curves as measured by Fermi (LAT and GBM) and Swift (BAT and XRT) for GRB130427A (top panel). The second panel shows the evolution in time of the spectral index for the power-law used for fitting Fermi-LAT data. The last panel shows individual photon energies in time recorded by the LAT. It is clear from the time axis extending up to over  $10^5$  s that the LAT emission is clearly extended in time. From Ackermann et al. (2014).

1. the Band model is not sufficient to describe the low and high-energy spectra together. An additional component or a cutoff are needed, with no unique solution for all LAT GRBs. Most of the times an extra power law is enough (GRB090510, GRB090902B) but in other cases a cutoff is needed (GRB100724B). Few other GRBs require the use of a thermal blackbody component.
2. LAT detected GRBs are among the brightest detected by the GBM. The energy released in high-energy gamma-rays ( $> 100$  MeV) in the extended temporal phase is about 10% of the total energy radiated in the prompt phase. The high- (100 MeV-10 GeV) to low-energy (10 keV-1 MeV) fluence ratio is  $\lesssim 20\%$ , with an exception for short GRBs (see Figure 5.14)
3. the high energy emission is extended in time well after the low-energy emission has faded. The temporal decay is consistent with a power law behavior  $t^{-\alpha_L}$  with  $\alpha_L \sim 1$
4. the onset of the high-energy emission is delayed with respect to the low-energy one.

These conclusions are the same resulting from the first Fermi-LAT GRB catalog, presented in Ackermann et al. (2013b), an in-depth systematic study of LAT-detected GRBs in the first three years of the mission.

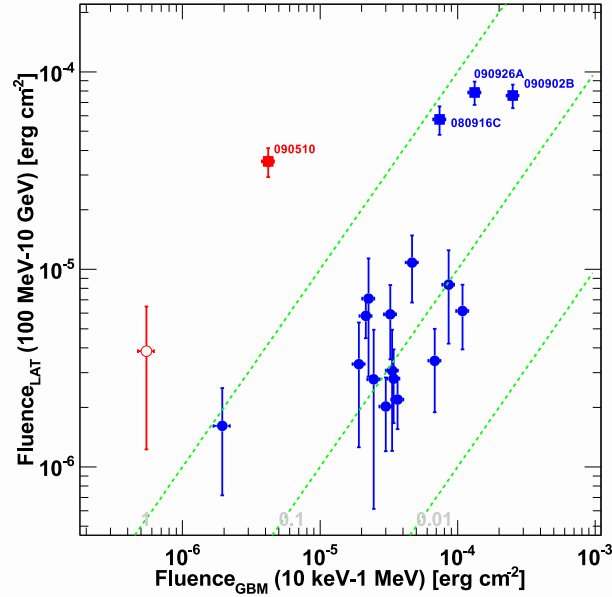


Figure 5.14: Fluence measured by Fermi-GBM (10 keV-1 MeV) versus the fluence measured by Fermi-LAT (100 MeV-10 GeV) for GRBs detected by both instruments. Blue points are long GRBs, while red ones are short GRBs. The green dashed lines correspond to 100%, 10% and 1% fluence ratios. From Ackermann et al. (2013b).

### 5.1.6 High and very high energy emission models for GRBs

In the previous section I focused on the observational status of GRBs at high energies with Fermi and AGILE. To justify the follow-up of GRBs at VHE by MAGIC, the fact that few GRBs detected by Fermi-LAT have photons at energies above few tens of GeV is not enough. For this reason one must also rely on theoretical models predicting emission from GRBs at very high energies. Usually these models are developed to explain the observation of particular bursts but they can also have a more generic application extended to other GRBs. For simplicity, theoretical models predicting high and very high energy emission from GRBs can be divided into two categories: models attributing the emission either to internal shocks or to external shocks. An additional subdivision is between leptonic and hadronic models, as described below. For a review, see Fan and Piran (2008). A generic scheme with the expected signature from GRBs at high energies is shown in Figure 5.15.

#### HE-VHE emission from internal shocks

One of the most popular explanations for HE-VHE emission from GRBs in the internal shock scenario is the synchrotron self Compton (SSC), that is the up-scattering of the synchrotron photons by their parent relativistic electrons to much higher energies. An example of this model is presented in Galli and Guetta (2008): the flow Lorentz factor  $\Gamma$  varies on a timescale  $t_v$  and has an amplitude of  $\delta\Gamma \sim \Gamma$ . The shells thus collide at a radius  $R \approx 2\Gamma^2 ct_v$  and in the collision there is a distribution among electrons, magnetic field and protons of the internal energy released. Electrons in particular are accelerated obtaining a power law distribution in energy and cool by both synchrotron and SSC mechanisms. The relative cooling importance of synchrotron and SSC is ruled by the Compton parameter  $Y$ . Both the opacity of the high-energy photons to pair production due to interaction with lower energy photons and the Thomson optical depth due to pair production are taken into account for the high-energy spectral cutoff. Detailed formulas for the synchrotron and SSC spectra are given in Guetta and Granot (2003a), while in Guetta and Granot (2003b) also the Klein-Nishina suppression

is taken into account. Depending on the values of  $\Gamma$  and  $t_v$ , the cutoff energy is shifted to lower or higher energies, giving the possibility to have GeV emission with  $\Gamma > 350$  and  $t_v = 1$  ms, with the SSC emission dominating above 100 MeV. An interesting possibility in this model is the delayed high-energy (MeV-GeV) emission in the internal shocks from the up-scattering of CMB photons by electrons or positrons produced by gamma rays with  $E \gg 300$  GeV in the prompt and IR background photons. This strongly depends from the strength of the intergalactic magnetic fields (IMGF) and it would be a detectable effect only at few Mpc from the GRB, see Dai and Lu (2002).

A collection of hadronic models is given in Razzaque, Dermer, and Finke (2010). The considered process is synchrotron radiation from cosmic ray protons accelerated in a magnetically-dominated shocked plasma with  $\Gamma \lesssim 1000$ . The resulting gamma rays will have GeV-TeV energies, but most of them will be lost due to pair production opacity. The delay seen in the high energy emission observed by AGILE and LAT is naturally explained within this model by the time needed to accelerate protons to sufficient energies for an efficient synchrotron radiation. An interesting result is that the energetics required is proportional to  $\Gamma^{16/3}$ , so that moderate values of the Lorentz factors are needed to find a matching with observations. A second example for hadronic models is given in Asano, Guiriec, and Mészáros (2009): the primary process is photomeson ( $p\gamma$ ) interaction but the resulting photon spectrum is due to either synchrotron emission or Inverse Compton from secondary  $e^+ - e^-$  pairs produced by the  $\gamma + \gamma \rightarrow e^+ - e^-$  process. GeV-TeV emission is expected (Asano and Inoue 2007; Asano, Inoue, and Mészáros 2009) and in this context the observations by Cherenkov telescopes is crucial to obtain photon statistics and resolve the spectrum both in time and energy. Despite this model looks very appealing, its initial luminosity requirement is very large ( $E > 10^{55}$  erg/s), which is hard to reconcile with observation (e.g. in the case of GRB090510).

### HE-VHE emission from external shocks

Within the external shock scenario, several possibilities of high and very high energy emission could arise due to the forward or the reverse shock.

In the forward shock, two popular models consider the synchrotron self Compton mechanism. In Sari and Esin (2001) the synchrotron self Compton mechanism is considered as the source of the high energy emission. Both the synchrotron and Inverse Compton spectra are computed in a detailed way in both the slow and fast cooling case. In Zhang and Mészáros (2001), three different emission mechanisms are considered: electron synchrotron, proton synchrotron and Inverse Compton. The last emission mechanism is computed starting from the work in Sari and Esin (2001). The three corresponding spectral components can dominate one above the other depending on the values of the microphysical parameters  $\epsilon_e$  and  $\epsilon_B$ . The conclusion of this study is that the electron IC component is the most likely origin of GeV gamma rays since it dominates above the other two components in a wide region of the  $\epsilon_e - \epsilon_B$  parameter space.

In the reverse shock scenario, a solution is again SSC emission (Wang, Dai, and Lu 2001) which peaks at few hundreds MeV, but fails in explaining the high energy components of some bursts like GRB941017, see Granot and Guetta (2003b).

Other models consider the emission from both the forward and reverse shock, as discussed in Fraija et al. (2016) to explain the emission of GRB090510.

Finally, also in the external shock scenario, hadronic models can explaining the origin of high energy gamma rays, as shown in Böttcher and Dermer (1998). Protons can be accelerated to very high energies and interact with photons to produce pions and eventually gamma rays, which can gain energy thanks to the SSC mechanism. Also, protons can radiate via synchrotron emission. The signatures of these processes, in particular the temporal decay rates, are different and could be distinguished thanks to HE and VHE observations.

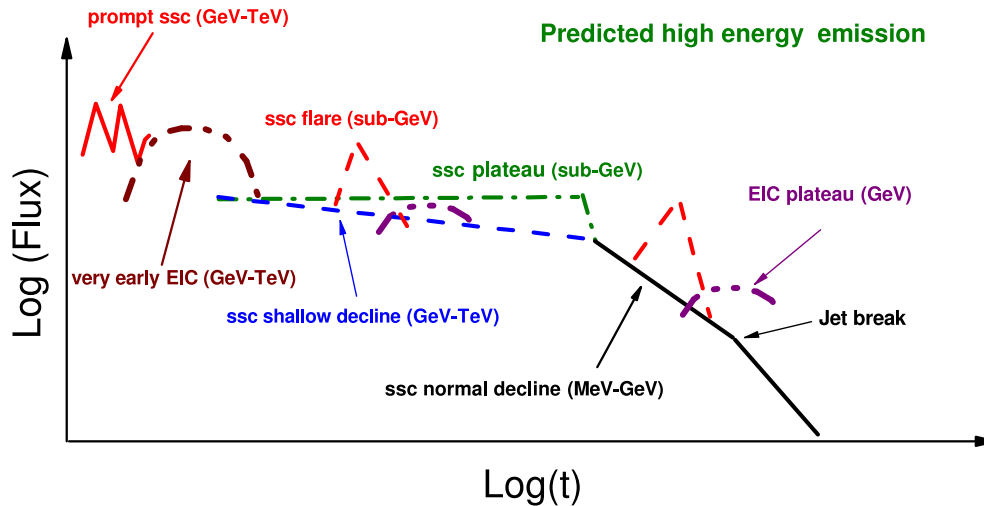


Figure 5.15: Expected high energy emission signatures from GRBs in different emission phases, from both the prompt and afterglow. From Fan and Piran (2008).

### Follow-up of GRBs at very-high energies: motivations and current status

Since their first light, IACTs have been trying to detect GRBs in the VHE range, setting up strategies for their follow-up thanks to the distribution of the coordinates from satellite-based experiments (in the beginning only by Swift and INTEGRAL, then AGILE and Fermi joined). Many models, as explained in the previous Section, were predicting that GRBs should have been VHE emitters and the predicted VHE fluxes seemed to be detectable by IACTs given their sensitivity. After the launch of Fermi and the detection of  $\sim 100$  GeV photons by Fermi-LAT, the follow-up of GRBs by IACTs became even more important. Cherenkov telescopes can reach low energy thresholds: MAGIC for example has an energy threshold at zenith and after analysis cuts of 70 GeV and its good sensitivity and collection area at low energies in principle allow to collect a large photon statistic. Since most GRBs are very distant, their flux is absorbed by the EBL and having a low energy threshold is essential in order to have a chance of detection. Nevertheless, it is not known if an extrapolation of power law spectra usually seen in Fermi-LAT GRBs is a suitable assumption, since spectral cutoffs can show up like in the case of GRB090926A. This problem is directly linked to the second motivation for following-up GRBs: a detection at VHE would allow to distinguish between the plethora of models discussed in the previous paragraphs and give more insights on GRBs emission mechanisms and jet physics (e.g. determine the Lorentz factor  $\Gamma$  of the outflow). Moreover, it would allow to study the EBL at redshifts which are not possible to reach with AGN and put tight constraints on processes which could possibly modify the propagation of  $\gamma$ -rays, like axion-like particles or Lorentz invariance violation, see De Angelis, Galanti, and Roncadelli (2011) and Kifune (1999).

As of today, no GRBs has been detected by IACTs (MAGIC, H.E.S.S. and VERITAS) or EAS arrays like HAWC and only upper limits could be computed (Aliu et al. 2014; Acciari et al. 2011b; Aharonian et al. 2009c; H.E.S.S. Collaboration et al. 2014; Aharonian et al. 2009b; Abeysekara et al. 2015b; Alfaro et al. 2017). The Milagro experiment found an evidence for TeV emission from GRB970417A, a burst detected by BATSE, with a chance probability of  $2.8 \cdot 10^{-5}$  for the excess to be a fluctuation of the background as stated in Atkins et al. (2000). This result is still under debate. As far as IACTs are concerned, the follow-up of GRBs is problematic due to GRBs serendipitous nature and to the small FoV of Cherenkov telescopes. This means that GRBs are observed with a certain delay and the observation conditions can be very different. In particular a large zenith angle of observation results in a high energy threshold and so in a stronger effect of the EBL on the possible VHE

emission of GRBs. Also, the poor localization in some cases (Fermi-GBM) can play a major role.

The past and recent follow-up of GRBs performed by MAGIC is presented in Section 5.1.8.

### 5.1.7 Other emission from GRBs

Beside electromagnetic radiation, GRBs are believed to be accompanied by other types of emission: high energy neutrinos, cosmic rays and gravitational waves. The first two messengers, together with photons, are probably related to the shock acceleration and can give us information about the shock model. Gravitational waves instead, if detected in coincidence with GRBs, can reveal the nature of the progenitor especially in the case of short GRBs (see Section 5.1.7). The emission of neutrinos, cosmic rays and gravitational waves will be briefly reviewed in this Section.

#### High energy neutrinos from GRBs

The fireball model described in Section 5.1.3 allows the presence of a certain amount of baryons, even if within a certain loading to let the relativistic outflow to be produced. So it means that together with electrons, protons are accelerated within the GRB jet. The maximum energy attainable by protons is greater than  $10^{20}$  eV, so in the ultra high energy range. The most relevant process, assuming that the acceleration of protons happens in a site where photon are also present, is the  $p\gamma$  interaction:

$$p\gamma \rightarrow \Delta^+ \rightarrow \begin{cases} n\pi^+ \rightarrow n\mu^+\nu_\mu \rightarrow ne^+\nu_e\bar{\nu}_\mu\nu_\mu \\ p\pi^0 \rightarrow p\gamma\gamma \end{cases} \quad (5.18)$$

This process is at play only if the condition:

$$E_p E_\gamma \gtrsim 0.147 \text{ GeV}^2 \left( \frac{\Gamma}{1+z} \right)^2 \quad (5.19)$$

Since in the decay of the  $\Delta$  resonance about 20% of the proton energy goes to the pion and its energy is then evenly distributed among four leptons, we have that the average energy of the resulting neutrinos from pion decay is  $E_\nu \sim 0.05E_p$ .

Beside the  $p\gamma$  interaction, also hadronic collisions can be responsible of neutrino production:

$$pp \rightarrow pn\pi^+/K^+ \rightarrow pn\mu^+\nu_\mu \rightarrow pne^+\nu_e\bar{\nu}_\mu\nu_\mu \quad (5.20)$$

$$pn \rightarrow pp\pi^-/K^- \rightarrow pn\mu^-\bar{\nu}_\mu \rightarrow ppe^-\bar{\nu}_e\bar{\nu}_\mu\nu_\mu \quad (5.21)$$

$$pn \rightarrow nn\pi^+/K^+ \rightarrow nn\mu^+\nu_\mu \rightarrow nne^+\nu_e\bar{\nu}_\mu\nu_\mu \quad (5.22)$$

Depending on the energy reached by the protons and on the photon energy (so depending on the site), the energy of neutrinos can be very different. Within the internal shock, where photon energies are of the order of hundreds of keV, neutrinos can reach sub-PeV and PeV. At the deceleration radius the typical photon energy is of the order of 1 eV, giving a final neutrino energy in the EeV regime. While the jet is still in the acceleration phase, the Lorentz factor is smaller ( $\sim 10$ ) and the photon energy is around 5 keV. In this case, TeV neutrinos will be produced. If the ejecta are neutron-rich, the decoupling of protons and neutrons can start inelastic collisions between them, resulting in the production of  $\sim 10-100$  GeV. Finally, MeV neutrinos are expected to be produced by the GRB central engine, like in core collapse events.

The neutrinos produced in GRBs span a wide energy range, so they could be detected by ground detectors. For MeV neutrinos, only very close GRBs could be targeted and this makes the event rate to be very low. In the case of GeV neutrinos the atmospheric background would

be a huge nuisance, but reducible if one restricts the search in temporal and spatial coincidence with GRBs. An interesting outcome would result from the observation of TeV neutrinos: they would be produced even if the GRB fails and would probe the jet creation failure in core collapse stars, as shown by MacFadyen, Woosley, and Heger (2001). Finally PeV and EeV neutrinos detection can probe the internal shocks and external shocks production process, see Mészáros and Razzaque (2007). In the former case the neutrino flux will strongly depend on the photon spectrum of the prompt phase.

Currently no neutrino from GRBs was detected. The upper limits set by IceCube help in constraining the internal shock model but at the same time raise doubts on the possible GRB origin for cosmic rays (Aartsen et al. 2016; Aartsen et al. 2017a). A detection of neutrinos from GRBs would have a huge impact, since will help in understanding the acceleration mechanism and favor matter-dominated outflows instead of magnetic-dominated ones.

### Cosmic rays from GRBs

Strongly linked with the previous discussion is the possible association of GRBs as the production sites of Ultra High Energy Cosmic Rays (UHECRs). The creation of UHECRs from sources like AGNs or GRBs belong to the so called *bottom-up* models. A first argument favoring GRBs as UHECRs producers is that the outflow properties like the high Lorentz factor and high magnetic field density, which are necessary for the gamma-ray production itself, are required to accelerate protons up to  $10^{20}$  eV. So no modification of the fireball scenario would be required. A second argument is the comparison of the energy generation rate of gamma-ray by GRBs,  $\sim 10^{44}$  erg Mpc $^{-3}$ yr $^{-1}$ , with the one observed for UHECRs,  $4.5 \pm 1.5 \times 10^{44}$  erg Mpc $^{-3}$ yr $^{-1}$  (see Nagano and Watson 2000). However it is not known if GRBs inject the same amount of energy in gamma rays and in cosmic rays. The situation is aggravated by the fact that UHECR, like protons of energies  $10^{20}$  eV, have a mean free path before interacting with CMB photons which is of the order of tens of Mpc. So if GRBs produce UHECRs, they should be at nearby (cosmological) distances. Also the interaction of UHECRs in the intergalactic magnetic fields must be take into account, so that an angular deflection and a temporal delay are expected between the GRB and UHECRs arrival. This means that GRBs could be “hidden sources” of UHECRs, because no direct association would be present. The only way to be certain that GRBs produce UHECRs is then detecting high-energy neutrinos in spatial and temporal coincidence with them, as discussed in Section 5.1.7. This will be a clear signature that protons are accelerated up to  $10^{20}$  eV, which in turn can interact with the photons or neutrons (if present) to generate neutrinos. The results by Auger seem to disfavor the idea of UHECRs produced by GRBs in support of an origin from AGNs.

### Gravitational waves from GRBs progenitors

As anticipated in Section 5.1.4, GRBs can be accompanied by gravitational waves if their progenitors are compact objects like neutron stars or black holes. The gravitational wave signal carries with itself information about the objects which produced it, like their nature, mass and spin. This means that detecting a gravitational and electromagnetic signal from a GRB in temporal and spatial coincidence would reveal the nature of the progenitor. This is exactly what happened with the recent discovery by LIGO/Virgo and many electromagnetic facilities: a gravitational wave signal, GW170817, was found to be near-simultaneous and spatially consistent with a short GRB detected by Fermi-GBM, GRB170817A, see Goldstein et al. (2017). With this event, the short GRB-binary neutron star systems connection has been proven. More events are expected to be detected during the third LIGO/Virgo run and will help to strengthen and understand more the depth of this connection, in particular if also neutron star-black hole binary system can power a short GRB.

The non detection of BH-NS and NS-NS binary systems in the first observing run of Advanced LIGO was used to set upper limits on the rate of these mergers in Abbott et al. (2016d). The constrain on the rate of NS-NS systems with component masses of  $1.35 \pm 0.13 M_{\odot}$  is  $R_{NSNS} < 12\,600 \text{ Gpc}^{-3} \text{ yr}^{-1}$ , while the one on BH-NS mergers is  $R_{BHNS} < 3600 \text{ Gpc}^{-3} \text{ yr}^{-1}$  with NS masses of  $1.4 M_{\odot}$  and BH masses greater than  $5 M_{\odot}$ , considering an isotropic distribution of spin directions. The authors moreover compared the rate of BH-NS and NS-NS mergers with the rate of short GRBs,  $R_{GRB} = 10_{-7}^{+20} \text{ Gpc}^{-3} \text{ yr}^{-1}$ , to infer a lower limit on the opening angle of gamma-ray radiation of  $\theta_{min} > 2.3_{-1.1}^{+1.7}$  or  $\theta_{min} > 4.3_{-1.9}^{+3.1}$  assuming that short GRBs are produced by NS-NS or BH-NS mergers alone respectively. With the detection of GW170817/GRB170817A the estimate on the BNS merger rate has been updated, using the previous upper limit as a prior, to  $R = 1540_{-1220}^{+3200} \text{ Gpc}^{-3} \text{ yr}^{-1}$ , see Abbott et al. (2017a). It is now proven that the sensitivity of Advanced LIGO and Virgo together is high enough to detect a signal from BNS systems. A GRB-GW signal was detected, a breakthrough in GRB and GW physics, which established the role of multi-messenger physics as the prominent one in modern astrophysics. More on the connection between GRBs and GWs will be described in Section 5.2, dedicated to the follow-up of gravitational waves candidate events by the MAGIC telescopes.

### 5.1.8 Observation of GRBs with MAGIC

The MAGIC telescopes were designed since the single-telescope era (2004-2009) to be light and fast during slewing in order to perform the follow-up of GRBs in the best possible way. The goal of GRBs observation is to detect a VHE gamma-ray signal from GRBs and find out the processes producing this possible signal. The follow-up of GRBs can be difficult for the following reason:

1. they are unpredictable and given the small FoV of MAGIC, an external trigger is needed and a delay in the observation is unavoidable
2. they are distant sources and so the EBL comes into play reducing the flux of VHE photons reaching Earth
3. the atmospheric conditions and hardware issues can affect the follow-up, sometimes compromising the data which cannot be analyzed.

To cope with these difficulties, the MAGIC collaboration adopted the following countermeasures:

1. MAGIC is continuously in alert to GRB/transient alerts from satellites thank to **GSPOT** to be able to point every observable trigger. The delay is reduced with the GRB speed mode, so that the telescopes can be repointed in tens of seconds. This makes possible to perform the observation of the early afterglow or even the prompt phase in few cases. Thanks to this, multi-wavelength observations can be carried together with other  $\gamma$ -ray, X-ray or optical instruments
2. depending on the redshift, the effect of the EBL starts to be non-negligible at different energies. In order to operate in a regime where the EBL does not affect the spectrum, the MAGIC telescopes were designed with a huge 17m reflector to have an energy threshold lower than 100 GeV (at low zenith). The trigger and readout systems and the analysis methods were optimized as well in this direction
3. MAGIC monitors the weather conditions with many instruments, especially with the LIDAR. Data can be corrected for the effects of a non-perfect atmospheric transmission (but does not affect the significance of the signal). To lower the chance of hardware failures, the automatic procedure was changed in 2013: the DAQ is not stopped during slewing and the trigger tables are changed in the same movement.

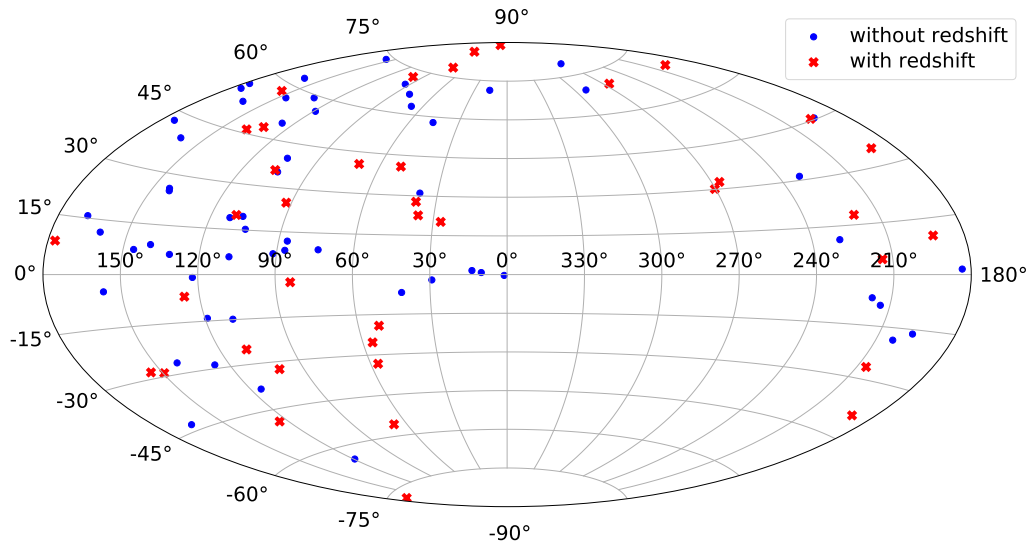


Figure 5.16: Skymap (Aitoff projection) in galactic coordinates of the GRBs observed by MAGIC between 2004 and August 2017 (only those with good data are shown). Crosses are GRBs without redshift, while circles are GRBs with redshift determination.

From this follows that GRBs are one of the most important science cases for MAGIC and for this reason they were one of the Key Observation Programs (KOP) up to 2017. Up to August 2017, MAGIC observed 97 GRBs. In this number only the bursts without major hardware issues and with acceptable weather conditions were included. The number of GRBs actually followed-up is higher. Figure 5.16 shows a skymap with the GRBs observed by MAGIC up to August 2017 including only the ones respecting the previous criteria. Following this rule, the rate of GRBs observed by MAGIC with no particular issue is 0.6 GRB/month.

Another interesting plot is the one showing the time delay ( $t_{\text{delay}}$ ) of GRB observation with respect to the onset versus the zenith angle of observation (see Figure 5.17). It can be seen that the region with delay lower than 100s is quite populated: out of 97 GRBs, 23 are in this region. Twelve of them have a redshift estimation and five of them have  $z < 1.5$ . The reasons of having not too many GRBs in the  $t_{\text{delay}} < 100$  s region are bad weather conditions or observational criteria not fulfilled at the moment of the GRB alert.

Finally, Figure 5.18 shows the cumulative distribution of the GRBs observed by MAGIC. Less than 20% of the total has a redshift lower than one. The highest redshift GRB observed by MAGIC is GRB050904 with  $z = 6.3$ , while the lowest redshift one is GRB160821B with  $z = 0.16$ .

Some remarkable bursts followed-up by MAGIC are:

- GRB050713A, which is the first GRB whose prompt emission was observed by any IACT. The burst had  $T_{90} = 129.2$  s and MAGIC started data taking at  $T_0 + 40$  s, see Albert et al. (2006);
- GRB050904, the burst observed by MAGIC with the highest redshift  $z = 6.3$  and one of the GRBs with the highest redshift ever measured;
- GRB160821B, which in the MAGIC GRB set holds two records: it is the closest ( $z = 0.16$ ) and the one observed with the minimum delay, just 24 s after  $T_0$ .

As far as past results are concerned, the GRBs observed in the first data cycle (2005-2006) were analyzed and their upper limits were presented in Albert et al. (2007). The flux upper

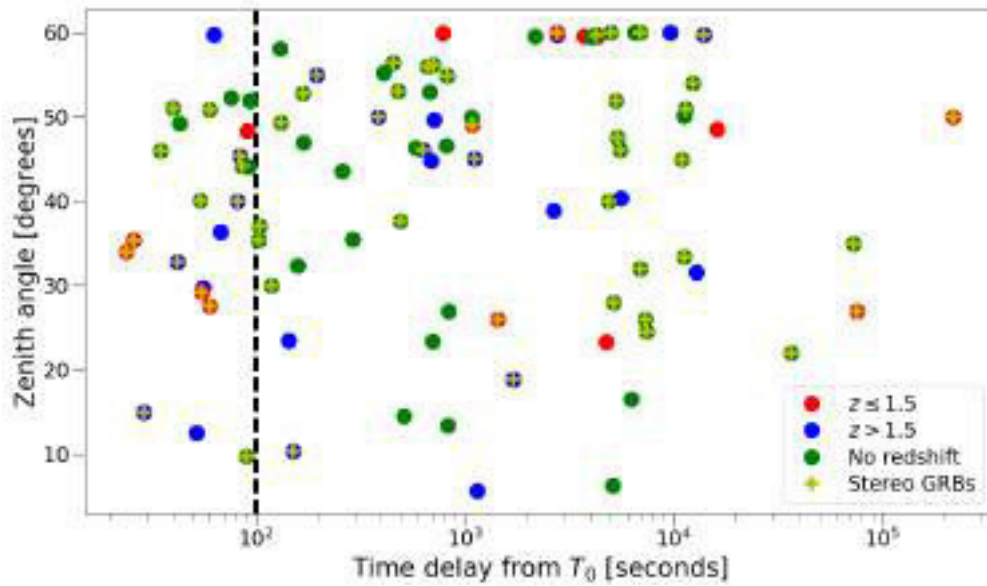


Figure 5.17: Delay of MAGIC observed GRBs with respect to the onset versus the zenith angle of observation. Red circles are bursts with  $z < 1.5$ , blue have  $z > 1.5$  while green ones do not have redshift determination. GRBs observed in stereo mode are denoted by a yellow cross.

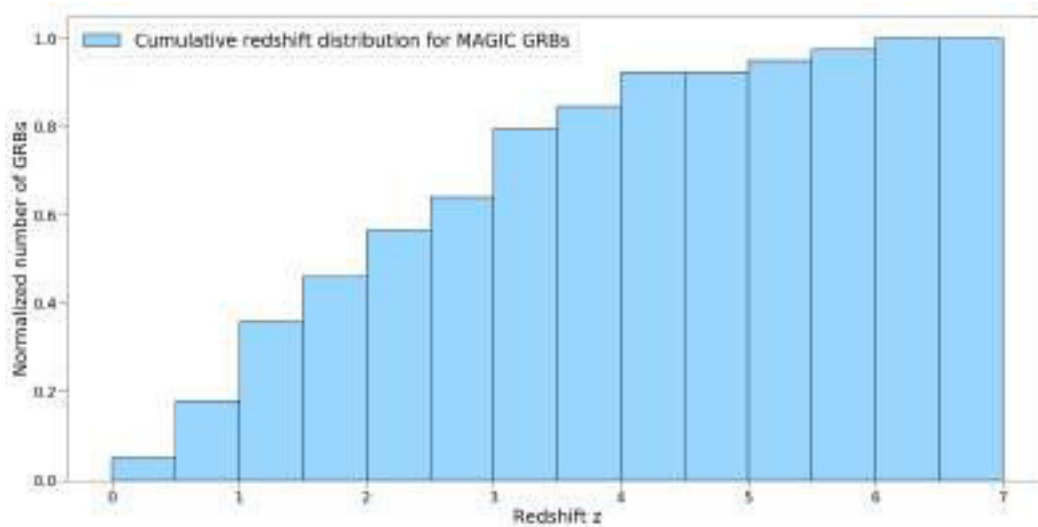


Figure 5.18: Cumulative redshift distribution of GRBs observed by MAGIC. The percentage of GRBs with  $z < 1.5$  is around 38%.

limits were compared, in the case of redshift estimation, with a power-law extrapolation from lower energies taking into account the EBL absorption and were found to be compatible with that assumption. Among the GRBs presented in Albert et al. (2007), GRB050713A was studied and analyzed in detail because, as already mentioned, its prompt emission was observed and it was the first time for any IACT, see Albert et al. (2006). Beside the standard analysis, a temporal one was performed to search for short-time variability in the possible  $\gamma$ -ray signal, but no evidence of it was found.

Other two bursts observed by MAGIC deserved more focus, namely GRB080430 and GRB090102. Both were observed in the mono era of MAGIC but data was taken simultaneously with other

instruments and the redshift was known for both of them. This allowed to perform a multi-wavelength observation and a detailed physical interpretation of the flux upper limits derived for the two bursts.

In Aleksić et al. (2010) it was possible to set an upper limit on the flux of GRB080430 in the energy bin from 80 GeV to 125 GeV, which is the most important upper limit in this case since the redshift of the event was  $z = 0.758$  and so for upper energy bins the EBL absorption is dominant. Since the event was observed starting from  $T_0 + 4753$  s, only the afterglow phase was observed and thus modeled as SSC emission, whose expected flux at different times was compared with MAGIC upper limits. In this particular case the huge delay (due to observational criteria, the Sun was still over the horizon) and moderate redshift played a major role. GRB090102 was the first GRB observed simultaneously by MAGIC, Swift and Fermi-LAT and MAGIC results are presented in Aleksić et al. (2014). The GRB was observed with the MAGIC-I sum trigger system, so that the energy threshold for the observation was as low as 30 GeV. Since the redshift of the burst was  $z = 1.547$ , having a low energy threshold allows to explore an energy range unaffected by the EBL. Both MAGIC and Fermi-LAT flux upper limits were derived and compared with a SSC emission by electrons with microphysical parameters obtained from X-ray observations. An hadronic scenario (SSC by protons) was considered as well, demonstrating that it was not possible to discriminate between leptonic and hadronic origin of the emission.

The recent MAGIC follow-up activity is briefly summarized in Berti and MAGIC GRB Group (2017). In 2016 in particular, few GRBs detected by LAT (GRB160310A, GRB160509A, GRB160623A, GRB160625B) were followed up at late times since, as mentioned in Section 5.1.5, long-lasting emission is observed in most LAT-detected GRBs. This new approach for GRBs follow-up is referred as *late-time observations*. Currently the MAGIC alert system is not updated for this new strategy so those four observations were triggered with a human in the loop. Implementing late-time observations for LAT-detected GRBs follow-up is one of the future prospects for the MAGIC alert system, see Section 6.6.

### 5.1.9 Analysis of MAGIC GRBs

In order to search for a possible VHE signal, a set of MAGIC observed GRBs, listed in Table 5.1, was considered. As it can be seen, all GRBs were observed between 2013 and 2015. The choice of taking GRBs after 2013 is due to the new automatic GRB procedure adopted. As far as the analysis is concerned, the most important change in the automatic procedure in 2013 was that GRBs were pointed in wobble mode and not in ON mode anymore. This means that the analysis of GRB data was somehow standardized: in particular there is no need for dedicated OFF observations affecting the observation time of other targets. The choice of taking GRBs up to the end of 2015 is because the number of GRBs observed and analyzable in this two years period is 19, 12 of which are in this thesis. 19 represents a large number, considering the reduced manpower in the MAGIC GRB working group.

As shown in Table 5.1, most of the GRBs were detected by Swift, except for GRB130903A and GRB150213A which were detected by INTEGRAL and Fermi-GBM respectively. All the GRBs in the set are long GRBs and half of them have a redshift estimation which is always greater than 1. They were observed in different conditions: the zenith of observation is in the low, medium, high and very high range ( $5^\circ$ - $35^\circ$ ,  $35^\circ$ - $50^\circ$ ,  $50^\circ$ - $62^\circ$  and  $62^\circ$ - $70^\circ$  respectively) while the background condition was dark for almost all of them, with some cases of Moon observation or low atmospheric transmission. These two parameters (zenith and background condition) are the ones mostly affecting the energy threshold of the observation. Finally, the last column of Table 5.1 lists the delay in seconds between the onset ( $T_0$ ) of the GRBs and the beginning of the observation. When the delay is large, the observational criteria were not respected or the weather conditions did not allow a safe operation of the telescopes. A remarkable case is GRB151215A, whose delay is 30 s: this is among the best repositioning

| GRB        | Satellite | $T_{90}$ [s] | Redshift | Zenith  | Condition            | Delay |
|------------|-----------|--------------|----------|---------|----------------------|-------|
| GRB130504A | Swift-BAT | 50           | -        | 44-57   | Dark, dim-moon       | 455   |
| GRB130606A | Swift-BAT | 276.58       | 5.913    | 5-43    | Dark                 | 634   |
| GRB130701A | Swift-BAT | 4.4          | 1.155    | 16-27   | Moderate moon        | 60    |
| GRB130903A | INTEGRAL  | 69           | -        | 51-63   | Dark                 | 11412 |
| GRB140430A | Swift-BAT | 173.6        | 1.60     | 45-54   | Dark                 | 1110  |
| GRB140709A | Swift-BAT | 98.6         | -        | 25-37   | Dark                 | 7414  |
| GRB141026A | Swift-BAT | 146          | 3.35     | 10-50   | Low $T_{9\text{km}}$ | 151   |
| GRB141220A | Swift-BAT | 7.21         | 1.32     | 19-29   | Dark                 | 55    |
| GRB150213A | Fermi-GBM | 4.1          | -        | 44-60.5 | Dark                 | 86    |
| GRB150819A | Swift-BAT | 52.1         | -        | 40-60   | Dark                 | 4888  |
| GRB151118A | Swift-BAT | 23.4         | -        | 40-58   | Dark                 | 54    |
| GRB151215A | Swift-BAT | 17.8         | 2.59     | 15-58   | Dark                 | 30    |

Table 5.1: List of MAGIC observed GRBs considered in this thesis. The columns are respectively: name of the GRB, satellite which detected the GRB,  $T_{90}$ , redshift, zenith range during the observation, background conditions and delay between the onset and the beginning of the observation. All the reported  $T_{90}$  are computed in the energy range 15 – 350 keV, except for GRB130903A and GRB150213A for which the energy range is 50 – 300 keV.

times that MAGIC can achieve. Of course lower delays are possible if the source observed before the GRB is very close to the previous target.

The goal of the analysis was to search for a possible signal in the VHE range from the GRBs considered. In the case of non detection, flux upper limits (both integral and differential) were computed using the Rolke method at a 95% C.L. and with a power law with spectral index  $-3.5$  as assumed spectrum. The choice of this spectrum is suggested by the fact that the observed spectrum should be quite soft given the high redshift and the EBL absorption effect.

The next sections will describe the observation and particular analysis issues of each GRB listed in Table 5.1. Table 5.2 shows the main observational parameters for each GRB. Finally, the results of the analysis will be presented in Section 5.1.11. Additional plots, like Swift-BAT and Swift-XRT lightcurves, are presented in Appendix B.

### GRB130504A

**Other observations** GRB130504A, a long GRB with duration of  $T_{90} = (50 \pm 10)$  s (15 – 350 keV), triggered Swift-BAT at 02:05:34 UTC and XRT began observation of the sky field 85.9 seconds after the trigger, without identifying at first an X-ray counterpart due to the proximity to the Galactic bulge (Cummings et al. 2013). The X-ray afterglow was detected afterwards in a different position than the one computed by BAT. After a refined analysis the BAT coordinates were found to be consistent with the XRT ones (D’Avanzo et al. 2013; Palmer et al. 2013). No optical afterglow was detected after observations done with Swift-UVOT, the Bassano Bresciano Observatory and the MITSuME telescope (Breeveld and Cummings 2013; Quadri et al. 2013; Kuroda et al. 2013), while a fading source was detected instead by the IAC80 telescope in a position coincident with the enhanced XRT position (Gorosabel et al. 2013). No redshift information is available for this burst.

The BAT light curve shows multiple peaks, while the spectrum is best fit by a power law with an exponential cutoff with photon index  $0.52 \pm 0.68$  and peak energy  $(85.4 \pm 47.6)$  keV, resulting in a fluence of  $(10 \pm 1) \cdot 10^{-7}$  erg/cm<sup>2</sup> in the 15-150 keV energy range. For more details, see [https://gcn.gsfc.nasa.gov/notices\\_s/555096/BA/](https://gcn.gsfc.nasa.gov/notices_s/555096/BA/).

The XRT light curve is best fit with a broken power law with  $t_{\text{break}} = 3828$  s and temporal

| GRB        | RA (J2000) | Dec (J2000) | $\theta_{90}$ | BAT Fluence [erg/cm <sup>2</sup> ] | BAT index  |
|------------|------------|-------------|---------------|------------------------------------|------------|
| GRB130504A | 272.459    | -16.32      | 1.7'          | $(10 \pm 1) \cdot 10^{-7}$         | 0.52 (CPL) |
| GRB130606A | 249.39     | 29.796      | 2.0'          | $(29 \pm 2) \cdot 10^{-7}$         | 1.52 (PL)  |
| GRB130701A | 357.224    | 36.1        | 1.0'          | $(44 \pm 1) \cdot 10^{-7}$         | 0.9 (CPL)  |
| GRB130903A | 82.13      | -0.125      | 1.5'          | -                                  | -          |
| GRB140430A | 102.942    | 23.033      | 1.0'          | $(11 \pm 2) \cdot 10^{-7}$         | 2.0 (PL)   |
| GRB140709A | 304.666    | 51.222      | 1.0'          | $(53 \pm 2) \cdot 10^{-7}$         | 1.23 (CPL) |
| GRB141026A | 44.049     | 26.925      | 1.9'          | $(13 \pm 1) \cdot 10^{-7}$         | 2.34 (PL)  |
| GRB141220A | 195.058    | 32.146      | 1.2'          | $(26 \pm 1) \cdot 10^{-7}$         | 0.62 (CPL) |
| GRB150213A | 95.29      | -4.85       | 1.0           | -                                  | -          |
| GRB150819A | 42.34      | 9.787       | 2.8'          | $(4.8 \pm 0.9) \cdot 10^{-7}$      | 1.72 (PL)  |
| GRB151118A | 57.169     | 65.889      | 1.4'          | $(4.5 \pm 0.6) \cdot 10^{-7}$      | 1.80 (PL)  |
| GRB151215A | 93.622     | 35.529      | 2.8'          | $(3.1 \pm 0.7) \cdot 10^{-7}$      | 1.99 (PL)  |

Table 5.2: Main parameters of MAGIC observed GRBs considered in this thesis. The columns are respectively: name of the GRB, right ascension, declination, uncertainty in the position in arcmin, fluence in BAT (15-150 keV energy range) and BAT photon index (PL and CPL stand for power-law and cutoff power-law respectively).

indexes  $\alpha_1 = 0.63 \pm 0.11$  and  $\alpha_2 = 1.64_{-0.16}^{+0.25}$  before and after the break respectively (see [http://www.swift.ac.uk/xrt\\_live\\_cat/00555096/](http://www.swift.ac.uk/xrt_live_cat/00555096/)).

**MAGIC observations** MAGIC received the alert for GRB130504A at 02:06:01 UTC and the telescopes promptly repointed, but observation could begin only at 02:13:09 UTC, after 455 s from the onset. The shift crew was performing the so called TPoint observation, so the lids of the camera were closed and the IPRC was disabled. The observation started in dark conditions but at about 02:50 UT Moon DT were used due to the Moon rising. At the end of observation, the rates began to decrease due to the L3 deadzone. The total observation time for this GRB was almost 3 h, stopped because of the upcoming sunrise.

There is no LIDAR info for this GRB, but shifters did not report any clouds in the observation runbook, so it is safe to suppose that the weather was good and the transmission of the atmosphere high. The observation was performed at medium-high zenith, between 45° and 56°, leading to an energy threshold of  $E_{\text{thr}} = 187$  GeV.

### GRB130606A

**Other observations** GRB130606A was detected by Swift-BAT at 21:04:39 UT (Ukwatta et al. 2013) and promptly observed by Swift-XRT after 72 s. The Swift-BAT refined analysis yielded an estimate of  $T_{90} = (276.58 \pm 19.31)$  s (15 – 350 keV, Barthelmy et al. 2013) and a light curve with multiple peaks (see [https://gcn.gsfc.nasa.gov/notices\\_s/557589/BA/](https://gcn.gsfc.nasa.gov/notices_s/557589/BA/)). The time averaged BAT spectrum from  $T_0 - 1.34$  s to  $T_0 + 297$  s is best fitted by a simple power law with index  $1.52 \pm 0.12$ , leading to a fluence of  $(29 \pm 2) \cdot 10^{-7}$  erg/cm<sup>2</sup> in the 15-150 keV in the range 15-150 keV.

The XRT light curve instead shows few peaks (flares) in the time window  $[T_0 + 78.7 \text{ s}; T_0 + 497 \text{ s}]$ . Excluding these data, the light curve can be fitted by a broken power law with three breaks at  $T_{b,1} = 729_{-85}^{+78}$  s,  $T_{b,2} = 1250_{-367}^{+690}$  s and  $T_{b,3} = 1.5_{-0.7}^{+0.5} \cdot 10^4$  s after the GRB onset and four temporal indexes  $\alpha_1 = -0.65_{-0.16}^{+0.13}$ ,  $\alpha_2 = -3_{-1}^{+2}$ ,  $\alpha_3 = -0.70_{-1.26}^{+0.28}$  and  $\alpha_4 = -1.78_{-0.16}^{+0.18}$  (see [http://www.swift.ac.uk/xrt\\_live\\_cat/557589](http://www.swift.ac.uk/xrt_live_cat/557589) and [https://gcn.gsfc.nasa.gov/reports/report\\_444\\_1.pdf](https://gcn.gsfc.nasa.gov/reports/report_444_1.pdf)). Chandra observed the burst about 10.3 d after the GRB trigger for 30 ks exposure and measured a flux of  $(2.4 \pm 0.4) \cdot 10^{-15}$  erg/cm<sup>2</sup>/s, consistent with the extrapolation of the Swift-XRT flux with a slope of  $-1.8 \pm 0.1$  (Fong et al. 2013).

Swift-UVOT did not detect any afterglow consistent with the optical position and it could only put upper limits (Pritchard and Ukwatta 2013). The afterglow was detected at first by NOT telescope (Xu et al. 2013a), then confirmed by Liverpool (Virgili, Mundell, and Melandri 2013) and other optical and NIR facilities (see <https://gcn.gsfc.nasa.gov/other/130606A.gcn3>).

The redshift of the bursts was estimated to be  $z = 5.91$  by spectroscopic observations performed by GTC, MMT and VLT (Castro-Tirado et al. 2013; Lunnan et al. 2013; Xu et al. 2013b). Given the high redshift, the optical and near-IR spectra were used to put constraints on the neutral hydrogen fraction  $f_{HI} \sim 0.05 - 0.1$  of the intergalactic medium (IGM) (Totani et al. 2016; Hartoog et al. 2015; Chornock et al. 2013).

**MAGIC observations** The BAT notice for GRB130606A arrived in the middle of the telescopes preparation at 21:05:02 UT. After completing the preparation, the observation started at 21:15:13 UT, with a total delay with respect to the onset of 634 s. Since it was not completely dark time at the beginning of the observation, the very first minutes were affected by low twilight. The observation proceeded smoothly until the end at 00:39:09 UT, for a total of about 2.8 h. Only a small technical issue arose about five minutes after the beginning of the observation when the DAQ aborted and data were not taken for few minutes in order to solve the problem.

The zenith angle of the observation spans the wide range from  $43^\circ$  to  $5^\circ$ . This results in a quite low energy threshold  $E_{thr} = 80$  GeV. Regarding the weather conditions, unfortunately no LIDAR information is available but the shifters did not report any clouds or high dust during the GRB observation.

### GRB130701A

**Other observations** GRB130701A triggered Swift-BAT at 04:17:43 UT (Kuin et al. 2013). Swift-XRT observed the field about 85.5 s after the trigger and imaging was performed with Swift-UVOT without finding any afterglow candidate. This was afterwards by NOT (Leloudas et al. 2013) and UVOT itself (Breeveld and Kuin 2013).

The redshift of the burst was estimated to be  $z = 1.155$  by VLT observations (Xu et al. 2013c). Also Konus-Wind was triggered by GRB130701A and it detected emission up to 0.5 MeV. The Konus-Wind time integrated spectrum from  $T_0$  to  $T_0 + 8.448$  s is best fitted with a cutoff power law with index  $-1.1 \pm 0.1$  and peak energy  $E_p = (89 \pm 4)$  keV (Golenetskii et al. 2013) while the light curve shows a multi-peaked pulse from  $T_0 - 0.5$  s to  $T_0 - 5$  s ([http://www.ioffe.ru/LEA/GRBs/GRB130701\\_T15462/](http://www.ioffe.ru/LEA/GRBs/GRB130701_T15462/)).

The duration of the burst was inferred by Swift-BAT data and estimated as  $T_{90} = (4.38 \pm 0.25)$  s in the 15-350 keV energy range. The Swift-BAT time averaged spectrum is compatible with the one measured by Konus-Wind (Sakamoto et al. 2013).

The X-ray light curve from Swift-XRT is best fitted by a broken power law with two breaks at  $T_{b,1} = 143_{-31}^{+12}$  s and  $T_{b,2} = 387_{-93}^{+410}$  s after the onset, corresponding to three temporal indexes  $\alpha_1 = -1.89_{-0.26}^{+0.88}$ ,  $\alpha_2 = -0.65_{-0.19}^{+0.30}$  and  $\alpha_3 = -1.25_{-0.04}^{+0.04}$  ([http://www.swift.ac.uk/xrt\\_live\\_cat/559482](http://www.swift.ac.uk/xrt_live_cat/559482)).

**MAGIC observations** GRB130701A was followed-up by MAGIC only 1 min after the burst trigger with the automatic GRB procedure. For this burst the NSB was quite high due to the presence of the Moon. The observation went on until 05:17:29 UT, when the DC of the PMTs was too high to continue the data taking. No technical issues arose during this follow-up.

The NSB level for this GRB is around 2-3 times the one in dark observations, meaning that the analysis should be customized to comply with the higher background level. For this reason, higher image cleaning were adopted for ON, OFF and MC data. For OFF and MC

data, noise was added to reproduce the right NSB level, as described in Section 4.4. A higher size cut was used at `odie` and `flute` level. The values used are the ones recommended in Ahnen et al. (2017).

The same analysis was applied to a Crab Nebula sample to check that the reproduced SED was compatible with the one reported for example in Aleksić et al. (2016b).

### GRB130903A

**Other observations** GRB130903A was detected by INTEGRAL at 00:47:20 UT, showing a FRED peak in the light curve (Mereghetti et al. 2013), as shown in <http://ibas.iasf-milano.inaf.it/130903A.html>. For this burst few X-ray measurements from Swift-XRT are available: the first one from  $T_0 + 39.6$  ks to  $T_0 + 46.4$  ks, the second one after  $3 \cdot 10^5$  s from the onset and a third one at about  $10^6$  s after the trigger. The first two measurements show a fading behavior with decay index  $0.8_{-0.4}^{+0.6}$ , while the third one is an upper limit confirming that the X-ray source is the afterglow of GRB130903A (see Grupe and Holland 2013; Grupe 2013 and [http://www.swift.ac.uk/xrt\\_curves/00020294/](http://www.swift.ac.uk/xrt_curves/00020294/)). The afterglow was also detected in the optical band by GROND and SANTEL-400AN (Tanga et al. 2013; Volnova et al. 2013), while Swift-UVOT could only put upper limits on the optical emission (Holland and Grupe 2013).

The burst was also detected by Fermi-GBM with coordinates consistent with the ones given by INTEGRAL and Swift and resulting in a duration of  $T_{90} = (68.61 \pm 0.72)$  s (50 – 300 keV). The time averaged spectrum from  $T_0 - 4.096$  s to  $T_0 + 49.152$  s is best fit by a power law with index  $-1.79 \pm 0.07$  while the fluence of the GRB in the 10-1000 keV energy range is  $(2.52 \pm 0.06)$  erg/cm<sup>2</sup> (see the Fermi-GBM catalog at the link <https://heasarc.gsfc.nasa.gov/W3Browse/fermi/fermigbrst.html> and data for GRB130903033).

**MAGIC observations** MAGIC observation for GRB130903A began at 03:57:32 UT, about 11 400 s after the INTEGRAL trigger, when it went below 60° in zenith. The observation lasted about one hour with no technical issues except for few car-flashes and a DAQ abort. The burst was observed under dark conditions in the high zenith range from 62° to 50°. The transmission  $T_{9\text{km}}$  was quite good around 0.8. The energy threshold for this burst is quite high,  $E_{\text{thr}} = 281$  GeV.

### GRB140430A

**Other observations** GRB140430A was detected by Swift-BAT at 20:33:36 UT and Swift-XRT began observations of the burst 50.8 s after the onset, finding an X-ray position within the error circle of Swift-BAT. Swift-UVOT imaged the field and found an optical afterglow (Siegel et al. 2014), also detected by the Liverpool Telescope, NOT, VLT, VATT, IAC80 and STELLA-I at different times from the onset (Melandri et al. 2014; Malesani et al. 2014; Kruehler et al. 2014; Kennedy 2014; Gorosabel et al. 2014a; Jarvinen and Gorosabel 2014). In particular, from VLT observations the redshift was estimated to be  $z = 1.60$ . Combining NOT and VATT optical observations, performed 86.5 min and 6.81 h after the trigger, the optical power-law decay index was estimated to be 0.76. After further VATT observations at 30.81 h from the onset of the burst, the optical light curve was found to have a steepening with power-law decay index of 1.0 (Kennedy and Garnavich 2014). The fast response of optical telescopes allowed to obtain data during the prompt or early afterglow phase of the GRB. The optical light curve resulted to be quite complex, with two long-lasting emission phases connected by a plateau at about 2000 s. Optical flares also appear in the first 300 s of the light curve, whose origin is more consistent with an internal shock origin (Kopač et al. 2015). The post-flares optical decay ( $\alpha_{\text{decay}} \sim 1$ ) is instead consistent with a forward-shock afterglow origin, while the plateau and following decline ( $\alpha_{\text{decay}} \sim 0.8$ ) could be explained as

continuous energy injection from the central engine.

The gamma-ray light curve by BAT shows two intense peaks, one between  $T_0 - 10$  s and  $T_0 + 10$  s and the other between  $T_0 + 140$  s and  $T_0 + 200$  s. Other two fainter peaks are centered at  $T_0 + 25$  s and  $T_0 + 575$  s. The duration of the burst and fluence resulting from BAT data are  $T_{90} = (174 \pm 4)$  s and  $(11 \pm 2) \cdot 10^{-7}$  erg/cm<sup>2</sup> in the 15-150 keV energy range respectively. The time-averaged spectrum between  $T_0 - 0.30$  s to  $T_0 + 177.58$  s is best fit by a power law model with index  $2.00 \pm 0.22$  (Krimm et al. 2014). The isotropic-equivalent energy for this burst, obtained by fitting the BAT time-averaged spectrum with a Band function is  $E_{\gamma, \text{iso}} = (1.3 \pm 0.4) \cdot 10^{52}$  erg (Kopač et al. 2015).

Finally, the X-ray light curve from XRT shows flaring activity in the first 250 s of the bursts with at least three bright flares. The first two are temporally coincident with the peaks in the BAT light curve. After the flaring phase, the X-ray light curve shows a steep decay and, after a gap in the data due to Earth occultation between  $T_0 + 500$  s and  $T_0 + 3900$  s, it has a shallower decay until  $T_0 + 10^5$  s. In the data gap, probably the canonical plateau of X-ray afterglow light curve is likely to be present. In the last time interval where Swift-XRT data were taken, from  $T_0 + 4000$  s to  $T_0 + 1.3 \cdot 10^5$  s, the decay of the light curve is best fit by a broken power law with break at  $T_b \sim 9700$  s and decay indexes  $\alpha_1 = 0.51 \pm 0.32$  and  $\alpha_2 = 0.85 \pm 0.06$  before and after the break respectively (Kopač et al. 2015).

**MAGIC observations** As happened for GRB130606A, the alert for GRB140430A arrived at 20:33:51 UT during the telescopes preparation. Observation could begin at 20:52:06 UT (1110 s after the burst trigger) and finished about 40 min after when the GRB reached almost 60° in zenith.

The weather conditions were perfect, with a very good atmospheric transmission and no clouds showed by the LIDAR. The moon was not present, so the background conditions were dark. Given the zenith range of the observation (45°-54°), the resulting energy threshold is  $E_{\text{thr}} = 188$  GeV.

### GRB140709A

**Other observations** GRB140709A was detected by Swift-BAT at 01:13:41 UT and after 82.9 s it was observed by Swift-XRT, which found an uncatalogued X-ray source (Hagen et al. 2014a). Swift-UVOT started observations after 92 s without finding any optical afterglow candidate, detected instead by other instruments as BOOTES-2, OSN, GTC, Virtual Telescope and Harold Johnson Telescope (Castro-Tirado et al. 2014b; Castro-Tirado et al. 2014a; Masi 2014; Butler et al. 2014a). Moreover a possible radio counterpart was detected 2.88 days post-trigger by AMI at 15 GHz with a flux of  $(0.35 \pm 0.06)$  mJy (Anderson et al. 2014). The Swift-BAT lightcurve is quite complex with several peaks: a first peak starts at  $\sim T_0 - 50$  s and peaks at  $T_0$ , then a second peak is present at  $\sim T_0 + 15$  s. Other two smaller peaks show up in the lightcurve at  $\sim T_0 + 55$  s and  $\sim T_0 + 75$  s (see [https://gcn.gsfc.nasa.gov/notices\\_s/603810/BA/](https://gcn.gsfc.nasa.gov/notices_s/603810/BA/)). From the counts evolution in time, the duration of the bursts was estimated to be  $T_{90} = (98.6 \pm 7.7)$  s (15-350 keV). The time integrated spectrum from  $T_0 - 46.1$  s to  $T_0 + 93.4$  s is instead well fit by a power law with photon index  $1.23 \pm 0.27$  and an exponential cutoff at  $E_p = (78.0 \pm 20.4)$  keV, resulting in a fluence of  $(5.3 \pm 0.2) \cdot 10^{-7}$  erg/cm<sup>2</sup> (15-150 keV) (Markwardt et al. 2014).

The Swift-XRT lightcurve shows two flaring episodes in the time interval [ $T_0 + 133$  s;  $T_0 + 304$  s]. Excluding these flares, the afterglow lightcurve can be fit with a broken power law with two breaks at  $T_{b,1} = 166_{-8}^{+9}$  s and  $T_{b,2} = 1.40_{-0.45}^{+0.28} \cdot 10^4$  s. The decay indexes are  $\alpha_1 = 6.7_{-0.6}^{+0.6}$ ,  $\alpha_2 = 0.54_{-0.05}^{+0.05}$  and  $\alpha_3 = 1.266_{-0.093}^{+0.102}$  respectively (see [http://www.swift.ac.uk/xrt\\_live\\_cat/603810](http://www.swift.ac.uk/xrt_live_cat/603810)).

The GRB was also detected by Fermi-GBM (Burns 2014) resulting in a lightcurve with two main peaks (see <https://heasarc.gsfc.nasa.gov/FTP/fermi/data/gbm/triggers/>

2014/bn140709051/quicklook/glg\_lc\_all\_bn140709051.gif). The time integrated spectrum from  $T_0 - 26.6$  s to  $T_0 + 21.5$  s is best fit by a smoothly broken power law with amplitude  $(4.03 \pm 0.16)$  photon/cm<sup>2</sup>/s/keV, break energy  $E_b = (44.3 \pm 10.9)$  keV and spectral indexes  $\beta_1 = -0.82 \pm 0.21$  and  $\beta_2 = -2.01 \pm 0.08$ . The fluence obtained for this spectrum is  $(8.14 \pm 0.32) \cdot 10^{-6}$  erg/cm<sup>2</sup> in the 10-1000 keV energy range (see the Fermi-GBM catalog at the link <https://heasarc.gsfc.nasa.gov/W3Browse/fermi/fermigbrst.html> and data for GRB140709051).

**MAGIC observations** The alert for GRB140709A arrived when the telescopes were parked due to strong wind gusts above 40 km h<sup>-1</sup>. The shifters prepared the telescopes for operation and waited until the safety limits were satisfied. Finally observation started at 03:17:15 UT, more than two hours after the burst trigger. Even if the wind was strong before the data taking of the GRB, during the observation the weather was quite stable and with a good transmission around 0.8. All the data were taken in dark conditions, except for the last minutes which are little affected by twilight. Observations ended close to the sunrise at 05:02:47 UT. The zenith of the observation was low, between 25° and 37°, so that the energy threshold for this GRB is  $E_{\text{thr}} = 92$  GeV.

### GRB141026A

**Other observations** GRB141026A was detected by Swift-BAT at 02:36:51 UT and an uncatalogued X-ray source was found afterwards by Swift-XRT, which began observations 157 s after the trigger. Swift-UVOT did not detect any optical counterpart in the first set of observations (Hagen et al. 2014b). A first possible candidate for the optical afterglow was found by P60 but it was not confirmed by any of the following observations. The second and real optical afterglow was detected by RATIR (Littlejohns et al. 2014b) and confirmed by other instruments with observations performed also before the RATIR one (see for example Varela, Kann, and Greiner 2014; Gorosabel et al. 2014b). From following observations, the RATIR candidate was found to be fading with a decay  $\sim t^{-0.5}$  (Butler et al. 2014b) and  $\sim t^{-0.9}$  (Littlejohns et al. 2014a). The afterglow was also detected in the radio band at 21.8 GHz and 6.2 GHz by VLA (Corsi 2014).

A possible redshift estimation of  $z = 3.35$  came from GTC observations performed about 4 h after the trigger (de Ugarte Postigo et al. 2014a).

The Swift-BAT lightcurve does not show any particular feature ([https://gcn.gsfc.nasa.gov/notices\\_s/616502/BA/](https://gcn.gsfc.nasa.gov/notices_s/616502/BA/)) and the resulting duration is  $T_{90} = (146 \pm 13)$  s (15–350 keV), which could be higher because the GRB went outside the Swift-BAT field of view at  $\sim T_0 + 250$  s, after which other emission episodes could be present. The BAT time-averaged spectrum from  $T_0 + 13.96$  s to  $T_0 + 177.75$  s can be fit by a power law with spectral index  $2.34 \pm 0.19$ , corresponding to a fluence of  $(13 \pm 1) \cdot 10^{-7}$  erg/cm<sup>2</sup> in the 15-150 keV energy range (Stamatikos et al. 2014a).

The Swift-XRT light curve shows small flares between  $T_0 + 160$  s and  $T_0 + 180$  s. The late time emission, from  $T_0 + 3.5$  ks to  $T_0 + 7 \cdot 10^5$  s, is well fit by a power law with decay index  $\alpha = 0.66 \pm 0.05$  (see [http://www.swift.ac.uk/xrt\\_live\\_cat/616502](http://www.swift.ac.uk/xrt_live_cat/616502)).

**MAGIC observations** MAGIC observation for GRB141026A started at 02:38:22 UT, 2.5 min after the BAT trigger. The repointing was very fast since the alert was received by GSPOT at 02:38:09 UT, resulting in a slewing time of just 13 s. For the first 1.5 h the data were affected by bad weather and a technical issue (DAQ inconsistency): many clouds were passing by at the MAGIC site, resulting in a low and unstable transmission of the atmosphere. After 04:00 UT the weather conditions were more stable as well as the atmospheric transmission ( $\sim 0.8$ ). The observation lasted until 05:57:36 UT after about 3.5 h of data taking.

For the analysis only data showing  $T_{9\text{km}} > 0.7$  were used and they were corrected for atmospheric extinction when running `flute`. Taking this fact into account, the actual zenith range of the data is between  $29^\circ$  and  $50^\circ$ . The resulting energy threshold is  $E_{\text{thr}} = 110 \text{ GeV}$ .

### GRB141220A

**Other observations** GRB141220A is a long burst ( $T_{90} = (7.21 \pm 0.48) \text{ s}$  in the 15–350 keV energy range, Stamatikos et al. 2014b) detected by Swift-BAT at 06:02:52 UT, 99.2 s afterwards it was observed by Swift-XRT and after 105 s by Swift-UVOT. An X-ray source and optical afterglow were clearly detected (Cummings et al. 2014; Gorosabel et al. 2014c; Guidorzi and Gomboc 2014; de Ugarte Postigo et al. 2014b; Marshall and Cummings 2014). After 50 min from the trigger the redshift was estimated to be  $z = 1.3195$  thanks to GTC observations (de Ugarte Postigo et al. 2014c).

The GRB triggered also Fermi-GBM and Konus-Wind (Yu 2014; Golenetskii et al. 2014). The time integrated spectrum for Fermi-GBM from  $T_0 - 1.024 \text{ s}$  to  $T_0 + 8.192 \text{ s}$  can be best fit with a power law of index  $-0.82 \pm 0.05$  with an exponential cutoff at  $E_c = (178.29 \pm 9.77) \text{ keV}$  while the fluence of the event in the 10-1000 keV energy range is  $(5.34 \pm 0.04) \cdot 10^{-6} \text{ erg/cm}^2$ . The BAT lightcurve shows two peaks at  $T_0 + 1 \text{ s}$  and  $T_0 + 3 \text{ s}$  (see [https://gcn.gsfc.nasa.gov/notices\\_s/621915/BA/](https://gcn.gsfc.nasa.gov/notices_s/621915/BA/)). Also in this case the time integrated spectrum can be fit with a power law with exponential cutoff (index  $0.62 \pm 0.38$  and cutoff energy  $E_c = (117.4 \pm 45.1) \text{ keV}$ ) from  $T_0 - 0.91 \text{ s}$  to  $T_0 + 7.30 \text{ s}$ , leading to a fluence of  $(26 \pm 1) \cdot 10^{-7} \text{ erg/cm}^2$  in the energy range 15-150 keV (Stamatikos et al. 2014b).

The Swift-XRT light curve show a simple decaying behavior after  $\sim 1500 \text{ s}$  from the trigger with decay index  $1.39_{-0.09}^{+0.10}$  (see [http://www.swift.ac.uk/xrt\\_live\\_cat/621915](http://www.swift.ac.uk/xrt_live_cat/621915)).

**MAGIC observations** The alert for GRB141220A arrived almost at the end of the night 06:03:17 UT, while the conditions were still dark. The telescope slewed immediately and the GRB was pointed in 30 s. The observational conditions for this GRB were very good: high atmospheric conditions ( $T_{9\text{km}} \sim 0.9$ ) and low zenith ( $29^\circ$ - $19^\circ$ ). The total observation time was 50 min, with twilight in the very last minutes of data taking due to sunrise. Given the very good conditions, the energy threshold is as low as 77 GeV. This makes GRB141220A one of the GRBs observed by MAGIC in the best possible conditions.

### GRB150213A

**Other observations** The only informations about GRB150213A comes from Fermi-GBM, which detected it at 00:01:48.70 UT. The duration of the burst in the 50-300 keV energy range is  $T_{90} = (4.096 \pm 0.091) \text{ s}$  (50–300 keV, Zhang 2015) as calculated from the light curve consisting of only one main FRED like pulse (see [https://heasarc.gsfc.nasa.gov/FTP/fermi/data/gbm/triggers/2015/bn150213001/quicklook/glg\\_lc\\_chan34\\_bn150213001.pdf](https://heasarc.gsfc.nasa.gov/FTP/fermi/data/gbm/triggers/2015/bn150213001/quicklook/glg_lc_chan34_bn150213001.pdf)).

The time-integrated spectrum from  $T_0 - 1.024 \text{ s}$  to  $T_0 + 13.312 \text{ s}$  is best fit by a Band function with energy peak  $E_p = (59.3 \pm 0.9) \text{ keV}$ , low energy index  $\alpha = -1.18 \pm 0.02$  and high energy index  $\beta = -2.66 \pm 0.04$ . The fluence for this burst is  $(2.876 \pm 0.001) \cdot 10^{-5} \text{ erg/cm}^2$  in the energy range 10 keV-1 MeV.

**MAGIC observations** The observation of GRB150213A started at 00:03:14 UTC (86 s after the GBM trigger; the GCN alert was received by GSPOT at 00:02:41 UTC) and finished at 01:33:28 UTC when the GRB reached  $60^\circ$  of zenith, for a total of about 1.5 h of observation. In the first two runs the coordinates used in the observation after the alert were (RA, Dec) = (06:20:58, -04:46:48), while for the remaining three runs the coordinates were adjusted to (RA, Dec) = (06:21:10, -04:50:59) as given in the GBM Final Position notice (<https://gcn.gsfc.nasa.gov/other/445478511.fermi>). The two set of coordinates are  $0.086^\circ$

away one from each other. For this reason only the last three runs were actually used in the high level analysis, reducing the effective time of observation to 0.96 h.

The weather conditions were very good, with low cloudiness and high transmission of the atmosphere ( $T_{9\text{km}} \sim 0.85 - 0.9$ ). The GRB was observed at medium-high zenith, between  $44^\circ$  and  $60^\circ$ , giving an energy threshold of  $E_{\text{thr}} = 203 \text{ GeV}$ .

The results of the analysis show no detection of any VHE  $\gamma$ -ray signal.

### GRB150819A

**Other observations** GR150819A was detected by Swift-BAT at 00:50:08 UT. Swift-XRT began observations 138.1 s after and detected a fading X-ray source within the BAT error circle (Ukwatta et al. 2015). No optical afterglow candidate was found by Swift-UVOT right after the initial trigger or from the follow-up of other optical facilities (MASTER-IAC, RATIR, NOT, Mondy and TSHAO).

The duration of the burst inferred from the Swift-BAT light curve, which shows a broad pulse peaking at  $\sim T_0 + 40 \text{ s}$ , is  $T_{90} = (52.1 \pm 12.9) \text{ s}$  in the 15 – 350 keV energy range. The time integrated spectrum from  $T_0 + 14.18 \text{ s}$  to  $T_0 + 73.46 \text{ s}$  is best fit by a power law with index  $1.72 \pm 0.27$  (Sakamoto et al. 2015).

The Swift-XRT lightcurve is very simple, since it can be fitted by a simple power law with decay index of  $1.65^{+0.10}_{-0.09}$  (see [http://www.swift.ac.uk/xrt\\_live\\_cat/652643](http://www.swift.ac.uk/xrt_live_cat/652643)). No flare episodes are present in the lightcurve.

**MAGIC observations** GRB150819A was observed by MAGIC starting from 02:11:36 UT with a delay of  $\sim 4900 \text{ s}$  with respect the burst onset due to the high zenith ( $> 60^\circ$ ) of the target at the time of arrival of the alert (00:51:27 UT). The observation lasted about 1.4 h with no technical issue and proceeded under dark conditions and good atmospheric transmission.

The zenith angle during observation was decreasing from  $60^\circ$  down to  $40^\circ$ . The energy threshold is around 175 GeV.

### GRB151118A

**Other observations** GRB151118A was detected by Swift-BAT at 03:06:30 UT and observed promptly by Swift-XRT after 66.2 s. A fading X-ray source was found, while Swift-UVOT did not detect any optical afterglow candidate in the first set of observations right after the trigger (Amaral-Rogers et al. 2015). Following optical observations by several telescopes (OSN, MASTER, ISON-NM, pt5m, AAO, MITSuME, iTelescope) did not reveal any afterglow candidate.

The Swift-BAT lightcurve shows two main peaks, one at  $\sim T_0$  and the other one at  $\sim T_0 + 7 \text{ s}$ , resulting in a duration of the burst of  $T_{90} = (23.4 \pm 10.5) \text{ s}$  (15-350 keV). A power law with index  $1.80 \pm 0.20$  is the best fit to the time-averaged spectrum from  $T_0$  to  $T_0 + 30.8 \text{ s}$ . The burst fluence, in the 15-150 keV energy range, is  $(4.5 \pm 0.6) \cdot 10^{-7} \text{ erg/cm}^2$  (Markwardt et al. 2015).

The Swift-XRT lightcurve shows a flaring episode between  $\sim T_0 + 94 \text{ s}$  and  $\sim T_0 + 319 \text{ s}$ . The late-time emission, from  $T_0 + 4.9 \text{ ks}$  to  $T_0 + 22.7 \text{ ks}$ , can be fitted by a power law with decay index  $1.07 \pm 0.26$  (Pagani et al. 2015).

**MAGIC observations** MAGIC started to observe GRB151118A just 54 s after the burst onset, so the automatic procedure worked fine without any issue. No problems were reported by the shifters in the observation runbook, except for a DAQ crash before the end of the observation.

The GRB was observed for around 11 200 s with very good weather conditions ( $T_{9\text{km}} > 0.8$ ).

The data taking for the burst was stopped when it reached almost  $60^\circ$  in zenith. The resulting energy threshold for this GRB is 170 GeV.

### GRB151215A

**Other observations** GRB151215A triggered Swift-BAT at 03:01:28 UT. Swift slewed almost immediately and after 169.1 s XRT began the observation of the burst finding a fading X-ray source (Gibson et al. 2015). The optical afterglow was first reported by the Palomar telescope, which began observations six minutes after the onset of the burst (Cenko 2015). Then it was confirmed by other optical facilities (MPG, NOT, MASTER II, pt5m, Zeiss-1000 and TAROT) and in particular NOT observations, performed 0.81 h after the GRB, resulted in a redshift estimate of  $z = 2.59$  (Xu et al. 2015).

The Swift-BAT lightcurve shows a broad peak centered at  $T_0$  (see [https://gcn.gsfc.nasa.gov/notices\\_s/667392/BA/](https://gcn.gsfc.nasa.gov/notices_s/667392/BA/)) and the duration of the burst is  $T_{90} = (17.8 \pm 1.0)$  s (15-350 keV). The time averaged spectrum can be fit with a power-law model with index  $1.99 \pm 0.33$  in the time range from  $T_0 - 15.46$  s to  $T_0 + 3.13$  s. The resulting fluence in the 15-150 keV energy range is  $(3.1 \pm 0.7) \cdot 10^{-7}$  erg/cm<sup>2</sup> (Cummings et al. 2015).

The Swift-XRT light curve does not show any flaring episode and can be fit by a simple power law with decay index  $0.94 \pm 0.05$  (see [http://www.swift.ac.uk/xrt\\_live\\_cat/667392](http://www.swift.ac.uk/xrt_live_cat/667392)).

**MAGIC observations** The reaction of MAGIC to GRB151215A was very fast, since it was followed-up just 30 s after the onset. As in the case of GRB141220A, GRB151215A was observed under very good conditions and in a wide range of zenith angles (from  $15^\circ$  to  $60^\circ$ ). Only in the last  $\sim 20$  min of observation the transmission was quite low, probably due to some passing clouds (not reported in the runbook). There was a small technical issue after the first wobble when the DAQ showed an inconsistent state between the two telescopes.

Since GRB151215A is one of the few GRBs observed in really good weather conditions and low zenith (at least at the beginning of data taking), it deserved a dedicated analysis. The work was done in collaboration with another MAGIC member, Koji Noda. The goal of the analysis was to check whether performing a custom analysis on this GRB could produce a significant improvement. For this purpose, Koji Noda analyzed the GRB with lower image cleanings at `star` level and lower size and hadronness cuts in `odie`. Moreover he adopted the so called *Extragalactic MC*, which consists of gamma rays simulated as in the standard MC but with a lower NSB level. To compare the results with Koji, I performed the analysis using the standard cuts (image cleanings, size, hadronness), excluding data with  $T_{9\text{km}} < 0.8$  in order to have the best quality ones and using both standard and Extragalactic MC (one at a time, so two analysis in total).

Unfortunately, the result of this study is that the gain of a custom analysis in terms of the significance of the signal is, at least for this particular GRB, negligible.

#### 5.1.10 Summary of the observation of MAGIC GRBs

In the table below I summarize the observations performed by MAGIC on the 12 GRBs considered in my thesis. The columns indicate in order: the name of the GRB, the date of observation, the trigger time  $T_0$ , the time  $T_{\text{alert}}$  when the GRB alert was received by GSPOT, the time of the beginning and end of observation ( $T_{\text{start}}$  and  $T_{\text{stop}}$ ) and the effective time of observation (after data quality cuts, like in the case of GRB141026A). All the times are in UTC, except for the effective time which is in hours. For all GRBs except GRB141026A, all data available were used since the observation were carried under good atmospheric conditions after inspecting them with `quate`. For GRB141026A, due to an unstable and low value of  $T_{9\text{km}}$  (affecting also the rates) during the first two hours of observations. In this case `quate`

was used to select data having  $T_{9\text{km}} > 0.7$  (this selection was done to have only the best quality data and for this reason the lower limit 0.7 was used), as shown in Figure D.8.

| GRB        | Date<br>YYYY-MM-DD | $T_0$<br>[UTC] | $T_{\text{alert}}$<br>[UTC] | $T_{\text{start}}$<br>[UTC] | $T_{\text{stop}}$<br>[UTC] | $T_{\text{eff}}$<br>[h] |
|------------|--------------------|----------------|-----------------------------|-----------------------------|----------------------------|-------------------------|
| GRB130504A | 2013-05-04         | 02:05:34       | 02:06:01                    | 02:13:09                    | 05:17:03                   | 2.91                    |
| GRB130606A | 2013-06-06         | 21:04:39       | 21:05:02                    | 21:15:13                    | 00:39:09                   | 2.78                    |
| GRB130701A | 2013-07-01         | 04:17:43       | 04:18:02                    | 04:18:43                    | 05:17:29                   | 0.66                    |
| GRB130903A | 2013-09-03         | 00:47:20       | 00:47:38                    | 03:57:32                    | 04:48:36                   | 0.71                    |
| GRB140430A | 2014-04-30         | 20:33:36       | 20:33:51                    | 20:52:06                    | 21:30:03                   | 0.52                    |
| GRB140709A | 2014-07-09         | 01:13:41       | 01:14:02                    | 03:17:15                    | 05:02:47                   | 1.62                    |
| GRB141026A | 2014-10-26         | 02:36:51       | 02:38:09                    | 02:38:22                    | 05:57:36                   | 1.74                    |
| GRB141220A | 2014-12-20         | 06:02:52       | 06:03:17                    | 06:03:47                    | 06:50:53                   | 0.76                    |
| GRB150213A | 2015-02-13         | 00:01:48       | 00:02:41                    | 00:03:14                    | 01:33:28                   | 0.93                    |
| GRB150819A | 2015-08-19         | 00:50:08       | 00:51:27                    | 02:11:36                    | 03:55:17                   | 1.43                    |
| GRB151118A | 2015-11-18         | 03:06:30       | 03:06:50                    | 03:07:24                    | 06:13:28                   | 2.98                    |
| GRB151215A | 2015-12-15         | 03:06:30       | 03:06:30                    | 03:01:58                    | 03:01:58                   | 2.89                    |

Table 5.3: Summary of the observations of the GRBs observed by MAGIC considered in this thesis. The explanation of the meaning of the columns is given in the text.

### 5.1.11 Summary of the analysis on MAGIC GRBs

All the GRBs listed in Table 5.1 were analyzed using the MAGIC software MARS and performing the standard analysis for GRBs. In few cases a dedicated analysis was needed: that is the case for GRB130701A and GRB151215A and the details of the analysis are reported in the respective sections devoted to those two bursts.

Unfortunately, no VHE gamma-ray signal was detected from any of the GRBs considered. The summary of the results of the analysis are shown in Table 5.4. The second column reports the significances of the GRBs as calculated by `odie` using standard LE cuts. The third column shows the energy threshold of the whole observation for each GRB: it depends mainly on the zenith range but also on the background conditions e.g. the presence of Moon (see Table 5.1 and the plots in Appendix D). Since no GRB shows signal, only flux upper limits could be computed using the Rolke method, setting the confidence level to 95%, and an assumed power-law spectrum with index  $-3.5$ : they are reported in the fourth column as integral flux upper limits above the energy threshold given in the third column. The differential upper limits are instead reported in Appendix E. Finally, to have an idea of the order of magnitude of the upper limits, the conversion in percentage of the Crab Unit (C.U.) above a particular energy threshold is given. The `odie` and `caspar` plots produced for each GRB are shown for completeness in Appendix C.

The natural question that could arise in this case is why there was no detection. There are two reasons, one is related to the detection technique and the other is physical.

The first reason is related to the reaction of the MAGIC telescopes (and IACTs in general) to GRBs and to the use of the Cherenkov atmospheric technique. Since GRBs are serendipitous sources not predictable in any way, the observational conditions at the time MAGIC receives the alerts are very different. Not all the GRBs were promptly observable but in half of the cases the delay from the onset was less than 3 min, with some remarkable bursts where the delay is even under 1 min. This confirms that the automatic procedure works fine and that the delay depends mostly on observational constraints like the zenith of the target or bad weather conditions. Despite this, MAGIC could not observe the prompt emission from these GRBs. Finally, the zenith range and background conditions affect the energy threshold

| GRB        | Significance [ $\sigma$ ] | $E_{\text{thr}}$ [GeV] | UL [ $\text{cm}^{-2} \text{s}^{-1}$ ] | C.U. [%] |
|------------|---------------------------|------------------------|---------------------------------------|----------|
| GRB130504A | -0.79                     | 187                    | $7.04 \cdot 10^{-12}$                 | 2.8      |
| GRB130606A | -1.03                     | 80                     | $1.99 \cdot 10^{-11}$                 | 2.8      |
| GRB130701A | +0.03                     | 100                    | $2.99 \cdot 10^{-11}$                 | 5.4      |
| GRB130903A | -0.73                     | 281                    | $1.04 \cdot 10^{-11}$                 | 7.3      |
| GRB140430A | -0.92                     | 188                    | $1.46 \cdot 10^{-11}$                 | 5.9      |
| GRB140709A | +0.65                     | 92                     | $6.17 \cdot 10^{-11}$                 | 10.1     |
| GRB141026A | -2.07                     | 110                    | $3.44 \cdot 10^{-11}$                 | 7.0      |
| GRB141220A | +2.10                     | 77                     | $4.74 \cdot 10^{-11}$                 | 6.3      |
| GRB150213A | +0.17                     | 203                    | $8.26 \cdot 10^{-12}$                 | 3.7      |
| GRB150819A | +0.57                     | 175                    | $3.17 \cdot 10^{-11}$                 | 11.7     |
| GRB151118A | -0.26                     | 170                    | $9.08 \cdot 10^{-12}$                 | 3.2      |
| GRB151215A | +0.66                     | 90                     | $3.24 \cdot 10^{-11}$                 | 5.2      |

Table 5.4: Summary of the results of the analysis performed on the GRBs listed in Table 5.1. The significance reported in the second column is the one computed using LE cuts in `odie`.

of the observations and it is intimately related to the second factor limiting the chance of detection. It is the physical effect due to the *Extragalactic Background Light* (EBL). Gamma rays interact with the EBL via the pair production process so that part of them will be lost in their propagation from the source to Earth. The absorption is redshift and energy dependent: in particular it increases with redshift and this causes the observed spectrum to present a cutoff at lower energies. This is true especially for MAGIC and IACTs in general, because the GeV-TeV range is the most affected by the EBL. Even for moderately distant sources ( $z \sim 0.3 - 0.4$ ) the absorption is quite high. For sources like GRBs this effect is even more pronounced because of their high redshift. The sample in this thesis unfortunately has only GRBs with  $z > 1$ : this means that the original spectrum in the MAGIC energy range is almost completely absorbed. Moreover the GRBs considered are not particularly bright bursts and no one was detected by Fermi-LAT, meaning that probably they were not emitting in the HE range as well or that the absorption in the Fermi energy range was already too high. For those GRBs without redshift a similar reasoning applies since, being long GRBs, they should have a high redshift.

### 5.1.12 Discussion and prospects for GRBs with MAGIC

From the previous sections, it is clear that MAGIC is very well suited to perform the follow-up of GRBs. The repointing time is as low as  $\sim 30$  s in the best cases except when the weather conditions or observational constraints prevent to begin immediately the observation. This is the result of the automatic procedure and of `GSPOT` working correctly. To this it should be added that the number of technical failures after the new automatic procedure drastically decreased and only small issues (usually with the DAQ) arise during GRB observation, which can happen in any case during the observation of other sources as well.

Moreover, the energy threshold of MAGIC for low zenith observations can be as low as 70-80 GeV after analysis cuts and this is crucial to observe GRBs in an energy range where the effect of the EBL is lower and this increases the chance of detection.

Despite these efforts, a detection of a GRB with the MAGIC telescopes is still missing. The high redshift of the events limits strongly the possibility to detect GRBs due to the absorption of gamma-rays by the EBL. This reduces as well the constraining power of the upper limits obtained from the analysis, especially in the cases when the redshift could not be determined. Nevertheless, the results of this analysis will be part of a publication where all GRBs observed by MAGIC in the two year period 2013-2015, containing other GRBs beside the ones in this

thesis.

As far as the future is concerned, the automatic procedure will be tested periodically to check its operation and the shifters reaction to GRB (transient) alerts. For GRBs, an improvement in the alert system is envisioned for GBM notices, currently the ones received in the highest number. More details about this topic are given in Section 6. Another improvement is expected at trigger level: currently the standard trigger is used to perform GRB observations, but the Sum Trigger will be used in the near future. This will allow to lower further the energy threshold of the telescopes and expand the gamma-ray horizon. Tests are being performed in this sense to check the stability of Sum Trigger when used in the automatic repointing procedure as well as for the Topological trigger.

## 5.2 Gravitational Waves

### 5.2.1 Introduction

The emission of Gravitational Waves (GWs) is one of the physical processes predicted by the General Theory of Relativity (usually called General Relativity, GR in short) proposed by Einstein in 1915. With the new concept of space-time introduced in GR to explain gravitational effects, GWs can be described as ripples in the curvature of space-time propagating at the speed of light and they are created by masses in accelerated motion.

The generation of GW is a direct consequence of the Einstein equation:

$$R_{\mu\nu} - \frac{1}{2}g_{\mu\nu}R = G_{\mu\nu} = \frac{8\pi G}{c^4}T_{\mu\nu} \quad (5.23)$$

where  $R_{\mu\nu}$  and  $R$  are the Ricci tensor and Ricci scalar respectively,  $g_{\mu\nu}$  is the metric tensor and  $T_{\mu\nu}$  is the stress-energy tensor. The Einstein equation relates the curvature of space-time and the energy density, describing how they are affected one by the other. A simple approximation to the Einstein equation is to consider a gravitational field in vacuum (i.e.  $T_{\mu\nu} = 0$ ) far from its source, so that the space-time can be described by the Minkowski metric  $\eta_{\mu\nu}$  plus a little perturbation  $h_{\mu\nu}$ , so that the metric  $g_{\mu\nu}$  can be written as:

$$g_{\mu\nu}(\mathbf{x}) = \eta_{\mu\nu} + h_{\mu\nu}(\mathbf{x}) \quad \eta_{\mu\nu} = \begin{pmatrix} -1 & 0 & 0 & 0 \\ 0 & 1 & 0 & 0 \\ 0 & 0 & 1 & 0 \\ 0 & 0 & 0 & 1 \end{pmatrix} \quad (5.24)$$

With this approximation, (5.23) becomes simply:

$$\square h_{\mu\nu}(\mathbf{x}) = 0 \quad \square = -\frac{1}{c^2} \frac{\partial}{\partial t^2} + \nabla^2 \quad (5.25)$$

This equation as wave-like solutions of the form  $h_{\mu\nu}(\mathbf{x}) = a_{\mu\nu}e^{i[\mathbf{k}\cdot\mathbf{x}-\omega t]}$  which, for a wave propagating along the  $z$  axis and using the *transverse-traceless gauge*, becomes (see Riles 2013):

$$h_{\mu\nu}(\mathbf{x}) = \begin{pmatrix} 0 & 0 & 0 & 0 \\ 0 & h_+ & h_\times & 0 \\ 0 & h_\times & -h_+ & 0 \\ 0 & 0 & 0 & 0 \end{pmatrix} \times e^{i[kz-\omega t]} \quad (5.26)$$

where  $h_+$   $h_\times$  are the constant amplitudes of the two polarizations of the gravitational wave. The effect of a gravitational wave propagating in space can be tested on a ring of free test masses: a GW with only the “+” or “ $\times$ ” polarization will stretch and compress the ring as it propagates in time as shown in Figure 5.19. This is the basic principle behind the detection technique of gravitational waves by interferometers, where sinusoidal-like waveforms are expected when a gravitational wave passes through the detector.

To understand the relation between a gravitational wave and its source, the inhomogeneous Einstein equation must be considered:

$$\square h_{\mu\nu}(\mathbf{x}) = -\frac{16\pi G}{c^4}T_{\mu\nu} \quad (5.27)$$

This equation is very similar to the wave equation for electrodynamics and indeed the Green function formalism can be applied, taking into account retarded times due to the finite speed of propagation of the wave. Under some approximations (distant source approximation, weak gravitational waves, source dominated by its rest-mass density  $\mu$ ) and using local energy/momentum conservation, the following is obtained:

$$h^{ij}(t, \mathbf{x}) \approx \frac{2G}{rc^4} \frac{d^2}{dt^2} [I^{ij}(t - r/c)] \quad I^{ij} \equiv \int d^3x \mu(t, \mathbf{x}) x^i x^j \quad (5.28)$$

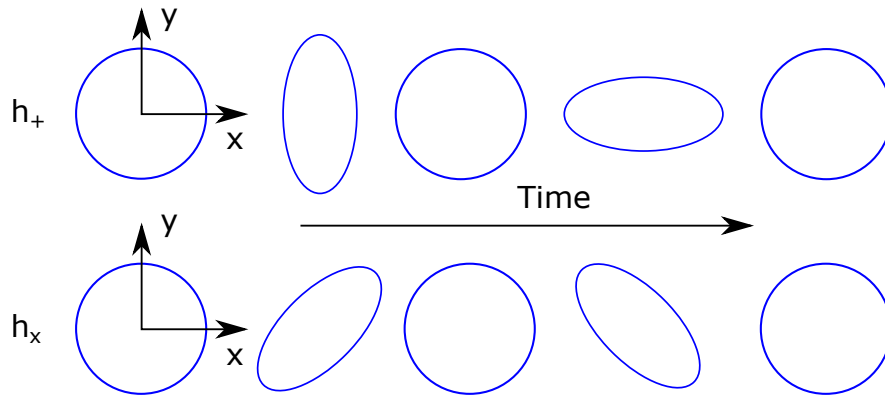


Figure 5.19: Effect of a gravitational wave having only the “+” or “x” polarization propagating through a ring of free test masses.

where  $r$  is the distance of the observer from the source and  $I^{ij}$  is the second mass moment. Finally, also the total energy luminosity  $\mathcal{L}$  can be computed (see Riles 2013):

$$\mathcal{L} = \frac{G}{5c^5} \langle \ddot{F}_{ij} \ddot{F}^{ij} \rangle \quad F^{ij} \equiv I^{ij} - \frac{1}{3} \delta^{ij} I_k^k \quad (5.29)$$

where the average  $\langle \rangle$  is performed over many cycles.

From (5.28), some properties of gravitational waves can be understood:

- they are a quadrupolar phenomenon.
- The amplitude of a gravitational wave, usually called *strain* and denoted by  $h$ , is proportional to  $2G/c^4 = 1.7 \cdot 10^{-44} \text{ s kg}^{-2} \text{ m}^{-1}$ , so that a huge second time derivative of the source quadrupole is needed to obtain a detectable signal. This is possible if the mass of the source is large, of the order of  $M_\odot$ , and its velocity is high.
- The amplitude of the gravitational wave decays as  $r^{-1}$ . This sets a limit to the distance of the source from which a gravitational wave signal can be detected.

The second and third point are especially important for the design of experiments dedicated to the detection of gravitational waves and give indications about the likely sources (see Section 5.2.2) whose gravitational signal could be effectively measured. In this regard, another important property of gravitational waves is that absorption, scattering and dispersion while they propagate through matter is negligible, so that they can be used to have information about the source from which they originated. Finally, despite the linear approximation used in the previous arguments gives a general idea of how gravitational waves originate and propagates, a full post-Newtonian perturbative approach is needed when dealing with relativistic sources and their numerical simulation, as shown in Sathyaprakash and Schutz (2009).

### 5.2.2 Sources of gravitational waves

Gravitational waves are produced by any mass in acceleration including spinning and orbiting objects. As anticipated in the previous section, the amplitude of gravitational waves is very small and only if the masses and velocities involved are large there is the chance of detecting them. Nonetheless, different systems will generate gravitational waves with specific properties, whose analysis can give information about the source(s) (e.g. type, mass and spin). For this reason, usually sources of gravitational waves are classified in four categories:

1. compact binary coalescences (CBCs), that is a binary system of two compact objects (e.g. black holes, neutron stars or white dwarfs);

2. continuous waves from spinning neutron stars;
3. stochastic waves from the Big Bang (relic gravitational waves);
4. burst gravitational waves, as the ones created by the explosion of a supernova.

In the following I will briefly review the properties of the CBC category, since it comprises systems of sources which are expected to emit both a gravitational and an electromagnetic signal, so that a follow-up can be performed from instruments like MAGIC. GW signal properties for the other three categories can be found in Riles (2013) or LVC collaboration (2016) and references therein.

**Compact binary coalescence (CBC)** Binary systems of compact objects, like Neutron Star-Neutron Star (NS-NS or BNS), Black Hole-Neutron Star (BH-NS) and Black Hole-Black Hole (BH-BH or BBH), are expected to be the ideal targets for the search of gravitational waves with ground interferometers. The modeling of the emission of gravitational waves from such systems is quite established and developed, so that matching filters techniques can be applied i.e. matching the possible signal waveform with a database of simulated waveforms with different parameters (e.g. mass, spin, distance).

The main unknown parameter in CBC searches is their occurrence: despite binary stellar systems are common in the Milky Way, not all of them will result in a binary system of compact objects. Few scenarios are for example the disruption of one star by the companion or a kick which removes the newly formed compact object from a bound orbit, preventing the formation or coalescence of the objects. Before the upgrade of LIGO and Virgo, the estimates for the coalescence rates of CBC systems were summarized in the review Abadie et al. (2010), which I report in Table 5.5. The coalescence rate then must be converted into detected coalescence rate taking into account the sensitivity of the detectors, the orientation of the emission and averaging over all sky positions.

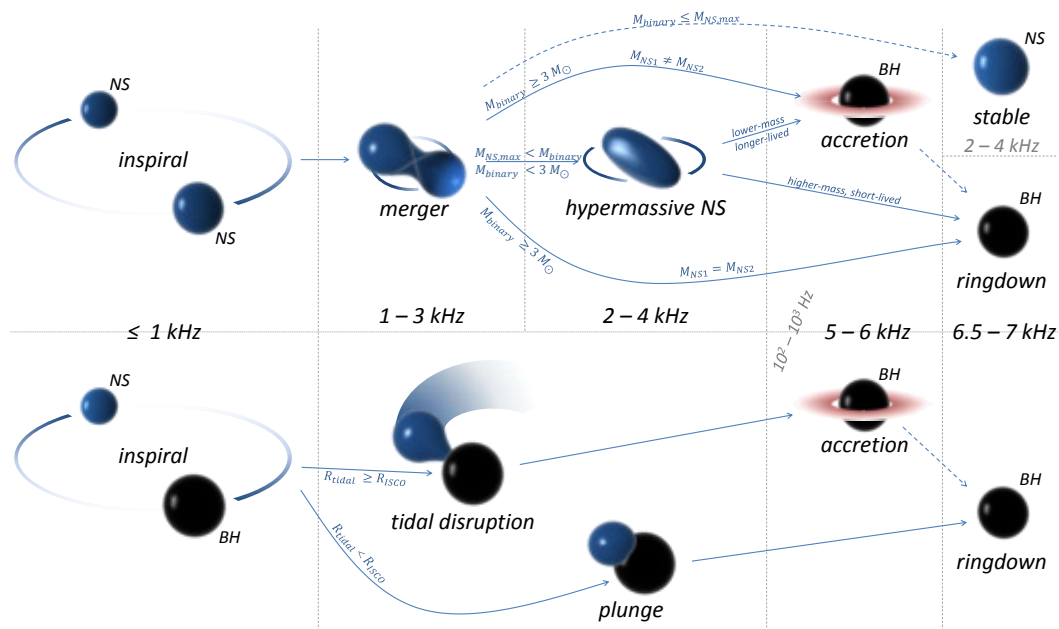


Figure 5.20: Scheme of the possible scenarios for the merging of a BNS (top) or NS-BH (bottom). From Bartos, Brady, and Márka (2013).

Recently the LIGO and Virgo collaboration estimated upper limits on the rate of BNS and NS-BH sources from the non-detection of gravitational signals from these signals in the first observing rung of LIGO, as shown in Abbott et al. (2016e). For BNS systems with objects

| Source | $R_{\text{low}}$<br>[Mpc <sup>-3</sup> Myr <sup>-1</sup> ] | $R_{\text{re}}$<br>[Mpc <sup>-3</sup> Myr <sup>-1</sup> ] | $R_{\text{high}}$<br>[Mpc <sup>-3</sup> Myr <sup>-1</sup> ] |
|--------|--|---|---|
| NS-NS  | 0.01   | 1   | 10  |
| NS-BH  | $6 \cdot 10^{-4}$  | 0.03  | 1   |
| BH-BH  | $10^{-4}$  | 0.005   | 0.3   |

Table 5.5: CBC rates for different systems.  $R_{\text{low}}$ ,  $R_{\text{re}}$  and  $R_{\text{high}}$  are defined as plausible pessimistic, realistic and optimistic estimates respectively. The rates were calculated assuming a mass of  $1.4M_{\odot}$  and  $10M_{\odot}$  for NS and BH respectively. From Abadie et al. (2010).

masses of  $1.35 \pm 0.13M_{\odot}$  the merger rate is less than  $12\,600 \text{ Gpc}^{-3} \text{ yr}^{-1}$ , while for NS-BH systems with NS mass of  $1.4M_{\odot}$  and BH mass of at least  $5M_{\odot}$  it is less than  $3600 \text{ Gpc}^{-3} \text{ yr}^{-1}$  considering an isotropic distribution of spin directions of the objects. The merger rate was updated recently with the detection of GW170817/GRB170817A to  $R = 1540^{+3200}_{-1220} \text{ Gpc}^{-3} \text{ yr}^{-1}$ , see Abbott et al. (2017a). For BBH systems, an estimate of their merger rate was inferred from the GW signal detections in the first and second observing runs (GW150914, GW151226, GW170104 and the less significant LVT151012) leading to a conservative range  $12 - 213 \text{ Gpc}^{-3} \text{ yr}^{-1}$ , see Abbott et al. (2017b). Regarding the coalescence of two compact objects, usually it is characterized by three stages: *inspiral*, *merger* and *ringdown*. When simulated, these three phases are treated in different ways, in particular for the merging phase, where strong relativistic effects need to be treated properly with a numerical relativity calculation. After the ringdown, a single black hole is left, whose mass will be the less than the sum of the two initial objects since part of the energy is radiated away as gravitational waves. Following Riles (2013), the frequency  $f_{\text{GW}}$  and the amplitude  $h_0$  evolution in time for two objects of mass  $M_1$  and  $M_2$  in circular orbits during the inspiral phase respectively are given by:

$$f_{\text{GW}}(t) = \frac{1}{8\pi} [1 \cdot 5^3]^{1/8} \left[ \frac{c^3}{GM_{\text{chirp}}} \right]^{1/8} \frac{1}{(t_{\text{coal}} - t)^{3/8}} \quad (5.30)$$

$$h_0(t) = \frac{1}{r} \left[ \frac{5G^5 M_{\text{chirp}}^5}{c^{11}} \right]^{1/4} \frac{1}{(t_{\text{coal}} - t)^{1/4}} \quad (5.31)$$

where  $M_{\text{chirp}} = (M_1 M_2)^{3/5} / (M_1 + M_2)^{1/5}$  is called *chirp mass* and  $t_{\text{coal}}$  is the coalescence time of the system. These are approximations which of course are not valid during the late inspiral and merging stages, where the orbit radius is close to zero and the objects move at relativistic speeds. In this phase, only post-Newtonian approaches can describe the time evolution of the orbital phase  $\phi(t)$ , see for example Sathyaprakash and Schutz (2009). It has to be noted that the approximated formulas for  $f_{\text{GW}}(t)$  and  $h_0(t)$  depend only on the chirp mass and not on the single masses  $M_1$  or  $M_2$  and so at that approximation level they cannot be estimated. Instead, from post-Newtonian methods the frequency computed as time derivative of the orbital phase  $\phi$  will depend on  $M_1$  and  $M_2$ , allowing in principle to infer them from the signal waveform. Finally, other effects to take into account which can modify the waveform are the possible elliptical orbit of the objects and their spin, particularly important in the case that at least one object is a black hole.

### 5.2.3 The interferometric technique for GW detection and localization

Measuring directly the effect of gravitational waves is very difficult due to their very small amplitude and for this reason the first searches were of indirect type. The first indirect proof of the existence of gravitational waves was given by Hulse and Taylor (1975) with the discovery of a binary system of pulsars (PSR B1913+16), the first of its kind. Emission

of gravitational waves in this kind of systems is expected and it results in a loss of orbital energy and consequently in a decrease of the orbital period. The system was monitored for few decades and the observed and theoretical (predicted by GR as emission of GW) orbital decays were found to be in perfect agreement, see Figure 5.21 and Weisberg and Taylor (2005).

The direct detection of gravitational waves required a huge technological effort. The first detectors for GW were developed by Weber and are usually called *resonant bars*, see Weber (1960). The name comes from the fact that the detector is a metal cylinder with piezo-electric crystals to measure small longitudinal vibrations of the bar due to the passage of a gravitational wave, to be compared with its baseline thermal motion which is one of the largest source of noise for GW measurement. A development of resonant bars are cryogenic detectors to reduce the thermal noise: the gain in sensitivity with respect to the first Weber-type resonant bar is about six order of magnitudes. Despite this, this kind of detectors were sensitive mainly to GW signals due to the collisions of black holes or supernovae collapses within our galaxy, so the expected rate is very low.

A second approach is based on the interferometric technique, see Pitkin et al. (2011). The separation  $L$  of two test masses is changed by  $\Delta L$  due to a gravitational wave, resulting in an amplitude:

$$h = \frac{2\Delta L}{L}$$

If the two masses (mirrors) are placed in two perpendicular arms at the same distance  $L$  from a light source like in a Michelson interferometer, a gravitational wave will change the length of the arms (depending on the orientation of the GW with respect to the detector) and the final light output measured will change accordingly. This detection technique allows at the end to have very good strain sensitivities in a wide range of frequencies, from few tens of Hz to few kHz. The main experimental challenge for GW interferometers are the several noise sources which must be properly taken into account and reduced as much as possible. These sources of noise can be divided in two categories:

- **displacement noises**, which comprise the seismic noise from Earth, thermal noise of the mirrors (Brownian motion, thermo-elastic noise from temperature fluctuations, thermo-refractive noise from changes in the refractive index) and the gravity gradient noise (gravitational coupling of mass density fluctuation around the detector with the test masses);
- **optical noises**, comprising quantum noises (shot noise in the detected photocurrent, radiation pressure noise on the test masses), laser noises, modulation noises and scattered light noises.

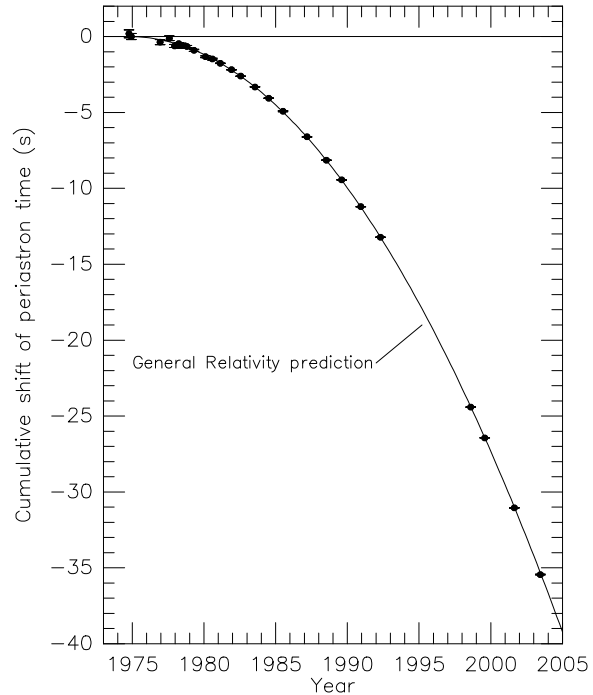


Figure 5.21: Decay of the orbital period from 1975 to 2005 in the binary system PSR B1913+16. The points are measurements, while the solid line is the theoretical prediction from the emission of gravitational waves. From Weisberg and Taylor (2005).

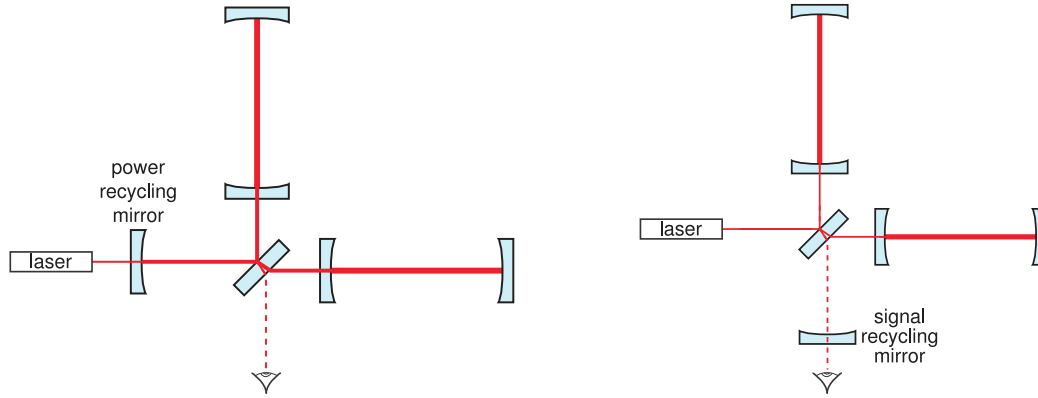


Figure 5.22: Working principle of a power and a signal recycling mirrors (left and right) respectively. From Pitkin et al. (2011)

In order to cope with these noises, special experimental apparatus must be considered. For example, the seismic noise can be reduced with a multi stage cantilever system with both active and passive isolation components. The gravity gradient noise can be reduced instead with two approaches: monitoring the ground motion with seismometers and properly subtract the noise signal measured or placing the detector in quiet places or better underground. The thermal noise mainly depends on the mirror coating material, which is chosen for its optical properties and not its mechanical or thermal one. In this case a compromise between the mechanical loss factors and optical noises and losses (radiation pressure, diffraction) must be found for both the mirror and suspension fiber materials. Optical noises mostly deal with the power of the laser used in the apparatus. Depending on the strain sensitivity to be achieved, a laser power  $P$  as high as 6 MW can be required (strain sensitivity is proportional to  $1/\sqrt{P}$ ). The radiation pressure depends on the laser power as well but also on the mass of the mirrors ( $\delta x^2 \propto P/m$ , with  $\delta x^2$  being the power spectral density of the fluctuating motion of each test mass), so having a low power laser or a large test mass can reduce this noise. Usually, at a given frequency, there is an optimum value of the laser power minimizing the effect of both shot and radiation pressure noise in the hypothesis that they are uncorrelated: the corresponding sensitivity limit (or strain noise) is called *Sensitivity Quantum Limit* (SQL). To cope with the difficult requirement of a laser with  $\mathcal{O}(10^6)$ W power, a power recycling mirror can be placed between the laser and the interferometer (see Figure 5.22). A resonant cavity is thus formed and the power required can be effectively reached with an input laser power orders of magnitude lower than  $10^6$  W. Another similar technique to enhance the sensitivity of interferometers is called *signal recycling*: a suitable mirror is placed at the output of the instrument so that any sideband created on the light by gravitational waves is sent back in the interferometer where it resonates and gets enhanced (see Figure 5.22). The number of light bounces inside the interferometers depends on the arm length and on the timescale expected for the signal. For an arm length of 3 km and a timescale of 1 ms, 50 bounces are enough to reduce the power requirement of the laser to  $\mathcal{O}(10^3)$ W.

As far as the response of the detector is concerned, since the wavelengths to be measured are way longer than the size of the detector, interferometers can be thought as antennas. For a generic GW coming from an arbitrary direction in the sky  $(\theta, \phi)$  with respect to a reference system centered on the detector,  $h_0$  can be replaced by  $|h_{yy} - h_{xx}|$ , where  $h_{xx}$  and  $h_{yy}$  are given by Blair et al. (2015):

$$h_{xx} = -\cos\theta \sin(2\phi)h_{\times} + (\cos^2\theta \cos^2\phi - \sin^2\phi)h_{+} \quad (5.32)$$

$$h_{yy} = \cos\theta \sin(2\phi)h_{\times} + (\cos^2\theta \sin^2\phi - \cos^2\phi)h_{+} \quad (5.33)$$

The antenna responses in an interferometer are shown in Figure 5.23 for different polarizations of the incoming GW. A consequence of this kind of response is that the localization capability of a single interferometer is very poor. Having a second detector or even more allows to triangulate the signal between pairs of detectors, improving the sky localization.

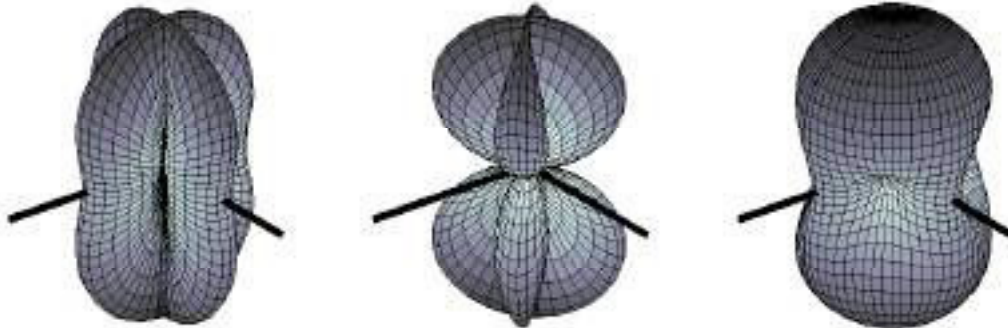


Figure 5.23: Antenna patterns in a Michelson interferometer. The beam-splitter is at the center of each pattern and the thick solid black lines denote the two interferometer arms. From left to right: + polarization,  $\times$  polarization and unpolarized waves. From Riles (2013).

The basic principles of an interferometer for GW measurement explained above are the basis of current generation interferometers: Advanced LIGO (aLIGO or simply LIGO) and Advanced Virgo (AdV or simply Virgo). Here I will just describe very briefly the main parameters of these instruments, but for a full description of the technical details of the two detectors see LIGO Scientific Collaboration et al. (2015) and Acernese et al. (2015). I will then focus more on the science case interesting for a follow-up from EM observatories like MAGIC, namely CBC sources as introduced in Section 5.2.2, and how the localization of GW events is provided. This is especially important when discussing a follow-up strategy as described in Section 5.2.4.

LIGO and Virgo are kilometer-scale interferometers built for a direct detection of GW signals. aLIGO (LIGO Scientific Collaboration et al. 2015) comprises two identical detectors placed in two different sites, one in Livingston (LA, USA) and the other in Hanford (WA, USA). The arms of the LIGO interferometers are 4 km long with Fabry-Perot resonant cavities and both power and signal recycling. A third detector was planned to be built in the Hanford site, but instead it will be installed in India (LIGO-India) in few years. Advanced LIGO is an enhancement of Initial LIGO with improved strain sensitivity and lower frequency end of the sensitivity band (10 Hz) thank to the replacement of several components and using new technologies to reduce the noise. In particular, in the low frequency band the seismic and thermal noises are reduced thanks to a better seismic isolation and test mass suspension. At mid and high frequencies up to 7000 Hz, the sensitivity was improved thanks to a higher power laser (up to 125 W at the power recycling mirror), larger test masses (40 kg) and better mirror coatings.

Advanced Virgo (Acernese et al. 2015) is a 3 km arm interferometer located in Cascina (Italy) and is the upgrade of the Virgo detector. Some of the technological improvements like signal recycling mirrors, increased laser power, heavier test masses, better coating and vibration isolation are very similar to the ones adopted by aLIGO. The sensitivity reachable by AdV is lower than the one by aLIGO: in the case of Virgo, thermal noise of the suspension wires, 50 Hz main line and harmonics and scattered light due to seismic noise are the main limitations at low frequencies. At high frequencies, shot noise from the primary and secondary beams is the main contribution to the overall noise.

The commissioning, upgrade and observation roadmaps for aLIGO and AdV can be found in Abbott et al. (2016c). The observations are divided in several runs, called *observation*

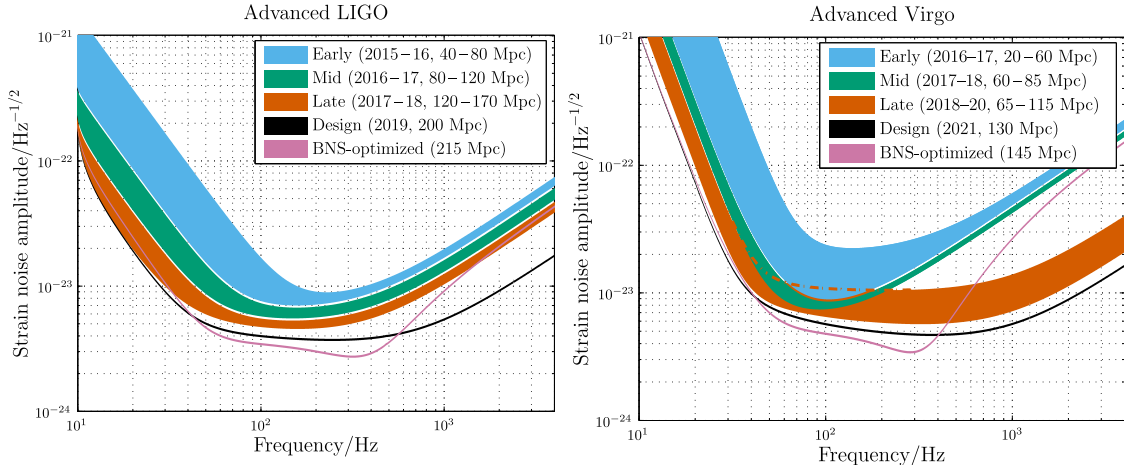


Figure 5.24.1

Figure 5.24.2

Figure 5.24: Prospects for the sensitivities achievable by aLIGO and AdV. From Abbott et al. (2016c).

*runs*, between which the detectors are progressively upgraded to reach their final design sensitivity which affects the effective volume that can be searched for GW signals, as shown in Figure 5.24. For the aLIGO-AdV network, three observation runs denoted as O1, O2 and O3 were envisioned. At the time of the writing of this thesis, both O1 and O2 have already ended. In O1 (from 18th September 2015 to 12th January 2016) only aLIGO was operative and it was the beginning of GW astronomy with the detection of two GW signals from binary systems of solar mass black holes: GW150914 (detected in the so called engineering run, Abbott et al. 2016b) and GW151226 (Abbott et al. 2016a). In O2 (from 30th November 2016 to 25th August 2017) the third GW signal was detected by aLIGO (GW170104, another binary black hole system, Abbott et al. 2017c). AdV joined the observations on 1st August 2017 leading to the first joint LIGO-Virgo detection of merging black holes (GW170814, Abbott et al. 2017d) and of a BNS system (GW170817, Abbott et al. 2017e). In O3, starting at the end of 2018 and with nine-month duration, both aLIGO and AdV will benefit of detector upgrades for a better sensitivity. By 2019 they will reach the full design sensitivity and in the following years other facilities will probably join the network (e.g. LIGO-India, KAGRA, Einstein Telescope). The predicted strain sensitivity and BNS range in Mpc are shown in Figure 5.24.

aLIGO and AdV search for many types of GW signals from different source types, as discussed in Section 5.2.2. Here I focus on the CBC category and on their localization by aLIGO and AdV: the search of GW signals is performed almost in real-time in order to rapidly identify GW event candidates and send alerts to EM partners for follow-up observations. The basic sky localization which can be performed by a network of interferometers is via triangulation: in the case of two detectors (like in O1 and most part of O2) this method results in an annulus in the sky and other informations that can be used to restrict the localization to parts of the annulus. If a third detector is added, the triangulation method provides two opposite sky positions, one of which can be discarded by requiring consistent amplitudes in the detectors. Moreover the localization depends on the SNR of the signal, so instruments with different sensitivities provide different accuracies in the localization estimates. With more detectors, the timing information is sufficient to have a very good localization of the event.

aLIGO and AdV provide the sky localizations of GW candidate events to EM observatories as posterior probability density skymaps. These are generated by different pipelines with either a low or high latency. For CBC, the sky localization is provided rapidly in few seconds with BAYESTAR, a Bayesian position reconstruction method described in Singer and Price (2016).

It uses the time arrival, the amplitude and the phase on arrival of a GW event and generates a likelihood function used for a Bayesian inference, obtaining the marginal posterior probability. This is performed for sky locations on a HEALPix grid. The advantage of BAYESTAR is that it does not use a Markov Chain Monte Carlo (MCMC) method which is computationally demanding. Moreover it can be parallelized very easily so that the run time can be reduced from few hundreds of seconds to few seconds. The BAYESTAR skymap is the first one to be sent to EM observatories for a rapid follow-up of GW events. An example of sky localization skymap produced by BAYESTAR is shown in Figure 5.25.

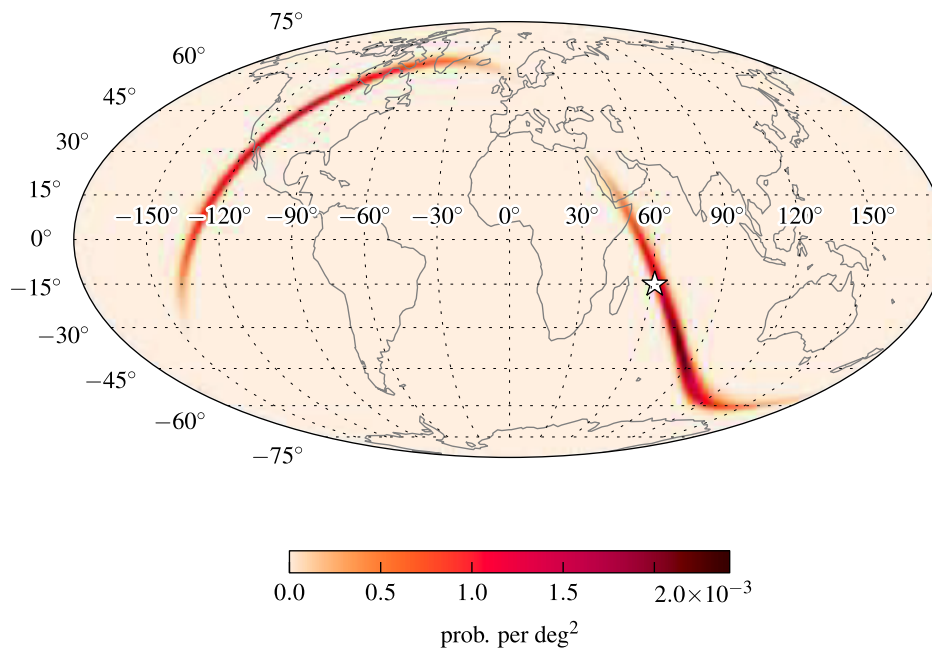


Figure 5.25: Example of a posterior probability density skymap of a simulated CBC event produced by the BAYESTAR pipeline. The star denotes the true location of the event, which is located at 266 Mpc. From Abbott et al. (2016c).

A second, high latency sky localization pipeline is LALInference, see Veitch et al. (2015). Compared to BAYESTAR, it uses full MCMC, nested sampling and Bayesian inference methods and beside sky locations, it can reconstruct the masses and the spin of the objects. Due to the high dimensionality of the parameter space, the time required to obtain a final skymap is longer than in the BAYESTAR case, ranging from few hours to days. A mid-latency LALInference analysis which does not take into account the spins of the object can provide a faster analysis with results comparable with BAYESTAR.

The skymaps produced by BAYESTAR or LALInference are privately distributed to EM partners via the GCN, so that follow-up observations can be performed, as described in the next Section.

Given a posterior probability density skymap, produced either with BAYESTAR or LALInference, the sky localization is described by the credible region  $CR_{0.9}$ , defined as the smallest area enclosing 90% of the total posterior probability (i.e. the sky area to be covered to have a 90% probability of enclosing the true location). The value of  $CR_{0.9}$  depends on the number of detectors detecting a GW signal, improving of orders of magnitude going from a two to a three-detectors network, as proven in Singer et al. (2014). While with Hanford and Livingston only  $CR_{0.9}$  is of the order of few thousands of square degrees, adding Virgo to the networks dramatically improves the localization to  $\sim 200 \text{ deg}^2$  or even to few tens of square degrees for signals with high SNR. This is particularly important for the follow-up of GW events by small FoV instruments like MAGIC, as described in the next Section.

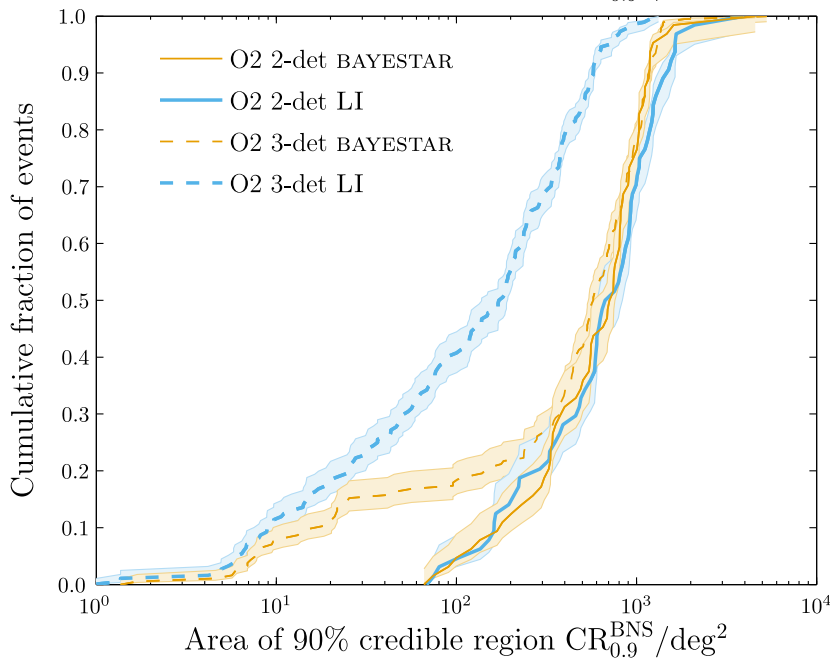


Figure 5.26: Binary neutron star sky localization in O2 with a 2 or 3 detectors network and for different pipelines (BAYESTAR and LALINFERENCE). The cumulative fraction of events is shown as a function of  $CR_{0.9}$ , the smallest area enclosing 90% of the total posterior probability. From Abbott et al. (2016c).

#### 5.2.4 MAGIC follow-up of GW candidate events from LVC: motivations and strategy

CBC systems (BBH, BNS and NS-BH) are thought to be able to emit gravitational waves detectable by aLIGO and AdV. At the time of the writing of this thesis, it is known that both BBH and BNS systems produce gravitational waves thanks to the detection of four and one event respectively. From systems with a NS and a black hole, a detection is still missing. The main reason for EM observers to perform a follow-up of GW candidate events is that EM emission is expected from these systems. Thus the link between GW and EM astronomy is crucial: the observation of the same event using different messengers (gravitational waves and photons, to which neutrinos and cosmic rays could be added) gives complementary informations about the source(s). While GW data can estimate several parameters of the sources like mass, spin, sky location (with accuracy depending on the number of detectors involved) and distance, EM observations could pinpoint the host galaxy, give a precise estimate of the redshift and information about the physical processes in the post-merger environment.

The importance of follow-up observations of GW candidate events became even more clear after the detection of the first GW signal, GW150914, when Fermi-GBM reported the possible detection of a weak gamma-ray transient after 0.4s from the GW trigger with a consistent sky localization (Connaughton et al. 2016). Since the GW signal was due to a BBH system, from which EM emission is not expected, the possible association (Savchenko et al. 2016) triggered many theoretical explanations for the electromagnetic emission from BBH systems. Some of these theories involve high-mass, low-metallicity stars undergoing a weak supernova explosions and producing a short GRB (Perna, Lazzati, and Giacomazzo 2016), clumps in a dumbbell configuration originated by the core of a rapidly rotating massive star (Loeb 2016) or Poynting-flux-dominated jets produced via the Blandford-Znajek mechanism (Yamazaki, Asano, and Ohira 2016) detectable as GRBs or Fast Radio Bursts (Zhang 2016).

Even more interesting is the case of BNS or NS-BH systems, because they are thought to be the progenitors of short GRBs. In this case the presence of a neutron star provides the

barionic matter which can then be accreted around the final BH, powering a collimated jet observable as a short GRB. Other possible electromagnetic counterparts for BNS and NS-BH systems comprise orphan optical or radio afterglows in the case the GRB is not energetic enough and *kilonovae* (Fernández and Metzger 2016; Metzger and Berger 2012). A picture of the possible EM counterparts of these systems is shown in Figure 5.27. In the particular case of GRBs, the detection of a GW signal will convey information about the central engine, while the EM emission can give information only about processes happening at large distances from the progenitor. For example, gravitational waves from BNS or NS-BH systems can be used to determine the source population and map it as a function of redshift in relation to the one for short GRBs, which is highly uncertain. The rate of binary mergers detected by GW detectors instead can help in constraining or determining the opening angle of short GRBs. The study of the GW signal finally can be used to reconstruct the properties of the neutron star (in particular its equation of state, on which the evolution of the merging depends strongly), of the magnetic fields in the inspiral or post-merger phase and of the accretion disk, see Bartos, Brady, and Márka (2013). So the GW-EM observation of the same event would give the full picture: the gravitational signal provides information about the progenitor and the central engine in the inspiral, merger and post-merger phases while the electromagnetic signal determines the properties of the outflow propagating from the central engine. This approach is the one used in the recent discovery of a gravitational wave by a BNS system, GW170817, associated with a short GRB, GRB170817A, observed with a delay of  $(1.74 \pm 0.05)$  s, see Abbott et al. (2017a). The event was also observed in optical as a kilonova (Arcavi et al. 2017; Coulter et al. 2017; Soares-Santos et al. 2017; Valenti et al. 2017; Tanvir et al. 2017; Pian et al. 2017; Lipunov et al. 2017; Covino et al. 2017), so as expected from predictions of the merging of a BNS system.

Given the relation between gravitational waves from binary mergers and short GRBs and the expected HE/VHE emission from sGRBs (Veres and Mészáros 2014; Takami, Kyutoku, and Ioka 2014), MAGIC is one of the facilities that signed a Memorandum of Understanding (MoU) with the Ligo and Virgo Collaboration (LVC) to receive alerts about GW candidate events through the GCN channel. These alerts contain a link to the skymaps generated by the localization pipelines discussed in the previous Section and basic parameters of the event. With this information, a follow-up can be planned.

In this regard, MAGIC must deal with the localization problem. As discussed in the previous section, the skymaps provided by LVC can have localizations as large as thousands of square degrees. Given the small field of view of MAGIC ( $3.5^\circ$  diameter), this poses a huge obstacle in performing a follow-up of a GW event. For this reason, a strategy must be set up to cope with this problem. Since MAGIC is one of the many EM partners joining the GW events follow-up, until the localization will be precise enough to cover the entire 90% credible region with a reasonable number of pointings, the current MAGIC follow-up strategy for GW candidate events is to exploit the follow-up observations of wide FoV instruments (e.g. Swift-BAT or Fermi-GBM) pointing possible counterparts detected by those detectors. As in the case of GRBs, EM counterparts from Fermi-GBM or Fermi-LAT are the obvious best candidates for a MAGIC follow-up, but also other bands (optical, radio, X) or even other messengers (neutrinos) are considered. This strategy was applied in the first and only follow-up observation performed by MAGIC during O1 after the detection of GW151226 by LIGO, as described in Section 5.2.6.

Regardless of the extension of the sky localization, it is useful to assess the visibility from the MAGIC site compared to the skymaps provided by LVC. For this reason I developed a Python script which reads the GW events skymap, saved as a `.fits` or `.fits.gz` all-sky image file with the HEALPix projection, and calculates the sky region visible from the MAGIC site below a certain zenith value to assess the overlapping with the 90% credibility region of the LVC skymap. The calculation is performed for different times in the night chosen for the computation in order to know when the highest probability region will be

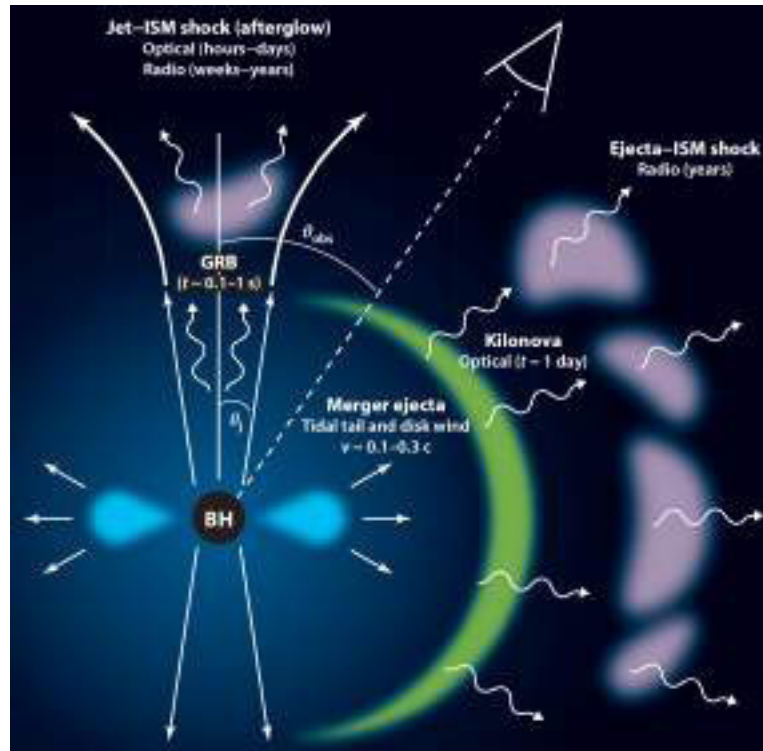


Figure 5.27: Possible electromagnetic counterparts of CBC mergers depending on the viewing angle  $\theta_{\text{obs}}$ . The possible GRB emission can be seen by observers with  $\theta_{\text{obs}} < \theta_j$  because of relativistic beaming. Optical and radio afterglow emission can be seen at different timescales. Another possible counterpart is a kilonova, emitting in the optical/IR bands due to the radioactive decay of r-process elements generated in the ejecta. From Berger (2014).

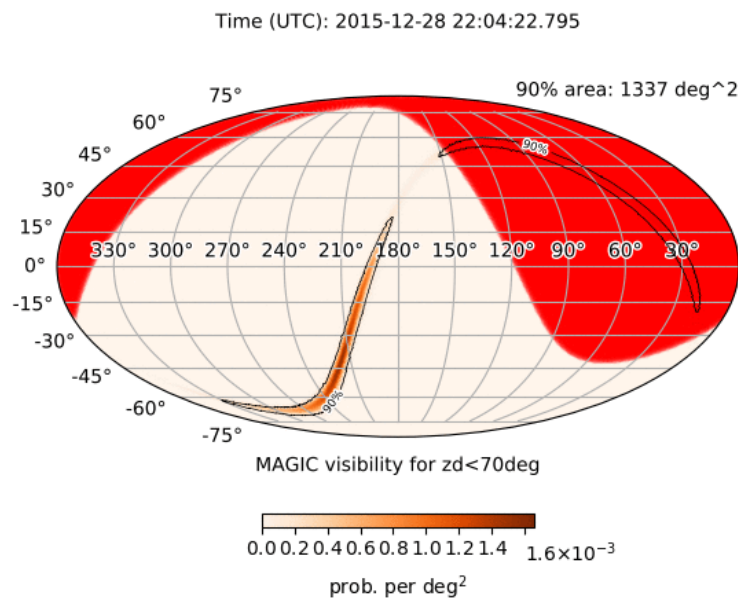


Figure 5.28: Example of the graphical output of the Python script developed by me to calculate the sky region visible by MAGIC below a certain zenith ( $70^\circ$  in this case, in red) at a certain time to assess the overlap with the LIGO/Virgo skymap. In this case the GW event is GW151226.

covered. To generate the sequence of pointings instead, already existing softwares can be used, like GWsky (<https://github.com/ggreco77/GWsky>).

After the follow-up, the data analysis is the next step. In most of the cases the localization will have a 90% credibility region larger than the MAGIC field of view. This poses a problem when analyzing the data, since the standard tools of the MAGIC software are well tuned and tested for point-like or moderately extended sources. Since the electromagnetic emission could come from any point of the FoV for GW follow-up given the huge sky areas involved, a new analysis approach is needed and it is the topic of the next Section.

### 5.2.5 Flux Upper Limits skymaps for Gravitational Waves candidate events

Since the localization of Gravitational Wave events is rather poor in the case of a two-site network of detectors, like in the case of the O1 run and part of the O2 run of aLIGO, there was the need to implement a new tool within the standard MAGIC analysis software MARS. The executable `flute`, which calculates fluxes, spectra and upper limits, has a limitation: the flux (or flux upper limits) of a source or, generally speaking, a target, is calculated only in its sky coordinates. There is the possibility to calculate fluxes in a different position, but unless the right Monte Carlo data are provided, the estimation of MC related quantities like the effective area and the migration matrix will not be correct. This is a consequence of the MAGIC wobble pointing mode. Standard MC data (wobble ring MC) for point-like sources are produced on a ring at a  $0.4^\circ$  degrees angular distance from the camera center and observations are performed at the same offset, except for particular sources. If wobble ring MC were used to calculate the flux on a different position from the target one, the effective area calculation would not be correct since the distance of the sky position selected from the camera center is different from the standard wobble offset. The problem can be solved using *diffuse Monte Carlo* data, in which MC events are generated over a viewcone of  $2.5^\circ$ . The MARS executable `selectmc` can then be used to select MC data with the proper source-camera distance and use them as an input to `flute` to calculate correctly the effective area and, at last, the flux and related quantities.

Given the limited MAGIC FoV and the largely imprecise localization of GW candidate events in the O1 run and most of the O2 run, the calculation of fluxes or flux upper limits only at the target position is not enough. Regardless of how the targets for the GW follow-up are chosen, what is searched for is a possible emission from a large portion of the MAGIC FoV and not only from the telescopes pointed sky position. This goal points out to the need of a tool calculating fluxes in a wide region of the FoV, which was not implemented in MARS before the beginning of the GW follow-up program.

The starting idea is to reuse already implemented, well tested MARS executables, namely `flute`, `selectmc` and `foam`. The tool performs the following steps:

1. select a number of sky positions around the target position. This number depends on some inputs parameters given by the user, in particular the radius of the sky region where fluxes will be calculated and the separation of the sky positions. I call the ensemble of these sky positions *grid*.
2. for each point of the grid, its distance from the target position and the camera center are calculated. This information is used to select appropriately MC data with `selectmc` from diffuse MC data (test sample).
3. once MC data are selected, `flute` can be run for each grid point. Since every MAGIC target is observed in different wobble positions, `flute` must be executed separately for each wobble position for each grid point with a MC ring with the proper distance from the camera center. The “off-from-wobble partner” method is used for background estimation. This choice is made based on the fact that for the follow-up of gravitational

waves events the targets will be observed for a time period not greater than 1 h, since the number of targets can be large in order to cover as much as possible the localization region with the highest a posteriori probability (in the case no other counterparts are found).

4. after running `flute`, results from different wobble pointings but same grid point must be merged. This is done by running accordingly `foam` on `flute` outputs. `foam` is a MARS executable which merges different `flute` output averaging and weighting the effective area according to the observation times of the inputs, calculating the merged spectrum and SED.
5. the last step is creating the flux and flux upper limits skymaps. A ROOT macro reads `foam` outputs and gathers the necessary information to accomplish the task.

In the previous list, no reference was made on how `melibea` files should be produced. For the tool it is needed to create Random Forest from diffuse MC data (train sample), so that a proper gamma/hadron separation can be performed.

During the developing phase of the tool, several tests<sup>3</sup> were performed to assess the compatibility of the results with the ones from other MARS executables, in particular `caspar`. The outcome of the tests are described in the next section.

### Tests performed on the tool

**MC rings thickness** The executable `selectmc` allows the user to select MC data according to the distance of the source from the camera center. This is done specifying two parameters,  $r_{\min}$  and  $r_{\max}$ , that is the minimum and maximum distance from the camera center respectively. As in the case of standard MC data, `selectmc` output is a MC ring. A proper calculation of the effective area needs enough MC statistics, so that the thickness of the ring must be suitable in order to have enough MC events.

In order to evaluate a suitable ring thickness, a test was performed taking `ST.03.06` MC data and looking at the distribution of the number of events  $N$  divided by the distance from the camera center  $R$  as a function of  $R$ . The ring thickness was computed for a dense sample of distances  $R_i$ : the thickness value at a distance  $R_i$  is the absolute value of the difference between  $R_i$  and the distance where  $N/R$  drops of a factor 0.2 with respect its value at  $R_i$ . The factor 0.2 was chosen to ensure a sufficient number of MC data in the ring.

The results of the test are shown in Figure 5.29 For small  $R$ , the distribution of MC data is almost flat, so that in principle the ring thickness should be high according to the aforementioned criterion. In this case, the flatness of the distribution ensures that even a small ring contains enough MC. So we focus on distances greater than  $\sim 0.6^\circ$ , where the distribution starts to drop. It can be seen that for  $R \gtrsim 0.6^\circ$ , the ring thickness can be taken to be  $0.2^\circ$ , having enough MC data for the effective area calculation.

**Grid points separation** The goal of this test is to assess the spacing between grid points in order not to lose too much sensitivity if the possible  $\gamma$ -ray source does not lie exactly on a grid point. The PSF of MAGIC is calculated from `ST.03.06` diffuse MC data and we look at the overlap of the PSF centered on a grid point and the PSF centered at a distance of  $s/\sqrt{2}$ , where  $s$  is the grid points separation. Taking MC rings at different distances and  $s = 0.04^\circ$ , the PSFs overlap is around 87% (see Table 5.6).

The way the sensitivity loss was estimated here is quantitatively rough, but it concludes that the choice of a grid spacing equal to  $0.04^\circ$  is good. For a more precise quantification of the sensitivity loss, another test was performed on Crab Nebula data (see below).

---

<sup>3</sup>For most of the tests, a crosscheck was performed by Konstancja Satalecka (DESY), who had the same idea on how to design the tool. Moreover, during the development phase of the tool, Koji Noda (MPI) tested

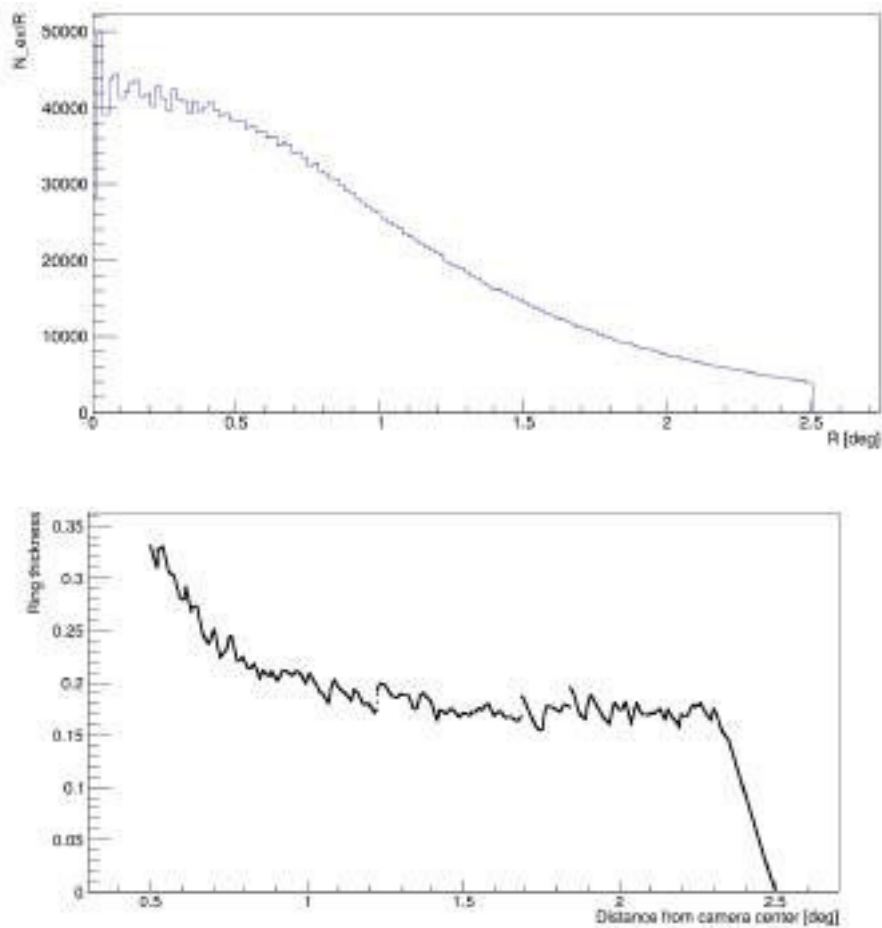


Figure 5.29: **Top:** distribution of the ratio of the number of MC events and the distance from the camera center  $R$  as a function of  $R$ . **ST.03.06** MC data were used. **Bottom:** values of the ring thickness for densely sampled values of  $R$ . Since the distribution of MC data is flat up to  $0.6^\circ$ , the focus is on larger radii (see text).

| Ring    | PSF value | overlap [%] |
|---------|-----------|-------------|
| 0.3-0.5 | 0.089     | 87.5        |
| 0.7-0.9 | 0.095     | 88          |
| 1.4-1.6 | 0.084     | 86.7        |
| 1.9-2.1 | 0.087     | 87.2        |

Table 5.6: Results of the test to determine the separation between grid points. The three columns are the chosen MC ring (with  $0.2^\circ$  thickness), the PSF value and the PSF overlap respectively.

**Crab Nebula spectrum reconstruction** After the determination of the values for the grid points separation and ring thickness, the next step was to try out if the tool was able to reconstruct properly the Crab Nebula spectrum. I took Crab Nebula data from the period ST0303 taken with different wobble offsets:

- $0.4^\circ$  (standard wobble offset): 2013-10-04, 2013-10-05, 2013-10-10, 2013-11-01, 2013-11-07, 2013-11-12, 2013-11-13, 2013-11-29

---

the tool and gave important comments and suggestions. I thank both of them.

---

- 0.7°: 2013-11-06, 2013-11-30, 2014-01-29
- 1.0°: 2013-11-04, 2013-11-08

In this case it is not important to create the full grid of points, but the one centered on the position of the Crab is enough to reproduce the spectrum. So the tool here is not tested in its entirety, but in any case some of its features are used and are therefore tested: calculating the distance of the source from the camera center, selecting the proper MC ring, running `flute` for each wobble position (in this specific case, Crab Nebula data are taken with two wobble positions) and finally running `foam` to merge the results. Of course a flux/UL skymap does not make sense with just one grid point.

The resulting spectra are compared with the Crab Nebula spectrum (in the range 65 GeV-13.5 TeV) reported in Aleksić et al. (2016b):

$$\frac{dN}{dE} = f_0 \left( \frac{E}{1 \text{ TeV}} \right)^{a+b \log_{10}(E/1 \text{ TeV})} \quad [\text{cm}^{-2} \text{ s}^{-1} \text{ TeV}^{-1}] \quad (5.34)$$

with parameters:

$$f_0 = (3.39 \pm 0.09) \cdot 10^{-11} \quad a = -2.51 \pm 0.02 \quad b = -0.21 \pm 0.03$$

$$F(E > 100 \text{ GeV}) = 5.52 \cdot 10^{-10} \text{ cm}^{-2} \text{ s}^{-1}$$

The results of the test are shown in Figures 5.30, 5.31 and 5.32 with the following fit values:

- 0.4°:  $f_0 = (3.35 \pm 0.05) \cdot 10^{-11}$     $a = -2.51 \pm 0.02$     $b = -0.22 \pm 0.02$

$$F(E > 100 \text{ GeV}) = 5.38 \cdot 10^{-10} \text{ cm}^{-2} \text{ s}^{-1}$$

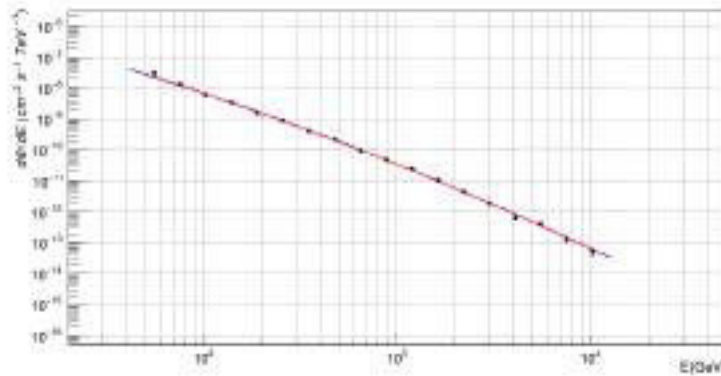


Figure 5.30: Crab Nebula spectrum at 0.4° offset. The red line is fit with the spectrum given by (5.34), while the blue line is the spectrum from Aleksić et al. 2016b.

- 0.7°:  $f_0 = (3.06 \pm 0.15) \cdot 10^{-11}$     $a = -2.54 \pm 0.07$     $b = -0.25 \pm 0.08$

$$F(E > 100 \text{ GeV}) = 4.96 \cdot 10^{-10} \text{ cm}^{-2} \text{ s}^{-1}$$

- 1.0°:  $f_0 = (3.22 \pm 0.13) \cdot 10^{-11}$     $a = -2.52 \pm 0.04$     $b = -0.27 \pm 0.06$

$$F(E > 100 \text{ GeV}) = 4.94 \cdot 10^{-10} \text{ cm}^{-2} \text{ s}^{-1}$$

All values are compatible within statistical and systematic uncertainties (18% at energies  $\lesssim 100$  GeV and 11% in the energy range of few hundreds of GeV for the flux normalization  $f_0$ ) with the values from Aleksić et al. (2016b).

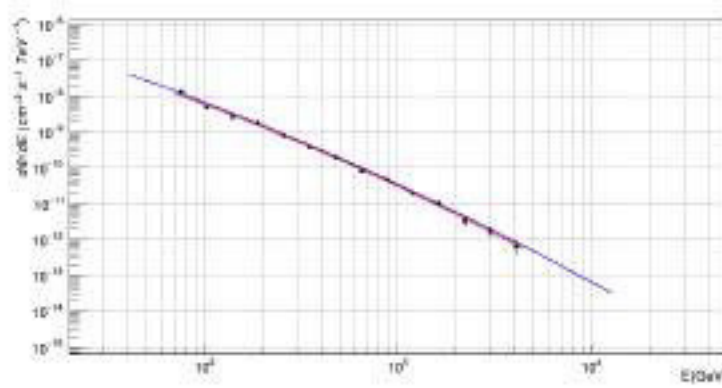


Figure 5.31: Crab Nebula spectrum at  $0.7^\circ$  offset. The red line is fit with the spectrum given by (5.34), while the blue line is the spectrum from Aleksić et al. 2016b.

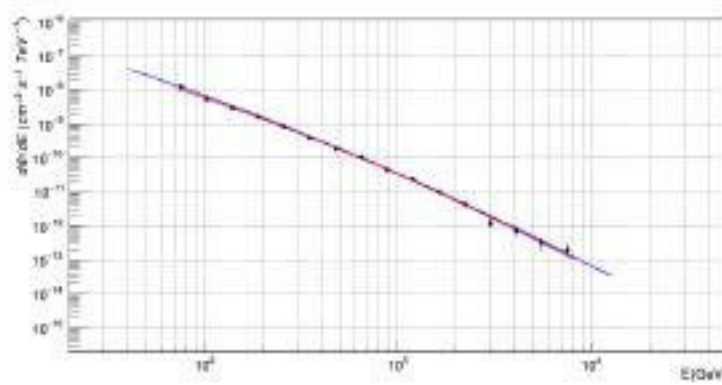


Figure 5.32: Crab Nebula spectrum at  $1.0^\circ$  offset. The red line is fit with the spectrum given by (5.34), while the blue line is the spectrum from Aleksić et al. 2016b.

**Sensitivity loss** One possible problem with the tool is the reconstruction of the spectrum of a possible source which does not lie on one of the grid points. So it is useful to take as before the Crab Nebula, but instead of centering it on one of the grid points, it is put on the center of a square whose vertexes are four points of the grid. So the Crab Nebula's distance from the grid points is  $s/\sqrt{2}$  (see Figure 5.33). The test is performed for the three Crab Nebula data sets taken with different wobble offsets.

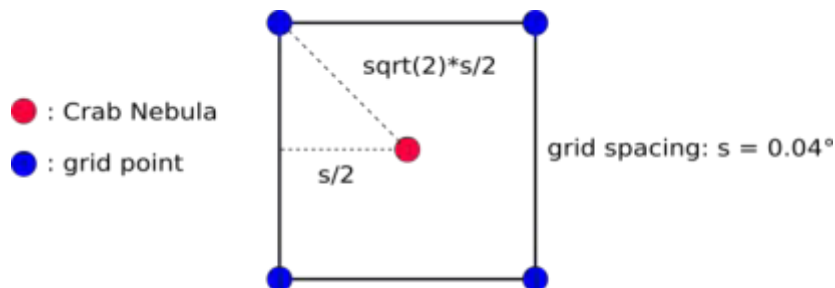


Figure 5.33: Graphical representation of the situation considered in the sensitivity loss test.

The results for the spectral parameters are shown in Table 5.7, 5.8 and 5.9.

Comparing the flux values obtained in this test with the ones calculated in the previous one, one can see that in the worst case the loss on the flux estimate induced by a grid with  $0.04^\circ$  spacing is  $\sim 6\%$ .

| Grid Point | $f_0$ [ $\cdot 10^{11}$ ] | $a$              | $b$              | $F(E > 100 \text{ GeV})$ [ $\text{cm}^{-2} \text{s}^{-1}$ ] |
|------------|---------------------------|------------------|------------------|---|
| 1st        | $3.27 \pm 0.05$           | $-2.50 \pm 0.02$ | $-0.19 \pm 0.02$ | $5.37 \cdot 10^{-10}$                                       |
| 2nd        | $3.21 \pm 0.05$           | $-2.51 \pm 0.02$ | $-0.20 \pm 0.02$ | $5.29 \cdot 10^{-10}$                                       |
| 3rd        | $3.22 \pm 0.05$           | $-2.52 \pm 0.02$ | $-0.21 \pm 0.02$ | $5.32 \cdot 10^{-10}$                                       |
| 4th        | $3.20 \pm 0.05$           | $-2.52 \pm 0.02$ | $-0.21 \pm 0.02$ | $5.29 \cdot 10^{-10}$                                       |

Table 5.7: Results from the test for the data set taken with  $0.4^\circ$  wobble offset.

| Grid Point | $f_0$ [ $\cdot 10^{11}$ ] | $a$              | $b$              | $F(E > 100 \text{ GeV})$ [ $\text{cm}^{-2} \text{s}^{-1}$ ] |
|------------|---------------------------|------------------|------------------|---|
| 1st        | $3.09 \pm 0.15$           | $-2.57 \pm 0.07$ | $-0.31 \pm 0.07$ | $4.87 \cdot 10^{-10}$                                       |
| 2nd        | $3.03 \pm 0.15$           | $-2.55 \pm 0.07$ | $-0.27 \pm 0.08$ | $4.87 \cdot 10^{-10}$                                       |
| 3rd        | $3.07 \pm 0.15$           | $-2.52 \pm 0.07$ | $-0.26 \pm 0.08$ | $4.77 \cdot 10^{-10}$                                       |
| 4th        | $3.03 \pm 0.05$           | $-2.49 \pm 0.06$ | $-0.23 \pm 0.08$ | $4.66 \cdot 10^{-10}$                                       |

Table 5.8: Results from the test for the data set taken with  $0.7^\circ$  wobble offset.

| Grid Point | $f_0$ [ $\cdot 10^{11}$ ] | $a$              | $b$              | $F(E > 100 \text{ GeV})$ [ $\text{cm}^{-2} \text{s}^{-1}$ ] |
|------------|---------------------------|------------------|------------------|---|
| 1st        | $3.37 \pm 0.13$           | $-2.49 \pm 0.04$ | $-0.27 \pm 0.06$ | $4.94 \cdot 10^{-10}$                                       |
| 2nd        | $3.17 \pm 0.12$           | $-2.53 \pm 0.05$ | $-0.27 \pm 0.06$ | $4.94 \cdot 10^{-10}$                                       |
| 3rd        | $3.27 \pm 0.13$           | $-2.51 \pm 0.04$ | $-0.27 \pm 0.06$ | $4.94 \cdot 10^{-10}$                                       |
| 4th        | $3.20 \pm 0.05$           | $-2.54 \pm 0.05$ | $-0.27 \pm 0.06$ | $4.94 \cdot 10^{-10}$                                       |

Table 5.9: Results from the test for the data set taken with  $1.0^\circ$  wobble offset.

**Full tool test on Crab Nebula data** The final test was meant to produce the final flux upper limits skymap using the tool, creating the whole grid and running the full procedure. One goal of test, beside obtaining correct skymaps, is to have a compatibility with the skymaps produced by the MARS executable `caspar`, in particular the one plotting the Test Statistics (TS) in a sky region around the source. What is expected is that regions in the TS skymap with “high” TS will correspond to higher values of the flux upper limits in our skymap. Indeed most of the FoV will be dominated by the background signal, so that the estimated number of excess events will be low or, most of times, negative. In this case the profile likelihood is no longer parabolic (but monotonically increasing) and the upper limit computed with the Rolke method will be lower. With a positive expected number of excess events, the profile likelihood will be parabolic and higher upper limits are expected, see for example figures 1 and 2 in Rolke, López, and Conrad (2005).

The issue here is that the background estimation used in `caspar` is very different from the one used in `flute`. So the upper limits skymap can show additional features that TS skymap do not have. However, both `flute` and `caspar` allow the user to select different values for the cuts, namely on  $\theta^2$ , hadronness and size of the image. So the same cuts were used for both `caspar` and `flute` to make a comparison between the maps. The values used for this test are:

- $\theta_{\text{cut}}^2 = 0.02$  (not used in `caspar`, otherwise a skymap cannot be obtained)
- hadronness cut: 0.28
- size cut: 60 (phe)
- energy threshold: 150 GeV.

For this test, the cuts applied at `flute` level are fixed and not computed with a desired level of efficiency for simplicity. The energy threshold was chosen to be 150 GeV since it is the energy threshold of the targets which were observed under dim moonlight conditions during

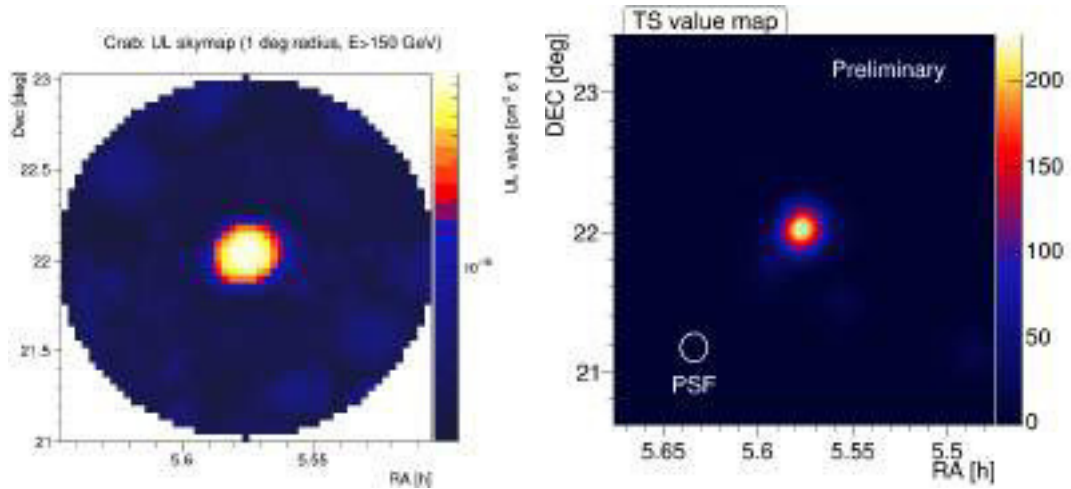


Figure 5.34: Flux upper limits skymap (left) and TS skymap (right) for the Crab Nebula using fixed cuts in `flute`.

the follow-up of the GW event GW151226.

To have enough sensitivity, usually the follow-up targets will be observed by MAGIC up to 1 h per target. So the Crab Nebula data set considered for this test corresponded to an observation time of about 40 min, that is two wobble positions. As determined from the first tests, the grid points spacing and the MC rings thickness were set to  $0.04^\circ$  and  $0.2^\circ$  respectively.

The flux upper limit skymap in a circular region of  $1^\circ$  radius around the source is shown in Figure 5.34 along with the TS skymap obtained with `caspar`.

A second test was performed on the same Crab Nebula dataset but in this case the cuts on  $\theta^2$  and hadronness are computed by `flute` according to a predefined efficiency (75% and 90% respectively) for each grid point. This is in principle a better approach compared to the one in which fixed global cuts are used for all grid points because it takes into account possible inefficiencies in the cameras and their degrading performance for sky positions observed at their edges. The only drawback is a slight longer time for the processing of MC files from which cuts are computed. The resulting upper limit skymap is shown in Figure 5.35. The only notable difference with the UL skymap in Figure 5.34 is that the region where ULs are above  $2 \cdot 10^{-10} \text{ cm}^{-2} \text{ s}^{-1}$  is slightly smaller and contained, whereas the ULs in the region where no signal is expected is almost unchanged.

This second method (cuts in `flute` computed from efficiencies) is the one used in the next analysis, namely the one for the targets observed as a follow-up of the GW event GW151226. This is presented in Section 5.2.6.

**Other details of the tool** In order to obtain conservative flux upper limits, when `foam` is run, if the number of excess events is negative, the number of ON events is set equal to the number of OFF events. In this way the UL will be slightly higher with respect to the case that the number of ON events is less than the OFF ones. This is to prevent having better upper limits which are created by negative excesses due to statistical fluctuations.

Moreover, if the resulting UL is less than 3% of the residual background, the UL will be set to that value. Even if the background estimation for MAGIC is at the 1% (or less) level, other systematics in its estimation can hide a real excess, especially in long observations. The resulting upper limit in this case would be too low. In the first versions of the tool, these features were not implemented in `flute` and `foam`, so the tests on the Crab Nebula were not performed using them. In any case, since the Crab Nebula is a quite strong source, it is not expected that imposing these additional constraints would have changed the results.

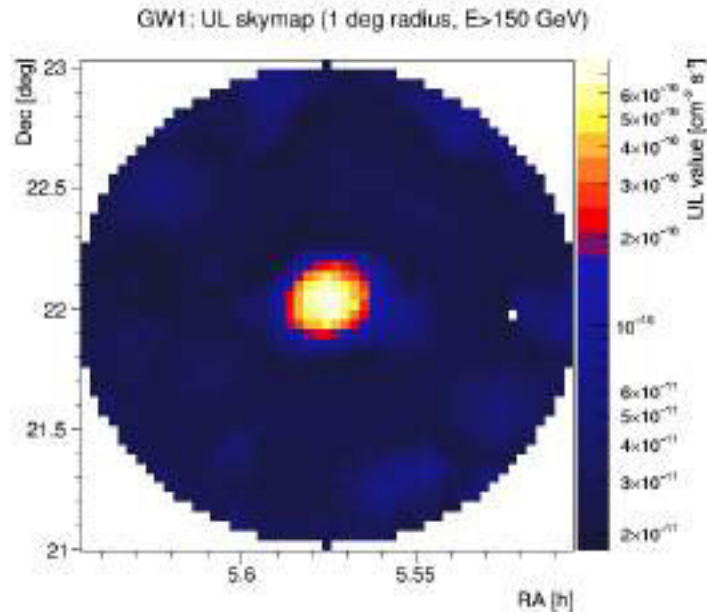


Figure 5.35: Flux upper limits skymap for the Crab Nebula using variable cuts from efficiency in flute.

### 5.2.6 MAGIC follow-up of GW151226

#### LIGO identification of GW151226

GW151226 (Abbott et al. 2016a) was identified by the online pipeline search GSTLAL CBC at 2015-12-26 03:38:53.647 UTC (coalescence time) with a False Alarm Rate of 1 per 950.84 years. The sky localization (Figure 5.36) covered at the 90% (50%) credible level about 1400 deg<sup>2</sup> (430 deg<sup>2</sup>).

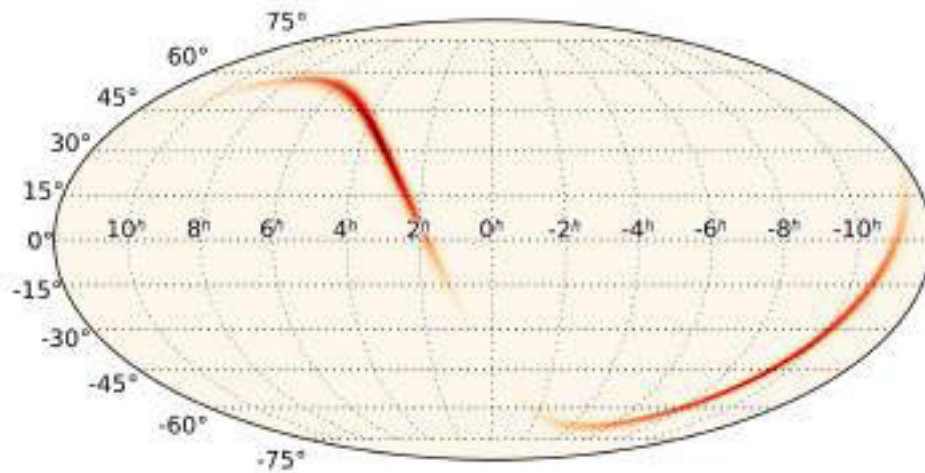


Figure 5.36: Sky localization provided by LIGO using the BAYESTAR algorithm. From <https://gracedb.ligo.org/events/view/G211117>.

After proper waveform modeling, the signal was identified to be due to the coalescence of two stellar mass black holes of masses  $m_1 = 14.2^{+8.3}_{-3.7} M_\odot$  and  $m_2 = 7.5^{+2.3}_{-2.3} M_\odot$  respectively. The final black hole mass is  $20.8^{+6.1}_{-1.7} M_\odot$ , placed at a luminosity distance of  $440^{+180}_{-190}$  Mpc. The main parameters characterizing GW151226 are summarized in Table 5.10.

| Parameter               | Value  |
|-------------------------|--|
| Primary BH mass $m_1$   | $14.2^{+8.3}_{-3.7} M_{\odot}$                   |
| Secondary BH mass $m_2$ | $7.5^{+2.3}_{-2.3} M_{\odot}$                    |
| Chirp mass              | $8.9^{+0.3}_{-0.3} M_{\odot}$                    |
| Total BH mass           | $21.8^{+5.9}_{-1.7} M_{\odot}$                   |
| Final BH mass           | $20.8^{+6.1}_{-1.7} M_{\odot}$                   |
| Radiated GW energy      | $1.0^{+0.1}_{-0.2} M_{\odot} c^2$                |
| Peak luminosity         | $3.3^{+0.8}_{-1.6} \times 10^{56} \text{ erg/s}$ |
| Final BH spin           | $0.74^{+0.06}_{-0.06}$                           |
| Luminosity distance     | $440^{+180}_{-190} \text{ Mpc}$                  |
| Source redshift $z$     | $0.09^{+0.03}_{-0.04}$                           |

Table 5.10: Summary of the values of the main parameters for GW151226. The reported numbers are median values with 90% credible intervals (statistical plus systematic errors). From Abbott et al. (2016a).

### MAGIC follow-up observations of GW151226

The identification of GW151226 was disseminated to all the EM observers, MAGIC included, with a GCN Circular (<https://gcn.gsfc.nasa.gov/gcn3/18728.gcn3>) including the links to the skymaps generated using both the BAYESTAR (online) and cWB (offline) algorithms. This first circular triggered the follow-up from the EM facilities searching for a possible counterpart of the GW event. As far as gamma-ray instruments are concerned, Fermi (both GBM and LAT), HAWC and MAGIC performed a follow-up of the event whose preliminary results were published as GCN Circular (no. 18741 and 18813 for Fermi-GBM and Fermi-LAT, no. 19156 for HAWC and no. 18776 for MAGIC). No EM counterpart was detected for this event (see <https://gcn.gsfc.nasa.gov/other/G211117.gcn3> for all the GCN Circulars related to GW151226).

From the skymap provided by LIGO, four positions were extracted which were visible at low zenith ( $< 30^\circ$ ) from the MAGIC site to ensure a low energy threshold. The positions were chosen according to few criteria like visibility, observations by other EM instruments, overlap with existing catalogs and using the LIGO localization skymap, as shown in Table 5.11. The MAGIC follow-up was later reported in a GCN Circular (<https://gcn.gsfc.nasa.gov/gcn3/18776.gcn3>).

The observations of the four targets (denoted as GW1, GW2, GW3 and GW4) were performed on December 28th 2015 starting at about 21:00 UT with the standard wobble-mode. GW1 was observed under dark conditions, while GW2 was observed under dim Moon conditions, but standard analysis could be applied. Both GW3 and GW4 were observed under moderate Moon conditions, so that higher cleaning levels (9-6 phe for M1 and 10-6 phe for M2) had to be applied and noise (mean and RMS: 3.8 (4.0) and 1.6 (1.7) for M1 (M2)) had to be added to MC and OFF data. The values of the cleaning and the noise mean and RMS differ from the ones given in Table 4.3 since at the time moon analysis was not yet standardized. Despite this, to prove that the analysis performed with these settings provides consistent results, the same settings were used on a Crab Nebula sample to reconstruct its spectrum and light curve (see Appendix F).

A first quick analysis of the four targets was performed right after the observation according to the standard MAGIC analysis, except for GW3 and GW4 for which a Moon-dedicated analysis was needed. No signal was found in the four datasets and the skymaps produced with *caspar* did not show any significant excess (see Figure 5.37 and Figure 5.38), so compatible with a background-only hypothesis. The results of the analysis are reported in Table 5.12.

| Tag | Target            | RA<br>HH:MM:SS.SSS | Dec (J2000)<br>DD:MM:SS.SS | Duration<br>[min] | Zd range |
|-----|-------------------|--------------------|----------------------------|-------------------|----------|
| GW1 | PGC1200980 (1)    | 02:09:05.800       | +01:38:03.00               | 48                | 27°-30°  |
| GW2 | strip from GW map | 02:38:38.930       | +16:36:59.27               | 59                | 13°-24°  |
| GW3 | Field VST (2)     | 02:38:02.210       | +19:13:12.00               | 30                | 22°-30°  |
| GW4 | Field VST (2)     | 03:18:23.712       | +31:13:12.00               | 30                | 19°-27°  |

Table 5.11: Summary of the four positions observed by MAGIC as a follow-up of GW151226. The second column shows the targets observed by optical partners and chosen to be observed by MAGIC. (1) <https://gcn.gsfc.nasa.gov/gcn3/18804.gcn3>. (2) <https://gcn.gsfc.nasa.gov/gcn3/18734.gcn3>

| Target | Significance [ $\sigma$ ] | $E_{\text{thr}}$ [GeV] | UL [ $\text{cm}^{-2} \text{s}^{-1}$ ] | C.U. [%] |
|--------|---------------------------|------------------------|---------------------------------------|----------|
| GW1    | +1.07                     | 100                    | $2.39 \cdot 10^{-11}$                 | 4.3      |
| GW2    | -2.24                     | 100                    | $1.29 \cdot 10^{-11}$                 | 2.3      |
| GW3    | -0.23                     | 150                    | $2.31 \cdot 10^{-11}$                 | 6.9      |
| GW4    | -0.33                     | 150                    | $1.41 \cdot 10^{-11}$                 | 4.3      |

Table 5.12: Summary of the results of the analysis performed on the four positions observed for the follow-up of GW151226 as listed in Table 5.11. The significance reported in the second column is the one computed using LE cuts in `odie`. The energy threshold for GW3 and GW4 is higher because of the higher NSB level due to the presence of the Moon during observations. Flux upper limits are calculated at the position of the targets.

### Upper limits skymaps for the GW151226 follow-up targets

After the first, standard analysis, the flux upper limits skymaps for the targets GW1, GW2, GW3 and GW4 were produced with the tool described in Section 5.2.5. Since it was already explained in detail, I just summarize the settings used:

- $0.2^\circ$  and  $0.04^\circ$  as MC rings thickness and spacing of the grid points respectively
- $\theta^2$  and hadronness cuts computed from efficiency in `flute`
- 150 GeV as the lower limit for the flux upper limit calculation
- assumed spectrum: power law with spectral index  $\beta = -2.6$
- $1^\circ$  radius.

The resulting upper limits skymaps are shown in Figure 5.39. It can be noted that for GW3 and GW4 the upper limits are globally higher since the observations were carried out under moderate moon conditions.

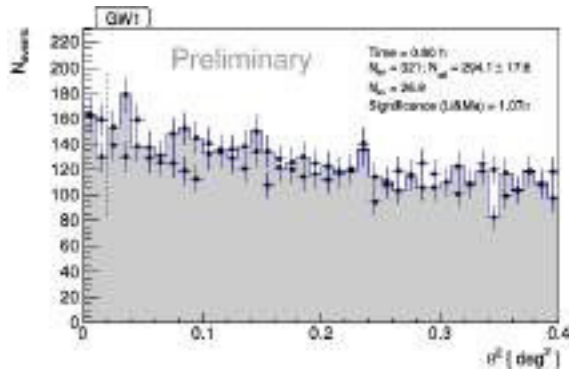


Figure 5.37.1: GW1

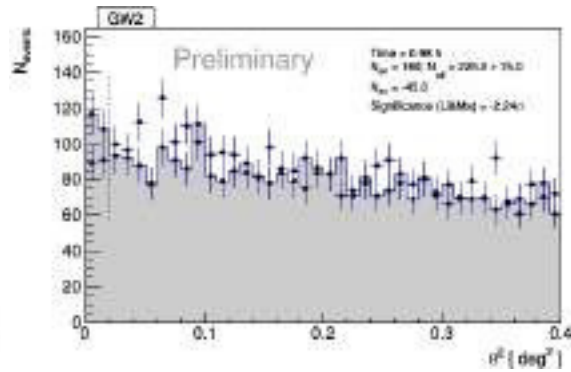


Figure 5.37.2: GW2

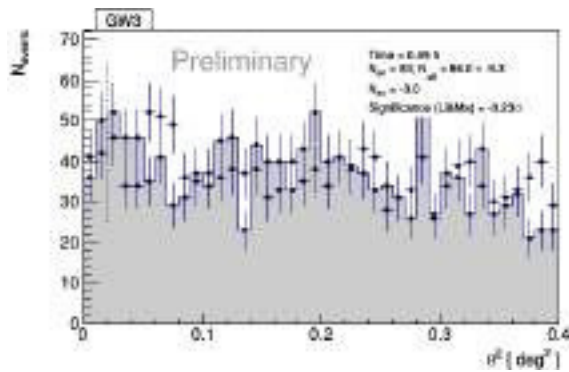


Figure 5.37.3: GW3

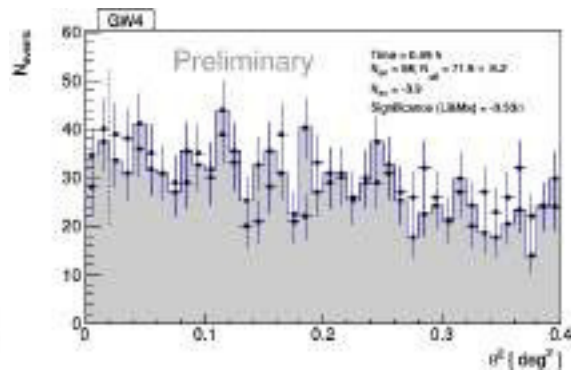


Figure 5.37.4: GW4

Figure 5.37:  $\theta^2$  plots (LE cuts) for the four targets observed by MAGIC in the follow-up of the gravitational event GW151226.

### 5.2.7 Discussion and prospects for GW follow-up with MAGIC

Currently the field of GW astronomy is open and in full development. The first four detections of binary systems brought excitement in the astrophysical community and triggered a collective effort in the follow-up of these events and gave for the first time a direct physical insight on these systems. The many theoretical predictions about electromagnetic signatures from compact binary mergers make the follow-up mandatory and could result in a high scientific reward. For this reason MAGIC joined the EM community in order to characterize in more detail the possible electromagnetic counterparts of GW events. In particular, the preferred targets would be BNS or NS-BH mergers, which are thought to be the progenitors of some short GRBs. In this regard, all the arguments discussed in Section 5.1 for GRBs are of course still valid: MAGIC has very good repointing capabilities and a very good sensitivity at low energies down to 50 GeV, making it suited for GRB and GW follow-up. Nonetheless, the still large localizations provided by aLIGO ( $\mathcal{O}(1000 \text{ deg}^2)$ ) prevent to have a fast follow-up due to the small MAGIC FoV. Covering the strips of GW skymaps with many pointings (tiling) would result in a small observation time per pointing and consequently in a quite low sensitivity (40% C.U. above 105 GeV in 6 min). Moreover, observational constraints like the one adopted for GRBs observation must be taken into account and also possible non-dark background conditions. For these reasons, the current strategy relies on the detection of EM counterparts of GW events from other observatories. The strategy could be changed only when smaller localizations ( $\mathcal{O}(10 \text{ deg}^2)$ ) will be provided i.e. with Virgo joining LIGO. At that point, a lower number of pointings would be needed to cover the 50% or 90% confidence region, allowing to observe for more time and with a better sensitivity at low energies. Nevertheless, checking for possible counterparts by other observatories will be still a good option

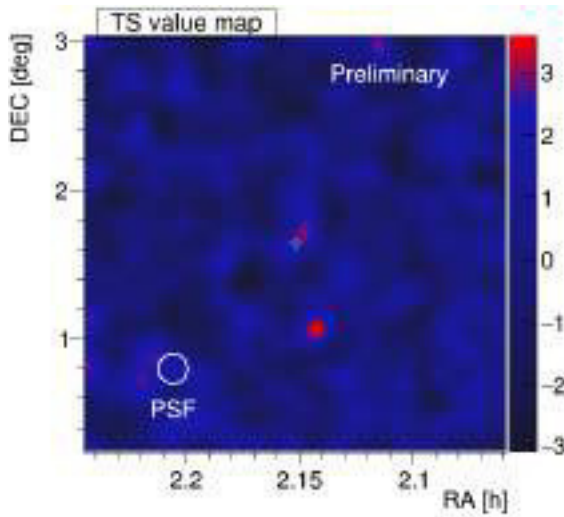


Figure 5.38.1: GW1

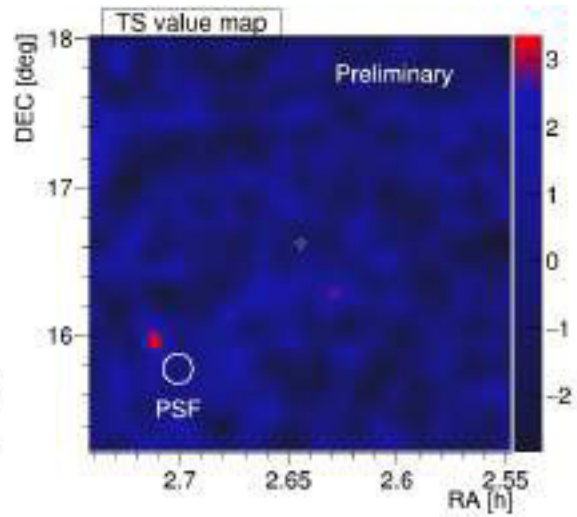


Figure 5.38.2: GW2

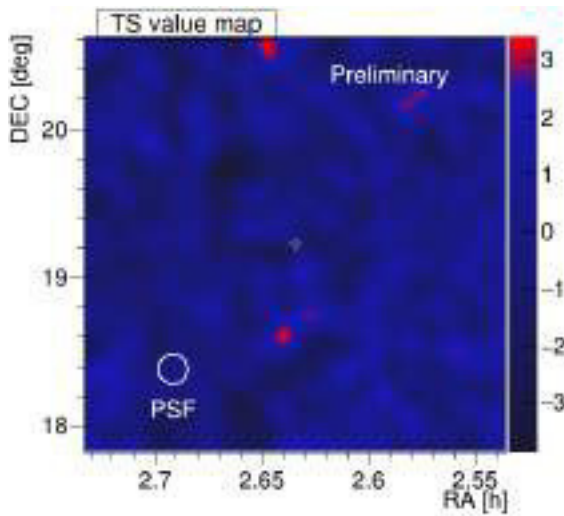


Figure 5.38.3: GW3

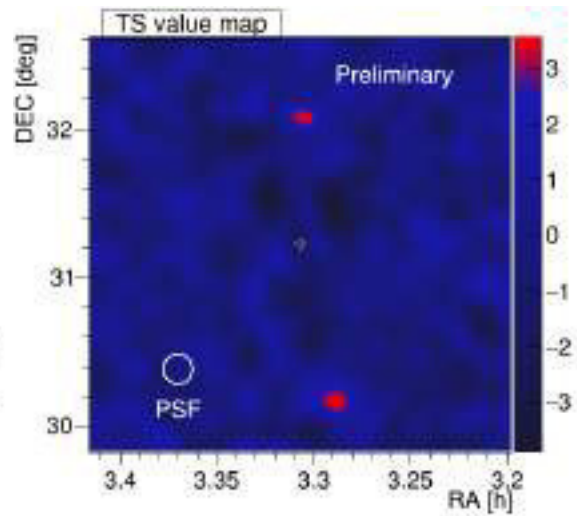


Figure 5.38.4: GW4

Figure 5.38: TS skymaps (LE cuts) for the four targets observed by MAGIC in the follow-up of the gravitational event GW151226.

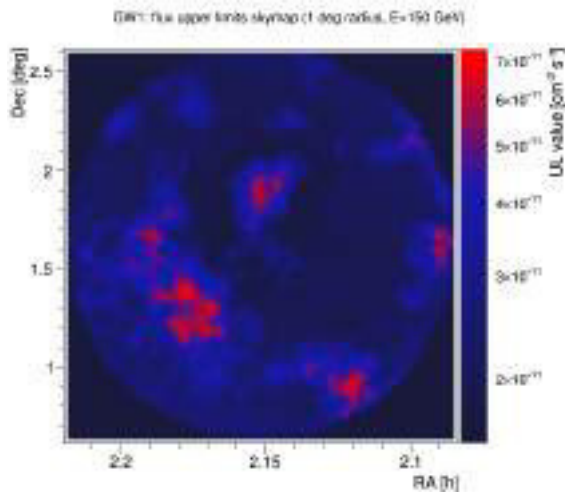


Figure 5.39.1: GW1

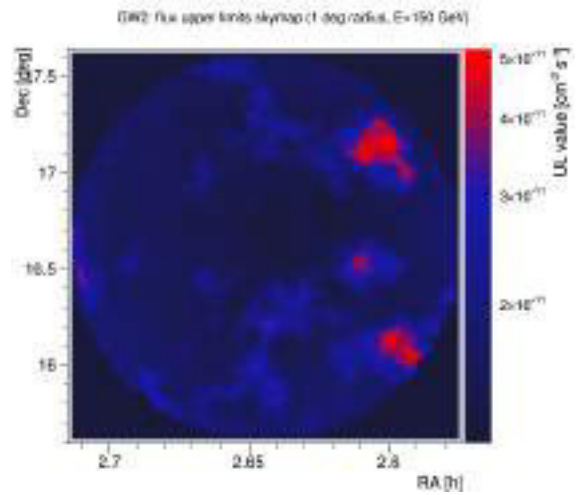


Figure 5.39.2: GW2

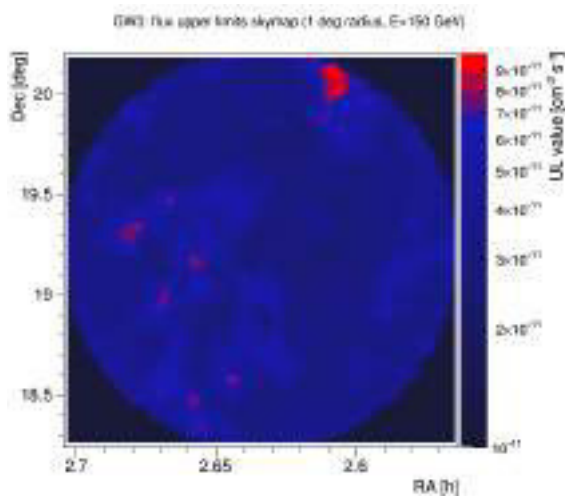


Figure 5.39.3: GW3

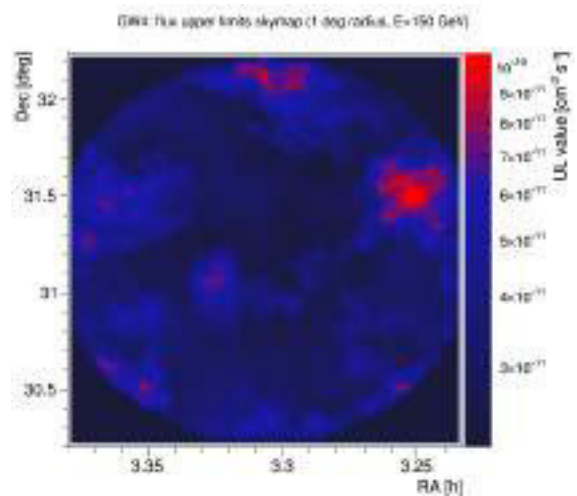


Figure 5.39.4: GW4

Figure 5.39: Flux upper limit skymaps for the four targets observed by MAGIC in the follow-up of the gravitational wave event GW151226.

especially in the case a GRB would be detected, like in the case of GW170817/GRB170817A. In this regard, an automatic reaction to GRB alerts is already working since 2004 in the MAGIC alert system, so nothing should be added, but the planning of tiling observations with several pointings is still not implemented (details will be discussed in Chapter 6). Another possible strategy in the case of large localizations would be using galaxy catalogs, weighting each galaxy choice based on the information provided by LVC like the distance of the event and again the localization skymap.

Finally, the next GW observations are quite close, since run O3 will start at the end of 2018. This period of time is crucial to improve and test the MAGIC follow-up strategy as discussed above. In the more distant future, more facilities are expected to join aLIGO and AdV in the gravitational wave detectors network, like KAGRA and ET (Einstein Telescope) (Aso et al. 2013; Sathyaprakash et al. 2012). A moderate boost in the localization is envisioned again, giving to small FoV instruments like MAGIC more possibilities for an efficient follow-up.

### 5.3 Conclusions and prospects for transient science with MAGIC

In this Chapter I dealt with the MAGIC follow-up programs for Gamma-Ray Bursts and gravitational waves candidate events. Given the unpredictable and serendipitous nature of GRBs, MAGIC was designed to be fast during slewing to follow-up as early as possible any observable trigger. The alert system listening to GRB alerts 24/7, described in Chapter 6, is thus fundamental to reduce the response time according to predefined observational criteria. The low energy threshold ( $\sim 50$  GeV) of the MAGIC telescopes gives the possibility to observe gamma-rays in an energy range where the absorption effect of the EBL is negligible, at least for GRBs with low or moderate redshift. Up to August 2017, MAGIC observed 97 GRBs in good conditions without specific hardware or technical problems. With the introduction of the new automatic procedure in 2013, failures in the follow-up just after the GRB alert were drastically reduced, allowing to observe without issue the emission during the first minutes, which are the most important due to the flux decay with time ( $\sim t^{-1}$  for the HE emission at late times).

Given the possibility of the presence of a VHE emission from GRBs, inferred from HE observation by Fermi-GBM and Fermi-LAT and predicted by many theoretical models, twelve GRBs observed by MAGIC were considered and analyzed to search for a possible  $\gamma$ -ray signal. None of the GRBs in the sample shows any hint of VHE emission, mostly due to their high redshift ( $z > 1$ ) leading to a strong absorption by the EBL already at energies around 100 GeV and to the huge delay between the onset and the beginning of the observation for some GRBs. This means that up to date a GRB detection is still missing by MAGIC (and the other IACT as well).

As far as future prospects for GRBs follow-up are concerned, they were already discussed in Section 5.1.12 but I give here a summary list:

- improving the alert system for GBM events
  - testing the automatic procedure using new triggers, namely the Sum Trigger and Topological trigger
  - making the Sum Trigger the default trigger for GRBs observations in order to lower the energy threshold
  - performing a dedicated low-energy analysis for the most promising GRBs, thus reducing the image cleaning levels and using MC data simulated with lower NSB level. This kind of study was performed inside the collaboration but it is not standardized within the MARS framework yet.
-

The efforts of the MAGIC collaboration for GRB follow-up are thus directed towards a more wise selection of the alerts in order to follow the most promising ones and to lower as much as possible the energy threshold to reduce the effect of the EBL and enhance the chance of detection for close GRBs.

The other class of transient sources considered is gravitational waves. More specifically the MAGIC follow-up of GW candidate events provided by aLIGO and AdV was discussed. The follow-up is crucial to detect the transient electromagnetic emission expected from some classes of gravitational wave emitting sources, CBC in particular. Theoretical models predict that compact binary mergers have many electromagnetic counterparts. Among them, short GRBs are the most interesting for MAGIC since in this case VHE emission could be produced. For these reasons MAGIC joined the EM community in the follow-up program of GW events. The most difficult problem to face for MAGIC is the large sky localizations, which cannot be covered easily due to its small FoV. For this reason the follow-up of GW151226 was performed choosing targets observed by other EM partners and this is the preferred strategy until better localizations will be provided. To deal with localizations larger than the MAGIC FoV, a new analysis tool was developed and fluxes or upper limits can be computed in a large region of the FoV. The targets observed after the GW151226 trigger did not show any gamma-ray signal so the tool was used to produce flux upper limits skymaps, which give more information not restricted to the positions of the targets only.

For the follow-up of GW events, the prospects were discussed in the previous section. The most promising candidates with EM counterparts are BNS or NS-BH systems, even if some scenarios predicts a possible electromagnetic emission from BBH systems. With more facilities joining the GW network, the localization of the events will improve dramatically (see Section 5.2.3), allowing MAGIC to cover the highest probability region with few pointings. If other observatories will detect a counterpart, the MAGIC alert system could be used to follow-up automatically these targets with the lowest delay possible. More on this topic will be discussed in Chapter 6.

Finally, I would like to stress that GRBs and GW events are not the only transients considered by MAGIC. A well established follow-up program is the one for AGN flares: the flux can be several times more than the Crab Nebula one and the typical timescale is of the order of days. Some AGN are monitored constantly and flares can be detected during the monitoring. Alerts (emails, ATELS) are then sent to other instruments for a better characterization of the event.

Another example are Fast Radio Bursts (FRBs): they are transient sources discovered recently in the radio band (GHz band) with durations of milliseconds but peak fluxes of the order of Jansky and dispersion measures exceeding the one of the Galaxy (Thornton et al. 2013). The number of detected events is currently quite limited<sup>4</sup>, see Petroff et al. (2016), but the number of FRBs expected per day is very high ( $\mathcal{O}(10000)$ ). Up to now, only one FRB was found to be repeating, FRB121102, see Spitler et al. (2016). There is still debate about their progenitors, since only FRB121102 has a precise redshift estimation (Chatterjee et al. 2017; Tendulkar et al. 2017). Some models predict that FRBs could be accompanied by VHE emission (Murase, Kashiyama, and Mészáros 2016; Lyubarsky 2014) and for this reason MAGIC is involved in their follow-up using as well the central pixel for optical observations to search for very fast variations, see Hassan et al. (2017).

Finally, another MAGIC multi-messenger follow-up program is related to very high energy neutrinos detected by IceCube. As in the case of GW events, the goal is to find a counterpart for astrophysical neutrinos and reveal their sources. AGNs seem to be favored but there is no definitive proof yet. The follow-up of neutrino events should be very similar to the GRB case, but the MAGIC alert system does not have an automatic response to neutrino alerts yet. This topic will be discussed in detail in the following Chapter.

---

<sup>4</sup>A FRB catalog is available at the link <http://www.astronomy.swin.edu.au/pulsar/frbcat/>.

## Chapter 6

# AUTOMATIC REPOINTING SYSTEM FOR MAGIC

The follow-up of transient sources by Cherenkov telescopes is a difficult task. Satellite-based instruments like *Swift*, *Fermi* and *INTEGRAL* have almost all-sky covering fields of view, so that almost no transient is left undetected. The same applies to neutrino detectors like IceCube or GW detectors like LIGO/Virgo. IACTs instead have a very narrow FoV: in the specific case of MAGIC, the FoV is  $3.5^\circ$  wide. For this reason, they need to point an exact position in the sky to try to catch a possible VHE emission from a transient source. An external trigger from the other observatories is then needed to allow IACTs to perform their follow-ups. The GRB Coordinate Network<sup>1</sup>, has been created for this purpose. Ground and satellite based instruments can subscribe to this stream and receive the alerts from other observatories containing the coordinates of the transient (in the case of GW, a probability skymap is provided). Each observatory then can parse the alerts and use the information according to a strategy to perform their follow up. In MAGIC, the alerts are received and processed by a daemon program called GSPOT (Gamma Sources POinting Trigger), already introduced briefly in Section 3.5.11. GSPOT checks if the coordinates contained in the alert are observable from the MAGIC site. If the check is positive, GSPOT communicates with the Central Control which repoints automatically the telescope to the target position. Here I will describe briefly the GCN system (Section 6.1), the GSPOT workflow (Section 6.2) and the work done to implement the automatic response to alerts containing neutrino transient sources (Section 6.3). After that, the preliminary offline tests performed on GSPOT, the Burst Advocate activity, some ideas for the future and the tests performed on GSPOT at the MAGIC site will be described in Sections 6.4, 6.5, 6.6 and 6.7 respectively.

### 6.1 The GCN system

The GCN is currently the main network used to distribute alerts about transient sources from space-based instrument to all the other observatories. Actually the GCN is the evolution of an older system called BACODINE (*BATse COordinates DIstribution NEtwork*), whose purpose was to disseminate to the interested parties the sky coordinates of the GRBs detected by the BATSE instrument onboard the CGRO. As soon as additional instruments for GRB science started operation, they were added to the stream and so BACODINE became the more generic GCN. Currently the GCN is not limited to GRB alerts, but other transients like Gravitational Waves and Neutrinos are included. For this reason, the complete name of the GCN is GCN/TAN, where TAN stands for *Transient Astronomy Network* but I will call it simply GCN from now on for simplicity.

---

<sup>1</sup><https://gcn.gsfc.nasa.gov/>

The GCN system is divided in two parts, the *GCN Notices* and the *GCN Circulars*. The GCN Notices distribute the sky positions of transient sources detected by several space or ground based instrument to the observatories interested in performing a follow-up. The distribution occurs via different methods: binary packets via socket, VOEvents via socket, emails or pagers. Since the binary packets is the protocol currently used by GSPOT to receive the alerts, they will be described in more detail. The GCN Notices are prepared and sent without any human in the loop: the info from the instruments is collected by the GCN, converted to a standard format (one of those listed previously) and distributed. Since the processing is automatized, the time-delay is minimized. This holds true for both the instrument part (the one sending the information) and the GCN part. The processing of the information by the instrument sending the coordinates is dependent on the instrument itself: in most cases (e.g. Swift-BAT, Fermi-GBM, Fermi-LAT, INTEGRAL) the time delay ranges from few seconds to few minutes (see Tables 1.1 and 1.4 in [https://gcn.gsfc.nasa.gov/gcn\\_describe.html](https://gcn.gsfc.nasa.gov/gcn_describe.html)). On the GCN part, the delay is less than 1 s for socket based connections (the fastest method) and up to 30s for emails. This means that the information is disseminated almost in real time. It is advisable that the observatories subscribed to the GCN Notices stream have an automatic system to parse the information contained to reduce the time needed to start the follow-up: for MAGIC, this automatic system is GSPOT.

There are many types of GCN Notices and each mission can produce more than one type of Notice. The full list of Notice types (some defunct) can be found at the following link: <https://gcn.gsfc.nasa.gov/filtering.html>. Each follow-up observer decides to receive all or a subset of the Notice types: for example, the list of Notices received by the MAGIC telescopes can be found at the link [https://gcn.gsfc.nasa.gov/sites2\\_cfg.html](https://gcn.gsfc.nasa.gov/sites2_cfg.html) (search for the string `SITE_NAME MAGIC`).

The GCN Circulars are prose-style email messages used to report about the results of the follow-ups or to coordinate the observations. The follow-up observers are in this case responsible to send their message to the GCN central queue, which then sends the Circular to the whole transient community. The GCN Circulars can be also used to send updated information about a specific event.

The BACODINE and the GCN systems allow to perform follow-ups of transient sources close to their onset, greatly enhancing the scientific discovery potential. For MAGIC, this is fundamental in the quest for high-energy emission from GRBs, GWs and neutrino sources.

### 6.1.1 Binary packets from the GCN

Currently GSPOT receives the alerts from the GCN system as GCN Notices. The protocol chosen for the transmission is the binary packets through socket connection. Each binary packet contains 160 bytes divided in 40 long words (or items) of 4 bytes each. The items contained in the packets are Notice type dependent because each instrument can put different information. For a detailed list of the items contained in the different binary packets, see [https://gcn.gsfc.nasa.gov/sock\\_pkt\\_def\\_doc.html](https://gcn.gsfc.nasa.gov/sock_pkt_def_doc.html). Despite this, some items are always the same and are always associated with the same position (index) in the binary packets. A list of these conserved items is in Table 6.1. Most of the items listed in Table 6.1 are also the most important ones because they hold the fundamental information about the event:

- `PKT_TYPE` tells which Notice type is represented by the binary packet. With this item, the mission/instrument sending the Circular can be promptly recognized;
  - `BURST_SOD` is the so called  $T_0$  for GRBs, but in general it is the trigger time of the event;
  - `BURST_RA` and `BURST_DEC` are the Right Ascension and Declination (J2000) of the target; the error on the position is `BURST_ERROR`;
-

| Item name   | Index | Definition                                      |
|-------------|-------|---|
| PKT_TYPE    | 0     | Packet type number                              |
| PKT_SERNUM  | 1     | Packet serial number                            |
| PKT_HOP_CNT | 2     | Packet hop counter                              |
| PKT_SOD     | 3     | Packet Sec-Of-Day [centi-sec] (sssss.sss*100)   |
| BURST_TRIG  | 4     | Trigger number                                  |
| BURST_TJD   | 5     | Truncated Julian Day                            |
| BURST_SOD   | 6     | Trigger Sec-of-Day [centi-secs] (sssss.sss*100) |
| BURST_RA    | 7     | RA [centi-deg] (0.0 to 359.999 *100)            |
| BURST_DEC   | 8     | Dec [centi-deg] (-90.0 to +90.0 *100)           |
| BURST_INTEN | 9     | Intensity [cnts]                                |
| BURST_ERROR | 11    | Location uncertainty [centi-deg]                |
| TRIGGER_ID  | 18    | Flag bits that identify the trigger type        |
| MISC        | 19    | Misc indicator flag bits                        |

Table 6.1: List of the items always contained in a binary packet, with the positions (indexes) in the packets (always the same for different types of packets).

- TRIGGER\_ID is an item used to tell if the event is of a certain type.

Of course, the other items could carry other informations (different from Notice to Notice) useful for the follow-up.

## 6.2 GSPOT

GSPOT is a multi-threaded C program (with some routines in Fortran and a program in C++) which takes care of the processing of the alerts (Notices) coming from the GCN system, see Galante (2006). In few words, gspot receives the alerts and, according to some predefined observational criteria, decides if the target is observable or not. If it is observable, it sends an alert string to the Central Control (CC) of the MAGIC telescopes, which automatically slew to the target position. The observability is computed thanks to the NOVAS (Naval Observatory Vector Astrometry Software) library.

The software of GSPOT was written and developed by Nicola Galante for his PhD thesis and then was maintained by Alessandro Carosi. When the latter left the MAGIC collaboration, I volunteered to become the next GSPOT maintainer, whose duty is to solve problems if they occur (GSPOT should run always, especially during night time at the MAGIC site) and to implement new features if needed.

In the following, I will describe in detail the workflow of GSPOT.

### 6.2.1 Threads in GSPOT

GSPOT functionalities are divided in different threads, which are initialized when the main program is launched. Each thread has its own scope, so they run in parallel independently. Nevertheless, some of them can modify a common data structure object one at a time. The four main threads created by GSPOT are the GCN thread, the CC client thread, the CC server thread and the Web thread. Other two threads are created, but they are not needed for the operation of GSPOT.

The GCN thread is responsible to establish (and maintain) the socket connection via TCP/IP between the machine where GSPOT runs and the GCN server. This connection is used by GSPOT to receive the binary packets from the GCN. The connection is not one-way, so that GSPOT can send back packets to the GCN. Once the connection is established, the GCN thread starts to read the data transmitted: if the number of bytes read is different from zero, the content of

the packet is put in a buffer for further processing. Moreover, the packet is echoed back to the GCN so that the roundtrip travel time can be computed and to inform that the packet was received. This information is used by the GCN to spot possible problems in the distribution of the Notices and for statistical purposes. Depending on the packet type, represented by the `PKT_TYPE` item, the packet buffer is processed in a different way to extract all the informations contained. An important packet sent by the GCN is the so called *iamalive* packet (type 3): the GCN sends an `iamalive` packet every 60s to check for the proper working of the connection with the receiving site. The GCN thread records the timestamp of the last `iamalive` packet received and if it does not receive a new `iamalive` packet within 15 min, it will close the connection and open it again.

Once the packet buffer is filled, it is processed by a different function depending on the packet type. The information contained in the buffer is used to fill the members of a C structure, which is one of the main objects in `GSPOT` because it resumes the target properties. The processing function will determine if the target is a GRB or a transient and if the packet contains coordinates (some do not, for example `GLAST_GBM_GRB_ALERT`). If the target is a GRB and the coordinates are present, the observability calculation is computed: if the source position is not visible at all, the alert content will be written into a log file and the processing will go on. If the target instead is observable, the alert is added to a list called `grblist`. The alert remains in the list until it expires (i.e. the end observation time is passed) or until an alert with better updated information is received. At this point, an alert email warning that a target is observable is sent. Even if the target is not observable, an email will be sent in any case. Finally the loop closes and the GCN thread waits for other packets.

The second thread is the CC client: it talks with the Central Control of the MAGIC telescopes via TCP/IP connection. When the connection is established, `GSPOT` sends a custom `iamalive` packet to the CC containing the global status of `GSPOT`. This is needed to know if the connection is working. The CC client thread now checks the list `grblist` for possible observable targets: if the list is not empty i.e. there are alerts with observable positions, it checks if the coordinates were sent or not to the CC. If more than one target is observable, it will choose the one with better observational conditions. A string called `GRB-ALARM` is built starting from the information contained in the alert and sent to the CC. With this, the operators do not have control anymore on the telescopes until they are pointed automatically to the position of the target. The CC client thread will also check for expired alerts inside `grblist` and removes them.

The third thread is the CC server thread, which listens to the CC for reports. The connection occurs in a different port with respect to the CC client thread connection. The reports that the CC sends are of two types:

- a normal CC report, which normally is sent every 1 s;
- an alert report sent from the CC client thread to the CC and sent back.

The CC reports are used to know if the communication between `GSPOT` and the CC is working. The alert reports sent from the CC client thread is echoed back as a confirmation that the CC received it correctly.

Finally, the Web thread creates the Burst Monitor webpage <http://www.magic.iac.es/site/grbm/index.html>, which contains the following information:

- the info about the last GRB observed (position and time);
- the status of the communication with the GCN;
- the communication status with the CC.

In case of an observable target, the table shown in the web page will turn red to warn the shifters and it will be filled with the information of the alert (position, end time of observation).

---

### 6.2.2 Observability computation and GRB observation strategy

The automatic reaction of GSPOT to the alerts coming from the GCN must be fast and reliable. For this reason a predefined set of rules must be followed by GSPOT when it checks if a target is observable. This set of rules are defined by the *GRB observation strategy*. Here we refer only to GRBs because currently GSPOT currently reacts automatically only to GRB Notices even if it receives correctly neutrino and GW related Notices.

The observability of the target is computed up to four hours starting from the time of the event trigger  $T_0$  and so the end time of the observation is at maximum four hours after the trigger. This is because GRBs have a prompt emission where the bulk of the photons is emitted and an afterglow where the flux decays with time approximately as  $t^{-1}$ . So it is possible that having a longer observation could result in a negative effect on the final result of the analysis, since the source flux is fading while the background level is approximately constant. Nonetheless, Fermi-LAT observation of GRBs showed that the HE emission can last up to many hours after the onset.

The other observational constraints are related to the target itself and to the position of the Sun and the Moon at the MAGIC site:

- the Sun must be at a zenith greater than  $103^\circ$  (so just when it enters the astronomical twilight);
- the Moon distance from the alert target must be greater than  $30^\circ$ ;
- the sky coordinates of the GRBs are converted in the local alt-azimuthal system of coordinates. The zenith of the target must be below  $60^\circ$ ;
- if the GRB is always above  $45^\circ$  during all the four hours observability window, then the observation time is reduced to 50 min.

The first constraint tells that at the MAGIC site must be nighttime. The second constraint follows from energy threshold considerations. As shown in Section 4.11.4, the energy threshold of the MAGIC telescopes increases with the zenith angle. If we assume that the spectrum of GRBs in the MAGIC energy range is simply a steep power law, it means that most of the gamma rays are produced at low energies. Moreover, since GRBs are distant sources, the effect of the EBL will create a dimming on the flux at the highest energies. For these reasons, the target should be at a reasonable zenith angle so that the energy threshold is as low as possible. Also the presence of the Moon increases the energy threshold, but at low zenith and with a moderate Moon level, GRBs observations can be performed anyway. In any case, the target cannot be too close to the Moon otherwise the moonlight would be too strong and from this follows the third constraint. The last constraint is related to the fact that we want the target to be observed at high energy threshold (above  $45^\circ$  of zenith it is around 200 GeV) for a short period of time.

According to these criteria, three situations can occur:

- the target is not observable during all four hours of the observability window;
- the target is not observable at the time of the alert receipt by GSPOT, but it becomes observable (e.g. its zenith goes below  $60^\circ$ ) during the observability window
- the target is observable during the whole observability window.

Another thing to be taken into account is that for some packet types there is a set of dedicated filters. If they are not satisfied, even if the target is observable, it will be not pointed by the telescopes. Currently, only Fermi-GBM packets, namely packets 111 and 112 (FERMI\_GBM\_FLT\_POS and FERMI\_GBM\_GND\_POS respectively), have filters. This is due to the large uncertainty on the localization and the small FoV of the MAGIC telescopes. Fermi

GBM packets filters are based on the values of the significance, hardness ratio (ratio between the number of counts in the energy bands 15 – 50 keV and 50 – 300 keV) and error on the position:

- for packet 111 (flight generated), the target is pointed if the significance is greater than 100, the hardness ratio is less than 1 and the error on the position is less than  $4^\circ$
- for packet 112 (ground generated), we have the automatic repointing if the position error is less than  $2^\circ$  and the significance is greater than 40.

For Swift and Fermi-LAT packets no filters are applied so that they are always followed-up. As noted, the previous discussion applies to GRBs only. Despite this, **GSPOT** is source agnostic in the sense that it is not focused on GRBs but can be adapted to handle other kind of transient, as explained in the next section.

### 6.3 Automatic reaction implementation for HESE and EHE alerts

Astrophysical neutrinos have been detected by the IceCube detector, yet the sources producing them is unknown. Several models predict a neutrino emission from AGNs, GRBs, flaring and transient sources. In order to understand which are the sources producing the neutrinos observed by IceCube, a fast follow-up from electromagnetic partners is fundamental. Neutrinos, very much like photons, are not deflected by the magnetic fields in the intergalactic medium and their low cross section allow them to reach Earth without interaction. So they point back directly to the source from where they originated. The detection of an electromagnetic emission directionally and temporally coincident with neutrinos will unveil the parent sources. The science outcome would be much greater, because high-energy neutrinos are produced with hadronic interactions. Nowadays, the debate between leptonic and hadronic models to explain the HE and VHE emission is still without clear solution. The detection of the sources producing neutrinos will clear this doubt. Moreover, in this hadronic interactions, high energy cosmic rays can be produced. With the study of neutrino sources, the origin of the cosmic rays at the highest energies could be unveiled.

The scientific reward in following-up the observation of high energy neutrinos is immensely huge. This is true in particular for IACT instruments like MAGIC: emission of gamma rays from flaring sources can produce, according to models, a neutrino flux comparable with the one measured by high-energy neutrino telescopes. For this reason, MAGIC joined as one of the electromagnetic observatories in the follow-up of neutrinos detected by IceCube.

MAGIC receives the alerts from IceCube as GCN Notices, so **GSPOT** should be responsible of processing them. There are two types of alerts sent from IceCube: the *High Energy Starting Event* (HESE) and the *Extreme High Energy* (EHE) events. These alerts are the result of a real time online analysis done right after data are collected and are distributed to the observational community via the Astrophysical Multimessenger Observatory Network (AMON) and the GCN, see Aartsen et al. (2017b).

HESE events are classified as track-like and shower-like events, both with the interaction vertex inside the fiducial volume of the detector. Track-like events originate from charged current interactions of muon neutrinos, while shower-like events are created by neutral and charged current interactions of electron and tau neutrinos. Most of HESE events are shower-like, but only track-like events are disseminated through the alerts. To determine if an event is more track-like or shower-like, a parameter called *signal\_trackness* is calculated: if 1, the event is certainly track-like. This parameter is included in the alert packet sent to the community. The alert is not sent if the *signal\_trackness* is lower than 0.1. The median angular resolution of HESE events is between  $0.4^\circ$  and  $0.6^\circ$ , because they usually have an energy greater than

60 TeV.

EHE events are the results of an analysis searching for PeV neutrinos with a track-like signature. A zenith dependent cut is applied in order to avoid contamination from atmospheric muons from cosmic rays. A parameter called *signalness* is used to estimate how likely the event is of astrophysical origin. For EHE alerts, the median angular resolution is  $0.22^\circ$ .

For both HESE and EHE events, the online alert analysis is followed by a more detailed offline analysis, so that updated information can be delivered few hours after the initial alert was sent. These kind of alerts started to be delivered in April 2016 and the expected rate is 4 alerts per year for both.

For all the reasons cited above, a follow-up of neutrino sources by MAGIC is fundamental to increase the chance of discovery. Currently GSPOT is able to receive HESE and EHE alerts (Notice types 158 and 169 respectively), but no automatic reaction was implemented yet. In order to implement it, a *neutrino observation strategy* similar to the one for GRBs is needed. This strategy was discussed among the MAGIC Neutrino Working Group and defines the observational constraints to apply when checking for the observability of a neutrino alert. The final strategy has the following constraints:

- the Sun must be at a zenith greater than  $103^\circ$ ;
- the Moon distance from the target must be greater than  $30^\circ$ ;
- the zenith of the target must be below  $50^\circ$ ;
- the maximum time of observation is up to 3 h starting from the time of the trigger.

The constraints are very similar to those of the GRB observation strategy. In this case nothing is known about the emission, so the strategy is fairly simple. Nonetheless, the energy threshold argument applies again if a flaring source is expected, if not in the generic case. Currently no dedicated filters on the event attributes e.g. `signal_trackness` are discussed.

## 6.4 Preliminary tests of the automatic reaction for neutrino alerts

As maintainer of GSPOT, my first work was to implement the neutrino observation strategy in the GSPOT code. Before changing the copy of GSPOT running in La Palma, offline tests can be performed with a program called `gcnsim`: it connects to GSPOT via socket connection and can be used to create fake GCN Notices of different type. This can be done with a local copy of GSPOT, even if the connection with the CC is not there. When an alert is created and sent with `gcnsim`, GSPOT will receive it and process it like it would normally do when running in La Palma. From the output of GSPOT, it can be understood if GSPOT is working correctly e.g. if it reads correctly the packet type and respects the constraints defined by the observation strategy.

To test if the implementation of the neutrino observation strategy worked correctly, first I adapted `gcnsim` to create fake HESE and EHE alerts and afterwards I tested the reaction of GSPOT to some alerts. Tests were performed during the first part of the night as soon as dark time started in La Palma. The dark time is defined as the time of astronomical twilight, when the sun is  $18^\circ$  below the horizon (so its zenith is greater than  $108^\circ$ ). Since the constraint on the sun zenith defined in GSPOT is to be greater than  $103^\circ$  (just after the nautical twilight, when the sun is  $12^\circ$  below the horizon), the tests can be performed a bit earlier before the dark time starts. Of course, since the tests were performed remotely from Italy, one must take into account that the local timezone and the La Palma one are different and consider that the time for disseminating and processing alerts is given in UTC. In the period when

---

the tests were performed, the time difference between the local time and the UTC one was 2 hours.

The first test was performed during the night of 14th of July 2017. According to the MAGIC nightly schedule, the dark time started at 21:43 UTC. As explained before, I could start the tests already at 23:20 (Rome timezone), corresponding to 21:20 UTC, so some 20 minutes before dark time. `gcnsim` allows the user to set the alert notice type, the target coordinates as right ascension and declination (equatorial coordinates) or as azimuth and zenith (local coordinates) and other items for some packet types, like the hardness ratio and significance for GBM notices. For the first test, the packet had the following items:

- PKT\_TYPE: 158
- PKT\_SOD: 76914 (corresponding to 21:21:54)
- BURST\_SOD: 76904 (`gcnsim` sets it to 10 seconds less than PKT\_SOD)
- coordinates were given in the local alt-azimuthal system as AZ=45.6 and ZD=20.3, corresponding to a right ascension and declination of 16.99 h and 41.61 deg (truncated to two decimal numbers)
- no coordinates error was set, so the default value (0) was used.

The (partial) output from GSPOT is listed below:

```

1  @@@@ FINAL CONDITIONS: zds=127.950363 grbzd=24.479795 moondst=104.955470
2  ----- GRB info -----
3  Type of alert: AMON_ICECUBE_HESE
4  GRB IS observable 9
5  R.A. = 16 h 59 m 29.712000 s
6  DEC. = 41 d 36 m 41.400000 s
7  GRB date : 2017/ 7/14 at 21:21:44.0
8  Trigger Time : Fri Jul 14 21:21:43 2017
9  Coordinate error 0
10 N_sigma = 0.000000
11 Zenith = 20 d 17 m 43.008799 s
12 Azimuth = 03 h 02 m 24.017471 s
13 Mean zenith during obs. time = 16.520810
14 Time of alert Thu Jan 1 00:00:00 1970
15 Initial time of observability: Fri Jul 14 21:21:54 2017 at ZA=20.3
16 Final time of observability: Sat Jul 15 00:21:42 2017 at ZA=24.5
17 Minimum ZA within 4 hours = 12.8
18 Alert already sent: no
19 ***** MARK = 1000.0
20 Total time of obs = 10788.000000, voto=1000.000, ti_zd=20.3 deg, tf_zd=24.5 deg
21 TELESCOPE DIRECT YES
22 tel ra = -1.000000 tel dec = -1.000000 ### tel az = 0.000000 tel zd = 0.000000
23 PKT INFO: Received: LT Fri Jul 14 23:21:54 2017
24 Type= 158 SN = 0
25 here sod= 76914 PKT_SOD= 76914.00 [sec] delta= 0.00
26 TRIG_NUM= 0
27 EVENT_TJD= 17948
28 EVENT_SOD= 76904.00 delta= 10.00
29 AMON ICECUBE HESE ALERT at 2017/07/14 21 h 21 m 44 s
30 EVENT R.A.= 16 h 59 m 29.712 s

```

```

31 EVENT Dec.= +41 deg 36 m 41.400 s
32 POSITION ERROR = 0.000000 deg
33 NUMBER OF EVENTS = 4434765
34
35 Nu Position IS observable, Zenith=20.295, Azimuth= 45.600
36 Begin of observation time Fri Jul 14 21:21:54 2017
37 End of observation time Sat Jul 15 00:21:42 2017
38 in the zenith range 20.3 --> 24.5

```

To show that the automatic reaction succeeded in this test, the following can be noted:

1. GSPOT recognized correctly the notice type, see line 3. AMON\_ICECUBE\_HESE is the name used internally by GSPOT for HESE alerts of type 158
2. the coordinates are the same as the ones in input, properly converted to the formats HH:MM:SS.SSSSSS and DD:DD:DD.DDDDDD for right ascension and declination respectively (see lines 5 and 6 or 30 and 31)
3. the PKT\_SOD and BURST\_SOD are correctly read by GSPOT (see lines 23 and 25 for the former and lines 7 and 29 for the latter)
4. the initial and final time of observation are 21:21:54 and 00:21:42 respectively, when the target is at zenith 20.3° and 24.5°, see lines 36 and 37
5. the mean zenith during the observation is 16.5°, while the minimum is 12.8°. According to the previous point, this means that the target culminates during observation
6. the total time of observation is 10 788 s, see line 20.

Regarding the last point, the total observation time is calculated as the difference between the final and initial time of observability, see lines 16 and 15. It can be noted that there is a 12s difference between the maximum observation time for neutrino notices (3 hours, 10 800 s) and the total observation time computed by GSPOT. 10 s are due to the time difference between PKT\_SOD and BURST\_SOD. The other 2 s are due to two reasons: the first is that the observability computation uses the difference between the trigger time of the burst, a `time_t` object, and another `time_t` object called `tgrb`. The trigger time is computed directly by BURST\_SOD and is the one printed at line 8: there is a 1 s difference between it and BURST\_SOD, which is due to a rounding effect. The second reason is that in the `while` loop for the observability computation, the condition requires that the difference `tgrb-trigger_time` is less than 10 800 s, and not less or equal. So here another 1 s difference is gained. So, adding up, 10 800 s are obtained. So GSPOT respects perfectly the maximum observation time constraint.

To verify the numbers in points 4 and 5, I wrote a small python script to compute the zenith angles of a given target at predefined times. The results from the script are 20.4°, 24.4°, 16.5° and 12.8° for the zenith at the start and end times of observation, mean zenith and minimum zenith during the observation. The values are not perfectly the same because of the different ephemeris used by GSPOT and by Astropy. The second set of tests was performed on 2017-07-16. The first goal was to check that GSPOT was correctly processing not only HESE alerts, but also EHE ones (type 169). The parameters used are summarized in Table 6.2.

| PKT_TYPE | PKT_SOD<br>[s] | PKT_TIME<br>[UTC] | BURST_SOD<br>[s] | AZ<br>[°] | ZD<br>[°] | RA<br>[hour] | DEC<br>[deg] |
|----------|----------------|-------------------|------------------|-----------|-----------|--------------|--------------|
| 169      | 76272          | 21:11:12          | 76262            | 120.4     | 30.4      | 17.4         | 10.9         |

Table 6.2: Summary of the parameters used for the first test performed on 2017-07-16

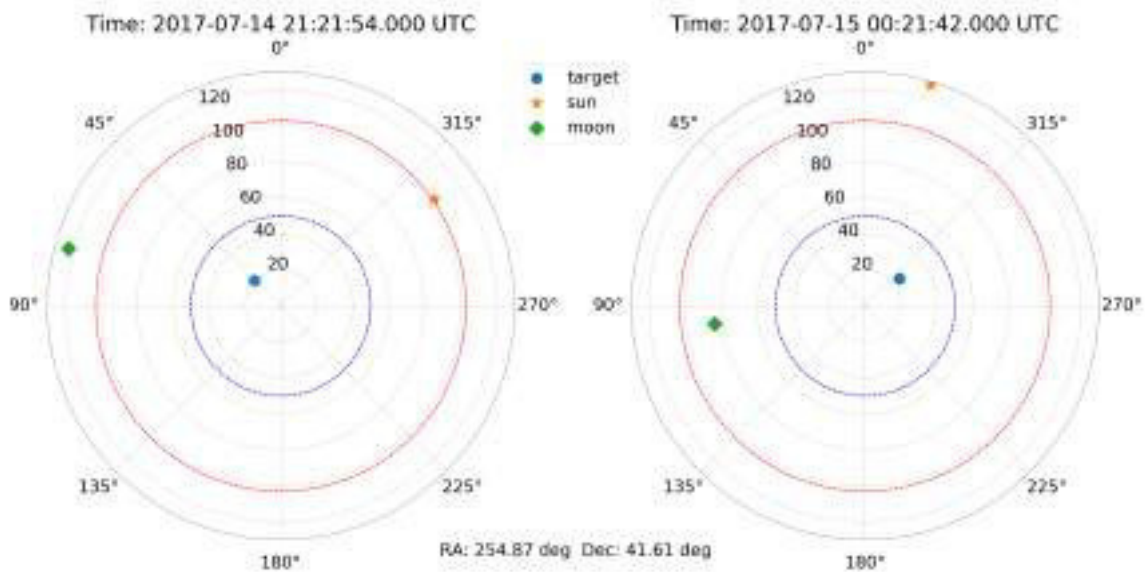


Figure 6.1: Positions of the target, the Sun and the Moon in the local azimuth-zenith reference system at the MAGIC site at the beginning and ending times as calculated by GSPOT for the test performed during 2017-07-14. The red dashed line is the zenith limit for the Sun ( $103^\circ$ ) while the blue one is the observability zenith limit for neutrino targets ( $50^\circ$ )

GSPOT output was:

```

1  @@@@ FINAL CONDITIONS: zds=127.520057 grbzd=24.908349 moondst=124.224567
2  ----- GRB info -----
3  Type of alert: AMON_ICECUBE_EHE
4  GRB IS observable 8
5  R.A. = 17 h 24 m 47.760000 s
6  DEC. = 10 d 59 m 3.120000 s
7  GRB date : 2017/ 7/16 at 21:11:02.0
8  Trigger Time : Sun Jul 16 21:11:01 2017
9  Coordinate error 0
10 N_sigma = 0.000000
11 Zenith = 30 d 23 m 22.043678 s
12 Azimuth = 08 h 01 m 37.283054 s
13 Mean zenith during obs. time = 21.397368
14 Time of alert Thu Jan 1 00:00:00 1970
15 Initial time of observability: Sun Jul 16 21:14:36 2017 at ZA=29.8
16 Final time of observability: Mon Jul 17 00:11:00 2017 at ZA=24.9
17 Minimum ZA within 4 hours = 17.8
18 Alert already sent: no
19 ***** MARK = 979.2
20 Total time of obs = 10584.000000, voto=985.903, ti_zd=29.8 deg, tf_zd=24.9 deg
21 TELESCOPE DIRECT YES
22 tel ra = -1.000000 tel dec = -1.000000 ### tel az = 0.000000 tel zd = 0.000000
23 PKT INFO: Received: LT Sun Jul 16 23:11:13 2017
24 Type= 169 SN = 0
25 here sod= 76273 PKT_SOD= 76272.00 [sec] delta= 1.00
26 TRIG_NUM= 0
27 EVENT_TJD= 17950
28 EVENT_SOD= 76262.00 delta= 11.00

```

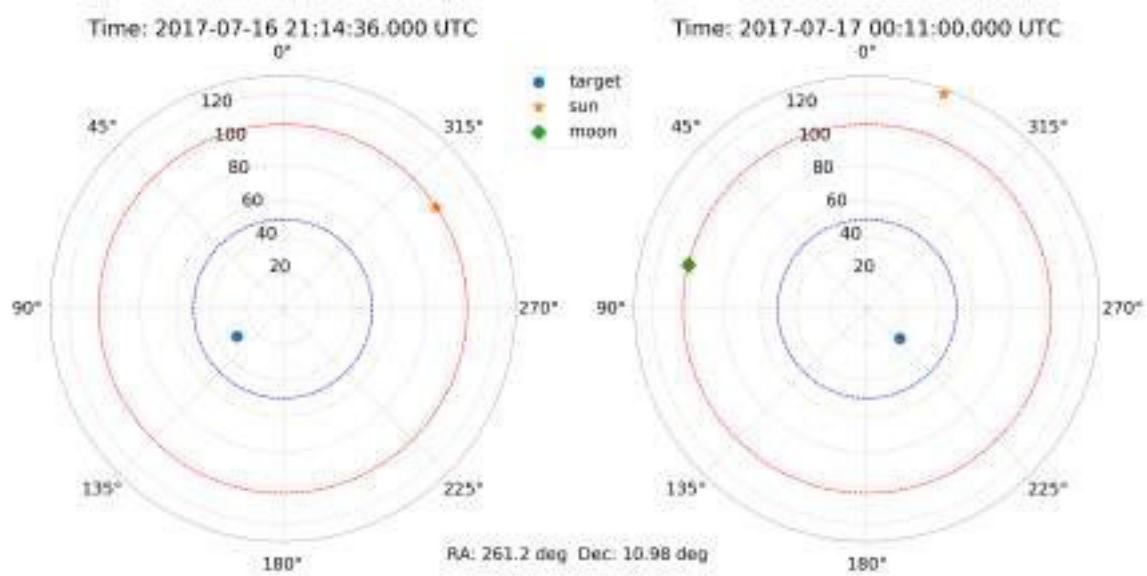


Figure 6.2: Positions of the target, the Sun and the Moon in the local azimuth-zenith reference system at the MAGIC site at the beginning and ending times as calculated by GSPOT for the first test performed during 2017-07-16. The red dashed line is the zenith limit for the Sun ( $103^\circ$ ) while the blue one is the observability zenith limit for neutrino targets ( $50^\circ$ )

```

29 AMON ICECUBE EHE ALERT at 2017/07/16 21 h 11 m 02 s
30 EVENT R.A.= 17 h 24 m 47.760 s
31 EVENT Dec.= +10 deg 59 m 3.120 s
32 POSITION ERROR = 0.000000 deg
33 NUMBER OF EVENTS = 4434765
34
35 Nu Position IS observable, Zenith=30.389, Azimuth=120.405
36 Begin of observation time Sun Jul 16 21:14:36 2017
37 End of observation time Mon Jul 17 00:11:00 2017
38 in the zenith range 29.8 --> 24.9

```

As done before, it is easy to check that also for EHE alerts GSPOT is behaving correctly. One detail to be noted is the start of observation time, which is few minutes shifted with respect to the time when the packet was received: the former is 21:14:36, the latter is 21:11:13. This is due to the fact that at 21:11:13 the Sun was not below  $103^\circ$  in zenith, but at  $102.38^\circ$ . So GSPOT correctly computed the first time for the observation: with the python script I obtained 21:14:35.

The second test of 2017-07-16 was focused on checking the behavior of GSPOT for HESE/EHE targets whose zenith was above  $50^\circ$  at the moment of the alert. The parameters used in this case are summarized in Table 6.3:

| PKT_TYPE | PKT_SOD<br>[s] | PKT_TIME<br>[UTC] | BURST_SOD<br>[s] | AZ<br>[ $^\circ$ ] | ZD<br>[ $^\circ$ ] | RA<br>[hour] | DEC<br>[deg] |
|----------|----------------|-------------------|------------------|--------------------|--------------------|--------------|--------------|
| 158      | 76465          | 21:14:25          | 76455            | 29.8               | 67.8               | 22.2         | 62.4         |

Table 6.3: Summary of the parameters used for the second test performed on 2017-07-16

The output from GSPOT was:

```

1 @@@@ FINAL CONDITIONS: zds=127.754113 grbzd=47.321297 moondst=69.524247
2 ----- GRB info -----

```

```

3  Type of alert: AMON_ICECUBE_HESE
4  GRB IS NOT observable 0
5  R.A. = 22 h 9 m 52.440000 s
6  DEC. = 62 d 23 m 23.280000 s
7  GRB date : 2017/ 7/16 at 21:14:15.0
8  Trigger Time : Sun Jul 16 21:14:15 2017
9  Coordinate error 0
10 N_sigma = 0.000000
11 Zenith = 67 d 46 m 9.352438 s
12 Azimuth = 01 h 59 m 12.019516 s
13 Mean zenith during obs. time = 48.651994
14 Time of alert Thu Jan 1 00:00:00 1970
15 Initial time of observability: Sun Jul 16 23:50:03 2017 at ZA=50.0
16 Final time of observability: Sun Jul 16 22:04:15 2017 at ZA=62.2
17 Minimum ZA within 4 hours = 47.3
18 Alert already sent: no
19 ***** MARK = 0.0
20 TELESCOPE DIRECT YES
21 tel ra = -1.000000 tel dec = -1.000000 ### tel az = 0.000000 tel zd = 0.000000
22 PKT INFO: Received: LT Sun Jul 16 23:14:25 2017
23 Type= 158 SN = 0
24 here sod= 76465 PKT_SOD= 76465.00 [sec] delta= 0.00
25 TRIG_NUM= 0
26 EVENT_TJD= 17950
27 EVENT_SOD= 76455.00 delta= 10.00
28 AMON ICECUBE HESE ALERT at 2017/07/16 21 h 14 m 15 s
29 EVENT R.A.= 22 h 9 m 52.440 s
30 EVENT Dec.= +62 deg 23 m 23.280 s
31 POSITION ERROR = 0.000000 deg
32 NUMBER OF EVENTS = 4434765
33
34 Nu Position IS NOT observable, Zenith=67.769, Azimuth= 29.800
35 Begin of observation time Sun Jul 16 23:50:03 2017
36 End of observation time Sun Jul 16 22:04:15 2017
37 in the zenith range 50.0 --> 62.2

```

One thing that can be immediately noted is that the start and end times of observations are not ordered: the latter should be after the former. In this case, the explanation is the following. The target trigger time is 21:14:15, so that it could be observed up to 00:14:15 of 2017-07-17. However, the target is above 50° until 23:50:03. So about 24 minutes would be available for the observation. Despite this, the target never gets below 45° before 00:14:15, so according to the strategy the total observation time is reduced to 50 minutes starting from the trigger time. Adding 50 minutes to 21:14:15 gives 22:04:15, which coincides with the end observation time computed by GSPOT. This test proves that GSPOT behaves correctly when the target is above the maximum zenith allowed by the observational strategy. The last set of tests was performed on 2017-07-17. The purpose was to check that GSPOT updates correctly the target information. In this case three alerts were sent in a row with different errors on the coordinates: 0.5°, 0.8° and 0.27° respectively. The expected behavior is the following. When an alert is observable, it is added to the alert list. If another alert corresponding to the same target is received but the error on the coordinates is larger, it is not added to the list. If instead the error is smaller, then the alert is added to the list. The first alert will eventually be removed from the list so that only the better one is left to be followed-up.

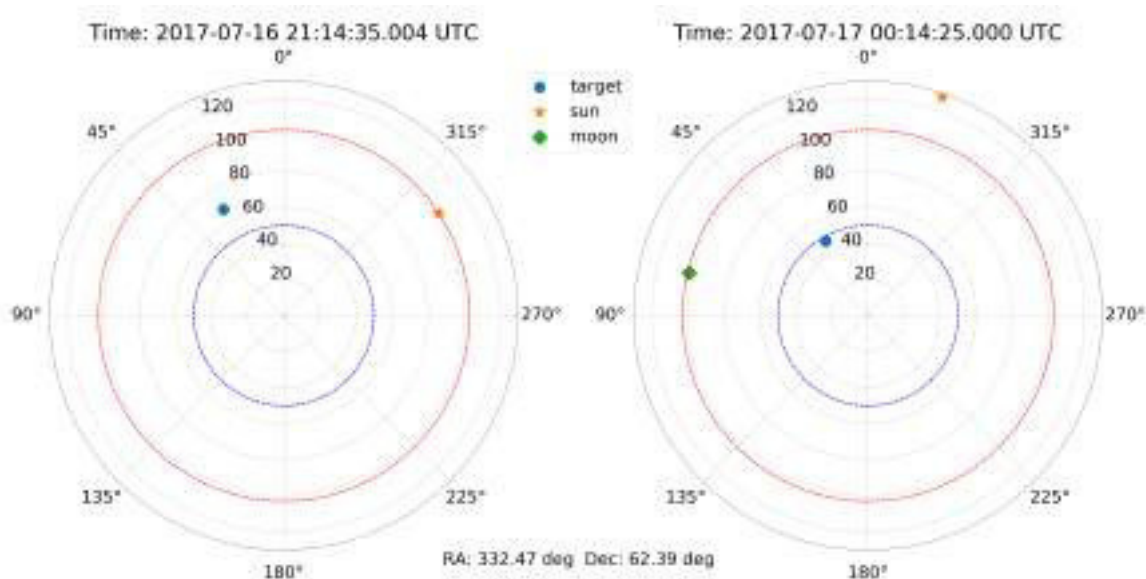


Figure 6.3: Positions of the target, the Sun and the Moon in the local azimuth-zenith reference system at the MAGIC site at the beginning and ending times as calculated by GSPOT for the second test performed during 2017-07-16. The red dashed line is the zenith limit for the Sun ( $103^\circ$ ) while the blue one is the observability zenith limit for neutrino targets ( $50^\circ$ )

The parameters used for the three alerts are summarized in Table 6.4.

| PKT_TYPE | PKT_SOD<br>[s] | PKT_TIME<br>[UTC] | BURST_SOD<br>[s] | AZ<br>[ $^\circ$ ] | ZD<br>[ $^\circ$ ] | RA<br>[hour] | DEC<br>[deg] | Error<br>[ $^\circ$ ] |
|----------|----------------|-------------------|------------------|--------------------|--------------------|--------------|--------------|-----------------------|
| 169      | 77083          | 21:24:43          | 77073            | 120.0              | 67.8               | 19.6         | -12.9        | 0.5                   |
| 169      | 77108          | 21:25:08          | 77098            | 120.0              | 70.0               | 19.8         | -14.3        | 0.8                   |
| 169      | 77130          | 21:25:30          | 77120            | 120.0              | 66.0               | 19.6         | -11.8        | 0.27                  |

Table 6.4: Summary of the parameters used for the test performed on 2017-07-17

To check if an alert is added to the alert list, it is enough to look at GSPOT output. For the first target in Table 6.4 the relevant output is:

```
adding...list size = 1
```

This means that the alert was added to the list and the number of alerts in it is returned. For the second target:

```
not added to list...list size = 1
```

So the alert was not added to the list. This is expected because the error on the position is larger than the one in the first alert. Finally, the third alert was sent:

```
adding...list size = 2
```

Since the error on the position is smaller than the first one, the alert is added to the list, which now contains two elements. GSPOT cycles constantly on the alert list to check if the alerts contained belong to the same GRB and if that is the case, will check which one has the worse error box and remove it. So in principle the alert list usually is empty or has one element. If the coordinates of the alerts are different, GSPOT will use the ones contained in the alert with better uncertainty in the position: this means that GSPOT can update the target position during observation.

## 6.5 Burst Advocate activity

GSPOT automatically handles transient alerts but it is not able (and was not conceived to do that) to judge if a transient source needs to be followed-up for more time or if the observation should be stopped before. Sometimes happens that an event whose origin was thought to be astrophysical in the first notice is found to be due to background fluctuations. In this case, a GCN Circular is sent, so GSPOT is not able to do anything because it does not receive them. In this case a human intervention is needed. For this reason, a person is in charge of monitoring the follow-up of transient sources. Among MAGIC this person is called *Burst Advocate* or simply BA. Originally her/his duty was to be on call during the night if a GRB is followed-up after GSPOT automatic reaction. The BA is contacted by the shifters at the MAGIC site and together with them checks that the observation has no fault. For example, the BA should verify that the trigger tables (i.e. the trigger used) and DT used are the correct ones, that the trigger and DAQ rates are within the limits and that the mirrors are correctly focused. This is important especially in the first minutes of the observations: if there is a problem, it should be spotted and solved as early as possible in order not to spoil the whole observation. If everything is fine, the BA should monitor the observation with the shifters until the end time suggested by GSPOT. Moreover the BA should check for Circulars about the same GRB coming from the GCN. As anticipated, a GRB detection can be retracted if further analysis from the instrument which sent the notice suggests that the GRB did not have astrophysical origin. If this is the case, the BA must stop the current GRB observation in order not to waste time which was scheduled for other sources. The GCN Circulars can also contain physical information from the follow-up of other instruments which can help the BA to decide if the observation should be prolonged beyond the default maximum observation time of 4 h. In some cases the results of follow-ups are not available immediately, but only after few hours. Another way to assess if the GRB should be observed further is to check the results of the MOLA online analysis. If a hint of a signal is shown in the  $\theta^2$  plots or in the skymaps produced by MOLA, it is worth to extend the observation time.

The BA should also check for GCN Notices and Circulars during the day. This is crucial for Fermi-LAT GRBs. Most of the GRB alerts received by GSPOT come from Swift-XRT/BAT and from Fermi-GBM. The latter, due to the special filters set in GSPOT, are almost always rejected. When a GRB is detected by GBM, usually Fermi-LAT data are analyzed in the same time window to search for a detection with the second instrument. In some cases, the GRB is detected by LAT as well and a GCN Circular is sent to the community. Since a LAT detected GRB is a very good candidate to be followed-up by MAGIC, even at late times (hours from the onset), the BA should request a Target of Opportunity (ToO) to observe the GRB as soon as possible, if observable. The same applies in the case LAT has an onboard trigger, that is it detects a GRB by its own. If it happens during the night, GSPOT will handle it but during the day the BA should be responsible of checking it and possibly requesting a ToO.

As mentioned, the BA role was originally created for GRBs follow-up only, but as soon other transient sources were added to the alert streams, other roles needed to be created to handle different kinds of transients. The reason is that each transient source has its own peculiarities from the physical point of view and so different expertise is needed from case to case. Because of this, recently the MAGIC Transients working group established additional types of BA. The role of the GRB Burst Advocate basically remained unchanged. As far as I am concerned, I took responsibilities as GRB BA, GW BA and neutrino Day-time BA. In the case of GW BA, the procedure is not automatic. Given the huge position uncertainty of the events detected by LIGO alone, small FoV telescopes like MAGIC cannot cover the whole high probability region in a reasonable time. For this reason, the MAGIC GW working group decided to perform only follow-ups of possible electromagnetic counterparts detected by other observatories until the uncertainty of the GW region would be accessible with a

reasonable number of pointings. This should happen with the simultaneous data taking of LIGO and Virgo. In order to check if the probability region given by LIGO (or LIGO+Virgo) is visible from the MAGIC site, I developed a Python script which computes the visibility below  $70^\circ$  of zenith from the MAGIC site at different times, superimposing it to the skymap given by the GW detectors (see Section 5.2.4). In this way it is easy to understand if the highest probability region is visible. Other existing tools can be used afterwards to build a list of pointings to be observe.

The day-time neutrino advocate is similar to the GRB BA duty during daytime. The neutrino advocate monitors the GCN stream for possible HESE or EHE notices. If a neutrino alert is received, she/he must check if the target is observable by MAGIC during the night according to the same criteria of the neutrino observation strategy. In positive case, the BA should issue a ToO to observe the position of the neutrino alert.

## 6.6 Future updates and prospects

As shown in Section 6.4, the preliminary tests performed on the automatic response to neutrino alerts had a positive result. The missing piece in the testing phase is the deployment of the new version of `GSPOT` in the La Palma servers, where the current version is running. After this, the tests on-site will be performed: they were scheduled in December 2017 during my stay at the MAGIC site for a data taking shift, because being on-site makes testing `GSPOT` easier compared to the case where the tests are done remotely. In case of successful on-site tests, `GSPOT` will be updated with the new version containing the neutrino automatic reaction. See next Section for details.

The maintainer of `GSPOT` has the duty to solve issues and implement new features requested by members of the collaboration. In this sense, beside the major work on the automatic reaction to neutrino alerts, I plan in the future (close or far) to update `GSPOT` following some suggestions by other members of the Transient working group as well as some personal ideas:

- Adding to the `GSPOT` output the reasons of the resulting observation times. Sometimes the output is not straightly readable and understandable by a non-expert of `GSPOT`. This is especially true when the observation time is reduced to 50 min and the observation times are reversed, as shown in the third test in Section 6.4. This rule is often forgotten and so the output can be deceiving. Moreover it can be helpful to have some graphical output (e.g. Figure 6.1), like the time evolution of the zenith and azimuth of the target and the Moon (if present): this information should be helpful in particular for the BA and also for the shifters, to understand when the GRB observation should be stopped and when the GRB culminates. These plots can be shown in the Burst Monitor webpage (<http://www.magic.iac.es/site/grbm/index.html>) for a quick inspection.
- Adding a correct interpretation of the `trigger_id` item in the Fermi-GBM packets 122 and 115. For these Notice types this item contains some important informations, for example if the GRB is in the FoV of the LAT or if the GRB is tagged as *bright hard burst* in the GBM. This second information is particularly important because it means that the burst could be detected by LAT. These bright GRBs are thus very good candidates for a follow-up. For GBM packets 111 a similar situation holds, since the item called `most_likely` is not well interpreted. As the name suggests, this item tells to which source class the target belongs e.g. GRB, generic transient, SGR, solar flare or others. Having this information is crucial because it could prevent to observe unwanted events and so not to lose precious observation time. In principle the BA should be able to get this information without `GSPOT` but of course in a longer time, so an automatic processing is needed.

- Adding an automatic response to Fermi-GBM packets 115, containing the final and best position of the GRB. Currently, there is no automatic response for such notice type. The reason is that in the past this Notice type was not sent for every GRB or sent with a huge delay because the position was calculated with a human in the loop. The decision was then left to the BA: she/he could ignore or use the coordinates of the Notice, depending on the situation. Nowadays these packets do not involve humans in the loop anymore, so everything is handled by an automatic software which reduces the delay from the first notice. This means that in principle an automatic response could be envisioned, but a careful design must be taken into account. A situation as the following could arise: a GBM alert is followed-up from the beginning of the night up to the end observation time computed by GSPOT and after some time, still during the night, that a GBM Notice of type 115 is received. Because the previous alert is already deleted from the alert list, according to GSPOT the incoming Notice will be considered a new alert and so it will be observed if the criteria are respected. Of course this situation must be avoided and so a non-trivial change in GSPOT is expected, given its current design.
  - Improving the follow-up of GW events. For Notices sent by LIGO/Virgo (LVC), which are still private but whose items are listed in [https://gcn.gsfc.nasa.gov/sock\\_pkt\\_def\\_doc.html](https://gcn.gsfc.nasa.gov/sock_pkt_def_doc.html), the output of GSPOT is incomplete due to information added at the end of 2016 and during 2017. An interesting example are LVC\_COUNTERPART Notices (154), containing information about counterpart sources of LIGO/Virgo GW candidate events from other instruments: in the particular case that the counterpart is detected by XRT, it will be given a rank from 1 to 4, with a low number meaning that the target is more likely to be related to the GW trigger. Such information is very useful for MAGIC follow-up observations because, given the small FoV, a rank 1 source could be a good target to be pointed after the GW trigger. Other two parameters missing in GSPOT output of GW related Notices are `ProbNS` and `ProbRemnant`: the former is the probability that at least one object in the event has a mass less than  $3M_{\odot}$  while the latter is the probability that there is matter in the surrounding central object. These values are crucial to understand if EM emission is expected. Since the third LIGO/Virgo run will start in late 2018, plenty of time is there to implement these changes on LVC Notices and find the best way to use all these informations to improve the follow-up of GW events.
  - Finding a way to automatize Fermi-LAT late time observations. As briefly mentioned in Section 5.1.8, in 2016 MAGIC performed few *late-time observations* of Fermi-LAT detected GRBs, that is the follow-up was extended up to some days after the LAT trigger. This is justified by the extended emission typical of LAT GRBs, as shown in Section 5.1.5. All the late-time observations performed in 2016 were triggered by the BA on shift, but an automatic response of GSPOT would be advisable: LAT GRBs are the most promising candidates for MAGIC follow-up and missing one event could mean losing the chance of discovery. The difficulty for late-time observations is the high number of variables such as redshift, not known at the moment of the event, weather conditions, zenith of observations and the number of hours to spend for the observations. Such a situation is difficult to automatize if a clear strategy is not found.
  - Adapting the system to receive VOEvents. The new protocol for disseminating alert among the astrophysical community will be the VOEvent (see <http://www.ivoa.net/documents/VOEvent/index.html> for a detailed description). VOEvents are XML based alerts, which means they have a hierarchical structure with parent and children tags containing the information about a generic transient event or source, see Figure 6.4. The advantages of using the XML files are several:
-

- they are both human and machine readable, because they can be easily parsed by already existing libraries (in C/C++, Python or Perl);
- they are more flexible because more information can be stored inside a VOEvent compared to the 160 byte binary packets and it can be done more easily, since a XML file is a text file;
- they are more suitable to plan follow-up observations, since a VOEvent can contain a reference to one or more previous VOEvents. Every VOEvent is uniquely defined by an identifier called *ivorn*, so a tree structure between VOEvents is created, which allows to plan different strategies for follow-up observations;
- they are not limited to GRBs or transient sources, but a VOEvent can contain an observation of an interesting source by a certain instrument.

VOEvents are very much like an extension of the GCN: indeed the GCN distributes also the VOEvent version of the binary packets which are sent to the different observatories. Since VOEvents will be the protocol used in the near future in alerts distribution, it is mandatory to migrate as soon as possible to this new way of receiving alerts. Preliminary tests were performed on a dedicated machine in Udine setup by Stefano Ansoldi, who also developed an automated system to receive and perform a first rough processing of VOEvents. I used this system to get confident with the VOEvent structure, in particular for GRBs and GW related VOEvents. Making GSPOT able to process VOEvent is not an easy task. In first place, only one distribution type can be chosen to be received from the GCN. In second place, many libraries specific for VOEvent parsing are available as open source codes in Python programming language, while for C/C++, the languages with which GSPOT was developed, this kind of libraries is not present. So a possibility would be to port GSPOT to Python, for which the development of the code is much easier and faster. Of course one must take into account that a Python code could be slower than a C code, because of the intrinsic properties of the languages: even few seconds can be crucial in the context of transient sources follow-up.

- Creating a database of alerts. The content of the alerts received by GSPOT, observable or not, are stored in ASCII files in the La Palma server. A database of alerts observed by MAGIC is not present yet, but it should be possible to create one starting from the ASCII files since the output of GSPOT is very similar for different packets: the important informations like  $T_0$ , arrival time, start and end observation times and so on are in the same format for all the packet types. With a database it should be easy to make queries and produce plots like those in Figure 5.16, 5.17 or 5.18, which were created by me with some Python scripts. Currently the list of MAGIC observed GRBs was created by hand by myself and Koji Noda starting from a private database hosted at ASDC and adding the missing GRBs, checking that the bursts contained in the list were not affected by technical problems or bad atmospheric conditions, so that they can be analyzed.
- Writing a User Manual for GSPOT. A documentation about GSPOT, its work-flow and how tests can be performed was missing since 2004. In order to let non-experts to understand in depth how GSPOT works, I decided to write a User Guide for GSPOT, which is almost complete (see Figure 6.5.1). While this will be helpful for all people involved with the follow-up of GRB, neutrino and GW alerts, it was a good starting point for me to learn how GSPOT works under the hood.
- Writing the documentation of GSPOT. Related to the previous point, GSPOT's code is usually inspected and thus modified only by the people maintaining it, but of course people interested in knowing all the details could ask to inspect GSPOT's code. For this purpose, I created the Doxygen (see <http://www.stack.nl/~dimitri/doxygen/>

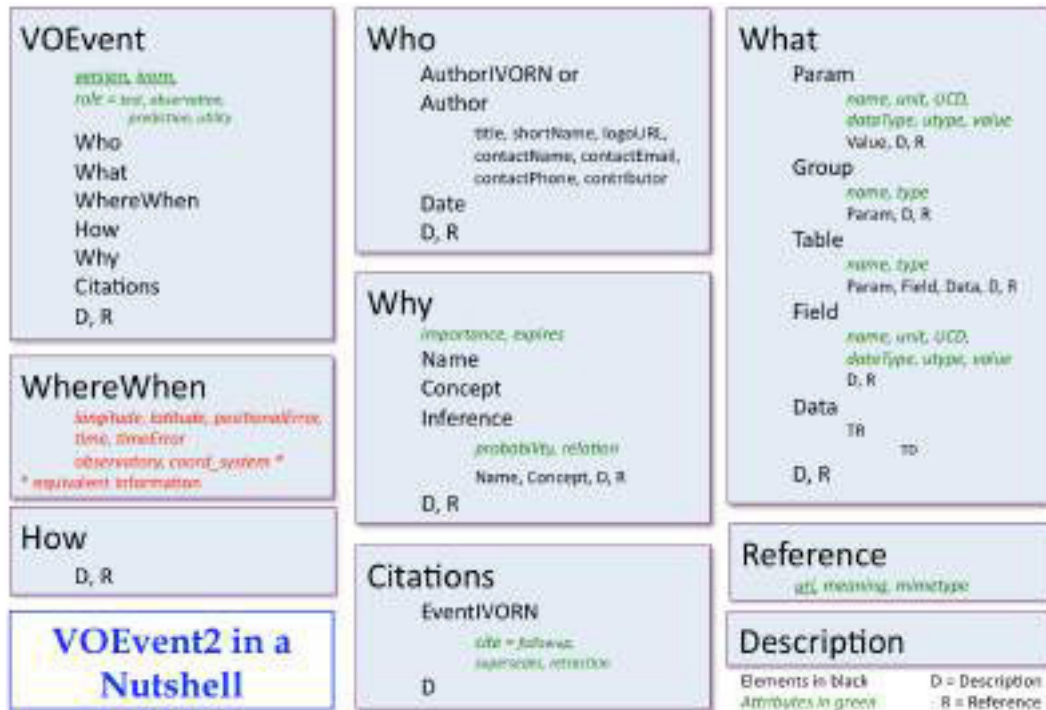


Figure 6.4: Schematic structure of a VOEvent alert. From <http://www.ivoa.net/documents/VOEvent/index.html>.

**Contents**

|   |    |
|---|----|
| Introduction  | 1  |
| 1 GCN system  | 1  |
| 2 gspot main program  | 2  |
| 3 GCN thread  | 3  |
| 3.1 List of the functions used for the processing of packets    | 4  |
| 3.2 Functions for the processing of inactive and kill packets   | 4  |
| 3.3 Functions for the processing of packets containing GRB info | 5  |
| 3.3.1 Processing of other instruments packets                   | 7  |
| 3.3.2 Dedicated filters for GBM packets                         | 7  |
| 4 CC client thread  | 7  |
| 5 CC server thread  | 8  |
| 5.1 The get_CCRReport() function                                | 9  |
| 6 Web thread  | 9  |
| 7 Details of observability calculation                          | 9  |
| 7.1 gspot observability criteria and strategy                   | 9  |
| 7.2 calc_grb_obs() function                                     | 10 |
| 8 Alarm string GRB-ALARM and abort string GRB-ABORT format      | 11 |

Figure 6.5.1

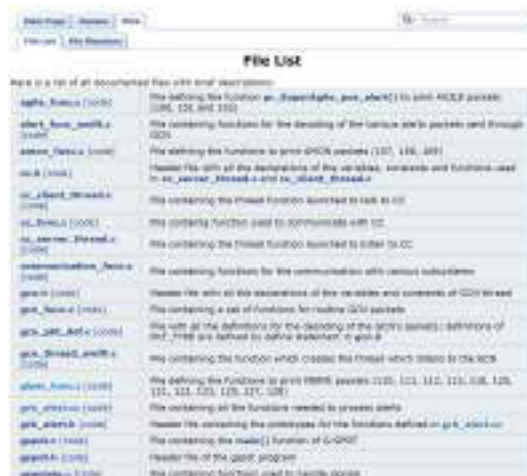


Figure 6.5.2

Figure 6.5: **Left:** extract of the table of contents of the GSPOT User Guide. **Right:** An example of the Doxygen online documentation for GSPOT.

index.html) documentation for GSPOT: almost all functions, classes and structure are described, see Figure 6.5.2 for an example.

- Developing GSPOT using version control systems. Being a software, GSPOT should be developed and maintained with the best available techniques. For this reason, the development will be hopefully carried in the future using a version control system like Git. In this way bugs, modifications and additions can be easily tracked and it is easier to go back to a working stable version if the newest one is unstable.

From the previous list it is clear that there is huge room for improvement, both on the

update and maintenance of GSPOT and on the strategy plan for follow-up observations. It will be crucial to use multi-messenger and multi-wavelength information to follow-up the best candidates, particularly for GW related events. This is especially true for the next generation Cherenkov telescopes, like the CTA array, which is expected to be particularly sensitive to transient phenomena.

## 6.7 On-site tests of GSPOT

As anticipated in the previous Section, on-site tests for GSPOT were scheduled in December 2017. Here I report the preliminary results of those tests, the first performed on the 7th of December and the second on the 22nd of December.

### 6.7.1 Test performed on 7th of December

The test of 7th of December was performed during the day, close to sunset and before the beginning of the night schedule. Before the test, the version of GSPOT containing the automatic response to neutrino alerts was deployed in the La Palma servers. Moreover, to be able to test GSPOT during the day, the constraints on the Sun and target zenith angles were relaxed. In this way, GSPOT will tag as observable almost all targets above the horizon (of course pointing the Sun is avoided). Since the test was performed close to sunset, when the sky brightness is still too high, the cameras of the MAGIC telescopes were kept closed. Indeed the goal of the test was to send few fake alerts to GSPOT and monitor the reaction of GSPOT itself but also of the other subsystems of the MAGIC telescopes. In particular, the expectation before the test was that GSPOT should have sent the target coordinates contained in the alert to *SuperArehucas*, after which the telescopes should have been repointed to the target position using the fast movement. In this way few aspects are checked:

- testing GSPOT behavior in a machine different from the one used for the offline tests performed in July 2017. In particular, the machine where GSPOT runs in the La Palma servers is a 32 bit one, which makes necessary some changes in the code;
- testing if GSPOT actually sends the GRB-ALARM string to the CC of the MAGIC telescopes;
- testing if the telescopes are repointed to the correct position in the sky.

In order to test the previous points, three fake alerts were sent with the parameters listed in Table 6.5.

| PKT_TYPE | PKT_SOD<br>[s] | PKT_TIME<br>[UTC] | BURST_SOD<br>[s] | RA<br>[hour] | DEC<br>[deg] | Name      | Error<br>[°] |
|----------|----------------|-------------------|------------------|--------------|--------------|-----------|--------------|
| 158      | 66860          | 18:34:20          | 66850            | 20.691       | +45.280      | Deneb     | 0.2          |
| 169      | 67196          | 18:39:56          | 67186            | 22.961       | -29.623      | Fomalhaut | 0.3          |
| 158      | 67482          | 18:44:42          | 67472            | 23.495       | +49.17       | NGC7686   | 0.27         |

Table 6.5: Summary of the parameters used for the test performed on 2017-12-07.

For the first alert the response of GSPOT together with the GRB-ALARM string sent to *SuperArehucas* is shown below:

```

1 PKT INFO: Received: LT Thu Dec 7 18:34:21 2017
2   Type= 158      SN = 0
3   here sod= 66861  PKT_SOD= 66860.00 [sec]   delta=      1.00
4   TRIG_NUM= 0

```

```

5  EVENT_TJD= 18094
6  EVENT_SOD= 66850.00    delta=    11.00
7  AMON ICECUBE HESE ALERT at 2017/12/07 18 h 34 m 10 s
8  EVENT R.A.= 20 h 41 m 27.600 s
9  EVENT Dec.= +45 deg 16 m 48.000 s
10 BURST LII = 84.29 deg BII = 1.99 deg
11 POSITION ERROR = 0.200000 deg
12 NUMBER OF EVENTS = 0.000000
13
14 Nu Position IS observable, Zenith=26.961, Azimuth=315.123
15 Begin of observation time Thu Dec 7 18:34:21 2017
16 End of observation time Thu Dec 7 21:34:08 2017
17 in the zenith range 27.0 --> 57.9
18
19 GRB-ALARM 09 2017 12 07 18 34 22 370 01 2017 12 07 18 34 09 999
20 000013 DIRECT 01 00 00.00 + 01 00 00.00 20 41 27.60 + 45 16 48.00
21 002000 315 07 21.18 26 57 40.28 84.29 1.99 OVER

```

From this output, the following can be noted:

- GSPOT respects the 3 hours limit set for neutrino alerts, but not the zenith one. This is because in the GSPOT version used for day-testing the zenith limit is relaxed to values greater than  $50^\circ$  as previously stated;
- the coordinates shown in GSPOT output correspond to the input ones shown in the first row of Table 6.5. The same can be found in the GRB-ALARM string (end of line 20).

After *SuperArehucas* received the GRB-ALARM string, the telescopes were repointed to the coordinates contained in it (to be precise, to a position  $0.4^\circ$  away from it, since the standard observation mode is the wobble one).

For the second alert the output was:

```

1  PKT INFO: Received: LT Thu Dec 7 18:39:57 2017
2  Type= 169    SN = 0
3  here sod= 67197    PKT_SOD= 67196.00 [sec]    delta=    1.00
4  TRIG_NUM= 0
5  EVENT_TJD= 18094
6  EVENT_SOD= 67186.00    delta=    11.00
7  AMON ICECUBE EHE ALERT at 2017/12/07 18 h 39 m 46 s
8  EVENT R.A.= 22 h 57 m 39.576 s
9  EVENT Dec.= -29 deg 37 m 22.800 s
10 BURST LII = 20.49 deg BII = -64.91 deg
11 POSITION ERROR = 0.299900 deg
12 NUMBER OF EVENTS = 0.000000
13
14 Nu Position IS observable, Zenith=58.608, Azimuth=174.301
15 Begin of observation time Thu Dec 7 18:39:57 2017
16 End of observation time Thu Dec 7 21:39:44 2017
17 in the zenith range 58.6 --> 69.5
18
19 GRB-ALARM 09 2017 12 07 18 39 57 745 01 2017 12 07 18 39 45 999
20 000012 DIRECT 01 00 00.00 + 01 00 00.00 22 57 39.58 - 29 37 22.80
21 002999 174 18 02.02 58 36 30.50 20.49 -64.91 OVER

```

Finally, for the third alert the output was:

```

1 PKT INFO: Received: LT Thu Dec 7 18:44:43 2017
2   Type= 158      SN = 0
3   here sod= 67483   PKT_SOD= 67482.00 [sec]   delta=      1.00
4   TRIG_NUM= 0
5   EVENT_TJD= 18094
6   EVENT_SOD= 67472.00   delta=      11.00
7   AMON ICECUBE HESE ALERT at 2017/12/07 18 h 44 m 32 s
8   EVENT R.A.= 23 h 29 m 42.000 s
9   EVENT Dec.= +49 deg 10 m 12.000 s
10  BURST LII = 109.46 deg BII = -11.55 deg
11  POSITION ERROR = 0.270000 deg
12  NUMBER OF EVENTS = 0.000000
13
14  Nu Position IS observable, Zenith=22.501, Azimuth= 21.540
15  Begin of observation time Thu Dec 7 18:44:43 2017
16  End of observation time Thu Dec 7 21:44:30 2017
17  in the zenith range 22.5 --> 32.1
18
19  GRB-ALARM 09 2017 12 07 18 44 44 085 01 2017 12 07 18 44 31 999
20  000013 DIRECT 01 00 00.00 + 01 00 00.00 23 29 42.00 + 49 10 12.00
21  002700 21 32 23.16 22 30 04.85 109.46 -11.55 OVER

```

For both the second and third alert, the same considerations valid for the first one apply. The tests performed on the 7th of December showed what was already tested offline in July: GSPOT receives and processes correctly neutrino alerts. With these on-site tests, it was proven that the right information is sent to *SuperArehucas*. So, the telescopes are repointed to the right coordinates in wobble mode.

To test GSPOT in a more realistic situation, a second round of tests was scheduled on the 22nd of December, as explained in the next Section.

### 6.7.2 Test performed on 22nd of December

On the 22nd of December, another test was performed on-site with the help of the shifters. This time GSPOT was tested during the night in a realistic situation, that is while telescopes were taking data on another source. The procedure used during this test was the following:

1. tracking a source in wobble mode and starting to take data. The source chosen was NGC1068 because the targets of the fake alerts lied on the Galactic plane, while NGC1068 lies outside it. In this way the telescopes have to move along a considerable path.
2. during data taking, a fake alert is sent. At this point GSPOT should react as described in the previous section, sending the GRB-ALARM string to the CC and so the telescopes are repointed to the target position.
3. after few minutes of data taking on the target of the fake alert, DAQ is stopped and telescopes are repositioned to NGC1068 and the procedure restarts.

This procedure was repeated twice, so that two alerts were sent, one for each neutrino notice type (HESE and EHE). The parameters of the two alerts are shown in Table 6.6. Here below I report the response of GSPOT and the GRB-ALARM string sent to the CC for the two alerts.

| PKT_TYPE | PKT_SOD<br>[s] | PKT_TIME<br>[UTC] | BURST_SOD<br>[s] | RA<br>[hour] | DEC<br>[deg] | Name             | Error<br>[°] |
|----------|----------------|-------------------|------------------|--------------|--------------|------------------|--------------|
| 169      | 80045          | 22:14:05          | 80035            | 4.4618       | +55.8277     | G150             | 0.1          |
| 158      | 81121          | 22:32:01          | 81111            | 5.966        | +18.4655     | TYC 1316-00147-1 | 0.2          |

Table 6.6: Summary of the parameters used for the test performed on 2017-12-22.

```

1 PKT INFO: Received: LT Fri Dec 22 22:14:06 2017
2   Type= 169      SN = 0
3   here sod= 80046   PKT_SOD= 80045.00 [sec]   delta=      1.00
4   TRIG_NUM= 0
5   EVENT_TJD= 18109
6   EVENT_SOD= 80035.00   delta=      11.00
7   AMON ICECUBE EHE ALERT at 2017/12/22 22 h 13 m 55 s
8   EVENT R.A.= 4 h 27 m 42.480 s
9   EVENT Dec.= +55 deg 49 m 39.720 s
10  BURST LII = 150.09 deg BII = 4.81 deg
11  POSITION ERROR = 0.100000 deg
12  NUMBER OF EVENTS = 0.000000
13
14 Nu Position IS observable, Zenith=30.469, Azimuth= 21.854
15 Begin of observation time Fri Dec 22 22:14:06 2017
16 End of observation time Sat Dec 23 01:13:53 2017
17 in the zenith range 30.5 --> 32.6
18
19 GRB-ALARM 09 2017 12 22 22 14 07 048 01 2017 12 22 22 13 54 999
20 000013 DIRECT 01 00 00.00 + 01 00 00.00 04 27 42.48 + 55 49 39.72
21 001000 21 51 13.83 30 28 08.48 150.09 4.81 OVER

1 PKT INFO: Received: LT Fri Dec 22 22:32:01 2017
2   Type= 158      SN = 0
3   here sod= 81121   PKT_SOD= 81121.00 [sec]   delta=      0.00
4   TRIG_NUM= 0
5   EVENT_TJD= 18109
6   EVENT_SOD= 81111.00   delta=      10.00
7   AMON ICECUBE HESE ALERT at 2017/12/22 22 h 31 m 51 s
8   EVENT R.A.= 5 h 57 m 57.600 s
9   EVENT Dec.= +18 deg 27 m 55.440 s
10  BURST LII = 190.45 deg BII = -2.91 deg
11  POSITION ERROR = 0.200000 deg
12  NUMBER OF EVENTS = 0.000000
13
14 Nu Position IS observable, Zenith=35.876, Azimuth= 98.180
15 Begin of observation time Fri Dec 22 22:32:01 2017
16 End of observation time Sat Dec 23 01:31:50 2017
17 in the zenith range 35.9 --> 12.3
18
19 GRB-ALARM 09 2017 12 22 22 32 01 615 01 2017 12 22 22 31 51 000
20 000010 DIRECT 01 00 00.00 + 01 00 00.00 05 57 57.60 + 18 27 55.44
21 002000 98 10 46.61 35 52 34.97 190.45 -2.91 OVER

```

As before, also in this situation GSPOT deals correctly with the neutrino alert packets and

sends the correct information to *SuperArehucas*. Moreover, a small bug, showing up when low observation times are set, was found and it will be investigated. Unfortunately, there was not enough time after the test to check other aspects of the automatic procedure, like the stability of rates after the repositioning or the correct setting of discriminator threshold. In any case, these are not handled by GSPOT but by the corresponding subsystems.

The conclusion from this test (and also from the previous one performed on the 7th of December) is that the new version of GSPOT works properly in a realistic situation. The preliminary results of the test were already reported to the MAGIC Technical Board, which will decide on the replacement of the current version of GSPOT with the new one containing the automatic response to neutrino notices.



## Chapter 7

# CONCLUSIONS AND FUTURE PROSPECTS

In this thesis I presented the results of the follow-up of GRBs and gravitational wave events performed with the MAGIC telescopes and of the technical work implemented to update the MAGIC automatic alert system.

The goal of GRBs follow-up was to search for a possible VHE  $\gamma$ -ray emission. The observation of GRBs is difficult due to their serendipitous nature, which results in very different observational conditions from GRB to GRB. Their fading emission makes it crucial to observe them as soon as possible and MAGIC has a fast repositioning system allowing to point GRBs in few tens of seconds. Moreover, the low energy threshold of the MAGIC telescopes allows to observe GRBs up to moderate redshift in an energy range where EBL absorption is lower. I pursued the search for VHE emission from GRBs taking into consideration 12 GRBs, which I analyzed with the MAGIC analysis software. The result of this analysis is that no GRB showed a significant signal and only upper limits on the flux could be obtained. This result can be explained given the quite high redshift of the GRBs ( $z > 1$ ) and the large delay of observation for some GRBs. Nonetheless, upper limits can be used to put constraints on the emission models: given a theoretical model, usually dependent on several parameters, upper limits can be used to constrain the parameter space. No definitive answer about the GRB HE emission process will be drawn until a GRB detection will be reached. To pursue this goal, one of the ways is to lower as much as possible the energy threshold of the MAGIC telescopes: different triggers could be used in the future to reach a threshold of 30 GeV for low zenith observations. This will expand the gamma-ray horizon observable by MAGIC and will increase the chances of detection for close GRBs ( $z < 1$ ). Another way to improve GRB observations is through the automatic alert system: on the one hand one must choose the best candidates, on the other the automatic procedure must be working flawlessly. For the latter point, regular tests with fake alerts are needed in order not to lose the golden chance of a GRB detection. Another important point in GRB observations is the role of MAGIC Burst Advocates. They are responsible for a flawless GRB observation to ensure good quality data especially in the first minutes of data: for this reason in the last period of my PhD I took this responsibility, not only for GRBs, but also for gravitational events and neutrinos (day-time advocate).

This thesis also reported the follow-up by MAGIC of gravitational wave events provided by LIGO. I directly participated as a data analyzer for the follow-up of GW151226 and I contributed with the creation of a tool for the analysis of such events whose localization is in most of the cases larger than the MAGIC field of view. The tool was created in collaboration with other two collaboration members: many tests were performed to tune the tool and obtain consistent results. The results of these tests were presented by me during several meetings of the MAGIC Software Board to reach the final blessing to use the tool on MAGIC data.

Finally I applied the tool to the four targets observed during the follow-up of GW151226. The result is compatible with a background-only emission, as expected by a BBH system. The tool is not limited to GW follow-up: indeed it was used also by the colleagues of the Neutrino Working Group (now inside the Transient Working Group) for the analysis of data taken after HESE and EHE alerts, where a similar situation to the GW follow-up arises. I also contributed to the follow-up strategy with a tool for the fast computation of the visibility from the MAGIC site for GW candidate events: it helps in considering which region of the localization sky map could be observable and in choosing promising targets. The follow-up strategy will be refined for sure before the start of the third LIGO/Virgo observation run. In particular, the distance information on the events shall be used to reduce the number of promising targets. A way to achieve this is using a catalog of known galaxies. The time before the beginning O3 will also be used to test the strategy with fake alerts in order to be prepared for real alerts.

Finally, this thesis presented the results of a technical work on the automatic alert system of the MAGIC telescopes, **GSPOT**. This system is crucial for the follow-up of GRBs and transient sources by MAGIC. I took over the responsibility as a maintainer of the system and I implemented the automatic response to neutrino alerts sent by IceCube. I also tested it offline, showing that it works properly. I will test the new procedure on my next shift in November/December 2017 and after it, hopefully MAGIC will have the automatic response to neutrino alerts. I envision other updates/upgrades for **GSPOT** if I will be given the possibility to keep working on it. In particular, it is important to refine the follow-up strategies for GRBs, GWs and Neutrinos and implement them automatically in **GSPOT**, so that no precious time is lost, which could hinder a huge scientific discovery. Moreover, the importance of tests with fake alerts must not be underestimated: as a matter of fact they are fundamental for a proper, flawless workflow of the automatic alert system. For this reason, making testing easier and faster is a way to both keep the system healthy and not to lose observation time which could be dedicated to the scheduled sources. Finally, in view of CTA, the passage to the new alert protocol **VOEvents** will be fundamental to keep **GSPOT** updated with the newest and best ways to perform follow-up observations.

Overall, this thesis gave me the opportunity to work in an experiment which is performing cutting edge research in gamma-ray astronomy and I tried to contribute to one of the topics for which a detection in the VHE range is still missing, namely GRBs. Moreover I contributed to the new challenge of GW follow-up, showing that new tools are required allowing to analyze data even with large localizations. I finally had the possibility to work on the automatic alert system of MAGIC, a high responsibility given its importance for the follow-up of transient sources. This work will for sure be the starting point for future improvements, which hopefully will lead to some great discoveries and increase our knowledge of the Universe. In this regard, soon the next generation experiment CTA will be operative and it will be the most sensitive Cherenkov array ever built. Its scientific potential will be tested with the first LST prototype in La Palma: with a low energy threshold ( $\sim 20$  GeV), fast repositioning ( $< 20$  s) and high sensitivity at low energies, it will be the key instrument for transient science in the future, opening a new era in the field of VHE  $\gamma$ -ray astronomy.

## Appendix A

# CASCADE THEORY

I resume here some functions which were used in Section 2.1.5, but which were not given the explicit functional form. For details see Rossi and Greisen (1941) and Lipari (2009).

The functions  $\lambda_{1,2}$  and the coefficients  $a_{1,2}$  and  $b_{1,2}$  present in equations (2.16) and (2.17) are given by:

$$\lambda_{1,2}(s) = -\frac{1}{2}[A(s) + \sigma_0] \pm \frac{1}{2}\sqrt{[A(s) - \sigma_0]^2 + 4B(s)C(s)} \quad (\text{A.1})$$

$$\frac{a_1}{b_1} = \frac{B(s)}{A(s) + \lambda_1(s)} \quad \frac{a_2}{b_2} = \frac{B(s)}{A(s) + \lambda_2(s)} \quad (\text{A.2})$$

Here we have introduced the functions  $A(s)$ ,  $B(s)$  and  $C(s)$ , which are defined as the momenta of the functions  $\varphi_0(y)$  and  $\psi_0(x)$ :

$$\begin{aligned} A(s) &= \int_0^1 dy \varphi_0(y) [1 - (1-y)^s] = \\ &= \left(\frac{4}{3} + 2b\right) \left(\frac{\Gamma'(1+s)}{\Gamma(1+s)} + \gamma\right) - \frac{5s^2 + 7s + 12b(s^2 + 2s)}{6(s+1)(s+2)} \end{aligned} \quad (\text{A.3})$$

$$B(s) = 2 \int_0^1 dx x^2 \psi_0(x) = \frac{6s^2 + 22s + 28 - 12b(s+1)}{3(s+1)(s+2)(s+3)} \quad (\text{A.4})$$

$$C(s) = \int_0^1 dy y^s \varphi_0(y) = \frac{3s^2 + 7s + 8 + 6b(2+s)}{3s(s+1)(s+2)} \quad (\text{A.5})$$

In  $A(s)$  the function  $\frac{\Gamma'(1+s)}{\Gamma(1+s)}$  is the digamma function (derivative of the logarithm of the Gamma function), while  $\gamma \simeq 0.577216$  is the Euler-Mascheroni constant. In equation (2.18) the functions  $G_\alpha$  were defined:

$$\begin{aligned} G_{e \rightarrow e}(s) &= \frac{[\sigma_0 + \lambda_1(s)]}{\lambda_1(s) - \lambda_2(s)} \\ G_{e \rightarrow \gamma}(s) &= \frac{C(s)}{\lambda_1(s) - \lambda_2(s)} \\ G_{\gamma \rightarrow e}(s) &= -\frac{1}{C(s)} \frac{[\sigma_0 + \lambda_1(s)][\sigma_0 + \lambda_2(s)]}{\lambda_1(s) - \lambda_2(s)} \\ G_{\gamma \rightarrow \gamma}(s) &= -\frac{[\sigma_0 + \lambda_2(s)]}{\lambda_1(s) - \lambda_2(s)} \end{aligned} \quad (\text{A.6})$$

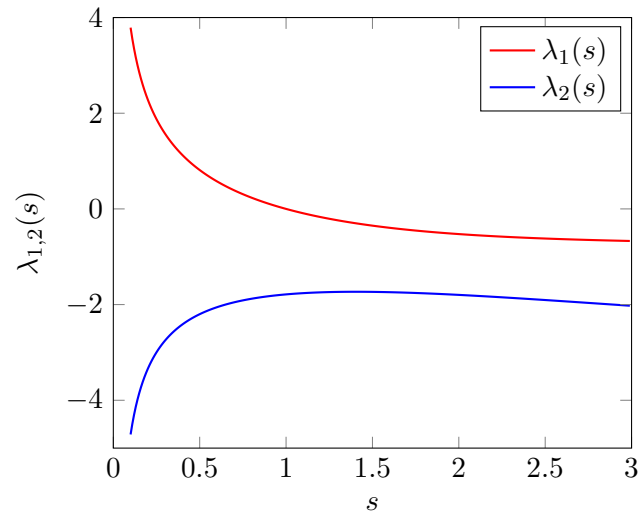


Figure A.1: Plot of the functions  $\lambda_1(s)$  and  $\lambda_2(s)$  defined in equation (A.1).

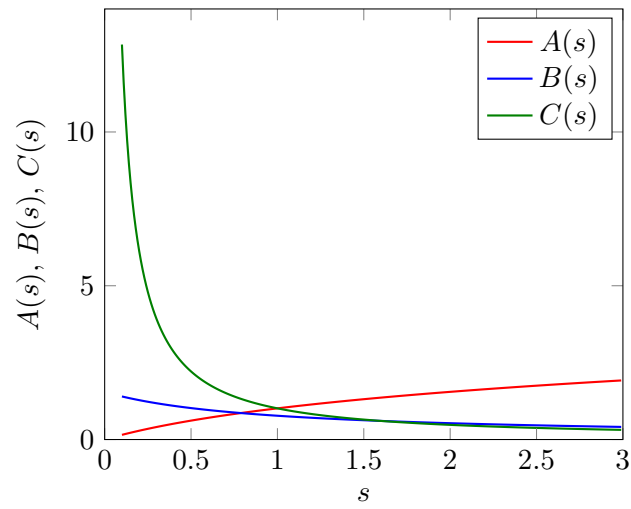


Figure A.2: Plot of the functions  $A(s)$ ,  $B(s)$  and  $C(s)$  defined in equations (A.3), (A.4) and (A.5) respectively.

## Appendix B

# GRB LIGHTCURVES

In this appendix, the lightcurves of the GRBs considered in this thesis and presented in Section 5.1.8 are shown. Most of them show the lightcurves from publicly available Swift-BAT and Swift-XRT data.

For GRB150213A, the Fermi-GBM lightcurve can be found at the link [https://heasarc.gsfc.nasa.gov/FTP/fermi/data/gbm/triggers/2015/bn150213001/quicklook/glg\\_lc\\_chan34\\_bn150213001.pdf](https://heasarc.gsfc.nasa.gov/FTP/fermi/data/gbm/triggers/2015/bn150213001/quicklook/glg_lc_chan34_bn150213001.pdf).

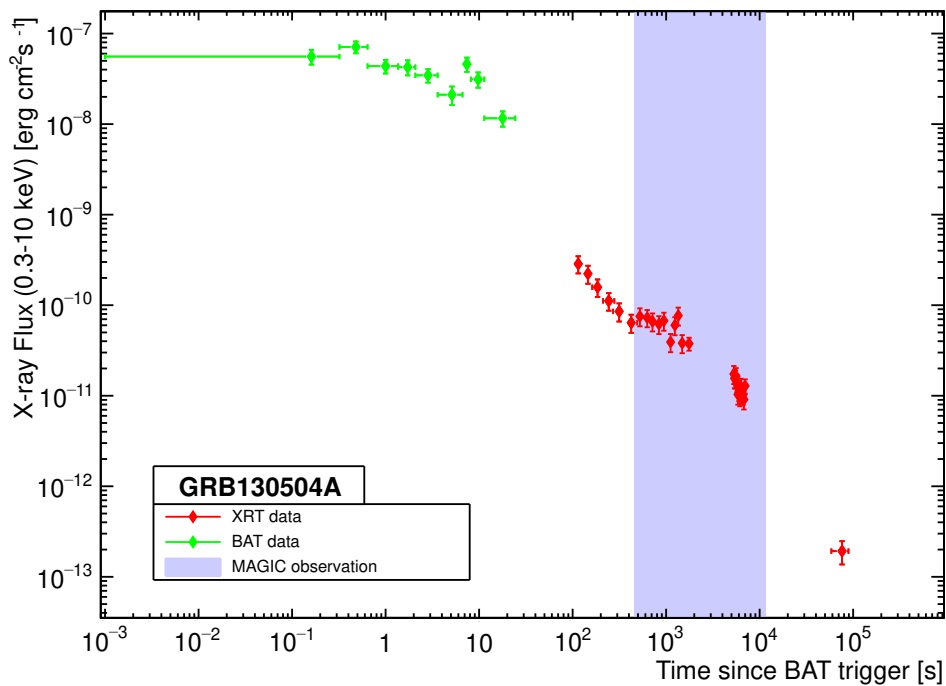


Figure B.1: Swift (BAT+XRT or XRT only) light curves for GRB130504A, with MAGIC observation window.

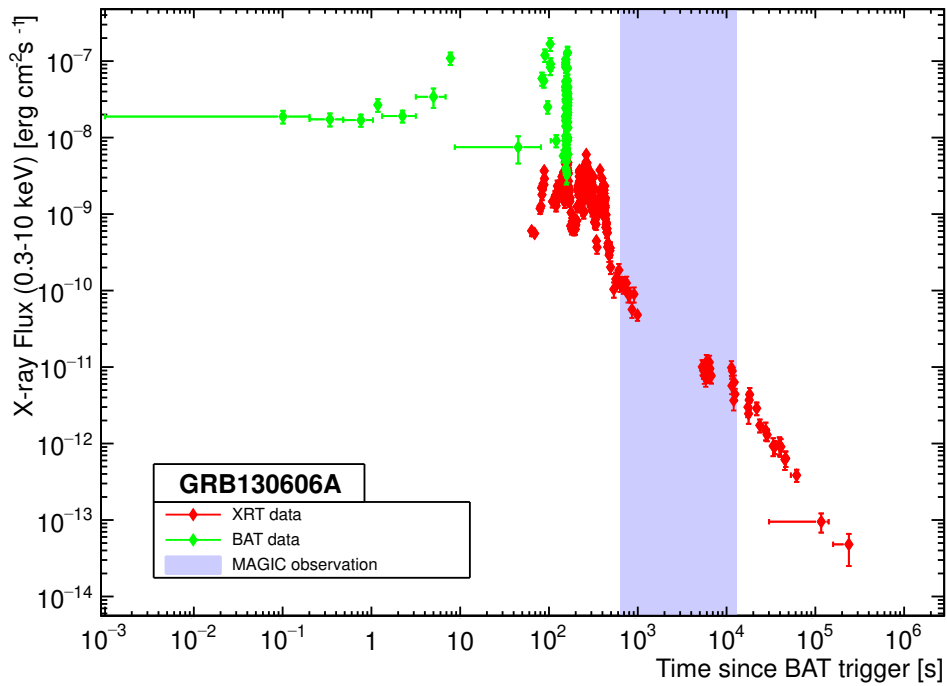


Figure B.2: Swift (BAT+XRT or XRT only) light curves for GRB130606A, with MAGIC observation window.

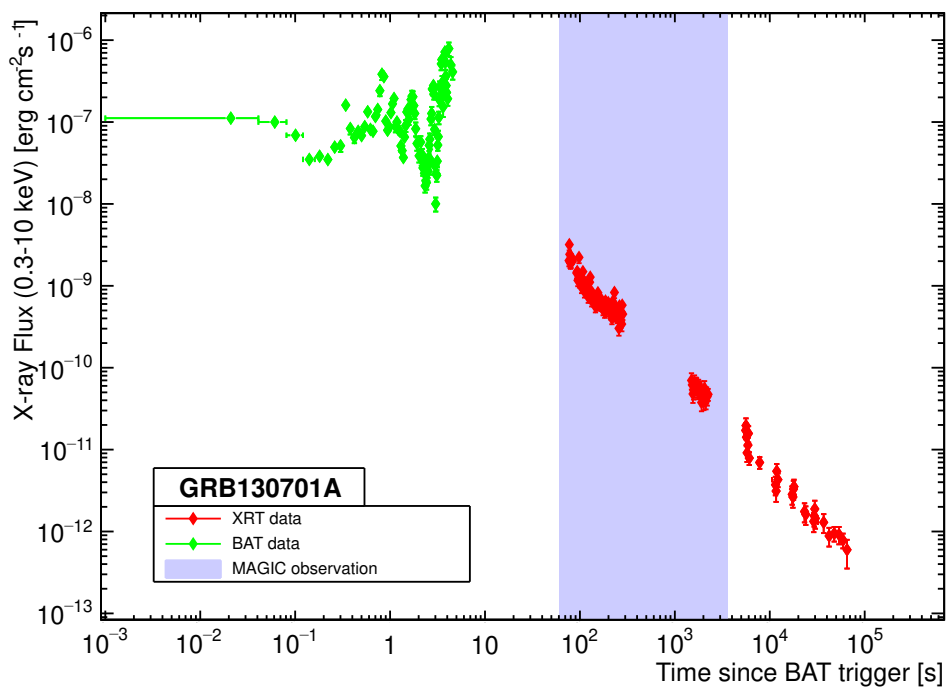


Figure B.3: Swift (BAT+XRT or XRT only) light curves for GRB130701A, with MAGIC observation window.

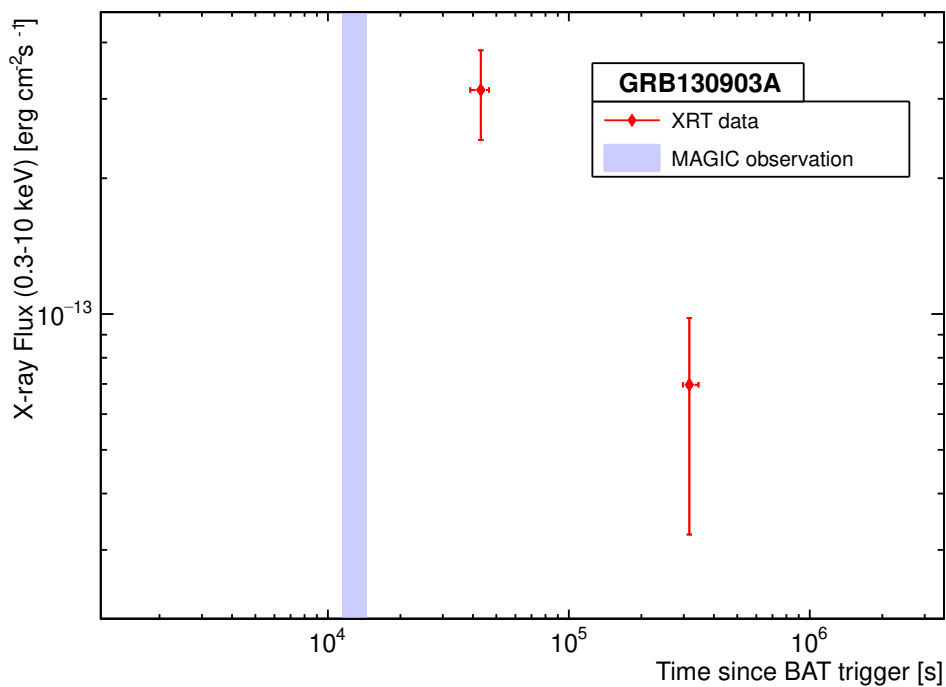


Figure B.4: Swift (BAT+XRT or XRT only) light curves for GRB130903A, with MAGIC observation window.

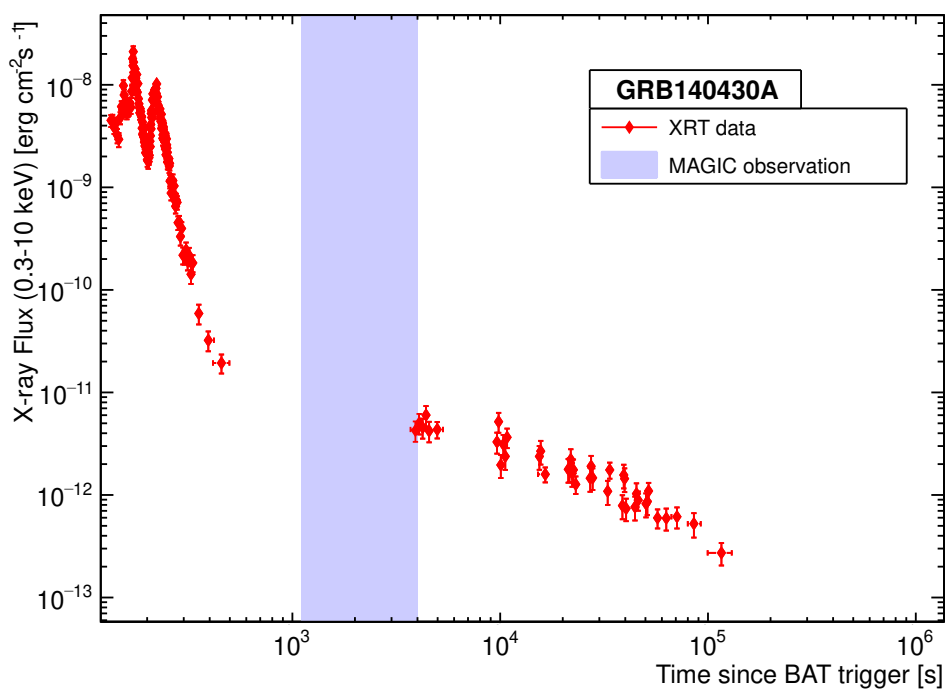


Figure B.5: Swift (BAT+XRT or XRT only) light curves for GRB140430A, with MAGIC observation window.

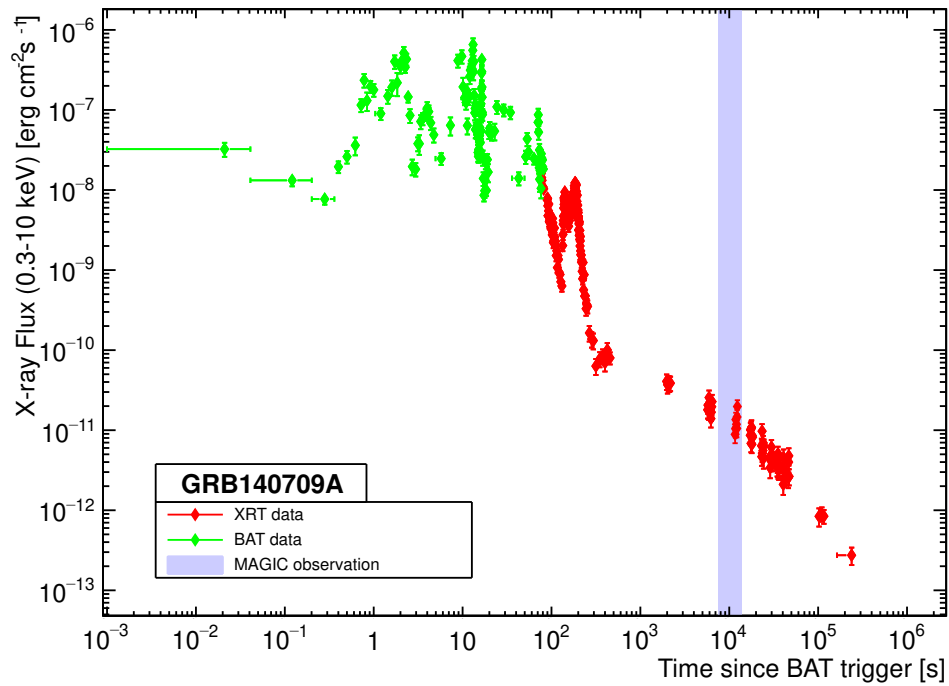


Figure B.6: Swift (BAT+XRT or XRT only) light curves for GRB140709A, with MAGIC observation window.

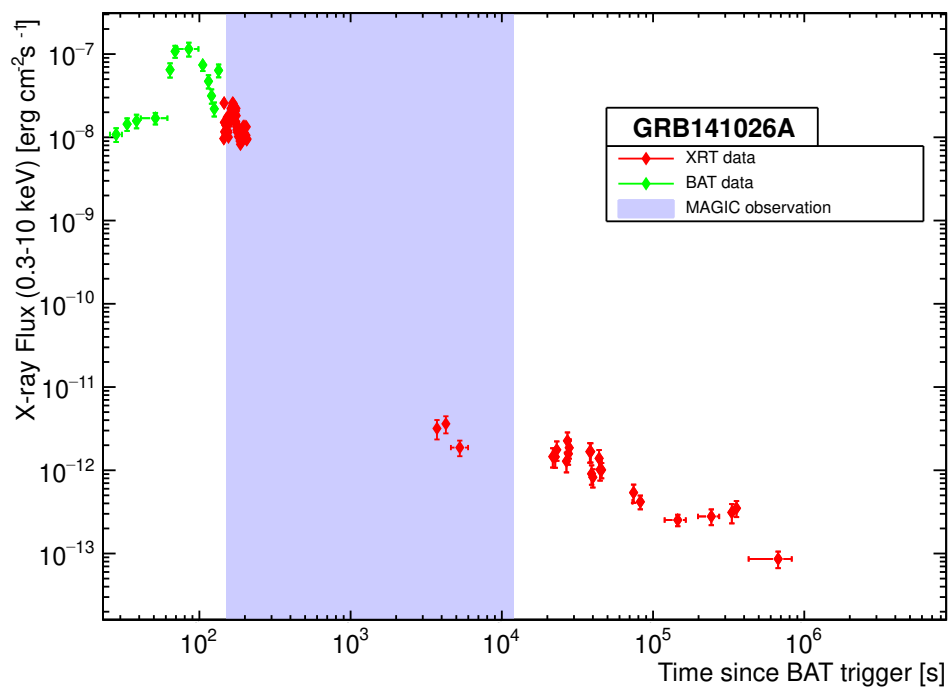


Figure B.7: Swift (BAT+XRT or XRT only) light curves for GRB141026A, with MAGIC observation window.

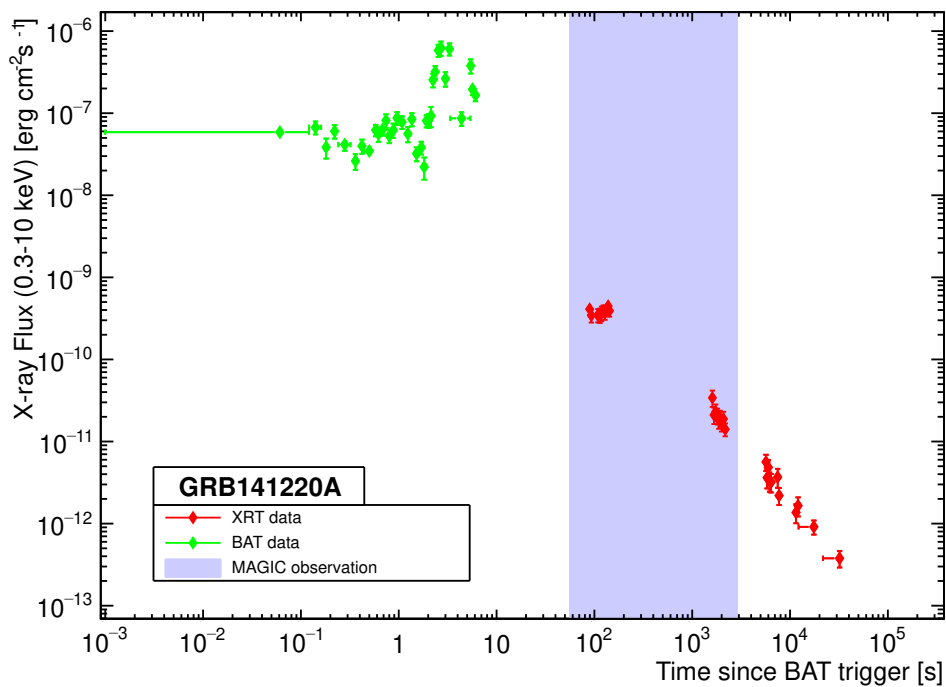


Figure B.8: Swift (BAT+XRT or XRT only) light curves for GRB141220A, with MAGIC observation window.

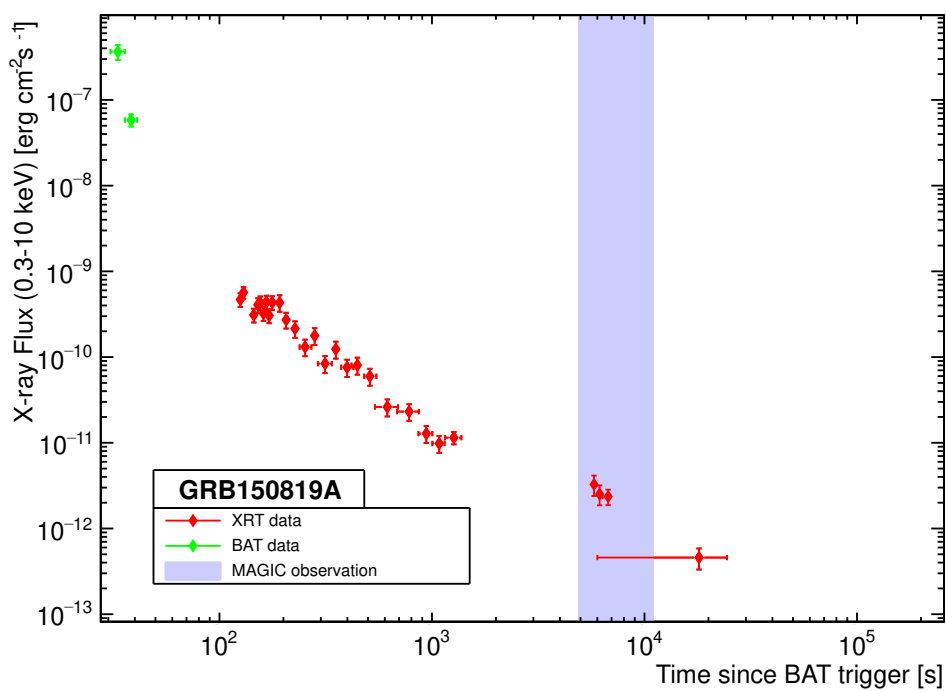


Figure B.9: Swift (BAT+XRT or XRT only) light curves for GRB150819A, with MAGIC observation window.

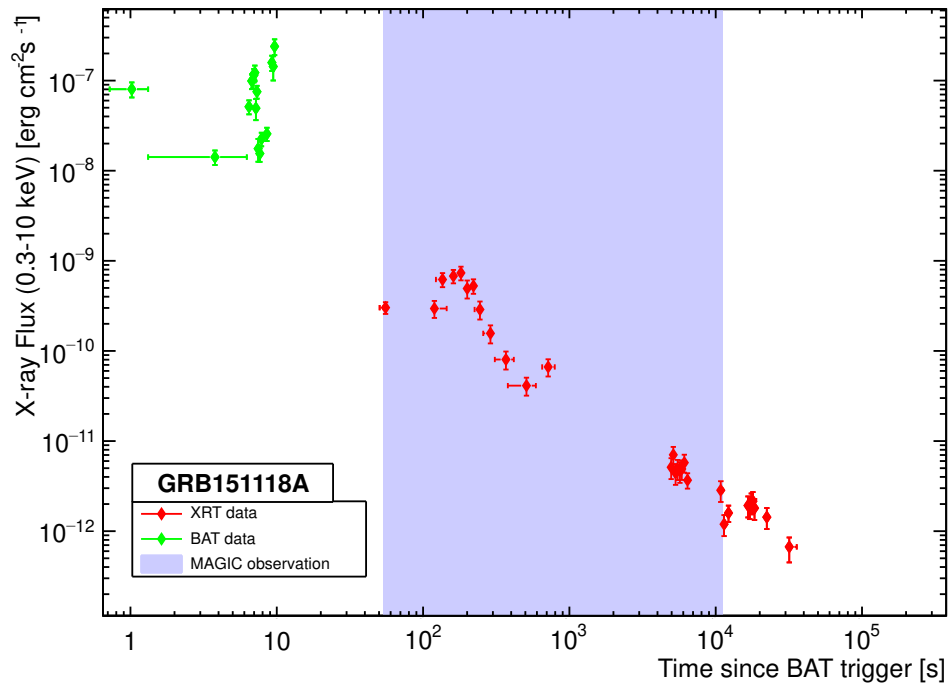


Figure B.10: Swift (BAT+XRT or XRT only) light curves for GRB151118A, with MAGIC observation window.

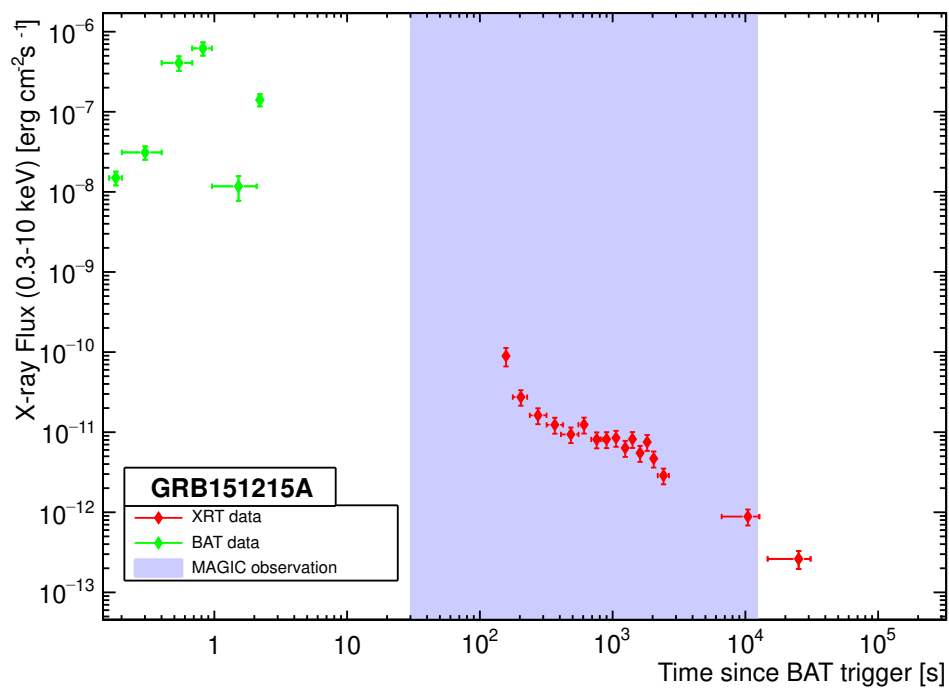


Figure B.11: Swift (BAT+XRT or XRT only) light curves for GRB151215A, with MAGIC observation window.

## Appendix C

# GRB ANALYSIS RESULTS

I present here the main plots for each GRB analyzed in my thesis, whose results are presented in Section 5.1.11. For each GRB four plots are presented:

- the  $\theta^2$  plot obtained from `odie` using LE cuts. The red dots represent the ON histogram, while the OFF histogram has black dots and corresponds to the grey filled histogram. On the top right inset, the observation time, total ON, OFF and excess events and significance calculated according to the Li&Ma formula are reported.
- TS skymap produced with `caspar` using LE cuts and specifying the coordinates of the GRB.
- TS value distribution: the null hypothesis distribution (i.e. data compatible with background emission) is the red solid line, while the distribution from the data is represented by white filled dots.
- Evolution in time of the significance (Li&Ma), excess events number, background events number and signal to noise ratio.

From the  $\theta^2$  plots one can understand that none of the GRBs considered has a signal compatible with a  $\gamma$ -ray emission hypothesis. The same holds for the TS skymaps: the TS value distributions are all compatible with a background-only hypothesis.

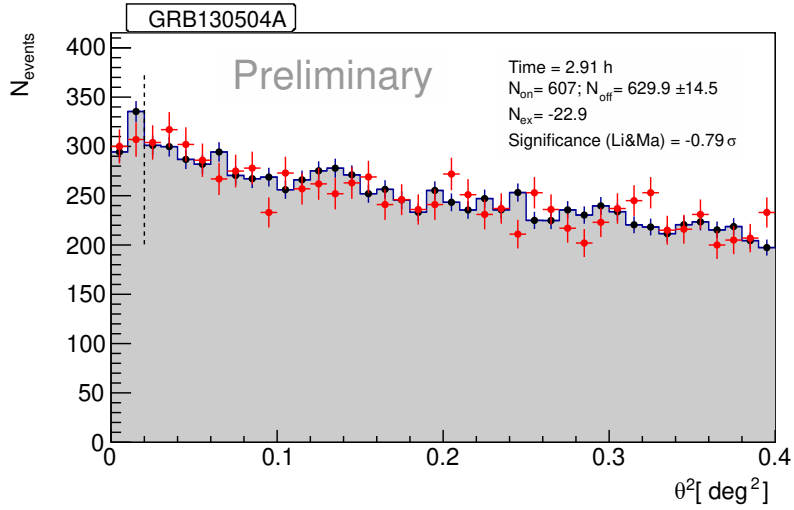


Figure C.1.1:  $\theta^2$  plot.

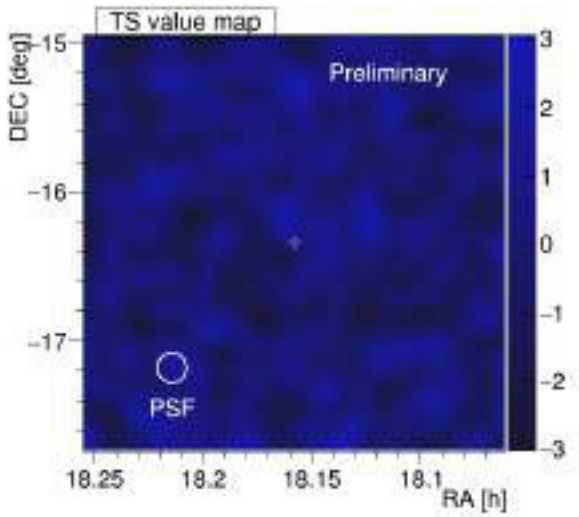


Figure C.1.2: TS skymap.

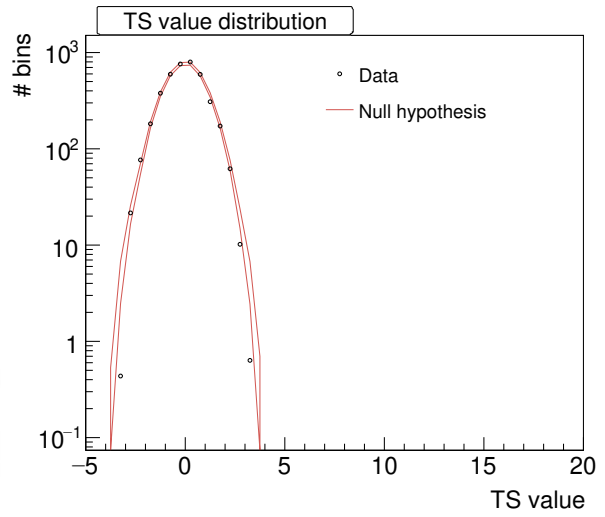


Figure C.1.3: TS distribution

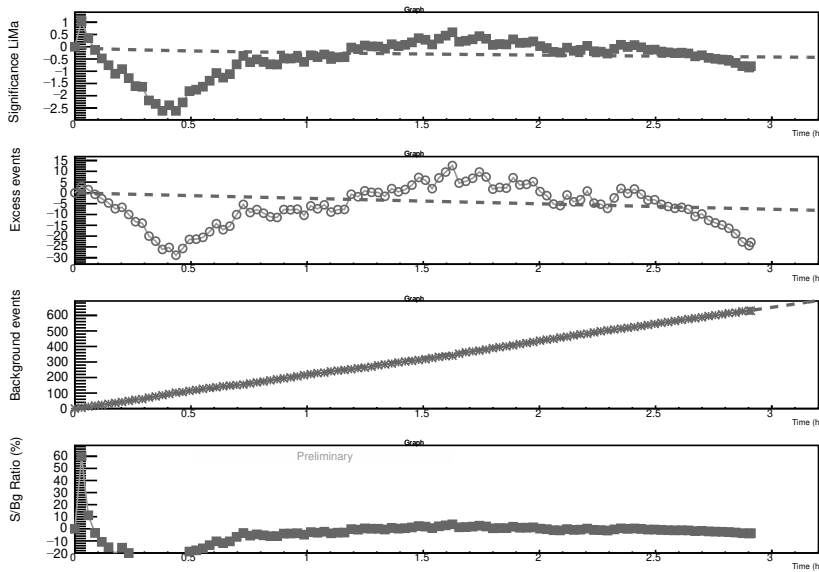


Figure C.1.4: Significance evolution in time.

Figure C.1:  $\theta^2$  plot, TS skymap and distribution and significance evolution in time for GRB130504A.

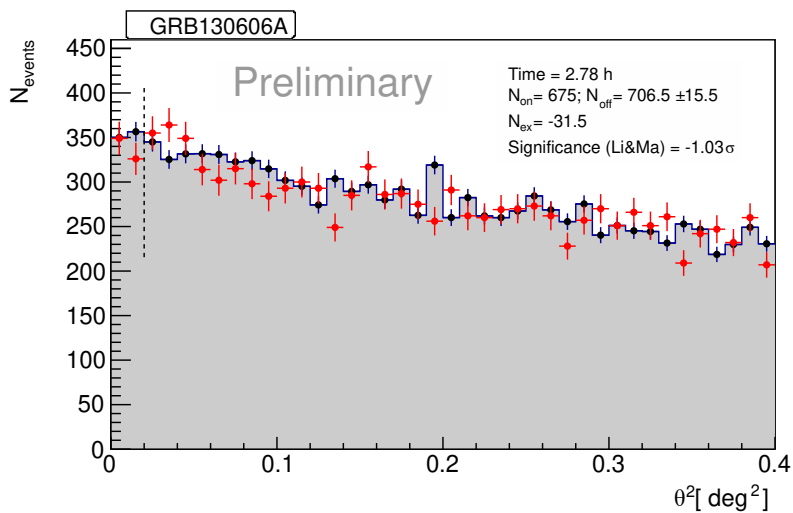
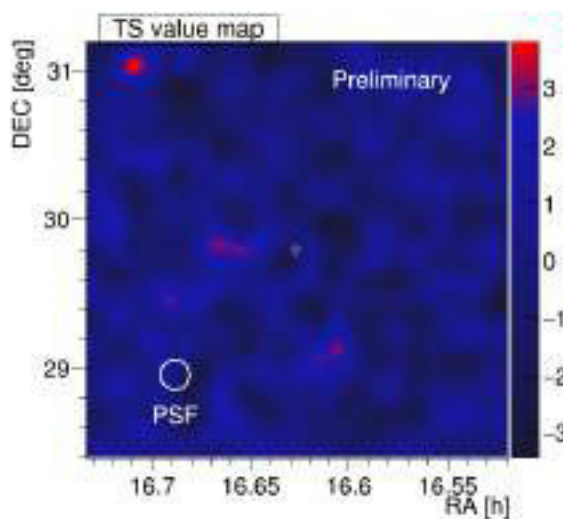
Figure C.2.1:  $\theta^2$  plot.

Figure C.2.2: TS skymap.

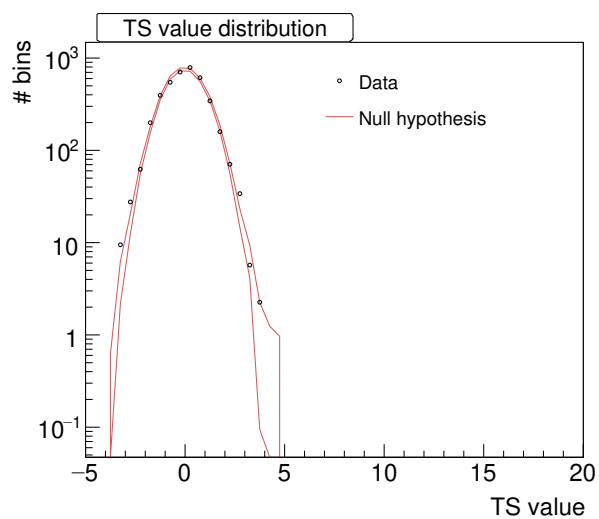


Figure C.2.3: TS distribution

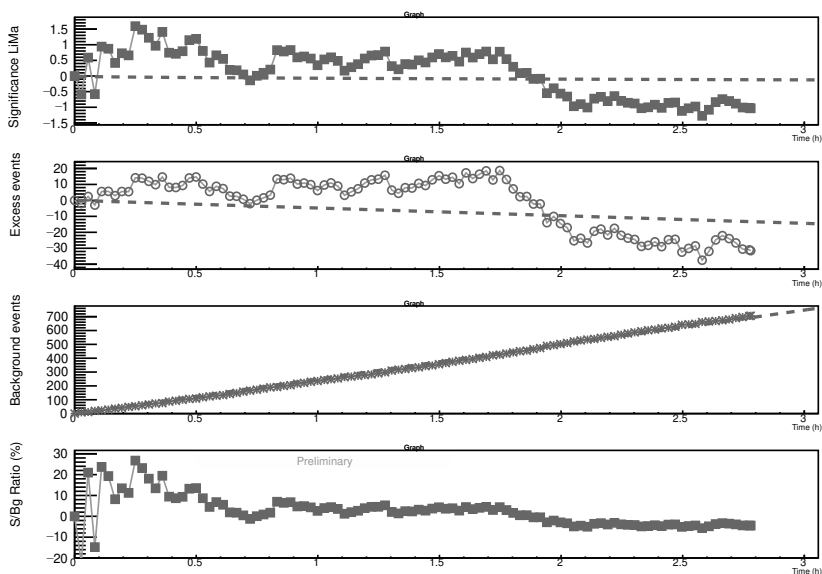


Figure C.2.4: Significance evolution in time.

Figure C.2:  $\theta^2$  plot, TS skymap and distribution and significance evolution in time for GRB130606A.

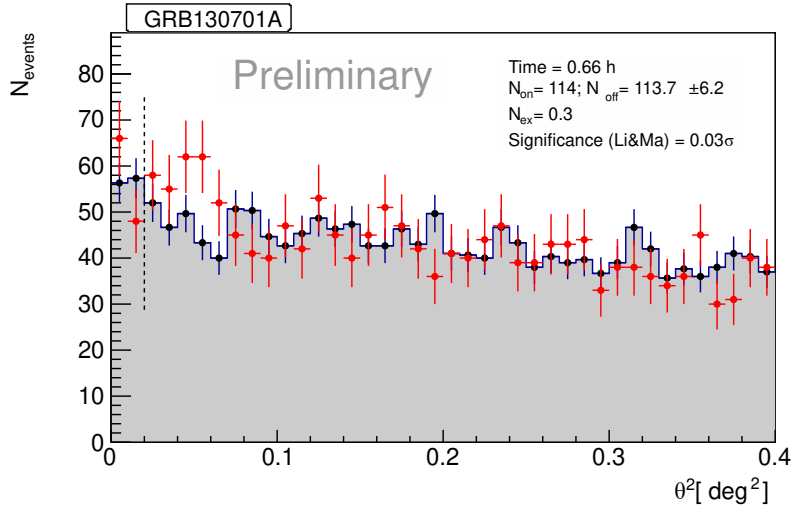


Figure C.3.1:  $\theta^2$  plot.

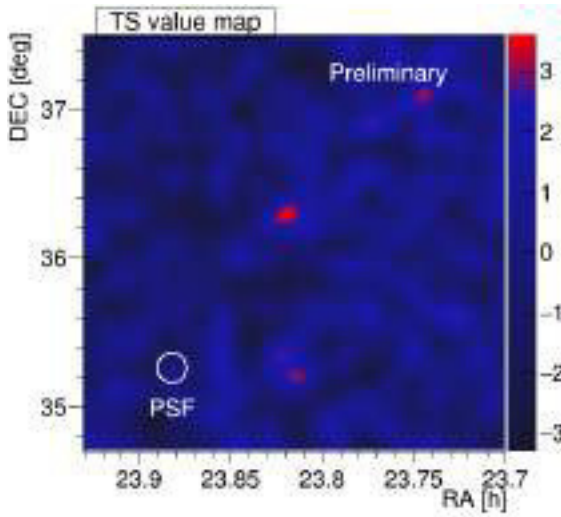


Figure C.3.2: TS skymap.

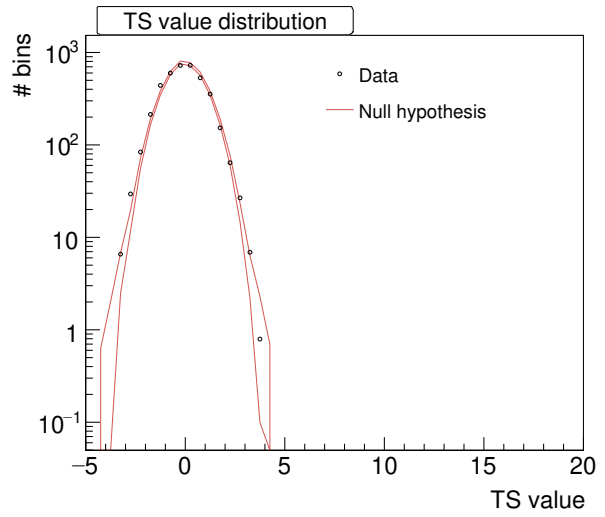


Figure C.3.3: TS distribution

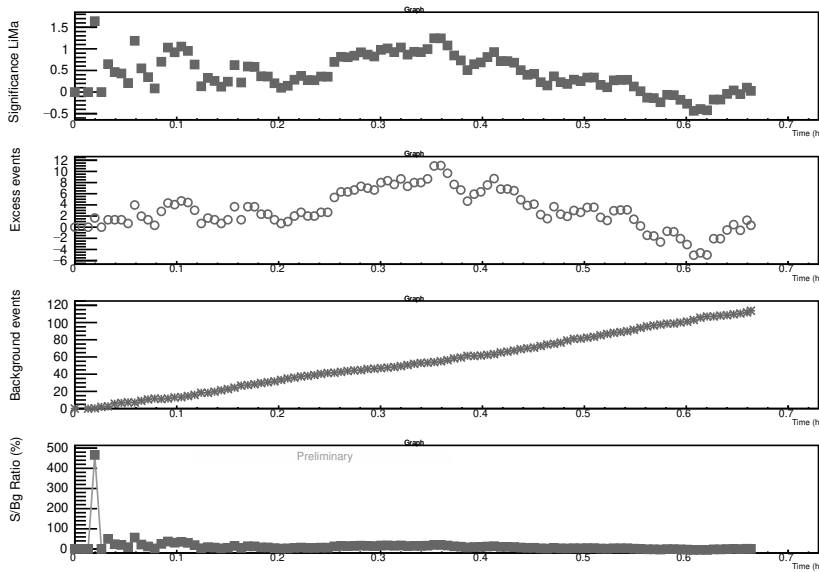


Figure C.3.4: Significance evolution in time.

Figure C.3:  $\theta^2$  plot, TS skymap and distribution and significance evolution in time for GRB130701A.

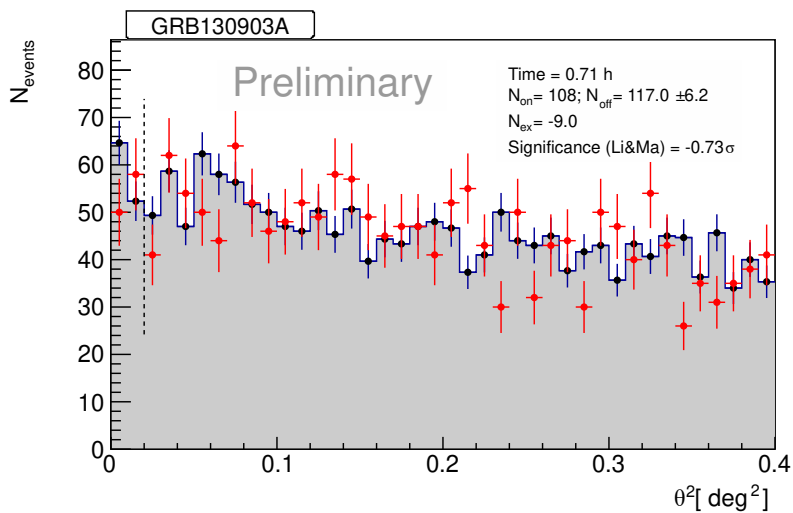
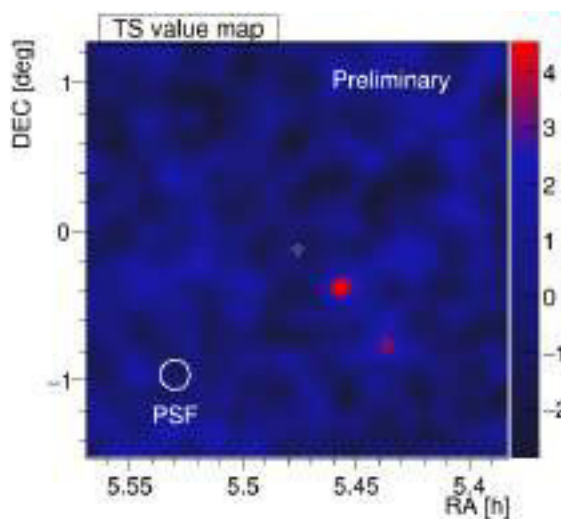
Figure C.4.1:  $\theta^2$  plot.

Figure C.4.2: TS skymap.

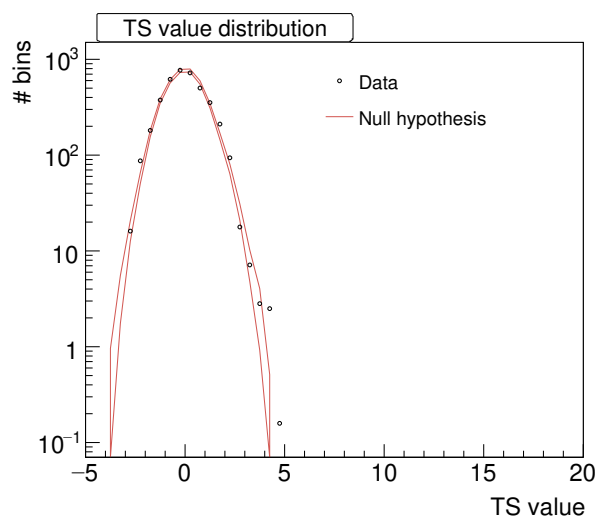


Figure C.4.3: TS distribution

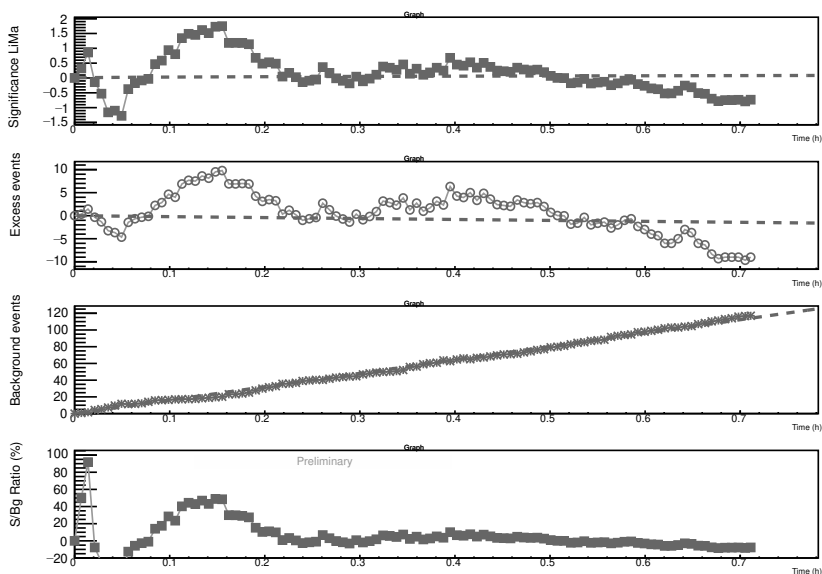


Figure C.4.4: Significance evolution in time.

Figure C.4:  $\theta^2$  plot, TS skymap and distribution and significance evolution in time for GRB130903A.

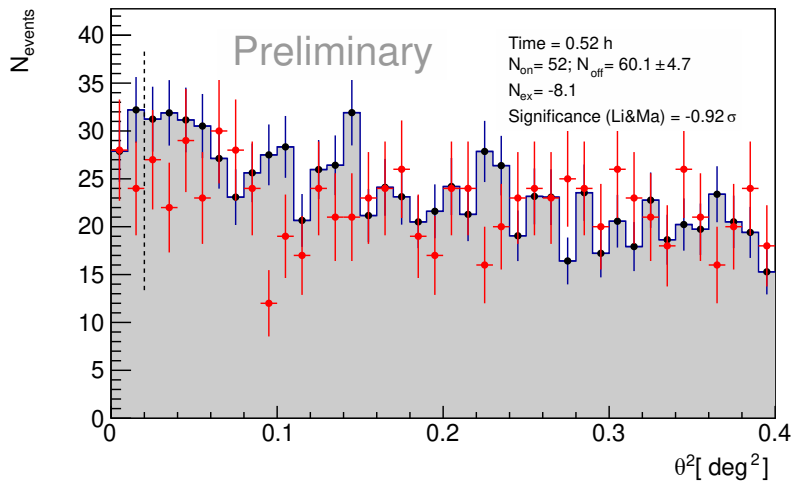


Figure C.5.1:  $\theta^2$  plot.

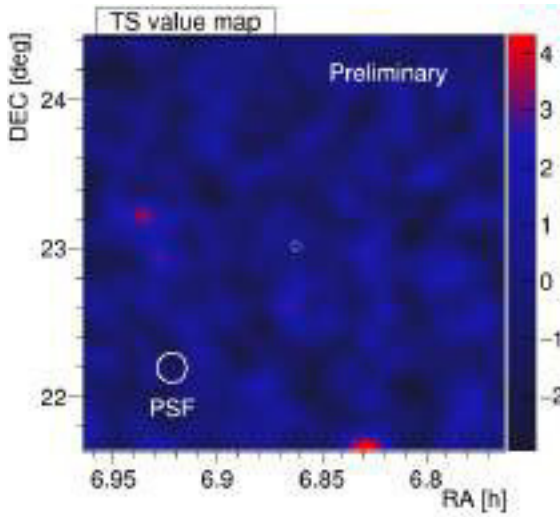


Figure C.5.2: TS skymap.

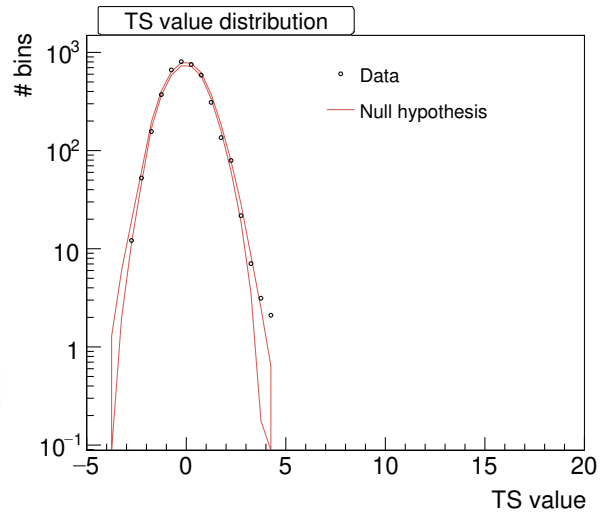


Figure C.5.3: TS distribution

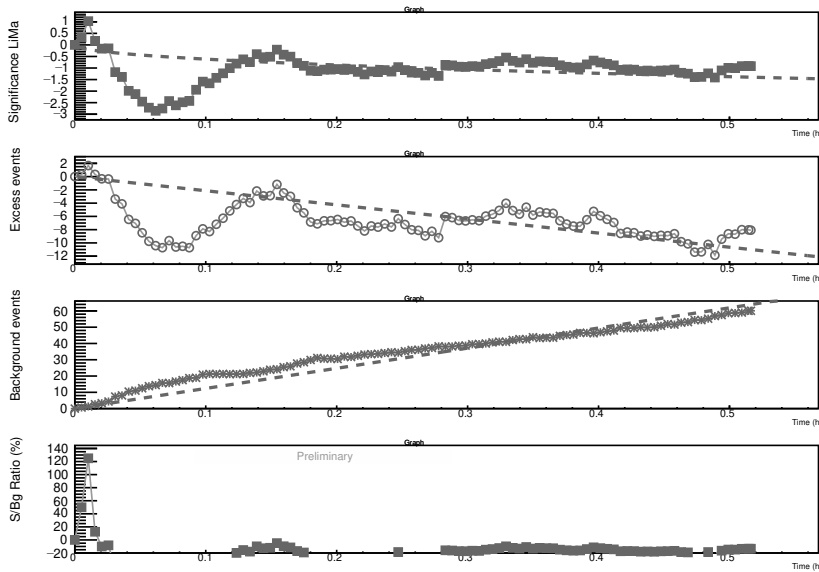


Figure C.5.4: Significance evolution in time.

Figure C.5:  $\theta^2$  plot, TS skymap and distribution and significance evolution in time for GRB140430A.

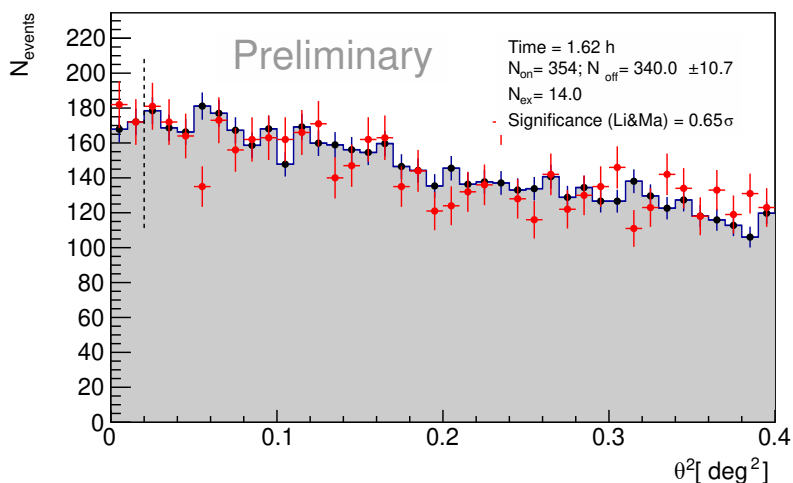


Figure C.6.1:  $\theta^2$  plot.

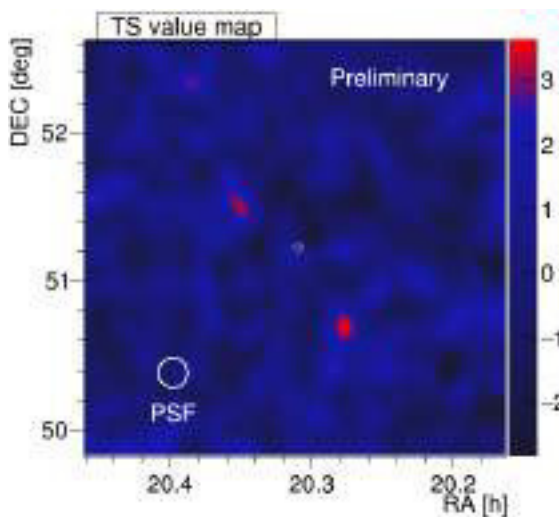


Figure C.6.2: TS skymap.

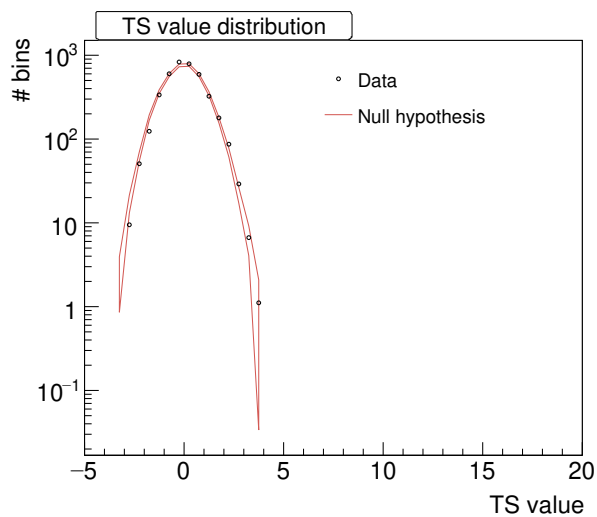


Figure C.6.3: TS distribution

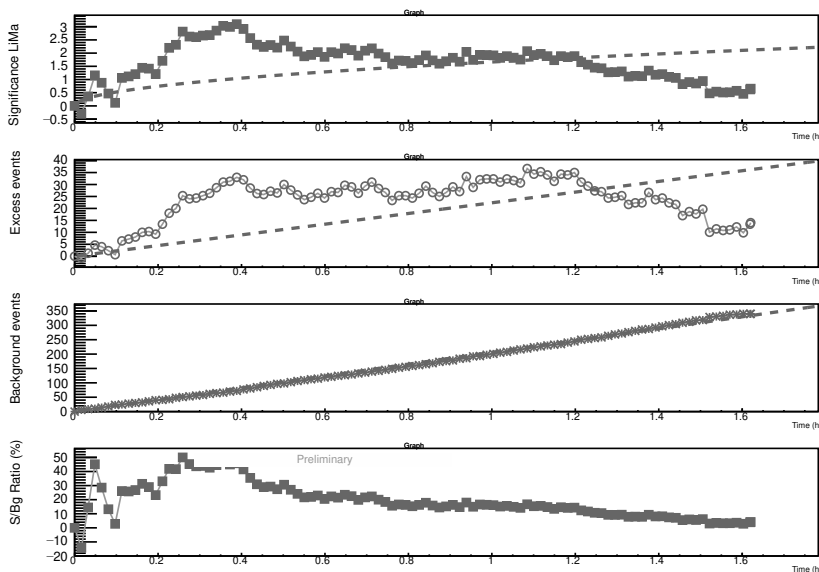


Figure C.6.4: Significance evolution in time.

Figure C.6:  $\theta^2$  plot, TS skymap and distribution and significance evolution in time for GRB140709A.

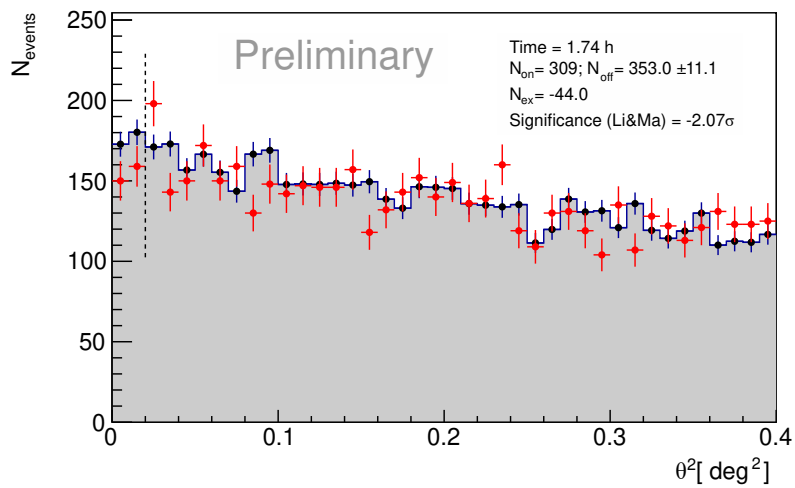


Figure C.7.1:  $\theta^2$  plot.

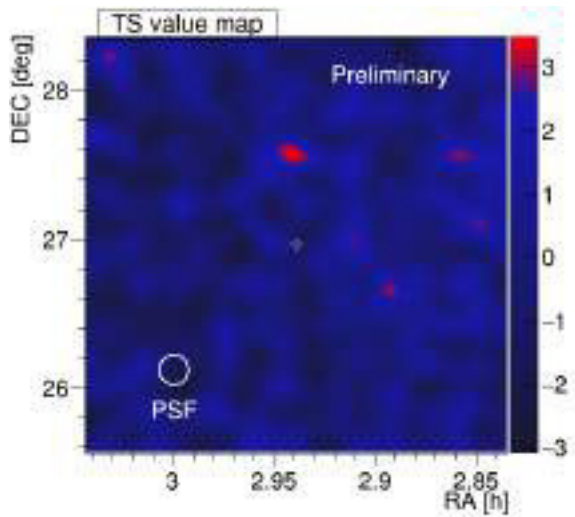


Figure C.7.2: TS skymap.

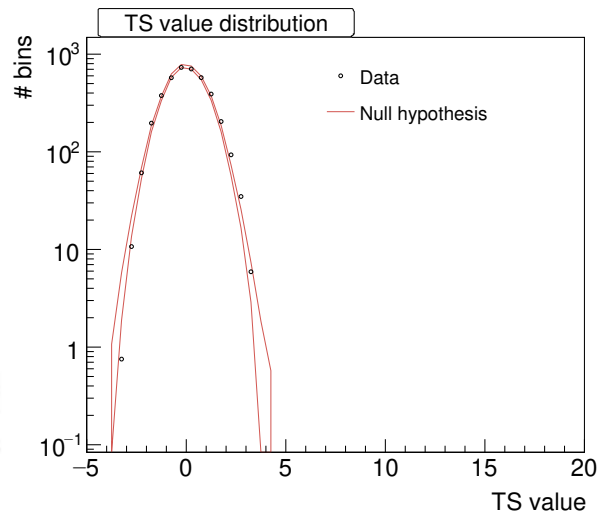


Figure C.7.3: TS distribution

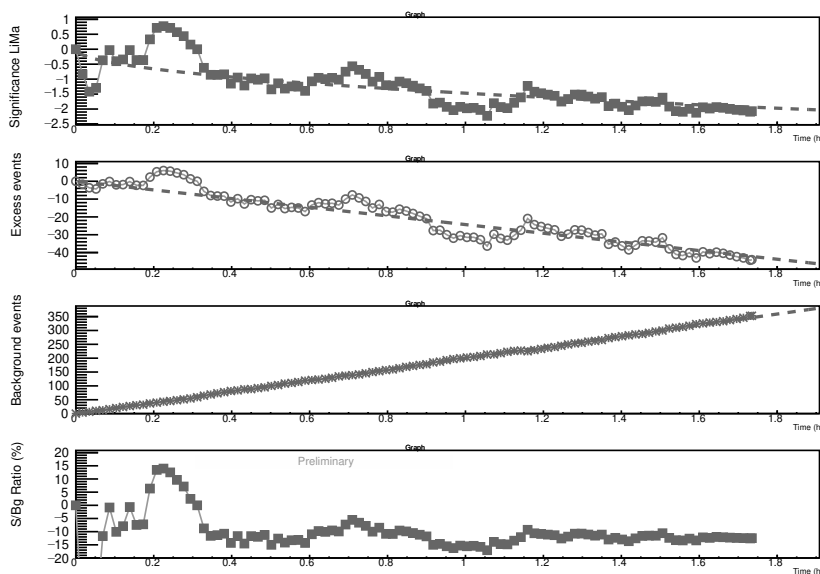


Figure C.7.4: Significance evolution in time.

Figure C.7:  $\theta^2$  plot, TS skymap and distribution and significance evolution in time for GRB141026A.

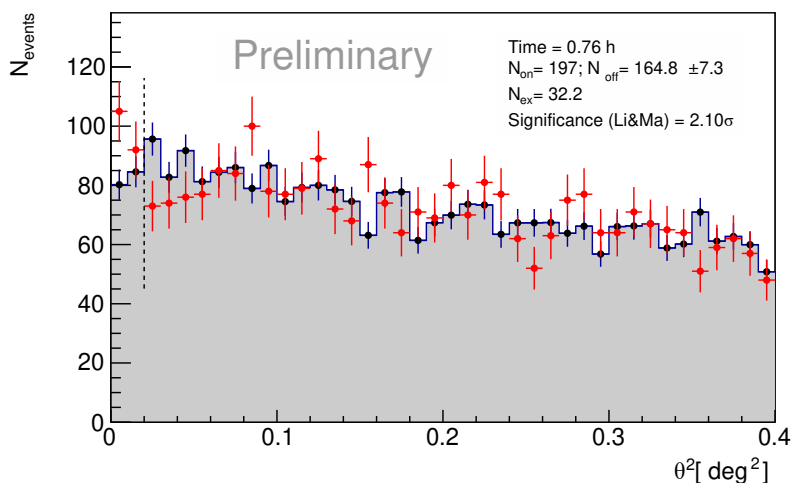


Figure C.8.1:  $\theta^2$  plot.

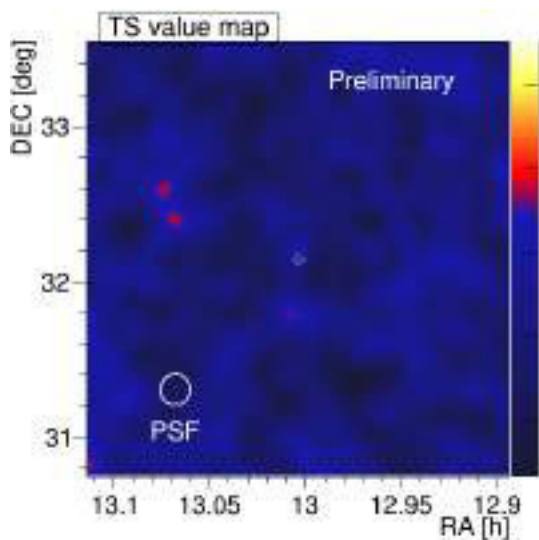


Figure C.8.2: Significance evolution in time.

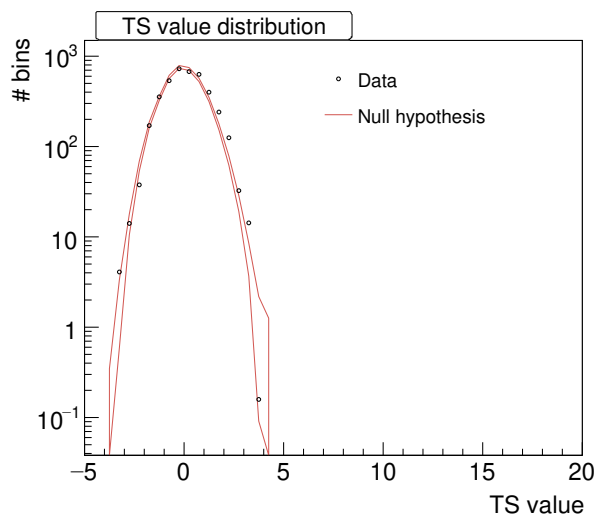


Figure C.8.3: TS skymap.

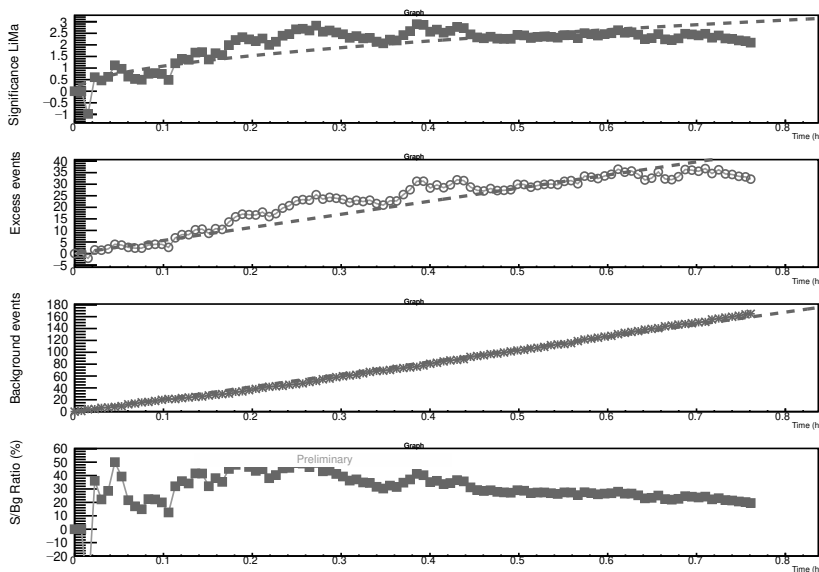


Figure C.8.4: Significance evolution in time.

Figure C.8:  $\theta^2$  plot, TS skymap and distribution and significance evolution in time for GRB141220A.

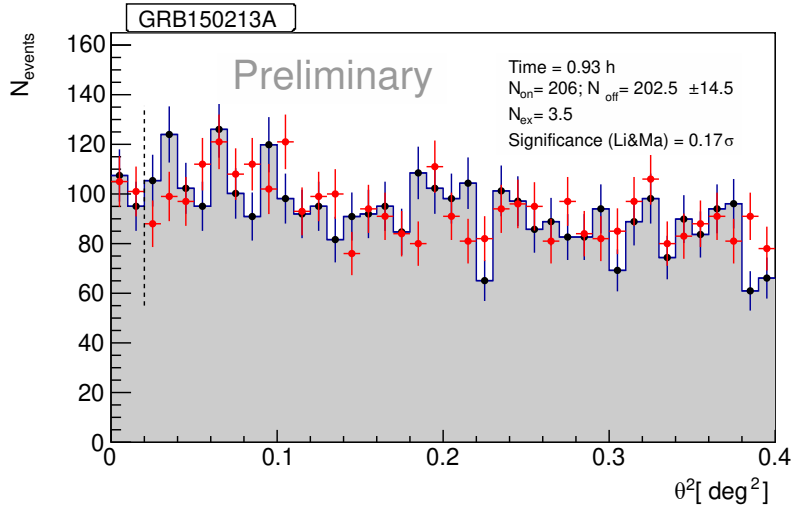


Figure C.9.1:  $\theta^2$  plot.

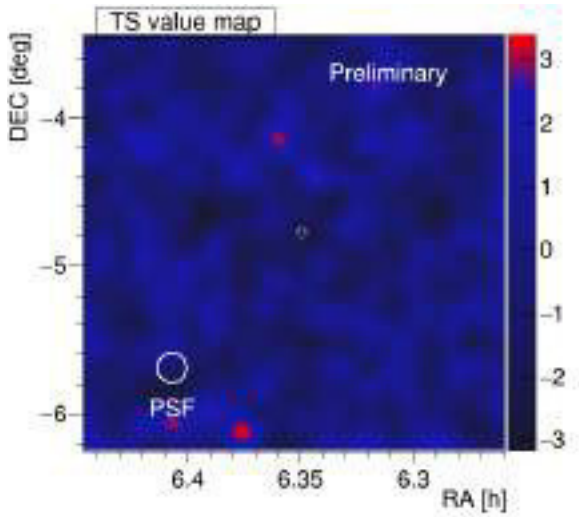


Figure C.9.2: TS skymap.

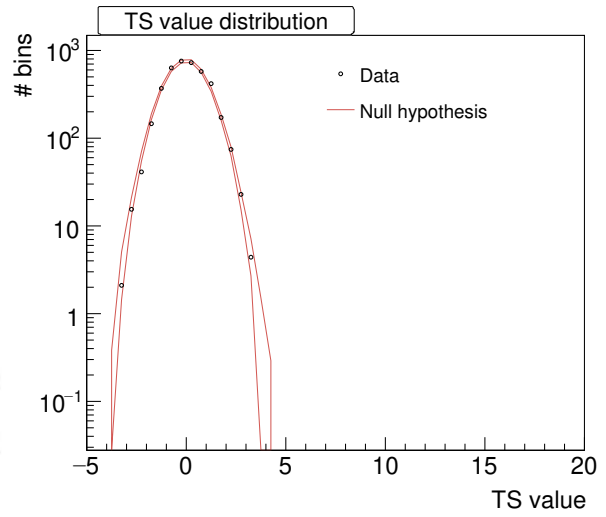


Figure C.9.3: TS distribution

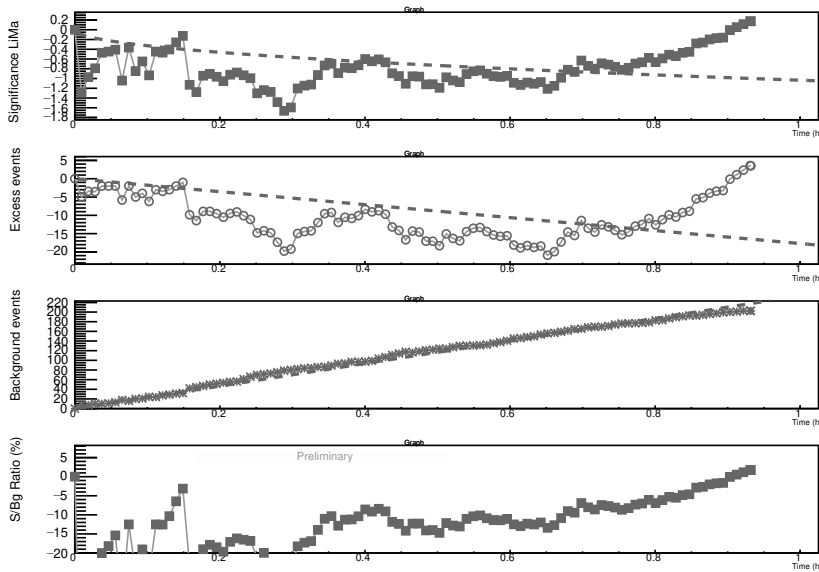


Figure C.9.4: Significance evolution in time.

Figure C.9:  $\theta^2$  plot, TS skymap and distribution and significance evolution in time for GRB150213A.

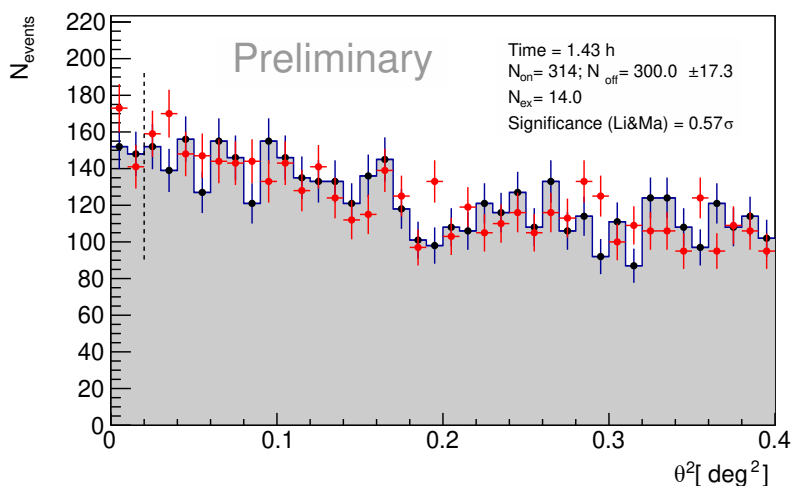


Figure C.10.1:  $\theta^2$  plot.

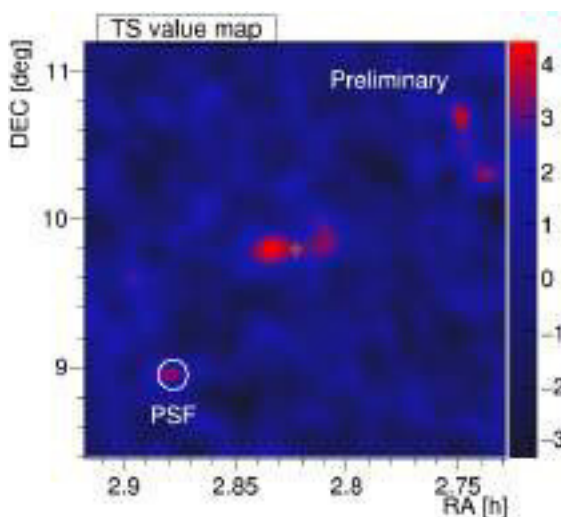


Figure C.10.2: TS skymap.

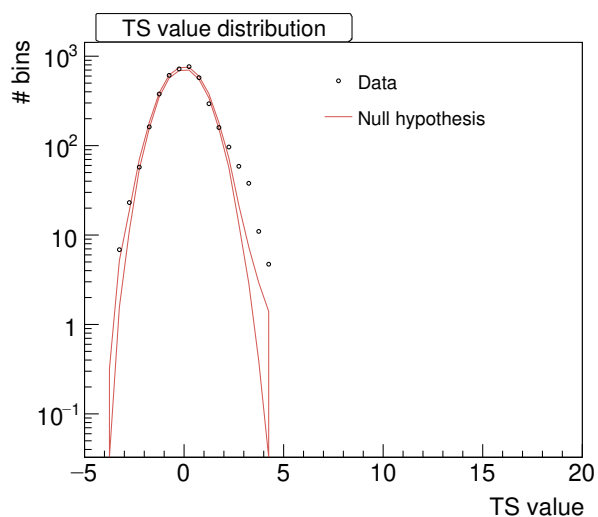


Figure C.10.3: TS distribution

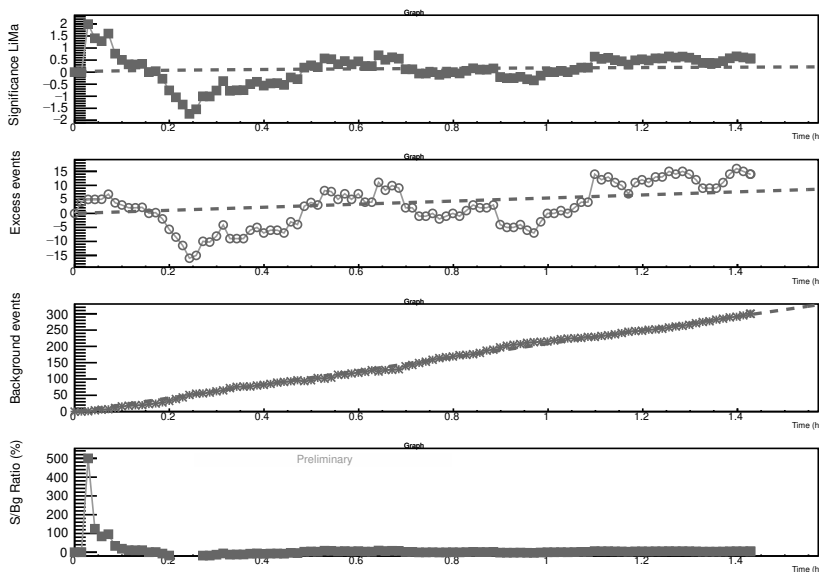


Figure C.10.4: Significance evolution in time.

Figure C.10:  $\theta^2$  plot, TS skymap and distribution and significance evolution in time for GRB150819A.

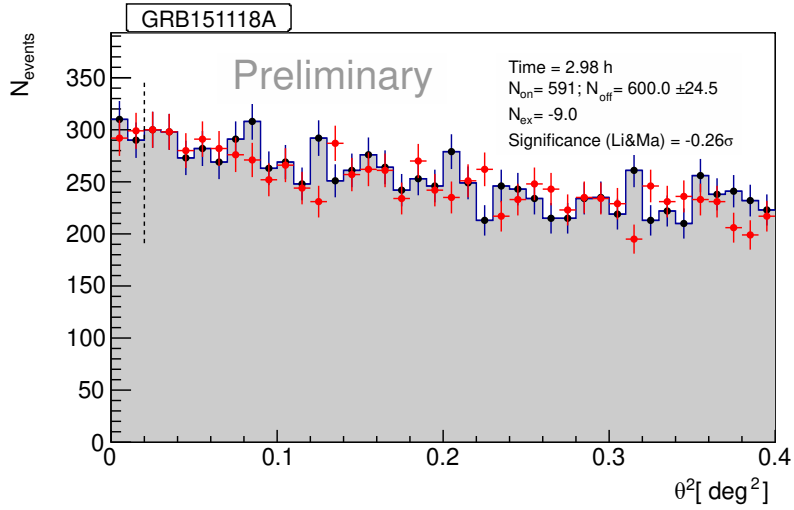


Figure C.11.1:  $\theta^2$  plot.

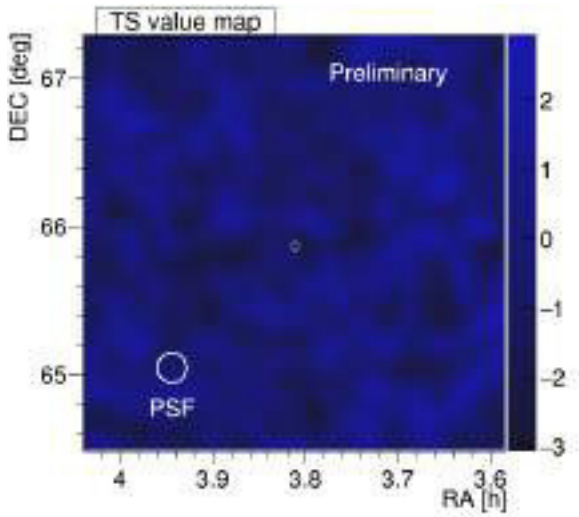


Figure C.11.2: TS skymap.

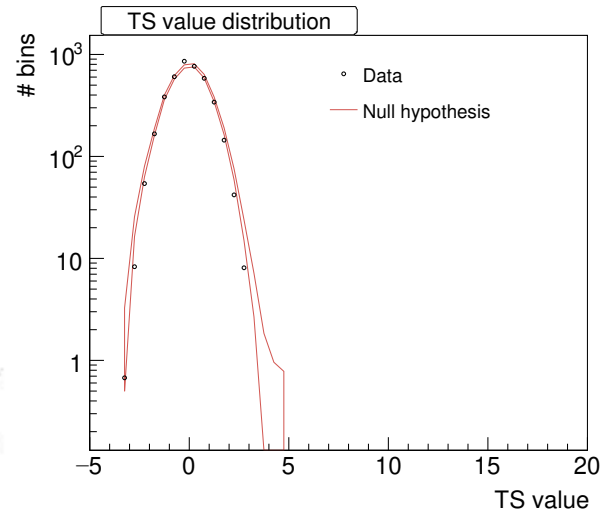


Figure C.11.3: TS distribution

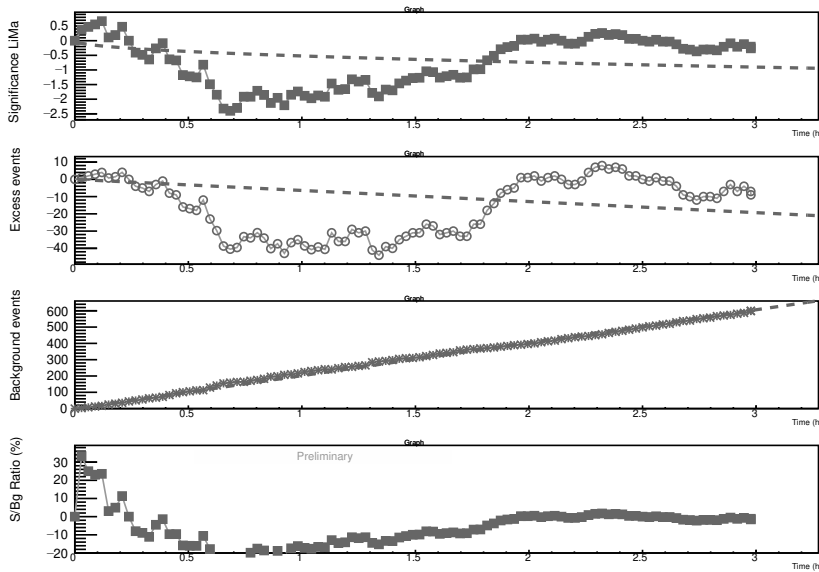


Figure C.11.4: Significance evolution in time.

Figure C.11:  $\theta^2$  plot, TS skymap and distribution and significance evolution in time for GRB151118A.

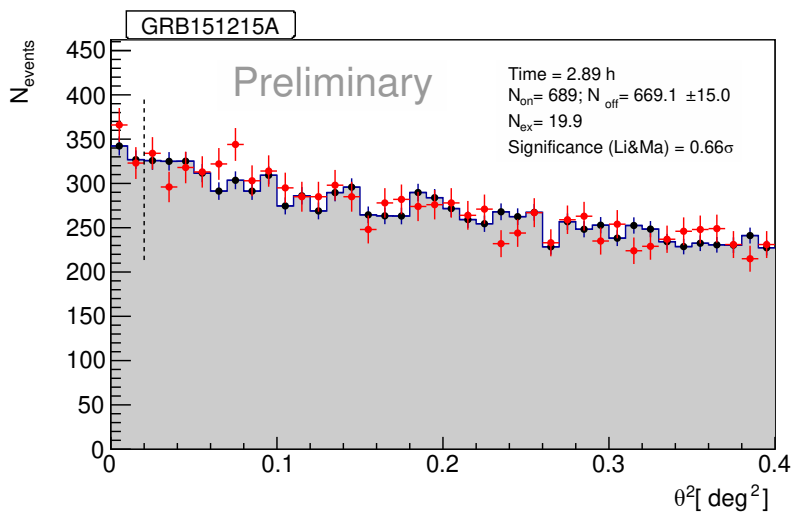
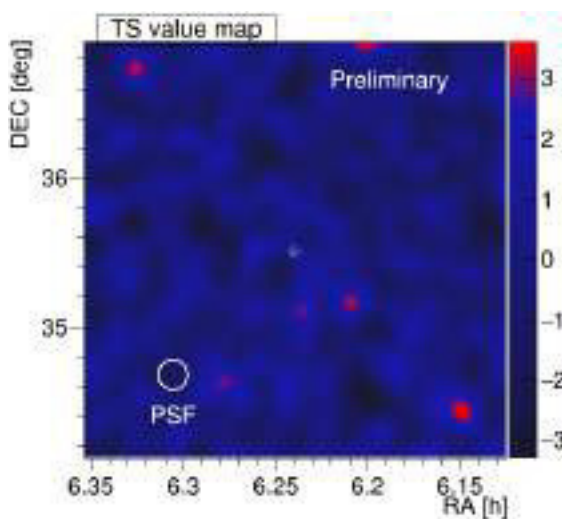
Figure C.12.1:  $\theta^2$  plot.

Figure C.12.2: TS skymap.

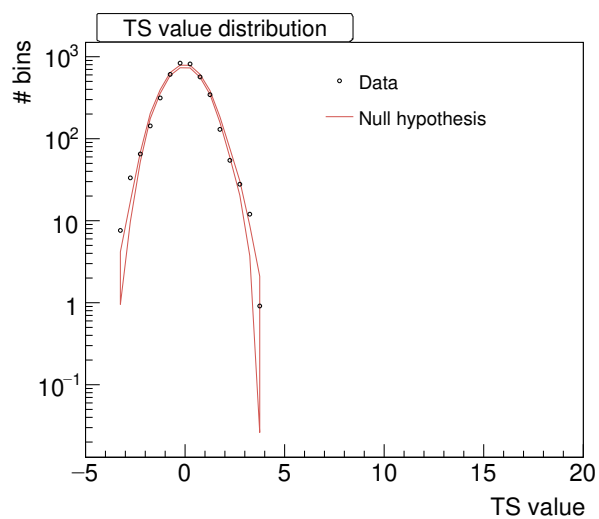


Figure C.12.3: TS distribution

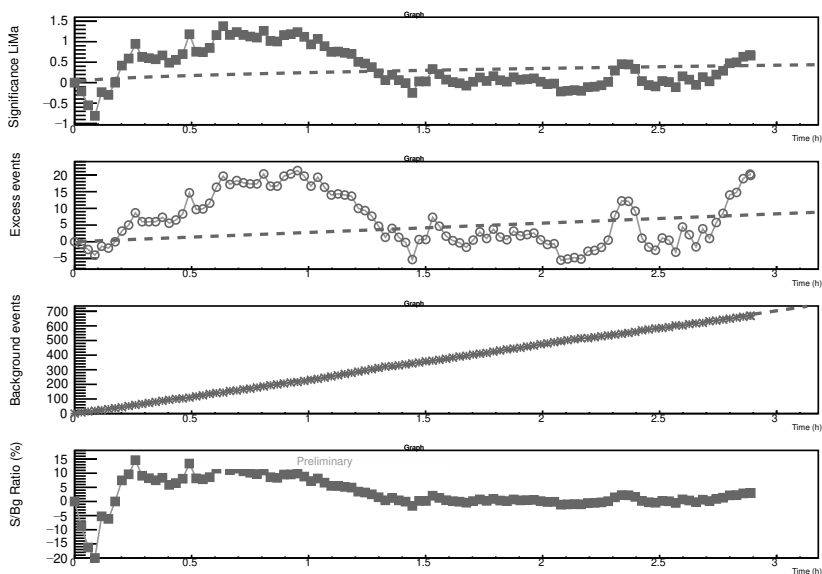


Figure C.12.4: Significance evolution in time.

Figure C.12:  $\theta^2$  plot, TS skymap and distribution and significance evolution in time for GRB151215A.



## Appendix D

# GRB ENERGY THRESHOLD

In this appendix, the energy thresholds obtained from MC data distribution in energy for each GRB are shown. The values are reported in Table 5.4 in Section 5.1.11. The energy threshold is obtained fitting the resulting MC distribution with a Landau function and taking the estimate of the peak as estimate of the energy threshold. The zenith angle, hadronness and size cuts are shown in the legend, as well as the energy threshold. To match the assumed spectrum used for upper limits calculation (power-law with index  $-3.5$ ), the MC distribution was weighted by a factor proportional to  $E^{-1.9}$ , where  $-1.9$  is the difference between the assumed spectrum spectral index ( $-3.5$ ) and the original spectral index of the MC data ( $-1.6$ ). The following MC production were used for the GRBs:

- ST.03.02: GRB130504A, GRB130606A, GRB130701A
- ST.03.03: GRB130903A, GRB140430A, GRB140709A
- ST.03.05: GRB141026A
- ST.03.06: GRB141220A, GRB150213A, GRB150819A, GRB151118A, GRB151215A

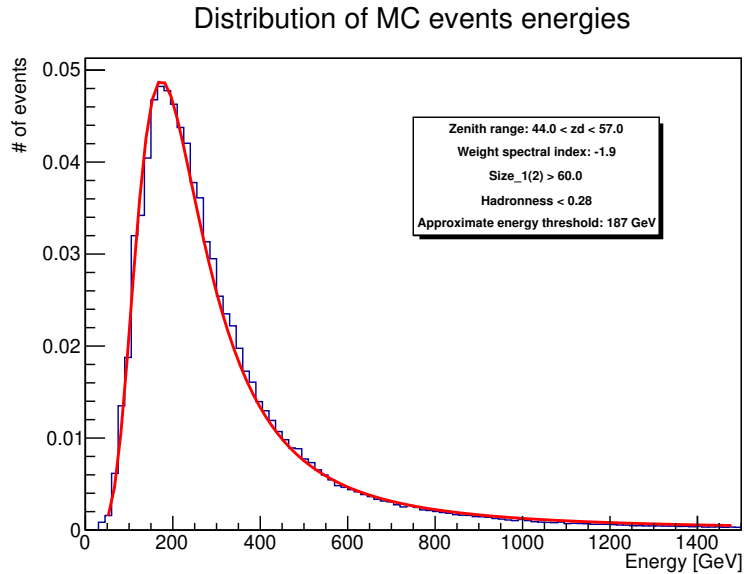


Figure D.1: Plot showing the MC data distribution in energy used for the calculation of the analysis energy threshold for GRB130504A.

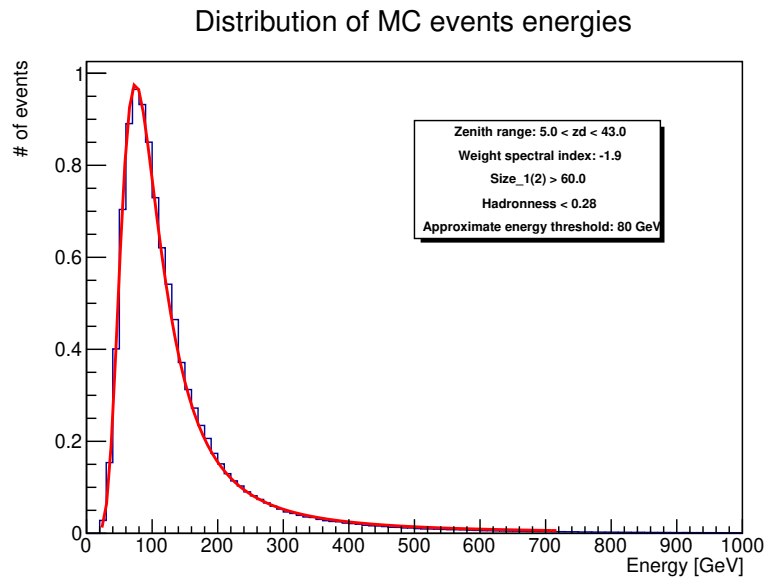


Figure D.2: Plot showing the MC data distribution in energy used for the calculation of the analysis energy threshold for GRB130606A.

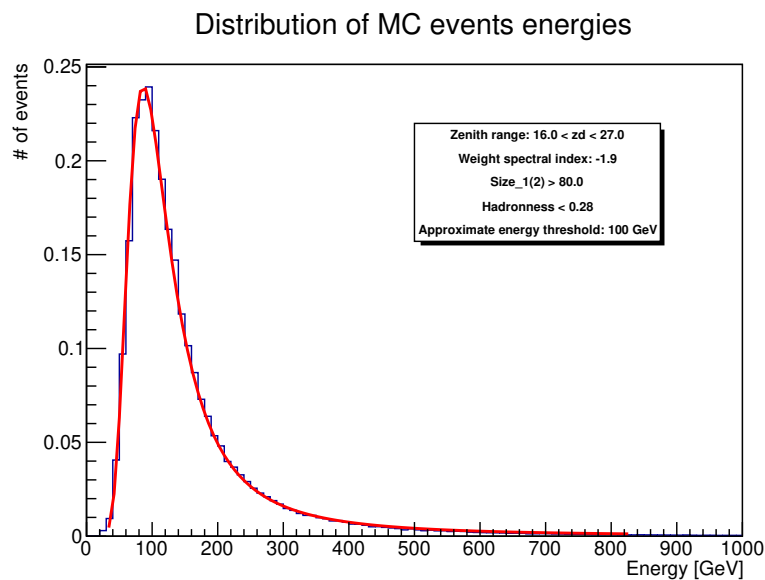


Figure D.3: Plot showing the MC data distribution in energy used for the calculation of the analysis energy threshold for GRB130701A. A higher cut size (80) was used because of the higher background due to the presence of the Moon, according to the values reported in Table 4.3.

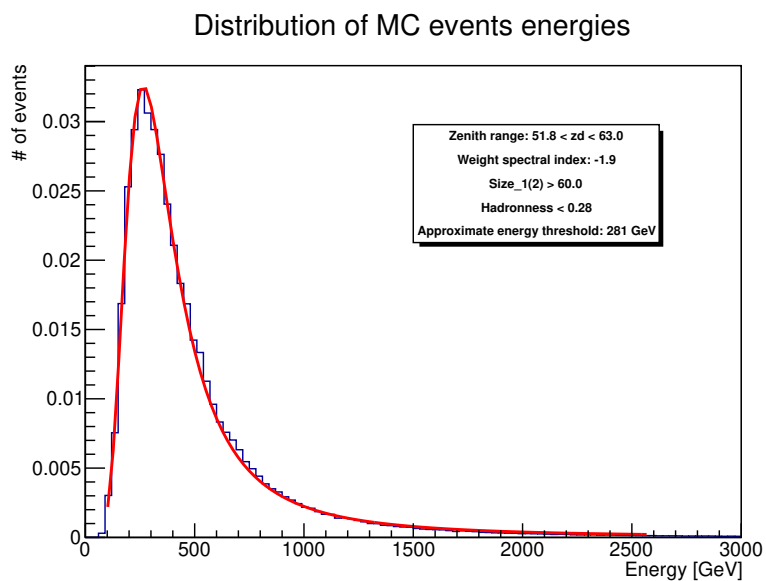


Figure D.4: Plot showing the MC data distribution in energy used for the calculation of the analysis energy threshold for GRB130903A.

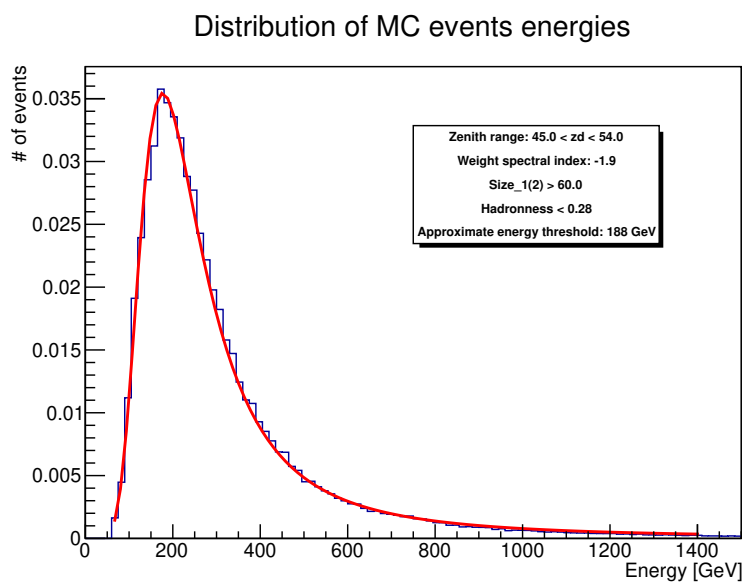


Figure D.5: Plot showing the MC data distribution in energy used for the calculation of the analysis energy threshold for GRB140430A.

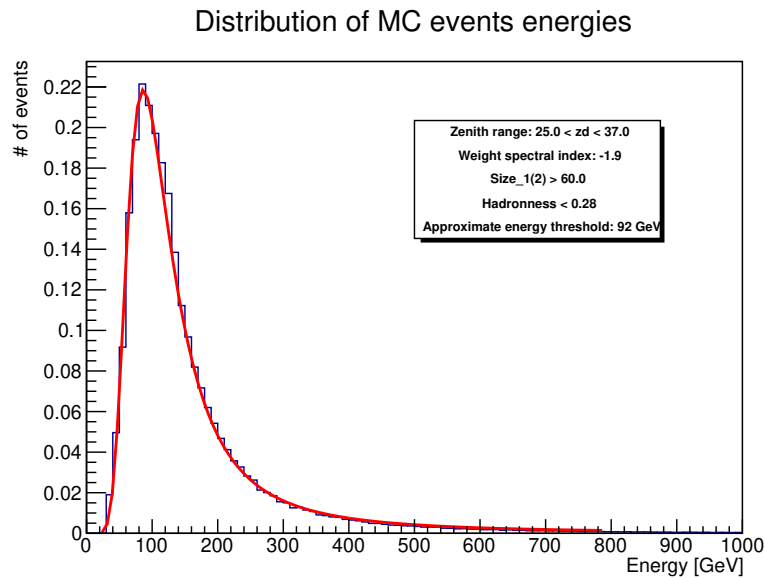


Figure D.6: Plot showing the MC data distribution in energy used for the calculation of the analysis energy threshold for GRB140709A.

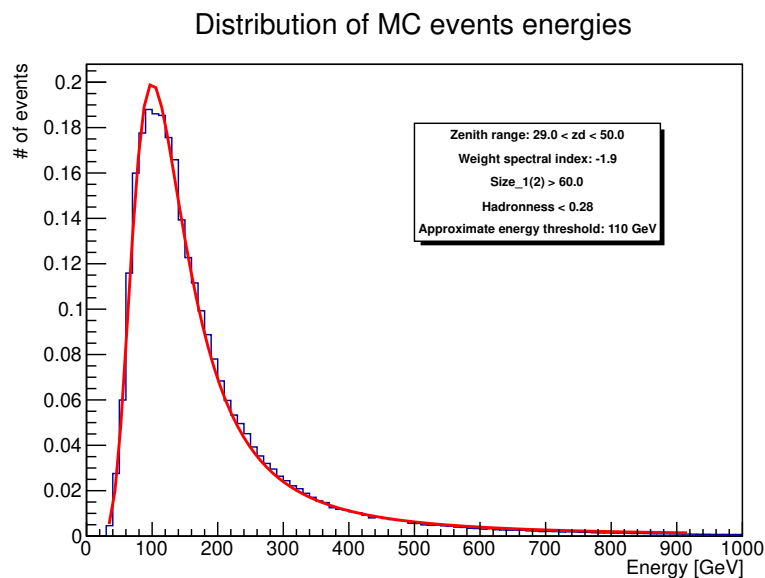


Figure D.7: Plot showing the MC data distribution in energy used for the calculation of the analysis energy threshold for GRB141026A. The zenith range used for the calculation of  $E_{\text{thr}}$  is not the same as shown in Table 5.1 ( $10^\circ$ - $50^\circ$ ), but it is different ( $29^\circ$ - $50^\circ$ ) to take into account the fact that most of the initial part of the data used were affected by low and unstable transmission (see Figure D.8).

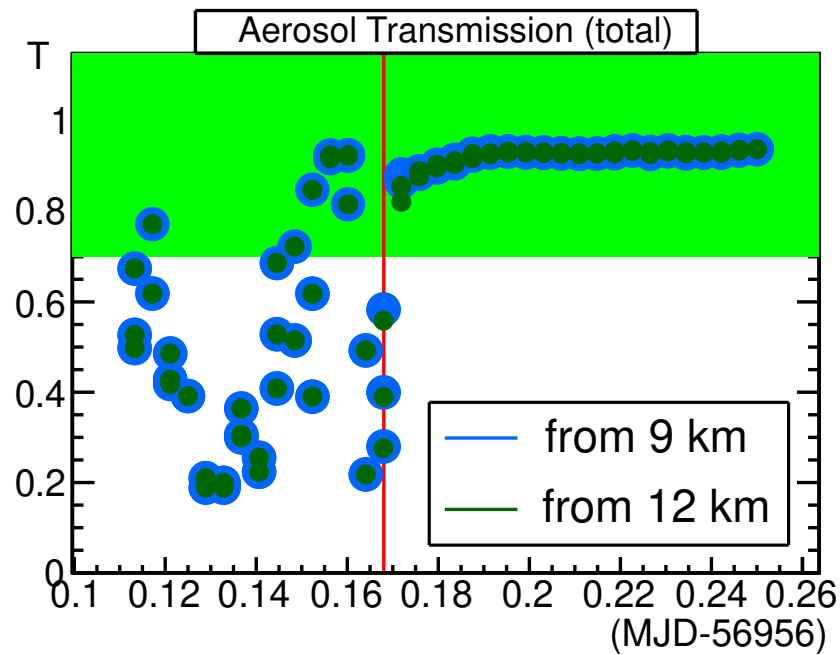


Figure D.8: Evolution in time of the atmospheric transmission at 9 km and 12 km for GRB141026A. The red line is the time at which the transmission becomes stable. The zenith of the GRB at that moment ( $29^\circ$ ) is the one taken as lower limit for the energy threshold calculation (see Figure D.7).

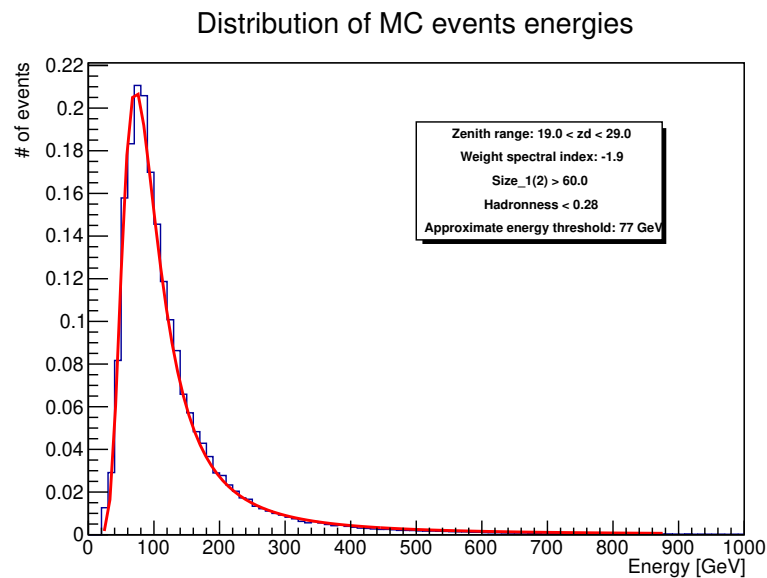


Figure D.9: Plot showing the MC data distribution in energy used for the calculation of the analysis energy threshold for GRB141220A.

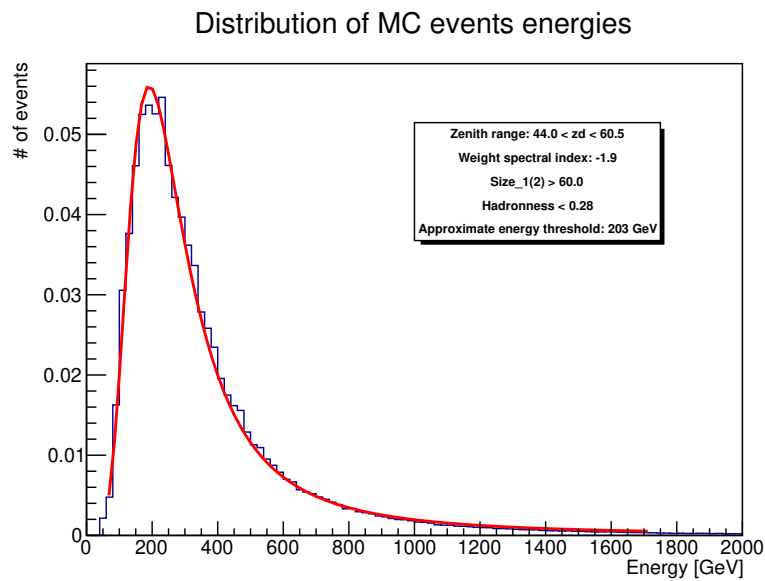


Figure D.10: Plot showing the MC data distribution in energy used for the calculation of the analysis energy threshold for GRB150213A.

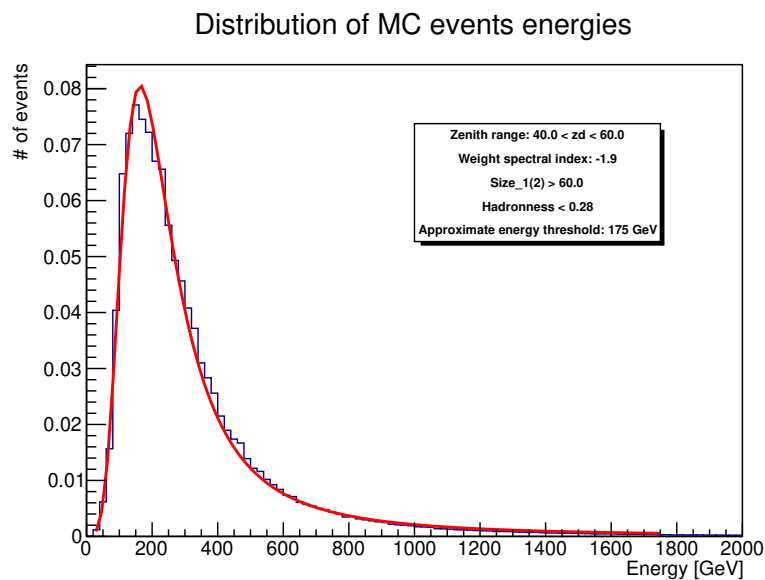


Figure D.11: Plot showing the MC data distribution in energy used for the calculation of the analysis energy threshold for GRB150819A.

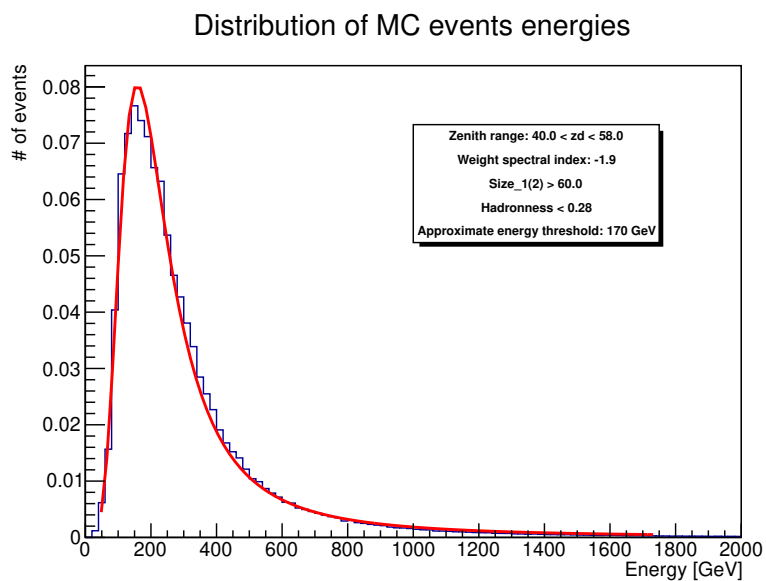


Figure D.12: Plot showing the MC data distribution in energy used for the calculation of the analysis energy threshold for GRB151118A.

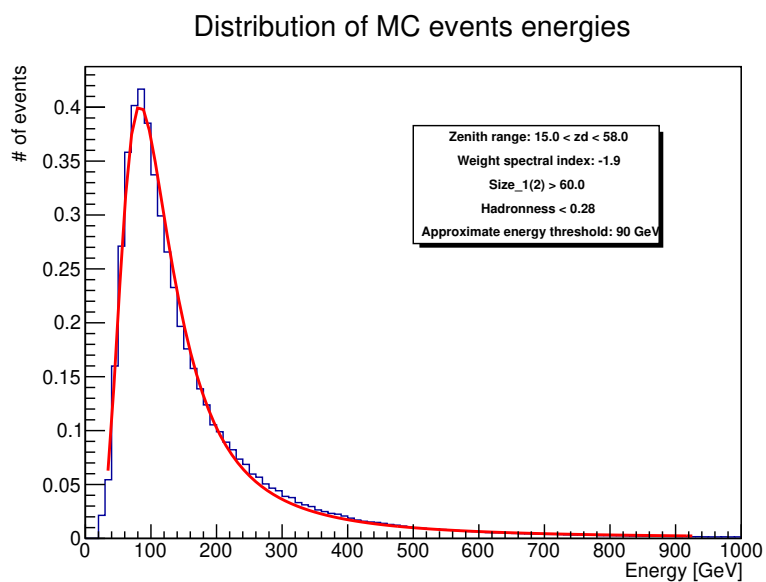


Figure D.13: Plot showing the MC data distribution in energy used for the calculation of the analysis energy threshold for GRB151215A.



## Appendix E

# GRB DIFFERENTIAL UPPER LIMITS

In this appendix I report the differential flux upper limits for the GRBs considered in the thesis. These values complete the results of the analysis of the GRBs shown in Table 5.4 in Section 5.1.11. As for integral flux upper limits, the assumed spectrum is a power law with index  $-3.5$  and the method used for the computation of upper limits is the Rolke prescription with 95% confidence level and 30% systematic error on the efficiency of analysis cuts.

| GRB130504A  |             |   |
|-------------|-------------|---|
| $E_1$ [GeV] | $E_2$ [GeV] | UL [ $\text{TeV cm}^{-2} \text{s}^{-1}$ ] |
| 187         | 254.2       | $3.70 \cdot 10^{-12}$                     |
| 254.2       | 345.548     | $7.95 \cdot 10^{-12}$                     |
| 345.548     | 469.723     | $1.76 \cdot 10^{-12}$                     |
| 469.723     | 638.521     | $2.10 \cdot 10^{-12}$                     |
| 638.521     | 867.977     | $1.39 \cdot 10^{-12}$                     |
| 867.977     | 1179.89     | $1.77 \cdot 10^{-12}$                     |
| 1179.89     | 1603.89     | $2.50 \cdot 10^{-12}$                     |
| 1603.89     | 2180.26     | $8.39 \cdot 10^{-13}$                     |
| 2180.26     | 2963.75     | $3.82 \cdot 10^{-13}$                     |
| 2963.75     | 4028.79     | $1.11 \cdot 10^{-12}$                     |
| 4028.79     | 5476.57     | $2.14 \cdot 10^{-12}$                     |
| 5476.57     | 7444.6      | $6.32 \cdot 10^{-13}$                     |
| 7444.6      | 10119.9     | $1.14 \cdot 10^{-12}$                     |
| 10119.9     | 13756.5     | $2.99 \cdot 10^{-12}$                     |
| 18700       | 25420       | $3.19 \cdot 10^{-12}$                     |

Table E.1: Differential flux upper limits in energy ranges  $[E_1; E_2]$  for GRB130504A. Only upper limits above the energy threshold are reported.

| GRB130606A  |             |   |
|-------------|-------------|---|
| $E_1$ [GeV] | $E_2$ [GeV] | UL [ $\text{TeV cm}^{-2} \text{s}^{-1}$ ] |
| 80          | 108.749     | $4.56 \cdot 10^{-12}$                     |
| 108.749     | 147.828     | $9.99 \cdot 10^{-12}$                     |
| 147.828     | 200.951     | $2.06 \cdot 10^{-12}$                     |
| 200.951     | 273.164     | $6.76 \cdot 10^{-12}$                     |
| 273.164     | 371.327     | $3.48 \cdot 10^{-12}$                     |
| 371.327     | 504.766     | $2.66 \cdot 10^{-12}$                     |
| 504.766     | 686.157     | $1.37 \cdot 10^{-12}$                     |
| 686.157     | 932.732     | $1.76 \cdot 10^{-12}$                     |
| 932.732     | 1267.91     | $1.34 \cdot 10^{-12}$                     |
| 1267.91     | 1723.55     | $6.25 \cdot 10^{-13}$                     |
| 1723.55     | 2342.92     | $8.12 \cdot 10^{-13}$                     |
| 2342.92     | 3184.86     | $1.49 \cdot 10^{-12}$                     |
| 3184.86     | 4329.36     | $4.00 \cdot 10^{-12}$                     |

Table E.2: Differential flux upper limits in energy ranges  $[E_1; E_2]$  for GRB130606A. Only upper limits above the energy threshold are reported.

| GRB130701A  |             |   |
|-------------|-------------|---|
| $E_1$ [GeV] | $E_2$ [GeV] | UL [ $\text{TeV cm}^{-2} \text{s}^{-1}$ ] |
| 100         | 135.936     | $7.85 \cdot 10^{-12}$                     |
| 135.936     | 184.785     | $1.95 \cdot 10^{-11}$                     |
| 184.785     | 251.189     | $3.17 \cdot 10^{-12}$                     |
| 251.189     | 341.455     | $3.49 \cdot 10^{-12}$                     |
| 341.455     | 464.159     | $3.67 \cdot 10^{-12}$                     |
| 464.159     | 630.957     | $8.51 \cdot 10^{-12}$                     |
| 630.957     | 857.696     | $5.28 \cdot 10^{-12}$                     |
| 1165.91     | 1584.89     | $7.47 \cdot 10^{-12}$                     |
| 5411.7      | 7356.42     | $1.24 \cdot 10^{-11}$                     |

Table E.3: Differential flux upper limits in energy ranges  $[E_1; E_2]$  for GRB130701A. Only upper limits above the energy threshold are reported.

| GRB130903A  |             |   |
|-------------|-------------|---|
| $E_1$ [GeV] | $E_2$ [GeV] | UL [ $\text{TeV cm}^{-2} \text{s}^{-1}$ ] |
| 281         | 381.979     | $6.59 \cdot 10^{-12}$                     |
| 381.979     | 519.246     | $6.75 \cdot 10^{-12}$                     |
| 519.246     | 705.84      | $1.09 \cdot 10^{-11}$                     |
| 705.84      | 959.488     | $4.83 \cdot 10^{-12}$                     |
| 959.488     | 1304.29     | $5.51 \cdot 10^{-12}$                     |
| 1304.29     | 1772.99     | $7.49 \cdot 10^{-12}$                     |
| 1772.99     | 2410.13     | $5.28 \cdot 10^{-12}$                     |
| 2410.13     | 3276.22     | $3.99 \cdot 10^{-12}$                     |
| 3276.22     | 4453.55     | $3.25 \cdot 10^{-12}$                     |
| 11186.8     | 15206.9     | $4.09 \cdot 10^{-12}$                     |

Table E.4: Differential flux upper limits in energy ranges  $[E_1; E_2]$  for GRB130903A. Only upper limits above the energy threshold are reported.

| GRB140430A  |             |  |
|-------------|-------------|--|
| $E_1$ [GeV] | $E_2$ [GeV] | UL [TeV cm <sup>-2</sup> s <sup>-1</sup> ] |
| 188         | 255.559     | $5.53 \cdot 10^{-12}$                      |
| 255.559     | 347.396     | $7.68 \cdot 10^{-12}$                      |
| 347.396     | 472.235     | $9.11 \cdot 10^{-12}$                      |
| 472.235     | 641.935     | $7.06 \cdot 10^{-12}$                      |
| 641.935     | 872.619     | $2.65 \cdot 10^{-12}$                      |
| 872.619     | 1186.2      | $1.13 \cdot 10^{-12}$                      |
| 1612.47     | 2191.92     | $2.63 \cdot 10^{-12}$                      |
| 2979.6      | 4050.34     | $3.03 \cdot 10^{-12}$                      |

Table E.5: Differential flux upper limits in energy ranges  $[E_1; E_2]$  for GRB140430A. Only upper limits above the energy threshold are reported.

| GRB140709A  |             |  |
|-------------|-------------|--|
| $E_1$ [GeV] | $E_2$ [GeV] | UL [TeV cm <sup>-2</sup> s <sup>-1</sup> ] |
| 92          | 125.061     | $1.06 \cdot 10^{-11}$                      |
| 125.061     | 170.002     | $1.67 \cdot 10^{-11}$                      |
| 170.002     | 231.094     | $9.97 \cdot 10^{-12}$                      |
| 231.094     | 314.138     | $2.39 \cdot 10^{-12}$                      |
| 314.138     | 427.026     | $5.31 \cdot 10^{-12}$                      |
| 427.026     | 580.481     | $1.38 \cdot 10^{-12}$                      |
| 580.481     | 789.08      | $2.93 \cdot 10^{-12}$                      |
| 789.08      | 1072.64     | $1.29 \cdot 10^{-12}$                      |
| 1072.64     | 1458.1      | $3.14 \cdot 10^{-12}$                      |
| 1458.1      | 1982.08     | $1.51 \cdot 10^{-12}$                      |
| 3662.59     | 4978.76     | $3.37 \cdot 10^{-12}$                      |

Table E.6: Differential flux upper limits in energy ranges  $[E_1; E_2]$  for GRB140709A. Only upper limits above the energy threshold are reported.

| GRB141026A  |             |  |
|-------------|-------------|--|
| $E_1$ [GeV] | $E_2$ [GeV] | UL [TeV cm <sup>-2</sup> s <sup>-1</sup> ] |
| 110         | 149.529     | $1.95 \cdot 10^{-11}$                      |
| 149.529     | 203.263     | $1.73 \cdot 10^{-11}$                      |
| 203.263     | 276.308     | $2.05 \cdot 10^{-12}$                      |
| 276.308     | 375.6       | $1.65 \cdot 10^{-12}$                      |
| 375.6       | 510.575     | $1.65 \cdot 10^{-12}$                      |
| 510.575     | 694.053     | $1.38 \cdot 10^{-12}$                      |
| 694.053     | 943.465     | $2.32 \cdot 10^{-12}$                      |
| 943.465     | 1282.51     | $3.27 \cdot 10^{-12}$                      |
| 1282.51     | 1743.38     | $1.97 \cdot 10^{-12}$                      |
| 1743.38     | 2369.88     | $1.19 \cdot 10^{-12}$                      |
| 2369.88     | 3221.51     | $1.49 \cdot 10^{-12}$                      |
| 5952.86     | 8092.06     | $2.86 \cdot 10^{-12}$                      |

Table E.7: Differential flux upper limits in energy ranges  $[E_1; E_2]$  for GRB141026A. Only upper limits above the energy threshold are reported.

| GRB141220A  |             |   |
|-------------|-------------|---|
| $E_1$ [GeV] | $E_2$ [GeV] | UL [ $\text{TeV cm}^{-2} \text{s}^{-1}$ ] |
| 77          | 104.67      | $1.75 \cdot 10^{-11}$                     |
| 104.67      | 142.284     | $7.51 \cdot 10^{-12}$                     |
| 142.284     | 193.415     | $1.22 \cdot 10^{-11}$                     |
| 193.415     | 262.92      | $2.90 \cdot 10^{-12}$                     |
| 262.92      | 357.402     | $5.08 \cdot 10^{-12}$                     |
| 357.402     | 485.837     | $6.49 \cdot 10^{-12}$                     |
| 485.837     | 660.426     | $1.16 \cdot 10^{-12}$                     |
| 660.426     | 897.754     | $5.59 \cdot 10^{-12}$                     |
| 897.754     | 1220.37     | $2.75 \cdot 10^{-12}$                     |
| 1220.37     | 1658.91     | $6.75 \cdot 10^{-12}$                     |
| 1658.91     | 2255.06     | $3.42 \cdot 10^{-12}$                     |

Table E.8: Differential flux upper limits in energy ranges  $[E_1; E_2]$  for GRB141220A. Only upper limits above the energy threshold are reported.

| GRB150213A  |             |   |
|-------------|-------------|---|
| $E_1$ [GeV] | $E_2$ [GeV] | UL [ $\text{TeV cm}^{-2} \text{s}^{-1}$ ] |
| 203         | 275.949     | $3.82 \cdot 10^{-12}$                     |
| 275.949     | 375.114     | $6.63 \cdot 10^{-12}$                     |
| 375.114     | 509.913     | $1.75 \cdot 10^{-11}$                     |
| 509.913     | 693.153     | $5.33 \cdot 10^{-12}$                     |
| 693.153     | 942.243     | $3.38 \cdot 10^{-12}$                     |
| 942.243     | 1280.84     | $2.85 \cdot 10^{-12}$                     |
| 1280.84     | 1741.12     | $5.73 \cdot 10^{-12}$                     |
| 1741.12     | 2366.81     | $3.31 \cdot 10^{-12}$                     |
| 2366.81     | 3217.33     | $1.02 \cdot 10^{-12}$                     |
| 3217.33     | 4373.5      | $2.79 \cdot 10^{-12}$                     |
| 4373.5      | 5945.15     | $3.21 \cdot 10^{-12}$                     |
| 5945.15     | 8081.58     | $1.52 \cdot 10^{-12}$                     |
| 8081.58     | 10985.7     | $1.10 \cdot 10^{-11}$                     |
| 20300       | 27594.9     | $5.59 \cdot 10^{-12}$                     |

Table E.9: Differential flux upper limits in energy ranges  $[E_1; E_2]$  for GRB150213A. Only upper limits above the energy threshold are reported.

| GRB150819A  |             |  |
|-------------|-------------|--|
| $E_1$ [GeV] | $E_2$ [GeV] | UL [TeV cm <sup>-2</sup> s <sup>-1</sup> ] |
| 175         | 237.887     | $2.52 \cdot 10^{-11}$                      |
| 237.887     | 323.374     | $4.57 \cdot 10^{-12}$                      |
| 323.374     | 439.58      | $9.91 \cdot 10^{-12}$                      |
| 439.58      | 597.546     | $1.57 \cdot 10^{-12}$                      |
| 597.546     | 812.278     | $4.48 \cdot 10^{-12}$                      |
| 812.278     | 1104.18     | $6.50 \cdot 10^{-12}$                      |
| 1104.18     | 1500.97     | $4.77 \cdot 10^{-12}$                      |
| 1500.97     | 2040.35     | $2.64 \cdot 10^{-12}$                      |
| 2040.35     | 2773.56     | $1.66 \cdot 10^{-12}$                      |
| 2773.56     | 3770.26     | $3.04 \cdot 10^{-12}$                      |
| 3770.26     | 5125.13     | $6.59 \cdot 10^{-12}$                      |
| 5125.13     | 6966.88     | $6.01 \cdot 10^{-12}$                      |
| 6966.88     | 9470.47     | $3.79 \cdot 10^{-12}$                      |
| 9470.47     | 12873.7     | $7.62 \cdot 10^{-12}$                      |
| 12873.      | 17500       | $3.12 \cdot 10^{-12}$                      |

Table E.10: Differential flux upper limits in energy ranges  $[E_1; E_2]$  for GRB150819A. Only upper limits above the energy threshold are reported.

| GRB151118A  |             |  |
|-------------|-------------|--|
| $E_1$ [GeV] | $E_2$ [GeV] | UL [TeV cm <sup>-2</sup> s <sup>-1</sup> ] |
| 170         | 231.091     | $5.73 \cdot 10^{-12}$                      |
| 231.091     | 314.134     | $8.29 \cdot 10^{-12}$                      |
| 314.134     | 427.021     | $2.77 \cdot 10^{-12}$                      |
| 427.021     | 580.473     | $2.09 \cdot 10^{-12}$                      |
| 580.473     | 789.07      | $1.97 \cdot 10^{-12}$                      |
| 789.07      | 1072.63     | $1.94 \cdot 10^{-12}$                      |
| 1072.63     | 1458.08     | $9.44 \cdot 10^{-13}$                      |
| 1458.08     | 1982.05     | $1.22 \cdot 10^{-12}$                      |
| 1982.05     | 2694.32     | $1.19 \cdot 10^{-12}$                      |
| 2694.32     | 3662.54     | $7.14 \cdot 10^{-13}$                      |
| 3662.54     | 4978.7      | $4.18 \cdot 10^{-13}$                      |
| 4978.7      | 6767.82     | $8.81 \cdot 10^{-13}$                      |
| 6767.82     | 9199.88     | $9.07 \cdot 10^{-13}$                      |
| 9199.88     | 12505.9     | $2.56 \cdot 10^{-12}$                      |
| 12505.9     | 17000       | $1.62 \cdot 10^{-12}$                      |
| 17000       | 23109.1     | $1.97 \cdot 10^{-12}$                      |

Table E.11: Differential flux upper limits in energy ranges  $[E_1; E_2]$  for GRB151118A. Only upper limits above the energy threshold are reported.

| GRB151215A  |             |   |
|-------------|-------------|---|
| $E_1$ [GeV] | $E_2$ [GeV] | UL [ $\text{TeV cm}^{-2} \text{s}^{-1}$ ] |
| 90          | 122.342     | $7.79 \cdot 10^{-12}$                     |
| 122.342     | 166.306     | $7.42 \cdot 10^{-12}$                     |
| 166.306     | 226.07      | $2.36 \cdot 10^{-12}$                     |
| 226.07      | 307.309     | $7.34 \cdot 10^{-12}$                     |
| 307.309     | 417.743     | $5.69 \cdot 10^{-12}$                     |
| 417.743     | 567.862     | $2.18 \cdot 10^{-12}$                     |
| 567.862     | 771.926     | $1.37 \cdot 10^{-12}$                     |
| 771.926     | 1049.32     | $2.14 \cdot 10^{-12}$                     |
| 1049.32     | 1426.4      | $2.87 \cdot 10^{-12}$                     |
| 1426.4      | 1938.99     | $3.02 \cdot 10^{-12}$                     |
| 1938.99     | 2635.78     | $2.04 \cdot 10^{-12}$                     |
| 2635.78     | 3582.96     | $1.29 \cdot 10^{-12}$                     |
| 4870.53     | 6620.78     | $1.34 \cdot 10^{-12}$                     |
| 9000        | 12234.2     | $2.39 \cdot 10^{-12}$                     |

Table E.12: Differential flux upper limits in energy ranges  $[E_1; E_2]$  for GRB151215A. Only upper limits above the energy threshold are reported.

## Appendix F

# CRAB NEBULA CROSS CHECK FOR GW151226 FOLLOW-UP

For the analysis of the targets denoted as GW3 and GW4, observed for the follow-up of the gravitational wave event GW151226, a dedicated moon analysis was performed, as discussed in Section 5.2.6. The reason is that the standardization of the analysis for data taken under moonlight described in Ahnen et al. (2017) was not available yet. So the cleaning levels used in `star` were computed according to the empirical formulas:

$$\text{Level 1} > \text{ped\_mean} + 3.0 \cdot \text{ped\_rms}$$

$$\text{Level 2} > \text{ped\_mean} + 1.0 \cdot \text{ped\_rms}$$

where `ped_mean` and `ped_rms` are the mean and RMS of the pedestal events distribution. The values obtained according to the pedestal events distribution for GW3 and GW4 are shown in Table F.1. These cleaning levels were used for ON, MC and OFF data. For MC

| Telescope | <code>ped_mean</code><br>[phe] | <code>ped_rms</code><br>[phe] | Lvl 1<br>[phe] | Lvl 2<br>[phe] |
|-----------|--------------------------------|-------------------------------|----------------|----------------|
| M1        | 3.8                            | 1.6                           | 9              | 6              |
| M2        | 4.0                            | 1.7                           | 10             | 6              |

Table F.1: Pedestal distribution mean and RMS and cleaning levels adopted for GW3 and GW4. The same settings were applied since the NSB level was similar for both targets.

and OFF data, noise was added at `star` level according to the pedestal distribution mean and RMS values in order to match the background level of the ON data. The same cleaning levels were applied to a Crab Nebula sample with the same NSB level as GW3 and GW4 in order check the consistency of the results. The set comprises a total of 5.91 h taken during the following dates:

- 2015-11-21: runs from 05048613 to 05048616
- 2015-11-22: runs from 05048661 to 05048667

The  $\theta^2$  plot, the resulting SED and the light curve are shown in Figure F.1.

Using the forward folding technique, the SED can be fitted with a function of the form:

$$\frac{dN}{dE} = f_0 \left( \frac{E}{1 \text{ TeV}} \right)^{a+b \log_{10}(E/1 \text{ TeV})} [\text{cm}^{-2} \text{ s}^{-1} \text{ TeV}^{-1}] \quad (\text{F.1})$$

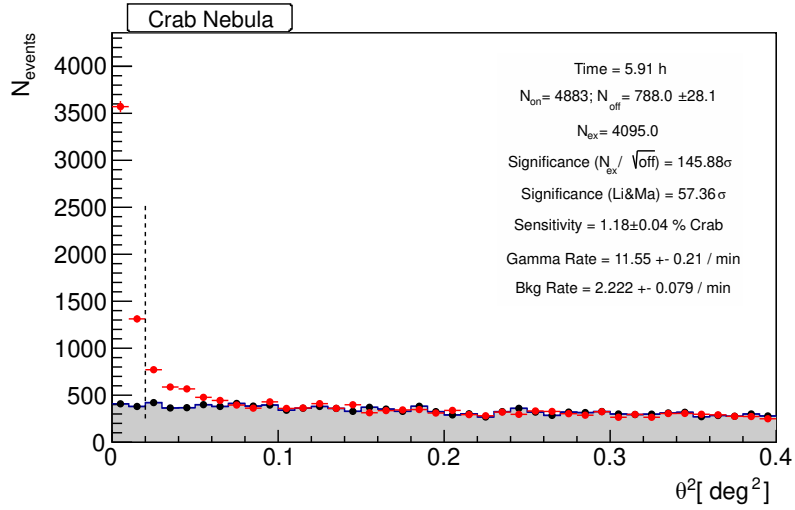


Figure F.1.1

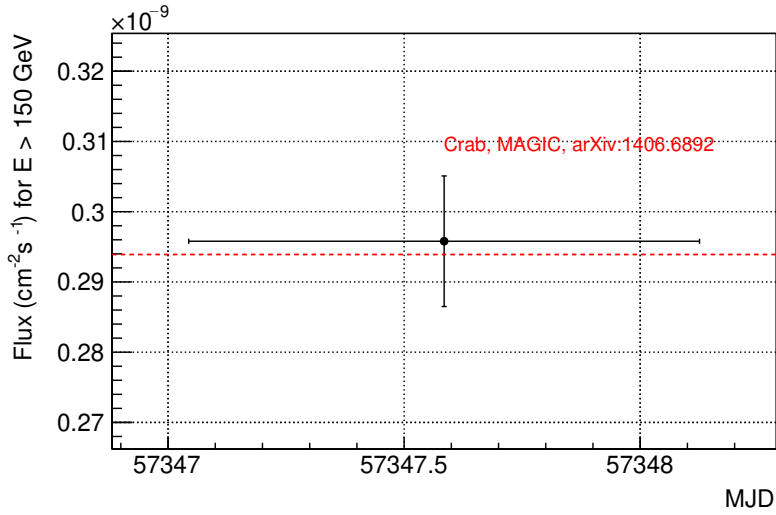


Figure F.1.2

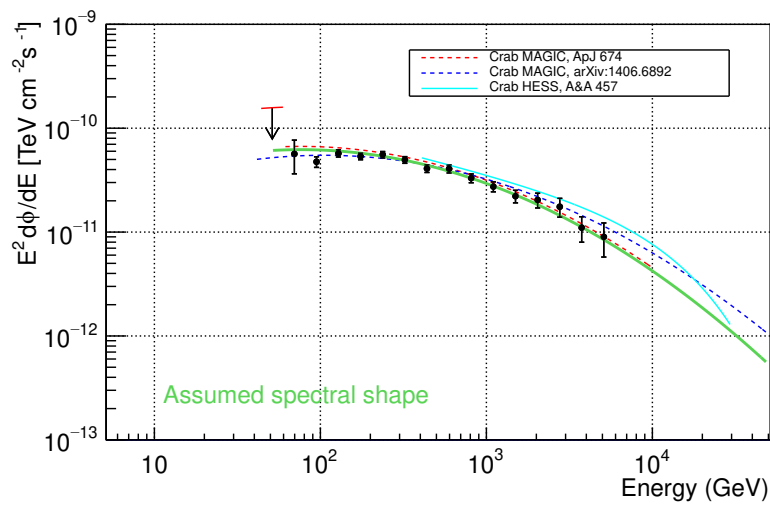


Figure F.1.3

Figure F.1:  $\theta^2$  plot (LE cuts), light curve and SED for the Crab Nebula sample considered for cross-checking the settings used for the analysis of the targets GW3 and GW4.

with best fit parameters:

$$f_0 = (2.97 \pm 0.13) \cdot 10^{-11} \quad a = -2.56 \pm 0.06 \quad b = -0.21 \pm 0.07 \quad \chi^2/\text{d.o.f} = 15.11/14$$

These values are compatible within statistical errors with the ones in Aleksić et al. (2016b).

---



# Acknowledgments

Here we go again: another thesis! The third one, to be precise. Someone asked me 'is it your last thesis?' and the answer is 'yes... I hope!'. In any case, being it the last or not, a thesis cannot be complete without acknowledgments.

First, I want to thank my supervisor Francesco Longo, Franz, 'proprio lui!'. I remember when I first met him to discuss the topic of my Bachelor thesis: this was the beginning of the scientific path that led me to this PhD thesis. During my PhD I had the opportunity to work closely with him, always giving precious advices. I thank him for creating a happy and relaxed atmosphere where people can work and express themselves without any constraint.

During the PhD I had the opportunity to become a member of a great collaboration: MAGIC. From the first time I met the other MAGICians in the software school in Lodz in February 2015, it was clear that it was the right place. Great scientists believing in young people, but also great people. I want to thank all the MAGICians for being more like a family and friends and not just a collaboration. In particular I want to thank the people who were together with me in La Palma during shifts (Simona, Alessandro, Marlene, Vandad, Cosimo, Antonio, Quim, Yusuke, Giovanni, Wriju, Koji, Alicia, Merve, Massimo, Michele, Lab, Victoria and Kazuma), the La Palma postdocs (Martin, Javier, Victor and Auni), Maestro Eduardo and all the people in the crazy nights after the social dinners in collaboration meetings.

I also thank the gamma-ray group in AREA: Franz, Guido, Thomas, Michele, Alice D., Davide, Lara, Stefano and Rafal. Tutti sempre sul pezzo. Especially when eating in osmiza. I spent most of my time in the INFN laboratories in AREA and there I had a great time with all the people working there, even if for a short period of time: Luigi, Luca, Massimo, Chiara, Shuddha, Chandra, Jinki, Anna, Damiano. I especially thank Luigi for giving me the opportunity of being tutor of the Physics course for Biology students: it was a great chance to work together with him and an experience I really enjoyed. What to say about our Italian Indians Shudda and Chandra? Crazy guys and nice people. I really liked listening to the stories bout India, a world so different from ours in certain aspects. And also hanging out with them, talking nonsense almost all the time. About physics as well, but no too much!

Now is the time to thank all my friends, who were with me almost from the first days when I started university. Here I can officially say to Baru that after all I was doing something during my PhD. There is a thesis here! Forget about the times I went to La Palma (four times, I bet that he counted them), to Barcelona, to Berlin, to Rome, to Catania, to Lodz, to Split, to Sexten, to all those places no one wants to visit. I went there to work! (I feel so good at trolling here!) Of course I cannot forget Debora, Aljaz, Giulia, Flavia, Daniel, Pietro, Stella, Ruggio, Luca, Batti, Alice G., Sara. We are in different places and in different situations, but we are doing quite a good job in keeping in contact and hanging out together when we have the chance.

I also thank my flatmates, Gabriele, Daniel and Francesco, for their patience when I was

playing drums after a long day. It is a way for me to think about something else, but I think that the people on the third floor thought to kill me. I am here, so I think they have even greater patience.

Last but not least, I thank my family: they know that I am studying something difficult, but they also trust that I know what I am doing. I am doing fine! As far as the future is concerned, who knows, the possibilities are so many. Finally, a special dedication to Nonna Lisetta, who is not with us anymore. Your last words to me were 'fa' il bravo'. I will try, my own way.

# References

- Aartsen, M. G. et al. (2016). “An All-sky Search for Three Flavors of Neutrinos from Gamma-ray Bursts with the IceCube Neutrino Observatory”. In: *The Astrophysical Journal* 824, 115, p. 115. DOI: 10.3847/0004-637X/824/2/115. arXiv: 1601.06484 [astro-ph.HE].
- Aartsen, M. G. et al. (2017a). “Extending the Search for Muon Neutrinos Coincident with Gamma-Ray Bursts in IceCube Data”. In: *The Astrophysical Journal* 843, 112, p. 112. DOI: 10.3847/1538-4357/aa7569. arXiv: 1702.06868 [astro-ph.HE].
- Aartsen, M. G. et al. (2017b). “The IceCube realtime alert system”. In: *Astroparticle Physics* 92, pp. 30–41. DOI: 10.1016/j.astropartphys.2017.05.002.
- Abadie, J. et al. (2010). “TOPICAL REVIEW: Predictions for the rates of compact binary coalescences observable by ground-based gravitational-wave detectors”. In: *Classical and Quantum Gravity* 27.17, 173001, p. 173001. DOI: 10.1088/0264-9381/27/17/173001. arXiv: 1003.2480 [astro-ph.HE].
- Abbott, B. P. et al. (2016a). “GW151226: Observation of Gravitational Waves from a 22-Solar-Mass Binary Black Hole Coalescence”. In: *Physical Review Letters* 116.24, 241103, p. 241103. DOI: 10.1103/PhysRevLett.116.241103. arXiv: 1606.04855 [gr-qc].
- Abbott, B. P. et al. (2016b). “Observation of Gravitational Waves from a Binary Black Hole Merger”. In: *Physical Review Letters* 116.6, 061102, p. 061102. DOI: 10.1103/PhysRevLett.116.061102. arXiv: 1602.03837 [gr-qc].
- Abbott, B. P. et al. (2016c). “Prospects for Observing and Localizing Gravitational-Wave Transients with Advanced LIGO and Advanced Virgo”. In: *Living Reviews in Relativity* 19, 1, p. 1. DOI: 10.1007/lrr-2016-1. arXiv: 1304.0670 [gr-qc].
- Abbott, B. P. et al. (2016d). “Upper Limits on the Rates of Binary Neutron Star and Neutron Star-Black Hole Mergers from Advanced LIGO’s First Observing Run”. In: *The Astrophysical Journal Letters* 832, L21, p. L21. DOI: 10.3847/2041-8205/832/2/L21. arXiv: 1607.07456 [astro-ph.HE].
- Abbott, B. P. et al. (2016e). “Upper Limits on the Rates of Binary Neutron Star and Neutron Star-Black Hole Mergers from Advanced LIGO’s First Observing Run”. In: *The Astrophysical Journal Letters* 832, L21, p. L21. DOI: 10.3847/2041-8205/832/2/L21. arXiv: 1607.07456 [astro-ph.HE].
- Abbott, B. P. et al. (2017a). “Gravitational Waves and Gamma-Rays from a Binary Neutron Star Merger: GW170817 and GRB 170817A”. In: *The Astrophysical Journal Letters* 848, L13, p. L13. DOI: 10.3847/2041-8213/aa920c. arXiv: 1710.05834 [astro-ph.HE].
- Abbott, B. P. et al. (2017b). “GW170104: Observation of a 50-Solar-Mass Binary Black Hole Coalescence at Redshift 0.2”. In: *Physical Review Letters* 118.22, 221101, p. 221101. DOI: 10.1103/PhysRevLett.118.221101. arXiv: 1706.01812 [gr-qc].
- Abbott, B. P. et al. (2017c). “GW170104: Observation of a 50-Solar-Mass Binary Black Hole Coalescence at Redshift 0.2”. In: *Physical Review Letters* 118.22, 221101, p. 221101. DOI: 10.1103/PhysRevLett.118.221101. arXiv: 1706.01812 [gr-qc].
- Abbott, B. P. et al. (2017d). “GW170814: A Three-Detector Observation of Gravitational Waves from a Binary Black Hole Coalescence”. In: *Physical Review Letters* 119 (14), p. 141101. DOI: 10.1103/PhysRevLett.119.141101. URL: <https://link.aps.org/doi/10.1103/PhysRevLett.119.141101>.

- Abbott, B. P. et al. (2017e). “GW170817: Observation of Gravitational Waves from a Binary Neutron Star Inspiral”. In: *Physical Review Letters* 119.16, 161101, p. 161101. DOI: 10.1103/PhysRevLett.119.161101.
- Abdo, A. A. et al. (2007). “Discovery of TeV Gamma-Ray Emission from the Cygnus Region of the Galaxy”. In: *The Astrophysical Journal Letters* 658.1, p. L33. URL: <http://stacks.iop.org/1538-4357/658/i=1/a=L33>.
- Abdo, A. A. et al. (2009a). “Fermi Observations of GRB 090902B: A Distinct Spectral Component in the Prompt and Delayed Emission”. In: *The Astrophysical Journal Letters* 706, pp. L138–L144. DOI: 10.1088/0004-637X/706/1/L138. arXiv: 0909.2470 [astro-ph.HE].
- Abdo, A. A. et al. (2009b). “Fermi Observations of High-energy Gamma-ray Emission from GRB 080825C”. In: *The Astrophysical Journal* 707, pp. 580–592. DOI: 10.1088/0004-637X/707/1/580. arXiv: 0910.4192 [astro-ph.HE].
- Abdo, A. A. et al. (2009c). “Fermi Observations of High-Energy Gamma-Ray Emission from GRB 080916C”. In: *Science* 323, p. 1688. DOI: 10.1126/science.1169101.
- Abdo, A. A. et al. (2010a). “Fermi Detection of Delayed GeV Emission from the Short Gamma-Ray Burst 081024B”. In: *The Astrophysical Journal* 712, pp. 558–564. DOI: 10.1088/0004-637X/712/1/558. arXiv: 1002.3205 [astro-ph.HE].
- Abdo, A. A. et al. (2010b). “Fermi Large Area Telescope Constraints on the Gamma-ray Opacity of the Universe”. In: *The Astrophysical Journal* 723, pp. 1082–1096. DOI: 10.1088/0004-637X/723/2/1082. arXiv: 1005.0996 [astro-ph.HE].
- Abdo, A. A. et al. (2010c). “Fermi Large Area Telescope Observation of a Gamma-ray Source at the Position of Eta Carinae”. In: *The Astrophysical Journal* 723, pp. 649–657. DOI: 10.1088/0004-637X/723/1/649. arXiv: 1008.3235 [astro-ph.HE].
- Abdo, A. A. et al. (2011). “Gamma-Ray Flares from the Crab Nebula”. In: *Science* 331, p. 739. DOI: 10.1126/science.1199705. arXiv: 1011.3855 [astro-ph.HE].
- Abdo, A. A. et al. (2013). “The Second Fermi Large Area Telescope Catalog of Gamma-Ray Pulsars”. In: *The Astrophysical Journal Supplement* 208, 17, p. 17. DOI: 10.1088/0067-0049/208/2/17. arXiv: 1305.4385 [astro-ph.HE].
- Abeysekara, A. U. et al. (2013). “Sensitivity of the high altitude water Cherenkov detector to sources of multi-TeV gamma rays”. In: *Astroparticle Physics* 50, pp. 26–32. DOI: 10.1016/j.astropartphys.2013.08.002. arXiv: 1306.5800 [astro-ph.HE].
- Abeysekara, A. U. et al. (2015a). “Gamma-Rays from the Quasar PKS 1441+25: Story of an Escape”. In: *The Astrophysical Journal Letters* 815, L22, p. L22. DOI: 10.1088/2041-8205/815/2/L22. arXiv: 1512.04434 [astro-ph.HE].
- Abeysekara, A. U. et al. (2015b). “Search for Gamma-Rays from the Unusually Bright GRB 130427A with the HAWC Gamma-Ray Observatory”. In: *The Astrophysical Journal* 800, 78, p. 78. DOI: 10.1088/0004-637X/800/2/78. arXiv: 1410.1536 [astro-ph.HE].
- Abeysekara, A. U. et al. (2017). “The 2HWC HAWC Observatory Gamma-Ray Catalog”. In: *The Astrophysical Journal* 843, 40, p. 40. DOI: 10.3847/1538-4357/aa7556. arXiv: 1702.02992 [astro-ph.HE].
- Abraham, J. et al. (2004). “Properties and performance of the prototype instrument for the Pierre Auger Observatory”. In: *Nuclear Instruments and Methods in Physics Research Section A: Accelerators, Spectrometers, Detectors and Associated Equipment* 523.1, pp. 50–95. ISSN: 0168-9002. DOI: <http://dx.doi.org/10.1016/j.nima.2003.12.012>. URL: <http://www.sciencedirect.com/science/article/pii/S0168900203033497>.
- Abraham, J. et al. (2010). “The fluorescence detector of the Pierre Auger Observatory”. In: *Nuclear Instruments and Methods in Physics Research A* 620, pp. 227–251. DOI: 10.1016/j.nima.2010.04.023.
- Abramowski, A. et al. (2015). “The exceptionally powerful TeV  $\gamma$ -ray emitters in the Large Magellanic Cloud”. In: *Science* 347, pp. 406–412. DOI: 10.1126/science.1261313. arXiv: 1501.06578 [astro-ph.HE].
-

- Acciari, V. A. et al. (2009). “A connection between star formation activity and cosmic rays in the starburst galaxy M82”. In: *Nature* 462, pp. 770–772. DOI: 10.1038/nature08557. arXiv: 0911.0873 [astro-ph.CO].
- Acciari, V. A. et al. (2011a). “Discovery of TeV Gamma-ray Emission from Tycho’s Supernova Remnant”. In: *Astrophysical Journal, Letters* 730, L20, p. L20. DOI: 10.1088/2041-8205/730/2/L20. arXiv: 1102.3871 [astro-ph.HE].
- Acciari, V. A. et al. (2011b). “VERITAS Observations of Gamma-Ray Bursts Detected by Swift”. In: *The Astrophysical Journal* 743, 62, p. 62. DOI: 10.1088/0004-637X/743/1/62. arXiv: 1109.0050 [astro-ph.HE].
- Acernese, F. et al. (2015). “Advanced Virgo: a second-generation interferometric gravitational wave detector”. In: *Classical and Quantum Gravity* 32.2, 024001, p. 024001. DOI: 10.1088/0264-9381/32/2/024001. arXiv: 1408.3978 [gr-qc].
- Acerro, F. et al. (2009). “Detection of Gamma Rays from a Starburst Galaxy”. In: *Science* 326, pp. 1080–. DOI: 10.1126/science.1178826. arXiv: 0909.4651 [astro-ph.HE].
- Acerro, F. et al. (2010). “First detection of VHE  $\gamma$ -rays from SN 1006 by HESS”. In: *Astronomy and Astrophysics* 516, A62, A62. DOI: 10.1051/0004-6361/200913916. arXiv: 1004.2124 [astro-ph.HE].
- Acharya, B. S. et al. (2013). “Introducing the CTA concept”. In: *Astroparticle Physics* 43, pp. 3–18. DOI: 10.1016/j.astropartphys.2013.01.007.
- Ackermann, M. et al. (2010). “Fermi Observations of GRB 090510: A Short-Hard Gamma-ray Burst with an Additional, Hard Power-law Component from 10 keV TO GeV Energies”. In: *The Astrophysical Journal* 716, pp. 1178–1190. DOI: 10.1088/0004-637X/716/2/1178. arXiv: 1005.2141 [astro-ph.HE].
- Ackermann, M. et al. (2011). “Detection of a Spectral Break in the Extra Hard Component of GRB 090926A”. In: *The Astrophysical Journal* 729, 114, p. 114. DOI: 10.1088/0004-637X/729/2/114. arXiv: 1101.2082 [astro-ph.HE].
- Ackermann, M. et al. (2013a). “Detection of the Characteristic Pion-Decay Signature in Supernova Remnants”. In: *Science* 339, pp. 807–811. DOI: 10.1126/science.1231160. arXiv: 1302.3307 [astro-ph.HE].
- Ackermann, M. et al. (2013b). “The First Fermi-LAT Gamma-Ray Burst Catalog”. In: *The Astrophysical Journal Supplement* 209, 11, p. 11. DOI: 10.1088/0067-0049/209/1/11. arXiv: 1303.2908 [astro-ph.HE].
- Ackermann, M. et al. (2014). “Fermi-LAT Observations of the Gamma-Ray Burst GRB 130427A”. In: *Science* 343, pp. 42–47. DOI: 10.1126/science.1242353. arXiv: 1311.5623 [astro-ph.HE].
- Aglietta, M. et al. (1989). “The EAS-TOP array at  $E_0 = 10^{14} - 10^{16}$  eV: Stability and resolutions”. In: *Nuclear Instruments and Methods in Physics Research A* 277, pp. 23–28. DOI: 10.1016/0168-9002(89)90531-7.
- Aguiar, M. et al. (2013). “First Result from the Alpha Magnetic Spectrometer on the International Space Station: Precision Measurement of the Positron Fraction in Primary Cosmic Rays of 0.5-350 GeV”. In: *Physical Review Letters* 110.14, 141102, p. 141102. DOI: 10.1103/PhysRevLett.110.141102.
- Aharonian, F. et al. (2001). “Evidence for TeV gamma ray emission from Cassiopeia A”. In: *Astronomy and Astrophysics* 370, pp. 112–120. DOI: 10.1051/0004-6361:20010243. eprint: astro-ph/0102391.
- Aharonian, F. et al. (2005a). “A New Population of Very High Energy Gamma-Ray Sources in the Milky Way”. In: *Science* 307, pp. 1938–1942. DOI: 10.1126/science.1108643. eprint: astro-ph/0504380.
- Aharonian, F. et al. (2005b). “Discovery of the binary pulsar PSR B1259-63 in very-high-energy gamma rays around periastron with HESS”. In: *Astronomy and Astrophysics* 442, pp. 1–10. DOI: 10.1051/0004-6361:20052983. eprint: astro-ph/0506280.
-

- Aharonian, F. et al. (2006). “Discovery of very-high-energy  $\gamma$ -rays from the Galactic Centre ridge”. In: *Nature* 439, pp. 695–698. DOI: 10.1038/nature04467. eprint: astro-ph/0603021.
- Aharonian, F. et al. (2009a). “Discovery of Gamma-Ray Emission From the Shell-Type Supernova Remnant RCW 86 With HESS”. In: *Astrophysical Journal* 692, pp. 1500–1505. DOI: 10.1088/0004-637X/692/2/1500. arXiv: 0810.2689.
- Aharonian, F. et al. (2009b). “HESS observations of  $\gamma$ -ray bursts in 2003-2007”. In: *Astronomy & Astrophysics* 495, pp. 505–512. DOI: 10.1051/0004-6361:200811072. arXiv: 0901.2187 [astro-ph.HE].
- Aharonian, F. et al. (2009c). “HESS Observations of the Prompt and Afterglow Phases of GRB 060602B”. In: *The Astrophysical Journal* 690, pp. 1068–1073. DOI: 10.1088/0004-637X/690/2/1068. arXiv: 0809.2334.
- Aharonian, F. et al. (2009d). “Spectrum and variability of the Galactic center VHE  $\gamma$ -ray source HESS J1745-290”. In: *Astronomy & Astrophysics* 503, pp. 817–825. DOI: 10.1051/0004-6361/200811569. arXiv: 0906.1247 [astro-ph.GA].
- Ahnen, M. L. et al. (2015). “Very High Energy  $\gamma$ -Rays from the Universe’s Middle Age: Detection of the  $z = 0.940$  Blazar PKS 1441+25 with MAGIC”. In: *The Astrophysical Journal Letters* 815, L23, p. L23. DOI: 10.1088/2041-8205/815/2/L23. arXiv: 1512.04435.
- Ahnen, M. L. et al. (2016). “Detection of very high energy gamma-ray emission from the gravitationally lensed blazar QSO B0218+357 with the MAGIC telescopes”. In: *Astronomy & Astrophysics* 595, A98, A98. DOI: 10.1051/0004-6361/201629461. arXiv: 1609.01095 [astro-ph.HE].
- Ahnen, M.L. et al. (2017). “Performance of the MAGIC telescopes under moonlight”. In: *Astroparticle Physics* 94, pp. 29–41. ISSN: 0927-6505. DOI: <http://dx.doi.org/10.1016/j.astropartphys.2017.08.001>. URL: <http://www.sciencedirect.com/science/article/pii/S092765051730110X>.
- Aielli, G. et al. (2010). “Gamma-ray Flares from Mrk421 in 2008 Observed with the ARGO-YBJ Detector”. In: *The Astrophysical Journal Letters* 714.2, p. L208. URL: <http://stacks.iop.org/2041-8205/714/i=2/a=L208>.
- Albert, J. et al. (2006). “Flux Upper Limit on Gamma-Ray Emission by GRB 050713a from MAGIC Telescope Observations”. In: *The Astrophysical Journal Letters* 641.1, p. L9. URL: <http://stacks.iop.org/1538-4357/641/i=1/a=L9>.
- Albert, J. et al. (2007). “MAGIC Upper Limits on the Very High Energy Emission from Gamma-Ray Bursts”. In: *The Astrophysical Journal* 667.1, p. 358. URL: <http://stacks.iop.org/0004-637X/667/i=1/a=358>.
- Albert, J. et al. (2007). “Very High Energy Gamma-Ray Radiation from the Stellar Mass Black Hole Binary Cygnus X-1”. In: *The Astrophysical Journal Letters* 665, pp. L51–L54. DOI: 10.1086/521145. arXiv: 0706.1505.
- Albert, J. et al. (2008a). “FADC signal reconstruction for the MAGIC telescope”. In: *Nuclear Instruments and Methods in Physics Research A* 594, pp. 407–419. DOI: 10.1016/j.nima.2008.06.043. eprint: astro-ph/0612385.
- Albert, J. et al. (2008b). “Implementation of the Random Forest method for the Imaging Atmospheric Cherenkov Telescope MAGIC”. In: *Nuclear Instruments and Methods in Physics Research A* 588, pp. 424–432. DOI: 10.1016/j.nima.2007.11.068. arXiv: 0709.3719.
- Aleksić, J. et al. (2010). “MAGIC observation of the GRB 080430 afterglow”. In: *Astronomy and Astrophysics* 517, A5, A5. DOI: 10.1051/0004-6361/200913461. arXiv: 1004.3665 [astro-ph.HE].
- Aleksić, J. et al. (2011a). “Observations of the Crab Pulsar between 25 and 100 GeV with the MAGIC I Telescope”. In: *The Astrophysical Journal* 742, 43, p. 43. DOI: 10.1088/0004-637X/742/1/43. arXiv: 1108.5391 [astro-ph.HE].
-

- Aleksić, J. et al. (2011b). “Observations of the Crab Pulsar between 25 and 100 GeV with the MAGIC I Telescope”. In: *The Astrophysical Journal* 742, 43, p. 43. DOI: 10.1088/0004-637X/742/1/43. arXiv: 1108.5391 [astro-ph.HE].
- Aleksić, J. et al. (2012). “Performance of the MAGIC stereo system obtained with Crab Nebula data”. In: *Astroparticle Physics* 35, pp. 435–448. DOI: 10.1016/j.astropartphys.2011.11.007. arXiv: 1108.1477 [astro-ph.IM].
- Aleksić, J. et al. (2016a). “The major upgrade of the MAGIC telescopes, Part I: The hardware improvements and the commissioning of the system”. In: *Astroparticle Physics* 72, pp. 61–75. DOI: 10.1016/j.astropartphys.2015.04.004. arXiv: 1409.6073 [astro-ph.IM].
- Aleksić, J. et al. (2016b). “The major upgrade of the MAGIC telescopes, Part II: A performance study using observations of the Crab Nebula”. In: *Astroparticle Physics* 72, pp. 76–94. DOI: 10.1016/j.astropartphys.2015.02.005. arXiv: 1409.5594 [astro-ph.IM].
- Aleksić, J. et al. (2014). “MAGIC upper limits on the GRB 090102 afterglow”. In: *Monthly Notices of the Royal Astronomical Society* 437.4, pp. 3103–3111. DOI: 10.1093/mnras/stt2041. eprint: /oup/backfile/content\_public/journal/mnras/437/4/10.1093\_mnras\_stt2041/4/stt2041.pdf. URL: +http://dx.doi.org/10.1093/mnras/stt2041.
- Alfaro, R. et al. (2017). “Search for Very-high-energy Emission from Gamma-Ray Bursts Using the First 18 Months of Data from the HAWC Gamma-Ray Observatory”. In: *The Astrophysical Journal* 843, 88, p. 88. DOI: 10.3847/1538-4357/aa756f. arXiv: 1705.01551 [astro-ph.HE].
- Aliu, E. et al. (2008a). “Observation of Pulsed  $\gamma$ -Rays Above 25 GeV from the Crab Pulsar with MAGIC”. In: *Science* 322, p. 1221. DOI: 10.1126/science.1164718. arXiv: 0809.2998.
- Aliu, E. et al. (2008b). “Observation of Pulsed  $\gamma$ -Rays Above 25 GeV from the Crab Pulsar with MAGIC”. In: *Science* 322, pp. 1221–. DOI: 10.1126/science.1164718. arXiv: 0809.2998.
- Aliu, E. et al. (2014). “Constraints on Very High Energy Emission from GRB 130427A”. In: *The Astrophysical Journal Letters* 795, L3, p. L3. DOI: 10.1088/2041-8205/795/1/L3. arXiv: 1410.5367 [astro-ph.HE].
- Amaral-Rogers, A. et al. (2015). “GRB 151118A: Swift detection of a burst.” In: *GRB Coordinates Network, Circular Service, No. 18611, #1 (2015)* 18611.
- Anderson, Carl D. (1933). “The Positive Electron”. In: *Phys. Rev.* 43 (6), pp. 491–494. DOI: 10.1103/PhysRev.43.491. URL: https://link.aps.org/doi/10.1103/PhysRev.43.491.
- Anderson, G. E. et al. (2014). “GRB 140709A: Possible AMI 15 GHz detection.” In: *GRB Coordinates Network, Circular Service, No. 16595, #1 (2014)* 16595.
- Antoni, T et al. (2003). “The cosmic-ray experiment KASCADE”. In: *Nuclear Instruments and Methods in Physics Research Section A: Accelerators, Spectrometers, Detectors and Associated Equipment* 513.3, pp. 490–510. ISSN: 0168-9002. DOI: http://dx.doi.org/10.1016/S0168-9002(03)02076-X. URL: http://www.sciencedirect.com/science/article/pii/S016890020302076X.
- Apel, W.D. et al. (2010). “The KASCADE-Grande experiment”. In: *Nuclear Instruments and Methods in Physics Research Section A: Accelerators, Spectrometers, Detectors and Associated Equipment* 620.2, pp. 202–216. ISSN: 0168-9002. DOI: http://dx.doi.org/10.1016/j.nima.2010.03.147. URL: http://www.sciencedirect.com/science/article/pii/S0168900210007734.
- Arcavi, I. et al. (2017). “Optical Follow-up of Gravitational-wave Events with Las Cumbres Observatory”. In: *The Astrophysical Journal Letters* 848, L33, p. L33. DOI: 10.3847/2041-8213/aa910f. arXiv: 1710.05842 [astro-ph.HE].
- Asano, K., S. Guiriec, and P. Mészáros (2009). “Hadronic Models for the Extra Spectral Component in the Short GRB 090510”. In: *The Astrophysical Journal Letters* 705, pp. L191–L194. DOI: 10.1088/0004-637X/705/2/L191. arXiv: 0909.0306 [astro-ph.HE].
-

- Asano, K. and S. Inoue (2007). “Prompt GeV-TeV Emission of Gamma-Ray Bursts Due to High-Energy Protons, Muons, and Electron-Positron Pairs”. In: *The Astrophysical Journal* 671, pp. 645–655. DOI: 10.1086/522939. arXiv: 0705.2910.
- Asano, K., S. Inoue, and P. Mészáros (2009). “Prompt High-Energy Emission from Proton-Dominated Gamma-Ray Bursts”. In: *The Astrophysical Journal* 699, pp. 953–957. DOI: 10.1088/0004-637X/699/2/953. arXiv: 0807.0951.
- Ascoli Balzanelli, A. and R. Ascoli (1954). “Esperienze sull’effetto Čerenkov nell’aria”. Italian. In: *Il Nuovo Cimento (1943-1954)* 11.5, pp. 562–564. DOI: 10.1007/BF02781049. URL: <http://dx.doi.org/10.1007/BF02781049>.
- Aso, Y. et al. (2013). “Interferometer design of the KAGRA gravitational wave detector”. In: *Physical Review D* 88.4, 043007, p. 043007. DOI: 10.1103/PhysRevD.88.043007. arXiv: 1306.6747 [gr-qc].
- Atkins, R. et al. (2000). “Evidence for TEV Emission from GRB 970417A”. In: *The Astrophysical Journal* 533, pp. L119–L122. DOI: 10.1086/312629.
- Atkins, R. et al. (2003). “Observation of TeV Gamma Rays from the Crab Nebula with Milagro Using a New Background Rejection Technique”. In: *The Astrophysical Journal* 595.2, p. 803. URL: <http://stacks.iop.org/0004-637X/595/i=2/a=803>.
- Atkins, R. et al. (2005). “Evidence for TeV Gamma-Ray Emission from a Region of the Galactic Plane”. In: *Phys. Rev. Lett.* 95 (25), p. 251103. DOI: 10.1103/PhysRevLett.95.251103. URL: <https://link.aps.org/doi/10.1103/PhysRevLett.95.251103>.
- Atwood, W. B. et al. (2009). “The Large Area Telescope on the Fermi Gamma-Ray Space Telescope Mission”. In: *The Astrophysical Journal* 697, pp. 1071–1102. DOI: 10.1088/0004-637X/697/2/1071. arXiv: 0902.1089 [astro-ph.IM].
- Bacci, C et al. (2002). “Results from the ARGO-YBJ test experiment”. In: *Astroparticle Physics* 17.2, pp. 151–165. ISSN: 0927-6505. DOI: [http://dx.doi.org/10.1016/S0927-6505\(01\)00145-1](http://dx.doi.org/10.1016/S0927-6505(01)00145-1). URL: <http://www.sciencedirect.com/science/article/pii/S0927650501001451>.
- Balzanelli, A. Ascoli and R. Ascoli (1953). “Effetto cerenkov in sostanze aeriformi”. Italian. In: *Il Nuovo Cimento (1943-1954)* 10.9, pp. 1345–1346. DOI: 10.1007/BF02773126. URL: <http://dx.doi.org/10.1007/BF02773126>.
- Band, D. et al. (1993). “BATSE observations of gamma-ray burst spectra. I - Spectral diversity”. In: *Astrophysical Journal* 413, pp. 281–292. DOI: 10.1086/172995.
- Barraud, C. et al. (2003). “Spectral analysis of 35 GRBs/XRFs observed with HETE-2/FREGATE”. In: *Astronomy and Astrophysics* 400, pp. 1021–1030. DOI: 10.1051/0004-6361:20030074. eprint: astro-ph/0206380.
- Barthelmy, S. D. et al. (2013). “GRB 130606A, Swift-BAT refined analysis.” In: *GRB Coordinates Network, Circular Service, No. 14819, #1 (2013)* 14819.
- Bartoli, B. et al. (2015). “Crab Nebula: Five-year Observation with ARGO-YBJ”. In: *The Astrophysical Journal* 798, 119, p. 119. DOI: 10.1088/0004-637X/798/2/119. arXiv: 1502.05665 [astro-ph.HE].
- Bartos, I., P. Brady, and S. Márka (2013). “How gravitational-wave observations can shape the gamma-ray burst paradigm”. In: *Classical and Quantum Gravity* 30.12, 123001, p. 123001. DOI: 10.1088/0264-9381/30/12/123001. arXiv: 1212.2289 [astro-ph.CO].
- Bauleo, P. M. and J. Rodríguez Martino (2009). “The dawn of the particle astronomy era in ultra-high-energy cosmic rays”. In: *Nature* 458, pp. 847–851. DOI: 10.1038/nature07948.
- Berger, E. (2014). “Short-Duration Gamma-Ray Bursts”. In: *Annual Review of Astronomy and Astrophysics* 52, pp. 43–105. DOI: 10.1146/annurev-astro-081913-035926. arXiv: 1311.2603 [astro-ph.HE].
- Bernlohr, K. (2000). “Impact of atmospheric parameters on the atmospheric Cherenkov technique”. In: *Astropart. Phys.* 12, pp. 255–268. DOI: 10.1016/S0927-6505(99)00093-6. arXiv: astro-ph/9908093 [astro-ph].
-

- Bertero, M. (1989). “Linear inverse and ill-posed problems”. In: ed. by P. W. Hawkes. Vol. 75. Academic Press, New York, pp. 1–120.
- Berti, A. and MAGIC GRB Group (2017). “Search for High Energy emission from GRBs with MAGIC”. In: *IAU Symposium*. Vol. 324. IAU Symposium, pp. 70–73. DOI: 10.1017/S1743921317001442.
- Biland, A. et al. (2008). “The Active Mirror Control of the MAGIC Telescopes”. In: *International Cosmic Ray Conference* 3, pp. 1353–1356. arXiv: 0709.1574.
- Bird, D. J. et al. (1995). “Detection of a cosmic ray with measured energy well beyond the expected spectral cutoff due to cosmic microwave radiation”. In: *The Astrophysical Journal* 441, pp. 144–150. DOI: 10.1086/175344. eprint: astro-ph/9410067.
- Bitossi, M., R. Paoletti, and D. Tesaro (2016). “Ultra-Fast Sampling and Data Acquisition Using the DRS4 Waveform Digitizer”. In: *IEEE Transactions on Nuclear Science* 63, pp. 2309–2316. DOI: 10.1109/TNS.2016.2578963.
- Blackett, P.M.S. (1948). In: *Phys. Soc. Gassiot Committee report 34*.
- Blair, D. et al. (2015). “Gravitational wave astronomy: the current status”. In: *Science China Physics, Mechanics, and Astronomy* 58, 5748, p. 5748. DOI: 10.1007/s11433-015-5748-6. arXiv: 1602.02872 [physics.ins-det].
- Blandford, R. D. and C. F. McKee (1976). “Fluid dynamics of relativistic blast waves”. In: *Physics of Fluids* 19, pp. 1130–1138. DOI: 10.1063/1.861619.
- Blandford, R. D. and D. G. Payne (1982). “Hydromagnetic flows from accretion discs and the production of radio jets”. In: *Monthly Notices of the Royal Astronomical Society* 199, pp. 883–903. DOI: 10.1093/mnras/199.4.883.
- Blandford, R. D. and R. L. Znajek (1977). “Electromagnetic extraction of energy from Kerr black holes”. In: *Monthly Notices of the Royal Astronomical Society* 179, pp. 433–456. DOI: 10.1093/mnras/179.3.433.
- Bleicher, M. et al. (1999). “Relativistic hadron-hadron collisions in the ultra-relativistic quantum molecular dynamics model”. In: *Journal of Physics G Nuclear Physics* 25, pp. 1859–1896. DOI: 10.1088/0954-3899/25/9/308. eprint: hep-ph/9909407.
- Bodaghee, A. et al. (2013). “Gamma-Ray Observations of the Microquasars Cygnus X-1, Cygnus X-3, GRS 1915+105, and GX 339-4 with the Fermi Large Area Telescope”. In: *The Astrophysical Journal* 775, 98, p. 98. DOI: 10.1088/0004-637X/775/2/98. arXiv: 1307.3264 [astro-ph.HE].
- Boella, G. et al. (1997). “BeppoSAX, the wide band mission for X-ray astronomy”. In: *Astronomy and Astrophysics, Suppl. Ser.* 122, pp. 299–307. DOI: 10.1051/aas:1997136.
- Boezio, M. and E. Mocchiutti (2012). “Chemical composition of galactic cosmic rays with space experiments”. In: *Astroparticle Physics* 39, pp. 95–108. DOI: 10.1016/j.astropartphys.2012.05.007. arXiv: 1208.1406 [astro-ph.HE].
- Borla Tridon, D. et al. (2009). “Performance of the Camera of the MAGIC II Telescope”. In: *ArXiv e-prints*. arXiv: 0906.5448 [astro-ph.HE].
- Böttcher, M. and C. Dermer (1998). “High Energy Gamma Rays from Ultrahigh Energy Cosmic Ray Protons in Gamma Ray Bursts”. In: *APS April Meeting Abstracts*.
- Breeveld, A. A. and J. R. Cummings (2013). “GRB 130504A: Swift/UVOT upper limits.” In: *GRB Coordinates Network, Circular Service, No. 14556, #1 (2013)* 14556.
- Breeveld, A. A. and N. P. M. Kuin (2013). “GRB 130701A: Swift/UVOT detection.” In: *GRB Coordinates Network, Circular Service, No. 14957, #1 (2013)* 14957.
- Breit, G. and J. A. Wheeler (1934). “Collision of Two Light Quanta”. In: *Physical Review* 46, pp. 1087–1091. DOI: 10.1103/PhysRev.46.1087.
- Bretz, T. et al. (2009). “The drive system of the major atmospheric gamma-ray imaging Cherenkov telescope”. In: *Astroparticle Physics* 31, pp. 92–101. DOI: 10.1016/j.astropartphys.2008.12.001. arXiv: 0810.4593.
-

- Briggs, M. S. et al. (1999). “Observations of GRB 990123 by the Compton Gamma Ray Observatory”. In: *The Astrophysical Journal* 524, pp. 82–91. DOI: 10.1086/307808. eprint: astro-ph/9903247.
- Burns, E. for the Fermi GBM team (2014). “GRB 140709A: Fermi GBM detection.” In: *GRB Coordinates Network, Circular Service, No. 16555, #1 (2014)* 16555.
- Buson, S. and C. C. Cheung (2014). “Fermi LAT Detection of a Hard Spectrum Gamma-ray Flare from Gravitationally Lensed Blazar S3 0218+357”. In: *The Astronomer’s Telegram* 6316.
- Butler, N. et al. (2014a). “GRB 140709A: Continued RATIR Optical and NIR Observations.” In: *GRB Coordinates Network, Circular Service, No. 16575, #1 (2014)* 16575.
- Butler, N. et al. (2014b). “GRB 141026A: Continued RATIR Optical and NIR Observations.” In: *GRB Coordinates Network, Circular Service, No. 16965, #1 (2014)* 16965.
- Castro-Tirado, A. J. et al. (2013). “GRB 130606A: 10.4m GTC refined redshift  $z = 5.91$ .” In: *GRB Coordinates Network, Circular Service, No. 14796, #1 (2013)* 14796.
- Castro-Tirado, A. J. et al. (2014a). “GRB 140709A: 10.4m GTC optical decay.” In: *GRB Coordinates Network, Circular Service, No. 16564, #1 (2014)* 16564.
- Castro-Tirado, A. J. et al. (2014b). “GRB 140709A: BOOTES-2 and OSN optical observations.” In: *GRB Coordinates Network, Circular Service, No. 16554, #1 (2014)* 16554.
- Cenko, S. B. (2015). “GRB151215A: P60 Optical Afterglow Candidate.” In: *GRB Coordinates Network, Circular Service, No. 18692, #1 (2015)* 18692.
- Chatterjee, S. et al. (2017). “A direct localization of a fast radio burst and its host”. In: *Nature* 541, pp. 58–61. DOI: 10.1038/nature20797. arXiv: 1701.01098 [astro-ph.HE].
- Cherenkov Telescope Array Consortium, T. et al. (2017). “Science with the Cherenkov Telescope Array”. In: *ArXiv e-prints*. arXiv: 1709.07997 [astro-ph.IM].
- Chiba, N. et al. (1992). “Akeno Giant Air Shower Array (AGASA) covering 100 km<sup>2</sup> area”. In: *Nuclear Instruments and Methods in Physics Research Section A: Accelerators, Spectrometers, Detectors and Associated Equipment* 311.1, pp. 338–349. ISSN: 0168-9002. DOI: [http://dx.doi.org/10.1016/0168-9002\(92\)90882-5](http://dx.doi.org/10.1016/0168-9002(92)90882-5). URL: <http://www.sciencedirect.com/science/article/pii/0168900292908825>.
- Chornock, R. et al. (2013). “GRB 130606A as a Probe of the Intergalactic Medium and the Interstellar Medium in a Star-forming Galaxy in the First Gyr after the Big Bang”. In: *The Astrophysical Journal* 774, 26, p. 26. DOI: 10.1088/0004-637X/774/1/26. arXiv: 1306.3949.
- Cocconi, G. (1960). “An air shower telescope and the detection of  $10^{12}$  eV photon sources”. In: *International Cosmic Ray Conference* 2, p. 309.
- Commichau, S.C. et al. (2008). “Monte Carlo studies of geomagnetic field effects on the imaging air Cherenkov technique for the MAGIC telescope site”. In: *Nuclear Instruments and Methods in Physics Research Section A: Accelerators, Spectrometers, Detectors and Associated Equipment* 595.3, pp. 572–586. ISSN: 0168-9002. DOI: <http://dx.doi.org/10.1016/j.nima.2008.07.144>. URL: <http://www.sciencedirect.com/science/article/pii/S0168900208010978>.
- Conceição, R. (2013). “The Pierre Auger Observatory: results on the highest energy particles”. In: *ArXiv e-prints*. arXiv: 1307.3956 [astro-ph.HE].
- Connaughton, V. et al. (2016). “Fermi GBM Observations of LIGO Gravitational-wave Event GW150914”. In: *The Astrophysical Journal Letters* 826, L6, p. L6. DOI: 10.3847/2041-8205/826/1/L6. arXiv: 1602.03920 [astro-ph.HE].
- Corsi, A. (2014). “GRB 141026A: VLA observations.” In: *GRB Coordinates Network, Circular Service, No. 17019, #1 (2014)* 17019.
- Cortina, J. and M. Teshima (2015). “Status of the Cherenkov Telescope Array Large Size Telescopes”. In: *34th International Cosmic Ray Conference (ICRC2015)*. Vol. 34. International Cosmic Ray Conference, p. 943.
- Costa, E. et al. (1997a). “GRB 970228”. In: *IAU Circ.* 6572.
-

- Costa, E. et al. (1997b). “GRB 970228”. In: *IAU Circ.* 6576.
- Coulter, D. A. et al. (2017). “Swope Supernova Survey 2017a (SSS17a), the optical counterpart to a gravitational wave source”. In: *Science*. ISSN: 0036-8075. DOI: 10.1126/science.aap9811. eprint: <http://science.sciencemag.org/content/early/2017/10/13/science.aap9811.full.pdf>. URL: <http://science.sciencemag.org/content/early/2017/10/13/science.aap9811>.
- Covino, S. et al. (2017). “The unpolarized macronova associated with the gravitational wave event GW170817”. In: *ArXiv e-prints*. arXiv: 1710.05849 [astro-ph.HE].
- Cummings, J. R. et al. (2013). “Trigger 555096: Swift detection of a possible burst.” In: *GRB Coordinates Network, Circular Service, No. 14551, #1 (2013)* 14551.
- Cummings, J. R. et al. (2014). “GRB 141220A: Swift detection of a burst with an optical afterglow.” In: *GRB Coordinates Network, Circular Service, No. 17196, #1 (2014)* 17196.
- Cummings, J. R. et al. (2015). “GRB 151215A: Swift-BAT refined analysis.” In: *GRB Coordinates Network, Circular Service, No. 18699, #1 (2015)* 18699.
- Dai, Z. G. and T. Lu (2002). “Spectrum and Duration of Delayed MeV-GeV Emission of Gamma-Ray Bursts in Cosmic Background Radiation Fields”. In: *The Astrophysical Journal* 580, pp. 1013–1016. DOI: 10.1086/343848. eprint: astro-ph/0203084.
- D’Avanzo, P. et al. (2013). “Swift-XRT X-ray afterglow candidate for GRB 130504A (BAT trigger 555096).” In: *GRB Coordinates Network, Circular Service, No. 14553, #1 (2013)* 14553.
- Daylan, T. et al. (2016). “The characterization of the gamma-ray signal from the central Milky Way: A case for annihilating dark matter”. In: *Physics of the Dark Universe* 12, pp. 1–23. DOI: 10.1016/j.dark.2015.12.005. arXiv: 1402.6703 [astro-ph.HE].
- De Angelis, A., G. Galanti, and M. Roncadelli (2011). “Relevance of axionlike particles for very-high-energy astrophysics”. In: *Physical Review D* 84.10, 105030, p. 105030. DOI: 10.1103/PhysRevD.84.105030. arXiv: 1106.1132 [astro-ph.HE].
- De Angelis, A. et al. (2017). “The e-ASTROGAM mission. Exploring the extreme Universe with gamma rays in the MeV - GeV range”. In: *Experimental Astronomy* 44, pp. 25–82. DOI: 10.1007/s10686-017-9533-6. arXiv: 1611.02232 [astro-ph.HE].
- De Angelis, Alessandro, Oriana Mansutti, and Massimo Persic (2008). “Very-High Energy Gamma Astrophysics”. In: *Riv. Nuovo Cim.* 31, p. 187. DOI: 10.1393/ncr/i2008-10032-2. arXiv: 0712.0315 [astro-ph].
- de Ugarte Postigo, A. et al. (2014a). “GRB 141026A: GTC spectroscopy.” In: *GRB Coordinates Network, Circular Service, No. 16968, #1 (2014)* 16968.
- de Ugarte Postigo, A. et al. (2014b). “GRB 141220A: Photometry from OSIRIS/GTC.” In: *GRB Coordinates Network, Circular Service, No. 17200, #1 (2014)* 17200.
- de Ugarte Postigo, A. et al. (2014c). “GRB 141220A: Redshift from OSIRIS at the 10.4m GTC.” In: *GRB Coordinates Network, Circular Service, No. 17198, #1 (2014)* 17198.
- Del Monte, E. et al. (2011). “The AGILE observations of the hard and bright GRB 100724B”. In: *Astronomy and Astrophysics* 535, A120, A120. DOI: 10.1051/0004-6361/201117053. arXiv: 1109.3018 [astro-ph.HE].
- Dermer, C. D. and B. Giebels (2016). “Active galactic nuclei at gamma-ray energies”. In: *Comptes Rendus Physique* 17, pp. 594–616. DOI: 10.1016/j.crhy.2016.04.004. arXiv: 1602.06592 [astro-ph.HE].
- Di Sciascio, G. (2016). “The LHAASO experiment: from Gamma-Ray Astronomy to Cosmic Rays”. In: *ArXiv e-prints*. arXiv: 1602.07600 [astro-ph.HE].
- Djannati-Ataï, A. et al. (2017). “Probing Vela pulsar down to 20 GeV with H.E.S.S. II observations”. In: *6th International Symposium on High Energy Gamma-Ray Astronomy*. Vol. 1792. American Institute of Physics Conference Series, p. 040028. DOI: 10.1063/1.4968932.
-

- Domínguez, A. et al. (2011). “Extragalactic background light inferred from AEGIS galaxy-SED-type fractions”. In: *Monthly Notices of the Royal Astronomical Society* 410, pp. 2556–2578. DOI: 10.1111/j.1365-2966.2010.17631.x. arXiv: 1007.1459 [astro-ph.CO].
- Doro, M. et al. (2008). “The reflective surface of the MAGIC telescope”. In: *Nuclear Instruments and Methods in Physics Research A* 595, pp. 200–203. DOI: 10.1016/j.nima.2008.07.073.
- Dubus, G. (2015). “Gamma-ray emission from binaries in context”. In: *Comptes Rendus Physique* 16, pp. 661–673. DOI: 10.1016/j.crhy.2015.08.014. arXiv: 1507.00935 [astro-ph.HE].
- Duncan, R. C. and C. Thompson (1992). “Formation of very strongly magnetized neutron stars - Implications for gamma-ray bursts”. In: *Astrophysical Journal Letters* 392, pp. L9–L13. DOI: 10.1086/186413.
- Dwek, E. and F. Krennrich (2013). “The extragalactic background light and the gamma-ray opacity of the universe”. In: *Astroparticle Physics* 43, pp. 112–133. DOI: 10.1016/j.astropartphys.2012.09.003. arXiv: 1209.4661 [astro-ph.CO].
- Fan, Y.-Z. and T. Piran (2008). “High-energy  $\gamma$ -ray emission from gamma-ray bursts – before GLAST”. In: *Frontiers of Physics in China* 3, pp. 306–330. DOI: 10.1007/s11467-008-0033-z. arXiv: 0805.2221.
- Fazio, G. G. et al. (1968). “An experiment to search for discrete sources of cosmic gamma rays in the  $10^{11}$  to  $10^{12}$ eV region”. In: *Canadian Journal of Physics* 46, p. 451.
- Fernández, R. and B. D. Metzger (2016). “Electromagnetic Signatures of Neutron Star Mergers in the Advanced LIGO Era”. In: *Annual Review of Nuclear and Particle Science* 66, pp. 23–45. DOI: 10.1146/annurev-nucl-102115-044819. arXiv: 1512.05435 [astro-ph.HE].
- Fernandez-Soto, A. et al. (2009). “GRB 090423: refined TNG analysis.” In: *GRB Coordinates Network* 9222.
- Fesefeldt, H. (1985). “The Simulation of Hadronic Showers: Physics and Applications”. In: Fishman, G. J. et al. (1985). “Burst and Transient Source Experiment (BATSE) for the Gamma Ray Observatory (GRO)”. In: *International Cosmic Ray Conference* 3.
- Fishman, G. J. et al. (1993). “Overview of Observations from BATSE on the Compton Observatory”. In: *Astronomy and Astrophysics, Suppl. Ser.* 97, p. 17.
- Fishman, G. J. et al. (1994). “The first BATSE gamma-ray burst catalog”. In: *Astrophysical Journal Supplement* 92, pp. 229–283. DOI: 10.1086/191968.
- Fletcher, R. S. et al. (1994). “sibyll: An event generator for simulation of high energy cosmic ray cascades”. In: *Physical Review D* 50, pp. 5710–5731. DOI: 10.1103/PhysRevD.50.5710.
- Fomin, V.P. et al. (1994). “New methods of atmospheric Cherenkov imaging for gamma-ray astronomy. I. The false source method”. In: *Astroparticle Physics* 2.2, pp. 137–150. ISSN: 0927-6505. DOI: [http://dx.doi.org/10.1016/0927-6505\(94\)90036-1](http://dx.doi.org/10.1016/0927-6505(94)90036-1). URL: <http://www.sciencedirect.com/science/article/pii/0927650594900361>.
- Fong, W. et al. (2013). “GRB 130606A: Chandra observation.” In: *GRB Coordinates Network, Circular Service, No. 15230, #1 (2013)* 15230.
- Fraija, N. et al. (2016). “Modeling the Early Afterglow in the Short and Hard GRB 090510”. In: *The Astrophysical Journal* 831, 22, p. 22. DOI: 10.3847/0004-637X/831/1/22. arXiv: 1608.01420 [astro-ph.HE].
- Frail, D. A. and S. R. Kulkarni (1997). “GRB 970508”. In: *IAU Circ.* 6662.
- Frail, D. A. et al. (2001). “Beaming in Gamma-Ray Bursts: Evidence for a Standard Energy Reservoir”. In: *The Astrophysical Journal* 562, pp. L55–L58. DOI: 10.1086/338119. eprint: astro-ph/0102282.
- Franceschini, A. and G. Rodighiero (2017). “The extragalactic background light revisited and the cosmic photon-photon opacity”. In: *Astronomy & Astrophysics* 603, A34, A34. DOI: 10.1051/0004-6361/201629684. arXiv: 1705.10256 [astro-ph.HE].

- Fruck, C. (2015). “The Galactic Center resolved with MAGIC and a new technique for Atmospheric Calibration”. PhD Thesis. Max-Planck-Institut für Physik. URL: <https://mediatum.ub.tum.de/doc/1237928/document.pdf>.
- Fruck, C. et al. (2014). “A novel LIDAR-based Atmospheric Calibration Method for Improving the Data Analysis of MAGIC”. In: *ArXiv e-prints*. arXiv: 1403.3591 [astro-ph.IM].
- Fryer, C. L. and S. E. Woosley (1998). “Helium Star/Black Hole Mergers: A New Gamma-Ray Burst Model”. In: *The Astrophysical Journal* 502, pp. L9–L12. DOI: 10.1086/311493. eprint: astro-ph/9804167.
- Fryer, C. L. et al. (1999). “Merging White Dwarf/Black Hole Binaries and Gamma-Ray Bursts”. In: *The Astrophysical Journal* 520, pp. 650–660. DOI: 10.1086/307467. eprint: astro-ph/9808094.
- Gaisser, T. K. (1990). *Cosmic Rays and Particle Physics*. Ed. by Cambridge University Press. ISBN: 0-521-33931-6.
- Galante, N. (2006). “Very High Energy observation of GRBs with the MAGIC Telescope”. PhD Thesis. Università degli studi di Siena.
- Galbraith, W. and J.V. Jelley (1953). “Light Pulses from the Night Sky associated with Cosmic Rays”. In: *Nature* 171.4347, pp. 349–350. DOI: <http://dx.doi.org/10.1038/171349a0>. URL: <http://www.nature.com/nature/journal/v171/n4347/abs/171349a0.html>.
- Galbraith, W. and J.V. Jelley (1955). “Light-pulses from the night sky and Čerenkov radiation: Part I”. In: *Journal of Atmospheric and Terrestrial Physics* 6.1, pp. 250–262. ISSN: 0021-9169. DOI: [http://dx.doi.org/10.1016/0021-9169\(55\)90038-6](http://dx.doi.org/10.1016/0021-9169(55)90038-6). URL: <http://www.sciencedirect.com/science/article/pii/0021916955900386>.
- Galli, A. and D. Guetta (2008). “Gamma-ray burst high energy emission from internal shocks”. In: *Astronomy & Astrophysics* 480, pp. 5–13. DOI: 10.1051/0004-6361:20078518. arXiv: 0709.4568.
- García, J. R. et al. (2014). “Status of the new Sum-Trigger system for the MAGIC telescopes”. In: *ArXiv e-prints*. arXiv: 1404.4219 [astro-ph.IM].
- Garczarczyk, M. et al. (2015). “Status of the Medium-Sized Telescopes for the Cherenkov Telescope Array”. In: *34th International Cosmic Ray Conference (ICRC2015)*. Vol. 34. International Cosmic Ray Conference, p. 959.
- Gehrels, N. et al. (2004). “The Swift Gamma-Ray Burst Mission”. In: *The Astrophysical Journal* 611, pp. 1005–1020. DOI: 10.1086/422091.
- Gibson, S. L. et al. (2015). “GRB 151215A: Swift detection of a burst.” In: *GRB Coordinates Network, Circular Service, No. 18691, #1 (2015)* 18691.
- Giuliani, A. et al. (2008). “AGILE detection of delayed gamma-ray emission from GRB 080514B”. In: *Astronomy and Astrophysics* 491, pp. L25–L28. DOI: 10.1051/0004-6361:200810737. arXiv: 0809.1230.
- Giuliani, A. et al. (2010). “AGILE Detection of Delayed Gamma-ray Emission From the Short Gamma-Ray Burst GRB 090510”. In: *The Astrophysical Journal* 708, pp. L84–L88. DOI: 10.1088/2041-8205/708/2/L84. arXiv: 0908.1908 [astro-ph.HE].
- Giuliani, A. et al. (2011). “Neutral Pion Emission from Accelerated Protons in the Supernova Remnant W44”. In: *The Astrophysical Journal Letters* 742, L30, p. L30. DOI: 10.1088/2041-8205/742/2/L30. arXiv: 1111.4868 [astro-ph.HE].
- Goldstein, A. et al. (2017). “An Ordinary Short Gamma-Ray Burst with Extraordinary Implications: Fermi-GBM Detection of GRB 170817A”. In: *The Astrophysical Journal Letters* 848, L14, p. L14. DOI: 10.3847/2041-8213/aa8f41. arXiv: 1710.05446 [astro-ph.HE].
- Golenetskii, S. et al. (2013). “Konus-wind observation of GRB 130701A.” In: *GRB Coordinates Network, Circular Service, No. 14958, #1 (2013)* 14958.
- Golenetskii, S. et al. (2014). “Konus-Wind observation of GRB 141220A.” In: *GRB Coordinates Network, Circular Service, No. 17207, #1 (2014)* 17207.
-

- Gomboc, A. (2012). “Unveiling the secrets of gamma ray bursts”. In: *Contemporary Physics* 53, pp. 339–355. DOI: 10.1080/00107514.2012.701453. arXiv: 1206.3127 [astro-ph.HE].
- González, M. M. et al. (2003). “A  $\gamma$ -ray burst with a high-energy spectral component inconsistent with the synchrotron shock model”. In: *Nature* 424, pp. 749–751. DOI: 10.1038/nature01869.
- Gorosabel, J. et al. (2013). “GRB 130504A: IAC80 optical candidate.” In: *GRB Coordinates Network, Circular Service, No. 14564, #1 (2013)* 14564.
- Gorosabel, J. et al. (2014a). “GRB 140430A: BVR-band IAC80 observations.” In: *GRB Coordinates Network, Circular Service, No. 16205, #1 (2014)* 16205.
- Gorosabel, J. et al. (2014b). “GRB 141026A: 1.23m CAHA I-band observations.” In: *GRB Coordinates Network, Circular Service, No. 16954, #1 (2014)* 16954.
- Gorosabel, J. et al. (2014c). “GRB141220A: 1.23m CAHA I-band observations.” In: *GRB Coordinates Network, Circular Service, No. 17197, #1 (2014)* 17197.
- Granot, J., J. Cohen-Tanugi, and E. d. C. e. Silva (2008). “Opacity Buildup in Impulsive Relativistic Sources”. In: *The Astrophysical Journal* 677, 92–126, pp. 92–126. DOI: 10.1086/526414. arXiv: 0708.4228.
- Granot, J. and D. Guetta (2003a). “Explaining the High-Energy Spectral Component in GRB 941017”. In: *The Astrophysical Journal* 598, pp. L11–L14. DOI: 10.1086/380499. eprint: astro-ph/0309231.
- Granot, J. and D. Guetta (2003b). “Explaining the High-Energy Spectral Component in GRB 941017”. In: *The Astrophysical Journal* 598, pp. L11–L14. DOI: 10.1086/380499. eprint: astro-ph/0309231.
- Greisen, K. (1960). “Cosmic Ray Showers”. In: *Annual Review of Nuclear and Particle Science* 10, pp. 63–108. DOI: 10.1146/annurev.ns.10.120160.000431.
- Greisen, K. (1966). “End to the Cosmic-Ray Spectrum?” In: *Physical Review Letters* 16, pp. 748–750. DOI: 10.1103/PhysRevLett.16.748.
- Grenier, I. A. and A. K. Harding (2015). “Gamma-ray pulsars: A gold mine”. In: *Comptes Rendus Physique* 16, pp. 641–660. DOI: 10.1016/j.crhy.2015.08.013. arXiv: 1509.08823 [astro-ph.HE].
- Grieder, P. K. F. (2010). *Extensive Air Showers. High Energy Phenomena and Astrophysical Aspects*. Ed. by Springer. ISBN: 978-3-540-76940-8. DOI: 10.1007/978-3-540-76941-5.
- Grindlay, J. E. (1971). “Extensive Air Shower Studies of Cosmic Gamma Rays and Cosmic Ray Composition”. In: *SAO Special Report* 334.
- Groot, P. J. et al. (1997). “GRB 970228”. In: *IAU Circ.* 6584.
- Groot, P. J. et al. (1998). “A Search for Optical Afterglow from GRB 970828”. In: *The Astrophysical Journal* 493, pp. L27–L30. DOI: 10.1086/311125. eprint: astro-ph/9711171.
- Grupe, D. (2013). “GRB 130903A: further Swift XRT observations.” In: *GRB Coordinates Network, Circular Service, No. 15231, #1 (2013)* 15231.
- Grupe, D. and S. Holland (2013). “GRB 130903A: Swift-XRT observations.” In: *GRB Coordinates Network, Circular Service, No. 15173, #1 (2013)* 15173.
- Guetta, D. and J. Granot (2003a). “High-Energy Emission from the Prompt Gamma-Ray Burst”. In: *The Astrophysical Journal* 585, pp. 885–889. DOI: 10.1086/346221. eprint: astro-ph/0209578.
- Guetta, D. and J. Granot (2003b). “Observational implications of a plerionic environment for gamma-ray bursts”. In: *Monthly Notice of the Royal Astronomical Society* 340, pp. 115–138. DOI: 10.1046/j.1365-8711.2003.06296.x. eprint: astro-ph/0208156.
- Guidorzi, C. and A. Gomboc (2014). “GRB 141220A: LT optical afterglow observations.” In: *GRB Coordinates Network, Circular Service, No. 17199, #1 (2014)* 17199.
- Guiriec, S. et al. (2011). “Detection of a Thermal Spectral Component in the Prompt Emission of GRB 100724B”. In: *The Astrophysical Journal Letters* 727, L33, p. L33. DOI: 10.1088/2041-8205/727/2/L33. arXiv: 1010.4601 [astro-ph.HE].
-

- Hagen, L. M. Z. et al. (2014a). “GRB 140709A: Swift detection of a burst.” In: *GRB Coordinates Network, Circular Service, No. 16546, #1 (2014)* 16546.
- Hagen, L. M. Z. et al. (2014b). “GRB 141026A: Swift detection of a burst.” In: *GRB Coordinates Network, Circular Service, No. 16950, #1 (2014)* 16950.
- Harrison, F. A. et al. (1999). “Optical and Radio Observations of the Afterglow from GRB 990510: Evidence for a Jet”. In: *The Astrophysical Journal* 523, pp. L121–L124. DOI: 10.1086/312282. eprint: astro-ph/9905306.
- Hartoog, O. E. et al. (2015). “VLT/X-Shooter spectroscopy of the afterglow of the Swift GRB 130606A. Chemical abundances and reionisation at  $z \sim 6$ ”. In: *Astronomy & Astrophysics* 580, A139, A139. DOI: 10.1051/0004-6361/201425001. arXiv: 1409.4804.
- Hassan, T. et al. (2017). “MAGIC sensitivity to millisecond-duration optical pulses”. In: *ArXiv e-prints*. arXiv: 1708.07698 [astro-ph.IM].
- Heck, D. et al. (1998). *CORSIKA: a Monte Carlo code to simulate extensive air showers*.
- Heise, J. et al. (2001). “X-Ray Flashes and X-Ray Rich Gamma Ray Bursts”. In: *Gamma-ray Bursts in the Afterglow Era*. Ed. by E. Costa, F. Frontera, and J. Hjorth, p. 16. DOI: 10.1007/10853853\_4.
- Heitler, Walter (1954). *The Quantum Theory of Radiation*. Monographs on Physics. Oxford University Press.
- H.E.S.S. Collaboration et al. (2011). “A new SNR with TeV shell-type morphology: HESS J1731-347”. In: *Astronomy & Astrophysics* 531, A81, A81. DOI: 10.1051/0004-6361/201016425. arXiv: 1105.3206 [astro-ph.HE].
- H.E.S.S. Collaboration et al. (2014). “Search for TeV Gamma-ray Emission from GRB 100621A, an extremely bright GRB in X-rays, with H.E.S.S.” In: *Astronomy & Astrophysics* 565, A16, A16. DOI: 10.1051/0004-6361/201322984. arXiv: 1405.0488 [astro-ph.HE].
- H.E.S.S. Collaboration et al. (2015). “The exceptionally powerful TeV  $\gamma$ -ray emitters in the Large Magellanic Cloud”. In: *Science* 347, pp. 406–412. DOI: 10.1126/science.1261313. arXiv: 1501.06578 [astro-ph.HE].
- Hewitt, J. W. and M. Lemoine-Goumard (2015). “Observations of supernova remnants and pulsar wind nebulae at gamma-ray energies”. In: *Comptes Rendus Physique* 16, pp. 674–685. DOI: 10.1016/j.crhy.2015.08.015. arXiv: 1510.01213 [astro-ph.HE].
- Hill, D. A. and N. A. Porter (1961). “Photography of Čerenkov Light from Extensive Air Showers in the Atmosphere”. In: *Nature* 191, p. 690. DOI: 10.1038/191690a0.
- Hillas, A M (1982). “The sensitivity of Cerenkov radiation pulses to the longitudinal development of cosmic-ray showers”. In: *Journal of Physics G: Nuclear Physics* 8.10, p. 1475. URL: <http://stacks.iop.org/0305-4616/8/i=10/a=017>.
- Hillas, A. M. (1985). “Cerenkov light images of EAS produced by primary gamma”. In: *International Cosmic Ray Conference* 3, pp. 445–448.
- Hjorth, J. et al. (2005). “The optical afterglow of the short  $\gamma$ -ray burst GRB 050709”. In: *Nature* 437, pp. 859–861. DOI: 10.1038/nature04174. eprint: astro-ph/0510096.
- Holland, S. T. and D. Grupe (2013). “GRB 130903A: Swift/UVOT upper limits.” In: *GRB Coordinates Network, Circular Service, No. 15181, #1 (2013)* 15181.
- Hughes, E. B. et al. (1980). “Characteristics of the telescope for high energy gamma-ray astronomy selected for definition studies on the Gamma Ray Observatory”. In: *IEEE Transactions on Nuclear Science* 27, pp. 364–369.
- Hulse, R. A. and J. H. Taylor (1975). “Discovery of a pulsar in a binary system”. In: *The Astrophysical Journal Letters* 195, pp. L51–L53. DOI: 10.1086/181708.
- Hurley, K. et al. (1994). “Detection of a  $\gamma$ -ray burst of very long duration and very high energy”. In: *Nature* 372, pp. 652–654. DOI: 10.1038/372652a0.
- Jarvinen, A. and J. Gorosabel (2014). “GRB 140430A: r'-band STELLA-I observations.” In: *GRB Coordinates Network, Circular Service, No. 16211, #1 (2014)* 16211.
-

- Jelley, J. V. and N. A. Porter (1963). “Cerenkov Radiation from the Night Sky”. In: *Quarterly Journal of the Royal Astronomical Society* 4, p. 275.
- Jelley, J.V. and W. Galbraith (1955). “Light pulses from the night sky and Čerenkov radiation: Part II”. In: *Journal of Atmospheric and Terrestrial Physics* 6.1–6, pp. 304–312. ISSN: 0021-9169. DOI: [http://dx.doi.org/10.1016/0021-9169\(55\)90047-7](http://dx.doi.org/10.1016/0021-9169(55)90047-7). URL: <http://www.sciencedirect.com/science/article/pii/0021916955900477>.
- Kalmykov, N. N., S. S. Ostapchenko, and A. I. Pavlov (1997). “Quark-Gluon-String Model and EAS Simulation Problems at Ultra-High Energies”. In: *Nuclear Physics B Proceedings Supplements* 52, pp. 17–28. DOI: 10.1016/S0920-5632(96)00846-8.
- Kamata, K. and J. Nishimura (1958). “The Lateral and the Angular Structure Functions of Electron Showers”. In: *Progress of Theoretical Physics Supplement* 6, pp. 93–155. DOI: 10.1143/PTPS.6.93.
- Kampert, Karl-Heinz and Alan A. Watson (2012). “Extensive air showers and ultra high-energy cosmic rays: a historical review”. In: *The European Physical Journal H* 37.3, pp. 359–412. ISSN: 2102-6467. DOI: 10.1140/epjh/e2012-30013-x. URL: <https://doi.org/10.1140/epjh/e2012-30013-x>.
- Katagiri, Hideaki et al. (2005). “Detection of gamma-rays around 1-TeV from RX J0852.0-4622 by CANGAROO-II”. In: *Astrophysical Journal* 619, pp. L163–L166. DOI: 10.1086/427980. eprint: [astro-ph/0412623](http://arxiv.org/abs/astro-ph/0412623).
- Kennedy, M. (2014). “GRB 140430A: VATT Optical Observations.” In: *GRB Coordinates Network, Circular Service, No. 16196, #1 (2014)* 16196.
- Kennedy, M. and P. Garnavich (2014). “GRB 140430A: Further VATT Optical Observations.” In: *GRB Coordinates Network, Circular Service, No. 16201, #1 (2014)* 16201.
- Kifune, T. (1999). “Invariance Violation Extends the Cosmic-Ray Horizon?” In: *The Astrophysical Journal Letters* 518, pp. L21–L24. DOI: 10.1086/312057. eprint: [astro-ph/9904164](http://arxiv.org/abs/astro-ph/9904164).
- Klebesadel, R. W., I. B. Strong, and R. A. Olson (1973). “Observations of Gamma-Ray Bursts of Cosmic Origin”. In: *Astrophysical Journal* 182, p. L85. DOI: 10.1086/181225.
- Koide, S., K. Shibata, and T. Kudoh (1999). “Relativistic Jet Formation from Black Hole Magnetized Accretion Disks: Method, Tests, and Applications of a General Relativistic-Magnetohydrodynamic Numerical Code”. In: *The Astrophysical Journal* 522, pp. 727–752. DOI: 10.1086/307667.
- Kopač, D. et al. (2015). “Limits on Optical Polarization during the Prompt Phase of GRB 140430A”. In: *The Astrophysical Journal* 813, 1, p. 1. DOI: 10.1088/0004-637X/813/1/1. arXiv: 1509.03099 [astro-ph.HE].
- Kouveliotou, C. et al. (2013). “NuSTAR Observations of GRB 130427A Establish a Single Component Synchrotron Afterglow Origin for the Late Optical to Multi-GeV Emission”. In: *The Astrophysical Journal Letters* 779, L1, p. L1. DOI: 10.1088/2041-8205/779/1/L1. arXiv: 1311.5245 [astro-ph.HE].
- Krimm, H. A. et al. (2014). “GRB 140430A: Swift-BAT refined analysis.” In: *GRB Coordinates Network, Circular Service, No. 16200, #1 (2014)* 16200.
- Kruehler, T. et al. (2014). “GRB 140430A: VLT/X-shooter redshift.” In: *GRB Coordinates Network, Circular Service, No. 16194, #1 (2014)* 16194.
- Kuin, N. P. M. et al. (2013). “GRB 130701A: Swift detection of a burst.” In: *GRB Coordinates Network, Circular Service, No. 14953, #1 (2013)* 14953.
- Kulkarni, S. R. et al. (1998). “Identification of a host galaxy at redshift  $z = 3.42$  for the  $\gamma$ -ray burst of 14 December 1997”. In: *Nature* 393, pp. 35–39. DOI: 10.1038/29927.
- Kumar, P. and B. Zhang (2015). “The physics of gamma-ray bursts and relativistic jets”. In: *Physics Reports* 561, pp. 1–109. DOI: 10.1016/j.physrep.2014.09.008. arXiv: 1410.0679 [astro-ph.HE].
- Kuroda, D. et al. (2013). “GRB 130504A: Mitsume okayama upper limits.” In: *GRB Coordinates Network, Circular Service, No. 14562, #1 (2013)* 14562.

- Lafferty, G.D. and T.R. Wyatt (1995). “Where to stick your data points: The treatment of measurements within wide bins”. In: *Nuclear Instruments and Methods in Physics Research Section A: Accelerators, Spectrometers, Detectors and Associated Equipment* 355.2, pp. 541–547. ISSN: 0168-9002. DOI: [http://dx.doi.org/10.1016/0168-9002\(94\)01112-5](http://dx.doi.org/10.1016/0168-9002(94)01112-5). URL: <http://www.sciencedirect.com/science/article/pii/S0168900294011125>.
- Lee, W. H. and W. Kluźniak (1999). “Newtonian hydrodynamics of the coalescence of black holes with neutron stars - II. Tidally locked binaries with a soft equation of state”. In: *Monthly Notices of the Royal Astronomical Society* 308, pp. 780–794. DOI: 10.1046/j.1365-8711.1999.02734.x. eprint: [astro-ph/9904328](http://arxiv.org/abs/astro-ph/9904328).
- Leloudas, G. et al. (2013). “GRB 130701A: optical afterglow from the NOT.” In: *GRB Coordinates Network, Circular Service, No. 14954, #1 (2013)* 14954.
- Lemoine, M. and G. Pelletier (2015). “On the origin of very-high-energy photons in astrophysics: A short introduction to acceleration and radiation physics”. In: *Comptes Rendus Physique* 16, pp. 628–640. DOI: 10.1016/j.crhy.2015.08.012.
- Li, T.-P. and Y.-Q. Ma (1983). “Analysis methods for results in gamma-ray astronomy”. In: *The Astrophysical Journal* 272, pp. 317–324. DOI: 10.1086/161295.
- LIGO Scientific Collaboration et al. (2015). “Advanced LIGO”. In: *Classical and Quantum Gravity* 32.7, 074001, p. 074001. DOI: 10.1088/0264-9381/32/7/074001. arXiv: 1411.4547 [gr-qc].
- Lipari, Paolo (2009). “Concepts of “age” and “universality” in cosmic ray showers”. In: *Phys. Rev. D* 79 (6), p. 063001. DOI: 10.1103/PhysRevD.79.063001. URL: <http://link.aps.org/doi/10.1103/PhysRevD.79.063001>.
- Lipunov, V. M. et al. (2017). “MASTER optical detection of the first LIGO/Virgo neutron stars merging GW170817”. In: *ArXiv e-prints*. arXiv: 1710.05461 [astro-ph.HE].
- Lithwick, Y. and R. Sari (2001). “Lower Limits on Lorentz Factors in Gamma-Ray Bursts”. In: *The Astrophysical Journal* 555, pp. 540–545. DOI: 10.1086/321455. eprint: [astro-ph/0011508](http://arxiv.org/abs/astro-ph/0011508).
- Littlejohns, O. et al. (2014a). “GRB 141026A: Continued RATIR Optical and NIR Observations.” In: *GRB Coordinates Network, Circular Service, No. 16970, #1 (2014)* 16970.
- Littlejohns, O. et al. (2014b). “GRB 141026A: RATIR Optical Observations.” In: *GRB Coordinates Network, Circular Service, No. 16952, #1 (2014)* 16952.
- Liu, R.-Y., X.-Y. Wang, and X.-F. Wu (2013). “Interpretation of the Unprecedentedly Long-lived High-energy Emission of GRB 130427A”. In: *The Astrophysical Journal Letters* 773, L20, p. L20. DOI: 10.1088/2041-8205/773/2/L20. arXiv: 1306.5207 [astro-ph.HE].
- Loeb, A. (2016). “Electromagnetic Counterparts to Black Hole Mergers Detected by LIGO”. In: *The Astrophysical Journal Letters* 819, L21, p. L21. DOI: 10.3847/2041-8205/819/2/L21. arXiv: 1602.04735 [astro-ph.HE].
- Longair, M. S. (2011). *High Energy Astrophysics*. Ed. by Cambridge University Press. ISBN: 9780521756181.
- Longo, F. et al. (2012). “Upper limits on the high-energy emission from gamma-ray bursts observed by AGILE-GRID”. In: *Astronomy and Astrophysics* 547, A95, A95. DOI: 10.1051/0004-6361/201016238.
- Lopez, M. (2013). “Simulations of the MAGIC Telescopes with Matelsim”. In: *Proceedings, 33rd International Cosmic Ray Conference (ICRC2013): Rio de Janeiro, Brazil, July 2-9, 2013*.
- López Coto, Rubén (2017). “Very-high-energy Gamma-ray Observations of Pulsar Wind Nebulae and Cataclysmic Variable Stars with MAGIC and Development of Trigger Systems for IACTs”. PhD thesis. Universitat Autònoma de Barcelona. DOI: 10.1007/978-3-319-44751-3.
- Lunnan, R. et al. (2013). “GRB 130606A: MMT spectroscopy.” In: *GRB Coordinates Network, Circular Service, No. 14798, #1 (2013)* 14798.
-

- LVC collaboration (2016). *The LSC-Virgo White Paper on Gravitational Wave Searches and Astrophysics (2016-2017 edition)*. URL: <https://dcc.ligo.org/LIGO-T1600115/public>.
- Lyne, A. et al. (2010). “Switched Magnetospheric Regulation of Pulsar Spin-Down”. In: *Science* 329, p. 408. DOI: 10.1126/science.1186683. arXiv: 1006.5184 [astro-ph.GA].
- Lyubarsky, Y. (2014). “A model for fast extragalactic radio bursts”. In: *Monthly Notices of the Royal Astronomical Society* 442, pp. L9–L13. DOI: 10.1093/mnrasl/slu046. arXiv: 1401.6674 [astro-ph.HE].
- MacFadyen, A. I. and S. E. Woosley (1999). “Collapsars: Gamma-Ray Bursts and Explosions in “Failed Supernovae””. In: *Astrophysical Journal* 524, pp. 262–289. DOI: 10.1086/307790. eprint: astro-ph/9810274.
- MacFadyen, A. I., S. E. Woosley, and A. Heger (2001). “Supernovae, Jets, and Collapsars”. In: *The Astrophysical Journal* 550, pp. 410–425. DOI: 10.1086/319698. eprint: astro-ph/9910034.
- Majumdar, P. et al. (2005). “Monte Carlo simulation for the MAGIC telescope”. In: *International Cosmic Ray Conference* 5, p. 203.
- Malesani, D. et al. (2014). “GRB 140430A: NOT optical observations.” In: *GRB Coordinates Network, Circular Service, No. 16193, #1 (2014)* 16193.
- Malyshev, D., A. A. Zdziarski, and M. Chernyakova (2013). “High-energy gamma-ray emission from Cyg X-1 measured by Fermi and its theoretical implications”. In: *Monthly Notices of the Royal Astronomical Society* 434, pp. 2380–2389. DOI: 10.1093/mnras/stt1184. arXiv: 1305.5920 [astro-ph.HE].
- Markwardt, C. B. et al. (2014). “GRB 140709A, Swift-BAT refined analysis.” In: *GRB Coordinates Network, Circular Service, No. 16553, #1 (2014)* 16553.
- Markwardt, C. B. et al. (2015). “GRB 151118A, Swift-BAT refined analysis.” In: *GRB Coordinates Network, Circular Service, No. 18622, #1 (2015)* 18622.
- Marshall, F. E. and J. R. Cummings (2014). “GRB 141220A: Swift/UVOT Detection.” In: *GRB Coordinates Network, Circular Service, No. 17201, #1 (2014)* 17201.
- Masi, G. (2014). “GRB 140709A : Virtual Telescope optical observations.” In: *GRB Coordinates Network, Circular Service, No. 16559, #1 (2014)* 16559.
- Matthews, J (2001). “Energy flow in extensive air showers”. In: *Proceedings of ICRC*. Vol. 2001. 261.
- Matthews, J. (2005). “A Heitler model of extensive air showers”. In: *Astroparticle Physics* 22, pp. 387–397. DOI: 10.1016/j.astropartphys.2004.09.003.
- Meegan, C. A. et al. (1996). “The Third BATSE Gamma-Ray Burst Catalog”. In: *Astrophysical Journal Supplement* 106, p. 65. DOI: 10.1086/192329.
- Meier, D. L. (1999). “A Magnetically Switched, Rotating Black Hole Model for the Production of Extragalactic Radio Jets and the Fanaroff and Riley Class Division”. In: *The Astrophysical Journal* 522, pp. 753–766. DOI: 10.1086/307671. eprint: astro-ph/9810352.
- Melandri, A. et al. (2014). “GRB 140430A : Liverpool Telescope optical afterglow observations.” In: *GRB Coordinates Network, Circular Service, No. 16192, #1 (2014)* 16192.
- Merck, M. et al. (1995). “Observations of High-energy Gamma-ray Bursts with EGRET”. In: *International Astronomical Union Colloquium* 151, 358–362. DOI: 10.1017/S0252921100035351.
- Mereghetti, S. et al. (2013). “GRB 130903A: a long GRB detected by INTEGRAL.” In: *GRB Coordinates Network, Circular Service, No. 15169, #1 (2013)* 15169.
- Mészáros, P. and S. Razzaque (2007). “Theoretical Aspects of High Energy Neutrinos and GRB”. In: *Energy Budget in the High Energy Universe*. Ed. by K. Sato and J. Hisano, pp. 84–93. DOI: 10.1142/9789812708342\_0009. eprint: astro-ph/0605166.
- Metzger, B. D. and E. Berger (2012). “What is the Most Promising Electromagnetic Counterpart of a Neutron Star Binary Merger?” In: *The Astrophysical Journal* 746, 48, p. 48. DOI: 10.1088/0004-637X/746/1/48. arXiv: 1108.6056 [astro-ph.HE].
-

- Metzger, M. R. et al. (1997). “GRB 970508”. In: *IAU Circ.* 6676.
- Mirzoyan, R. (2012). “Beginnings of the Atmospheric Air Cherenkov Technique”. URL: <https://agenda.infn.it/getFile.py/access?contribId=45&sessionId=3&resId=0&materialId=slides&confId=4267>.
- Mirzoyan, R. (2014). “Discovery of Very High Energy Gamma-Ray Emission From Gravitationally Lensed Blazar S3 0218+357 With the MAGIC Telescopes”. In: *The Astronomer’s Telegram* 6349, p. 1.
- Mirzoyan, R. (2015). “Discovery of Very High Energy Gamma-Ray Emission from the distant FSRQ PKS 1441+25 with the MAGIC telescopes”. In: *The Astronomer’s Telegram* 7416, p. 1.
- Mirzoyan, R. and E. Lorenz (1997). “On the Calibration Accuracy of Light Sensors in Atmospheric Cherenkov Fluorescence and Neutrino Experiments”. In: *International Cosmic Ray Conference* 7, p. 265.
- Montaruli, T. et al. (2015). “The small size telescope projects for the Cherenkov Telescope Array”. In: *34th International Cosmic Ray Conference (ICRC2015)*. Vol. 34. International Cosmic Ray Conference, p. 1043.
- Muraishi, H. et al. (2000). “Evidence for TeV gamma-ray emission from the shell type SNR RX J1713.7-3946”. In: *Astronomy and Astrophysics* 354, pp. L57–L61. eprint: [astro-ph/0001047](https://arxiv.org/abs/astro-ph/0001047).
- Murase, K., K. Kashiyama, and P. Mészáros (2016). “A burst in a wind bubble and the impact on baryonic ejecta: high-energy gamma-ray flashes and afterglows from fast radio bursts and pulsar-driven supernova remnants”. In: *Monthly Notices of the Royal Astronomical Society* 461, pp. 1498–1511. DOI: 10.1093/mnras/stw1328. arXiv: 1603.08875 [astro-ph.HE].
- Nagano, M. and A. A. Watson (2000). “Observations and implications of the ultrahigh-energy cosmic rays”. In: *Reviews of Modern Physics* 72, pp. 689–732. DOI: 10.1103/RevModPhys.72.689.
- Naurois, Mathieu de and Daniel Mazin (2015). “Ground-based detectors in very-high-energy gamma-ray astronomy”. In: *Comptes Rendus Physique* 16.6–7. Gamma-ray astronomy / Astronomie des rayons gamma, pp. 610–627. ISSN: 1631-0705. DOI: <http://dx.doi.org/10.1016/j.crhy.2015.08.011>. URL: <http://www.sciencedirect.com/science/article/pii/S1631070515001462>.
- Nesterova, N.M. and A.E. Chudakov (1955). “On the Observation of Cerenkov Radiation Accompanying Broad Atmospheric Showers of Cosmic Rays”. English. In: *Journal of Experimental and Theoretical Physics* 1.2, pp. 388–389. URL: [http://www.jetp.ac.ru/cgi-bin/dn/e\\_001\\_02\\_0388.pdf](http://www.jetp.ac.ru/cgi-bin/dn/e_001_02_0388.pdf).
- Netzer, H. (2015). “Revisiting the Unified Model of Active Galactic Nuclei”. In: *Annual Review of Astronomy and Astrophysics* 53, pp. 365–408. DOI: 10.1146/annurev-astro-082214-122302. arXiv: 1505.00811.
- Nozzoli, F. (2017). “Precision measurement of antiproton to proton ratio with the Alpha Magnetic Spectrometer on the International Space Station”. In: *ArXiv e-prints*. arXiv: 1701.00086 [astro-ph.HE].
- Ohm, S. (2016). “Starburst galaxies as seen by gamma-ray telescopes”. In: *Comptes Rendus Physique* 17, pp. 585–593. DOI: 10.1016/j.crhy.2016.04.003. arXiv: 1601.06386 [astro-ph.HE].
- Olive, K. A. et al. (2014). “Review of Particle Physics”. In: *Chin. Phys.* C38, p. 090001. DOI: 10.1088/1674-1137/38/9/090001.
- Paciesas, W. S. et al. (1999). “The Fourth BATSE Gamma-Ray Burst Catalog (Revised)”. In: *The Astrophysical Journal Supplement Series* 122, pp. 465–495. DOI: 10.1086/313224. eprint: [astro-ph/9903205](https://arxiv.org/abs/astro-ph/9903205).
- Padovani, P. et al. (2017). “Active galactic nuclei: what’s in a name?” In: *The Astronomy and Astrophysics Review* 25, 2, p. 2. DOI: 10.1007/s00159-017-0102-9. arXiv: 1707.07134.
-

- Pagani, C. et al. (2015). “GRB 151118A: Swift-XRT refined Analysis.” In: *GRB Coordinates Network, Circular Service, No. 18617, #1 (2015)* 18617.
- Palmer, D. M. et al. (2013). “GRB 130504A, Swift-BAT refined analysis.” In: *GRB Coordinates Network, Circular Service, No. 14554, #1 (2013)* 14554.
- Pe’er, A. and E. Waxman (2004). “The High-Energy Tail of GRB 941017: Comptonization of Synchrotron Self-absorbed Photons”. In: *The Astrophysical Journal* 603, pp. L1–L4. DOI: 10.1086/382872. eprint: astro-ph/0310836.
- Perna, R., D. Lazzati, and B. Giacomazzo (2016). “Short Gamma-Ray Bursts from the Merger of Two Black Holes”. In: *The Astrophysical Journal Letters* 821, L18, p. L18. DOI: 10.3847/2041-8205/821/1/L18. arXiv: 1602.05140 [astro-ph.HE].
- Petroff, E. et al. (2016). “FRBCAT: The Fast Radio Burst Catalogue”. In: *Publications of the Astronomical Society of Australia* 33, e045, e045. DOI: 10.1017/pasa.2016.35. arXiv: 1601.03547 [astro-ph.HE].
- Pian, E. et al. (1999). “BeppoSAX detection and follow-up of GRB 980425”. In: *Astronomy and Astrophysics Supplement* 138, pp. 463–464. DOI: 10.1051/aas:1999310. eprint: astro-ph/9903113.
- Pian, E. et al. (2017). “Spectroscopic identification of r-process nucleosynthesis in a double neutron star merger”. In: *ArXiv e-prints*. arXiv: 1710.05858 [astro-ph.HE].
- Piran, T. (2004). “The physics of gamma-ray bursts”. In: *Reviews of Modern Physics* 76, pp. 1143–1210. DOI: 10.1103/RevModPhys.76.1143. eprint: astro-ph/0405503.
- Piro, L. et al. (1996). “GRB 960720”. In: *IAU Circ.* 6480.
- Pitkin, M. et al. (2011). “Gravitational Wave Detection by Interferometry (Ground and Space)”. In: *Living Reviews in Relativity* 14, 5, p. 5. DOI: 10.12942/lrr-2011-5. arXiv: 1102.3355 [astro-ph.IM].
- Plyasheshnikov, A.V. and G.F. Bignami (1985). “Investigation on the effectiveness of VHE gamma-ray astronomy techniques based on imaging of Čerenkov light flashes”. English. In: *Il Nuovo Cimento C* 8.1, pp. 39–54. ISSN: 0390-5551. DOI: 10.1007/BF02507701. URL: <http://dx.doi.org/10.1007/BF02507701>.
- Pritchard, T. A. and T. N. Ukwatta (2013). “GRB 130606A: Swift/UVOT upper limits.” In: *GRB Coordinates Network, Circular Service, No. 14814, #1 (2013)* 14814.
- Punch, M. et al. (1992). “Detection of TeV photons from the active galaxy Markarian 421”. In: *Nature* 358, p. 477. DOI: 10.1038/358477a0.
- Quadri, U. et al. (2013). “GRB 130504A: bassano bresciano observatory optical upper limit.” In: *GRB Coordinates Network, Circular Service, No. 14559, #1 (2013)* 14559.
- Ranft, J. (1995). “Dual parton model at cosmic ray energies”. In: *Physical Review D* 51, pp. 64–84. DOI: 10.1103/PhysRevD.51.64.
- Razzaque, S., C. D. Dermer, and J. D. Finke (2010). “Synchrotron Radiation from Ultra-High Energy Protons and the Fermi Observations of GRB 080916C”. In: *The Open Astronomy Journal* 3, pp. 150–155. DOI: 10.2174/1874381101003010150. arXiv: 0908.0513 [astro-ph.HE].
- Rees, M. J. and P. Meszaros (1992). “Relativistic fireballs - Energy conversion and time-scales”. In: *Monthly Notices of the Royal Astronomical Society* 258, 41P–43P. DOI: 10.1093/mnras/258.1.41P.
- Rees, M. J. and P. Meszaros (1994). “Unsteady outflow models for cosmological gamma-ray bursts”. In: *Astrophysical Journal Letters* 430, pp. L93–L96. DOI: 10.1086/187446. eprint: astro-ph/9404038.
- Ricker, G. R. et al. (2003). “The High Energy Transient Explorer (HETE): Mission and Science Overview”. In: *Gamma-Ray Burst and Afterglow Astronomy 2001: A Workshop Celebrating the First Year of the HETE Mission*. Ed. by G. R. Ricker and R. K. Vanderpek. Vol. 662. American Institute of Physics Conference Series, pp. 3–16. DOI: 10.1063/1.1579291.

- Riles, K. (2013). “Gravitational waves: Sources, detectors and searches”. In: *Progress in Particle and Nuclear Physics* 68, pp. 1–54. DOI: 10.1016/j.ppnp.2012.08.001. arXiv: 1209.0667 [hep-ex].
- Rolke, W. A., A. M. López, and J. Conrad (2005). “Limits and confidence intervals in the presence of nuisance parameters”. In: *Nuclear Instruments and Methods in Physics Research A* 551, pp. 493–503. DOI: 10.1016/j.nima.2005.05.068. eprint: physics/0403059.
- Rossi, Bruno and Kenneth Greisen (1941). “Cosmic-Ray Theory”. In: *Rev. Mod. Phys.* 13 (4), pp. 240–309. DOI: 10.1103/RevModPhys.13.240. URL: <http://link.aps.org/doi/10.1103/RevModPhys.13.240>.
- Sakamoto, T. et al. (2005). “Global Characteristics of X-Ray Flashes and X-Ray-Rich Gamma-Ray Bursts Observed by HETE-2”. In: *The Astrophysical Journal* 629, pp. 311–327. DOI: 10.1086/431235.
- Sakamoto, T. et al. (2013). “GRB 130701A, Swift-BAT refined analysis.” In: *GRB Coordinates Network, Circular Service, No. 14959, #1 (2013)* 14959.
- Sakamoto, T. et al. (2015). “GRB 150819A: Swift-BAT refined analysis.” In: *GRB Coordinates Network, Circular Service, No. 18170, #1 (2015)* 18170.
- Sari, R. and A. A. Esin (2001). “On the Synchrotron Self-Compton Emission from Relativistic Shocks and Its Implications for Gamma-Ray Burst Afterglows”. In: *The Astrophysical Journal* 548, pp. 787–799. DOI: 10.1086/319003. eprint: astro-ph/0005253.
- Sathyaprakash, B. et al. (2012). “Scientific objectives of Einstein Telescope”. In: *Classical and Quantum Gravity* 29.12, 124013, p. 124013. DOI: 10.1088/0264-9381/29/12/124013. arXiv: 1206.0331 [gr-qc].
- Sathyaprakash, B. S. and B. F. Schutz (2009). “Physics, Astrophysics and Cosmology with Gravitational Waves”. In: *Living Reviews in Relativity* 12, 2, p. 2. DOI: 10.12942/lrr-2009-2. arXiv: 0903.0338 [gr-qc].
- Savchenko, V. et al. (2016). “INTEGRAL Upper Limits on Gamma-Ray Emission Associated with the Gravitational Wave Event GW150914”. In: *The Astrophysical Journal Letters* 820, L36, p. L36. DOI: 10.3847/2041-8205/820/2/L36. arXiv: 1602.04180 [astro-ph.HE].
- Schmelling, M. (1994). “The method of reduced cross-entropy A general approach to unfold probability distributions”. In: *Nuclear Instruments and Methods in Physics Research A* 340, pp. 400–412. DOI: 10.1016/0168-9002(94)90119-8.
- Siegel, M. H. et al. (2014). “GRB140430A: Swift detection of a burst with an optical counterpart.” In: *GRB Coordinates Network, Circular Service, No. 16190, #1 (2014)* 16190.
- Singer, L. P. and L. R. Price (2016). “Rapid Bayesian position reconstruction for gravitational-wave transients”. In: *Physical Review D* 93.2, 024013, p. 024013. DOI: 10.1103/PhysRevD.93.024013. arXiv: 1508.03634 [gr-qc].
- Singer, L. P. et al. (2014). “The First Two Years of Electromagnetic Follow-up with Advanced LIGO and Virgo”. In: *The Astrophysical Journal* 795, 105, p. 105. DOI: 10.1088/0004-637X/795/2/105. arXiv: 1404.5623 [astro-ph.HE].
- Sitarek, J. et al. (2013). “Analysis techniques and performance of the Domino Ring Sampler version 4 based readout for the MAGIC telescopes”. In: *Nuclear Instruments and Methods in Physics Research A* 723, pp. 109–120. DOI: 10.1016/j.nima.2013.05.014. arXiv: 1305.1007 [astro-ph.IM].
- Soares-Santos, M. et al. (2017). “The Electromagnetic Counterpart of the Binary Neutron Star Merger LIGO/Virgo GW170817. I. Discovery of the Optical Counterpart Using the Dark Energy Camera”. In: *The Astrophysical Journal Letters* 848.2, p. L16. URL: <http://stacks.iop.org/2041-8205/848/i=2/a=L16>.
- Sokolsky, P. and HiRes Collaboration (2011). “Final Results from the High resolution Fly#700s Eye (HiRes) Experiment”. In: *Nuclear Physics B Proceedings Supplements* 212, pp. 74–78. DOI: 10.1016/j.nuclphysbps.2011.03.010. arXiv: 1010.2690 [astro-ph.HE].
-

- Spitler, L. G. et al. (2016). “A repeating fast radio burst”. In: *Nature* 531, pp. 202–205. DOI: 10.1038/nature17168. arXiv: 1603.00581 [astro-ph.HE].
- Spurio, M. (2015). *Particles and Astrophysics. A Multi-Messenger Approach*. Ed. by Springer. ISBN: 978-3-319-08050-5. DOI: 10.1007/978-3-319-08051-2.
- Stamatikos, M. et al. (2014a). “GRB 141026A: Swift-BAT refined analysis.” In: *GRB Coordinates Network, Circular Service, No. 16960, #1 (2014)* 16960.
- Stamatikos, M. et al. (2014b). “GRB 141220A: Swift-BAT refined analysis.” In: *GRB Coordinates Network, Circular Service, No. 17202, #1 (2014)* 17202.
- Stanek, K. Z. et al. (2003). “Spectroscopic Discovery of the Supernova 2003dh Associated with GRB 030329”. In: *The Astrophysical Journal* 591, pp. L17–L20. DOI: 10.1086/376976. eprint: astro-ph/0304173.
- Su, M. and C. van Eldik (2015). “Gamma rays from the Galactic Centre region”. In: *Comptes Rendus Physique* 16, pp. 686–703. DOI: 10.1016/j.crhy.2015.09.001.
- Syrovatskii, S. I. (1971). “Cosmic Rays of Ultra-High Energy”. In: *Comments on Astrophysics and Space Physics* 3, p. 155.
- Szanecki, M. et al. (2013). “Influence of the geomagnetic field on the {IACT} detection technique for possible sites of {CTA} observatories”. In: *Astroparticle Physics* 45, pp. 1–12. ISSN: 0927-6505. DOI: <http://dx.doi.org/10.1016/j.astropartphys.2013.02.002>. URL: <http://www.sciencedirect.com/science/article/pii/S0927650513000285>.
- Takami, H., K. Kyutoku, and K. Ioka (2014). “High-energy radiation from remnants of neutron star binary mergers”. In: *Physical Review D* 89.6, 063006, p. 063006. DOI: 10.1103/PhysRevD.89.063006. arXiv: 1307.6805 [astro-ph.HE].
- Takeda, M. et al. (1998). “Extension of the Cosmic-Ray Energy Spectrum beyond the Predicted Greisen-Zatsepin-Kuz’min Cutoff”. In: *Physical Review Letters* 81, pp. 1163–1166. DOI: 10.1103/PhysRevLett.81.1163. eprint: astro-ph/9807193.
- Tameda, Y. (2009). “Telescope Array Experiment”. In: *Nuclear Physics B - Proceedings Supplements* 196. Proceedings of the XV International Symposium on Very High Energy Cosmic Ray Interactions (ISVHECRI 2008), pp. 74–79. ISSN: 0920-5632. DOI: <http://dx.doi.org/10.1016/j.nuclphysbps.2009.09.011>. URL: <http://www.sciencedirect.com/science/article/pii/S0920563209006471>.
- Tanga, M. et al. (2013). “GRB 130903A: GROND afterglow discovery.” In: *GRB Coordinates Network, Circular Service, No. 15177, #1 (2013)* 15177.
- Tanvir, N. R. et al. (2017). “The Emergence of a Lanthanide-rich Kilonova Following the Merger of Two Neutron Stars”. In: *The Astrophysical Journal Letters* 848, L27, p. L27. DOI: 10.3847/2041-8213/aa90b6. arXiv: 1710.05455 [astro-ph.HE].
- Tavani, M. et al. (2009a). “Detection of Gamma-Ray Emission from the Eta-Carinae Region”. In: *The Astrophysical Journal Letters* 698, pp. L142–L146. DOI: 10.1088/0004-637X/698/2/L142. arXiv: 0904.2736 [astro-ph.HE].
- Tavani, M. et al. (2009b). “The AGILE Mission”. In: *Astronomy and Astrophysics* 502, pp. 995–1013. DOI: 10.1051/0004-6361/200810527. arXiv: 0807.4254.
- Tavani, M. et al. (2011). “Discovery of Powerful Gamma-Ray Flares from the Crab Nebula”. In: *Science* 331, p. 736. DOI: 10.1126/science.1200083. arXiv: 1101.2311 [astro-ph.HE].
- Tendulkar, S. P. et al. (2017). “The Host Galaxy and Redshift of the Repeating Fast Radio Burst FRB 121102”. In: *The Astrophysical Journal Letters* 834, L7, p. L7. DOI: 10.3847/2041-8213/834/2/L7. arXiv: 1701.01100 [astro-ph.HE].
- Tescaro, D. et al. (2013). “The MAGIC telescopes DAQ software and the on-the-fly online analysis client”. In: *ArXiv e-prints*. arXiv: 1310.1565 [astro-ph.IM].
- Thornton, D. et al. (2013). “A Population of Fast Radio Bursts at Cosmological Distances”. In: *Science* 341, pp. 53–56. DOI: 10.1126/science.1236789. arXiv: 1307.1628 [astro-ph.HE].
- Tikhonov, A. N. and V. I. Arsenin (1977). *Solutions of Ill-posed Problems*.
-

- Totani, T. et al. (2016). “High-precision analyses of Ly $\alpha$  damping wing of gamma-ray bursts in the reionization era: On the controversial results from GRB 130606A at  $z = 5.91$ ”. In: *Publications of the Astronomical Society of Japan* 68, 15, p. 15. DOI: 10.1093/pasj/psv123. arXiv: 1508.05067.
- Tsai, Y.-S. (1974). “Pair production and bremsstrahlung of charged leptons”. In: *Reviews of Modern Physics* 46, pp. 815–851. DOI: 10.1103/RevModPhys.46.815.
- Ukwatta, T. N. et al. (2013). “GRB 130606A: Swift detection of a burst.” In: *GRB Coordinates Network, Circular Service, No. 14781, #1 (2013)* 14781.
- Ukwatta, T. N. et al. (2015). “GRB 150819A: Swift detection of a burst.” In: *GRB Coordinates Network, Circular Service, No. 18163, #1 (2015)* 18163.
- Urry, C. M. and P. Padovani (1995). “Unified Schemes for Radio-Loud Active Galactic Nuclei”. In: *Publications of the Astronomical Society of the Pacific* 107, p. 803. DOI: 10.1086/133630. eprint: astro-ph/9506063.
- Usov, V. V. (1992). “Millisecond pulsars with extremely strong magnetic fields as a cosmological source of gamma-ray bursts”. In: *Nature* 357, pp. 472–474. DOI: 10.1038/357472a0.
- Valenti, S. et al. (2017). “The Discovery of the Electromagnetic Counterpart of GW170817: Kilonova AT 2017gfo/DLT17ck”. In: *The Astrophysical Journal Letters* 848, L24, p. L24. DOI: 10.3847/2041-8213/aa8edf. arXiv: 1710.05854 [astro-ph.HE].
- Varela, K., D. A. Kann, and J. Greiner (2014). “GRB 141026A: GROND observations.” In: *GRB Coordinates Network, Circular Service, No. 16953, #1 (2014)* 16953.
- Vedrenne, G. and J. Atteia (2009). *Gamma-Ray Bursts: The brightest explosions in the Universe*.
- Veitch, J. et al. (2015). “Parameter estimation for compact binaries with ground-based gravitational-wave observations using the LALInference software library”. In: *Physical Review D* 91.4, 042003, p. 042003. DOI: 10.1103/PhysRevD.91.042003. arXiv: 1409.7215 [gr-qc].
- Veres, P. and P. Mészáros (2014). “Prospects for GeV-TeV Detection of Short Gamma-Ray Bursts with Extended Emission”. In: *The Astrophysical Journal* 787, 168, p. 168. DOI: 10.1088/0004-637X/787/2/168. arXiv: 1312.0590 [astro-ph.HE].
- Vianello, G. et al. (2017). “The Bright and the Slow – GRBs 100724B & 160509A with high-energy cutoffs at  $\lesssim 100$  MeV”. In: *ArXiv e-prints*. arXiv: 1706.01481 [astro-ph.HE].
- Vietri, M. (1997). “The Afterglow of Gamma-Ray Bursts: The Cases of GRB 970228 and GRB 970508”. In: *The Astrophysical Journal* 488, pp. L105–L108. DOI: 10.1086/310931. eprint: astro-ph/9706060.
- Vietri, M. and L. Stella (1998). “A Gamma-Ray Burst Model with Small Baryon Contamination”. In: *The Astrophysical Journal* 507, pp. L45–L48. DOI: 10.1086/311674. eprint: astro-ph/9808355.
- Virgili, F. J., C. G. Mundell, and A. Melandri (2013). “GRB 130606A - Liverpool telescope optical afterglow confirmation.” In: *GRB Coordinates Network, Circular Service, No. 14785, #1 (2013)* 14785.
- Volnova, A. et al. (2013). “GRB 130903A: optical observations.” In: *GRB Coordinates Network, Circular Service, No. 15241, #1 (2013)* 15241.
- Wang, X. Y., Z. G. Dai, and T. Lu (2001). “Prompt High-Energy Gamma-Ray Emission from the Synchrotron Self-Compton Process in the Reverse Shocks of Gamma-Ray Bursts”. In: *The Astrophysical Journal Letters* 546, pp. L33–L37. DOI: 10.1086/318064. eprint: astro-ph/0010320.
- Weber, J. (1960). “Detection and Generation of Gravitational Waves”. In: *Physical Review* 117, pp. 306–313. DOI: 10.1103/PhysRev.117.306.
- Weekes, T. C. (1985). “A third generation VHE Gamma Ray Observatory”. In: *Cosmic Ray and High Energy Gamma Ray Experiments for the Space Station Era*. Ed. by W. V. Jones and J. P. Wefel, pp. 497–503.
-

- Weekes, T. C. (1996). “The Atmospheric Cherenkov Technique in Very High Energy Gamma-Ray Astronomy”. In: *Space Science Reviews* 75, pp. 1–15. DOI: 10.1007/BF00195020.
- Weekes, T. C. et al. (1989). “Observation of TeV gamma rays from the Crab nebula using the atmospheric Cerenkov imaging technique”. In: *The Astrophysical Journal* 342, pp. 379–395. DOI: 10.1086/167599.
- Weisberg, J. M. and J. H. Taylor (2005). “The Relativistic Binary Pulsar B1913+16: Thirty Years of Observations and Analysis”. In: *Binary Radio Pulsars*. Ed. by F. A. Rasio and I. H. Stairs. Vol. 328. Astronomical Society of the Pacific Conference Series, p. 25. eprint: astro-ph/0407149.
- Werner, K. (1993). “Strings, pomerons and the VENUS model of hadronic interactions at ultrarelativistic energies”. In: *Physics Reports* 232, pp. 87–299. DOI: 10.1016/0370-1573(93)90078-R.
- Wilson-Hodge, C. A. et al. (2011). “When a Standard Candle Flickers”. In: *The Astrophysical Journal Letters* 727, L40, p. L40. DOI: 10.1088/2041-8205/727/2/L40. arXiv: 1010.2679 [astro-ph.HE].
- Woosley, S. E. (1993). “Gamma-ray bursts from stellar mass accretion disks around black holes”. In: *Astrophysical Journal* 405, pp. 273–277. DOI: 10.1086/172359.
- Xu, D. et al. (2013a). “GRB 130606A: NOT afterglow detection.” In: *GRB Coordinates Network, Circular Service, No. 14783, #1 (2013)* 14783.
- Xu, D. et al. (2013b). “GRB 130606A: VLT/X-shooter redshift confirmation.” In: *GRB Coordinates Network, Circular Service, No. 14816, #1 (2013)* 14816.
- Xu, D. et al. (2013c). “GRB 130701A: VLT/X-shooter redshift.” In: *GRB Coordinates Network, Circular Service, No. 14956, #1 (2013)* 14956.
- Xu, D. et al. (2015). “GRB 151215A: NOT spectroscopy and redshift.” In: *GRB Coordinates Network, Circular Service, No. 18696, #1 (2015)* 18696.
- Yamazaki, R., K. Asano, and Y. Ohira (2016). “Electromagnetic afterglows associated with gamma-ray emission coincident with binary black hole merger event GW150914”. In: *Progress of Theoretical and Experimental Physics* 2016.5, 051E01, 051E01. DOI: 10.1093/ptep/ptw042. arXiv: 1602.05050 [astro-ph.HE].
- Yu, H.-F. (2014). “GRB 141220A: Fermi GBM observation.” In: *GRB Coordinates Network, Circular Service, No. 17205, #1 (2014)* 17205.
- Zanin, R. (2013). “MARS, the MAGIC analysis and reconstruction software”. In: *Proceedings, 33rd International Cosmic Ray Conference (ICRC2013): Rio de Janeiro, Brazil, July 2-9, 2013*.
- Zatsepin, G. T. and V. A. Kuz'min (1966). “Upper Limit of the Spectrum of Cosmic Rays”. In: *Soviet Journal of Experimental and Theoretical Physics Letters* 4, p. 78.
- Zhang, B. (2016). “Mergers of Charged Black Holes: Gravitational-wave Events, Short Gamma-Ray Bursts, and Fast Radio Bursts”. In: *The Astrophysical Journal Letters* 827, L31, p. L31. DOI: 10.3847/2041-8205/827/2/L31. arXiv: 1602.04542 [astro-ph.HE].
- Zhang, B. and P. Mészáros (2001). “High-Energy Spectral Components in Gamma-Ray Burst Afterglows”. In: *The Astrophysical Journal* 559, pp. 110–122. DOI: 10.1086/322400. eprint: astro-ph/0103229.
- Zhang, B. et al. (2006). “Physical Processes Shaping Gamma-Ray Burst X-Ray Afterglow Light Curves: Theoretical Implications from the Swift X-Ray Telescope Observations”. In: *The Astrophysical Journal* 642, pp. 354–370. DOI: 10.1086/500723. eprint: astro-ph/0508321.
- Zhang, B.-B. (2015). “GRB 150213A: Fermi GBM detection.” In: *GRB Coordinates Network, Circular Service, No. 17463, #1 (2015)* 17463.
-